Physics Area - PhD course in Theoretical Particle Physics

SISSA, Trieste

Ultrarelativistic Phase Transitions in the early Universe

The faster the better

Supervisor:
Aleksandr Azatov

Candidate:
Giulio Barni

ACADEMIC YEAR 2023/2024

When the scientist is dealing with the central problem of his field, he may become so absorbed in his work that he cannot recognise any alternatives to the current paradigm. Only when the problems of the paradigm become more and more severe and the alternative paradigms become more and more promising do the scientists begin to question the prevailing view (?)

— Thomas Khun, *The Structure of Scientific Revolutions*

Acknowledgments

I would like to begin by thanking my supervisor, Alex. I felt guided and introduced to the world of research with patience, practicality, and intellectual honesty. I am grateful for making this my first real research experience both stimulating and fulfilling.

Quisiera agradecer a Javi y a José Miguel (aka Josemi) por su confianza, su paciencia y su conocimiento. Les agradezco porque mi tiempo en Madrid ha sido importante para mí, especialmente a nivel académico, y espero en el futuro próximo poder cumplir con todas las expectativas que han depositado en mí. ¡Hasta pronto!

Vorrei ringraziare la mia famiglia per il continuo e costante sostegno durante tutti questi anni. Loro sanno quanto sia stato alto il prezzo del sacrificio per arrivare fino a qui, ma sanno anche la mia soddisfazione dopo ogni obiettivo raggiunto e la caparbietà di non fermarsi mai. Mi hanno domandato a più riprese come funzionasse la parte di Universo che stavo studiando, spero di aver risposto con pazienza e chiarezza. Li ringrazio per la loro vicinanza e stima che ho sentito e sento tutt'ora più che mai. Voglio ringraziare i miei zii e i miei cugini, per essermi stati vicini ed essersi interessati a me sempre in questi anni.

I would like to thank my collaborators and friends who have actively contributed to my research and to my positive experiences. Miguel, you have truly been my launchpad. Your drive and positivity have done me a lot of good, but above all, your patience has been fundamental to me. Time passes, but our "caffettino" that turns into a "progettino" remains. Rudin, your determination and genuine interest in physics have always fascinated me. I want to thank you for taking care of me academically, and for giving me advice and feedback on myself and my work. Simone, after defeating Taub, well, nothing can stop us! Working with you is both stimulating and a lot of fun.

I would like to thank Andrea Tesi, my former supervisor, for his help and support over the years and during my search for my first PostDoc. Your support and assistance have been invaluable. I greatly appreciate and cherish your academic advice every time we meet.

Mi sento immensamente grato all'ufficio 431, aka "I freschi di zona". Francesco, Fabiana e Saman, oltre ad essere stati compagni quotidiani di lavoro, vita, disgrazie e gioe, siete e sempre sarete casa per me. Francesco tu sei stato compagno di studi e discussioni, ci sei sempre per me, per tutti i miei dubbi e tutte le volte che ti chiedo sostegno. Prima o poi finiremo le nostre dispense di BSM. Fabiana, mi ha riempito di gioia essere prima il segretario dell'armocromia, poi consulente per imparare a dire no, ma soprattutto amico tuo. Le tue parole, la tua premura e sensibilità sono stati importanti per me. Saman, maestro di vita, di memes, di basket, ricorderò con immenso affetto i momenti passiati assieme. Grazie davvero!

Voglio ringraziare Ludo per tutta la sua vicinanza, empatia, stimolo e soprattutto amore, fiducia e trasparenza. Una volta mi hai detto che per chi ha complicità non serveno parole ne gesti, ma basta uno sguardo, e per questo motivo non dirò altro.

Voglio ringraziare Andrea, aka Solfa, ma ho questa abitudine che nel momento in cui

entro in relazione con qualcuno non posso non chiamarlo con il suo vero nome. Ti ringrazio per essere mio amico, anima gemella accademica, compagno di viaggio e poi coinquilino (e non coinqui di merda). Spero che quello che abbiamo costruito in questi ultimi 10 anni possa resistere al tempo e alla distanza. Forse non saremo mai più coinquilini, ma forse lo continueremo ad essere un po' per sempre. Grazie!

Voglio ringraziare Daniele, amico prima sul dance floor e poi nella vita. Ammiro come affronti la vita, i problemi e le difficoltà, con il tuo metterti in discussione. Grazie per il sostegno, la discussione e la premura che hai avuto nei miei confronti, sono stati per me preziosi.

Voglio ringraziare i miei compagni e colleghi di PhD con cui abbiamo vissuto a stretto contatto questi anni meravigliosi: Francesco D., Cristiano, Davide, Valentina, Andrea, Giovanni, Giuà, Vania, Mavi, Daniele, Costanza, Stephane, Cristoforo, Diego B., Diego S., Max, Alice D., Alfredo e per ultimo, ma non meno importante Samuele. Ognuno di voi, a suo modo, ha contribuito a rendere questa mia narrazione speciale. Ho condiviso parti di vita che rimarranno indelebili nei miei ricordi, grazie a tutti voi!

Voglio ringraziare altre persone in SISSA tra cui Alessandro, Guido, Francesco A., Martina, Marcin, Michele. Con voi ho condiviso serate, chiacchierate e problemi quotidiani e non. Vi ringrazio per le persone che siete e per i pensieri, valori e affetti trasmessi.

Voglio ringraziare il bar e la mensa della SISSA con le persone che ci lavorano. Patrizia, Barbara, Francesca e Deborah, voi mi avete visto in tutte le condizioni, da felice e sereno a stressato e preoccupato, tutte le volte che sono venuto a prendere un caffè, tutti i giorni più volte al giorno, e mi avete sostenuto con qualche domanda, chiacchiera o banalmente un sorriso. Vi ringrazio perché mi sono sentito sempre accolto da voi!

I would like to thank friends and colleagues around the world whom I have met thanks to the fortune of being able to travel. Angel, it was love at first sight with you; your way of being, your Spanish nature, and your thoughts brought us together immediately. We found each other all over Europe, visiting and supporting one another, discussing physics, philosophy, politics, and our lives. I am grateful for the trust and the part of your life that you have shared with me.

Francesco C., the relationship we have built is rare. We have talked a lot, sought each other out, and supported one another, for which I am thankful, especially in the last year when it was fundamental. I hope we will continue to meet around the world to climb, dance swing (even as a couple), and soon discuss physics in a project together. Thank you!

I would also like to thank (in no particular order) Martin, Macej, Francesco S., Piergiuseppe, Yusuke, Antonio J. I., Sara B., Marco M., Simone M., Giulio B., Xavier, Carlo T., Claudio T., Gabriele L., Jaime, Federico C., Andrea O., Martina C., Lorenzo, Luca, Matilda, Alexander, and Alejandro.

Voglio ringraziare Marco ed Enrico. Voi, amici di una vita, in cui non c'è stato solo supporto costante, ma condivisione sincera e profonda, siamo cresciuti in parte insieme e continueremo a farlo, anche se un po' a distanza. Vi ringrazio perché siete stati parte della mia vita e del mio percorso personale che mi ha permesso di affrontare e coltivare questa mia passione. Vi ringrazio dal più profondo del cuore.

Voglio fare un ringraziamento particolare a Gianluca, amico, padre e guida, con cui ho condiviso aspetti importanti e profondi della mia persona e della mia spiritualità. Ho sempre sentito tanta fiducia e stima da parte tua, spero di averla ricambiata almeno in parte.

E voglio ringraziare anche tutti gli altri che di questo percorso fanno parte e sono stati perle preziose: Ciccio, Alice, Chiara B., Dimitri, Noemi, Alessia, Guglielmo, Cosimo,

David, Arianna, Andrea, Gabriele, Chiara A., Silvia, Daniela, Eleonora, Serena, Lorenzo Caruso, Lorenzo Calistri, Giovanni, Beatrice, Alessio P., ma anche tutti gli altri che non fanno parte della mia comunità fra cui Martina S., Lorenzo B., Chiara M., Virginia, Alessandro, Leonardo N., Giada, Clara e tutti gli altri. Voglio anche ringraziare il gruppo di ragazzi qui a Trieste con cui ho speso e condiviso tanto tempo di qualità: Paola, Massimiliamo T., Maddalena, Marta, Giulia P., Filippo, Angelica, Giulia M., Luca, Marco, Franz, Francesco C., Michele, Chiara M., Chiara R., Giovanni, Massimiliano P., Henry e tutti gli altri.

Voglio ringraziare Sara, compagna di Swing e di chiacchierate. Condivido con te lo squardo per le cose, instancabile voglia di fare e la vitalità che esce da ogni tuo poro. Ti ringrazio per il sostegno e l'affetto ricevuto!

Voglio ringraziare Fiorella. Anche se ci siamo visti poco in questi anni, nutro per te una profonda stima e affetto. Ho sentito la tua attenzione e il tuo sguardo, anche da lontano, come se fossi una nonna per me. Questo lavoro è in parte anche tuo, e di cuore ti ringrazio.

Voglio ringraziare Marina, bibliotecaria che ha saputo trasmettermi tanto affetto e cura. Non credo mi dimenticherò mai alcune procedure (soprattutto durante il Covid) che ci hai dovuto insengare.

Vorrei ringraziare la SISSA e Trieste. Credo sia raro trovare un posto simile nel mondo. Il senso di casa e appartenenza che ho provato in questi anni sarà difficile da replicare altrove. Porterò sempre con me un po' di nostalgia per questo periodo della mia vita trascorso qui.

A tutte le persone che sopra citate (e quelle dimenticate) che hanno contribuito a plasmare la mia persona in tutti i suoi lati dico grazie! Tutto questo lavoro non sarebbe stato possibile senza di voi!

Vostro Giulio,
Lunedì 23 Settembre 2024

Abstract

Our understanding of the earliest moments of the Universe relies on General Relativity (GR) and the Standard Model (SM) of particle physics, which together allowed us to trace its history from the first minutes to the date. Gravitational waves (GWs), predicted by GR and detected for the first time in 2015, offer a unique way to probe the very early Universe, providing insights about phenomena beyond the reach of direct measurements and beyond the cosmic microwave background (CMB). Cosmological phase transitions during the evolution of the Universe are particularly significant as they can generate a stochastic background of GWs, revealing critical information about the fundamental forces of the Universe and its early dynamic processes.

This thesis presents a self-consistent study of cosmological first-order phase transitions (FOPTs) and their implications for the early Universe. We begin with an overview of the standard Hot Big Bang theory, the thermal history of the Universe, and its expansion. The basics of Quantum Field Theory at finite temperature are introduced to understand the effective potential and the dynamics of phase transitions. We particularly focus on FOPTs and the complexities of computing the velocity of the expanding bubbles. An in-depth examination is conducted on FOPTs within the Standard Model augmented with a real scalar singlet, identifying the region in parameter space where bubbles can achieve relativistic velocities, which is crucial for recently discussed baryogenesis and Dark Matter production mechanisms. We then present a more sophisticated analysis regarding the computation of the friction exerted by the plasma on the expanding bubbles. Additionally, we quantise field theories on a bubble wall background, focusing on spontaneous gauge symmetry–breaking and computing the momentum transfer from transition radiation. This will lead towards an understanding of bubble expansion during FOPTs. Furthermore, we move to analyse symmetry–restoring phase transitions and the friction exerted from the plasma to relativistic expanding bubbles demonstrating that next-to-leading order effects result in positive pressure scaling with the wall's Lorentz boost factor, as it will happen in the more vanilla symmetry–breaking case. In the final part, we take a different perspective regarding the problem and we utilise a hydrodynamic approach to characterise various expansion modes for direct and inverse phase transitions, analysing their hydrodynamics, energy budget, and the possibility of runaway walls.

This work aims at providing a sufficiently detailed framework for understanding part of the intricate dynamics of FOPTs, therefore contributing to the broader scope of understanding of the early Universe.

List of Publications

I hereby declare that, except where specific reference is made to the work of others, the contents of this thesis are original and have not been submitted in whole or in part for consideration for any other degree or qualification in this, or any other university.

The discussion is based on the following published works:

- A. Azatov, G. Barni, S. Chakraborty, M. Vanvlasselaer, W. Yin, *Ultra-relativistic bubbles from the simplest Higgs portal and their cosmological consequences*, JHEP **10** (2022) 017, [arXiv:2207.02230] [1]

- A. Azatov, G. Barni, R. Petrossian-Byrne, M. Vanvlasselaer, *Quantisation Across Bubble walls and Friction*, JHEP **05** (2024) 294, [arXiv:2310.06972] [2]

- A. Azatov, G. Barni, R. Petrossian-Byrne, *NLO friction in symmetry restoring phase transitions*, [arXiv:2405.19447] [3]

- G. Barni, S. Blasi, M.Vanvlasselaer, *The hydrodynamics of inverse phase transitions*, [arXiv:2406.01596] [4]

Contents

Chapter 0

Introduction

Our understanding of the Universe, particularly its earliest moments, is grounded in two fundamental pillars of theoretical physics: General Relativity (GR) and the Standard Model (SM) of particle physics. Einstein's theory of gravitation, among other things, enables us to comprehend one intriguing aspect of our Universe—its expansion. The SM, in turn, provided a more comprehensive understanding of pivotal events in the early Universe, such as the formation of the first nuclei during Big Bang Nucleosynthesis and the creation of the cosmic microwave background (CMB). Remarkably, GR and the SM together allowed us to reconstruct a precise history of the Universe from its first minutes to the date, spanning almost 14 billion years.

Making experimental progress and penetrating the optically thick barrier of the CMB is challenging. How can we investigate the very first moments of the existence of the Universe? Currently, we cannot perform direct measurements of those moments. However, GR predicts the existence of gravitational radiation, manifesting as tiny ripples in spacetime that propagate at the speed of light. Gravitational waves (GWs) are so weakly coupled to us that, once formed, they proceed undisturbed and constitute an important source of information if detected and traced till their origin. In 2015, the LIGO experiment made the first detection of gravitational waves originating from a binary black hole merger, making the start of a new era of astronomical and cosmological research. Astrophysical objects of interest now include massive binaries, inspirals, supernovae, and spinning neutron stars. Additionally, cosmological phenomena such as inflation and cosmological phase transitions might have generated a stochastic background of gravitational radiation. Observing such a background provides a direct probe into the very early Universe, looking back far beyond the CMB and involving energies beyond the reach of any ground-based laboratory.

This thesis focuses on the cosmological impact of phase transitions associated with the spontaneous symmetry breaking of global and local symmetries. As it is well known from thermodynamics, phase transitions can be of various types. We will mostly focus on first-order ones, that occur abruptly and proceed through the nucleation of bubbles of the new phase. These transitions move from a metastable vacuum to a stable one, with bubbles representing regions of the new phase expanding into the old phase of the Universe. After nucleation, these bubbles expand and eventually collide. This process must compete with the expansion of the Universe; if it is too slow, the bubbles never collide. The collisions generate anisotropies that act as sources of gravitational radiation. Once produced, GWs propagate undisturbed through space until they might be detected today as a redshifted stochastic background. Present and future ground-based and space-based interferometers are actively searching for such signals.

Cosmological FOPTs have the peculiar feature that the Universe spends a certain amount of time in a metastable state, known as the false vacuum. The phase ends, in most cases, when the probability per unit time and unit volume of nucleating bubbles in the expanding Universe becomes significant.

A critical open question in the study of FOPTs in the early Universe is to determine the velocity of the bubble walls as they expand. This quantity is essential for understanding the dynamics of the transition and its observational signatures, but it remains unclear how to compute it accurately. The velocity of the bubble wall is influenced by several factors, including the pressure difference between the two phases, the friction from interactions with the surrounding plasma, and the transfer of energy from the bubble wall to the surrounding medium. Accurately modelling these effects is crucial for predicting the outcomes of the phase transition, such as the characteristics of the gravitational wave signal.

In this thesis, we tackle this problem from different perspectives. We explore various theoretical approaches to compute the friction exerted on the bubble wall, which is a key factor in determining the wall velocity. One approach is to use effective field theory techniques to derive simplified models that capture the essential physics of the problem, providing a more tractable framework for analytic calculations. Another approach involves the characterisation of the microphysics of the plasma surrounding the bubble wall in terms of a fluid description, considering the interactions between the particles in the plasma and the field driving the phase transition.

With this latter approach, we also investigate the role of hydrodynamic effects in the expansion of the bubble walls. The motion of the bubble wall can induce shock waves and rarefaction waves in the surrounding plasma, which can affect the energy transfer and the friction experienced by the wall. Understanding these hydrodynamic effects is important for developing a complete picture of the bubble wall dynamics.

Furthermore, we examine the impact of different models of new physics beyond the Standard Model on the bubble wall velocity. Various extensions of the SM predict different behaviours for the phase transition, including variations in the strength of the transition and the nature of the interactions in the plasma. By studying these models, we aim at identifying common features and key differences that could help in constraining new physics from future gravitational wave observations.

This thesis is structured as follows: in chapter 1, we introduce the necessary framework for this work to be self-consistent. We start with an overview of the standard Hot Big Bang theory, detailing the thermal history of the Universe and describing its expansion as understood to date. We then introduce the basics of Quantum Field Theory (QFT) at finite temperature, essential for computing the effective potential of a given theory—a key component for quantitatively studying the dynamics of phase transitions. We discuss different types of phase transitions and the role of symmetries. We then focus on first-order phase transitions, introducing all the elements needed to describe their dynamics. The chapter concludes with the challenging task of computing the velocity of bubble expansion during a FOPT, reviewing existing approaches in the literature, and discussing their weaknesses.

The remainder of this thesis is structured into three main sections, each one exploring different facets of FOPTs. In the first part, in chapter 2, we investigate an explicit FOPT, focusing on the fine-tuning necessary to achieve ultrarelativistic expansion of the bubble wall. The second part, made of chapter 3 and chapter 4, builds on the previous results by thoroughly analysing the friction exerted by plasma particles on the wall in this high-velocity limit, both in symmetry–breaking and symmetry–restoring phase transitions.

The final part, in chapter 5, approaches the dynamics from a different angle, treating the plasma particles as a continuous fluid moving in response to the expanding bubble wall.

In more detail, in chapter 2, we study an explicit example of a FOPT in the SM augmented with a real scalar singlet. The novelty of our study is the identification and analysis of the parameter space region where a first-order phase transition can occur, particularly where bubbles of true vacuum can reach relativistic velocities. This region is interesting because it can lead to the recently discussed mechanisms for baryogenesis and Dark Matter production. We thoroughly analyse different models for Dark Matter production and baryogenesis, as well as the possible discoveries in current and future experiments.

In chapter 3, we quantise from first principles the field theories existing on the background of a bubble wall in the planar limit, focusing on spontaneous gauge symmetry breaking. Using these tools, we compute the average momentum transfer from transition radiation—the soft emission of radiation by an energetic particle passing across the wall—with a focus on the longitudinal polarisation of vectors. We find these to be comparable to transverse polarisations in symmetry-breaking transitions with mild supercooling, and dominant in broken-to-broken transitions with thin walls. Our results have phenomenological applications for bubble expansion during first-order phase transitions. Our framework allows for robust calculation of any particle processes of interest in such translation-breaking backgrounds.

In chapter 4, we analyse for the first time the friction pressure on relativistic walls in phase transitions where gauge symmetry is restored. This is particularly motivated by the observation that this pressure can, in principle, be negative at leading order as some particles lose mass crossing into the new phase. We find, however, that at next-to-leading order (NLO) the soft emission of vectors from a charged current leads to positive pressure scaling with the wall's Lorentz boost factor γ_w, similar to the case of gauge symmetry breaking. Unlike the latter case, the dominant contribution in single emission is safe from infrared divergences and exhibits a much stronger dependence on the wall shape. Finally, we argue that in any phase transition, no multi-particle process on the wall can impart negative pressure greater than the leading-order result in the asymptotic limit of large velocity.

In chapter 5, we study the hydrodynamic approach to bubble expansion to characterise all expansion modes. We review the literature on direct phase transitions (PT) and extend the study to inverse PTs. In a direct PT, a local vacuum transitions to a deeper vacuum of the zero-temperature potential, with the energy difference manifesting as bubble wall acceleration, driven by vacuum energy release. In an inverse PT, a deeper minimum transitions to a higher one of the zero temperature potential, with bubbles expanding against vacuum energy, driven purely by thermal corrections. We study, for the first time, the hydrodynamics and energy budget of inverse PTs. We find several expansion modes for inverse bubbles, related to known modes for direct transitions by mirror symmetry. We also investigate the friction on the bubble wall and discuss the possibility of runaway walls in inverse PTs.

In summary, this thesis will contribute to advancing our understanding of FOPTs in the early Universe by partially addressing the challenging problem of bubble wall velocity from multiple angles. By effective field theory approaches, semi–analytic computations, and hydrodynamic considerations, we aim to provide a comprehensive framework for predicting the dynamics of bubble walls during cosmological phase transitions. This work represents a small but hopefully significant step forward in comprehending the complex and intriguing dynamics of FOPTs, by ultimately helping us to unlock the secrets of the

early Universe and the fundamental forces that shaped its evolution.

Chapter 1

Basics of phase transitions in the early Universe

In this opening chapter, we start exploring part of the intricate dynamics of the early Universe. At the heart of our investigation lies the compelling scenario of FOPTs and their profound implications for understanding the evolution of the Universe. These transitions, occurring in the primordial plasma, could have profoundly shaped the thermal and cosmological history of the Universe.

Throughout this chapter, we will lay the groundwork by introducing concepts, tools, and notation essential for our exploration. We begin with a review of the thermal evolution of the Universe, highlighting key thermodynamic principles that govern its early stages. Moving beyond to conventional QFT and then its version at finite temperature. These foundational tools will enable us to investigate the intricate dynamics of FOPT bubbles, including their formation, expansion, and the subsequent emission of gravitational waves.

This introductory chapter sets the stage for comprehending the broader implications of FOPTs in theoretical model building and experimental observations. It serves as a concise and comprehensive guide, useful for both newcomers and seasoned researchers delving into the interplay between cosmology and high-energy physics.

The chapter is organised as follows: in section 1.1, we provide an overview of the standard cosmological and thermal history of the Universe, emphasising key thermodynamic quantities essential for understanding the processes that occur in such an environment. In section 1.2, we introduce fundamental computational tools used to quantitatively explore the early stages of the Universe. This includes computing the effective potential in quantum field theory and understanding how the surrounding thermal environment influences the fields potential. In section 1.3, we delve into the concept of phase transitions that may have occurred in the early Universe, their connection to symmetry breaking, and their impact on cosmological dynamics. We conduct a quantitative analysis to characterise first-order phase transitions, illustrated with a specific example.

Moving on to section 1.4, we examine the dynamics of nucleated bubbles, which expand while experiencing frictional forces from the plasma. We also review the production of gravitational wave signals from linearised Einstein equations, their relationship with FOPTs, and methods for computing sensitivity curves for present and future experiments. In section 1.5, we try to address the complex task of calculating bubble wall velocities, a topic still under active investigation in the literature. We review existing approaches and their limitations.

In section 1.6, we focus on the case of ultrarelativistic expanding bubbles, where computations are simplified. We discuss the current state of the art of friction computa-

tions for individual particles impacting the walls, highlighting strengths, weaknesses, and approximations used. Finally, in section 1.7, we summarise the findings presented and outline the objectives and structure of the subsequent chapters of this thesis.

Notations

Throughout this thesis, we will work in natural units and use the convention of setting

$$\hbar = c = k_B = 1 \ , \tag{1.1}$$

unless otherwise stated. When necessary for comparison with real numbers, we will temporarily restore the usual dimensions.

1.1 Cosmological setup

The standard cosmological history of the Universe provides a comprehensive framework that describes the evolution of the Universe from its earliest moments to its current state. This model, grounded in the Hot Big Bang theory, combines principles from general relativity, particle physics, and observational astronomy to offer a coherent narrative of the history of the Universe. In this section, we aim to provide a concise review of the standard cosmological framework within which the phenomena we will study occur. The discussion will follow ref. [5].

1.1.1 Expansion of the Universe

The expansion of the Universe is a fundamental concept in cosmology, first observed by Edwin Hubble in the 1920s. Through his observations of distant galaxies, Hubble discovered that galaxies are receding from us at velocities proportional to their distances. This led to the formulation of Hubble's Law, which states that the velocity of a galaxy v is directly proportional to its distance d from the observer, expressed as $v = H_0 d$. The proportionality constant, H_0, known as the Hubble constant, quantifies the rate of expansion of the Universe. The Hubble constant is crucial for understanding the scale and age of the Universe, as it provides a measure of how fast space is expanding. Current estimates of H_0 are derived from various methods, including observations of the cosmic microwave background, supernovae, and galaxy redshift surveys. The precise value of the Hubble constant remains a topic of ongoing research and debate, with implications for our understanding of cosmological parameters and the overall dynamics of the Universe.

The Universe, as we observe it, when examined at sufficiently large scales ($\sim$ Mpc), starts to exhibit the same properties regardless of the direction we look. This observation led to the formulation of the *cosmological principle*. The cosmological principle is a foundational assumption in cosmology that asserts the Universe is both isotropic and homogeneous when viewed on sufficiently large scales. Isotropy means that the Universe looks the same in all directions; there is no preferred direction in the cosmos, and the large-scale distribution of matter and radiation is uniform. Homogeneity, on the other hand, implies that the Universe has a consistent composition and structure regardless of the location within it. These principles suggest that the laws of physics are universal and that any observer, regardless of their position, would perceive a similar large-scale structure of the Universe. The cosmological principle simplifies the mathematical modelling of the Universe and underpins many of our current cosmological theories. Observations of the cosmic microwave background radiation and the large-scale distribution of galaxies provide

strong empirical support for the isotropy and homogeneity of the Universe, validating the cosmological principle as a robust framework for understanding the cosmos.

A key ingredient for understanding the expansion of the Universe and seeing the cosmological principle applied is the set of *Einstein equations.*. These equations, formulated by Albert Einstein as part of his general theory of relativity, describe how matter and energy influence, and are influenced by, the curvature of spacetime. The Einstein field equations are given by

$$G_{\mu\nu} + \Lambda g_{\mu\nu} = 8\pi G_N T_{\mu\nu} \ , \tag{1.2}$$

where $G_{\mu\nu} = R_{\mu\nu} - \frac{1}{2}\mathcal{R}g_{\mu\nu}$ is the Einstein tensor that encodes the curvature of spacetime, where $R_{\mu\nu}$ and $\mathcal{R}$ are the Ricci tensor and the Ricci scalar, respectively, Λ is the cosmological constant, $g_{\mu\nu}$ is the metric tensor describing the geometry of spacetime, G_N is the Newton gravitational constant, and $T_{\mu\nu}$ is the stress-energy tensor that represents the distribution of matter and energy. We use a mostly minus metric for flat space $(+,-,-,-)$.

Among all solutions to the Einstein equations, one that embodies the assumptions of isotropy and homogeneity is the Friedmann-Robertson-Lamaitre-Walker (FRLW) metric, which can be expressed as

$$ds^2 = dt^2 - a(t)^2 \left[\frac{dr^2}{1-kr^2} + r^2 d\Omega^2\right] \ , \tag{1.3}$$

where ds is the spacetime interval, $a(t)$ is the scale factor that describes how distances in the Universe change with time, k is the curvature parameter (with $k = 0, +1, -1$ corresponding to flat, closed, and open universes, respectively), r is the radial coordinate, and $d\Omega$ represents the angular part of the metric. If we describe the Universe as a perfect fluid, characterised by having no shear stress, no viscosity, and no heat conduction (compatible with isotropy and homogeneity), this approximation is not only suitable for its contents, including radiation and dark energy, but also simplifies the Einstein equations, allowing for tractable solutions that can describe the expansion of the Universe. The stress-energy tensor is then given by

$$T^{\mu\nu} = (\rho + p)u_\mu u_\nu - p g_{\mu\nu} \ , \tag{1.4}$$

where ρ and p are the energy and pressure density, respectively, and u_μ is the 4–velocity of the fluid. It can be shown that the energy-momentum tensor is covariantly conserved, $\nabla_\mu T^{\mu\nu} = 0$. Such conservation law leads to the continuity equation describing the evolution of the energy density in an expanding Universe that reads

$$\dot{\rho} = -3\frac{\dot{a}}{a}(\rho + p) \ . \tag{1.5}$$

Since in general $\dot{a} \neq 0$, we can clearly see that the energy is not conserved, due to the non-time translational invariance of the metric.

Substituting the FRLW metric into the Einstein equations yields the Friedmann equations, which govern the dynamics of the scale factor $a(t)$ and thus the expansion of the Universe. They read

$$\left(\frac{\dot{a}}{a}\right)^2 = \frac{8\pi G_N}{3}\rho - \frac{k}{a^2} + \frac{\Lambda}{3} \ , \tag{1.6}$$

$$\frac{\ddot{a}}{a} = -\frac{4\pi G_N}{3}(\rho + 3p) + \frac{\Lambda}{3} \ . \tag{1.7}$$

Here, $\dot{a}$ and $\ddot{a}$ are the first and second time derivatives of the scale factor. The first Friedmann equation relates the expansion rate to the energy density, curvature, and cosmological constant, indicating how the expansion speed of the Universe depends on its contents and geometry. The second Friedmann equation provides information about the acceleration or deceleration of this expansion, influenced by the energy density, pressure, and cosmological constant.

Now, we can define the Hubble factor, in terms of the scale factor,

$$H(t) = \frac{\dot{a}(t)}{a(t)} \ , \tag{1.8}$$

and specifying the matter content of the Universe, that is introducing an equation of state (EoS), where we relate the pressure with the energy density through

$$p = w\rho \ , \tag{1.9}$$

where w is the quantity defining the type of content, assumed to be a constant. Now, combining eq. (1.6) and eq. (1.7) with the previous expression we can write down the evolution of the energy density of the Universe

$$\dot{\rho} = -3H\left(\rho + p\right) = -3H\rho(1+w) \ , \tag{1.10}$$

whose solution, if w is time–independent, is just

$$\rho \propto a^{-3(1+w)} \ , \qquad a(t) \propto t^{2/3(1+w)} \ . \tag{1.11}$$

Depending on the value of w it describes different types of energy, that are:

- $w = 1/3$: this describe pure radiation, since for it the EoS reads $\rho = p/3$. The energy density of radiation scales as $\rho \propto a^{-4}$ because, in addition to the dilution effect due to expansion, the energy of each photon also redshifts (decreases) with the expansion of the Universe.

- $w = 0$: this describes non-relativistic matter (dust), where the pressure is negligible compared to the energy density, $p \approx 0$. The energy density of matter scales as $\rho \propto a^{-3}$ as the Universe expands.

- $w = -1$: for dark energy (cosmological constant), the pressure is $p = -\rho$, where $\rho \propto$ const. The energy density of the dark energy remains constant as the Universe expands, then leading to an accelerated expansion.

Other values of w are (generically) more exotics, such as $w = 1$ describes a period of kination, i.e. when the dominant component is the kinetic energy of a scalar field, or $w = -1/3$ where it describes the contribution from the curvature of the Universe, that anyway it is measured to be roughly flat, $k \approx 0$.

Therefore, the Hubble parameter $H(t)$ evolves differently depending on the dominant component of the Universe, and then it is instructive to recast eq. (1.6) in the following form

$$H^2 = \sum_i \frac{8\pi G_N}{3}\rho_i \ , \tag{1.12}$$

where we have defined

$$\rho_k = -\frac{k}{8\pi G a^2} \ , \qquad \rho_\Lambda = \frac{3\Lambda}{8\pi G a^2} \ . \tag{1.13}$$

In this way, eq. (1.6) reads

$$H^2 = H_0^2(\Omega_{0,\text{rad}}a^{-4} + \Omega_{0,m}a^{-3} + \Omega_{0,k}a^{-2} + \Omega_{0,\Lambda}a^0) \ , \tag{1.14}$$

where we have defined the ratio of the energy densities with the critical energy density

$$\Omega_{0,i} = \frac{\rho_i}{\rho_c} \ , \qquad \rho_c = \frac{3H_0^2}{8\pi G_N} \ , \tag{1.15}$$

and where the subscript '0' refers to the present epoch, having normalised $a_0 = 1$. The precise value of H_0 is still under debate, but it is measured to be roughly $H_0 \sim 70\,\text{km}\ \text{s}^{-1}\text{Mpc}^{-1}$.

The expression in eq. (1.7) tells us that an isotropic and homogeneous Universe cannot be static for standard matter, i.e. matter satisfying the so-called strong energy condition $\rho + 3p > 0$, or in other words, when neglecting curvature and the cosmological constant. Moreover, since today $\dot{a} > 0$ and $\ddot{a} < 0$, we can deduce that the Universe is expanding. If the expansion were at a constant rate, the inverse of the Hubble rate, $1/H_0$, would give us the age of the Universe.

1.1.2 Thermal history of the Universe

When the expansion rate is relatively slow compared to the characteristic time scale of subnuclear processes, that is $\Gamma_{\text{int}} \gg H$ with Γ_{int} interaction rate of such processes, and the departure from thermal equilibrium is small, then the particles involved can be accurately described by equilibrium thermodynamics. The key quantity for deriving all thermodynamic properties is the phase space distribution function $f = f(\boldsymbol{x}, \boldsymbol{k})$, defined as

$$dN = f_i(\boldsymbol{x}, \boldsymbol{k})\, d^3\boldsymbol{x} d^3\boldsymbol{k} \ , \tag{1.16}$$

where i refers to the particular species of particles and dN is the number of particles in a box of volume $d^3\boldsymbol{x}d^3\boldsymbol{k}$ in the phase space. As we said, from here we can derive the thermodynamical properties, such as the number density

$$n_i = \frac{g_i}{(2\pi)^3}\int \frac{d^3\boldsymbol{x}d^3\boldsymbol{k}}{V} f_i(\boldsymbol{x}, \boldsymbol{k}) \ , \tag{1.17}$$

where g_i are the degrees of freedom of the i particle. Alongside the number density, we can define the energy density and the pressure density

$$\rho_i = \frac{g_i}{(2\pi)^3}\int \frac{d^3\boldsymbol{x}d^3\boldsymbol{k}}{V} E_i(p) f_i(\boldsymbol{x}, \boldsymbol{k}) \ , \tag{1.18}$$

$$p_i = \frac{g_i}{(2\pi)^3}\int \frac{d^3\boldsymbol{x}d^3\boldsymbol{k}}{V} \frac{|\boldsymbol{k}|^2}{3E_i(p)} f_i(\boldsymbol{x}, \boldsymbol{k}) \ , \tag{1.19}$$

where $E_i^2 = \boldsymbol{k}^2 + m_i^2$ and where m_i is its mass. At a microscopical level, at the equilibrium, there are two different families of species described by[1]

$$f_i^{\text{eq}}(p) = \frac{1}{e^{(E_i - \mu_i)/T} \pm 1} \ , \tag{1.20}$$

[1]The functional form of f, at equilibrium, that is it depends only on p and not on $\boldsymbol{k}$ and $\boldsymbol{x}$, is a direct consequence from the assumption of a homogeneous and isotropic Universe, i.e. from the cosmological principle.

where $\mp$ refers to bosons and fermions, respectively, and μ_i is the chemical potential associated to the species i[2].

We can explicitly compute two relevant limits for the thermodynamic quantities above derived. There are two relevant scales appearing in the distribution function, that are the mass m_i and the temperature T_i of the i species, so

$$\text{non–relativistic}: \quad m_i \gg T_i \qquad \begin{cases} n_i = g_i \left(\frac{m_i T_i}{2\pi}\right)^{3/2} e^{-(m_i+\mu_i)/T_i} \ , \\ \rho_i = m_i \, n_i \ , \\ p_i = T_i \, n_i \ , \end{cases} \tag{1.21}$$

$$\text{relativistic}: \quad m_i \ll T_i \qquad \begin{cases} n_i = c_i g_i \frac{\zeta(3)}{\pi^2} T_i^3 \ , \\ \rho_i = d_i g_i \frac{\pi^2}{30} T_i^4 \ , \\ p_i = \frac{\rho_i}{3} \ , \end{cases} \tag{1.22}$$

with $c_i = 1(3/4)$ and $d_i = 1(7/8)$ for bosons (fermions). Moreover, it is convenient to define the energy density of all radiation present in the Universe at a certain temperature, considering only the relativistic species, since the non relativistic ones are exponentially suppressed, that is

$$\rho_{\rm rad} = g_\star(T) \frac{\pi^2}{30} T^4 \ , \qquad g_\star(T) = \sum_{i=B} g_i \left(\frac{T_i}{T}\right)^4 + \frac{7}{8} \sum_{j=F} \left(\frac{T_j}{T}\right)^4 \ , \tag{1.23}$$

where the sums run over all the bosons and fermions coupled to the thermal bath, where T is the temperature of the bath, and T_i is the temperature of the species i. Then, $g_\star(T)$ can be seen as the effective number of relativistic dofs that are active at a temperature T.

It is instructive to see, from eq. (1.8), that in a radiation dominated Universe the Hubble rate depends on the temperature as

$$H(T) = \sqrt{\frac{\pi^2}{90} g_\star(T)} \frac{T^2}{M_{\rm Pl}} \ , \tag{1.24}$$

where $M_{\rm Pl} = (8\pi G_N)^{-1/2} = 2.4 \times 10^{18}$ GeV is the reduced Planck mass.

As an example we compute the relativistic dofs for the SM at $T \geq 300$ GeV $\geq M_W$, where all the species are non-decoupled, *i.e.* all the $T_i = T$, then

$$\begin{aligned} g_*^{\rm SM}(T \gg M_W) = & \underbrace{2 \cdot 8}_{\text{gluons}} + \underbrace{3 \cdot 3}_{W^\pm, Z} + \underbrace{2}_{A} + \underbrace{1}_{h} + \\ & + \frac{7}{8} \left(\underbrace{4 \cdot 6 \cdot 3}_{g_q, \text{ quarks, colour}} + \underbrace{4 \cdot 3}_{g_l, \text{ leptons}} + \underbrace{2 \cdot 3}_{g_\nu, \text{ neutrinos}} \right) = 106.75 \ , \end{aligned} \tag{1.25}$$

while the value today can be computed to be $g_\star^0 \simeq 3.36$.

[2]This distribution is valid if the component is at *chemical* and *kinetic* equilibrium at temperature T. With *chemical* equilibrium we mean that if there is some particle changing interaction $i + j \leftrightarrow m + n$ we also have $\mu_i + \mu_j = \mu_m + \mu_n$. With *kinetic* equilibrium we mean that the scattering interactions in processes like $i + j \leftrightarrow i + j$ are in equilibrium, meaning that for every process that occurs, the reverse process occurs at the same rate. This equilibrium ensures that their momentum distributions are characterised by a common temperature.

Entropy in an expanding Universe

Another useful quantity, both in thermodynamics and in the evolution of the Universe, is the entropy. Neglecting the chemical potential, from thermodynamics we know that the entropy variation can be written as

$$TdS = dU + pdV = d(\rho V) + pdV = d[(\rho + p)V] - Vdp \ , \tag{1.26}$$

where ρ and p are quantities defined at equilibrium. Moreover, from the integrability conditions $\frac{\partial^2 S}{\partial T \partial V} = \frac{\partial^2 S}{\partial V \partial T}$ we find a relation between energy density and pressure

$$dp = \frac{\rho + p}{T} dT \ . \tag{1.27}$$

Then substituting above we get

$$dS = \frac{1}{T} d[(\rho + p)V] - (\rho + p)V \frac{dT}{T^2} = d\left[\frac{\rho + p}{T} V + const.\right] \ . \tag{1.28}$$

This tells us that the entropy per comoving volume is given by

$$S = a^3 \frac{(\rho + p)}{T} \ , \tag{1.29}$$

then recalling the energy conservation

$$d[(\rho + p)V] = \rho V \quad \rightarrow \quad d\left[\frac{\rho + p}{T} V\right] = 0 \ ,$$

thus, this implies that at the thermal equilibrium, the entropy per comoving volume is conserved[3].
It is useful to introduce the entropy density

$$s = \frac{S}{V} = \frac{(\rho + p)}{T} \quad \rightarrow \quad \frac{d(sa^3)}{dt} = 0 \ . \tag{1.31}$$

The entropy density is dominated by the contribution of relativistic species, i.e.

$$s = \frac{2\pi^2}{45} g_{\star,s} T^3, \qquad g_{*,s}(T) = \sum_{i=B} g_i^B \left(\frac{T_i}{T}\right)^3 + \frac{7}{8} \sum_{j=F} g_j^F \left(\frac{T_j}{T}\right)^3 \ . \tag{1.32}$$

In general, $g_\star \neq g_{\star,s}$, but what is important is to underline that the entropy is conserved for both species at equilibrium and decoupled species, separately. Now that we know the behaviour of s and n_a in terms of the scale factor $a(t)$ we can define a conserved quantity, the yield

$$Y_a = \frac{n_a}{s} \rightarrow \frac{dY_a}{dt} = 0 \ , \tag{1.33}$$

where

$$Y_a = \begin{cases} \frac{45\zeta(3) g_a}{2\pi^4 g_{*,s}} & T \gg m, \mu \ , \\ \frac{45 g_a}{4\sqrt{2}\pi^5 g_{*,s}} \left(\frac{m}{T}\right)^{\frac{3}{2}} e^{-(m-\mu)/T} & T \ll m \ , \end{cases} \tag{1.34}$$

[3]We have neglected the chemical potential since in general $|\mu| \ll T$, but we can easily generalise to the case with chemical potential

$$TdS = dU + pdV = d(\rho V) + pdV - \mu d(nV) \quad \rightarrow \quad S = a^3 \frac{(\rho + p - \mu n)}{T} \ , \tag{1.30}$$

where n is the number density of particles.

thus if the particle number of a given species a does not change in a comoving volume, Y_a is constant. Moreover, the fact that $s \sim g_{\star,s} T^3 a^3 = const.$ implies that the temperature of the Universe evolves as

$$T \sim g_{\star,s}^{-1/3} a^{-1} \ , \tag{1.35}$$

where the factor $g_{\star,s}^{-1/3}$ enters since every time a species becomes non−relativistic and it decouples from the thermal bath, it injects entropy to other relativistic particles present in the plasma.

1.1.3 Timeline of Cosmological Evolution

Understanding the history of the universe is crucial for comprehending its current state and predicting its future development. This section outlines the key eras of the evolution of the Universe, highlighting the major physical processes and transitions that have occurred since the "beginning". With the theoretical tools we have gathered, we can now describe the expected history of the universe, particularly within the first second. As we progress through the timeline, we move from the well-understood Big Bang Nucleosynthesis (BBN) to the more speculative aspects of inflation. The time and temperature intervals (expressed in energy units) for each era are provided in table 1.1 to give a detailed picture of how the universe has changed over time.

Era	**Time Interval** ($\approx$)	**Temperature Interval** ($\approx$)	**Description**
Planck Era (???)	$t < 10^{-43}$ s	$T > 10^{19}$ GeV	Quantum gravitational effects dominate.
Grand Unification Era (?)	10^{-43} s to 10^{-36} s	10^{19} GeV to 10^{16} GeV	Strong, weak, and electromagnetic forces are unified.
Inflationary Era (?)	10^{-36} s to 10^{-32} s	10^{16} GeV	Exponential expansion of the universe driven by the potential of some scalar field.
Electroweak Era	10^{-32} s to 10^{-12} s	10^{16} GeV to 100 GeV	Electroweak force separates into weak and electromagnetic forces.
Quark Era	10^{-12} s to 10^{-6} s	100 GeV to 200 MeV	Universe filled with a quark-gluon plasma.
Hadron Era	10^{-6} s to 0.1 s	200 MeV to 10 MeV	Quarks combine to form protons and neutrons.
BBN	0.1 s to 10 s	10 MeV to 100 keV	The neutrons and the protons combine in nuclei to form the light elements: D, He^3, He^4, Li^7.
Recombination	10 s to $380,000$ years	100 keV to 0.3 eV	Photons dominate. The Universe becomes transparent.
Dark Ages	$380,000$ years to 150 million years	0.3 eV to 10^{-3} eV	No stars or galaxies have formed yet.
Reionisation Era	150 million years to 1 billion years	10^{-3} eV	First stars and galaxies form.
Galaxy Formation	1 billion years to present	10^{-3} eV to 2.7 K	Galaxies form and evolve.
Current Era	Present	2.7 K (2.3×10^{-4} eV)	Dominated by dark energy, causing accelerated expansion.

Table 1.1: Timeline of Cosmological evolution.

1.2 Introduction to finite temperature QFT

The early Universe was a hot and dense environment where high-energy interactions played a significant role in the evolution of matter and energy. To properly study cosmological phase transitions, it is essential to understand the behaviour of quantum fields at finite temperatures. The early Universe was characterised by extremely high temperatures, where thermal effects significantly influenced the dynamics of fields and particles. Finite temperature quantum field theory (QFT) provides the framework necessary to describe these thermal effects and analyse phase transitions that may have occurred in the early Universe. We start by reviewing the case at zero temperature, explaining how to compute the effective potential of a QFT, and then, introducing the finite temperature effects, how it is affected by the presence of a thermal bath.

1.2.1 Basics of zero temperature QFT

In the path integral representation of a QFT [6, 7], the vacuum-to-vacuum transition amplitude for a scalar field in the presence of a source $J(x)$ is given by

$$\langle 0^+|0^-\rangle_J = \mathcal{Z}[J] = \int \mathcal{D}\phi \, \exp\left[iS[\phi] + \int d^4x \, J(x)\phi(x)\right] \, , \tag{1.36}$$

where $\mathcal{Z}$ is the generating functional of Green's functions, represented by a functional integral over configuration space and $S[\phi]$ is the action describing the theory. The generating functional of connected Green's functions $W[J]$ is related to $\mathcal{Z}$ via exponentiation

$$\mathcal{Z} = e^{iW[J]} \, . \tag{1.37}$$

Expanding W in a functional Taylor series gives

$$W[J] = \sum_n \frac{1}{n!} \int d^4x_1 \dots d^4x_n \, G^{(n)}(x_1, \dots, x_n) J(x_1) \dots J(x_n) \, , \tag{1.38}$$

where $G^{(n)}$ is a connected Feynman diagram with n external lines and the sum runs over all the connected diagrams. The effective action $\Gamma[\bar{\phi}(x)]$ is obtained from $W[J]$ via a Legendre transformation

$$\Gamma[\bar{\phi}(x)] = W[J] - \int d^4x \, J(x)\bar{\phi}(x) \, , \tag{1.39}$$

where $\bar{\phi}(x)$ is the classical field defined as

$$\bar{\phi}(x) = \frac{\delta W}{\delta J(x)} = \frac{\langle 0^+|\phi(x)|0^-\rangle_J}{\langle 0^+|0^-\rangle_J} \, . \tag{1.40}$$

From the definition (1.40), it follows that

$$\frac{\delta \Gamma}{\delta \bar{\phi}(x)} = -J(x) \, . \tag{1.41}$$

This equation is crucial in the study of spontaneous symmetry breaking (SSB), as minimising $\Gamma[\bar{\phi}]$ corresponds to finding the minima of the effective potential, which will be defined shortly. The effective action $\Gamma[\bar{\phi}]$ can be expanded similarly to W

$$\Gamma[\bar{\phi}] = \sum_n \frac{1}{n!} \int d^4x_1 \dots d^4x_n \, \Gamma^{(n)}(x_1, \dots, x_n) \bar{\phi}(x_1) \dots \bar{\phi}(x_n) \, , \tag{1.42}$$

where $\Gamma^{(n)}$ is an one-particle-irreducible (1PI) Feynman diagrams with n external lines and the sum runs over all the 1PI diagrams. The effective action can also be expanded in terms of momentum rather than powers of $\bar{\phi}$[4], yielding

$$\Gamma[\bar{\phi}] = \int d^4x \left[-V_{\text{eff}}(\bar{\phi}) + \frac{1}{2}(\partial_\mu \bar{\phi})^2 Z(\bar{\phi}) + \cdots \right] , \tag{1.43}$$

where $Z(\bar{\phi})$ is the wavefunction renormalisation factor and $V_{\text{eff}}(\bar{\phi})$ is the effective potential. For a constant classical field, this reduces to $\Gamma[\bar{\phi}] = -V_4 V_{\text{eff}}(\bar{\phi})$, where V_4 is the 4−volume containing the system.

Using the background-field method involves expanding the action around a constant configuration ϕ_b, shifting $\phi \to \phi_b + \phi$

$$e^{i\Gamma[\phi_b]} = e^{i\int d^4x \left(-\frac{1}{2}\phi_b \Box \phi_b - V[\phi_b]\right)} \int \mathcal{D}\phi \, e^{i\int d^4x \left(-\frac{1}{2}\phi\Box\phi - \frac{1}{2}\phi^2 V''(\phi_b) - \frac{1}{3!}\phi^3 V'''(\phi_b) + \cdots\right)} . \tag{1.44}$$

At one-loop order, this simplifies to

$$e^{i\Gamma[\phi_b]} = e^{i\int d^4x \left(-\frac{1}{2}\phi_b \Box \phi_b - V[\phi_b]\right)} \int \mathcal{D}\phi \, \exp\left\{ i \int d^4x \left(-\frac{1}{2}\phi\Box\phi - \frac{1}{2}\phi^2 V''(\phi_b) \right) \right\} , \tag{1.45}$$

that leads to a Gaussian integral

$$e^{i\Gamma[\phi_b]} = \text{const.} \times e^{i\int d^4x \left(-\frac{1}{2}\phi_b \Box \phi_b - V[\phi_b]\right)} \frac{1}{\sqrt{\det(\Box + V''[\phi_b])}} . \tag{1.46}$$

The effective potential $\Gamma[\phi]$ is computed by taking the logarithm

$$\Gamma[\phi] = S[\phi_b] + \Delta\Gamma[\phi_b] . \tag{1.47}$$

The one-loop effective potential in momentum space is given by

$$\Delta V_{\text{eff}}(\phi_b) = -\frac{i}{2} \int \frac{d^4p}{(2\pi)^4} \log(p^2 + V''[\phi_b]) , \tag{1.48}$$

where $\Delta\Gamma[\phi_b] = -V_4 \Delta V_{\text{eff}}(\phi_b)$.

$\overline{\text{MS}}$ renormalisation scheme

Given the divergence of the integral above, we need to renormalise the theory by fixing the value of the couplings appearing in $V''[\phi_b]$ at a specific scale μ_R, known as the renormalisation scale. Utilising dimensional regularisation with the $\overline{\text{MS}}$ scheme, for a theory with a general particle content, the effective potential is

$$V_{\text{eff}}(\phi_b) = V_0(\phi_b) + \frac{1}{64\pi^2} \sum_i (-1)^F n_i m_i^4(\phi_b) \left[\log \frac{m_i^2(\phi_b)}{\mu_R^2} - C_i \right] , \tag{1.49}$$

where n_i are the degrees of freedom for each field, coupled with ϕ, and C_i are $C_F = C_S = \frac{3}{2}$ for scalars and fermions, $C_g = \frac{5}{6}$ for gauge bosons and $F = 0(1)$ for bosons (fermions). Moreover, $m_i(\phi_b)$ are the tree-level field–dependent masses of each particle in the theory. The correction to the tree-level potential is typically referred to as Coleman-Weinberg (CW) potential [8, 9].

[4]In the Local Potential Approximation (LPA), the effective action is simplified by assuming that the dependence of the field on space-time derivatives can be neglected, focusing instead on the potential term. This means that only the local interactions of the fields are considered, while gradient terms are ignored.

On-shell renormalisation scheme

While the $\overline{\text{MS}}$ scheme is often computationally simpler due to its regularisation and renormalisation techniques, other regularisation schemes that directly connect to physical observables can sometimes simplify result interpretation and reduce calculation complexity, especially in phenomenological studies. Therefore, the on-shell renormalisation scheme is useful. The on-shell scheme directly relates renormalised parameters to physically measurable quantities, such as particle masses and physical couplings. This offers a clearer and more intuitive physical interpretation compared to the $\overline{\text{MS}}$ scheme, where we impose the renormalisation conditions:

$$\left.\frac{dV_{\text{eff}}}{d\phi}\right|_{\phi=v} = 0 \ , \tag{1.50}$$

$$\left.\frac{d^2V_{\text{eff}}}{d\phi^2}\right|_{\phi=v} = M_\phi^2 \ , \tag{1.51}$$

where v is the minimum of the tree-level potential, and M_ϕ is the physical ϕ mass. We can easily derive that the CW potential becomes

$$V_{\text{CW}} = \sum_i \frac{n_i(-1)^F}{64\pi^2}\left[M_i^4\left(\log\frac{M_i^2}{M_{i0}^2} - \frac{3}{2}\right) + 2M_i^2M_{i0}^2\right] \ . \tag{1.52}$$

In this expression, M_i represents the masses as functions of the scalar field values, $M_i \equiv M_i(\phi)$, and M_{i0} are the masses evaluated at the tree-level vacuum expectation value, $M_{i0} \equiv M_i(v)$, in the true vacuum of the theory. This setup is preferred for the study of phase transitions (PTs) since radiative corrections do not modify the tree-level position of the ground state and the masses in the true vacuum of the theory.

The above formula (1.52), is not applicable to particles that are massless in the true vacuum, such as Goldstone bosons[5], because the normalisation scale in the logarithm becomes ill-defined. We will address this issue more thoroughly in the next Chapter, in section 2.1, when discussing an explicit theory, such as the singlet extension of the Standard Model, and propose a resolution method for this problem.

1.2.2 Adding a thermal bath

At finite temperatures, the properties of quantum fields are modified by the presence of a thermal bath. The key idea in FTQFT is to incorporate temperature effects into the standard QFT by working in a modified space-time framework, [6, 10–13].

In QFT's path integral representation, the partition function $\mathcal{Z}(\beta)$ is defined as

$$\mathcal{Z}(\beta) = \text{Tr}\, e^{-\beta H} \ , \qquad \rho(\beta) = \frac{1}{\mathcal{Z}} e^{-\beta H} \ , \tag{1.53}$$

where H is the Hamiltonian of the system, and $\beta^{-1} = T$ represents the temperature. Here, $\rho(\beta)$ denotes the density matrix operator. In a statistical ensemble, ensemble averages for any observable O are defined as

$$\langle O\rangle_\beta = \text{Tr}\,\rho(\beta)O \ . \tag{1.54}$$

[5]This is also referred to as the IR catastrophe.

The cyclicity of the trace in the partition function leads to the Kubo-Martin-Schwinger (KMS) formula

$$\langle O_1(t)O_2(t')\rangle_\beta = \langle O_2(t')O_1(t+i\beta)\rangle_\beta \ . \tag{1.55}$$

This relation highlights that the partition function exhibits periodicity along the imaginary time axis with period β. After performing the Wick rotation $t \to -i\tau$ in the time direction, the partition function's periodicity is reflected in the action

$$\mathcal{Z}(\beta) = \int \mathcal{D}\phi\, e^{-S_E[\phi]} \ , \quad S_E[\phi] = \int_0^\beta d\tau \int d^3\boldsymbol{x}\, \mathcal{L}[\phi] \ , \tag{1.56}$$

where $\phi(\tau = 0, \boldsymbol{x}) = \phi(\tau = \beta, \boldsymbol{x})$ ensures periodic boundary conditions.

For a fermionic system, the partition function in the imaginary formalism introduces anti-periodic boundary conditions:

$$\psi(\beta, \boldsymbol{x}) = -\psi(0, \boldsymbol{x}) \ , \quad \bar{\psi}(\beta, \boldsymbol{x}) = -\bar{\psi}(0, \boldsymbol{x}) \ . \tag{1.57}$$

The fields' Fourier expansion in the time direction results in discrete frequencies:

$$\phi(\boldsymbol{x}, \tau) = \sum_{\omega_n = 2n\pi/\beta} e^{-i\omega_n \tau}\phi_n(\boldsymbol{x}) \quad \text{(bosons)} \ , \tag{1.58}$$

$$\psi(\boldsymbol{x}, \tau) = \sum_{\omega_n = (2n+1)\pi/\beta} e^{-i\omega_n \tau}\psi_n(\boldsymbol{x}) \quad \text{(fermions)} \ . \tag{1.59}$$

The Fourier transform of the propagator is then

$$G(\tau, \boldsymbol{x}) = \frac{1}{\beta}\sum_n e^{-i\omega_n\tau}\tilde{G}(\omega_n, \boldsymbol{x}) \ , \tag{1.60}$$

where $\omega_n = \frac{2n\pi}{\beta}$ for bosons and $\omega_n = \frac{(2n+1)\pi}{\beta}$ for fermions, are the Matsubara frequencies. Then, the propagators for bosonic and fermionic field theories in the Matsubara formalism (in momentum space) are given by

$$\tilde{G}(\omega_n, \boldsymbol{p}) = \frac{-i}{\omega_n^2 + \boldsymbol{p}^2 + m^2} \ , \quad \tilde{S}(\omega_n, \boldsymbol{p}) = \frac{-i(\not{p} + m)}{\omega_n^2 + \boldsymbol{p}^2 + m^2} \ . \tag{1.61}$$

Therefore, at finite temperature, the integration over internal energies is replaced by a sum over discrete Matsubara frequencies, leading to

$$\int \frac{d^4p}{(2\pi)^4} \quad \to \quad \frac{1}{\beta}\sum_n \int \frac{d^3p}{(2\pi)^3} \ . \tag{1.62}$$

For bosonic fields, a mode $\omega_B(n = 0) = 0$ is permitted, known as soft bosons. These soft bosons are crucial in determining the plasma properties during the phase transition, which will be elaborated further in this thesis. Modes with $n > 0$ are referred to as hard modes. Therefore, using the imaginary time formalism, we can derive the Feynman rules that incorporate finite-temperature corrections. These rules are summarised as follows:

- **Boson propagator**: $\dfrac{-i}{\omega_n^2 + \boldsymbol{p}^2 + m^2}$
- **Fermion propagator**: $\dfrac{-i(\not{p} + m)}{\omega_n^2 + \boldsymbol{p}^2 + m^2}$

- **Loop integration**: $iT \sum_{n=-\infty}^{\infty} \int \frac{d^3\boldsymbol{p}}{(2\pi)^3}$
- **Vertex factor**: $-iT\delta\left(\sum_i \omega_i\right)\delta^{(3)}\left(\sum_i p_i\right)$

With these Feynman rules, we can perturbatively compute the finite-temperature corrections to the effective potential. Then, we can easily extend the result in eq. (1.48) and get

$$\Delta V_{\text{eff}}^{\beta}(\phi_b) = \frac{1}{2\beta}\sum_n \int \frac{d^3\boldsymbol{p}}{(2\pi)^3}\log(\omega_n^2 + \boldsymbol{p}^2 + V''[\phi_b]) \ . \tag{1.63}$$

It can be shown that by summing over the Matsubara frequencies we get

$$\Delta V_{\text{eff}}^{\beta}(\phi_b) = \int \frac{d^3\boldsymbol{p}}{(2\pi)^3}\left[\frac{\omega}{2} + \frac{1}{\beta}\log(1 \pm e^{-\beta\omega})\right] \ , \tag{1.64}$$

where $\pm$ refers to bosons and fermions respectively, and $\omega^2 = \boldsymbol{p}^2 + V''[\phi_b]$. One can see that the first temperature-independent term in (1.64) corresponds to the CW potential, indeed it can be computed that

$$\int \frac{d^3\boldsymbol{p}}{(2\pi)^3}\frac{\omega}{2} = \frac{1}{2}\int \frac{d^4p}{(2\pi)^4}\log(p^2 + V''[\phi_b]) \ . \tag{1.65}$$

The second term in (1.64) is related to the thermal corrections to the potential as follows

$$\frac{1}{\beta}\int \frac{d^3\boldsymbol{p}}{(2\pi)^3}\log(1 \pm e^{-\beta\omega}) = \frac{1}{2\pi^2\beta^4}J_{B,F}[V''(\phi_b)\beta^2] \ . \tag{1.66}$$

The integral (1.66) and therefore the thermal bosonic (fermionic) effective potential admits a high-temperature expansion which will be very useful for practical applications.

It is important to highlight that in the high-temperature limit, the thermal corrections to the effective potential take the form

$$\Delta V_T \overset{T\gg m_i}{\longrightarrow} \text{const.} + \sum_{i=B,F} c_i g_i \frac{m_i^2}{24}T^2 + \dots \ , \tag{1.67}$$

where $c_i = 1(1/2)$ for bosons (fermions) and g_i are the dofs of the i-th particle. The terms proportional to T^2 in this expansion can be interpreted as thermal masses. At very high temperatures, these terms contribute significantly to the free energy density and to the curvature of the effective potential at the origin, stabilising it. In other words, the large thermal contributions cause the potential's minima to shift towards the origin (i.e., the symmetric phase), thus restoring the symmetry. This phenomenon is known as high-temperature symmetry restoration.

This approach allows for a comprehensive study of QFT at finite temperature, incorporating both statistical mechanics and field theory techniques.

1.2.3 Daisy resummation and higher order loops

Incorporating finite-temperature corrections is crucial for understanding symmetry restoration at high temperatures. However, the perturbative expansion becomes problematic in this regime due to infrared (IR) divergences caused by soft bosons. The presence of the

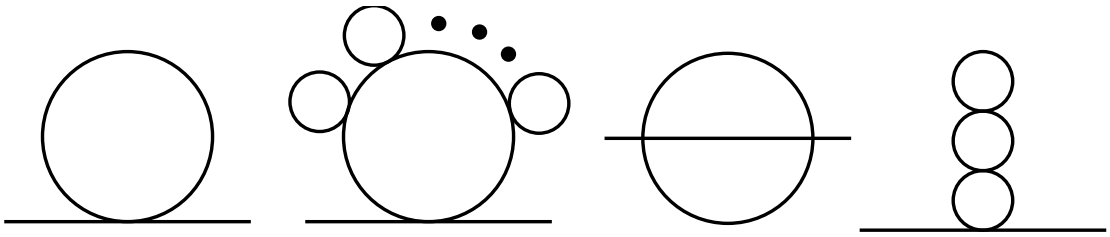

Figure 1.1: Here are shown the different higher-loops contributions to the effective potential: (from left to right) the thermal correction to the mass, the daisy diagrams, the lollipop and the superdaisy contribution.

additional scale parameter, the temperature T, disrupts the usual connection between the powers of the coupling and the loop order, leading to the breakdown of the perturbative series. To address this problem, a resummation procedure is necessary to account for all thermal effects correctly.

A systematic approach to this problem involves the resummation of "daisy diagrams". This full dressing resummation procedure has been developed in the literature, providing a consistent perturbative framework for studying phase transitions, [14].

The thermal potential, while straightforward to implement, faces IR challenges illustrated by specific diagrams as shown in fig. 1.1. The scaling behaviour of these diagrams can be analysed using finite-temperature Feynman rules. For example, a diagram with a zero-temperature superficial degree of divergence[6] $D > 0$ scales as T^D, whereas a diagram with $D \leq 0$ scales as T. This analysis confirms that the thermal mass diagram, with $D = 2$, scales as $\sim \lambda T^2$. Similar scaling behaviour can be computed for other relevant diagrams, assuming the loop connecting to the external legs is soft, or $n = 0$ in terms of Matsubara modes. Under these conditions, the scaling for various diagrams can be computed as follows:

- For daisy diagrams with n petals, the scaling is $\sim \lambda^n T^{2n-1}/m_\phi^{2n-3}$.
- For two-loop lollipop diagrams, the scaling is $\sim \lambda^2 T^2$.
- For three-loop superdaisy diagrams, the scaling is $\sim \lambda^3 T^4/m_\phi^2$.

It is important to note that the m_ϕ in the denominator only appears if the first loop contains a soft boson. Fermion loops, even with $n = 0$, include a πT in the denominator, preventing them from becoming soft.

The phase transition is driven by the interplay between tree-level masses $-m_\phi^2$ and thermal corrections λT^2. The transition occurs when these quantities are of the same order, i.e., $m_\phi^2 \sim \lambda T_{\rm PT}^2$. At the phase transition temperature $T_{\rm PT}$, we can evaluate the scaling of the diagrams:

[6] In QFT, the superficial degree of divergence D of a Feynman diagram provides a measure of how the diagram's amplitude behaves under changes in the momentum scale. It is determined by the power counting of momenta in the integrals that define the diagram. Specifically, D is given by

$$D = 4 - E_\phi(d_\phi - 1) - E_\psi\left(d_\psi - \frac{3}{2}\right) - E_A(d_A - 1)\ ,$$

where E_ϕ, E_ψ, and E_A are the numbers of external scalar, fermion, and gauge boson lines, respectively, and d_ϕ, d_ψ, and d_A are the corresponding field dimensions. The superficial degree of divergence indicates whether a diagram is convergent or divergent: if $D < 0$, the diagram is convergent; if $D \geq 0$, it is divergent. This analysis helps identify which diagrams require renormalisation and guides the development of renormalisation procedures to handle these divergences systematically.

- For daisy diagrams with n petals, the scaling becomes $\sim \lambda^{1/2} m_\phi^2$.
- For two-loop lollipop diagrams, the scaling remains $\sim \lambda m_\phi^2$.
- For three-loop superdaisy diagrams, the scaling also remains $\sim \lambda m_\phi^2$.

We observe that while two-loop lollipops and three-loop superdaisies remain under perturbative control, the daisy diagrams have the same value at each order in the perturbation expansion n. This indicates a significant breakdown of the perturbative expansion. In the following, we show how to address this problem neglecting the contribution from $2-$loop lollipop and $3-$loop super daisy diagrams.

It can be shown that resumming all the daisy diagrams one gets

$$\delta V_{\text{daisies}} = -\frac{T}{12\pi}\left(m_\phi^2 + \frac{\lambda T^2}{24}\right)^{3/2} = -\frac{T}{12\pi}\left(m_\phi^2 + \Pi(T)\right)^{3/2} \ . \tag{1.68}$$

Here, $\Pi(T) = \frac{\lambda T^2}{24}$ represents the thermal correction to the scalar field mass. Examining the thermal mass correction of the scalar field, we find that the resummation of the daisy diagrams effectively shifts the mass

$$m_\phi^2 \to m_\phi^2 + \Pi(T) \ . \tag{1.69}$$

This shift can be applied to the full thermal potential. At high temperatures, shifting m_ϕ^2 in the potential mainly adds a field-independent term, which can be ignored. Additionally, the m_ϕ^4 term contributions from the thermal potential and the zero-temperature Coleman-Weinberg potential cancel each other out, making them irrelevant. At low temperatures, this shift becomes inconsequential.

However, it's important to note that thermal corrections slow the convergence of the perturbation series. When $m_\phi \to 0$ in the above expression, the one-loop correction scales as $\lambda^{3/2}$, rather than the usual λ^2 at higher orders.

To summarise, to account for higher loops due to the Daisy diagrams at finite temperature, we can follow the so-called "Truncated-Full-Dressing" procedure [14]. Doing so, the full one-loop potential becomes

$$V_{\text{eff}}(\phi, T) = V_{\text{tree}} + \sum_i V_{\text{CW}}\left(M_i^2(\phi) + \Pi_i\right) + V_T\left(M_i^2(\phi) + \Pi_i\right) \ , \tag{1.70}$$

where Π_i are the thermal masses, dependent on the VEV ϕ and the temperature for each degree of freedom.

Despite its effectiveness, the full dressing procedure does not completely resolve all IR issues in the effective potential. Additional techniques are required to manage the IR behaviour of transverse gauge bosons, since they do not receive thermal correction perturbatively, and sensitivity to IR cutoffs. Alternative methods have been proposed to further mitigate these issues [15–20]. Although a comprehensive discussion of these methods is beyond our scope, it is important to note their relevance and the ongoing efforts to refine them.

1.2.4 Imaginary potential

As scalar masses become negative, the quantum potential develops imaginary parts at both zero and finite temperatures [21]. At zero temperature, the imaginary part of the

quantum potential is given by

$$\mathrm{Im}\, V_{1-\mathrm{loop}}^{T=0}(\phi) = \sum_i \Theta(-m_i^2(\phi)) n_i \frac{|m_i(\phi)|^4}{64\pi} \ . \tag{1.71}$$

Here, $\Theta(-m_i^2(\phi))$ is the Heaviside function, indicating when the field i is tachyonic. The Higgs boson can have a negative mass squared due to the non-convex nature of the classical potential, leading to an unstable origin or a potential barrier. Goldstone bosons can also become tachyonic, adding to the imaginary part. However, this imaginary part is cancelled by finite temperature corrections within the temperature range relevant for phase transitions.

At finite temperature, the imaginary parts arise in both the integrals and the daisy resummed contributions when scalar fields are tachyonic. The high-temperature limit of the finite temperature correction is

$$\mathrm{Im}\, V_{1-\mathrm{loop}}^{T\neq 0}(\phi, T) \approx \sum_i \Theta(-m_i^2(\phi)) n_i \left(-\frac{|m_i(\phi)|^4}{64\pi} + \frac{|m_i(\phi)|^3 T}{12\pi} \right) \ . \tag{1.72}$$

The first term cancels the zero-temperature imaginary part, while the second term is compensated by the ring diagrams' imaginary part, given by

$$\mathrm{Im}\, V_{\mathrm{daisy}}(\phi, T) = -\sum_i \Theta(-m_i^2(\phi)) n_i \frac{T|m_i(\phi)|^3}{12\pi} \ . \tag{1.73}$$

This cancellation holds as long as $m_i^2(\phi) + \Pi_i(T) > 0$ for all ϕ. However, for certain values of T and ϕ, $m_i^2(\phi) + \Pi_i(T)$ can become negative, leading to an imaginary part from the daisy resummed corrections.

The imaginary part of the potential represents a decay rate of quantum states [22]. We rely on the real part of the potential for stability during the phase transition, as the imaginary part remains small. Thus, the system's dynamics are driven by the real part of the one-loop potential, ensuring stability throughout the transition.

1.3 Phase transitions in the early Universe

Having established the essential concepts for understanding early Universe dynamics, we can now step into the cosmological PTs. The notion that the universe underwent a PT is both intriguing and significant, offering a myriad of phenomenological implications such as baryon asymmetry, dark matter, GW signals, and various cosmological relics. Phase transitions in the early Universe, particularly FOPT, are especially compelling due to their potential to produce strong GW signals through bubble collisions and the formation of topological defects. In contrast, second-order phase transitions (SOPTs), which occur without a barrier in the effective potential separating different phases, do not break thermal equilibrium and hence do not produce baryogenesis.

A key feature of QFT is its ability to exhibit different phases, even in simple settings, resulting in distinct phenomenologies depending on the phase. This is due to the necessity of expanding the theory around the minimum of the potential to make predictions, with each phase corresponding to a different minimum. The role of symmetries and their breaking is fundamental in physics, exemplified by the electroweak (EW) symmetry breaking via the Higgs mechanism, which provides mass to fermions in the Standard Model (SM). At high energies, such as those present in the primordial plasma after inflation and reheating, the fate of broken symmetries like the EW symmetry becomes crucial.

High-temperature expansions of the thermal potential suggest symmetry restoration at high temperatures, leading to the necessity of a phase transition as the universe cools.

This section explores the effective potentials characterising crossovers, SOPTs and FOPTs, equipping the reader with the necessary tools to understand the electroweak phase transition (EWPT) and other important phenomena discussed in subsequent sections. We also review the broader implications of these PTs in the early Universe, emphasising their unique properties and significant cosmological impacts.

1.3.1 Symmetry Paradigm in Phase Transitions and Their Role

Symmetry and its breaking are fundamental concepts in understanding phase transitions within the framework of QFT. Symmetry principles guide the behaviour of physical systems, dictating how fields and particles interact. In the context of cosmological phase transitions, symmetries play a crucial role in shaping the dynamics of the early Universe.

A symmetry in a physical system implies that certain transformations leave the system unchanged. For example, a rotational symmetry means that the system's properties do not change if it is rotated. In QFT, symmetries are often described by groups of transformations under which the action of the theory remains invariant. When a symmetry is spontaneously broken, the system's ground state (vacuum state) does not exhibit the symmetry of the underlying theory. This phenomenon is central to many important processes in particle physics and cosmology. The Higgs mechanism, which breaks the electroweak symmetry, is a prime example. By introducing a scalar field (the Higgs field) that acquires a non-zero vacuum expectation value (VEV), the Higgs mechanism provides mass to the gauge bosons and fermions in the Standard Model.

In the early Universe, as it cooled from the hot, dense state following the (hot) Big Bang, various symmetries that were initially unbroken could have been broken through phase transitions. These transitions are driven by changes in temperature and other environmental conditions, causing the universe to shift from one phase to another. The type of phase transition depends on the nature of the symmetry breaking:

- **Crossovers:**
  - They refer to smooth transitions between different phases of matter, where no latent heat is released and no distinct phase boundary is formed.
  - During a crossover, physical properties such as energy density and pressure change smoothly (and also all their derivatives) as the temperature varies. This means there is no abrupt change in the state of the system, but rather a continuous transformation from one phase to another.
- **Second-Order Phase Transitions:**
  - SOPTs involve a continuous change in the order parameter (e.g., the VEV of a field) without any discontinuity. It is characterised by having the second derivative of the free energy density discontinuous. There is no latent heat released, and the transition does not involve the coexistence of phases.
  - Symmetries are restored smoothly as the temperature increases. For instance, the high-temperature expansion of the effective potential typically includes a term proportional to $T^2\phi^2$, which tends to stabilise the symmetric phase ($\phi = 0$) at high temperatures.

  - During a SOPT, the effective potential's minima are connected, allowing the system to transition smoothly between phases. This type of transition does not generate significant non-equilibrium phenomena, making it less effective for processes like baryogenesis, but they can produce a significant amount of topological defects [23] resulting in a non trivial dynamics after the PT, i.e. production of a gravitational wave signal, among the other things.

- **First-Order Phase Transitions:**
  - FOPTs are characterised by a discontinuous change in the order parameter, involving a latent heat and the coexistence of different phases. This transition typically requires a barrier in the effective potential separating the symmetric and broken phases.
  - At a critical temperature, bubbles of the new phase nucleate within the old phase. These bubbles expand, collide, and eventually fill the entire universe, releasing latent heat and potentially generating GWs.
  - The presence of a barrier and the resulting bubble dynamics create conditions far from equilibrium, which are necessary for mechanisms like baryogenesis. This makes FOPTs particularly significant in cosmology, as they can lead to the production of matter-antimatter asymmetry and other cosmological relics.

The breaking of symmetries and the resulting phase transitions have profound implications for the early Universe:

- **QCD PT:** An example of a crossover in cosmology is the quark-hadron transition in QCD, which is believed to have occurred in the early Universe. At high temperatures, quarks and gluons exist in a deconfined state known as the quark-gluon plasma. As the universe cooled, these particles gradually combined to form hadrons (protons and neutrons) in a process that was not a sharp phase transition but rather a smooth crossover.

- **Electroweak Phase Transition (EWPT):** The EWPT is a crucial event in the history of the universe. If it is a first-order transition, it can provide the necessary conditions for electroweak baryogenesis, a process that could explain the observed baryon asymmetry of the universe.

- **Gravitational Waves:** FOPTs can (directly) generate a stochastic background of GWs through bubble collisions and turbulence in the primordial plasma. These GWs provide a unique probe of the early Universe, potentially observable by future detectors. GWs are be also produced in SOPTs, but their signal is much more suppressed compared to the one generated during FOPTs, but as already mentioned, topological defects originated during the PT could possibly lead to GW production, e.g. [24–27].

- **Topological Defects:** Symmetry breaking during phase transitions can lead to the formation of topological defects such as cosmic strings, domain walls, and monopoles. These defects can have significant cosmological consequences and offer insights into the symmetry structure of fundamental theories.

In summary, the paradigm of symmetry and its breaking plays a pivotal role in phase transitions, influencing the behaviour and evolution of the universe. Understanding these transitions helps us uncover the fundamental processes that shaped the cosmos, providing key insights into the underlying symmetries of nature.

1.3.2 Nucleation rates

As already stated FOPTs in the early Universe are crucial phenomena characterised by the nucleation of bubbles of a new phase within the old phase through the tunnelling between these two phases.

In QFT, tunnelling decay processes are often studied using the Euclidean path integral approach. The path integral formulation often employs the *saddle point approximation* (or the *method of steepest descent*) to evaluate integrals. The dominant contributions to the path integral come from the paths near the classical solution that extremise the action, i.e., the paths for which the first variation of the action vanishes ($\delta S_E = 0$). The bounce solution ϕ_{bounce} is a non-trivial solution to the Euclidean field equations

$$\frac{\delta S_E[\phi_{\text{bounce}}]}{\delta \phi} = 0 \ . \tag{1.74}$$

This solution corresponds to a configuration where the field tunnels through a potential barrier from a false vacuum state to a true vacuum state. For ϕ_{bounce}, the Euclidean action is at an extremum. This means that the first derivative of the action with respect to the field configuration vanishes. The second variation of the action around the bounce solution determines the nature of the extremum. For the bounce solution, the second variation (or the Hessian matrix of the action) has both positive and negative eigenvalues. This mixed signature indicates that the bounce is a saddle point rather than a local minimum or maximum. The presence of negative eigenvalues corresponds to directions in which the action decreases, signifying the instability of the false vacuum state.

The fact that the bounce solution is a saddle point means that it represents a metastable state with respect to the tunnelling process. The negative mode in the spectrum of fluctuations around the bounce solution is associated with the decay of the false vacuum through quantum tunnelling.

Then, to quantitatively describe this process, we compute the tunnelling rate, which represents the probability per unit volume and unit time that a phase transition occurs [28–31]. The tunnelling rate, Γ, is expressed as

$$\Gamma = A e^{-S_E} \ , \tag{1.75}$$

where A has the dimension of energy to the fourth power, and S_E is the Euclidean action evaluated on the solution of the Euclidean EOM. This rate encapsulates the dynamics of bubble nucleation in a scalar field theory described by the Lagrangian

$$\mathcal{L} = \frac{1}{2}(\partial_\mu \varphi)^2 - V(\varphi) \ . \tag{1.76}$$

To understand the tunnelling process, we need to study the decay of the metastable (false) vacuum. The process can be visualised as classical motion in imaginary time, where the field evolves according to the Euclidean equation of motion

$$\Box \varphi = \frac{d^2\varphi}{d\tau^2} + \nabla^2 \varphi = \frac{dV(\varphi)}{d\varphi} \equiv V'(\varphi) \ , \tag{1.77}$$

with boundary conditions

$$\varphi(\pm\infty, \boldsymbol{x}) = 0 \ , \quad \frac{d\varphi}{d\tau}(0, \boldsymbol{x}) = 0 \ . \tag{1.78}$$

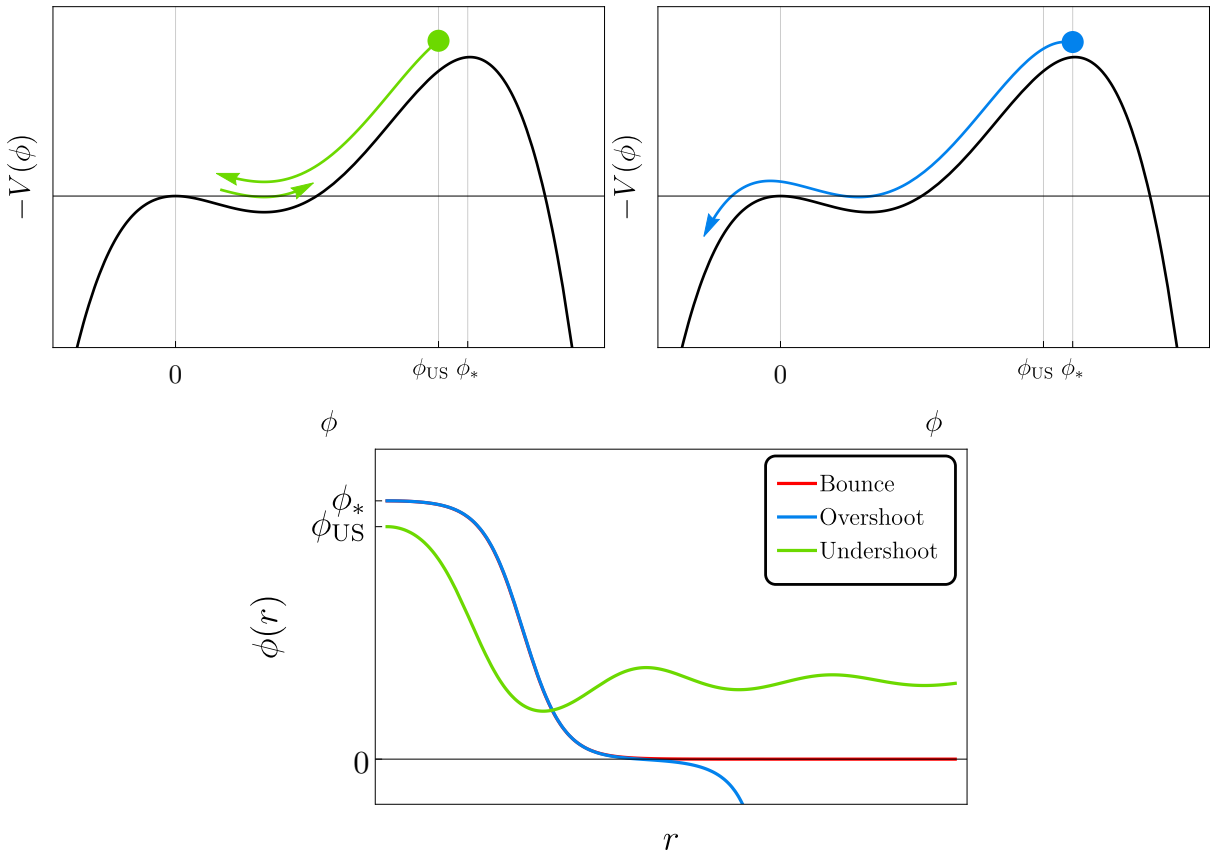

Figure 1.2: Top: sketch of the analogy with classical mechanics. Solving the problem of a particle subjected to the inverted potential $-V(\phi)$, released at rest at some point, is analogous. If the release point is to the left of ϕ_*, we end up in an undershoot configuration (left panel). If the release point is to the right of ϕ_*, we end up in an overshoot configuration (right panel). **Bottom**: The field profiles for each configuration mentioned above, where the only solution is the (red) one when the release (escape) point is exactly at ϕ_*.

The solution to this equation, known as the bounce, describes the field starting from the false vacuum, reaching near the true vacuum, and returning to the false vacuum. The Euclidean action evaluated on the bounce solution is given by

$$S_E(\varphi) = \int d\tau d^3x \left[\frac{1}{2}\left(\frac{d\varphi}{d\tau}\right)^2 + \frac{1}{2}(\nabla\varphi)^2 + V(\varphi)\right]_{\rm bounce} . \tag{1.79}$$

As Coleman showed in [28], the solution with minimal action typically exhibits spherical symmetry, $O(d)$, simplifying the equation to

$$\frac{d^2\varphi}{dr^2} + \frac{d-1}{r}\frac{d\varphi}{dr} = \frac{dV}{d\varphi} , \tag{1.80}$$

with the boundary conditions

$$\frac{d\varphi}{dr}(r=0) = 0, \quad \varphi(r=\infty) = 0 . \tag{1.81}$$

This equation has an analogy in classical mechanics, where φ is the position of a particle moving under an inverted potential $-V(\varphi)$ with a friction term. The particle must start at

the escape point and reach the origin at rest. Since the bounce equation cannot generally be solved analytically, numerical methods like the overshoot/undershoot technique are employed, as sketched in fig. 1.2. This method converts a boundary value problem into an initial value problem, iteratively adjusting the starting point to find the correct bounce solution.

Given the spherical symmetry, the bounce action simplifies to

$$S_E \equiv \frac{S_d}{T^{4-d}} = \Omega_d \int_0^\infty dr\, r^{d-1} \left[\frac{1}{2} \left(\frac{d\varphi}{dr} \right)^2 + V(\varphi) \right] , \tag{1.82}$$

where Ω_d is the solid angle in d-dimensions.

To be more clear, the total solution is a sum over all possible field configurations in the path integral. However, since tunnelling processes are exponentially suppressed by the Euclidean action S_E, the dominant contribution comes from the configuration with minimal Euclidean action. At zero temperature ($T = 0$), the system respects full Euclidean symmetry, and we typically consider the solution with $O(4)$ symmetry, which minimizes the action in four-dimensional Euclidean space.

At finite temperature ($T > 0$), time is compactified and periodic with a period $\beta = 1/T$, reducing the symmetry of the system. In this case, we should consider both $O(4)$– and $O(3)$–symmetric solutions, but generally the latter ones, which have only spatial symmetry, dominate when the thermal fluctuations become significant. Therefore, at high temperatures, the $O(3)$ bounce typically dominates the tunnelling rate.

Then, at finite temperatures, the tunnelling process requires the evaluation of both four-dimensional and three-dimensional actions

$$S_4 = 2\pi^2 \int_0^\infty dr\, r^3 \left[\frac{1}{2} \left(\frac{d\varphi}{dr} \right)^2 + V(\varphi) \right] , \tag{1.83}$$

$$\frac{S_3}{T} = \frac{4\pi}{T} \int_0^\infty dr\, r^2 \left[\frac{1}{2} \left(\frac{d\varphi}{dr} \right)^2 + V(\varphi) \right] . \tag{1.84}$$

In summary, FOPTs in the early Universe are described by the tunnelling of the scalar field through a potential barrier, a process quantified by the tunnelling rate. The bounce solution, which minimises the Euclidean action, provides a detailed understanding of the dynamics of bubble nucleation.

Explicit example To illustrate the concepts of a FOPT, we consider a specific potential where thermal corrections introduce a term proportional to φ^3. This potential is expressed as:

$$V(\varphi, T) = \frac{M^2}{2}\varphi^2 - \frac{A(T)}{3}\varphi^3 + \frac{\lambda}{4}\varphi^4 , \tag{1.85}$$

and shown in (left panel of) fig. 1.3.

Here, $M^2 \equiv M^2(T) = c(T^2 - T_0^2)$ with $c > 0$, $A(T) \propto T > 0$, and $\lambda > 0$ for stability at zero temperature. At low temperatures where $A(T)$ is negligible, the phase transition is second order since the quartic term dominates. However, at higher temperatures, the φ^3 term creates a thermal barrier, potentially leading to a FOPT.

The potential's extrema are

$$\varphi_{\min} = \left\{ 0, \varphi_* \equiv \frac{A}{2\lambda} \left(1 + \sqrt{1 - \frac{4M^2\lambda}{A^2}} \right) \right\} , \quad \varphi_{\max} = \frac{A}{2\lambda} \left(1 - \sqrt{1 - \frac{4M^2\lambda}{A^2}} \right) . \tag{1.86}$$

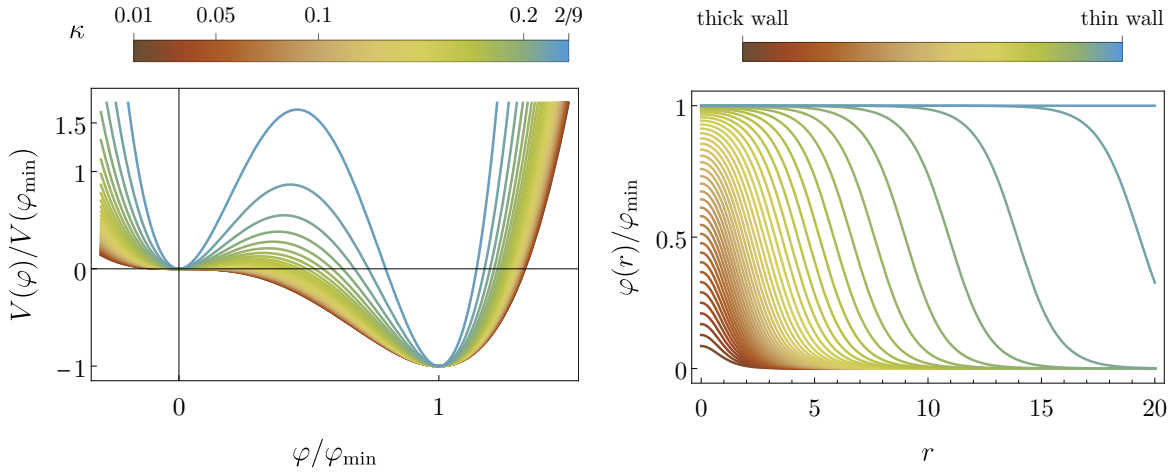

Figure 1.3: Left: toy (rescaled) potential, properly normalised, for studying the main features of a FOPT, as a function of the parameter κ. It is worth noting that the limit $\kappa \to 2/9$ corresponds to a barrier of infinite height, resulting in the system being stuck in the false vacuum, or in other words, the system has a temperature above the critical one. **Right**: bounce profiles as a function of κ. For $\kappa \to 0$, the barrier becomes smaller and smaller, resulting in a thick wall configuration, while in the other limit, the bubble wall becomes thinner and thinner.

The critical temperature T_c is when the potential has two degenerate minima, defined by

$$\frac{\lambda M^2}{A^2} = \frac{2}{9} \,. \tag{1.87}$$

For $T_0 < T < T_c$, the potential has a first-order transition if tunnelling occurs before the temperature drops to T_0. A FOPT is characterised by a discontinuous change in the VEV of φ, leading to a singularity in the first derivative of the free energy. The latent heat, or the difference in free energy between the two minima, is $\Delta V = V(0) - V(\varphi_*) \geq 0$. We define $\kappa \equiv \lambda M^2/A^2$, making the critical condition $\kappa \leq 2/9$. The tunnelling action must be calculated to determine if the transition happens. The nucleation temperature lies between T_c and T_0 when the potential has a thermal barrier. By rescaling the variables

$$r = \frac{\xi}{\mu} \,, \quad \varphi = \frac{M^2}{A}\phi \,, \tag{1.88}$$

the actions in four and three dimensions are

$$S_4 = 2\pi^2 \frac{M^2}{A^2} I_4(\kappa) \,, \qquad \frac{S_3}{T} = 4\pi \frac{M^3}{TA^2} I_3(\kappa) \,, \tag{1.89}$$

where

$$I_d(\kappa) \equiv \int_0^\infty d\xi \, \xi^{d-1} \left[\frac{1}{2} \left(\frac{d\phi}{d\xi} \right)^2 + \frac{\phi^2}{2} - \frac{\phi^3}{3} + \frac{\kappa\phi^4}{4} \right] \,. \tag{1.90}$$

These integrals must be evaluated on the bounce solution of (1.80) where the field profiles solving the Euclidean EOM, as a function of the parameter κ, have been reported in the right panel of fig. 1.3. The potential in terms of rescaled variables is then

$$\hat{V}(\phi) = \frac{\phi^2}{2} - \frac{\phi^3}{3} + \frac{\kappa\phi^4}{4} \,, \tag{1.91}$$

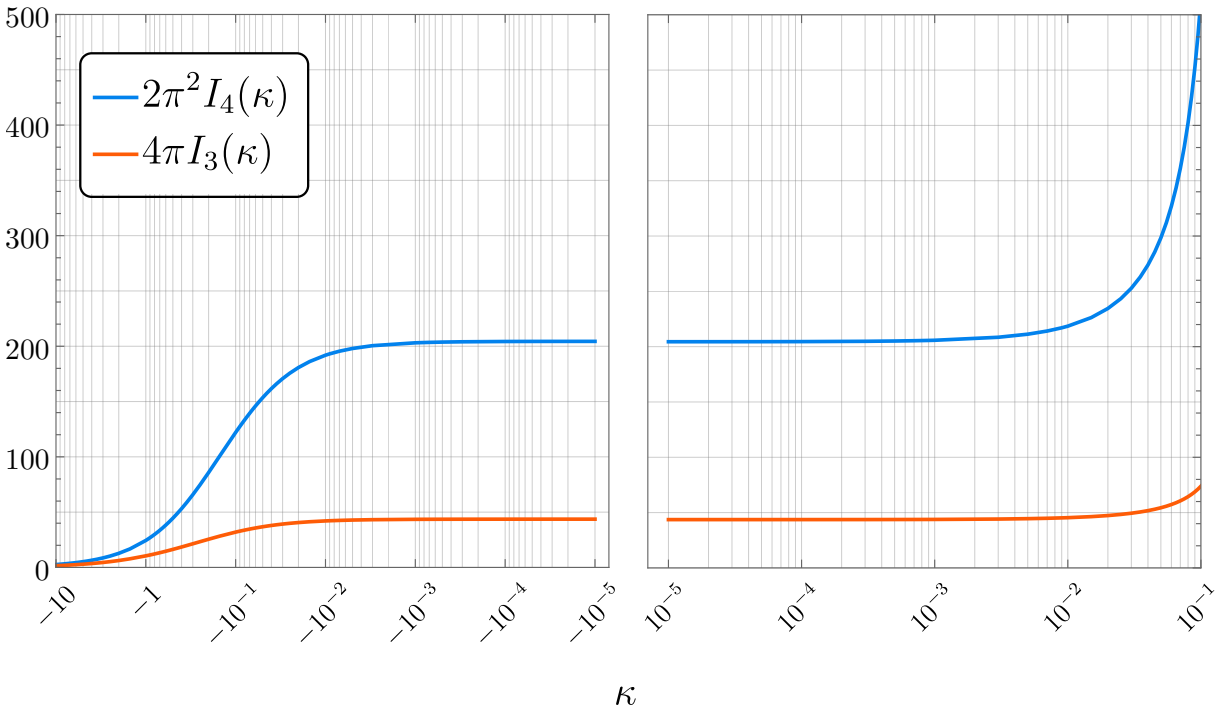

Figure 1.4: Here, we report the dimensionless integrals $I_{3,4}(\kappa)$ as in (1.90). It is evident that in the limit $\kappa \to 2/9$, these integrals diverge. The limit $\kappa \to 0$, both from above and from below, corresponds to thick wall configurations.

with a false vacuum at the origin if $\kappa < 2/9$. For $\kappa = 2/9$, the potential develops two degenerate minima, causing $I_{3,4}$ to diverge. When $\kappa \to 0$, it transitions into a thick-wall configuration as the quartic term becomes negligible. Numerical solutions, as in fig. 1.4, yield $I_3(0) \approx 3.47$ and $I_4(0) \approx 10.36$. In the figure has also been reported the case with $\kappa < 0$. Here, even if the potential is not bounded from below, we can in principle compute the tunnelling decay rate of the system, as computed in [32].

This example clearly demonstrates how thermal corrections can induce a FOPT, highlighting the critical concepts and calculations involved.

1.3.3 Parameters of the PT

A FOPT can be quantitatively described by several key parameters. These parameters provide insights into the dynamics and physical consequences of the transition. Below, we introduce and define these parameters [33, 34].

After having defined the nucleation rate as in (1.75), we can define the nucleation temperature, T_n, as the temperature at which the phase transition effectively begins. It is defined as the temperature at which the probability of nucleating a critical bubble of the new phase within a Hubble volume per Hubble time becomes order one. Mathematically, this condition is expressed as

$$\int_{T_c}^{T_n} \frac{dT}{T} \frac{\Gamma}{H^4} = 1 \ , \tag{1.92}$$

where H is the Hubble parameter. By considering the exponential growth of the tunnelling rate [29], $\Gamma \sim T^4 \left(\frac{S_E}{2\pi}\right)^{d/2} e^{-S_E}$, for the relevant temperatures one can approximate the

nucleation condition by

$$\frac{\Gamma(T_n)}{H(T_n)^4} = 1 \quad \rightarrow \quad \frac{S_d}{T_n^{4-d}} - \frac{d}{2}\ln\left(\frac{S_d}{2\pi T_n^{4-d}}\right) = 4\ln\frac{T_n}{H(T_n)} \ , \tag{1.93}$$

where we used that $S_E = S_d/T^{4-d}$. Assuming radiation domination and neglecting the first logarithm in the LHS of the previous expression we can roughly estimate the value of the bounce action for a temperature $T \sim$TeV

$$S_E \simeq 4\ln\left(\frac{M_{\rm Pl}}{T_n}\right) \approx 140 \ . \tag{1.94}$$

Now, the probability $P(T)$ of a specific point in the Universe remaining in the false vacuum at temperature T can be derived by considering the nucleation and growth of bubbles of the true vacuum [35]. When a bubble nucleates, it expands spherically with a volume $V = \frac{4\pi}{3}R^3$. The comoving volume affected by a bubble nucleated at temperature T' expands as the Universe expands, proportional to $\frac{1}{H(T')^3}$, where $H(T')$ is the Hubble parameter. The number of bubbles nucleated per unit comoving volume, between a time t and a time $t + dt$, is then given by

$$dN = \Gamma(t)V(t)\,dt = \Gamma\cdot\frac{4\pi}{3}\frac{v_w^3}{H(T')^3}\left|\frac{dt}{dT'}\right|dT' = \Gamma(T')\frac{dT'}{T'}\frac{1}{H(T')^4} \ , \tag{1.95}$$

where we have used that

$$\frac{dT}{dt} = -H(T)T \ . \tag{1.96}$$

The volume fraction of the false vacuum decays exponentially because the nucleation events are Poisson distributed[7] in space and time. Therefore, the probability $P(T)$ can be written as an exponential of the integral of the nucleation rate. Integrating this from T to the critical temperature T_c gives the exponential suppression factor

$$P(T) = \exp\left(-\int_T^{T_c} dN(T')\right) = \exp\left(-\frac{4\pi}{3}v_w^3\int_T^{T_c}\frac{\Gamma(T')}{H(T')^4}\frac{dT'}{T'}\right) \ . \tag{1.98}$$

Therefore, the probability, $P(T)$, of a specific point in the Universe remaining in the false vacuum at temperature T is given by

$$P(T) = \exp\left[-I(T)\right] \ , \qquad I(T) = -\frac{4\pi}{3}v_w^3\int_T^{T_c}\frac{\Gamma(T')}{H(T')^4}\frac{dT'}{T'} \ . \tag{1.99}$$

[7] The bubble nucleation rate depends on the temperature but can be considered locally constant within a small enough time or temperature interval. In each such interval, the nucleation events occur with a constant average rate. Each bubble nucleation event is independent of other nucleation events. This independence arises because the nucleation of a bubble in one region does not directly influence the nucleation of bubbles in distant regions of the Universe, especially in the early stages of nucleation before bubbles start to grow and overlap significantly. For a Poisson process, the probability $P(n;\lambda)$ of observing n events in a given interval is given by:

$$P(n;\lambda) = \frac{\lambda e^{-\lambda}}{n!} \ , \tag{1.97}$$

where λ is the average number of events in the interval. Consider a small volume element V in the Universe and a small time interval Δt, then the expected number of bubble nucleation events in this volume and time interval is $\lambda = \Gamma(T)V\Delta t$. The probability of no bubble nucleation events occurring in the volume V during the time interval Δt, i.e. the probability of a specific point in the Universe remaining in the false vacuum, is $P(0;\lambda)$.

This probability decreases as the Universe cools and more regions transition to the true vacuum. The percolation temperature, T_p, is the temperature at which bubbles of the new phase have expanded sufficiently to overlap and fill a significant fraction of the Universe. It is defined by the condition

$$P(T_p) \approx 0.71 \ , \qquad I(T_p) \approx 0.34 \ . \tag{1.100}$$

This refers to the fraction of space filled by randomly distributed, equal-sized spheres (including overlaps) in three-dimensional Euclidean space, marking the onset of percolation. It indicates that at least 34% of the comoving volume must have transitioned to the true vacuum state for percolation to occur.

In a vacuum-dominated scenario, as reported in [36], the simple percolation criterion can be misleading. While the probability of being in the false vacuum, $P(t)$, decreases over time and may reach the desired value, percolation might never occur due to the continued inflation of the false vacuum. This issue arises because, despite the reduction in $P(t)$, the physical volume of the false vacuum, $V_{\rm false} \propto a(t)^3 P(t)$, may continue to grow as space expands. For the phase transition to successfully complete, it is not enough for $P(t)$ to decrease; the physical volume of the false vacuum must also shrink after or around percolation.

This sets a stringent condition: $P(t)$ must decrease faster than the rate of expansion of space in the vacuum-dominated phase. Specifically, the condition for the successful completion of the phase transition is that the rate of change of the false vacuum volume must satisfy

$$\frac{1}{V_{\rm false}}\frac{dV_{\rm false}}{dt} = 3H(t) - \frac{dI(t)}{dt} = H(T)\left(3 + T\frac{dI(T)}{dT}\right) < 0 \, . \tag{1.101}$$

This implies that the decrease in $P(t)$ must outpace the growth in the physical volume due to inflation.

The strength of the phase transition, denoted by α, quantifies the latent heat released during the transition relative to the radiation energy density. It is defined as[8]

$$\alpha = \frac{\varepsilon}{\rho_{\rm rad}} = \frac{\Delta V - T\frac{d\Delta V(\phi)}{dT}}{\rho_{\rm rad}} \approx \frac{\Delta V}{\rho_{\rm rad}} \ , \tag{1.105}$$

where ΔV is the difference in energy density between the false and true vacua, and $\rho_{\rm rad}$ is the radiation energy density at the transition temperature. This parameter, which

[8]There is an intuitive and physical way to understand this definition. Starting from basic thermodynamics, from the definition of the internal energy of a system $U = TS - pV$ and dividing by the volume we get

$$u = Ts - p \ , \tag{1.102}$$

where now we have that u is the internal energy density, s the entropy density and p the pressure. At the transition, the change in internal energy is the latent heat, ε, while

$$\Delta p = -\Delta V(\phi) = -(V(\phi_{TV}) - V(\phi_{FV}) \ , \qquad \Delta s \equiv -\frac{d\Delta\mathcal{F}}{dT} = -\frac{d\Delta V(\phi)}{dT} \ , \tag{1.103}$$

so that we get

$$\varepsilon = \Delta V - T\frac{d\Delta V(\phi)}{dT} \ . \tag{1.104}$$

must be computed at the percolation temperature, plays a significant role in determining the energy budget of the phase transition. The α parameter, defined as the latent heat liberated during the transition divided by the radiation energy density of the universe, is influenced by the extent of supercooling. As the temperature drops below the critical point, the energy difference between the true and false vacua, ΔV, remains relatively stable. In contrast, the radiation energy density, $\rho_{\rm rad} \propto T^4$, decreases rapidly due to the expansion of the universe. As a result, $\alpha \propto 1/T^4$, implying that more significant supercooling leads to a higher α, which indicates a larger energy budget for the transition.

Another important parameter is the inverse duration of the phase transition, β/H, which characterises how rapidly the transition proceeds. It is defined as

$$\frac{\beta}{H} = T\frac{d(S_E/T)}{dT} \ . \tag{1.106}$$

A larger β/H implies a faster transition, which affects the resulting GW signals and the formation of other cosmological relics. It is generically computed at the nucleation temperature, since in all realistic cases the percolation temperature is almost always equal to the nucleation one. If this is not true, as we will see in chapter 2, the inverse duration of the PT can be estimated to be

$$\left.\frac{\beta}{H}\right|_{T_p} \approx \frac{(8\pi)^{1/3}v_w}{H(T_p)R_\star} \ , \qquad R_\star = \left(\int_{T_p}^{T_c} \frac{dT}{T}\,\frac{\Gamma(T)}{H(T)}\left(\frac{T_p}{T}\right)^3\right)^{1/3} \ . \tag{1.107}$$

Together, these parameters provide a comprehensive description of a FOPT, capturing the dynamics, timescales, and physical implications of the transition.

The temperature at the end of the phase transition, called reheating temperature ($T_{\rm reh}$), critically influences the redshift of the GW signal. Assuming the transition completes within a time frame shorter than the Hubble time, we can apply conservation of energy arguments to estimate the reheating temperature $T_{\rm reh}$

$$(1-\Omega_{\rm GW})(\Delta V + \rho_{\rm rad}\Big|_{T=T_p}) = \rho_{\rm rad}\Big|_{T=T_{\rm reh}} \ , \quad \longrightarrow \quad T_{\rm reh} \approx (1+\alpha)^{1/4}T_p \ , \tag{1.108}$$

where $\Omega_{\rm GW}$ represents the fraction of the critical energy density in gravitational waves. In the second step, we assumed the energy lost in GW signal to be negligible. Then, gravitational waves generated during the phase transition redshift as the universe expands, lowering their observed frequency today. The reheating temperature $T_{\rm reh}$ signifies the temperature at which the universe is reheated after the phase transition, affecting subsequent cosmological evolution and the relic abundance of particles. In the context of cosmological models, $T_{\rm reh}$, plays a crucial role in scenarios involving baryogenesis, dark matter production, and the thermal history of the Universe.

1.4 Bubble dynamics - expansion of the bubble and GW signal

After introducing the essential tools to define bubble properties during a FOPT and their nucleation, we now turn to their evolution and expansion within the primordial thermal plasma. We will begin by reviewing the evidence for bubble expansion and identifying the final expansion regimes. As bubbles collide, they generate a stochastic background of GWs. We will explore how the linearised Einstein equations describe GW propagation and production, and review the contributions to the overall GW signal expected from bubble collisions, sound wave generation, and turbulence. Finally, we will discuss the prospects of detecting these signals with future space-based and ground-based interferometers.

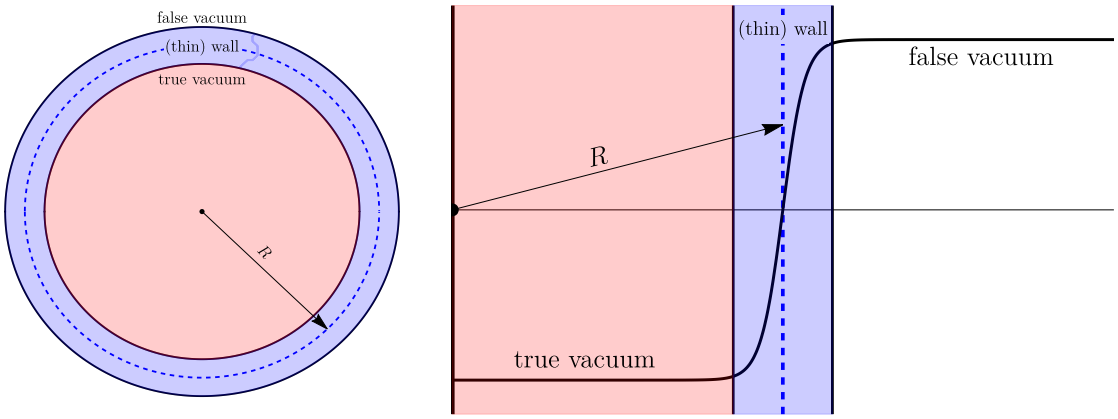

Figure 1.5: General structure of a (thin) bubble configuration. Inside the bubble (red shaded region) the system is in the true vacuum, $\langle\phi\rangle \neq 0$, while outside the bubble, $r \gtrsim R$, in the false vacuum, $\langle\phi\rangle = 0$. The thickness of the wall is defined as the transient region for which $\phi'(r) \neq 0$.

1.4.1 Bubble expansion

Once bubbles are nucleated in a FOPT, their dynamics play a crucial role in the completion of the transition. Understanding how these bubbles evolve involves considering their formation in Euclidean space and then translating these dynamics to Minkowski spacetime. This section details the nucleation process, the critical radius, and distinguishes between $O(4)$ symmetric bubbles in vacuum and $O(3)$ symmetric bubbles in a thermal primordial plasma.

In the context of QFT, bubble nucleation is initially studied in Euclidean space, where time is treated as an imaginary quantity. The nucleation process involves the creation of a bubble of true vacuum within the false vacuum. The bounce solution has $O(4)$ symmetry in vacuum, meaning it is spherically symmetric in four-dimensional Euclidean space. After performing a Wick rotation to Minkowski spacetime, the $O(4)$ symmetry becomes a hyperbolic symmetry in three spatial dimensions and one time dimension. This can be easily seen by looking at the profile solution of the scalar field $\phi \equiv \phi(r)$ where $r = \sqrt{\tau^2 + \boldsymbol{x}^2}$ is the Euclidean radius. At first glance, we can treat the bubble wall as thin, i.e. we can approximate the transition of $\phi(r)$ from $\phi(r = 0) = \phi_*$ to $\phi(r = \infty) = 0$ as happening instantaneously at $r = R$

$$\phi(r) = \begin{cases} \phi_* & \text{for } r \lesssim R \ , \\ 0 & \text{for } r \gtrsim R \ , \end{cases} \tag{1.109}$$

as one can see from the sketch in fig. 1.5. When we rotate back to Minkowski and this radius is written in terms of the Minkowski time we have

$$\phi(r) = \phi\left(\sqrt{t^2 - \boldsymbol{x}^2}\right) \ , \tag{1.110}$$

and we can clearly figure out the interpretation: the solution $\phi(r)$ describes the nucleation of a bubble of true vacuum of radius R. The interpretation in terms of bubbles is possible thanks to the spherical symmetry of the least action solution. This can be seen as the formation of a bubble with value ϕ_*, with the surface located at $R = \sqrt{x^2_{\text{surface}} - t^2}$ in real space. In the vacuum, the surface then expands, reaching asymptotically the speed of light

$$x_{\text{surface}} = \sqrt{R^2 + t^2} \quad \to \quad \lim_{t\to\infty} \frac{dx_{\text{surface}}}{dt} = 1 \ . \tag{1.111}$$

Outside of the bubble, $|\boldsymbol{x}| \gtrsim |x_{\text{surface}}|$, there is still the false vacuum; inside, there is the true one.

In a thermal context, where the phase transition occurs in a hot, early Universe plasma, the system is studied in three spatial dimensions with time periodically identified with period $1/T$. This periodicity breaks the $O(4)$ symmetry to $O(3)$, resulting in bubbles that are spherically symmetric in three-dimensional space. Since time has been compactified, the solutions are stationary. Therefore, for the $O(3)$ symmetric solution, upon rotating back to Minkowski spacetime, we observe that a bubble with exactly the critical radius will not expand. It is generally believed [37] that thermal fluctuations will slightly deform the radius $R_c \to R_c + \delta$, causing the expansion to begin.

Critical radius The concept of a critical radius is pivotal in understanding the dynamics of nucleated bubbles. The critical radius, R_c, is the radius at which a bubble is energetically favourable to grow rather than shrink. This balance is determined by the competition between volume energy and surface tension.

- **Volume Energy:** The volume energy difference between the false vacuum (high energy state) and the true vacuum (low energy state) provides a driving force for the bubble to expand. The energy gain per unit volume is ΔV, the difference in potential energy between the two vacua.

- **Surface Tension:** The bubble wall has a surface tension σ, which represents the energy cost of creating the interface between the true and false vacua. The energy cost per unit area is proportional to

$$\sigma = \int_0^\infty dr \left[\frac{1}{2}\left(\frac{d\phi}{dr}\right)^2 + V(\phi, T)\right] = \int_0^{\phi_\star} d\phi \, \sqrt{2V(\phi, T)} \, , \tag{1.112}$$

  where $\phi_\star$ is the escape point.

The total energy $E(R)$ of a bubble of radius R is given by the sum of the volume energy and the surface energy

$$E(R) = -\frac{4\pi}{3} R^3 \Delta V + 4\pi R^2 \sigma \, . \tag{1.113}$$

To find the critical radius, we set the derivative of $E(R)$ with respect to R to zero

$$\frac{dE(R)}{dR} = -4\pi R^2 \Delta V + 8\pi R \sigma = 0 \, . \tag{1.114}$$

Solving for R, we get the critical radius

$$R_c = \frac{2\sigma}{\Delta V} \, . \tag{1.115}$$

A bubble with $R < R_c$ will shrink and disappear, while a bubble with $R > R_c$ will grow, converting the false vacuum into the true vacuum.

Driving Force of Bubble Expansion Once a bubble of true vacuum nucleates, the expansion is driven by the pressure difference between the true vacuum inside the bubble and the false vacuum outside. This pressure difference acts as the driving force pushing the bubble walls outward.

The effective equation for bubble expansion in thermal equilibrium can be derived from an effective Lagrangian[9]

$$L = -4\pi\sigma R^2\sqrt{1-\dot{R}^2} + \frac{4}{3}\pi R^3 \Delta p_{\rm dr} \ . \tag{1.119}$$

Here, $\Delta p_{\rm dr}$ represents the change in driving pressure, defined as $\Delta p_{\rm dr} = \Delta V_{\rm eff}$. The Euler-Lagrange equation derived from this is

$$\ddot{R} + \frac{2}{R}(1-\dot{R}^2) = \frac{\Delta p_{\rm dr}}{\sigma}(1-\dot{R}^2)^{3/2} \ . \tag{1.120}$$

Expressed in terms of the Lorentz factor $\gamma = 1/\sqrt{1-\dot{R}^2}$, this becomes

$$\frac{d\gamma}{dR} = \frac{\Delta p_{\rm dr}}{\sigma} - \frac{2\gamma}{R} \ . \tag{1.121}$$

Solving this, we get

$$\gamma(R) = \frac{\Delta p_{\rm dr}}{3\sigma}R + \frac{C}{R} \ , \tag{1.122}$$

with the constant C determined by the initial condition $\gamma(R_0) = 1$. The initial static bubble radius $R_0 = R_c$ has been defined in (1.115). Simplifying the solution for $\gamma(R)$ and normalising with respect to R_0 we get

$$\gamma(R) = \frac{2}{3}R + \frac{1}{3R^2} \ . \tag{1.123}$$

This indicates that the bubble velocity

$$\dot{R}(t) = \sqrt{1 - \frac{9R^4}{(1+2R^3)^2}} \ , \tag{1.124}$$

rapidly approaches the speed of light after nucleation if $\Delta p_{\rm dr} > 0$. Although this effective equation can also describe bubble expansion in a vacuum by substituting the driving

[9] In order to derive this effective Lagrangian, following [38, 39], we introduce the radial variable $\rho^2 = x^2 + y^2 + z^2$ and in the action with Lagrangian in (1.76), we split the contribution inside the wall and outside of it assuming that all the gradients far from the wall vanish, then

$$S[\phi] = \int d^4x \left[\frac{1}{2}(\partial\phi)^2 - V(\phi)\right] \tag{1.116}$$

$$= 4\pi \int_{\rm wall} dt d\rho\, \rho^2 \left[\frac{1}{2}\left(\dot{\phi}^2 - (\partial_\rho\phi)^2\right) - V(\phi)\right] - \frac{4\pi}{3}R^3 \int dt \Delta V \ . \tag{1.117}$$

Now change the basis from $(\hat{t}, \hat{\rho})$ to $(\hat{\boldsymbol{e}}_\perp, \hat{\boldsymbol{e}}_{||})$ defined by

$$\hat{\boldsymbol{e}}_\perp = \frac{1}{\sqrt{1-\dot{R}^2}}(-\dot{R}\hat{t} + \hat{\rho}) \ , \qquad \hat{\boldsymbol{e}}_{||} = \frac{1}{\sqrt{1-\dot{R}^2}}(\hat{t} + \dot{R}\hat{\rho}) \ . \tag{1.118}$$

Integrating over ϕ the EOM, neglecting friction terms, and assuming the thin wall limit we arrive at the relation $2V(\phi) = (\partial_\perp\phi)^2$. Plugging this in the action above and performing the integral, with the definition of sigma as in (1.112), we arrive at (1.119).

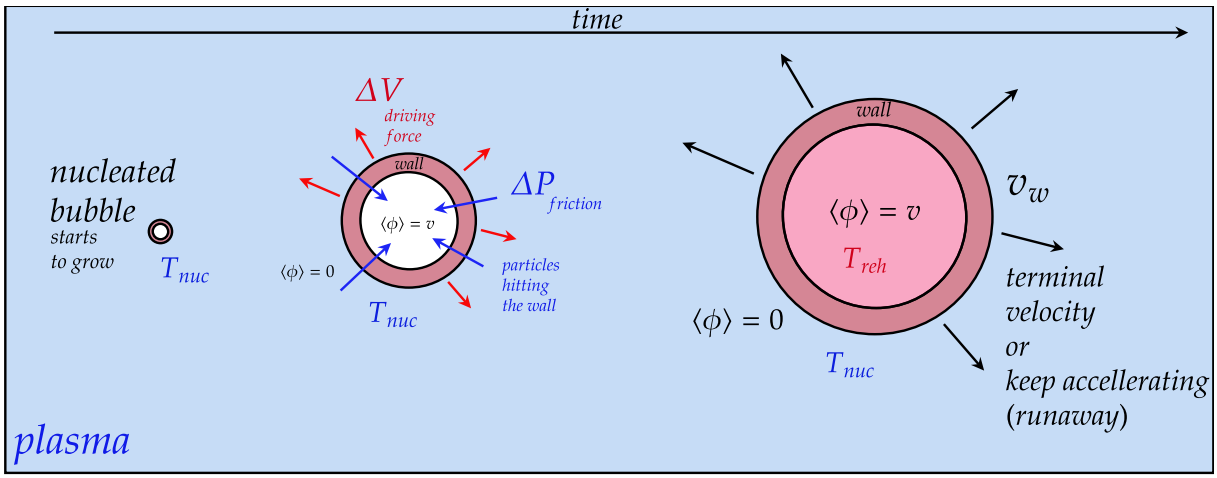

Figure 1.6: Sketch of the dynamics of a nucleated bubble in the primordial plasma. Once a bubble is nucleated, it starts to expand due to the initial driving force, ΔV. All the particles around it described either as individual ones or through collective action in terms of a fluid, exert a friction force on the expansion. The end of the picture signals two different possibilities: either the driving force is so large that the expansion is never stopped and the bubbles keep accelerating until they collide (so-called runaway regime), or there is a balance between these forces and a terminal velocity is reached.

pressure with its vacuum part, it's important to note that true thermal equilibrium is not realistic near the bubble wall. This necessitates the inclusion of friction terms in the effective equation of motion due to out-of-equilibrium effects, which will be further discussed.

For $O(4)$ symmetric bubbles, which nucleate in a vacuum, there is no surrounding plasma to exert any frictional force, $\Delta p_{\rm dr} = \Delta V_{\rm eff}$. As a result, once these bubbles nucleate and start to grow, they are expected to continuously accelerate until they collide with other bubbles. The lack of resistance allows the bubble walls to move outward increasingly faster as the pressure difference drives the expansion.

In contrast, $O(3)$ symmetric bubbles, which nucleate in a thermal primordial plasma, experience a different dynamic. The presence of the plasma introduces frictional forces due to interactions with the surrounding particles. As the bubble expands, this frictional force opposes the driving force of the pressure difference, $\Delta p_{\rm dr} = \Delta V_{\rm eff} - \Delta \mathcal{P}_{\rm plasma}$. This resistance can alter the dynamics significantly. If the bubble starts to grow, the friction from the plasma and surrounding particles will eventually produce a balance with the driving force, leading to the bubble reaching a terminal velocity, found by solving

$$\lim_{\gamma_w \to \infty} \Delta p_{\rm dr} = 0 \ . \tag{1.125}$$

This terminal velocity is the speed at which the driving force and the frictional force are in equilibrium, preventing further acceleration. However, if bubbles collide before this equilibrium is reached, the dynamics are altered.

Then, as sketched in fig. 1.6, there are two primary regimes for the dynamics of expanding bubbles [33, 40, 41]

- **Runaway Regime**: In this regime, the bubbles continue to accelerate until they collide, reaching very high velocities. This occurs when the driving force remains dominant over any resisting forces, typically in a vacuum scenario.

- **Terminal Velocity Regime**: In this regime, the bubbles reach a terminal velocity where the driving force is balanced by the frictional force from the plasma. This prevents further acceleration and is characteristic of bubbles expanding in a thermal primordial plasma.

In summary, the distinction between $O(4)$ symmetric bubbles in vacuum and $O(3)$ symmetric bubbles in a thermal primordial plasma reflects the different symmetries and dynamics involved in these environments. Understanding these dynamics is essential for studying the early Universe and the resulting cosmological implications.

Interior of the bubble

After discussing the evolution of the bubble wall, which expands due to the balance between the driving force and the friction from the plasma, it's essential to understand the dynamics inside the bubble as well [42, 43].

The lightlike hypersurface $r = r_*(t)$, where the field takes the value ϕ_*, that is the tunnelling point, separates the solution $\phi = \tilde{\phi}(\sqrt{t^2 - r^2})$ for $r < t$ from $\phi = \bar{\phi}(\sqrt{r^2 - t^2})$ for $r > t$. Inside this lightcone, field oscillations occur, while outside, the bubble wall reaches the asymptotic value $\phi_{\rm FV}$. The evolution of a single bubble configuration after nucleation at $t = 0$ is as follows:

- **Outside of the Bubble**: The scalar configuration is related to the bounce configuration $\bar{\phi}$ through SO(1,3) symmetry

$$\phi(t, r) = \bar{\phi}\left(\sqrt{-t^2 + r^2}\right) \ , \tag{1.126}$$

  where $\bar{\phi}(s = \sqrt{-t^2 + r^2})$ satisfies the bounce equation of motion

$$\frac{d^2\bar{\phi}}{ds^2} + \frac{3}{s}\frac{d\bar{\phi}}{ds} - \frac{dV}{d\bar{\phi}} = 0 \ . \tag{1.127}$$

- **Inside of the Bubble**: The scalar configuration is again related through SO(1,3) symmetry

$$\phi(t, r) = \tilde{\phi}\left(\sqrt{t^2 - r^2}\right) \ , \tag{1.128}$$

  where $\tilde{\phi}(s = \sqrt{t^2 - r^2})$ satisfies:

$$\frac{d^2\tilde{\phi}}{ds^2} + \frac{3}{s}\frac{d\tilde{\phi}}{ds} + \frac{dV}{d\tilde{\phi}} = 0 \ . \tag{1.129}$$

  In this region, the field oscillates around the new local minimum of the potential.

Thus, the dynamics of the bubble interior involve field oscillations, distinct from the exterior where the bubble wall propagates. The exact solution of the field equation reveals oscillations generated behind the wall, decaying towards the bubble centre, as we can see from fig. 1.7. For spherical symmetry, this behaviour is significant when the ratio $\Delta V/V_{\rm max}$ is high enough, or in other words, if ϕ_* is sufficiently far from $\phi_{\rm TV}$.

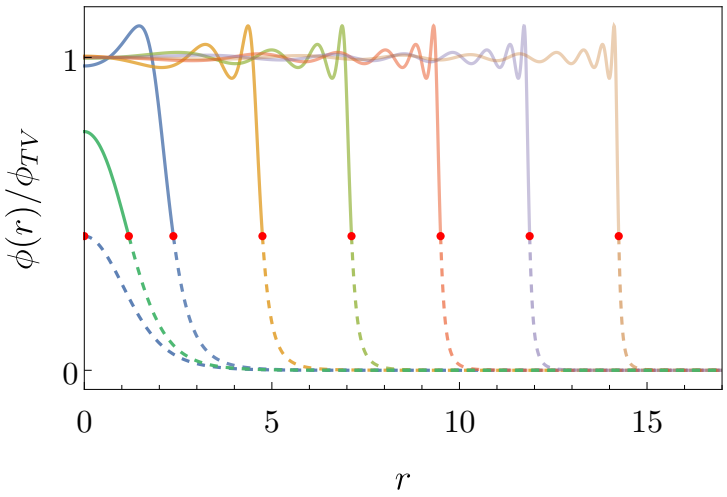

Figure 1.7: This figure illustrates the time evolution of a bubble wall at different time slices in the $O(4)$ symmetric case. The dashed section represents the exterior of the bubble, described by $\phi = \bar{\phi}(\sqrt{r^2 - t^2})$, while the solid line represents the interior, described by $\phi = \tilde{\phi}(\sqrt{t^2 - r^2})$. If the nucleated bubble is thick, meaning the escape point is far from the true vacuum, the field rolls down classically, producing a tail of oscillations. As time progresses, these oscillations compress towards the wall position.

1.4.2 GW from linearised Einstein equations

In this section, we first review the prediction of gravitational radiation emission within the weak field limit of GR. We then explore the essential characteristics of GW signals that arise from FOPTs. Specifically, we investigate how the GW spectrum depends on key parameters directly associated with the effective potential governing the order parameter. Additionally, we analyse the sensitivity curves of current and future experiments, crucial for assessing the detectability of GWs [44, 45].

Gravitational Wave Emission

Starting from Einstein's equations without the cosmological constant, we focus on the linearised theory by expanding the metric around flat spacetime. This approach predicts gravitational radiation, neglecting self-gravitational interaction via radiation.

Linearising the metric, $g_{\mu\nu} = \eta_{\mu\nu} + h_{\mu\nu}$ where $|h_{\mu\nu}| \ll 1$, $h_{\mu\nu}$ is treated as a perturbation, and $\eta_{\mu\nu}$ is the Minkowski metric. In this regime, the Ricci tensor $R_{\mu\nu}$ and Ricci scalar $\mathcal{R}$ yield

$$G_{\mu\nu} = R_{\mu\nu} - \frac{1}{2}\eta_{\mu\nu}\mathcal{R} = -\frac{1}{2}\left(\Box h_{\mu\nu} - \frac{1}{2}\eta_{\mu\nu}\Box h\right) = \frac{1}{M_{\rm Pl}}T_{\mu\nu} \ , \tag{1.130}$$

where $h = h^{\mu}{}_{\mu}$. Introducing the trace-reversed field tensor

$$\bar{h}_{\mu\nu} = h_{\mu\nu} - \frac{1}{2}\eta_{\mu\nu}h \ , \quad \text{and} \quad \partial_\mu \bar{h}^{\mu}{}_{\nu} = 0 \ , \tag{1.131}$$

where $\bar{h} = -h$. The linearised field equations become

$$\Box \bar{h}_{\mu\nu} = -16\pi G_N T_{\mu\nu} \ , \tag{1.132}$$

where $M_{\rm Pl} = (8\pi G_N)^{-1/2}$. In this gauge, the equation of motion for $h_{\mu\nu}$ is a standard wave equation. The key implication of equation (1.130) is the prediction of gravitational radiation. In vacuum, this simplifies to

$$\Box \bar{h}_{\mu\nu} = (-\partial_t^2 + \nabla^2)\bar{h}_{\mu\nu} = 0 \ , \tag{1.133}$$

which describes 10 equations for GWs propagating at the speed of light. The simplest solution is sought in the form of plane waves

$$\bar{h}_{\mu\nu} = A_{\mu\nu} e^{ikx} \ , \tag{1.134}$$

where $A_{\mu\nu}$ is the amplitude tensor and $k^\mu = (\omega, \boldsymbol{k})$ is the wave four-vector satisfying $k_\mu k^\mu = 0$ leading to $\omega^2 = |\boldsymbol{k}|^2$.

It can be shown that only 6 of the 10 equations are independent, allowing the choice of a gauge such as the Lorenz gauge $A_{\mu\nu}k^\mu = 0$. This gauge ensures that $A_{\mu\nu}$ is transverse and traceless (TT).

The effect of GWs on free-falling particles in the TT gauge is null for a single particle. However, for two nearby particles initially at rest, the proper distance between them evolves over time[10].

Gravitational Wave Radiation

Here, we briefly discuss the emission of GWs from a general distribution characterised by the stress-energy tensor $T_{\mu\nu}$. We will see that radiation correlates with the quadrupole moment tensor $\mathcal{I}_{ij} = \int d^3\boldsymbol{x}\ \rho(\boldsymbol{x}) x_i x_j$.

Similar to Maxwell's equations, we seek retarded solutions for an observer far from the source at position $\boldsymbol{r}$ and time t. Under the assumption $|\boldsymbol{x}| \ll r$, the retarded solution of equation (1.130) approximates to

$$\bar{h}_{\mu\nu}(t, r) \simeq \frac{4G_N}{r} \int_V T_{\mu\nu}(t - r, \boldsymbol{x}) d^3\boldsymbol{x} \ , \tag{1.136}$$

where V denotes the volume containing the source. Considering momentum-energy conservation, the spatial components $\bar{h}_{ij}$ are meaningful, leading to the tensor virial theorem

$$\partial_t^2 \int_V T^{00} x^i x^j d^3\boldsymbol{x} \simeq 2 \int_V T^{ij} d^3\boldsymbol{x} \ . \tag{1.137}$$

This, together with the definition of the quadrupole moment, results in the emitted GW

$$\bar{h}_{ij}(t, r) = \frac{2G_N}{r} \ddot{\mathcal{I}}_{ij}(t - r) \ , \tag{1.138}$$

known as the quadrupole emission formula. Enforcing the TT gauge, we obtain

$$\bar{h}^{\rm TT}_{ij}(t, r) = \frac{2G_N}{r} \ddot{\mathcal{I}}^{\rm TT}_{ij}(t - r) \ . \tag{1.139}$$

[10]The proper distance, computed at the same time, between two nearby particles is

$$\Delta L = \int |ds^2|^{1/2} = \int \sqrt{|g_{\mu\nu} dx^\mu dx^\nu|} \simeq |g_{xx}(x = 0)|^{1/2} \cdot \epsilon \simeq \left[1 + \frac{1}{2} h^{\rm TT}_{xx}(x = 0)\right] \cdot \epsilon \ , \tag{1.135}$$

where $h^{\rm TT}_{xx}(x = 0) = A^+ e^{-i\omega t}$. Then the displacement is proportional to the initial separation, ϵ, of the masses in a possible detector and the sensitivity must be such to distinguish A^+ from 1, where this is expected to be of order $10^{-23} - 10^{-21}$.

When the time-dependent components of $\mathcal{I}_{ij}$ lie in the transverse plane with respect to the z-axis, the two polarisations of GW radiation are

$$h^{+}(t,r) = \frac{2G_N}{r}\ddot{\mathcal{I}}^{\mathrm{TT}}_{xx}(t-r) \ , \quad h^{\times}(t,r) = \frac{2G_N}{r}\ddot{\mathcal{I}}^{\mathrm{TT}}_{xy}(t-r) \ , \tag{1.140}$$

with linear polarisation for a single component and elliptical polarisation otherwise.

Power Emitted

GWs carry energy and induce spacetime deformations. In the TT gauge of the linearised theory, the stress-energy tensor for GWs is given by

$$T^{GW}_{\mu\nu} = \frac{1}{32\pi}\frac{c^2}{G_N}\langle(\partial_\mu \bar{h}^{\mathrm{TT}}_{ij})(\partial_\nu \bar{h}^{\mathrm{TT}}_{ij})\rangle \ , \tag{1.141}$$

with averaging over several wavelengths indicated by angular brackets. For a plane wave propagating in the z-direction, the stress-energy tensor has three non-zero components. We focus on the 00 component, corresponding to the energy density

$$T^{GW}_{00} = \rho_{GW} = \frac{1}{32\pi}\frac{\omega^2 c^2}{G_N}(A^2_{+} + A^2_{\times}) \ . \tag{1.142}$$

Using this, the power emitted by GWs is derived as

$$P_{GW} = -\frac{dE}{dt} = \frac{G_N}{5c^5}\langle(\dddot{\mathcal{I}}^{\mathrm{TT}}_{ij})(\dddot{\mathcal{I}}^{\mathrm{TT}}_{ij})\rangle \ . \tag{1.143}$$

This formula highlights that the quadrupole moment of a system relates to the emitted power, reflecting the system's kinetic energy relative to the timescale of its non-spherical internal motions. The fundamental constant G_N/c^5 is inversely related to a characteristic luminosity L_0, emphasising the immense scale of gravitational radiation compared to other forms of energy emission in the Universe.

1.4.3 Stochastic Gravitational Wave Background from FOPTs

After briefly exploring the origins of GW predictions, we categorise them into three main sources:

(i) GWs produced by astrophysical events like compact binary systems orbiting or supernova explosions.

(ii) Primordial GWs generated during the early Universe by inflation, leaving a distinct imprint on the Cosmic Microwave Background.

(iii) GWs stemming from cosmological phase transitions.

Cosmological FOPTs can generate a stochastic background of GWs via bubble nucleation—a highly inhomogeneous process— where some of the kinetic energy from rapidly expanding bubbles transfers to the cosmic plasma, creating turbulence. A stochastic background of GWs arises from the superposition of numerous independent and uncorrelated sources, making them indistinguishable from random noise. Ground-based detectors detect these by coordinating measurements across multiple interferometers to identify sources of correlated noise [46–56].

In this section, we outline the primary characteristics of the GW spectrum and the signals expected from FOPTs. We start with the energy-momentum tensor associated with the scalar field ϕ

$$T_{\mu\nu} = \partial_\mu\phi\partial_\nu\phi - \eta_{\mu\nu}\left(\frac{1}{2}(\partial\phi)^2 - V(\phi)\right) \ , \tag{1.144}$$

where $\eta_{\mu\nu}$ is the Minkowski metric. The GW energy density is then given by

$$\rho_{GW}(t,\boldsymbol{x}) = \frac{1}{32\pi G_N}\langle \dot{h}_{ij}^{TT}(t,\boldsymbol{x})\dot{h}_{ij}^{TT}(t,\boldsymbol{x})\rangle \ . \tag{1.145}$$

To compute the GW power spectrum, we assume the cosmological stochastic background is statistically isotropic, stationary, and Gaussian[11]. The spectral density of the time derivative of metric perturbations $P_{\dot{h}}$ is defined as

$$\langle \dot{h}_{ij}^{TT}(\boldsymbol{k},t)\dot{h}_{ij}^{TT}(\boldsymbol{k}',t)\rangle = P_{\dot{h}}(\boldsymbol{k},t)(2\pi)^3\delta(\boldsymbol{k}-\boldsymbol{k}') \ , \tag{1.146}$$

resulting in the energy density

$$\frac{d\rho_{GW}}{d\ln(k)} = \frac{1}{32\pi G_N}\frac{k^3}{2\pi^2}P_{\dot{h}}(\boldsymbol{k},t) \ , \tag{1.147}$$

and dividing by the critical energy density ρ_c

$$\frac{d\Omega_{GW}}{d\ln(k)} = \frac{1}{32\pi G_N\rho_c}\frac{k^3}{2\pi^2}P_{\dot{h}}(\boldsymbol{k},t) \ . \tag{1.148}$$

The stochastic GW background's magnitude is typically expressed in terms of its energy density per logarithmic frequency interval relative to the critical energy density of the Universe:

$$\Omega_{GW}(f) = \frac{f}{\rho_c}\frac{d\rho_{GW}}{df} \ , \tag{1.149}$$

where $\rho_c = 3M_{\rm Pl}^2H_0^2$, with H_0 being the Hubble rate today.

To conclude this section, we note that GWs produced at temperature T_*, with a characteristic frequency f_*, propagate through the Universe unchanged, with their energy density scaling as a^{-4} and their frequency as a^{-1}. The characteristic frequency and the fraction of critical energy density in GWs today are

$$f = f_*\left(\frac{g_{0,s}}{g_{*,s}}\right)^{1/3}\frac{T_0}{T_*} \ , \tag{1.150}$$

$$\Omega_{GW} = \Omega_{GW}^*\left(\frac{a_*}{a_0}\right)^4\left(\frac{H_*}{H_0}\right)^2 \ , \tag{1.151}$$

where H_* and $g_{*,s}$ are the Hubble parameter and the number of relativistic degrees of freedom at T_*, respectively.

[11]Statistically isotropic means that the statistical properties of the system can be determined by looking at any section of the sky. Stationarity implies that these properties do not change over time. Gaussianity arises from the central limit theorem for independent events: the radiation arriving at a detector is the sum of the amplitudes of the radiation produced by each independent process, leading to a Gaussian signal.

GW Spectrum from FOPTs

FOPTs are particularly intriguing because their GW spectrum depends on two key parameters. The first parameter, β, represents the rate of change of the bubble nucleation rate—or the inverse period of the phase transition—which sets the characteristic timescale and the bubble size at collision time, determining the characteristic frequency f_* of the GW spectrum. The second crucial parameter is α, defined as in (1.105). Both α and β are evaluated at the nucleation temperature[12] $T_{\rm nuc}$ and dictate the functional form of the GW spectrum. These parameters are computed from the effective action describing bubble nucleation, found for any scalar potential governing the phase transition.

The primary sources contributing to the GW power spectrum from FOPTs include [54]:

1. Bubble wall collisions. These collisions are often approximated using the envelope approximation [57].

2. Sound waves in the plasma are generated after bubble collisions but before the plasma's kinetic energy dissipates [46].

3. Magnetohydrodynamic (MHD) turbulence in the plasma developing post-bubble collisions [58].

These processes coexist, and their contributions to the stochastic GW background linearly combine to give

$$h^2\Omega_{GW} \approx h^2\Omega_{\phi} + h^2\Omega_{\rm sw} + h^2\Omega_{\rm turb} \ . \tag{1.152}$$

In strong FOPTs, when no terminal velocity is reached, the scalar contribution often dominates, especially when bubble expansion proceeds via detonation ($v_w > c_s$, where v_w is the wall velocity and c_s is the sound speed in the plasma).

This section highlights that GWs from FOPTs offer unique insights into the dynamics of the early Universe. They carry information about high-energy particle physics and remain largely undisturbed since their production, owing to their weak interaction with matter.

Scalar field contribution

The GW contribution from the scalar field involved in a PT can be approximated using the *envelope approximation* [57, 59, 60]. In this method, a fraction κ of the latent heat from the PT is concentrated in a thin shell near the PT front, neglecting the dynamics of the interior collision regions. The kinetic energy is assumed to be stored only in the bubble walls that have not yet collided. The first collision of a surface element determines the point at which the energy density will start to fade away. Therefore, in the envelope approximation, the anisotropic stress is abruptly removed at this point. When bubble walls collide, they push the plasma to scales comparable to their radius at the collision time, causing turbulence that generates gravitational radiation.

To understand the spectrum's dependence on key quantities, first we use dimensional analysis. The energy density of GWs equals the energy radiated by GW emission divided by the volume where this energy is located. The radiated energy is the emitted power times the problem's timescale. Thus, the relevant quantities are the timescale β^{-1} and

[12] Actually, they have to be evaluated at the percolation temperature, T_p, but since generically, they are almost the same, here, we make no distinction between them.

the typical bubble size $v_w\beta^{-1}$, where v_w is the bubble wall velocity. Therefore, the GW energy density today can be expressed as

$$\rho_{GW,*} = \frac{P_{GW}\beta^{-1}}{(v_w\beta^{-1})^3} \ , \tag{1.153}$$

where P_{GW} is the power emitted during GW emission. From dimensional analysis, we can see that

$$\dddot{\mathcal{I}} \sim \frac{\text{mass} \times (\text{size})^3}{(\text{time})^3} \sim \kappa\varepsilon v_w^3\beta \ , \qquad P_{GW} \sim G_N(\kappa\varepsilon v_w^3\beta)^2 \ , \tag{1.154}$$

where we used that $[\varepsilon] = ML^{-1}T^2$ and, as previously mentioned, the kinetic energy of accelerating bubbles is typically a fraction κ of the latent heat ε of the phase transition, then we get

$$\rho_{GW,*} \sim G_N\kappa^2\frac{\varepsilon^2}{\beta^2}v_w^3 \ . \tag{1.155}$$

It is useful to express G_N as a function of the Hubble rate, $G_N \sim \frac{H_*^2}{\rho_{tot}}$, allowing us to estimate

$$\Omega_{GW,*} \sim \left(\frac{H_*}{\beta}\right)^2\left(\frac{\kappa\varepsilon}{\rho_{\text{rad}}+\varepsilon}\right)^2 v_w^3 \ . \tag{1.156}$$

Numerical simulations suggest the power spectrum can be described by the fit

$$\Omega_{\text{env}}^{\phi}(f) = \Omega_{\text{env}}^{\phi,\text{peak}}\frac{(a+b)\tilde{f}_\phi^b f^a}{b\tilde{f}_\phi^{a+b} + af^{a+b}} \ , \tag{1.157}$$

where $a = 3$, $b = 1.51$, and $\tilde{f}$ and $\Omega_{\text{env}}^{\phi,\text{peak}}$ are the peak frequency and amplitude respectively[13]. The peak amplitude $\Omega_{\text{env}}^{\phi,\text{peak}}$ is given by

$$h^2\Omega_{\text{env}}^{\phi,\text{peak}} = 1.67\times10^{-5}\times\frac{0.44v_w^3}{1+8.28v_w^3}\kappa^2\left(\frac{H}{\beta}\right)^2\left(\frac{\alpha}{\alpha+1}\right)^2\left(\frac{100}{g_*}\right)^{1/3} \ , \tag{1.158}$$

and the peak frequency $\tilde{f}_\phi$ is

$$\tilde{f}_\phi = 2.62\times10^{-3}\times\frac{1.96}{1-0.51v_w+0.88v_w^2}\left(\frac{1}{H_*}\right)\left(\frac{T_*}{100\,\text{GeV}}\right)\left(\frac{g_*}{100}\right)^{1/6}\text{mHz} \ . \tag{1.159}$$

Here, H_* is the Hubble parameter at the time of bubble collision, g_* is the number of relativistic degrees of freedom, and κ is the fraction of latent heat converted into the kinetic energy of the bubble walls. This mechanism predominantly contributes to the GW spectrum in the so-called runaway regime, where bubble walls continue to accelerate until they collide. This process is brief but significant in generating gravitational radiation.

[13] In the literature, gravitational wave spectra from bubble dynamics are often estimated using simulations that employ thin-wall and envelope approximations within a flat background metric. However, in [61] it has been shown that these spectra can be analytically derived under the same assumptions.

Sound waves contribution

After the merger of bubbles, the subsequent phase, known as the “acoustic" mechanism, becomes crucial for the generation of GWs. In this phase, sound waves produced by the dynamics of the bubble propagate through the plasma, overlapping and contributing to the generation of additional GWs. Unlike the brief collision mechanism, the acoustic phase lasts much longer, typically on the order of the Hubble time, making it a dominant contributor to the GW spectrum when the bubble wall reaches a terminal velocity v_w.

The GW spectrum from the acoustic mechanism is described by

$$\frac{d\Omega_{sw}}{d\ln f} = 0.687 F_{\mathrm{gw},0}\Omega_{sw} C\left(\frac{f}{\tilde{f}_{sw}}\right)\begin{cases} K^2\left(\frac{H_* R_*}{c_s}\right) & \tau_{\mathrm{sh}} > 1/H_* \ , \\ K^{3/2}\left(\frac{H_* R_*}{\sqrt{c_s}}\right)^2 & \tau_{\mathrm{sh}} < 1/H_* \ , \end{cases} \tag{1.160}$$

where the efficiency parameter K for GW production in this stage is defined as

$$K = \frac{\kappa_{sw}\alpha}{1+\alpha} \ , \quad \kappa_{sw} = \frac{3}{\epsilon \xi_w}\int w(\xi) v_p^2 \gamma_p^2 \xi^2 d\xi \ , \tag{1.161}$$

where γ represents the Lorentz factor, $\xi = r/t$ with r as the bubble radius and t as the time since nucleation, v_p is the velocity of the plasma. This quantity will be largely studied in the last chapter. Moreover, τ_{sh} denotes the time scale for shock formation, and $\Omega_{\mathrm{gw}} \approx 10^{-2}$ is determined from numerical simulations. The mean bubble separation is $R_* = (8\pi)^{1/3}\max(v_w, c_s)/\beta$, with c_s being the speed of sound. The factor $F_{\mathrm{gw},0}$ scales the emitted signal to the observable spectrum today

$$F_{\mathrm{gw},0} = \Omega_{\gamma,0}\left(\frac{g_{0,s}}{g_{*,s}}\right)^{4/3}\left(\frac{g_*}{g_0}\right) \approx 3.57\times 10^{-5}\left(\frac{g_*}{100}\right)^{1/3} \ , \tag{1.162}$$

The spectral shape $C(s)$ and peak frequency $\tilde{f}_{sw}$ are given by

$$C(s) = s^3\left(\frac{7}{4+3s^2}\right)^{7/2} \ , \quad \tilde{f}_{sw} \approx 26\left(\frac{1}{H_* R_*}\right)\left(\frac{z_p}{10}\right)\left(\frac{T_*}{100\ \mathrm{GeV}}\right)\left(\frac{g_*}{100}\right)^{1/6}\mu\mathrm{Hz} \ , \tag{1.163}$$

where $z_p \approx 10$ is determined by simulations.

In finding the case $\tau_{\mathrm{sh}} > H_*^{-1}$, it has been assumed that the sourced lasted for $\tau_{\mathrm{sh}} \sim H_*^{-1}$. If the shock formation timescale is less than a Hubble time the total GW power should be reduced by a factor $\tau_{\mathrm{sh}} H_* = H_* R_\star / K^{1/2}$.

Initially, the prevailing view attributed the primary generation of GWs to the kinetic energy of bubble walls during their collisions, especially in scenarios with strong FOPTs. This perspective led to the formulation of the envelope approximation model, which posits that shear stresses are concentrated in thin shells near the phase boundary and dissipate rapidly upon collision. However, it is now recognised that GWs produced during the collision phase are often overshadowed by radiation generated by fluid dynamics in subsequent phases of the transition unless the plasma friction is minimal enough to allow for a runaway scenario. In runaway scenarios, where the bubble walls accelerate continuously, most of the transition's energy is converted into kinetic energy of the walls, thereby amplifying gravitational radiation from the collision phase. Nevertheless, recent numerical simulations indicate that shear stresses in the collision region exhibit a more intricate behaviour than originally envisioned by the envelope approximation.

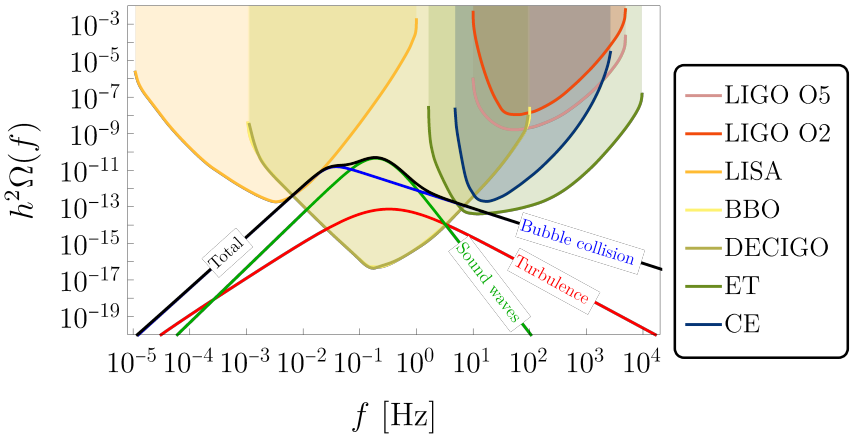

Figure 1.8: This figure illustrates a typical GW signal from a FOPT, separated into its various contributions: bubble collisions (blue), sound waves (green), and turbulence (red). The sensitivity curves for current and future ground- and space-based interferometers are also shown. The method for constructing these sensitivity curves is discussed in sec. 1.4.4.

Turbulence contribution

The final stage of GW production is the turbulent phase, where the non-linearities of fluid equations become significant. This phase is the most challenging to model accurately due to the complexity of numerical simulations, which often rely on untested assumptions. One key uncertainty in this phase is the generation and role of vorticity, which leads to turbulence and subsequently contributes to the GW spectrum. In the turbulent phase, the motion of the fluid becomes chaotic, leading to the generation of turbulence, which can further enhance the production of GWs. This chaotic motion is characterised by vortices that create anisotropic stress-energy components, essential for GW generation. However, the exact mechanisms by which vorticity is produced and its relative importance in the overall GW spectrum remain areas of active research.

Numerical simulations have provided some insights into the GW spectrum from turbulence, though these models are still subject to significant uncertainties. For instance, current models suggest that the efficiency of GW production from turbulence can be parameterised in terms of the turbulent kinetic energy fraction and the properties of the phase transition, such as the terminal wall velocity v_w and the strength parameter α. The GW energy density spectrum from turbulence is often modelled using a power-law behaviour with a peak frequency determined by the characteristic length scale of the turbulent vortices. The peak amplitude and frequency can be fit from numerical simulations, typically yielding results that depend on the specifics of the phase transition dynamics and the properties of the fluid involved. For a more accurate modelling of the GW spectrum, it is crucial to determine the terminal velocity v_w with precision. The terminal velocity influences the efficiency of energy transfer to the fluid and thus affects the resultant turbulence. Determining v_w requires a detailed understanding of the bubble wall dynamics during the phase transition, which involves complex interactions between the bubble wall and the surrounding plasma.

Here are the relevant equations and fits from numerical simulations for the GW signal

produced during the turbulent phase

$$\frac{d\Omega_{\rm turb}}{d\ln f} \sim \left(\frac{H_*}{\beta}\right)^2 \left(\frac{\kappa_{\rm turb}\alpha}{1+\alpha}\right)^{3/2} \left(\frac{100}{g_*}\right)^{1/3} \left(\frac{f}{\tilde{f}_{\rm turb}}\right)^3 \left(\frac{1}{1+\left(f/\tilde{f}_{\rm turb}\right)^2}\right)^{11/3} , \quad (1.164)$$

where $\kappa_{\rm turb}$ is the efficiency factor for turbulence and $\tilde{f}_{\rm turb}$ is the peak frequency of the turbulent GW spectrum, given by

$$\tilde{f}_{\rm turb} \approx 27\,\mu{\rm Hz} \left(\frac{\beta}{H_*}\right) \left(\frac{T_*}{100\,{\rm GeV}}\right) \left(\frac{g_*}{100}\right)^{1/6} . \quad (1.165)$$

This provides a numerical fit for the GW signal from turbulence based on current understanding and simulations, highlighting the ongoing need for refined models and simulations to reduce uncertainties and improve accuracy.

In summary, while the turbulent phase of GW production is the least understood and modelled with the greatest uncertainty, it is a critical component of the overall GW spectrum from a FOPT. Further advancements in numerical simulations and theoretical models are necessary to improve our understanding and predictions of this phase. This includes refining the models of vorticity generation and turbulence and obtaining more accurate values for key parameters such as the terminal velocity v_w.

1.4.4 Sensitivity Curves for GW Experiments

In this section, we derive the sensitivity curves for current and future experiments designed to detect GW signals. Our goal is to assess the detectability of GW signals originating from cosmological PTs by evaluating their signal-to-noise ratio (SNR) [41, 62]. The central issue revolves around whether the GW signals generated by PTs fall within the detectable range of sensitivity for present and future experiments.

A stochastic background of GWs becomes detectable in an experiment running for a duration $t_{\rm obs}$ if the SNR exceeds a specified threshold value

$$\mathrm{SNR} \geq \mathrm{SNR}_{\rm thr} = 10 , \quad (1.166)$$

where the SNR is calculated as

$$\mathrm{SNR} = \sqrt{t_{\rm obs} \int_{f_{\rm min}}^{f_{\rm max}} df \left(\frac{h^2\Omega_{GW}(f)}{h^2\Omega_{\rm noise}(f)}\right)^2} . \quad (1.167)$$

Here, $h^2\Omega_{GW}(f)$ denotes the dimensionless spectral energy density of GWs, while $h^2\Omega_{\rm noise}(f)$ represents the spectral noise energy density. $t_{\rm obs}$ accounts for the observational time integrated over multiple interferometers used in the experiment.

To derive the sensitivity, we assume a power-law form for the GW spectrum:

$$\Omega_{GW}(f) = \Omega_b(f_{\rm ref}) \left(\frac{f}{f_{\rm ref}}\right)^b , \quad (1.168)$$

where $f_{\rm ref}$ is a reference frequency. The sensitivity can then be determined by maximising $\Omega_b(f_{\rm ref})$ for each $f_{\rm ref}$ to achieve the required SNR threshold $\mathrm{SNR}_{\rm thr}$.

The Power-Law Integrated (PLI) sensitivity curve $h^2\Omega_{PLI}(f_{\rm ref})$ is defined as

$$h^2\Omega_{PLI}(f_{\rm ref}) \equiv h^2 \max_b[\Omega_b^{\rm thr}] , \quad (1.169)$$

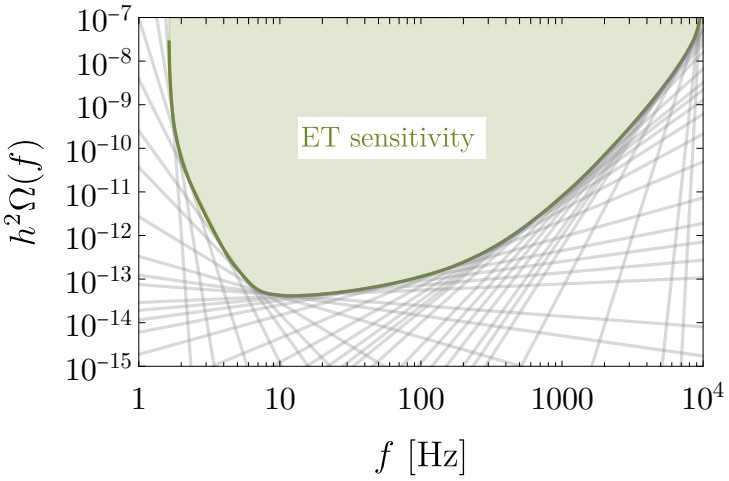

Figure 1.9: Here is presented the Power-Law Integrated (PLI) sensitivity curve for the Einstein Telescope (ET) experiment [63]. The PLI sensitivity in (1.169) is obtained considering, for each reference frequency $f_{\rm ref}$, between the range of accessible frequencies, the power-law relation $\Omega_{GW}(f) = \Omega_b(f_{\rm ref})(f/f_{\rm ref})^b$, find the spectral index b that maximises the threshold value $\Omega_b^{\rm thr}$, and then take the envelope of the family of curves.

	LIGO O2	LIGO O5	LISA	CE	BBO	DECIGO	ET
$t_{\rm obs}$ (months)	6	20	48	60	48	48	60
$h^2\Omega_{\rm noise}(f)$	[64]	[65]	[66]	[67]	[68]	[69]	[63]

Table 1.2: Observational times ($t_{\rm obs}$) and $h^2\Omega_{\rm noise}(f)$ values for each experiment, with SNR threshold $\mathrm{SNR}_{\rm thr} = 10$.

where $\Omega_b^{\rm thr}$ represents the threshold value of $\Omega_b(f_{\rm ref})$ for detection. Experimental sensitivities are often presented in terms of characteristic strain noise $h_c(f)$

$$h_c(f) = \sqrt{f S_{\rm noise}(f)} \ , \tag{1.170}$$

where $S_{\rm noise}(f)$ is the one-sided noise power spectral density. The relationship with $\Omega_{\rm noise}(f)$ is given by

$$\Omega_{\rm noise}(f) = \frac{2\pi^2}{3H_0^2} f^3 S_{\rm noise}(f) \ , \tag{1.171}$$

with $H_0 = 2.176 \times 10^{18}$ Hz being the Hubble rate today. Table 1.2 summarises the observational times $t_{\rm obs}$ considered for each experiment, along with the corresponding values of $h^2\Omega_{\rm noise}(f)$ used in our calculations.

In conclusion, by analysing the sensitivity curves across various experiments, we can determine the detectability of GW signals from cosmological Phase Transitions. These analyses play a crucial role in understanding the potential of current and future observatories in unveiling these elusive cosmic phenomena.

1.5 Interaction with the surroundings: friction

After summarising all the relevant information needed to compute the GW signals from cosmological phase transitions, we realised that the wall velocity is a crucial parameter.

It significantly influences the dynamics of the phase transition and the resulting GW spectrum. To accurately determine it, it is essential to consider the interaction between the bubble wall and the surrounding plasma. Various methods and approximations have been employed in the literature to estimate the wall velocity, each with its own set of assumptions and limitations. In this section, we will explore and summarise the key approaches used to compute the wall velocity, highlighting their assumptions and the conditions under which they are reliable.

The dynamic of the bubble wall is governed by its interaction with the plasma. As the bubble expands, the wall encounters resistance from the surrounding plasma, which affects its velocity. The key factors influencing this interaction include:

- **Friction from Plasma Particles**: The particles in the plasma exert a frictional force on the bubble wall, slowing it down. This friction depends on the nature of the particles and their interactions with the wall.
- **Thermal and Pressure Effects**: The temperature and pressure differences between the inside and outside of the bubble contribute to the driving force and the opposing frictional force.
- **Energy Transfer**: The energy transferred from the bubble wall to the plasma can affect the wall's velocity. This includes energy lost as heat or converted into kinetic energy of the plasma particles.

These components—friction from plasma particles, thermal and pressure effects, and energy transfer—are interdependent. For instance, higher temperatures result in more energetic plasma particles, increasing friction, while energy transfer can change the thermal state of the plasma, affecting both the frictional force and pressure. Thus, the interplay between these factors creates a complex, dynamic system where changes in one aspect, such as temperature, can significantly impact others, like friction and pressure, underscoring the importance of understanding these interdependencies for accurately modelling bubble wall dynamics.

Several methods have been proposed in the literature to model these interactions and to compute the wall velocity. Here, we discuss the most relevant ones, outlining their assumptions and applicability:

1. **Hydrodynamic Approximations**: These models, [33, 70–73], classify the phase transition based on the speed of the bubble wall relative to the speed of sound in the plasma. There are two main classes of expansions that are detonations, when the wall velocity exceeds the speed of sound, leading to a supersonic expansion, and deflagrations when the wall velocity is subsonic. These models assume specific forms of energy transfer and friction between the wall and plasma. They are reliable when the interactions can be approximated by ideal hydrodynamic flows.

2. **Microphysical Approaches**: These approaches, [74–79], compute the friction force from first principles, considering the detailed particle interactions at the microscopic level. Using effective field theories, these methods incorporate particle physics details to estimate the wall velocity. These methods require detailed knowledge of the particle physics involved and are reliable when such detailed information is available and accurate.

3. **Numerical Simulations**:

- **Lattice Simulations**: These simulations model the phase transition on a discrete space-time lattice, allowing for a detailed study of the bubble dynamics and wall velocity, [80–84].
- **Hydrodynamic Simulations**: Using computational fluid dynamics, these simulations solve the hydrodynamic equations to model the bubble expansion and wall velocity, [46–50, 85–90].

In the following, we will briefly review the hydrodynamic approach, which will be mostly presented in the last chapter, and we will also discuss the (semi-classical) approach using the Boltzmann equations for the plasma. We will conclude the chapter by analysing how the situation changes when we consider ultrarelativistic bubbles and how the computations simplify.

1.5.1 Hydrodynamics description

This section introduces, in the context of the hydrodynamic description of the plasma, the key thermodynamic variables, examines the role of the scalar field driving the phase transition, and emphasises the necessity of an equation of state to determine the bubble expansion dynamics.

To classify FOPTs, it is important to analyse the plasma's behaviour around the bubble wall. The bubble wall acts as a boundary between two phases of the plasma, modelled as a perfect fluid characterised by bulk velocity v, temperature T, and pressure p. For large bubbles, the relevant bulk velocity is primarily along the wall's direction, which we refer to as the z-direction.

The interface between the phases is a sharp boundary, considered infinitely thin in hydrodynamic terms. As a result, the values of $(T,\, v,\, p)$ can differ on either side of the interface. The hydrodynamic model aims to relate the properties inside the bubble (denoted as higgsed, $(T,\, v,\, p)_h$) with those outside the bubble (denoted as symmetric, $(T,\, v,\, p)_s$) and the energy parameters of the transition described in the previous sections. The main variables in this analysis include the shape of the scalar field, the temperatures inside T_h and outside T_s the bubble, the plasma velocities inside v_h and outside v_s, and the pressures inside p_h and outside p_s. The hydrodynamic approach usually leaves the wall velocity v_w as an undetermined parameter, requiring additional methods and approximations to find its value.

In this section, we will explore various established techniques to understand these relationships and their impact on bubble expansion dynamics. Further, we will address the determination of wall velocity in the subsequent part of this chapter, examining different methods and assumptions used to compute it.

Thermodynamic quantities To describe the hydrodynamic behaviour of the bubble wall, we first introduce the key thermodynamic quantities

$$w = T\frac{\partial p}{\partial T}\,, \quad s = \frac{w}{T}\,, \quad e = w - p\,, \quad \mathcal{F} = -p = V_T(\phi, T)\,, \tag{1.172}$$

where, in order, we defined the enthalpy, the entropy density, the energy density and the free-energy density.

The Scalar field The phase transition is driven by a scalar field, ϕ, which changes its value from the false vacuum (ϕ_{false}) to the true vacuum (ϕ_{true}) as the bubble expands. The

dynamics of the scalar field are governed by its potential, $V(\phi, T)$, which is temperature-dependent and dictates the energetics of the phase transition.

Hydrodynamic Equations

The combined system of the scalar field condensate and the surrounding plasma can be described by their contribution to the energy-momentum tensor [73]. For the scalar field, we have

$$T_{\phi}^{\mu\nu} = (\partial^{\mu}\phi)\partial^{\nu}\phi - g^{\mu\nu}\left[\frac{1}{2}(\partial\phi)^2 - V(\phi)\right] \ , \tag{1.173}$$

where $V(\phi)$ is the zero temperature potential. The stress-energy tensor of a gas described by a distribution function f is generically defined as

$$T^{\mu\nu} = \int \frac{d^3\boldsymbol{k}}{(2\pi)^3 2E}\, k^{\mu}k^{\nu} f(\boldsymbol{k}, x) \ . \tag{1.174}$$

For a perfect fluid, it can also be written as

$$T_{f}^{\mu\nu} = (e_f + p_f)u^{\mu}u^{\nu} - g^{\mu\nu}p_f \ , \tag{1.175}$$

where u^{μ} is the plasma four-velocity. Then, the total stress-energy tensor is the sum of two contributions, the scalar field condensates and plasma. The hydrodynamic equations are derived from the conservation of the total energy-momentum tensor of the system and the rest mass current density

$$\nabla_{\mu}T^{\mu\nu} = 0 \ , \qquad \nabla_{\mu}J^{\mu} = 0 \ , \tag{1.176}$$

where $J^{\mu} = \rho u^{\mu}$ and ρ is the rest mass energy density. Solving such a set of equations will allow us to describe continuous waves.

However, in such a hydrodynamic description, the shape of the wall is described by a sudden step, mathematically parameterised by a discontinuity. This will induce discontinuities in the thermodynamic quantity describing the fluid, so we need to deal with such discontinuity. As an explicit example, we can consider the case of a steady planar wall, moving in the $z-$direction. Then the conservation of the stress-energy tensor implies

$$\partial_z T^{zz} = \partial_z T^{zt} = 0 \ . \tag{1.177}$$

By integrating the above equations across the wall one gets the following useful relations, also called junction conditions, that connect the plasma velocity and the other thermodynamic quantities between the two sides of the discontinuity

$$w_+ v_+ \gamma_+^2 = w_- v_- \gamma_-^2 \ , \qquad w_+ v_+^2 \gamma_+^2 + p_+ = w_- v_-^2 \gamma_-^2 + p_- \ , \tag{1.178}$$

where $\pm$ refers to the two different sides of the interface.

To close the set of hydrodynamic equations, an equation of state (EoS) is required. The EoS relates the thermodynamic quantities and provides a functional relationship between them. A commonly used form of the EoS in the context of cosmological phase transitions is

$$p = p(\rho, T) \ . \tag{1.179}$$

The specific form of the EoS depends on the properties of the plasma and the nature of the phase transition. In such a context the relativistic gas approximation, where a bag equation of state[14] is used, is a good description of the system. Therefore

$$p = \frac{1}{3}(e - 4\epsilon) \ , \tag{1.180}$$

where ϵ is the vacuum energy difference between the two phases. It is worth noticing that the vacuum energy contribution will be present only in the old phase, i.e. outside of the bubble, while inside, in the new phase, only the contribution coming from the relativistic gas will be present.

Given appropriate initial conditions, the hydrodynamic equations fully describe the temperature and fluid velocity distributions. These equations define the various hydrodynamic phases that occur during a FOPT. Therefore, the interaction between the bubble wall and the surrounding plasma results in distinct expansion modes, categorised by the wall's velocity in relation to the speed of sound in the plasma (c_s):

- **Deflagration**: The bubble wall expands subsonically ($v_w < c_s$). The phase transition front moves slower than the speed of sound, creating a compression wave ahead of the bubble ending in a shock.
- **Detonation**: The bubble wall expands supersonically ($v_w > c_s$). The phase transition front moves faster than the speed of sound, generating a tail behind the front.
- **Hybrid Modes**: Intermediate scenarios where the wall velocity is bigger than the speed of sound, but a compression wave in front of the bubble wall is still present.

To determine the expansion mode of the bubbles, we solve the hydrodynamic equations subject to the boundary conditions at the bubble wall, imposing that, in the plasma frame, the fluid is at rest at the centre of the bubble and very far from the bubble wall.

In summary, the hydrodynamic description of bubble wall expansion requires the introduction of key thermodynamic quantities, the scalar field dynamics, and an appropriate equation of state. By solving the conservation equations for energy and momentum, we can determine the expansion modes of the bubbles, which is crucial for predicting the resulting GW signals. In Chapter 5, we will analyse this approach in detail, extending it to the case of *inverse* phase transitions, which will be defined there.

1.5.2 Boltzmann equations

Determining the velocity of the bubble wall, v_w, and accurately modelling the friction necessitates a detailed understanding of the out-of-equilibrium disturbances within the plasma, governed by effective kinetic theory. This theory involves solving a set of Boltzmann equations, which are intricate integro-differential equations. Addressing these challenges, this section delves into various methods and approaches used in the literature, providing a thorough overview of the techniques employed to determine the wall velocity under different conditions and assumptions.

[14]The bag EoS is a model used primarily in the context of quark-gluon plasma and in the study of hadrons. The EoS reads $p = (\rho - 4B)/3$ where B is referred to as the bag constant, a parameter representing the vacuum energy difference between the perturbative vacuum (free quarks and gluons) and the true vacuum (inside hadrons where quarks are confined). The term "bag" comes from the fact that hadrons are described as regions (bags) of space where quarks are confined by the vacuum pressure but are free to move within the "bag".

The friction between the plasma and the bubble wall is a complex physical process. In equilibrium, each plasma component can be described by a distribution function $f_{\mathrm{eq},i}$. However, when the scalar condensate interacts with the plasma, it drives the system out of equilibrium, causing the distribution function f_i to differ from $f_{\mathrm{eq},i}$. Simultaneously, the dynamics of the scalar condensate are influenced by these distribution functions, creating a feedback loop that complicates solving the system. To tackle this, we start with the fundamental equations. The equation of motion for the Higgs classical background φ, derived at leading order[15], is given by

$$\Box\varphi + \frac{dV_0}{d\varphi} + \sum_i \frac{dm_i^2(\varphi)}{d\varphi} \int \frac{d^3\boldsymbol{k}}{(2\pi)^3 E_i} f_i(\boldsymbol{k}, x) = 0 \ , \tag{1.181}$$

where the sum includes all light particles interacting with the wall, f_i represents their distribution functions, and V_0 is the renormalised vacuum potential. The coupling between the condensate and the plasma particles is represented by the last term on the left-hand side. Additionally, the Boltzmann equations governing the plasma distributions are essential for a comprehensive understanding.

The Boltzmann equation tracks the evolution of the distribution in phase space $f_a(\boldsymbol{x}, \boldsymbol{p}, t)$ according to the interaction between the species a and the other species (and possibly according to the expansion of the Universe). Formally the Boltzmann equation[16] is written as

$$L[f] = \mathcal{C}[f] \ , \tag{1.183}$$

where L is the Liouville operator, while $\mathcal{C}$ is the collision term. The non$-$ relativistic Liouville operator[17] for $f(\boldsymbol{x}, \boldsymbol{v})$ of a species of mass m subjected to a force $\boldsymbol{F} = \frac{d\boldsymbol{p}}{dt}$ is

$$L[f] = \left(\frac{\partial}{\partial t} + \dot{\boldsymbol{x}} \cdot \nabla_{\boldsymbol{x}} + \dot{\boldsymbol{v}} \cdot \nabla_{\boldsymbol{v}}\right) f = \left(\frac{\partial}{\partial t} + \boldsymbol{v} \cdot \nabla_{\boldsymbol{x}} + \frac{\boldsymbol{F}}{m} \cdot \nabla_{\boldsymbol{v}}\right) f \ . \tag{1.185}$$

Now the covariant generalisation of the Liouville operator, under the assumption of a smooth Universe, i.e. f will be $\boldsymbol{x}-$independent, is given by

$$L = p^\mu \frac{\partial}{\partial x^\mu} + mF^\mu \frac{\partial}{\partial p^\mu} \ , \tag{1.186}$$

[15] In order to get this expression, following [91], one needs to compute the operator equation of motion, that should annihilate the physical thermal state, and then split the Higgs (quantum) field in its classical background and a fluctuation part, such that $\langle \delta\phi \rangle = 0$. We then evaluate the trace of the operator equation of motion over the out-of-equilibrium thermal density matrix that describes the propagating bubble wall. Assuming there are no charge conjugation-violating gauge condensates, we have $\langle A_\mu \rangle = 0$. Finally, we use WKB wave functions to evaluate the thermally averaged operators. This can be found in [92]. This approach is justified because the background field φ varies on a scale much longer than T^{-1}, which characterises the reciprocal momenta of particles in the plasma.

[16] At the kinetic equilibrium, this equation, for a species a will be a differential equation for the number density, that can be seen as

$$J^\mu = (n, \boldsymbol{J}) \ , \qquad \nabla_\mu J^\mu = \dot{n} + 3Hn = [source - loss] \ . \tag{1.182}$$

[17] In order to justify the structure of this operator we need to use the gas kinetic theory. Consider the evolution of f_a describing a gas of N particles with mass m in a box of volume V, subjected to the force $\boldsymbol{F}$. In the dilute gas limit, for which we can neglect the collisions between particles, all the particles contained in an elementary volume centred in $(\boldsymbol{x}, \boldsymbol{p})$, after a time dt, will be in an elementary volume centred in $(\boldsymbol{x'} = \boldsymbol{x} + \boldsymbol{v}dt, \boldsymbol{p'} = \boldsymbol{p} + \boldsymbol{F}dt)$. Then

$$f_a(\boldsymbol{x}, \boldsymbol{p}, t) = f_a(\boldsymbol{x} + \boldsymbol{v}dt, \boldsymbol{p} + \boldsymbol{F}dt, t + dt) \ , \tag{1.184}$$

and expanding to the first order we recover the previous expression.

where the Liouville operator L governs the evolution of the distribution function f of a particle in position space $\boldsymbol{x}$, with momentum $\boldsymbol{p}$ and mass m, under the influence of an external force F^μ. The collision operator $\mathcal{C}[f]$ accounts for the interactions occurring within the plasma. Its general form read

$$\mathcal{C}[f_a] = \sum_{n,m} \frac{1}{S} \int d\Pi_{\text{ALL}}\, \delta^{(4)}(p_i^{\text{tot}} - p_j^{\text{tot}}) \left[|\mathcal{M}_{n\to m}|^2 \mathcal{P}[n,m] - (n \leftrightarrow m) \right] \ , \tag{1.187}$$

where we have defined

$$d\Pi_{\text{ALL}} = \prod_{i=1, i\neq a}^{n} \frac{d^3\boldsymbol{p}_i}{(2\pi)^3 2E_i} \prod_{j=1}^{m} \frac{d^3\boldsymbol{p}_j}{(2\pi)^3 2E_j} \ . \tag{1.188}$$

and the population factor

$$\mathcal{P}[n,m] = \prod_{i=1}^{n} f_i \prod_{j=1}^{m} (1 \pm f_j) \ , \tag{1.189}$$

and where the sum over n, m denotes all possible interaction processes and takes into account all the particles except for the a for which we are trying to solve the Boltzmann equation, the $\delta^{(4)}$ ensures the conservation of four-momentum and the factor $1 \pm f$ in the population factor account for quantum statistical effects, like Bose-Einstein condensate or fermion degeneracy. S is a symmetry factor accounting for identical particles in the initial and final state and it is defined as $S = \prod_i n_i! \prod_j n_j!$.

In the literature, the Boltzmann equations are often simplified by primarily considering $2 \to 2$ scattering processes due to the relative tractability of these interactions and due to the fact that they are very efficient in thermalising the plasma in front of the bubble wall. During the EWPT the relevant processes that have been considered in previous studies [74–76] are

- top interactions: $t\bar{t} \to gg$, $tg \to tg$, $tq \to tq$ (summing over all massless quarks).
- W interactions: $Wq \to gg$, $Wg \to qg$, $WW \to \bar{f}f$ and $Wf \to Wf$.

In summary, the interaction between the bubble wall and the plasma is then captured by a complex set of equations. The Boltzmann equations include a force term, which is related to the momentum change of particles as they collide with the wall, leading to a departure from equilibrium in their distribution functions. The collision term, on the other hand, represents the interactions among plasma particles within the wall and acts to restore equilibrium. The scalar field equation incorporates various physical aspects: the wall's acceleration, the energy released from the phase transition (which drives the acceleration), and the departure from equilibrium (which provides friction against the wall). When the deviation from equilibrium δf_i approaches zero, the dissipative friction term disappears, simplifying the scenario. Solving these coupled equations is extremely challenging due to the complexity of the collision term, which necessitates tracking numerous interactions within the wall. This problem can be approached by considering two different scales: the wall thickness L_w and the mean free path λ_{mfp} of plasma particles. When the wall thickness is much greater than the mean free path, the particles tend to thermalise, and their distribution remains close to equilibrium, simplifying the equations. Conversely, if the mean free path is much longer than the wall thickness, the collision term can be approximated as zero, a situation known as the semi-classical approximation, which significantly reduces the complexity of the problem.

In this last case, considering $\mathcal{C}[f] = 0$, a simple solution can be found. We can consider a planar wall along the z-direction, and then the Boltzmann equation simplifies significantly. The equation reduces to

$$\frac{p_z}{E}\partial_z f_i(p,z) - \frac{1}{2E_i}\frac{dm_i^2}{dz}\partial_{p_z} f_i(p,z) = 0 \ , \tag{1.190}$$

where $m_i(z)$ is the position-dependent mass. This equation can be solved by knowing only the shape of the wall, which controls $m_i^2(z)$. The term containing the mass derivative acts as a classical force, pushing the distribution functions away from equilibrium. It can be shown that the solution to this equation should be expressed in terms of the transverse momentum $\boldsymbol{p}_\perp$ and the quantity $\sqrt{p_z^2 + m^2(z)}$

$$f_i\left(\boldsymbol{p}_\perp, \sqrt{p_z^2 + m^2(z)}\right) \ . \tag{1.191}$$

This form indicates that the distribution function depends on the transverse momentum and the effective energy, which includes the position-dependent mass. Then, the distribution function, in the wall frame, will take the form

$$f_i(E,p,T) = f_i\left(\frac{p^\mu u_\mu}{T}\right) = f_i\left(\frac{\gamma_w(E + v_w p_z)}{T}\right) \ , \tag{1.192}$$

where v_w is the velocity of the wall and $u^\mu = \gamma_w(1,0,0,-v_w)$.

Despite his usefulness and complexity, this approach overlooks other potentially significant processes, such as $1 \to 2$ interactions (e.g. decays or transition radiation processes). We will see that these latter ones (at least in the ultrarelativistic limit) are highly relevant and can change qualitatively the dynamics. This will be the subject of the next section.

1.6 Ultrarelativistic Bubbles

In the context of FOPTs, the study of ultrarelativistic bubbles provides significant simplifications in the computations of bubble dynamics and interactions with the plasma. Ultrarelativistic bubbles are characterised by bubble wall velocities approaching the speed of light, $v_w \approx 1$. This regime is particularly interesting because the dynamics of the phase transition and the resulting GW production can be markedly different from those involving non-relativistic bubbles.

In this regime, the computation simplifies greatly because the interaction of the plasma with the wall can be described in terms of individual particles colliding with the wall, rather than through collective hydrodynamic effects. Then, what we generally do is to set aside the Boltzmann distribution functions for the active species and focus on solving the EOM for the scalar degrees of freedom undergoing the PT using the effective potential. The condition for a runaway or non-runaway scenario is determined by the relation

$$\Delta V \gtrless \mathcal{P} \ , \tag{1.193}$$

where $\mathcal{P}$ is the total pressure acting on the wall. For sufficiently fast and large bubbles, compared to their initial radius, the wall shape can be approximated as planar. This approximation is valid because, at these high velocities, the curvature of the bubble

becomes negligible over the relevant scales of interaction. Consequently, we can simplify the problem by considering the bubble wall as an infinitely large plane moving through the plasma. In this planar wall limit, the computation of the friction force can be organised by considering the process of a single particle transforming into another (others) as it passes through the wall.

To be as general as possible, we derive a master equation for $\mathcal{P}$ that will be used throughout this thesis [93]. The pressure exerted on the expanding wall by single particles hitting it can be understood as the momentum exchanged with the wall during the interaction, averaged over the phase space[18] where such a process can occur, and then integrated over the flux of the incoming particles. Thus, it reads

$$\mathcal{P} = \underbrace{\sum_i \int \prod_{A\in i} g_A \frac{d^3\boldsymbol{p}_A}{(2\pi)^3} \frac{p_A^z}{p_{0,A}} f_A(p_A)}_{\text{incoming flux}} \times \underbrace{\sum_f \int d\mathbb{P}_{i\to f} \Delta p^z}_{\langle \Delta p^z \rangle} , \tag{1.194}$$

where A represents the particles present in the initial state, the sums run over all possible initial and final states allowed by the theory. To provide a precise expression for the differential splitting probability $d\mathbb{P}_{i\to f}$, consider a single particle interacting with the bubble wall. We begin by integrating the improperly normalised momentum-space states

$$\langle \boldsymbol{p}' | \boldsymbol{p} \rangle = 2p^0 (2\pi)^3 \delta^3(\boldsymbol{p} - \boldsymbol{p}') , \tag{1.195}$$

over a wave packet to construct a properly normalised single particle initial state

$$|\phi\rangle \equiv \int \frac{d^3\boldsymbol{p}}{(2\pi)^3 2p^0} \phi(\boldsymbol{p}) |\boldsymbol{p}\rangle , \tag{1.196}$$

with the normalisation condition

$$\int \frac{d^3\boldsymbol{p}}{(2\pi)^3 2p^0} |\phi(\boldsymbol{p})|^2 = 1 . \tag{1.197}$$

We label momentum-space states in terms of their incoming symmetric-phase momentum. Due to the presence of a bubble wall, these states exhibit nontrivial dependence on the z-direction

$$\langle \boldsymbol{r} | \boldsymbol{p} \rangle = \sqrt{2p^0} e^{i\boldsymbol{p}_\perp \cdot \boldsymbol{r}_\perp} \chi_p(z) \quad \text{(scalars)}, \tag{1.198}$$

where $\chi_p(z)$ has to be determined by solving the corresponding free particle evolution equation in the presence of the bubble wall. For spinor or vector fields, χ_p should be replaced with the appropriate spinor or vector solution to the Dirac or Yang-Mills equation in the wall background.

The splitting probability is then given by integrating over the final state phase space of the squared $\mathcal{T}-$matrix element of the initial state transitioning to the multiparticle final state

$$d\mathbb{P}_{i\to f} \equiv \int \prod_{X\in f} \frac{d^3\boldsymbol{p}_X}{(2\pi)^3 2p_X^0} \langle \phi | \mathcal{T} | \{\boldsymbol{p}_X\} \rangle \langle \{\boldsymbol{p}_X\} | \mathcal{T} | \phi \rangle , \tag{1.199}$$

implicitly summing over final state spin and colour indices and where X represents the particles present in the final state and $\{\boldsymbol{p}_X\}$ the collection of their momenta. Since

[18] The phase space considered includes the non-conservation of momentum along the z-direction, making it larger than the Lorentz-invariant phase space.

the bubble wall is invariant in time and the transverse directions, energy and transverse momentum are conserved. Therefore, the transition matrix element between momentum states is

$$\langle\{\boldsymbol{p}_X\}|\mathcal{T}|\boldsymbol{p}\rangle = \int d^4x \langle\{\boldsymbol{p}_X\}|\mathcal{H}_{\rm int}|\boldsymbol{p}\rangle \tag{1.200}$$

$$= (2\pi)^3\delta^{(2)}\left(\boldsymbol{p}_\perp - \sum_{X\in f}\boldsymbol{p}_{\perp,X}\right)\delta\left(p^0 - \sum_{x\in f}p^0_X\right)\mathcal{M}_{i\to f}\ . \tag{1.201}$$

Then the differential probability of the process $i \to f$ takes the following form

$$d\mathbb{P}_{i\to f} = \prod_{X\in f}\left(\frac{d^3\boldsymbol{p}_X}{(2\pi)^3 2p_{0,X}}\right)(2\pi)^3\delta^{(3)}(p_i^{\rm tot} - p_f^{\rm tot})|\mathcal{M}_{i\to f}|^2\ , \tag{1.202}$$

where $\mathcal{M}_{i\to f}$ is the amplitude of the process taking into account the fact that in the z-direction, there is a wall background breaking translation symmetry along this direction. Therefore, it is defined as

$$\mathcal{M}_{i\to f} = \int dz\, V(z)\prod_{A\in i}\zeta(p_A)\prod_{X\in f}\zeta^*(p_X)\ , \tag{1.203}$$

where $\zeta(p)$ are the eigenmodes describing the incoming/outgoing particles, found by solving the EOM for the specific particle, while $V(z)$ is the (generally) space-dependent vertex function.

1.6.1 Review computation for LO and NLO

In this section, we review the computations for the $1 \to 1$ (LO) and $1 \to 2$ (NLO) processes shown in fig. 1.10, as it has been done in the literature [94–99]. We start by reviewing how the WKB approximation works and what is the form of the eigenmodes of the particles in such approximation.

WKB approximation

The Wentzel-Kramers-Brillouin (WKB) approximation is a widely used method in quantum mechanics for solving the Schrödinger equation in cases where the potential varies slowly compared to the wavelength of the particle. This semi-classical approximation is particularly useful in scenarios where exact solutions to the Schrödinger equation are difficult or impossible to obtain.

The fundamental idea of the WKB approximation is to express the wave function as an exponential function whose exponent is expanded in powers of $\hbar$, the reduced Planck constant. This leads to an approximate solution that can be interpreted in terms of classical mechanics with quantum corrections. Outside the wall, far from the bubble wall, the mode functions are expected to be a superposition of plane waves. These plane waves are solutions to the Klein-Gordon equation:

$$\chi''(z) + \left(\frac{p_z^2(z)}{\hbar^2}\right)\chi(z) = 0\ . \tag{1.204}$$

Inside the wall, the situation is more complex due to the spatially varying potential. In the literature has been proposed the WKB approximation where we express the wave function $\chi(z)$ in the form

$$\chi(z) = e^{\frac{i}{\hbar}(S_0+\hbar S_1+\hbar^2 S_2+\cdots)}\ , \tag{1.205}$$

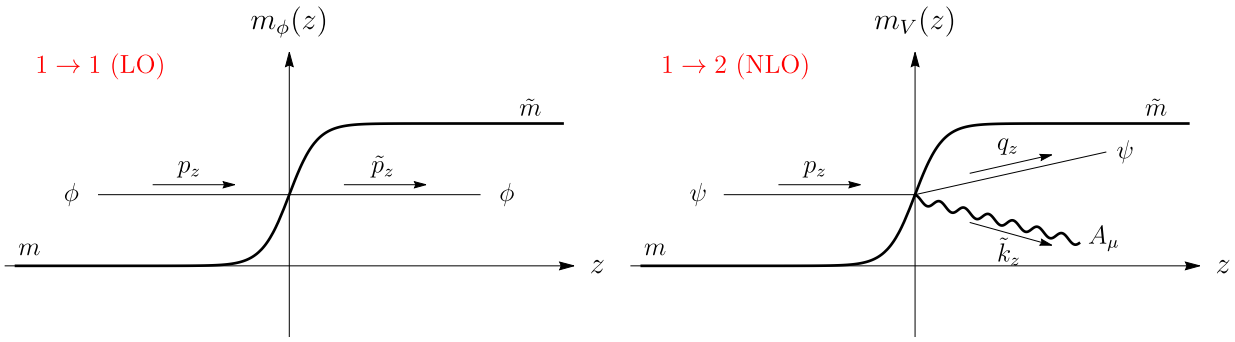

Figure 1.10: Sketch of the processes $1 \to 1$ (left) and $1 \to 2$ (right), also referred to as LO and NLO processes. In the LO one, a particle changes its mass (and thus its momentum) as it passes through the wall, while in the NLO, an incoming particle a approaching the bubble wall radiates a vector boson c, which acquires mass in the Higgs phase.

and then substituting this expression into the differential equation, matching terms of the same order in $\hbar$. This process yields an infinite set of equations that can be solved order by order in $\hbar$. To the leading order, the solution is

$$\chi(z) = \sqrt{\frac{p_z^s}{p_z(z)}} \exp\left[\frac{i}{\hbar}\int_0^z dz'\, p_z(z') + \cdots\right] . \tag{1.206}$$

The assumptions underlying the WKB approximation are:

- The potential varies slowly on the scale of the particle's wavelength, which is quantified by the condition $\hbar p_z''/p_z^2 \ll 1$.
- The solution can be locally approximated by plane waves whose amplitude and phase vary slowly compared to the wavelength.

In the context of bubbles in a FOPT, these conditions are typically satisfied as soon as the bubble walls are thin compared to the characteristic length scales of the phase transition, but still large enough for the slowly varying potential assumption to hold, and the scalar field in the vicinity of the bubble wall changes smoothly.

Thus, when the WKB approximation is justified and allows us to simplify the problem significantly by treating the interaction of the particles with the bubble wall in terms of quasi-classical particle trajectories.

LO contribution

At leading order (LO), i.e. $1 \to 1$ process, the computation involves calculating the momentum transfer from particles hitting the wall and changing their mass. The friction force at this order is relatively straightforward to compute because it involves only the direct interactions of particles with the wall. The amplitude for the process, using the WKB approximation for the eigenmodes, reads

$$\mathcal{M}_{1\to1} = 2p_0 , \tag{1.207}$$

then the average exchanged momentum is

$$\langle \Delta p_z \rangle = \int \frac{d^3\boldsymbol{q}}{(2\pi)^3 2q_0}\, (2\pi)^3 \delta^{(3)}(p-q) \cdot 4p_0^2 \cdot \Delta p_z \simeq 2p_0 \cdot \Delta p_z . \tag{1.208}$$

From here to get the friction we just need to integrate over the incoming flux

$$\mathcal{P}_{LO} = \int \frac{d^3\boldsymbol{p}}{(2\pi)^3 2p_0} \cdot \frac{p^z}{p_0} f(p) \cdot 2p_0 \cdot \Delta p_z \tag{1.209}$$

$$= \frac{\Delta m^2}{24} T_{\rm nuc}^2 \ , \tag{1.210}$$

where $\Delta m^2 = m_b^2 - m_s^2$ is the difference in mass across the different phases and where we used that the momentum change is given by

$$\Delta p_z = p^z - q^z \approx p_0 - \sqrt{p_0^2 - \Delta m^2} \approx \frac{\Delta m^2}{2p_0} \ , \tag{1.211}$$

where we assumed the relativistic limit $p_0 \gg \Delta m$ and

$$\int_0^\infty \frac{4\pi p^2 dp}{(2\pi)^3} \frac{1}{e^{p/T_{\rm nuc}} \pm 1} \frac{\Delta m^2}{2p} = \frac{\Delta m^2 T_{\rm nuc}^2}{24} \times \begin{cases} 1 & \text{boson} \\ \frac{1}{2} & \text{fermion} \end{cases} \ , \tag{1.212}$$

where $T_{\rm nuc}$ is the nucleation temperature. Thus, extending to a general particle content, we obtain

$$\mathcal{P}_{LO} = \sum_i \frac{n_i c_i}{24} \left(m_i^2(\text{TV}) - m_i^2(\text{FV}) \right) T_{\rm nuc}^2 \ , \tag{1.213}$$

where i runs over all the particles present in the thermal plasma, n_i is the number of d.o.f.s of the particle i, $c_i = 1(1/2)$ for bosons(fermions) while $m_i^2(\text{TV}, \text{FV})$ are the tree level field dependent masses computed at the true (false) vacuum.

NLO contribution

For next-to-leading order (NLO) computation, the process is commonly referred to as *transition radiation*[19], i.e. the splitting of a particle passing through the wall. This introduces additional complexity as one must account for the particles not only interacting with the wall but also emitting radiation. We will see that the NLO friction can be significantly higher than the LO friction, especially when emitting a gauge boson.

For a general splitting $1 \to 2$ it is convenient to parameterise the kinematics of the particles' momenta in the following way

$$p^\mu = \left(p_0, 0, 0, \sqrt{p_0^2 - m_a(z)^2} \right) \ , \tag{1.214}$$

$$q^\mu = \left((1-x)p_0, -k_\perp, 0, \sqrt{(1-x)^2 p_0^2 - m_b(z)^2 - k_\perp^2} \right) \ , \tag{1.215}$$

$$k^\mu = \left(x p_0, k_\perp, \sqrt{x^2 p_0^2 - m_c(z)^2 - k_\perp^2} \right) \ , \tag{1.216}$$

where we defined $x = k_0/p_0$ and we already used the conservation of energy $p_0 = q_0 + k_0$. Moreover, $m_i(z)$ are the masses of the three particles involved in the vertex as a function

[19] Transition radiation occurs when a charged particle crosses the boundary between two different media with varying electromagnetic properties. The sudden change in velocity of the particle as it moves from one medium to another results in the emission of radiation due to the disruption of the particle's electromagnetic field. The energy and frequency of the emitted radiation depend on the properties of the media and the energy of the charged particle.

of z, and $k_\perp = |\boldsymbol{k}_\perp|$. The mass change through the wall will be approximated as a sudden step

$$m_i(z) = m_{i,s}\,\theta(-z) + m_{i,b}\,\theta(z) \ . \tag{1.217}$$

Imposing the reality of q^z and k^z alongside the conservation of energy, $0 < x < 1$, we get the explicit shape of the allowed phase space, that is

$$\frac{\sqrt{k_\perp^2 + m_c(z)^2}}{p_0} \leq \ x \ \leq 1 - \frac{\sqrt{k_\perp^2 + m_b(z)^2}}{p_0} \ , \tag{1.218}$$

$$0 \leq k_\perp^2 \leq \frac{p_0^2}{4} - \frac{m_b(z)^2 + m_c(z)^2}{2} + \frac{\left(m_b(z)^2 - m_c(z)^2\right)^2}{4p_0^2} \ . \tag{1.219}$$

Now, one last ingredient that is missing is the amplitude of the process $a \to bc$, which reads

$$\mathcal{M} \equiv \int dz\, \chi_p(z) V(z) \chi_q^*(z) \chi_k^*(z) \ , \tag{1.220}$$

where χ_p, χ_q, and χ_k are the particles' wave functions, and $V(z)$ is the vertex function. The product of three wave functions in the $1 \to 2$ splitting is given by

$$\chi_p(z)\chi_q^*(z)\chi_k^*(z) \sim \exp\left[\int_{z_0}^{z} \left(\frac{m_a^2}{2p_0} - \frac{m_b^2 + k_\perp^2}{2k_0} - \frac{m_c^2 + k_\perp^2}{2k_0}\right) dz'\right] \ . \tag{1.221}$$

Then, the matrix element is expressed as:

$$\mathcal{M} = V_s \int_{-\infty}^{0} \exp\left[iz\frac{A_s}{p_0}\right] dz + V_h \int_0^{\infty} \exp\left[iz\frac{A_h}{p_0}\right] dz = 2ip_0 \left(\frac{V_h}{A_h} - \frac{V_s}{A_s}\right) \ , \tag{1.222}$$

where

$$A = m_a^2 - \frac{m_b^2}{x} - \frac{m_c^2}{1-x} - \frac{k_\perp^2}{x(1-x)} \ , \tag{1.223}$$

and $s(h)$ refers to the symmetric (higgsed) phase. The squared matrix element becomes

$$|\mathcal{M}|^2 = 4p_0^2 \left|\frac{V_b}{A_b} - \frac{V_s}{A_s}\right|^2 \ . \tag{1.224}$$

It has been emphasised in [95] that among all the possible emissions the one contributing the most to the pressure at high energies p_0 involves the emission of a (transverse) vector boson $X(p) \to X(q) + A_T(k)$, where A_T represents a transversely polarised vector boson and X can be a fermion, scalar, or a boson. For the case of a trilinear interaction involving a vector boson, we report a brief derivation here, while for all the rest we refer to [95, 96]. The interaction we have in mind is present in the scalar-QED theory, with a complex scalar field charged under a local $U(1)$, where the Lagrangian contains

$$\mathcal{L} \supset -ig(\phi^\dagger \partial_\mu \phi - \phi \partial_\mu \phi^\dagger) A^\mu \ , \tag{1.225}$$

producing a vertex function as follows

$$iV_\pm = g(p_\mu + q_\mu)\epsilon_\pm^\mu(k) \ , \tag{1.226}$$

where $\epsilon_\pm$ refers to the two polarisations for the transverse modes[20] and where the vertex function remains independent of phase (both V_b and V_s are identical) and squaring, contracting and summing over initial and final spins can be expressed as

$$|V|^2 = 4g^2 \frac{k_\perp^2}{x^2} \ , \tag{1.229}$$

where g denotes the gauge coupling constant. Then, the amplitude takes the form

$$|\mathcal{M}|^2 \approx 16 g^2 p_0^2 \frac{m_V^4}{k_\perp^2 (k_\perp^2 + m_V^2)^2} \ , \tag{1.230}$$

where $m_V = m_{c,h}$ and $m_{c,s} = 0$. Finally, we have all the ingredients to compute the friction from the process $\phi \to \phi + A_T$

$$\mathcal{P}_{NLO} = \int \frac{d^3\boldsymbol{p}}{(2\pi)^3 (4 p_0 q_0)} f(p) \int \frac{d^3\boldsymbol{k}}{(2\pi)^3 2k_0} \cdot |\mathcal{M}|^2 \cdot (p^z - q^z - k^z) \tag{1.231}$$

$$\approx \int \frac{d^3\boldsymbol{p}}{(2\pi)^3 4p_0^2} f(p) \int \frac{dx}{2x} \int \frac{\pi dk_\perp^2}{(2\pi)^3} \cdot \frac{16 g^2 p_0^2 m_V^4}{k_\perp^2 (k_\perp^2 + m_V^2)^2} \cdot \frac{k_\perp^2 + m_V^2}{2x p_0} \tag{1.232}$$

$$\approx \int \frac{d^3\boldsymbol{p}}{(2\pi)^3 2p_0} f(p) \cdot \frac{m_V p_0}{2\pi^2} \log\left(\frac{m_V}{gT}\right) \ , \tag{1.233}$$

where in the previous steps we integrated over the allowed PS and the integral over $k_\perp$, being divergent, has been regularised by cutting the integration at $k_\perp^{\min} \sim gT$, being the minimal value of the transverse momenta is cut in the IR. This has been done since we cannot trust our QFT at zero temperature for momenta lower than the typical momentum of the plasma particles in equilibrium, due to the screening of the long wavelength modes by the temperature effects and a proper treatment at finite temperature is needed. We can, then, schematically say that

$$\mathcal{P}_{NLO} \sim \frac{g^2}{2\pi^2} m_V \gamma_w T_{\text{nuc}}^3 \ . \tag{1.234}$$

We can observe that the pressure is primarily affected by the emission of *soft* vector bosons, resulting in the characteristic γ_w enhancement.

In summary, if the plasma does not exert sufficient friction on the bubble wall to halt its acceleration, the wall will continue to accelerate, reaching high γ factors. At leading order, the backward friction exerted by the medium on the bubble wall scales as $P_{1\to1} \sim m^2 T^2$, which attains a finite limit at large γ. The pressure driving the wall forward is generally of the same order, but it can be numerically larger, leading to a scenario where γ increases indefinitely, suggesting a potential "runaway" situation.

However, at the next order, transition radiation of wall-frame soft, massive vector bosons introduces an additional friction term, $P_{1\to2} \sim \gamma g^2 m T^3$. This term increases linearly with γ, thereby limiting the γ-factor of the wall and preventing an actual runaway.

[20] Starting from the functional form of k^μ in order to find the polarisation vectors we need to solve the system of equations

$$\epsilon(k) \cdot k = 0 \ , \qquad \epsilon^*(k) \cdot \epsilon(k) = -1 \ , \tag{1.227}$$

so that they take the following form, as found in ref. [96]

$$\epsilon_\pm(k) = \frac{1}{\sqrt{2 - 2\mu_c^2}} \left(0, \sqrt{1 - \mu_c^2 - \theta^2}, \pm i \sqrt{1 - \mu_c^2}, -\theta\right) \simeq \frac{1}{\sqrt{2}} (0, 1, \pm i, -\theta) \ , \tag{1.228}$$

where $\theta \equiv \frac{k_\perp}{x E_a}$ is the emission angle and $\mu_c \equiv \frac{m_c}{x E_a}$ is the mass fraction.

1.7 Summary and outlook

A FOPT proceeds through the nucleation and subsequent expansion of bubbles of the new phase, driven by the free-energy density difference, ΔV, between phases. If friction from the surrounding matter can be ignored, the bubble wall interpolating between the two phases will continue to expand with constant proper acceleration until the bubbles collide. In this scenario, most of the vacuum energy released is converted into the kinetic energy of the walls, a situation known as *runaway*. Conversely, if friction causes a pressure $\mathcal{P}$ that equilibrates the driving force $\mathcal{P} \simeq \Delta V$, the bubble wall reaches a constant subluminal terminal velocity, and energy is efficiently transferred to the medium.

The bubble velocity and the realisation of either regime critically affect the phenomenological consequences, such as the strength and spectral shape of the stochastic GW signal. Therefore, understanding the dynamics of an expanding domain wall in a medium is essential[21]. Analysing bubble-medium interactions is complex and remains an active area of research [74, 75, 77, 78, 94–96, 99–113]. Friction is generally a complex function of bubble velocity v_w and the surrounding degrees of freedom (d.o.f.). However, a distinction can be made between the low v_w regime, where a fluid description is appropriate, and the ultra-relativistic regime, $\gamma_w \equiv 1/\sqrt{1-v_w^2} \gg L_w \Gamma_{\text{int.}}$, where L_w is the wall thickness in its rest frame and $\Gamma_{\text{int.}}$ is the interaction rate between particles in the medium [114]. The third chapter focuses on the latter regime, where the wall interacts with individual particles.

A particle hitting the wall from the old phase can undergo several processes, organised as a perturbative expansion in the theory's couplings defined in the wall's background. The spontaneous breaking of translation symmetry means momentum perpendicular to the wall is no longer conserved. The average momentum lost $\langle \Delta p \rangle$ times the flux of incoming particles yields the pressure opposing the bubble's expansion. It is most convenient to work in the wall's rest frame.

At leading order, incoming particles either cross the wall or reflect. When reflections are neglected[22], we find:

$$\mathcal{P}^{\text{LO}}_{\gamma_w \to \infty} \simeq (\gamma_w n v_w) \langle \Delta p \rangle \simeq (\gamma_w n v_w) \frac{\Delta m^2}{2 \langle p^0 \rangle} \,, \tag{1.235}$$

where $\langle p^0 \rangle \propto \gamma_w T$ is the boosted energy of the incoming particle in the wall frame, $\Delta m \equiv \sqrt{\tilde{m}^2 - m^2}$ is the mass change between phases, and n is the number density in the plasma frame. This LO pressure is independent of γ_w and scales like $\propto T^2 \tilde{v}^2$ in the case of a thermal bath, where $\tilde{v}$ is the vacuum expectation value in the broken phase[23] [94, 106].

Later, the same authors analysed the next-to-leading order $1 \to 2$ processes in the same ultra-relativistic regime. Despite the cost of the coupling, they found that the emission of soft vector bosons gaining mass during the transition leads to a friction pressure scaling like $\mathcal{P}^{\text{NLO}} \propto \gamma_w$ [95], which eventually dominates over the LO effect. This soft emission is known as *transition radiation*. While [95] focused on particles emitted forward into the wall, [96, 115] also considered reflected emission and argued it was larger by a factor of four.

[21] In this thesis, we refer to any bubble wall interpolating between different phases of a theory in the planar limit as a domain wall, otherwise stated

[22] Reflections can be important and even dominant for intermediate relativistic γ_w [79].

[23] This leads to the so-called Bodeker-Moore (BM) criterion, $\mathcal{P}^{\text{LO}} < \Delta V$, for the wall to become relativistic. Assuming pressure monotonically increases with γ_w, the BM criterion was used as a rough *runaway* condition.

Subsequent studies only considered the emission of transverse vector polarisations, ignoring the effects of longitudinal ones. Analysing these modes is complicated by the rearrangement of particle d.o.f. across a gauge symmetry-breaking transition [116], particularly in the case of greatest interest. Moreover, amplitudes involving Nambu-Goldstone bosons (NGBs) can produce spurious divergences without proper care. Recently, it was shown that LO effects from longitudinal modes significantly impact pressure [79]. Thus, it becomes essential to properly account for their contribution at NLO. Additionally, frequent reliance on WKB approximations, which break down for the soft momenta dominating the emission phase space, weakens previous treatments.

1.7.1 Thesis structure

In this thesis, we will tackle all these features regarding cosmological FOPTs from different perspectives. In the next chapter, we analyse phase transitions in the minimal extension of the SM with a real singlet scalar field. The novelty of our study is that we identify and analyse in detail the region of parameter space where the FOPT can occur, particularly where the bubbles of true vacuum can reach relativistic velocities. The aim is to investigate how much fine-tuning is needed to have ultrarelativistic expanding bubbles. Moreover, this region is interesting as it can lead to the newly discussed baryogenesis and dark matter production mechanisms [97, 98].

After this study, we will come back to the weaknesses presented above in the computation of the friction in such ultrarelativistic limit. We will approach the calculation of transition radiation by quantising field theories in the translation-breaking background of a domain wall from first principles. We construct a complete orthonormal basis of 'left' and 'right' mover energy eigenstates[24], each wave mode having 'reflected' and 'transmitted' parts. We then relate these to *in* and *out* asymptotic eigenstates of four-momentum in the S-matrix language. In the case of vectors, the degrees of freedom across the wall are best described in terms of 'wall polarisations' τ and λ, as noted in [116]. The advantage is that $\tau_{1,2}$ and λ are not mixed with each other in the presence of the domain wall. The two sets coincide only for zero transverse momentum $\boldsymbol{k}_\perp = 0$ (normal incidence on the wall), where rotations around the direction of propagation are symmetric[25]. Additionally, in the case of gauge symmetry breaking, λ smoothly transitions from a Higgs d.o.f. on the symmetric side to a third massive vector d.o.f. on the broken side. We demonstrate how to perform calculations using this basis consistently and avoid the divergences that appear in a naive analysis.

In the fourth chapter, we analyse for the first time friction pressure on relativistic walls in phase transitions where gauge symmetry is restored, particularly motivated by the observation that this pressure can, in principle, be negative at leading order, since some particles lose mass by definition as they cross into the new phase. We find, however, that at NLO, the soft emission of vectors from a charged current leads to positive pressure scaling as the wall's Lorentz boost factor γ_w, similar to the case of gauge symmetry breaking. Contrary to the latter case, we find that the dominant contribution in single emission is safe from IR divergences and exhibits a much stronger dependence on the wall shape. Finally, we argue that in any phase transition, no multi-particle process on the

[24] Throughout this chapter, 'right-moving' denotes positive z-momentum particles and 'left-moving' denotes negative z-momentum particles.

[25] Starting from $\boldsymbol{k}_\perp = 0$, the general τ and λ polarisation vectors can be obtained by general transverse Lorentz boosts, a good symmetry of the theory. Thus orthogonality is obvious. In general, they are also distinguished by whether in unitary gauge the z-component of the vector A^μ is zero or not. See section 3.2.2.

wall can impart negative pressure greater than the leading order result, in the asymptotic limit of large velocity.

In the fifth and last chapter, we will present a different perspective on the friction acting on the bubble walls, i.e. from a hydrodynamic point of view. We will also extend the treatment at what we will define to be *inverse* PTs.

Chapter 2

Ultrarelativistic bubbles and some cosmological consequences

As mentioned earlier, this chapter will focus on the study of ultrarelativistic FOPTs and the degree of fine-tuning required to achieve such rapidly expanding bubbles. Among the many motivations for exploring this intriguing question, the origins of dark matter (DM) and the matter–antimatter asymmetry remain some of the most significant unresolved puzzles in early Universe cosmology. We will also investigate in detail the novel mechanisms proposed in [97, 98, 117] for DM production and baryon asymmetry generation during FOPTs.

FOPTs are known to be particularly useful for constructing baryogenesis models since they inherently satisfy the out-of-equilibrium condition required by one of Sakharov's criteria [118]. Applications of this mechanism to the electroweak phase transition have led to the seminal scenarios of electroweak baryogenesis [119, 120]. In the SM, the EWPT is expected to be a smooth crossover [121, 122]. However, this is not the case for various BSM frameworks, where successful scenarios of electroweak baryogenesis can be constructed (for a recent review, see [123]). The connection between DM and phase transitions is less direct, but there are classes of models where these two phenomena are strongly related (see, for example, [124–145]).

The focus of this chapter will be EWFOPT with very relativistic bubbles. In this context, collision between bubbles and particles in the plasma, as was shown recently [115], can lead to the production of new states with mass scale significantly larger than the scale of the phase transition[1]. These heavy states can serve as DM candidates [97] or their production and subsequent decay [98, 117], if accompanied with C, CP and baryon number violating interactions can lead to baryon asymmetry generation. The successful realisation of this scenario requires bubble expansion with ultra-relativistic velocities. Such bubble wall motion is known to be possible and is expected within certain classes of the potentials ([33, 62, 107, 147, 148]). However, in the case of electroweak phase transition, the requirement of ultra-relativistic velocities leads to very non-trivial constraints on the effective potential. In this chapter, we analyze in detail the simplest extension of the SM that can lead to a FOPT: real singlet scalar field. There have been numerous studies of phase transition in this type of scenario [149–161]. The Lagrangian can be restricted further by considering Z_2 [162] or Z_3 symmetries [163, 164]. Interestingly such a real singlet scalar field can appear in composite Higgs models [165] (see also [166–168] for studies pertaining to phase transition). However, most of the above mentioned works

[1]Note that this effect is different from the mechanism presented in [139, 146] where the heavy fields are produced by the collisions between different bubble walls.

did not analyze in detail the region of parameter space with relativistic bubbles since slow bubble wall velocities are preferred [119, 120] for the usual electroweak baryogenesis. We fill this gap by analysing in detail phase transitions in the real singlet extension of SM with an approximate Z_2 discrete symmetry, focusing on the parameter space which results in very fast bubble expansions.

This will permit us to evaluate the region of parameter space where Baryogenesis via relativistic bubble walls is viable and to put constraints on the mass scale of the dark sector responsible for CP and B violation. Implications for non-thermal DM production from bubble wall plasma particle collisions will also be considered.

The chapter is organised as follows: in section 2.1, we review the singlet extension of the SM and write the two field potential with thermal corrections. In section 2.2, we present the computation of the terminal velocity of the bubble wall in the ultra-relativistic regime, for the generic case and for SM. In section 2.3, we qualitatively discuss the different patterns of phase transitions and argue that only a two-steps PT can yield ultra-relativistic bubble wall motion. In section 2.4 we present a numerical study of the two-step PT analysing in detail the region with fast bubble motion. In section 2.5, we draw the consequences of our previous results for the production of heavy DM and Baryogenesis and in section 2.6, we comment on the GW signal induced by such strong transitions. Finally, in section 5.5, we summarise and conclude.

2.1 Review of the singlet extension of the SM

Let us start by reviewing the effective potential of the SM with a real scalar field (s). The scalar potential will be given by

$$V(\mathcal{H}, s) = -\frac{m_h^2}{2}(\mathcal{H}^\dagger\mathcal{H}) + \lambda(\mathcal{H}^\dagger\mathcal{H})^2 - \frac{m_s^2}{4}s^2 + \frac{\lambda_{hs}}{2}s^2(\mathcal{H}^\dagger\mathcal{H}) + \frac{\lambda_s}{4}s^4 \,, \tag{2.1}$$

where $\mathcal{H}$ is the SM Higgs doublet and $m_h \approx 125$ GeV is the physical mass of the Higgs. For simplicity, we will impose Z_2 symmetry on the potential to avoid the terms with odd powers of s field. As a result, when $\langle s\rangle = 0$, we avoid any scalar mixing terms which are constrained by the recent Higgs signal strength measurements [169]. The Higgs doublet can be decomposed as usual

$$\mathcal{H}^T = \left(G^+, \frac{h + iG^0}{\sqrt{2}}\right) , \tag{2.2}$$

where h is the usual Higgs boson getting a vev which is given by $v_{EW} = \sqrt{m_h^2/2\lambda} \approx 246$ GeV if $\langle s\rangle \equiv v_s = 0$.

2.1.1 Coleman–Weinberg potential

Next, we take into account 1-loop corrections which are encapsulated by the Coleman-Weinberg (CW) potential [9]

$$V_{CW} = \sum_{i=Z,h,W,t} \frac{n_i(-1)^F}{64\pi^2}\left[M_i^4\left(\log\frac{M_i^2}{M_{i0}^2} - \frac{3}{2}\right) + 2M_i^2M_{i0}^2\right] . \tag{2.3}$$

In this expression, M_i stands for the masses depending on the Higgs and singlet fields values, $M_i \equiv M_i(h, s)$, and M_{i0} are the field values from the tree-level vev, $M_{i0} \equiv M_i(v_{EW}, 0)$.

Then one can easily check that this potential corresponds to the following renormalisation conditions

$$\begin{aligned} &V_{\rm eff} = V_0 + V_{CW}, \\ &\left.\frac{dV_{\rm eff}}{dh}\right|_{(h,s)=(v_{EW},0)} = 0, \qquad \left.\frac{d^2V_{\rm eff}}{dh^2}\right|_{(h,s)=(v_{EW},0)} = m_h^2 \,. \end{aligned} \tag{2.4}$$

eq.(2.3) cannot be used directly for contributions of the Goldstone bosons, since their masses vanish in the true vacuum and the CW potential is IR divergent. However, the solution to this issue was suggested in ref. [21] which emphasised that the physical Higgs mass is defined at $p^2 = m_h^2$ and the effective potential at $p^2 = 0$ (see for details ref. [21]). Thus it would be better to use a modified renormalisation condition

$$\left.\frac{d^2V_{\rm eff}}{dh^2}\right|_{(h,s)=(v_{EW},0)} = m_h^2 - \Sigma\left(p^2 = m_h^2\right) + \Sigma\left(0\right) \,, \tag{2.5}$$

where the differences in self-energies are taking into account the running of self-energy from $p^2 = 0$ to $p^2 = m_h^2$. In this case, the IR divergences in $\Sigma(0)$ due to the virtual Goldstone bosons are cancelled against the IR divergences of $V_{\rm eff}$. In practice, at the end of this renormalisation procedure, the contribution of the Goldstone bosons is given by

$$V_{CW}^{GB}(h) = \sum_{i=G} \frac{n_G}{64\pi^2} M_{G^{\pm},0}^4(h)\left[\log\frac{M_G^2}{m_h^2} - \frac{3}{2}\right] . \tag{2.6}$$

The number of d.o.f, masses of various particles and the scalar mass matrix as a functions of h, s are given by

$$\begin{aligned} &n_{W^\pm} = 6, \qquad n_Z = 3, \qquad n_{G^{\pm},0} = 3, \qquad n_t = 12 \,, \\ &M_{W^\pm}^2(h) = \frac{g^2h^2}{4}, \quad M_Z^2(h) = \frac{g^2+g'^2}{4}h^2, \quad M_{G^{\pm},0}^2(h) = -\frac{m_h^2}{2} + \lambda h^2 + \lambda_{hs}s^2, \quad M_t^2(h) = \frac{y_t^2h^2}{2} \,, \\ &M^2(h,s) = \begin{pmatrix} 3\lambda h^2 + \frac{\lambda_{hs}}{2}s^2 - \frac{m_h^2}{2} & \lambda_{hs}sh \\ \lambda_{hs}sh & 3\lambda_s s^2 + \frac{\lambda_{hs}}{2}h^2 - \frac{m_s^2}{2} \end{pmatrix} . \end{aligned} \tag{2.7}$$

As a side remark, in the region where the Higgs $h \to 0$ and $s \sim O(v_{EW})$, there will be two scales involved in the problem: the value of the singlet field s and the masses of the SM particles $M_{W,Z,t}(h \to 0, s) \to 0 \ll s$. This type of two scale potential has been studied in the past [170], by using two different renormalisation scales. It was concluded that resummation is needed when the $\log\left(M_i(0,s)/s\right)$ is large enough to cancel the loop suppression. Although we have two largely separated scales, we have checked that for our region of the parameter space, such a resummation is not necessary.

2.1.2 Finite temperature potential

The temperature and the density effects can be taken into account by complementing the zero temperature potential with thermal corrections (see for example [6, 14]),

$$V(T, M_i) = V_{\rm eff}^{T=0}(M_i) + V_T(M_i) \,. \tag{2.8}$$

In eq.(2.8), $V_{\rm eff}^{T=0}(M_i)$ is the potential we computed in the previous subsection and the thermal potential $V_T(M_i)$ is given by

$$V_T(M_i(h,s)) = \sum_{i\in B}\frac{n_i}{2\pi^2}T^4 J_B\left(\frac{M_i^2(h,s)}{T^2}\right) - \sum_{i\in F}\frac{n_i}{2\pi^2}T^4 J_F\left(\frac{M_i^2(h,s)}{T^2}\right),$$
$$J_{B/F}(y^2) = \int_0^\infty dx\; x^2 \log\left[1 \mp \exp\left(-\sqrt{x^2+y^2}\right)\right]. \tag{2.9}$$

However, to save computation time, we use the approximate expansion of the function $J_{B/F}(y^2)$ as given in ref. [14]:

$$J_B(y^2) = \begin{cases} -\frac{\pi^4}{45} + \frac{\pi^2}{12}y^2 - \frac{\pi}{6}y^3 - \frac{y^4}{32}\log\left[\frac{y^2}{16\pi^2\exp[3/2-2\gamma]}\right], & y^2 \ll 1, \\ -\sum_{n=1}^{m>3}\frac{1}{n^2}y^2 K_2(yn), & y^2 \gg 1, \end{cases}$$
$$J_F(y^2) = \begin{cases} \frac{7\pi^4}{360} - \frac{\pi^2}{24}y^2 - \frac{y^4}{32}\log\left[\frac{y^2}{\pi^2\exp[3/2-2\gamma]}\right], & y^2 \ll 1, \\ -\sum_{n=1}^{m>3}\frac{(-1)^n}{n^2}y^2 K_2(yn), & y^2 \gg 1. \end{cases} \tag{2.10}$$

where $\gamma \approx 0.577$ is the *Euler constant*, and $K_2(z)$ are the second-kind Bessel function. To account for dangerously divergent higher loops due to the Daisy diagrams at finite temperature, we follow the so-called "Truncated-Full-Dressing" procedure [14][2]. Doing so, the full one-loop potential becomes

$$V(h,s,T) = V_{\rm tree}(h,s) + \sum_i\left[V_{CW}\left(M_i^2(h,s)+\Pi_i(h,T)\right) + V_T\left(M_i^2(h,s)+\Pi_i(h,T)\right)\right], \tag{2.11}$$

where $\Pi_i(T)$ are the thermal masses of various degrees of freedom. In the real singlet extension of the SM [14], the expressions of the thermal masses read

$$\text{Scalar:}\qquad \Pi_h(T) = T^2\left(\frac{3g^2}{16}+\frac{g'^2}{16}+\frac{\lambda}{2}+\frac{y_t^2}{4}+\frac{\lambda_{hs}}{24}\right), \qquad \Pi_s(T) = T^2\left(\frac{\lambda_{hs}}{6}+\frac{\lambda_s}{4}\right), \tag{2.12}$$

$$\text{Gauge:}\qquad \Pi_g^L(T) = T^2\,\mathrm{diag}\left(\frac{11}{6}g^2, \frac{11}{6}(g^2+g'^2)\right), \qquad \Pi_g^T(T) = 0, \tag{2.13}$$

where $\Pi_g^L(T)$ denote the thermal mass of the *longitudinal* mode of the gauge bosons, while transverse modes $\Pi_g^T(T)$ are protected by gauge invariance and thus do not receive a mass at leading order in perturbation theory.

2.2 Velocity of the EW bubbles

After having introduced all the necessary concepts and ingredients to quantitatively study the FOPTs, like in section 1.3 and section 1.4, let us proceed to the computation of the

[2]Recently for the singlet scalar extensions of the SM have been proposed more sophisticated method for computing the thermal potential with two loop dimensional reduction to the three dimensional effective field theory see [171, 172].

bubble wall velocity v_w. The dynamics of the bubble wall motion is controlled by the driving force due to the potential differences between the false and true vacuum

$$\Delta V \equiv V_{\rm false} - V_{\rm true} \ , \tag{2.14}$$

and the friction due to finite temperature effects. As already stated in the previous chapter, the calculation of the friction is generically a very complicated problem, however for the ultra-relativistic bubble motion at leading order (LO - tree level) very simple expressions have been obtained [94, 106] for the pressure force from friction,

$$\Delta \mathcal{P}_{\rm LO} \simeq \sum_i g_i c_i \frac{\Delta M_i^2}{24} T_{\rm nuc}^2 \ , \tag{2.15}$$

where ΔM_i^2 is the change in the mass of the particle i during the PT, $c_i = 1\,(1/2)$ for bosons (fermions) and g_i is the number of d.o.f of the incoming particle. eq.(2.15) assumes that the masses of the particles outside of the bubble are less than the temperature, otherwise, the friction will have an additional Boltzmann suppression $\propto \exp[-M_{\rm false}/T]$. Interestingly the production of heavy particles can also contribute to the friction at the same order [115]

$$\Delta \mathcal{P}_{\rm LO}^{\rm mixing} \propto v^2 T^2 \Theta(\gamma_w T_{\rm nuc} - M_{\rm heavy}^2/v) \ , \tag{2.16}$$

where v is the vev of the Higgs field and we review the heavy particle production later in the section 2.5.1. One can see that the friction (pressure from plasma on the bubble wall) becomes velocity independent so that permanent accelerating (runaway) behaviour of the bubble expansion becomes possible. However, for theories where the gauge bosons receive a mass during the phase transition, this is not the case and the effect with multiple gauge boson emissions, leads to the additional contribution (NLO) to the pressure which scales as [95, 96, 115, 134]

$$\Delta \mathcal{P}_{\rm NLO} \propto \sum_a g_a g_{gauge}^3 \gamma_w T_{\rm nuc}^3 v \ . \tag{2.17}$$

At this point, we can see that bubbles will keep accelerating till the moment when NLO friction becomes large enough to balance the driving force

$$\Delta V = \Delta \mathcal{P}_{\rm LO} + \Delta \mathcal{P}_{\rm LO}^{\rm mixing} + \Delta \mathcal{P}_{\rm NLO} \ , \tag{2.18}$$

which will set the $\gamma_w^{\rm terminal}$ the bubble can reach,

$$\gamma_w^{\rm terminal} \sim \left(\frac{\Delta V - \Delta \mathcal{P}_{\rm LO} - \Delta \mathcal{P}_{\rm LO}^{\rm mixing}}{T_{\rm nuc}^3 v} \right) . \tag{2.19}$$

Note that we can be as well in the situation where the percolation (bubble collision) starts before the terminal $\gamma_w^{\rm terminal}$ is reached.

2.2.1 Friction forces during the electroweak phase transitions

Let us apply the discussion of the previous section to the EWPT. Our main interest will be the possibility of heavy particle production which can later source baryogenesis and DM production following the ideas in [97, 98, 115, 117]. The heavy particle production (see also the discussion in section 2.5.1) happens due to the collision between the plasma particles and the bubble wall. The typical centre of mass energy for such a process will

be roughly $\sim \sqrt{\gamma_w T v_{EW}}$, thus γ_w will be controlling the maximal mass of the new fields that can be produced. To calculate γ_w in the context of the EWPT, we need to know the forces acting on the bubble wall.

The LO friction from the top, Z, and W takes the form

$$\Delta\mathcal{P}^{SM}_{\rm LO} \approx T^2_{\rm nuc} v^2_{EW}\left(\frac{y_t^2}{8}+\frac{g^2+g'^2}{32}+\frac{g^2}{16}\right) \approx 0.17\, T^2_{\rm nuc} v^2_{EW}. \tag{2.20}$$

There is also a contribution to the LO friction from the singlet and Higgs scalars, however, it depends on the masses of these fields in the false vacuum and we find it to be numerically subleading compared to the estimate in eq.(2.20)[3]. In our numerical calculation we took this additional contribution into account, however, for the current discussion it is sufficient to use eq.(2.20). This gives a rough condition on the nucleation temperature for the transition to become ultra-relativistic

$$\Delta V > 0.17\, T^2_{\rm nuc} v^2_{EW} \qquad \text{(relativistic wall condition)}. \tag{2.21}$$

The computation of the NLO friction in the SM has been carried out in [96] and the following approximate expression has been derived:

$$\Delta\mathcal{P}^{SM}_{\rm NLO} \approx \left[\sum_{abc} \nu_a g_a \beta_c C_{abc}\right] \frac{\kappa\zeta(3)}{\pi^3} \alpha M_Z(v_{EW}) \gamma_w \log\frac{M_Z(v_{EW})}{\mu} T^3_{\rm nuc}\,, \tag{2.22}$$

where $\nu_a = 1(3/4)$ for a a boson (fermion), g_a is the number of degrees of freedom of a and $M_{g,i}(v_{EW})$ is the mass of the gauge boson inside the bubble. C_{abc} represents the coupling which appears in the vertex (see appendix 2.C), $\beta_{c=Z^0} = 1$, and $\beta_{c=W^\pm} = \cos\theta_W = M_W/M_Z$, $\alpha = e^2(v_{EW})/4\pi \sim 1/128$ is the electromagnetic fine structure constant. The renormalisation scale μ has to be understood as the lower cut-off for the integration over soft momentum, typically the thermal mass $\mu \propto \alpha_i^{1/2} T_{\rm nuc}$ [115]. The κ factor is introduced [96] to account for the contributions of both reflected and transmitted bosons and is approximately equal to $\kappa \sim 4$. The sum in the square brackets is approximately equal to

$$\left[\sum_{abc} \nu_a g_a \beta_c C_{abc}\right] \approx 157\,, \tag{2.23}$$

see appendix 2.C for details. At this point, we can compute the terminal wall velocity by balancing the pressure against the driving force

$$\Delta V - \Delta\mathcal{P}^{SM}_{\rm LO} = \Delta\mathcal{P}^{SM}_{\rm NLO}(\gamma_w = \gamma_w^{\rm terminal}) \quad \text{(Terminal velocity criterion)} \tag{2.24}$$

$$\Rightarrow \gamma^{\rm terminal} \sim 6 \times \left(\frac{\Delta V - \Delta\mathcal{P}^{SM}_{\rm LO}}{(100\text{ GeV})^4}\right)\left(\frac{100\text{GeV}}{T_{\rm nuc}}\right)^3 \frac{1}{\log\frac{M_z}{gT}}\,. \tag{2.25}$$

Taking into account that $(\Delta V - \Delta\mathcal{P}_{\rm LO})/(100\text{ GeV})^4 \lesssim \mathcal{O}(1)$, we can see that the bubbles will become ultra-relativistic, *i.e.* $\gamma^{\rm terminal} \gg 1$ only if $T_{\rm nuc}$ is significantly lower than the scale of the phase transition ~ 100 GeV.

[3] These contributions are smaller due to the number of d.o.f. and possible Boltzmann suppression factors $\propto \exp[-M_{\rm false}/T]$.

2.3 Phase transition in the singlet extension

After the preparatory discussion in the previous sections 2.1 and 2.2, we can proceed to the analysis of phase transition in the model with the singlet field, eq.(2.1). Our analysis will be focused on the region of parameter space with relativistic bubble expansion, for other studies of phase transition in SM plus Z_2 real singlet scalar, see Refs. [162, 173–175].

In the previous section 2.2, we have seen that the velocity of the bubble expansion is fixed by the balance between the friction from the plasma and the driving force. At low temperatures the friction is suppressed (see eq.(2.20)-(2.22)) so that we expect the bubbles to become relativistic (large Lorentz $\gamma_w^{\text{terminal}}$ factor).

Let us check whether low nucleation temperatures are feasible in the singlet extension. We will assume that Z_2 remains unbroken in the true vacuum in order to avoid to constraints from the Higgs-scalar mixing (see for example [176]). Then in the model with Z_2 odd singlet, the phase transition can occur in two ways: one-step $(\langle h\rangle = 0, \langle s\rangle = 0) \to (v_{EW}, 0)$ and two-steps[4] $(\langle h\rangle = 0, \langle s\rangle = 0) \to (0, \langle s\rangle|_{\neq 0}) \to (v_{EW}, 0)$ [157, 162, 174], and each of these phase transitions can be first or the second order. We review both of these scenarios of phase transitions in order to understand in what case it is possible to obtain relativistic bubbles.

2.3.1 One-step phase transition

This case has been largely studied in the literature [162, 174] and we will not provide a complete description of it. In this scenario, the singlet never gets a vev, and all of its effects reduce to the additional contributions to the Higgs potential from Coleman-Weinberg terms and thermal corrections. However, it turns out that relativistic bubbles are very unlikely for such phase transitions (see also results in [162]). In the limit when $|m_s| \ll T_c$ we can show analytically that this is indeed the case. Near the origin $h \to 0$, the potential in h direction is dominated by the $\propto h^2$ terms

$$V_{\text{dominant}}(h \to 0, s = 0, T) = \frac{m^2_{\text{eff}}(T)}{2} h^2 + \dots \ . \tag{2.26}$$

The effective mass m^2_{eff} include the tree-level terms and the leading thermal contributions and is approximately equal to

$$m^2_{\text{eff}}(T) \simeq -m_h^2 + T^2 \left(\frac{m_h^2}{4v_{EW}^2} + \frac{y_t^2}{4} + \frac{g^2 + g'^2}{16} + \frac{g^2}{8} + \frac{\lambda_{hs}}{24} \right) > 0 \ . \tag{2.27}$$

The FOPT can happen only if $m^2_{\text{eff}}(T) > 0$. Then assuming perturbative values of the coupling λ_{hs} we can estimate the lowest temperature where the FOPT can occur to be $T^{\text{nuc}}_{\text{min}} \gtrsim 100$ GeV. Comparing this value with the discussion in the section 2.2.1 we can see that the bubble wall velocities will always satisfy $\gamma_w \lesssim 10$. As mentioned before, we are interested in the expansions with much larger γ_w factors, so that we do not discuss one step phase transition further.

2.3.2 Two step FOPT with relativistic bubbles

Two-steps realisations of the EWPT have already been studied in many works, see for example [157, 162, 174, 177–181]. The novelty of our study is that we will be focusing

[4] We will see later that at temperatures $T \ll T_c$ Coleman-Weinberg potential can shift a little bit the false vacuum position to $(\delta v_h, v_s)$ where $\delta v_h \ll v_s, v_h$.

on the parameter space with relativistic bubbles which was previously ignored. We organise the discussion as follows: In section 2.3.2, we show qualitative results based on the approximate treatment of the potential and then in section 2.4 we present the exact numerical results obtained with our code. The two step phase transition

$$(0,0) \to (0,\langle s\rangle) \to (v_{EW},0)\ , \tag{2.28}$$

can happen if the m_s^2 parameter of eq.(2.1) is positive. In this case, it is convenient to parameterise the Lagrangian in the following way

$$V_{\rm tree}(h,s) = -\frac{m_h^2}{4}h^2 + \frac{m_h^2}{8v_{EW}^2}h^4 - \frac{m_s^2}{4}s^2 + \frac{\lambda_{hs}}{4}s^2h^2 + \frac{m_s^2}{8v_s^2}s^4\ . \tag{2.29}$$

where $v_{EW} = \sqrt{m_h^2/2\lambda}$ GeV and $v_s = \sqrt{m_s^2/2\lambda_s}$ correspond to the local minima at $(\langle h\rangle = v_{EW}, \langle s\rangle = 0)$ and $(\langle h\rangle = 0, \langle s\rangle = v_s)$ respectively. The origin of two-step PT can be intuitively understood from the following considerations. For simplicity let us ignore the Coleman-Weinberg potential and restrict the discussion by considering only the thermal masses. Then the potential will be given by

$$\begin{aligned} V(\mathcal{H},s) &\approx V_{\rm tree}(\mathcal{H},s) + \frac{T^2}{24}\left[\sum_{bosons} n_i M_i^2(\mathcal{H},s)) + \frac{1}{2}\sum_{fermions} n_F M_F^2(\mathcal{H},s)\right]\ , \\ &= V_{\rm tree}(\mathcal{H},s) \\ &+ T^2\left[h^2\left(\frac{g'^2}{32} + \frac{3g^2}{32} + \frac{m_h^2}{8v_{EW}^2} + \frac{y_t^2}{8} + \frac{\lambda_{hs}}{48}\right) + s^2\left(\frac{m_s^2}{16v_s^2} + \frac{\lambda_{hs}}{12}\right)\right]. \end{aligned} \tag{2.30}$$

From this expression, we can clearly see that the temperatures when the minima with non zero vevs appear for the Higgs and singlet fields can be different. Then it can happen that the Z_2 breaking phase transition occurs before the EW one. This means that there will be first a phase transition from $(0,0) \to (0,v_s)$. After this phase transition, the Universe keeps cooling down and the minimum with $\langle h\rangle \neq 0$ will be generated. By choosing the appropriate values of masses and couplings we can make sure that the minimum with $(v_{EW},0)$ is the true minimum of the system. The transition $(0,v_s) \to (v_{EW},0)$ will be of the first order if there is a potential barrier between the two minima. One of the necessary condition in this case will be $\partial^2 V/\partial h^2|_{s=v_s,h\to 0} > 0$, which using eq.(2.30) we get

$$\frac{-m_h^2}{4} + \frac{\lambda_{hs}v_s^2}{4} + T^2\left(\frac{g'^2}{32} + \frac{3g^2}{32} + \frac{m_h^2}{8v^2} + \frac{y_t^2}{8} + \frac{\lambda_{hs}}{48}\right) > 0\ . \tag{2.31}$$

From this discussion, we can see that there are qualitatively two different cases depending on whether the potential barrier between two minima remains or disappears at zero temperature, *i.e.* when $m_h^2 \gtrless \lambda_{hs}v_s^2$. In the first case, the phase transition will necessarily happen before the "No Barrier"(NB) temperature

$$T^{\rm NB} = \sqrt{\frac{m_h^2 - \lambda_{hs}v_s^2}{\frac{g'^2}{8} + \frac{3g^2}{8} + \frac{m_h^2}{2v^2} + \frac{y_t^2}{2} + \frac{\lambda_{hs}}{12}}} \sim \frac{v_s\sqrt{-\lambda_{hs} + \left(\frac{m_h}{v_s}\right)^2}}{0.8}\ , \tag{2.32}$$

since the bounce action drops once the potential barrier between two minima reduces.

In the other case, when the barrier remains even for zero temperature potential, the phase transition is obviously of the first order. However, it might happen that the tunnelling rate is too slow and the system remains stuck in the false vacuum.

From eq.(2.31) we can see that the size of the potential barrier between the two minima is controlled by the coupling λ_{hs}. Increasing this parameter will enhance the potential barrier and will lead to the reduction of $T^{\rm NB}$ so that $(v_s, 0)$ remains a local minimum even at zero temperature. At some point we expect the potential barrier to become so large that the system will remain trapped in the false vacuum forever. From this discussion, we can expect that the lowest temperatures will be achieved at the boundary of the region where no PT can occur. The lowest temperature will correspond to the (global) minimum of S_3/T controlling the tunnelling rate, as explained later in section 2.4. If this minimum happens at temperatures much lower than $T_{\rm crit}$, then there will be super-cooling ($T_{\rm nuc} \ll T_{\rm crit}$). Even though this discussion was made by considering only the thermal masses in the potential, numerically we find that for the effective potential with truncated full dressing [14] the qualitative behaviour does not change, and only explicit conditions for m_h^2 and $T_{\rm min}^{\rm nuc}$ are modified.

At last, we always check whether the condition for the EWSB minimum to be the global minimum at zero temperature is satisfied:

$$m_s^2 v_s^2 < m_h^2 v_{EW}^2 \qquad \text{(EWSB is global minimum)}\,, \tag{2.33}$$

where the above equation is valid up to small loop-level corrections.

2.4 Numerical results

After the qualitative discussion, let us proceed to the numerical calculations. The bounce action for $(0, v_s) \to (v_{EW}, 0)$ was computed using our own dedicated code (cross checked against `FindBounce` [182]) and we relegate the details and methods of this calculation to Appendix 2.A. We parameterise our model in terms of (m_s, λ_{hs}, v_s) parameters (see eq.(2.29)). Instead of analysing all the possible values of m_s, in this section we report the results (see fig.2.1 left panel) by fixing $m_s = 125$ GeV (there is no particular reason for this value of m_s and the results for the other values of m_s are similar and are shown in the appendix 2.B). In the plane (see fig.2.1) $v_s - \lambda_{hs}$, we identify four regions with different behaviours under the phase transition. The blue region shows second order transition when there is no barrier between the two separated vacuum. Next to it there is a light red region where the transition is of the first order. We indicate separately (dark red) the region, where the transition is of the first order and the bubbles are relativistic. In particular, the boundary between the regions with relativistic and non-relativistic bubbles is defined by the criteria of eq.(2.21), *i.e.* when the LO pressure for relativistically expanding bubbles is less than the driving force. At last, there is NO PT region, where the system remains stuck in the false vacuum since the tunnelling rate is too small.

The structure of the diagram (on the fig.2.1 top−left panel) can be easily understood from the qualitative discussion in the previous section. Indeed, keeping v_s fixed, the size of the potential barrier is controlled by the coupling λ_{hs}. Moving from left to right the size of the potential barrier increases and we are gradually moving from the region of second order phase transition → FOPT → FOPT with relativistic bubbles → no PT region. Similarly moving up (increasing v_s for fixed values of λ_{hs}) also corresponds to the increase of the potential barrier as we pass through the regions with different PT in the same order. On the upper axis, we report the physical mass of the singlet in the true

vacuum $M_s(v_{EW}, 0)$ and exclude the constrained region where $h \to ss$ is kinematically allowed (the grey meshed region).

Next we plot the values of $T_{\rm nuc}$ and $\gamma_w^{\rm terminal}$ as a function of (λ_{hs}, v_s) (fig.2.1). As discussed in the previous section, the region with the smallest values of the nucleation temperature (thus the fastest bubbles) is located near the "NO PT" region, *i.e.* where the system remains trapped in the false vacuum. The blue dot on the $T_{\rm nuc}$ plot indicates the last point we have found before the system enters the regime of no phase transition (NO PT). In the bottom right we plot $M_{\rm max} = \sqrt{\gamma_w T_{\rm nuc} v_{EW}}$ quantity which indicates the maximal energy in the c.o.m frame for the plasma particle−bubble wall collision, which corresponds to the largest mass of the heavy particles we can produce (see discussion in sec 2.5.1).

In order to better understand the dependencies of $T_{\rm nuc}$ and γ_w on the parameters of the model, it is useful to separate further the parameter space depending on whether the potential barrier disappears at zero temperature or not. This is important since the bounce action in such cases has very different dependencies on the temperature. See for example fig.2.2, where we have plotted the S_3/T for $v_s = 170, m_s = 125$ GeV for the various couplings λ_{hs}. In the case when the potential barrier disappears at some temperature $T^{\rm NB}$ the function S_3/T drops to zero, but if the barrier remains even at zero temperature S_3/T has a global minimum for $T \neq 0$ which will be controlling the lowest nucleation temperature possible.

2.4.1 No potential barrier at zero temperature

Let us start by defining the region where there is no potential barrier at zero temperature. In fig.2.1, we demonstrate the curves where the barrier disappears for various values of the temperatures ($T^{\rm NB}$). For $T^{\rm NB} = 0$ case, the approximate curve can be obtained analytically by looking at the leading terms in the zero temperature CW potential

$$\lambda_{hs} \lesssim \frac{m_h^2}{v_s^2} - \frac{n_t y_t^4}{32\pi^2} \frac{v_{EW}^2}{v_s^2} \,. \tag{2.34}$$

The agreement between this equation and the exact $T^{\rm NB} = 0$ curve is at the level of a few permille discrepancies. To the right of $T^{\rm NB} = 0$ curve, the potential barrier between the two minima remains even at zero temperatures. For the values $v_s \gtrsim 200$ GeV, we find that the line $T^{\rm NB} = 0$ approximately coincides with the boundary of no phase transition region (where the system remains stuck in the false vacuum) but obviously the boundary of "NO PT" is always to the right of $T^{\rm NB} = 0$ curve. The size of this narrow strip is of the order 10^{-4} in λ_{hs} values. One can see it from the $T_{\rm nuc}$ panel of fig.2.1 where we have indicated the value of λ_{hs} when $T_{\rm NB} = 0$ by vertical thin line and red dot (for intersection) and the position of the blue dot which is the last point where the transition is of the first order before we enter NO PT region. The boundaries of this region were obtained by numerical calculations where we have scanned λ_{hs} parameter with a step 10^{-6}. We postpone the discussion of the FOPT in this narrow region to the next section 2.4.2.

In this section, we restrict our discussion only on the region to the left of $T^{\rm NB} = 0$ curve. Then the phase transition will be always completed before the Universe cools down to $T^{\rm NB}$, *i.e.* $T^{\rm NB} < T_{\rm nuc}$, which provides a lower bound for the nucleation temperature. At the same time, the velocity of the bubbles becomes largest for the smallest possible values for the nucleation temperature. So that the fastest bubbles will be near $T^{\rm NB} = 0$ curve. Looking at fig.2.1 we can see that the largest γ_w (Lorentz boost factor) and lowest nucleation temperatures happen for $v_s \gtrsim 200$ GeV, where the $T^{\rm NB} = 0$ curve passes

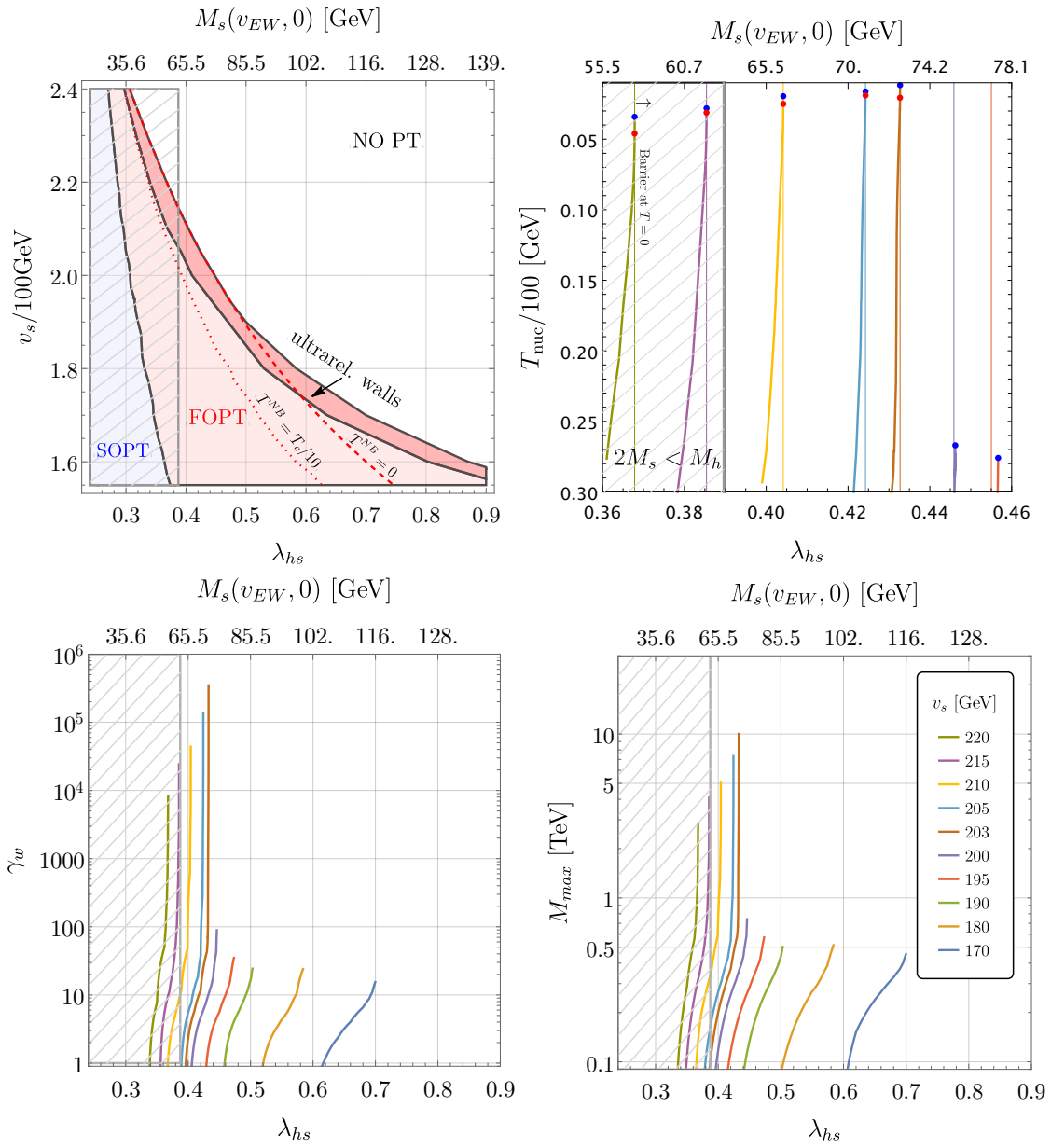

Figure 2.1: Top-Left: Scan of the parameter space in the plane $\lambda_{hs} - v_s$ for $m_s = 125$ GeV. The four regions are as follows: i) white - NO PT, the region where the transition never completes because the barrier remains at zero temperature and the function S_3/T never passes below the nucleation condition, ii) light and dark red are the regions where the FOPT happens. Dark (light) red corresponds to the region with relativistic (non-relativistic) bubble expansion. The boundary between two regions is given by eq.(2.21) iv) blue - the phase transition is of the second order. The grey meshed region is the one in which $M_s(v_{EW},0) < m_h/2$, that is constrained from collider experiments. **Top-Right and Bottom**: the dependencies of $T_{\rm nuc}, \gamma_w,\ M_{max}$ on the λ_{hs} coupling for $m_s = 125$ GeV. The blue dot on the Top-Right plot designates the end of the curve when the tuning becomes 10^{-6} and the red dot signals the appearance of a barrier at zero temperature (all the points above the red dot have a barrier at $T = 0$). For the last three plots, we varied the λ_{hs} parameter with the steps of 10^{-6}. The value of v_s is encoded in colour according to the bottom-right plot.

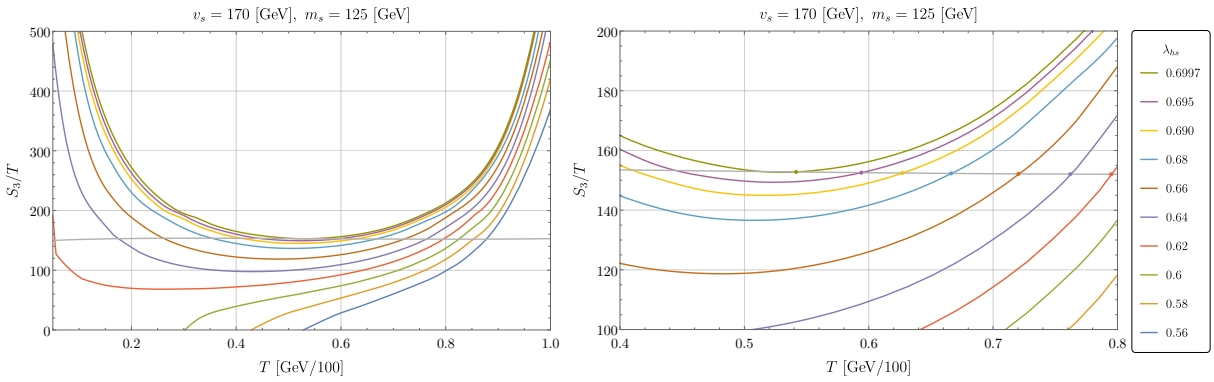

Figure 2.2: Left: S_3/T function with $v_s = 170$ GeV and $m_s = 125$ GeV. We observe that the nucleation temperature saturates around $T_{\rm nuc} \approx 54$ GeV. The horizontal gray line satisfy the nucleation condition $S_3/T_{\rm nuc} = \frac{3}{2}\log\left(S_3/2\pi T_{\rm nuc}\right) + 4\log\left(T_{\rm nuc}/H\right)$. **Right**: Zooming in on the region with lower nucleation temperatures.

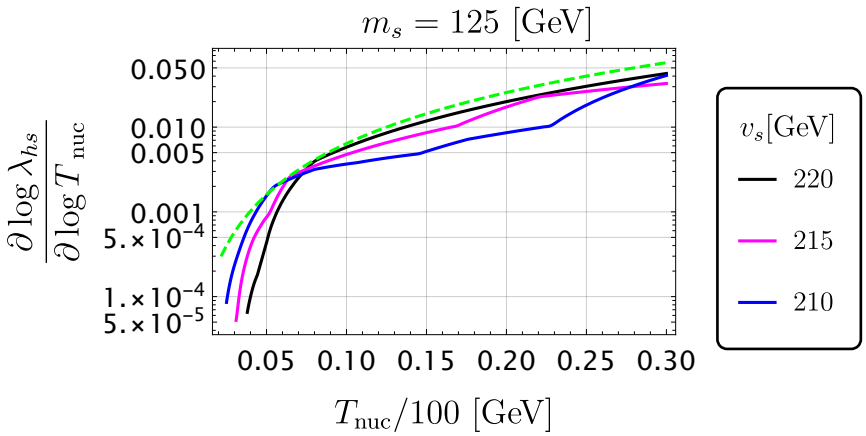

Figure 2.3: Tuning of the coupling λ_{hs} as a function of the nucleation temperature. The dashed green line represents the naive tuning $\sim (T_{\rm nuc}/m_h)^2$. We observe that this naive estimation for the tuning is rather precise at large nucleation temperature but can underestimate the tuning by one order of magnitude for very low nucleation temperature.

very close to the NO PT boundary. The shape of the lines in fig.2.1 clearly indicates the necessity of tuning in order to obtain low nucleation temperatures (large γ_w). In particular, for the values of $v_s \gtrsim 200$ GeV we can see that the nucleation temperature drops by choosing λ_{hs} close to the NB value (similarly γ_w becomes maximal see fig.2.1). We can estimate this tuning by looking at $\partial \log \lambda_{hs}/\partial \log T_{\rm nuc}$ quantity (analogue of Giudice-Barbieri [183] measure of the tuning) as a function of $T_{\rm nuc}$. This result agrees with our expectation from the steepness of the curves in the fig.2.3 and with the naive tuning expectation which scales as $\sim \left(T_{\rm nuc}/m_h\right)^2$[5].

At last, we would like to remind that the discussion in this section always assumed that the phase transition completes before the potential barrier disappears. We have checked numerically that this is always the case. Indeed the time of the phase transition

[5]This expression follows eq.(2.31) if we require the cancellation between the terms independent of temperature.

is given approximately by the bubble radius at the moment of percolation [36, 184]

$$R_\star \equiv \frac{(8\pi)^{1/3}}{\tilde{\beta}} = \left(\int_{T_{\rm per}}^{T_{\rm crit}} \frac{dT}{T} \frac{\Gamma(T)}{H(T)} \left(\frac{T_{\rm per}}{T} \right)^3 \right)^{-1/3} . \tag{2.35}$$

This radius is related to the $\beta \equiv -\frac{d}{dt}\frac{S_3}{T} = HT\frac{d}{dT}\frac{S_3}{T}$ parameter by an approximate relation [184]

$$\left.\frac{\beta}{H}\right|_{T_{\rm per}} \simeq \frac{\tilde{\beta}}{H} = \frac{(8\pi)^{1/3}}{R_\star H} , \tag{2.36}$$

where we find $R_\star^{-1} \sim \beta_{\rm typical} \sim (10 - 10^4)H$. At this point, the temperature drop during the bubble expansion will scale as

$$\Delta T \sim T_{\rm nuc}(H\Delta t) \sim \frac{T_{\rm nuc} H}{\beta} . \tag{2.37}$$

Due to the large value of β/H we find numerically that this drop of the temperature is not enough for the barrier to disappear or in other words

$$T_{\rm nuc} - \Delta T > T^{\rm NB} . \tag{2.38}$$

Such behaviour can be understood from the following consideration: near $T_{\rm NB}$ the bounce action drops very quickly and so that the tunnelling becomes very efficient almost instantaneous and typical bubble radiuses are much smaller than the Hubble scale. This leads to another prediction that GW signal will be suppressed as well since it is controlled by the (β/H) quantity eq.(2.36). As we will see, even with this suppression the GW signal is efficient enough to be detected in the future.

2.4.2 Tunnelling with potential barrier at zero temperature

Let us proceed to the analysis of the case when the potential barrier does not disappear at zero temperature. The parameter space with the lowest nucleation temperatures (fastest bubbles) will be located again near the "NO PT" boundary. However in this case the nucleation temperature will be controlled by the local minima of the S_3/T function, see fig.2.2. At least a minimum is expected since the potential at low temperature becomes fully temperature independent and $S_3(T \to 0) \to$ const., so that S_3/T necessarily starts to grow for $T \to 0$.

Numerically (see fig.2.1) for the value of $m_s = 125$ GeV we find that for $v_s \lesssim 170$ GeV entire region with the fast bubbles has a potential barrier at zero temperature. In fig.2.2, we present the euclidean action for $v_s = 170$ GeV and $m_s = 125$ GeV. Going back to fig.2.1, we see that for those values the "NO PT" curve and the "$T_{\rm NB} = 0$" curve are largely separated. This is not a surprise since in this region of parameter space the bounce action $S_3/T \sim O(10^2)$ is small enough to guarantee the successful tunnelling even when the barrier remains at zero temperature. In the range of λ_{hs} from 0.5 to 0.7, numerically we find that nucleation temperatures are $\gtrsim 30$ GeV, and the corresponding maximal Lorentz factors for the velocities of the bubble expansion in the ranges of $\lesssim 30$, see Table 2.1. Interestingly we find that in this case the bubble radius $R_\star \sim \frac{(8\pi)^{1/3} v_w}{\beta}$ are a little bit larger than the ones discussed in the section 2.4.1, corresponding to a bit smaller values of β/H parameter.

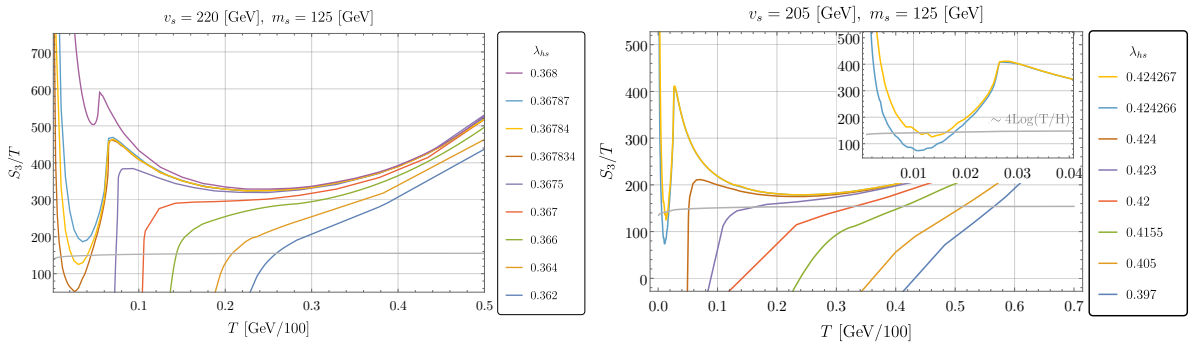

Figure 2.4: Left: Plot of $S_3(T)/T$ as a function of the temperature, for different values of λ_{hs} in the case where $m_s = 125$ GeV and $v_s = 220$ GeV. As we increase the value of the coupling λ_{hs}, the disappearance of the potential barrier happens later, allowing for longer supercooling, until it is large enough to remain even at zero temperature. For the first four curves from the top, we observe a second drop in the function at very low temperature. This second drop corresponds to the displacement on the false minimum that we describe in this section. **Right**: Same plot as in the left panel, but with a lower value for v_s. The pattern we found is the same, but lowering v_s causes a lowering of the curves and the displacement of the false minimum is less pronounced.

Super fine-tuned region We finally comment on the parameter space with $v_s \gtrsim 200$ GeV (again we are fixing $m_s = 125$ GeV), where the curves "NO PT" and "$T_{\rm NB} = 0$" almost superimpose (the region between red and blue dots on the $T_{\rm nuc}$ panel of the fig.2.1). There will be a very narrow strip between the curves "NO PT" and "$T_{\rm NB} = 0$" regions, where the tunnelling will happen even though the barrier remains at zero temperature. We find (see fig.2.4) that the region corresponds to the variations of the λ_{hs} parameter of the order $\delta\lambda_{hs} \sim O(10^{-4})$, *i.e.* two order of magnitude smaller than the full region with relativistic bubbles. In this very small region, various additional effects can start playing a role. For example, let us look at the fig.2.4 we can see that the bounce action S_3/T has a local maximum and a deeper (global) minimum with respect to the standard scenario. Such behaviour of the action is coming from the cancellations of various terms in the effective potential. For simplicity let us look at $T = 0$ case. Then there is a region of parameter space where purely polynomial potential has no local minimum at $(0, v_s)$, but the effects of the $\frac{-3M_t^4(h)}{8\pi^2}\left(\log\frac{M_t(h)}{M_t(v_{EW})}\right)$ terms in Coleman-Weinberg contribution lead to the appearance of the local minimum at $(\delta v_h, v_s)$. In fig.2.5 we plot the contributions of the various terms in the effective potential leading to the appearance of this local minimum and the trajectory of the typical bounce solution in this case. As a result, the distance in the fields space between the two minima decreases and the tunnelling becomes faster, which leads to the appearance of the second (global) minimum in S_3/T.

Benchmark points

In Table 2.1 and 2.2, we give typical values of the nucleation temperature, the Lorentz factor γ_w, the β/H factor, and we indicate if the barrier remains at zero temperature, applying the criterion in eq.(2.38). We can see that the largest bubble radius at the collision (smallest β) corresponds to the case when S_3/T is monotonic and very flat near the tunnelling temperature (c.f. the right panel of fig. 2.4).

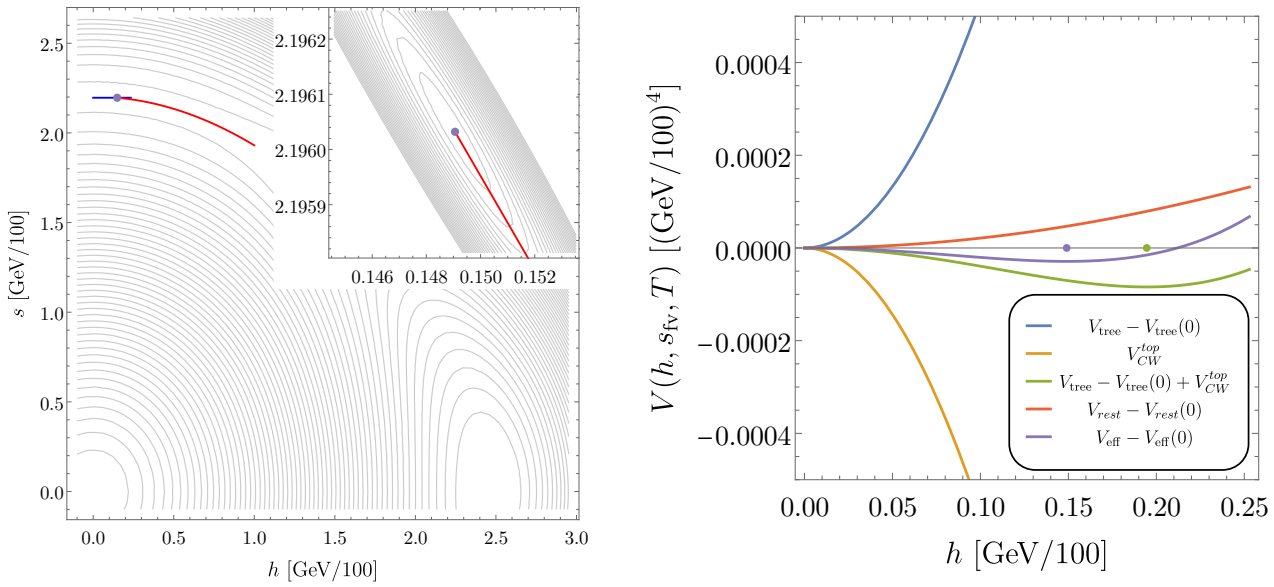

Figure 2.5: Here is presented an explicit example of displacement of the false vacuum for $\{\lambda_{hs}, v_s, T\} = \{0.36784, 220\text{ GeV}, 3\text{ GeV}\}$. **Left**: we show the 2D potential where the blue line corresponds to the part of the potential plotted in the right panel and the (purple) dot is the position of the displaced false minimum, in both plots. Red line indicates the bounce trajectory. **Right**: plot of the different contributions to the potential. We see that a displaced minimum can be generated by balancing the tree level and the CW potential of the top quark, for low enough temperature, in such a way all the other particles, that are massless in the false vacuum, have a negligible contribution. It can be shown that they cause, as the temperature increases, the shift of the local minimum towards $h = 0$.

$m_s = 125$ GeV, $v_s = 170$ GeV							
λ_{hs}	$\frac{T_{\rm reh}}{100\text{GeV}}$	$\frac{T_{\rm nuc}}{100\text{GeV}}$	$\frac{T_{\rm per}}{100\text{GeV}}$	γ_w	$\frac{\tilde{\beta}}{H} = \frac{(8\pi)^{1/3}}{R_\star H}$	$m_H^{\rm False}$/GeV	FM_0
0.56	0.880	0.877	0.850	–	434	35.4	No
0.58	0.855	0.851	0.822	–	355	37.3	No
0.6	0.829	0.824	0.790	–	296	39.2	No
0.62	0.800	0.795	0.762	1.2	209	40.1	No
0.64	0.769	0.762	0.714	2.4	158	42.5	No
0.66	0.729	0.720	0.661	4	108	43.4	No
0.68	0.678	0.666	0.582	6.6	51	44.8	No
0.69	0.642	0.627	0.506	8.8	18	45.0	No
0.695	0.612	0.594	0.412	11	5	44.7	No
0.6997	0.566	0.542	0.237	15	1.4	43.8	No

Table 2.1: We report for fig.2.2, $m_s = 125$ GeV and $v_s = 170$ GeV, reheating, nucleation and percolation temperatures, respectively, for different values of λ_{hs} and γ_w reached by the expanding walls as well as the parameter $\tilde{\beta}/H$ computed using eq.(2.36). We also show the effective Higgs mass in the false vacuum at the nucleation temperature defined as $(m_H^{\rm False})^2 = \frac{\partial^2 V}{\partial h^2}\Big|_{T=T_{\rm nuc}}$, relevant for DM production explained in section 2.5.2. In the last column, FM_0 concerns the displacement of the false minimum. 'No' if it is at the (Higgs) origin, 'Yes' if it moved. In this case, the minimum is always at the origin.

$m_s = 125$ GeV, $v_s = 205$ GeV							
λ_{hs}	$\frac{T_{\rm reh}}{100\rm GeV}$	$\frac{T_{\rm nuc}}{100\rm GeV}$	$\frac{T_{\rm per}}{100\rm GeV}$	γ_w	$\frac{\tilde{\beta}}{H} = \frac{(8\pi)^{1/3}}{R_\star H}$	$m_H^{\rm False}/\rm GeV$	$\rm FM_0$
0.397	0.577	0.564	0.544	4	371	19.1	No
0.405	0.530	0.512	0.488	8	268	19.1	No
0.4155	0.448	0.412	0.379	18	130	17.7	No
0.42	0.393	0.330	0.290	37	72	15.2	No
0.423	0.339	0.161	0.124	270	66	7.1	No
0.4234	0.335	0.107	0.095	805	109	3.9	No
0.424	0.335	0.051	0.051	$5.7 \cdot 10^3$	$3.3 \cdot 10^3$	0.7	No
0.4242	0.335	0.0337	0.0337	$1.8 \cdot 10^4$	$3.2 \cdot 10^4$	0.25	No
0.42424	0.335	0.028	0.0279	$3.0 \cdot 10^4$	$1.8 \cdot 10^3$	4.4	No
0.424266	0.335	0.018	0.017	$1.0 \cdot 10^5$	99	6.2	Yes
0.424267	0.335	0.016	0.014	$1.3 \cdot 10^5$	44	6.3	Yes

Table 2.2: Same as Table 2.1, but for fig.2.4 and with $v_s = 205$ GeV. We observe that the last two points display a displacement of the false minimum.

2.5 Consequences for production of dark matter and Baryogenesis

One of the motivations for the study of a model of EWPT with relativistic bubbles is the relation between relativistic expansion and the out-of-equilibrium production of heavy states presented for the first time in [115], when the field undergoing the PT (here the Higgs) is coupled to some heavy dark sector at typical mass M_N. In this section, we remind the principle of the production mechanism and we study the scenario of the production of Dark Matter [97] and Baryogenesis [98], which were previously agnostic about the EWPT realisation.

First of all, the strong FOPT involves a supercooling represented by a dilution factor,

$$D \equiv \frac{g_{\star s}^{\rm sym}(T_{\rm nuc})}{g_{\star s}(T_{\rm reh})} \left(\frac{T_{\rm nuc}}{T_{\rm reh}}\right)^3 , \tag{2.39}$$

with $g_{\star s}(T)$ ($g_{\star s}^{\rm sym}(T)$) being the number of relativistic degrees of freedom of the entropy in the broken (symmetric) phase. This means that with $D \ll 1$, any type of dark matter production or Baryogenesis mechanism that happens much earlier than the PT should provide values denser than the conventional estimation by a factor of $1/D$ (see for example [133, 185]). For instance, the WIMP cross section should be $\sigma \sim \frac{D}{10^{-3}} 10^{-29} \rm cm^3/s$ to produce a correct dark matter abundance. This is the case when freeze-out happens at temperatures much higher than the reheating.

2.5.1 Production of heavy states during ultra-relativistic expansion

There are a few mechanisms which can lead to heavy particle production during FOPT. This can happen if the incoming massless particle in the unbroken phase gets a very large mass from the Higgs vev [94, 117] (mass gain), or due to the bubble- bubble collision [139, 146] or due to the plasma particle−bubble collision [115]. Our study will be focused on the later one.

Let us assume that FOPT happens and the bubble expansion is indeed relativistic with $\gamma_w^{\rm terminal} \gg 1$. The simplest model where the production of heavy particles

during plasma−bubble wall collision can be realised is described by the following Lagrangian [115]:

$$\mathcal{L} = \frac{1}{2}(\partial_\mu h)^2 + i\bar{q}\partial\!\!\!/ q + i\bar{N}\partial\!\!\!/ N - M_N\bar{N}N - Yh\bar{N}q - V(h)\ , \tag{2.40}$$

where q is a massless particle in the symmetric phase and N is a heavy field with large vev−independent mass $M_N \gg v_{EW}$. h is the Higgs field undergoing a FOPT. With no loss of generality, we go to the basis where fermion masses are real. Before the strong phase transition starts, the abundance of heavy states N in the plasma is strongly Boltzmann suppressed and they would naively seem irrelevant to the dynamics of the transition. In a homogeneous vacuum, the transition from light to heavy state $q \to N$ is obviously forbidden by the conservation of momentum. However, in the presence of the bubble wall, the conservation of momentum along the z direction is broken (assuming a planar wall expanding in the $x-y$ plane) and a computation using WKB phases for the q and N fields demonstrates that the probability $\mathcal{P}(q \to N)$ is non-vanishing [115] and is given by

$$\mathcal{P}(q \to N) \approx \frac{Y^2 v_{EW}^2}{M_N^2}\Theta(\gamma_w T_{\rm nuc} - M_N^2 L_w)\ , \tag{2.41}$$

with $L_w \sim 1/v_{EW}$ the width of the wall. Behind the bubble wall a large abundance of N and $\bar{N}$, n_N^{BE} is produced. Let us emphasise that this abundance is much larger than its equilibrium value.

Another possibility of the heavy particle production can be realised for the following interaction

$$\Delta\mathcal{L} \supset \frac{\lambda_{h\phi}}{2}\phi^2 h^2 + \frac{1}{2}M_\phi^2\phi^2\ . \tag{2.42}$$

In this case ϕ is a heavy scalar field with mass $M_\phi \gg v_{EW}$, then in the vicinity of the wall, the process $h \to \phi\phi$ has the probability [115]

$$\mathcal{P}(h \to \phi^2) \approx \left(\frac{\lambda_{h\phi} v_{EW}}{M_\phi}\right)^2 \frac{1}{24\pi^2}\Theta(\gamma_w T_{\rm nuc} - M_\phi^2 L_w^h)\ . \tag{2.43}$$

The results in section 2.2 on the terminal velocity in the singlet extension of SM allows us to compute the maximal mass of the particles which can be produced during the electroweak FOPT in the singlet extension. Indeed saturating the step function in the above equation and assuming the $L_w \sim 1/v_{EW}$ we get approximately:

$$M^{MAX} \approx \frac{400\ \text{GeV}}{\log^{1/2}\frac{M_Z}{gT_{\rm nuc}}}\left(\frac{\Delta V - \Delta P_{\rm LO}}{(100\ \text{GeV})^4}\right)^{1/2}\left(\frac{100\text{GeV}}{T_{\rm nuc}}\right). \tag{2.44}$$

Numerical results for the maximal mass $M^{\rm MAX}$ are reported in fig.2.1. We can see that the maximal mass we can produce is roughly ~ 10 TeV scale.

We would like to note that our results can be easily applied for the mass gain mechanism of the heavy state production [117]. Indeed, in this case, the maximal mass will be $M_{\text{mass gain}} \simeq \gamma_w T$, and can be read off from the bottom right plot of the fig.2.1 by noting that it will scale as $M_{\text{mass gain}} \sim M_{\rm MAX}^2/v_{EW}$. Since the mass of the heavy field comes from the vev of the Higgs, it will additionally be bounded by the unitarity considerations to be below $\lesssim 2$ TeV.

2.5.2 Dark Matter production

In this section, we will apply the results for the velocity of the bubble expansion for DM model building.

Scalar DM coupled to the Higgs portal

We assume a heavy scalar ϕ coupled to the SM via the traditional Higgs portal

$$\mathcal{L}_{DM} = \frac{1}{2}(\partial_\mu \phi)^2 - \frac{M_\phi^2 \phi^2}{2} - \frac{\lambda_{h\phi}}{2} h^2 \phi^2 \ . \tag{2.45}$$

The DM (ϕ) field is stabilised by some additional Z_2^ϕ (we use this subscript to differentiate it from Z_2 of the singlet potential). After the Higgs transition, the abundance of massive ϕ, $n_\phi^{\rm BE}$, behind the wall is given by

$$n_\phi^{\rm BE} \approx \frac{2}{\gamma_w v_w} \int \frac{d^3p}{(2\pi)^3} \frac{p_z}{p_0} \mathcal{P}(h \to \phi^2) \times f_h(p, T_{\rm nuc}) \ . \tag{2.46}$$

We can see that DM production during the bubble expansion is strongly dependent on the density of the Higgs field available at the nucleation temperature $f_h(p, T_{\rm nuc})$. The relevant parameter for the discussion is the ratio

$$\sqrt{\left.\frac{d^2V}{dh^2}\right|_{\rm fv}} \frac{1}{T} \equiv \frac{m_H^{\rm False}}{T} \ , \tag{2.47}$$

where fv denotes the position of the false vacuum and $\sqrt{\left.d^2V/dh^2\right|_{\rm fv}}$ is the mass of the Higgs $m_H^{\rm False}$ in the false vacuum. As soon as this quantity becomes larger than 1, we expect exponential suppression of the Higgs abundance

$$C_{\rm eff} \frac{\zeta(3) T_{\rm nuc}^3}{\pi^2} \equiv \int \frac{d^3p}{(2\pi)^3} f_h(p, T_{\rm nuc}) \approx \begin{cases} \frac{\zeta(3) T_{\rm nuc}^3}{\pi^2} & \text{if} \quad m_H^{\rm False} < T \ , \\ \left(\frac{m_H^{\rm False} T_{\rm nuc}}{2\pi}\right)^{3/2} e^{-m_H^{\rm False}/T_{\rm nuc}} & \text{if} \quad m_H^{\rm False} > T \ . \end{cases} \tag{2.48}$$

Here we define $C_{\rm eff}$ to take into account the Boltzmann suppression. After redshifting to today, the stable produced abundance takes the form

$$\begin{aligned} \Omega_{\phi,{\rm BE}}^{\rm today} h^2 &= \frac{M_\phi n_\phi^{\rm BE}}{\rho_c/h^2} \frac{g_{\star S0} T_0^3}{g_{\star S}(T_{\rm reh}) T_{\rm reh}^3} \approx 6.3 \times 10^8 \ \frac{M_\phi n_\phi^{\rm BE}}{\rm GeV} \frac{1}{g_{\star S}(T_{\rm reh}) T_{\rm reh}^3} \ , \\ &\approx 5.4 \times 10^5 \times \left(\frac{C_{\rm eff} \lambda_{h\phi}^2 v_{EW}}{M_\phi g_{\star S}(T_{\rm reh})}\right) \left(\frac{v_{EW}}{\rm GeV}\right) \left(\frac{T_{\rm nuc}}{T_{\rm reh}}\right)^3 \times e^{-\frac{M_\phi^2}{2\gamma_w v_{EW} T_{\rm nuc}}} \ . \end{aligned} \tag{2.49}$$

This expression has to be supplemented with the *freeze-out*(FO) contribution which is produced *before* the phase transition

$$\begin{aligned} &\Omega_{\phi,{\rm FO}}^{\rm today} h^2 \approx 0.1 \times \left(\frac{T_{\rm nuc}}{T_{\rm reh}}\right)^3 \times \left(\frac{0.03}{\lambda_{h\phi}}\right)^2 \left(\frac{M_\phi}{100 \ {\rm GeV}}\right)^2 \ , \\ &\Omega_{\phi,{\rm tot}}^{\rm today} h^2 = \Omega_{\phi,{\rm BE}}^{\rm today} h^2 + \Omega_{\phi,{\rm FO}}^{\rm today} h^2 \ . \end{aligned} \tag{2.50}$$

Note that the FO contribution is suppressed by the factor $\left(T_{\rm nuc}/T_{\rm reh}\right)^3$ due to the brief stage of inflation during the phase transition. Obviously the prediction for relic density

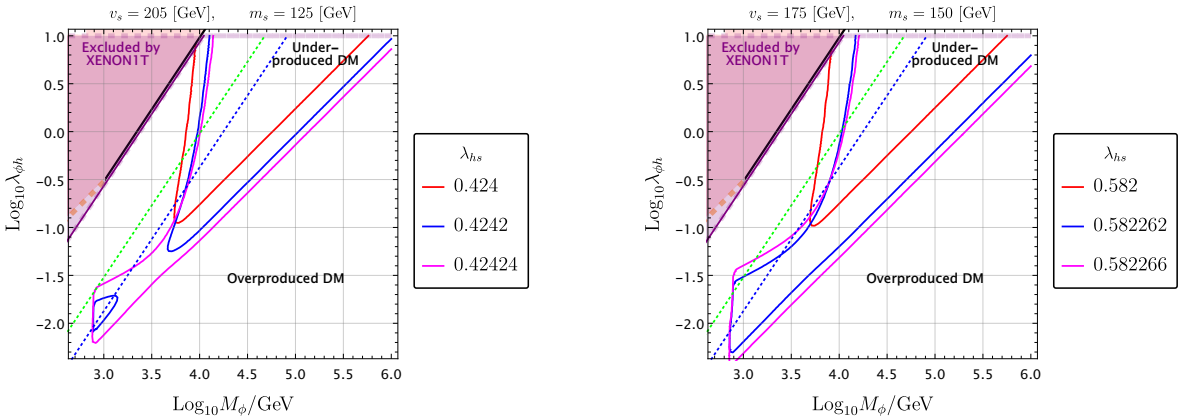

Figure 2.6: Left: DM abundance in the parameter space $\lambda_{h\phi} - M_\phi$ for different values of λ_{hs} by fixing $v_s = 205$ GeV and $m_s = 125$ GeV (that fixes the values of $T_{\rm nuc}, T_{\rm reh}$ and $\gamma_w^{\rm terminal}$). The solid lines represent correct DM abundance, while underproduced inside and overproduced outside. The lower part of each contour is dominated by freeze-out and the upper part via bubble expansion. The connecting vertical line (independent of the portal) comes from thermal production after the reheating of the transition. The magenta shaded region is excluded by XENON1T while the dotted green and blue lines are projected limits from XENONnT and DARWIN respectively. **Right**: same plot for $v_s = 175$ GeV and $m_s = 150$ GeV. As expected, increasing the tuning from red to magenta increases the amplitude of the curve. The values used are extracted from Table 2.B.1.

must match the experimental observations: $\Omega^{\rm today}_{\phi,\rm tot}h^2 \approx 0.1$. We can see from eqs.(2.49),(2.50) that for small values of the portal coupling $\lambda_{h\phi}$, DM production will be dominated by the freeze-out mechanism while bubble expansion takes over for larger values of $\lambda_{h\phi}$.

Next, we can check whether this mechanism for DM production can lead to viable phenomenology, given the results on bubble dynamics in section 2.4. Instead of making a scan of the parameter space, we will just focus on a few representative benchmark points.

For $m_s = 125$ GeV, $v_s = 205$ GeV, we show in fig.2.6 the isocontours reproducing the correct relic density for three reference values of λ_{hs} (corresponding nucleation temperatures can be found in the Table 2.1). Firstly, $C_{\rm eff} \simeq 1$ for all three reference points. For $\lambda_{hs} = 0.424$ the upper red curve corresponds to the case when DM production is dominated by the BE (bubble expansion) and the lower curve by FO. The steepness of the upper red curve (BE) comes from the fact that we are always in the region of parameter space where $\exp\left[-M_\phi^2/(2\gamma_w v_{EW} T_{\rm nuc})\right] \ll 1$, leading to a very strong sensitivity on M_ϕ mass. Physically this means that the model generically predicts large overproduction of DM in BE process unless the Boltzmann suppression $\exp\left[-M_\phi^2/(2\gamma_w v_{EW} T_{\rm nuc})\right]$ is playing a role. For the other two reference points $\lambda_{hs} = 0.4242, 0.42424$ we can see that there is an additional part of parameter space for the DM masses $M_\phi \sim 1-4$ TeV, which corresponds to the region without the Boltzmann suppression $\exp\left[-M_\phi^2/(2\gamma_w v_{EW} T_{\rm nuc})\right] \sim 1$. This is related to larger values of $M^{\rm MAX} \sim \sqrt{\gamma_w v_{EW} T_{\rm nuc}}$ and smaller values of the nucleation temperature, reducing the excess of the DM abundance. On the right panel of fig.2.6, we report similar plots for $v_s = 175$ GeV, $m_s = 150$ GeV.

Finally, before closing this section, we comment on the possibility of considering the singlet s itself, in the limit of very precise Z_2, as DM. After the phase transition $T \sim 40$ GeV, the singlet is in thermal equilibrium and we can apply straightforwardly the

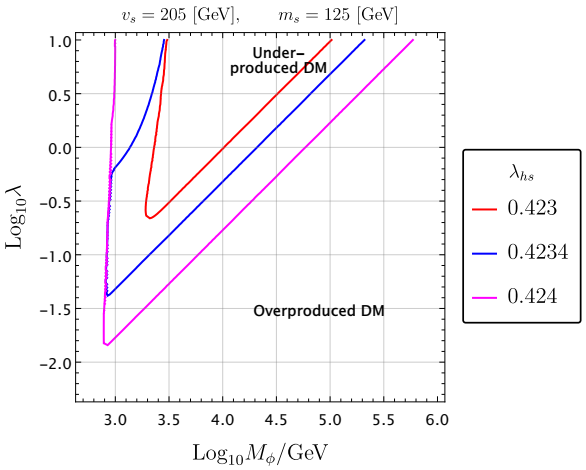

Figure 2.7: DM production for the singlet portal model. In this context, the Boltzmann suppression $\sim e^{-m_s/T_{\rm nuc}}$ plays a strong role and allows for bubble expansion produced DM with much higher nucleation temperature $T_{\rm nuc} \sim 15$ GeV.

freeze-out expression:

$$\Omega^{\rm today}_{s,\ \rm FO} h^2 \approx 0.1 \left(\frac{0.06}{\lambda_{hs}}\right)^2 \left(\frac{M_s(v_{EW},0)}{100\ \rm GeV}\right)^2 . \tag{2.51}$$

From this estimate of the FO abundance for s and recalling that we considered $\lambda_{hs} \sim 0.3 - 0.6$ and $M_s(v_{EW},0) \sim 100$ GeV, we conclude that the abundance of s produced in this fashion, today, is underproduced by one or two orders of magnitude to fit the observed amount of DM $\Omega^{\rm today}_{s,\ \rm FO} h^2 \approx 0.1$. Even in this underproduced case, there are severe bounds from the direct detection experiments except for the resonant region, where (2.51) is overestimated. However, as we will discuss in the Appendix. 2.D, we will have a Z_2 explicit breaking which makes s decay much before today.

Singlet portal DM

In this section, we mention an alternate possibility of coupling the DM (ϕ) to the singlet field s via the "singlet portal"

$$\Delta\mathcal{L} \supset \frac{\lambda_{s\phi}}{2}\phi^2 s^2 + \frac{1}{2}M_\phi^2\phi^2 , \quad \mathcal{P}(s \to \phi^2) \approx \left(\frac{\lambda_{s\phi} v_s}{M_\phi}\right)^2 \frac{1}{24\pi^2}\Theta(\gamma_w T_{\rm nuc} - M_\phi^2 L_w^s) , \tag{2.52}$$

where the width of the singlet wall is similar to the length of the Higgs wall L_w. Interestingly even though FOPT is from $(0, v_s) \to (v_{EW}, 0)$, the singlet scattering of the wall can lead to the production of the ϕ field. The phenomenology of DM production is very similar to the Higgs portal case discussed in the previous section, with one main difference: in the false vacuum, the mass of the singlet is not small and the factor $C_{\rm eff}$ introduced in the eq.(5.71) plays an important role. The results are shown in fig.2.7. For example, if we compare the curves for $\lambda_{hs} = 0.424$, $m_s = 125$ GeV, $v_s = 205$ GeV in fig.2.7 and in fig.2.6, we can see that, for the Higgs portal DM, the isocontour has the same shape, but with the larger values of DM M_ϕ masses. As shown in eq.(2.49), this is due to the proportionality between the DM relic abundance produced during the bubble expansion with $\propto C_{\rm eff}/M_\phi$.

Singlet portal with additional field A slight modification of this scenario is to further introduce a light scalar $\tilde{s}$. Then we can have,

$$\mathcal{L} = \mathcal{L}_{SM} - \tilde{\lambda}\tilde{s}s\phi^2 - \frac{M_\phi^2}{2}\phi^2, \tag{2.53}$$

where again ϕ is the DM and we did not write down the mass terms for simplicity of notation. We assume that $\tilde{s}$ is in the thermal bath before the PT. Then due to the field change of s in the bubble wall, the momentum conservation violating process $\tilde{s} \to \phi\phi$ can occur ($h \to \phi\phi$ may also occur if there is the $h^2\phi^2$ term). In this model, $s \to \tilde{s} + SM$ particles happen via the DM loop.

Fermion-mediated Dark Matter

In the previous section, we noticed that the DM production during bubble expansion strongly depends on the mass of the incoming particle in the symmetric phase, due to the Boltzmann suppression factor. In the case of an incoming scalar, generically this effect is relevant and crucially modifies the phenomenology, as we have seen in the section 2.5.2. In this section, we construct a model where the incoming particle is a massless fermion in the symmetric phase so that $C_{\text{eff}} \equiv 1$ by definition. The model consists of a vector-like neutral fermion N which is a singlet under SM and a couple of Z_2 odd fields ϕ and χ:

$$\mathcal{L} = \mathcal{L}_{SM} + Y_* \bar{L} H N + M_N \bar{N} N + Y_{DM} \bar{N} \chi \phi \ . \tag{2.54}$$

Here, L, H are SM lepton and Higgs doublets, respectively. The production mechanism works as follows: the heavy field N is produced during the phase transition $L \to N$ and it will subsequently decay into $N \to \chi\phi, N \to LH$. The field N can be Majorana or Dirac (in the former case there will be a relation to neutrino masses and in the latter it will be completely independent of neutrinos).

In this model, heavy N are produced via $L \to N$ with a probability

$$\mathcal{P}^{\text{tree}}(L \to N) \approx \frac{Y_\star^2 v_{EW}^2}{M_N^2} \Theta(\gamma_w T_{\text{nuc}} - M_N^2 L_w) \ . \tag{2.55}$$

As a consequence, unstable heavy N accumulate behind the wall with initial density given by

$$\begin{aligned} n_N^{\text{BE}} &\approx \frac{Y_\star^2 v_{EW}^2}{M_N^2 \gamma_w v_w} \int \frac{d^3p}{(2\pi)^3} \frac{p_z}{p_0} \times f_L(p, T_{\text{nuc}}) \Theta(p_z - M_N^2/v_{EW}) \ , \\ &\approx \frac{Y_\star^2 v_{EW}^2 T_{\text{nuc}}^3}{2\pi^2 M_N^2} e^{-\frac{M_N^2}{2 v_{EW} T_{\text{nuc}} \gamma_w}} + \mathcal{O}(1/\gamma_w) \ , \end{aligned} \tag{2.56}$$

where $v_w = \sqrt{1 - 1/\gamma_w^2}$, we expanded for large γ_w and approximated the Fermi-Dirac distribution as a Boltzmann distribution. Compared to the original proposal in ref. [97], the density of the heavy fields inside the bubble will be additionally enhanced by $\sim 16\pi^2$ factor since $1 \to 1$ transitions are more effective than $1 \to 2$. Let us assume that $M_\phi < M_\chi$ so that ϕ is the DM candidate, then DM production will happen via the following chain of processes:

$$L \underset{\text{via PT}}{\to} N \underset{\text{via decay}}{\to} \phi\chi \to \phi\phi + \text{SM} \ . \tag{2.57}$$

However, the heavy N has two channels of decay: toward the heavy dark sector ϕ, χ and back to the light L. The abundance of ϕ, χ after the transition is thus suppressed and given by

$$n_\chi \approx n_\phi \approx \frac{Y_{DM}^2 Y_\star^2}{Y_{DM}^2 + Y_\star^2} \frac{v_{EW}^2 T_{\rm nuc}^3}{2\pi^2 M_N^2} e^{-\frac{M_N^2}{2v_{EW} T_{\rm nuc}\gamma_w}} + \mathcal{O}(1/\gamma_w) \,, \tag{2.58}$$

and the final relic abundance redshifted to today thus reads

$$\Omega_{\phi,\rm BE}^{\rm today} h^2 \approx 1.5 \times 10^8 \times \frac{Y_\star^2 Y_{DM}^2}{Y_\star^2 + Y_{DM}^2} \frac{2M_\phi}{M_N} \left(\frac{v_{EW}}{M_N}\right) \left(\frac{v_{EW}}{246\text{GeV}}\right) \left(\frac{T_{\rm nuc}}{T_{\rm reh}}\right)^3 e^{-\frac{M_N^2}{2v_{EW} T_{\rm nuc}\gamma_w}} \,. \tag{2.59}$$

For the freeze-out process in the symmetric phase, we have $\phi\phi \to LHLH$ by neglecting co-annihilation. The cross-section is highly phase space suppressed (closing a loop for a 2 to 2 annihilation gives a similar scaling): $\sigma_{\phi\phi\to(LH)^* LH} \sim \frac{M_\chi^2 (Y_{\rm DM} Y_*)^2}{(16\pi^2)^2 4\pi M_N^4}$. The abundance by taking into account the supercooling is

$$\Omega_{\phi,\rm FO}^{\rm today} h^2 = 10^3 \left(\frac{T_{\rm nuc}}{T_{\rm reh}}\right)^3 \frac{M_N^4/M_\chi^2}{(6\text{TeV})^2} \frac{10}{(Y_{\rm DM} Y_*)^4} \,. \tag{2.60}$$

The total DM density today will be given by the sum of eq.(2.59)-(2.60). Therefore, this scenario leads to the over-production of DM unless $M_\phi, M_\chi \lesssim 10$ GeV. However, note that these equations are valid only for the heavy DM candidates which do not go back to equilibrium after the phase transition. Otherwise, the final density will be given by eq.(2.60) only without $\left(T_{\rm nuc}/T_{\rm reh}\right)^3$ and we are going back to the normal freeze-out scenario.

Let us now investigate the regime $M_\phi \simeq M_\chi$, precisely $|M_\phi - M_\chi| \lesssim M_\phi/20$, where the co-annihilation takes place. In this case, we have the channel $\phi\chi \to H\bar{L}$ to decrease the abundance of ϕ as well as χ. The cross-section is $\sigma_{\phi\chi\to H\bar{L}} \sim \frac{(Y_{\rm DM} Y_*)^2}{4\pi M_N^2}$. Therefore, we have

$$\Omega_{\phi,\rm FO,Co}^{\rm today} h^2 \sim 0.1 \left(\frac{T_{\rm nuc}}{T_{\rm reh}}\right)^3 \times \frac{M_N^2}{(10\text{TeV})^2} \frac{1}{(Y_{\rm DM} Y_*)^2} \,. \tag{2.61}$$

Summing this estimate with the $\Omega_{\phi,\rm BE}^{\rm today} h^2$ in eq.(2.59) we find that it becomes possible to reproduce the observed DM abundance. However, we see that bubble expansion tends to overproduce the DM and the relic abundance in BE can be reproduced if only the factor $\exp[-M_N^2/(2v_{EW} T_{\rm nuc}\gamma_w)]$ starts playing a role in suppressing DM relic density (left boundary of fig.2.8 is almost vertical).

2.5.3 Baryogenesis mechanism

Now we remind the reader, the scenario of Baryogenesis with relativistic bubble walls that was proposed in [98]. As a prototype, we worked with the following model, reminiscent of the toy model of eq.(2.40), (omitting the kinetic terms)

$$\begin{aligned} \mathcal{L} = \; & \mathcal{L}_{SM} + m_\eta^2 |\eta|^2 + \sum_{I=1,2} M_I \bar{B}_I B_I \\ & + \left(\sum_{I=1,2} Y_I (\bar{B}_I H) P_L Q + y_I \eta^* \bar{B}_I P_R \chi + \kappa \eta^c d u + \frac{1}{2} m_\chi \bar{\chi^c} \chi + h.c. \right) . \end{aligned} \tag{2.62}$$

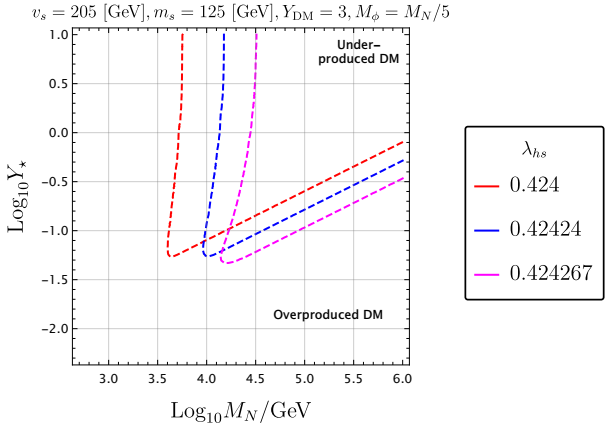

Figure 2.8: DM production in the fermionic portal model. We fix $M_{\rm DM} = M_N/5$, and $Y_{\rm DM} = 3$. Only the co-annihilation regime where $|M_\phi - M_\chi| \lesssim M_\phi/20$ appears to be viable and shown by dashed lines.

Thus, additionally to the SM and the singlet sector, the model contains a Majorana field χ and two vector-like B quarks with the masses $M_{1,2} \sim m_\chi$. η is a scalar field in the fundamental representation of QCD and with electric charge $Q(\eta) = 1/3$. We defined Q, u, d as the SM quark doublet and singlets respectively, and ignored the flavour indices. H is the SM Higgs.

We first proved that the production mechanism, when computed up to one loop-level, indeed transforms a CP-violating phase into a chiral asymmetry in the abundances produced, in a fashion very similar to usual leptogenesis decay. Let us now sketch the mechanism in itself. First, $b-$quarks collide with the relativistic wall and produce B_I, B_I^c via the mechanism explained above. Thus inside the bubble, we have

$$n_{B_I} - n_{B_I^c} = -\left(\frac{Y_I v_{EW}}{M_I}\right)^2 \epsilon_I n_b^{\rm inc} \,, \qquad n_b - n_{b^c} = \sum_I \left(\frac{Y_I v_{EW}}{M_I}\right)^2 \epsilon_I n_b^{\rm inc} \,, \tag{2.63}$$

where $n_b^{\rm inc}$ is the number density of the bottom-type quark colliding with the wall from outside, n_b and n_B are the abundances inside of the bubble and ϵ is a loop suppressed coefficient which parametrises the CP violating phase and the resonance between one-loop and tree-level diagrams. After the passage through the wall, the following asymmetric abundances are then generated

$$\sum_I \left(n_{B_I} - n_{B_I^c}\right) = -(n_b - n_{b^c}) \,. \tag{2.64}$$

From this expression we can read an apparent asymmetry in the bottom quark abundances. However, if the heavy B freshly produced were to decay back into b, the asymmetry would be washed out. This is however not the case if they decay in a dark sector containing χ, η, where the asymmetry is enhanced by the presence of a Majorana mass for χ. The final unsuppressed produced asymmetry is given by

$$\begin{aligned} \frac{\Delta n_{\rm Baryon}}{s} \approx \; & \frac{135\zeta(3)}{8\pi^4} \sum_{I,J} \left(\frac{Y_I \langle H\rangle}{M_I}\right)^2 \frac{|y_I|^2}{|y_I|^2 + |Y_I|^2} \times \frac{g_b}{g_\star}\left(\frac{T_{\rm nuc}}{T_{reh}}\right)^3 \\ & \times {\rm Im}(Y_I Y_J^* y_I^* y_J) \left(-\frac{2{\rm Im}[f_B^{IJ}]}{|Y_I|^2} + \frac{4{\rm Im}[f_B^{IJ}]|_{m_{\chi,\eta}\to 0}}{|y_I|^2}\right) \,, \end{aligned} \tag{2.65}$$

where s is the entropy at the moment of the production, g_b is the number of degrees of freedom of the bottom and $g_\star$ the number of relativistic degrees of freedom. The loop functions f_B^{IJ} have been computed in [98] and are controlled by the CP-violating sector. Absence of strong wash-out conditions

$$M_{B,\chi,\eta} \gtrsim 30 T_{\rm reh} \sim 10^3 \text{ GeV} , \qquad \text{(suppressed wash-out)} \tag{2.66}$$

as well as experimental signatures (direct production in colliders, flavor violation, neutron oscillations) pushed the heavy particles to be

$$M_{B,\chi,\eta} \gtrsim 2 \times 10^3 \text{ GeV} . \tag{2.67}$$

In the context of singlet extension with Z_2 that we studied, this opens up the range

$$M_{B,\chi,\eta} \in [2, 10] \text{ TeV} , \tag{2.68}$$

where the Baryogenesis mechanism proposed above is operative.

2.5.4 Impact of the heavy sector on the phase transition

The models we are considering by construction have new heavy fields coupled to the Higgs boson. These will lead to the finite corrections to the scalar parameters of the form (assuming a Yukawa type connection $yBHb$)

$$\delta m_h^2 \sim \frac{-8 g_N M_N^2 y^2}{64\pi^2}\left(\log\frac{M_N^2}{v_{EW}^2} - \frac{3}{2}\right), \qquad \delta\lambda \sim 4 g_N \frac{y^4}{64\pi^2}\left(\log\frac{M_N^2}{v_{EW}^2} - \frac{3}{2}\right), \tag{2.69}$$

where g_N is the number of heavy degrees of freedom and M_N is the typical mass of the heavy sector. One can wonder how these corrections can affect the tuning of the Higgs potential. However, note that in our model the Higgs mass hierarchy problem is not addressed and generically we expect the size of m_h^2 to be of the order of the cut off scale ($M_{\rm pl}$ in SM). So the corrections in eq.(2.69) do not make the tuning worse.

In case the Higgs hierarchy problem is solved at the scale of the heavy fields in eq.(2.45),(2.62) the tuning in the Higgs potential will be roughly,

$$\text{tuning} \sim \frac{m_h^2}{\Delta_{\text{Heavy physics}} m_h^2} \sim \frac{8\pi^2 m_h^2}{y^2 M_N^2}. \tag{2.70}$$

We can combine this estimate with a tuning for low nucleation temperatures (see discussion in section 2.4.1) which are necessary for the heavy field production and the tuning estimate becomes:

$$\text{tuning} \sim \frac{T_{\rm nuc}^2}{\Delta_{\text{Heavy physics}} m_h^2} \sim \frac{8\pi^2 T_{\rm nuc}^2}{y^2 M_N^2}. \tag{2.71}$$

Using the estimates of the maximal values of γ_w and the maximal mass of heavy particles which can be produced during the bubble-plasma collisions (see eq.(2.25) and eq.(2.41)) we get the following estimate for the maximal tuning in the model

$$\text{tuning}^{MAX} \sim \left(\frac{T_{\rm nuc}}{20\text{GeV}}\right)^4, \tag{2.72}$$

where we remind the reader that this estimate is valid only if the Higgs hierarchy problem is solved at the heavy fields scale.

2.6 Gravitational waves emitted

It is well known that strong gravitational waves background will be emitted, with peak frequency around the mHz if the EWPT happens to be strongly first order. This is the optimal range of sensitivity of the forthcoming LISA detector [54, 186] and also GW detectors such as LIGO [187, 188], BBO [189, 190], DECIGO [191–193], ET [63, 194, 195], AION [196], AEDGE [197].

The signal produced at the moment of the transition, as presented in section 1.4, can be separated into different contributions: the *bubble collision* [49] contribution, the *plasma sound waves* [54] and finally the *turbulence*. Only the two first sources of GW are well understood. Another nice feature of those two sources is that they are expected to dominate in different physical situations; the bubble collision would dominate in case of a runaway wall and the sound waves if the wall reaches a terminal velocity. We have already mentioned that the EWPT, if first order, will always happen in the regime of terminal velocity, because of the large number of strongly coupled vector bosons[6]. For GW produced by plasma sound wave, the peak frequency and amplitude are given by

$$\begin{aligned}\Omega^{\rm peak}_{\rm plasma}h^2 &\approx 0.7\times 10^{-5}\left(\frac{100}{g_\star}\right)^{1/3}\left(\frac{\kappa_{sw}\alpha}{1+\alpha}\right)^2 (H_{\rm reh}R_\star)\ ,\\ f_{\rm peak} &\approx 2.6\times 10^{-5}\left(\frac{1}{H_{\rm reh}R_\star}\right)\left(\frac{z_p}{10}\right)\left(\frac{T_{\rm reh}}{100\ {\rm GeV}}\right)\left(\frac{g_\star}{100}\right)^{1/6}{\rm Hz}\ ,\end{aligned} \tag{2.73}$$

with $z_p \sim 10$, κ_{sw} is the efficiency factor for the production of sound waves in the plasma [73],

$$\kappa_{sw} \approx \frac{\alpha}{0.73+0.083\sqrt{\alpha}+\alpha}\ , \tag{2.74}$$

α and $R_\star$ have been defined in eqs.(1.105) and (2.35) respectively, $R_\star \sim \mathcal{O}(10^{-1}-10^{-4})H^{-1}$ is the approximate size of the bubble at collision and all quantities $(T, H, g_\star)$ have to be evaluated at *reheating*.

As we have seen in sections 2.5.3–2.5.2, for the baryogenesis and DM production we need relativistic walls with relatively low nucleation temperature $\lesssim 10$ GeV. In this context, $\alpha \gg 1$ and $\kappa_{sw} \to 1$. The peak frequency and the signal amplitude are only functions of the size of the bubbles at collision, which are reported in Table 2.2 and 2.B.1. We can observe that in this range β/H spans the value between $[50, 10^4]$, with a preference for lower values. Going back to eq.(2.73), emitted amplitude and frequencies will be of the order

$$\Omega^{\rm peak}_{\rm plasma}h^2 \in [5\times 10^{-7}, 2\times 10^{-9}]\ , \qquad f_{\rm peak}\in[10^{-4}, 0.03]\quad {\rm Hz}\ , \tag{2.75}$$

where we set $z_p = 10, g_\star = 100$. This range of frequencies and amplitude are largely in the expected sensitivity of the coming observer LISA [54, 198], as expected for this class of models [33]. We thus conclude that a strong GW signal in the LISA with a spectrum controlled by the plasma sound waves is a generic prediction of baryogenesis with relativistic bubble walls. This is in sharp opposition with the general expectation that usual EWBG demands slow walls, and thus suppressed signals.

As a final comment, it should however be noticed that the current simulations do not directly provide solutions for the regime of large α, and we only have an extrapolation of the numerical result. Thus, the conclusion above should be taken with a grain of salt.

[6] A possible exception would be the case of extreme cooling, as hinted in [96] where even the pressure from gauge bosons cannot stop the acceleration of the wall. However, in our study, we do not find such a situation.

2.7 Summary

In this chapter, we have presented the first explicit realisation of the baryogenesis and DM production during electroweak phase transition for ultra-relativistic bubble expansion. The work is based on the proposals in [97, 98, 115, 117] where new heavy particles are produced in plasma−bubble wall collisions. We have shown that the model with SM extended by a real singlet with a Z_2 symmetry can indeed lead to ultra-relativistic bubbles, where the Lorentz factor γ_w can reach the values $\sim 10^{5-6}$. Such fast bubbles can appear if the symmetry–breaking occurs in two steps: first discrete Z_2 is spontaneously broken and in the second step electroweak symmetry–breaking is accompanied by Z_2 restoration $(0,0) \xrightarrow{SOPT} (0, v_s) \xrightarrow{FOPT} (v_{EW}, 0)$. We find that there exists a region of parameter space where the nucleation temperature can become as low as $1-2$ GeV and the collision of the bubble wall with the plasma particles can lead to the non-thermal heavy particle production with the masses up to ~ 10 TeV. Interestingly we find that the mechanism is most efficient for relatively low masses of the singlet field $M_s(v_{EW}, 0) \sim 70 - 100$ GeV, close to the region excluded by the Higgs invisible decays. Subsequently, this region of parameter space will be probed by HL-LHC ([174, 199]) in the singlet production mediated by off-shell Higgs boson. By noting the slight Z_2 breaking, s, if produced, can decay into $b\bar{b}$ in collider experiments. Depending on the size of the breaking displaced vertices of $b\bar{b}$ may be probed. We find the typical bubble radius parameter of the order of $R_\star \sim (10^{-4}-1)H^{-1}$ so that stochastic gravitational background signal becomes observable at GW experiments like LISA [54, 198].

The model necessarily requires tuning $\propto (T_{\rm nuc}/m_h)^2$ which numerically turns out to be of the order of $10^{-4} - 10^{-2}$ (using Giudice-Barbieri measure) for successful baryogenesis and DM production mechanism. In spite of this, we believe it can provide an useful guidance for more appealing models where these hierarchies can appear naturally.

Appendix

2.A The bounce in two dimensions

In this chapter, we studied numerically the phase transition from the minimum $(0, v_s)$ (or in the vicinity of it) to $(v_{EW}, 0)$. The bounce computation can be done using existing codes for example `FindBounce` or `CosmoTransition`. However, we have found that in the regime of large supercooling where the potential around the false vacuum is very flat, the existing codes are often not stable and lead to numerical errors. Thus we have developed our own code (more stable for the flat potentials), following the procedure described in [200], while cross-checking the available values with `FindBounce`.

2.A.1 Computation of the bounce profile

In this Appendix, we briefly review the standard computation of the bounce action with only one field before describing the algorithm we used for the same computation but for the case of two fields PT. In order to compute the vacuum tunnelling probability from the false vacuum to the true one in d dimensions, we need to minimise the Euclidean action given by

$$S_E = \int d^d x \left[\frac{1}{2} (\partial_\mu \phi)^2 + V[\phi] \right] . \tag{2.76}$$

It is known that the field configurations leading to the minimal action are the ones that exhibit an $O(d)$ spherical symmetry, then the so-called bounce solution is the solution of the following Cauchy problem

$$\frac{d^2\phi}{dr^2} + \frac{d-1}{r}\frac{d\phi}{dr} = \frac{dV[\phi]}{d\phi} , \qquad \lim_{r\to\infty} \phi(r) = 0 , \qquad \left.\frac{d\phi}{dr}\right|_{r=0} = 0 , \tag{2.77}$$

where we have chosen the false minimum to be at $\phi = 0$. If we interpret the parameter r as a time and ϕ as a position, this problem becomes formally equivalent to the evolution of a mechanical ball in a potential $-V[\phi]$ undergoing a friction $\frac{d-1}{r}\frac{d\phi}{dr}$, released with vanishing velocity and stopping its evolution for $r \to \infty$ at $\phi = 0$. It is well known that this problem can be solved by applying numerically an overshoot/undershoot method on the position of the released point. Releasing the ball too close to the true vacuum would induce an overshoot configuration (the ball would continue after crossing $\phi = 0$), we would thus shift the release point toward the false vacuum, while releasing it too close to it would end up in an undershoot configuration (the ball would never reach $\phi = 0$ and starts oscillate around the minimum of $-V[\phi]$) and we correct it by shifting the release point farther from the false vacuum. Iterating between those two situations, we are able to find the correct release point and obtain the *bounce solution*.

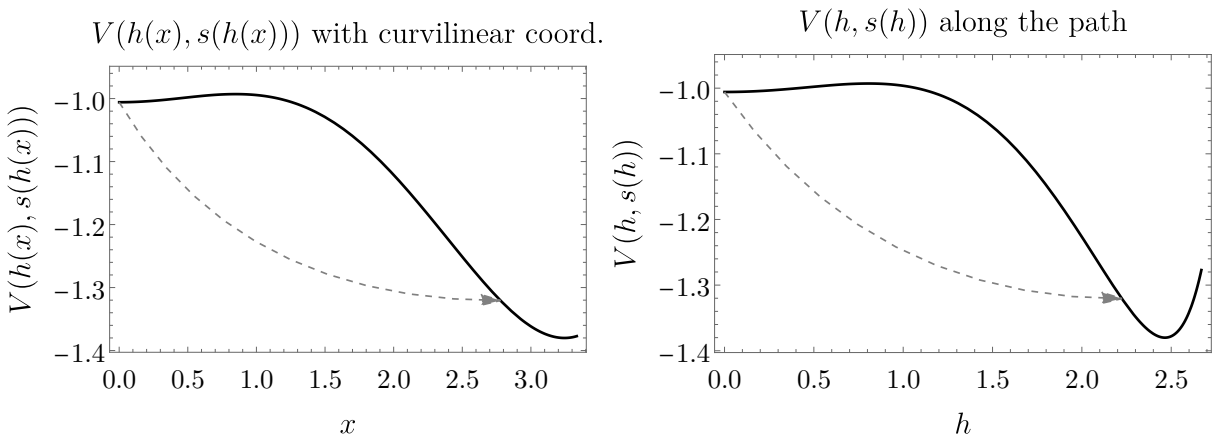

Figure 2.A.1: On the left, the potential, along the path, experienced by the field x and the corresponding escape point $x_\star$. On the right the potential, along the path, is projected in the h direction.

2.A.2 Bounce action in two dimensions and path deformation

The problem complexifies when the transition involves many fields. Here there is no straightforward intuition for the path followed by the fields in field space during the tunnelling. One can think that a straight line, connecting the two minima, could be a reasonable guess, but it turns out that it cannot be considered a good approximation of the tunnelling path[7]. Here we thus describe the algorithm [200] to find the right path in field space. In a multi-field case, the eq.(2.77) becomes

$$\frac{d^2\vec{\phi}}{dr^2} + \frac{d-1}{r}\frac{d\vec{\phi}}{dr} = \vec{\nabla}V[\vec{\phi}] \ , \qquad \lim_{r\to\infty}\vec{\phi}(r) = 0 \ , \qquad \left.\frac{d\vec{\phi}}{dr}\right|_{r=0} = 0 \ . \tag{2.78}$$

Since in this case an overshoot/undershoot procedure cannot be easily applied, the idea is to reduce the problem to one dimensional tunnelling. In order to do so we start guessing the path, $\vec{\phi}_g(x)$, where x is now to be understood as the parameter that measures the distance along the path, *i.e.* the so-called curvilinear abscissa. For the present case, if we parametrise the path in the field space as $(h(t), s(t)) = (t, f(t)) \equiv (h, s(h))$ it is defined as

$$x(h) = \int_{h_{fm}}^{h} \sqrt{1 + \left(\frac{ds(h')}{dh'}\right)^2}\, dh' \ , \tag{2.79}$$

where h_{fm} is the value of the Higgs field in the false minimum. With this choice of field coordinates to parametrise the path, the condition $\left|\frac{d\vec{\phi}(x)}{dx}\right|^2 = 1$ is satisfied, and the Euclidean equation of motion in eq. (2.78) can be rewritten along the parallel and the perpendicular direction

$$\begin{aligned} &\frac{d^2x}{dr^2} + \frac{d-1}{r}\frac{dx}{dr} = \partial_x V[\vec{\phi}_g(x)] \ , \\ &\frac{d^2\vec{\phi}_g(x)}{dx^2}\left(\frac{dx}{dr}\right)^2 = \vec{\nabla}_\perp V[\vec{\phi}_g(x)] \ . \end{aligned} \tag{2.80}$$

[7]Let us emphasise that in the region of the parameter space we studied, the straight line between the false and the true vacuum gives a Euclidean action which is often wrong by *orders of magnitudes*, as the path is often very far from the straight line, as a consequence, we cannot dispense from the effort of studying the exact 2D path in field space.

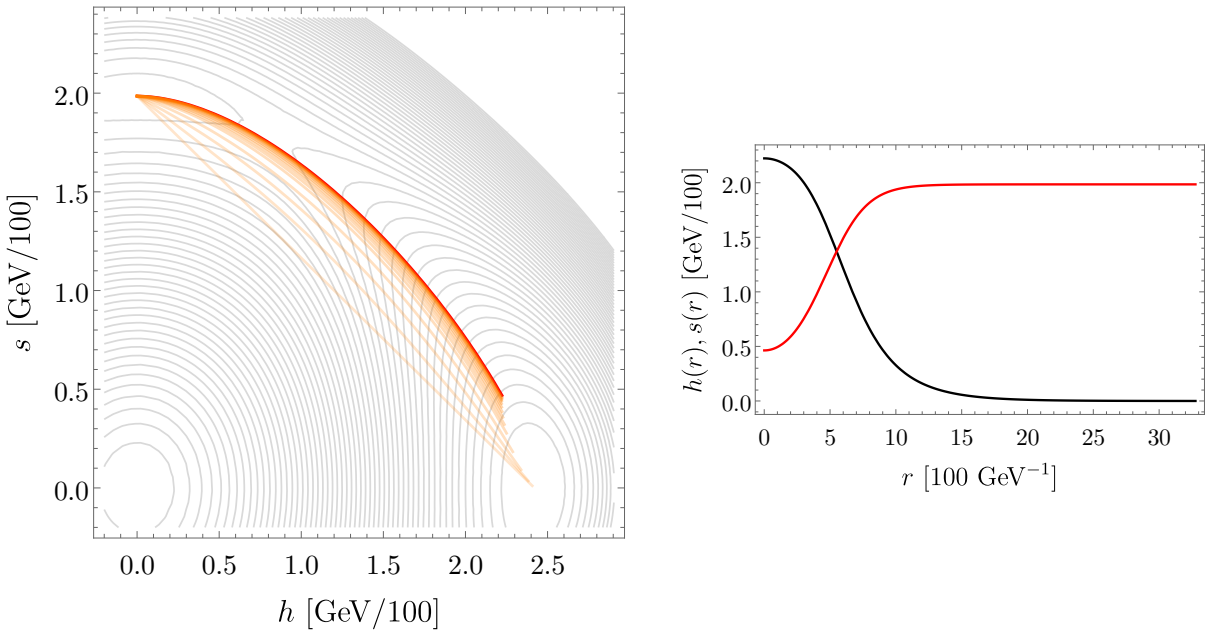

Figure 2.A.2: Left: iterative procedure for the correct path, starting from the straight line connecting the two minima and then modified according to the field $\vec{N}$. **Right**: bounce profile of the fields (black for $h(r)$ and red for $s(r)$) on the correct path.

Here, we have been able to separate the dynamics along the parallel and perpendicular direction in such a way the first equation defines a new undershoot/overshoot problem, that we solve to obtain the value of the *escape point*, $\vec{\phi}_0(x_\star)$, and the Euclidean action corresponding to the potential along the path considered $\vec{\phi}_g$, as in fig.2.A.1. On the other hand, the second equation can be seen as a condition that the bounce solution has to satisfy and can be thought of as a force field acting on the path, defined as following

$$\vec{N} \equiv \frac{d^2\vec{\phi}_g(x)}{dx^2}\left(\frac{dx}{dr}\right)^2 - \vec{\nabla}_\perp V[\vec{\phi}_g(x)] \ . \tag{2.81}$$

The right path will be the one where $\vec{N}$ is vanishing. The algorithm proceeds iteratively: first, we guess a path, the straight line connecting the two minima, then we find the bounce solution along this path, we compute the normal force and deform the guessed path according to it. In practice, to define the path at the step n, $\vec{\phi}_n$, we need to solve for the bounce profile for the path at $\vec{\phi}_{n-1}$, extract the escape point $x_{\star,n-1}$, that is $(h(x_{\star,n-1}), s(x_{\star,n-1}))$ in field space, we then discretise the path in the interval $x \in [0, x_{\star,n-1}]$, creating a series $(\vec{\phi}_{n-1})_j$, for $j = 1, ..., N$ and a series of values for the normal force $(\vec{N}_{n-1})_j$. We then shift each point of the discretised path by

$$(\vec{\phi}_n)_j = (\vec{\phi}_{n-1})_j + \rho(\vec{N}_{n-1})_j \qquad j = 1, \dots, N \ . \tag{2.82}$$

In the end, we fit a path $\vec{\phi}_n$ along the shifted points from $(\vec{\phi}_{n-1})_j$. The procedure of deformation of the path will produce a series of paths $\vec{\phi}_i[x]$, over which we compute the Euclidean action according to eq.(2.76) at each step of the deformation, like in fig.2.A.2. The algorithm stops when the difference in the bounce action, S_3, between two successive iterations is below some imposed precision. At a definite temperature T, we start by identifying the two minima, the false and the true ones

$$(\langle h\rangle, \langle s\rangle)_{\rm fm} = (v(T), v_s(T)) \to (v_{EW}, 0) \ , \tag{2.83}$$

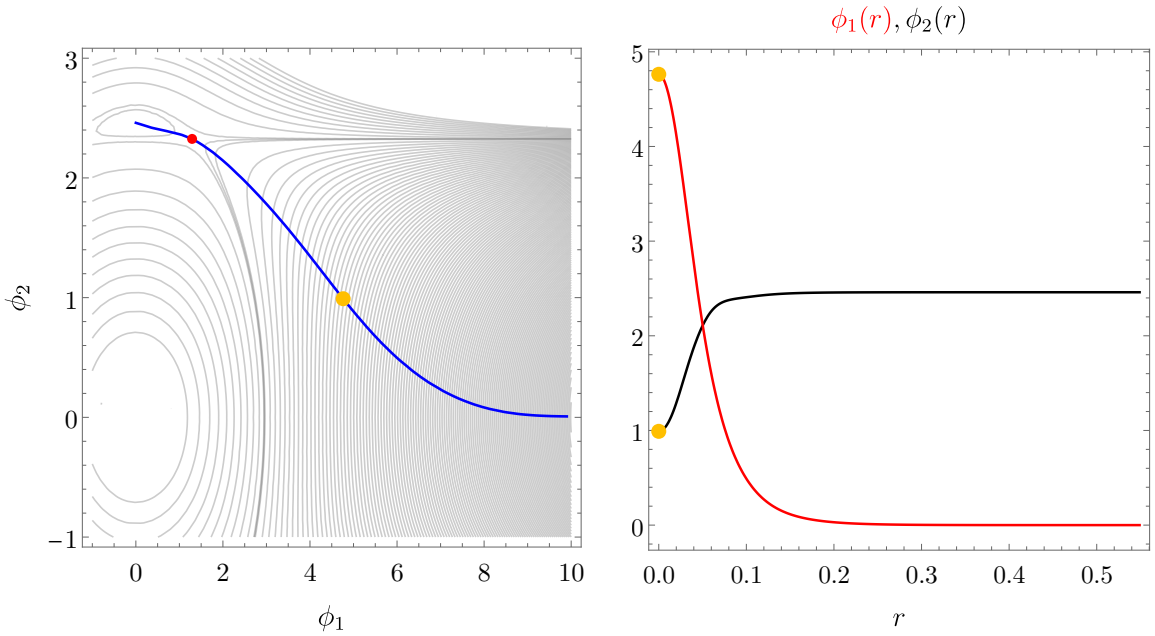

Figure 2.A.3: Left: in blue the initial guessed path with a straight line connecting the false vacuum and the saddle-point, showed in red, and then the steepest path computed from the saddle-point. We used a polynomial potential with arbitrary units, not relevant for the qualitative picture we are presenting in this section. **Right**: fields profile along the final tunnelling path that it is not shown in the right panel, since it almost super-imposes with the initial path. In yellow it is depicted the release point.

and will keep the false minimum fixed during the whole procedure of deformation. Generally, especially when we have a sizable amount of supercooling, the escape point is just behind the barrier, so the escape point $(v_\star(T_n), v_{s,\star}(T_n))$ will be different from the, zero-temperature, EWSB vacuum, but when the tunnelling happens the system will classically roll down towards the global minimum, as we can see from fig.2.A.2. We do not track the evolution of the fields profile after the tunnelling.

2.A.3 Unbounded potentials

When dealing with an unbounded potential, conceptually there is nothing particularly different compared to a very deep minimum scenario. At some point, the escape point does not change significantly as the minimum becomes deeper. However, we encountered two specific issues:

- The initial path cannot be a straight line connecting the two minima, as we cannot guess the slope of the line without knowing the global minimum.
- Even if we intuitively select a straight initial line, the code we developed often becomes unstable if the guessed path is significantly different from the real one.

To address these issues, we devised an initial path consisting of two segments. First, a straight line connecting the false vacuum and the saddle point. Then, from the saddle point, we used the steepest descent path. This is achieved by solving the following equation:

$$\frac{d\vec{\phi}(t)}{dt} = -\vec{\nabla} V[\vec{\phi}(t)] \ , \qquad \vec{\phi}(0) = \text{saddle point} \ . \tag{2.84}$$

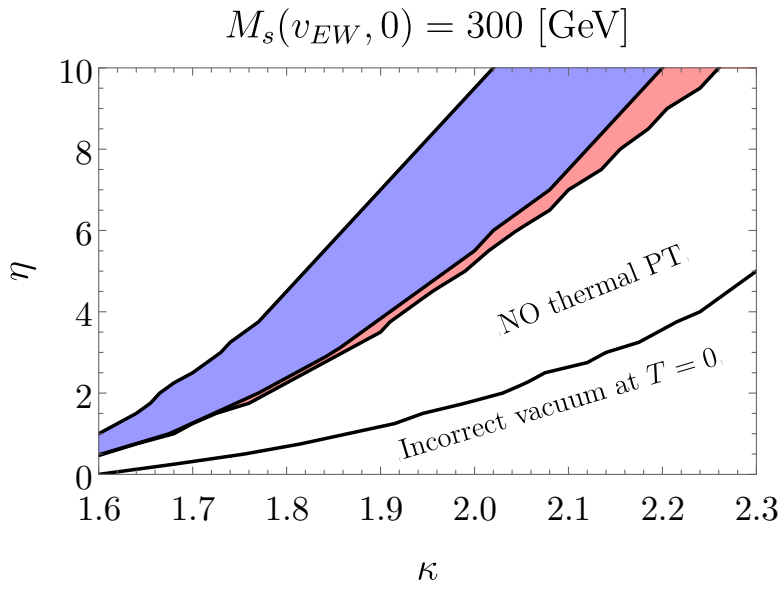

Figure 2.B.1: Here is presented the same results found in fig. 6 of ref. [162]. It has to be noted that these results are obtained with only the thermal potential and without Daisy resummation, *i.e.* without thermal masses. The relation with our parameters is $(\lambda_s,\ \lambda_{hs}) = (\eta,\ 2\kappa)$ and $M_s(v_{EW}, 0) = 300$ GeV.

$m_s = 150$ GeV, $v_s = 175$ GeV							
λ_{hs}	$\frac{T_{\rm reh}}{100\rm GeV}$	$\frac{T_{\rm nuc}}{100\rm GeV}$	$\frac{T_{\rm per}}{100\rm GeV}$	γ_w	$\frac{\tilde{\beta}}{H} = \frac{(8\pi)^{1/3}}{R_\star H}$	$m_H^{\rm False}/\rm GeV$	$\rm FM_0$
0.53	0.616	0.608	0.592	–	580	17.4	No
0.54	0.581	0.570	0.552	3	420	17.8	No
0.56	0.492	0.470	0.444	9	228	17.7	No
0.58	0.329	0.141	0.130	348	160	4.7	No
0.582	0.327	0.051	0.0508	$5.3 \cdot 10^3$	$9.5 \cdot 10^3$	0.4	No
0.582262	0.327	0.025	0.0236	$3.7 \cdot 10^4$	194	8.2	Yes
0.582264	0.327	0.024	0.0219	$4.3 \cdot 10^4$	130	8.3	Yes
0.582266	0.327	0.021	0.017	$5.7 \cdot 10^4$	24	8.5	Yes

Table 2.B.1: Same as Tables 2.1 and 2.2, but with $m_s = 150$ GeV and $v_s = 175$ GeV.

With this initial guess, the algorithm proceeds as previously described, and the code stabilises. Figure 2.A.3 provides a pictorial understanding of the case with two fields, ϕ_1 and ϕ_2. The blue path represents the first straight segment from the false vacuum to the saddle point, followed by the steepest descent path. The red point marks the saddle point, while the yellow point indicates the release point. The right panel shows the field profiles along the final path.

2.B Supplemental numerical results

In this Appendix, we present all our supplemental numerical results. First, although we focused mostly on a more weakly coupled part of the parameter space, we would like to compare our findings with the ones in the ref. [162] and argue that we observed only small changes, due to the inclusion of loop-corrections and Daisy resummation. In fig.2.B.1 we make a reproduction of the scan of fig.6 of [162] using our potential and emphasise the close similarities. The relations between the parameters κ, η and the couplings in the

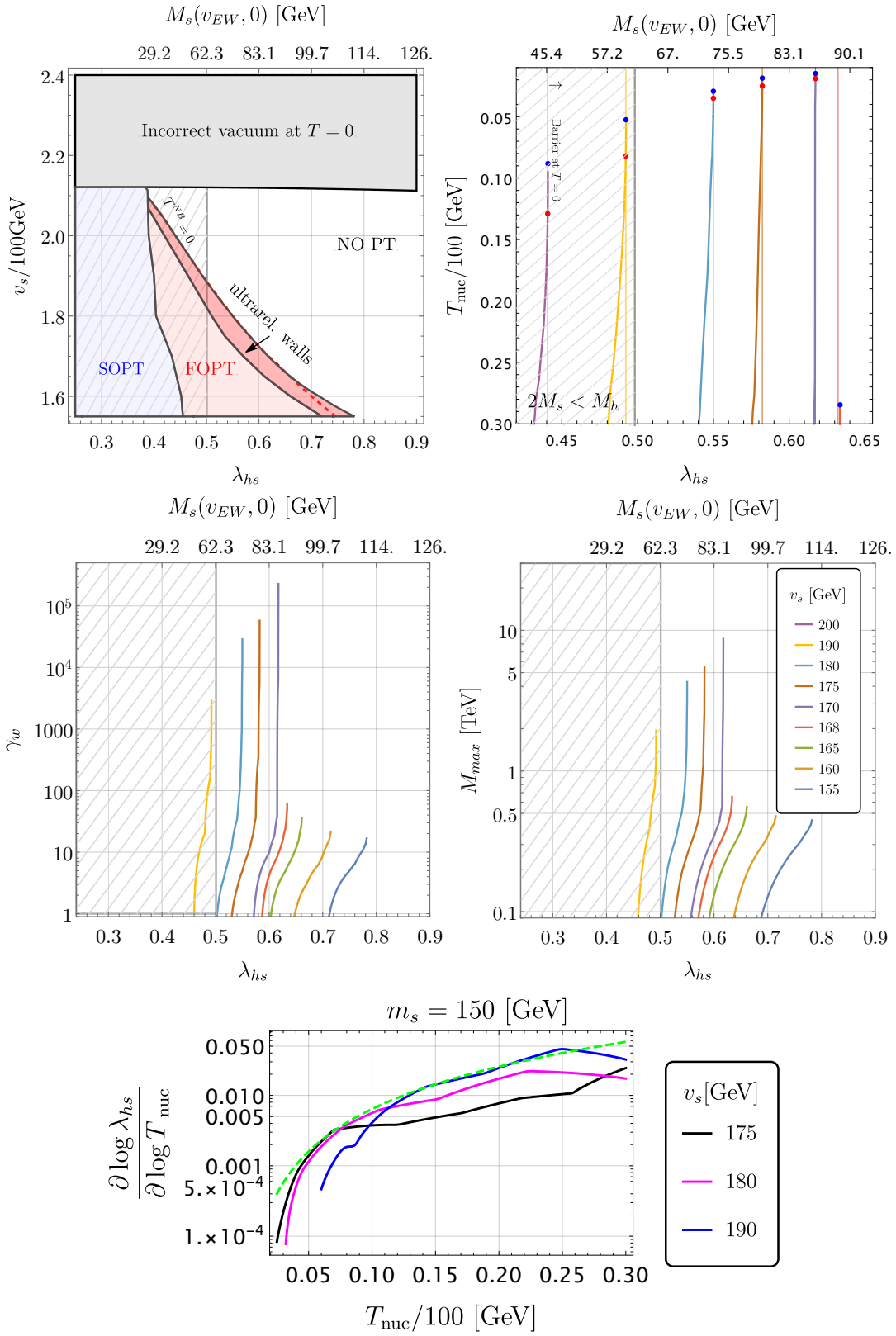

Figure 2.B.2: Similar plots than in fig.2.1 and fig.2.3 for the value of $m_s = 150$ GeV.

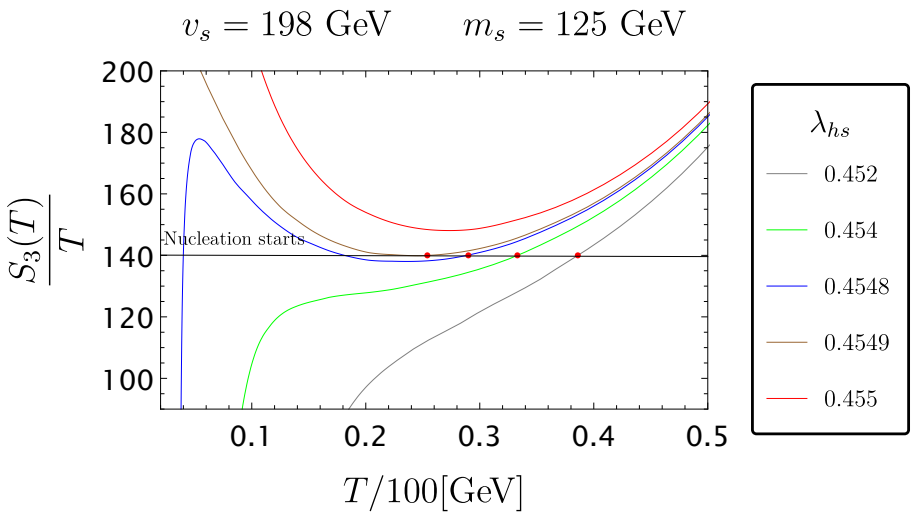

Figure 2.B.3: In this plot we show the regime of transition. We observe that several points display a disappearance of the barrier which is typical of the regime of no barrier at $T = 0$. However, the nucleation temperature is controlled by the first minimum of S_3/T, which is typical of the regime with a barrier at $T = 0$.

eq.(2.1) is as follows

$$\kappa \text{ [162]} = \frac{\lambda_{hs}}{2} , \quad \eta \text{ [162]} = \lambda_s . \tag{2.85}$$

In the main text, we studied specifically the case where the parameter $m_s = 125$ GeV, we observed that for this value, the region of deep supercooling displayed small masses of the singlet in the real vacuum, being on the verge of detection due to $h \to ss$ at $M_s \lesssim 62$ GeV. We also concluded in section 2.4 that this region was closing around $M_s \approx 75$ GeV. We could wonder if this conclusion would change if we modify the value of the parameter m_s, and if so in which direction. In fig.2.B.2 we show similar plots than in fig.2.1 and 2.3 for the case of $m_s = 150$ GeV. Thus, increasing the value of m_s pushes the deep supercooling region to $M_s \approx 90$ GeV, at the price of increasing the portal coupling λ_{hs}. However, we can observe on the last plot of fig.2.B.2 that the typical tuning remains roughly the same and that we can still trust our naive $(T_{\text{nuc}}/m_h)^2$ for an order-of-magnitude estimate of the tuning.

On the other hand, we also observed that decreasing the parameter m_s to ≈ 100 GeV was pushing all the deep supercooling region inside $M_s \lesssim 62$ GeV, which is thus strongly disfavoured by colliders. We hope that this trend can be extrapolated to larger values of m_s, until we hit perturbativity bounds for λ_{hs}.

We could also wonder what happens at the *upper* boundary of the deep supercooling region, as we have observed in fig.2.1 a sharp decrease in the supercooling allowed around $v_s \lesssim 200$ GeV (for $m_s = 125$ GeV). This transition regime can be understood if we plot the explicit S_3/T functions in fig.2.B.3. Comparing the plot in fig.2.B.3 with the one in fig.2.4, we see that as we decrease v_s, the full pattern of S_3/T is shifted toward smaller values. At some critical point around $v_s \approx 200$ GeV, the nucleation becomes controlled by the first minimum in the function S_3/T and not by the disappearance of the barrier. This largely suppresses the possibility of large supercooling.

Finally, in Table 2.B.1, we provide the value of the velocity, reheating and nucleation temperature for $m_s = 150$ GeV and $v_s = 175$ GeV that was used in fig.2.6.

2.C The coefficient of NLO pressure

In this appendix, we will review the calculation of the friction coefficient for the NLO pressure for EW phase transition. We will follow closely the discussion in [96] and report the quantity

$$\left[\sum_{abc} \nu_a g_a \beta_c C_{abc}\right] , \tag{2.86}$$

where $\nu_a = 1(3/4)$ for a a boson (fermion), $\beta_c \equiv \frac{M_c}{M_Z}$and C_{abc} stands for the couplings appearing in the vertex. Normalisation of the C_{abc} coefficient is the following: for a chiral fermion coupled to the vector field the amplitude for the process $\psi \to \psi A_{soft}$ is equal to

$$g_\psi \bar{\psi}_L A_\mu \psi_L \Rightarrow \quad C_{\psi\psi A} = \frac{g_\psi^2}{4\pi\alpha_{em}} . \tag{2.87}$$

The relation eq.(2.87) is written only for one polarisation of the vector field. Similarly for the scalar field

$$i g_\phi (\phi^* \partial_\mu \phi - \partial_\mu \phi^* \phi) A^\mu \Rightarrow \quad C_{\phi\phi A} = \frac{g_\psi^2}{4\pi\alpha_{em}} , \tag{2.88}$$

and the vector fields

$$g_{V^1V^2A^3} \left(V^1_{\mu\nu} V^2_\mu A_\nu + V^2_{\mu\nu} A_\mu V^1_\nu + A_{\mu\nu} V^1_\mu V^2_\nu\right) \Rightarrow C_{V_1V_2A} = \frac{g^2_{V^1V^2A}}{4\pi\alpha_{em}} , \tag{2.89}$$

where in all of these formulas C_{abc} coefficients are reported only for one polarisation of the vector fields both in the initial and the final states. Summing all of these contributions and taking care of the multiplicities of the initial and final states we find

$$\left[\sum_{abc} \nu_a g_a \beta_c C_{abc}\right] = 2\left(\frac{7 + 14 c_w}{s_w^2} - \frac{7 - 15 s_w^2}{c_w^2}\right) \simeq 157 . \tag{2.90}$$

For the interested reader, we refer various individual contributions in the Table 2.C.1. If in the false vacuum the Higgs doublet $\mathcal{H}$ is too heavy its contribution must be subtracted and the sum in eq.(2.90) reduces to

$$\left[\sum_{abc} \nu_a g_a \beta_c C_{abc}\right]_{\text{No Higgs}} \simeq 145 . \tag{2.91}$$

At last, we would like to emphasise that these results include only the transverse polarisations of the vector fields. NLO effects of the longitudinal polarisations are not fully established and we omit them here, however, these cannot qualitatively modify the results.

2.D Domain wall collapse

Our main discussion was focused on the two step phase transition $(0,0) \to (0, v_s) \to (v_h, 0)$ where the first phase transition is Z_2 breaking. Obviously during such a phase transition domain walls will be formed which can drastically modify the cosmology of the system. We can avoid the stable domain walls if we assume some small Z_2 breaking, however in

Process	$\sum g_a C_{abc}$	β	ν	Result
$\psi \to W^{\pm}\psi$	$\frac{24}{s_w^2}$	c_w	$\frac{3}{4}$	$\frac{18c_w}{s_w^2}$
$\psi \to Z\psi$	$\frac{4(3-6s_w^2+8s_w^4)}{s_w^2 c_w^2}$	1	$\frac{3}{4}$	$\frac{3(3-6s_w^2+8s_w^4)}{s_w^2 c_w^2}$
$\mathcal{H} \to W\mathcal{H}$	$\frac{2}{s_w^2}$	c_w	1	$\frac{2c_w}{s_w^2}$
$\mathcal{H} \to Z\mathcal{H}$	$\frac{1-2s_w^2c_w^2+c_w^4+s_w^4}{2s_w^2c_w^2}$	1	1	$\frac{1-2s_w^2c_w^2+c_w^4+s_w^4}{2s_w^2c_w^2}$
$A \to W_{soft}W$ & $W \to W_{soft}A$	8	c_w	1	$8c_w$
$Z \to W_{soft}W$ & $W \to W_{soft}Z$	$\frac{8c_w^2}{s_w^2}$	c_w	1	$\frac{8c_w^3}{s_w^2}$
$W \to Z_{soft}W$	$\frac{4c_w^2}{s_w^2}$	1	1	$\frac{4c_w^2}{s_w^2}$
Total:				$2\left(\frac{7+14c_w}{s_w^2} - \frac{7-15s_w^2}{c_w^2}\right) \simeq 157$

Table 2.C.1: Different contributions to the sum in eq.(2.22).

this case the question arises about the timescale for the stability of the domain walls. This is particularly important since recently it was shown [201] that for singlet extension of the SM the domain walls (if still present) will become seeds of the secondary phase transition $(0, v_s) \to (v_h, 0)$ and will dominate the phase transition. We will follow closely the discussion in section 2.3.2 using only the tree-level potential and the thermal corrections to the masses. Then the Z_2 breaking phase transition will occur at the temperatures

$$T_{Z_2} \simeq v_s \left(\frac{12}{3 + 4\lambda_{hs}\frac{v_s^2}{m_s^2}}\right)^{1/2} \simeq 200 - 300 \ \ \text{GeV}, \tag{2.92}$$

which is the temperature of the domain wall formation. The domain wall-mediated transition will happen at the temperature T_w which is found to be order one different from T_{Z_2}. The exact mechanism of the transition depends on the values of the couplings and can proceed either with the classical rolling or 2D bounces localised on the domain wall. The temperature when the classical rolling can start is reported in ref. [201] and is equal to

$$T_w^{\text{rolling}} \simeq T_{Z_2}\left[\frac{4m_h^2 + m_s^2\left(1 - \sqrt{1 + \frac{8v_s^2\lambda_{hs}}{m_s^2}}\right)}{8\Pi_h(T_{Z_2}) + m_s^2\left(1 - \sqrt{1 + \frac{8v_s^2\lambda_{hs}}{m_s^2}}\right)}\right]^{1/2} . \tag{2.93}$$

The nucleation temperature (T_w^{2D}) of $2D$ bounces should be found numerically (ref. [201]) however it will be obviously smaller than T_{crit} (of $(0, v_s) \to (v_h, 0)$ phase transition). At this point, we can safely ignore the seeded phase transition effects if all of the domain walls annihilate in the interval of temperatures

$$[T_w, T_{Z_2}] \ , \quad T_w < T_{\text{crit}} \ , \tag{2.94}$$

where T_w is the temperature when the seeded phase transition will be completed and it is obviously less than $T_{\rm crit}$ of EW phase transition. Let us estimate how strong the bias ΔV_B should be between the potential energies of the two minima of Z_2 potential so that all of the walls can disappear. For these estimates, it is sufficient to assume that there is order one difference between T_w and T_{Z_2}, which is generically the case. The critical radius (above which) areas with the true vacuum will start to expand is roughly

$$R_c \sim \frac{\sigma}{\Delta V_B} \ , \tag{2.95}$$

where σ is the surface energy density of the wall. So the domain walls will exist on the time scale of

$$\Delta t_w \sim \frac{R_c}{u} \sim \frac{\sigma}{u \Delta V_B} \ , \tag{2.96}$$

where u is the velocity of the wall motion. The change of the temperature during the wall annihilation will be roughly

$$\Delta T \sim T_{\rm crit} H \Delta t_w \ . \tag{2.97}$$

So if $\Delta t_w H \ll 1 \Rightarrow \Delta T \ll T_{\rm crit}$ the wall annihilation happens almost instantaneously. Assuming $\sigma \sim T_{\rm crit}^3$ and $H \sim \frac{T_{\rm crit}^2}{M_{\rm pl}}$ we get

$$\frac{\Delta V}{T_{\rm crit}^4} \gg \frac{T_{\rm crit}}{u M_{\rm pl}} \ . \tag{2.98}$$

Balancing the pressure against the friction forces $\Delta V_B \sim u T_{\rm crit}^4$ we can estimate the velocity and then the condition for the quick wall annihilation becomes

$$\frac{\Delta V_B}{T_{\rm crit}^4} \gg \sqrt{\frac{T_{\rm crit}}{M_{\rm pl}}} \sim 10^{-8} \ , \tag{2.99}$$

which is not restrictive at all.

Chapter 3

Quantisation across the bubble wall and friction

The progression of a FOPT involves the nucleation and expansion of bubbles of a new phase, driven by the free-energy density difference ΔV between phases. If there is no friction from surrounding matter, the bubble walls expand with constant acceleration, a scenario known as *runaway*. However, if friction generates a pressure $\mathcal{P}$ balancing the driving force ($\mathcal{P} \simeq \Delta V$), the bubbles reach a constant subluminal velocity.

Understanding bubble dynamics is crucial for predicting phenomena like GW signals. Friction depends on the bubble velocity v_w and the surrounding dofs. At low v_w, a fluid description can be suitable, but in the ultra-relativistic regime, individual particle interactions become significant. Incoming particles can either cross the wall or reflect, with the resulting momentum loss providing the pressure opposing the expansion.

At leading order (LO), for processes $1 \to 1$, the pressure is independent of γ_w, scaling with temperature and the vev in the broken phase, see (1.213). Next-to-leading order (NLO) processes, i.e. $1 \to 2$, involving the emission of soft vector bosons, lead to a friction pressure scaling with γ_w, known as *transition radiation*, which can dominate the LO effect, see (1.234). In fig. 3.0.1 is presented a sketch of such processes. This study will point out that longitudinal modes and soft momenta, often neglected in previous analyses, can significantly impact pressure calculations.

In this chapter, we approach the calculation of transition radiation by quantising field theories in the translation-breaking background of a domain wall from first principles. A complete orthonormal basis is constructed from 'left' and 'right' mover energy eigenstates, with each wave mode having 'reflected' and 'transmitted' parts. We then carefully relate these to *in* and *out* asymptotic eigenstates of 4-momentum, understood in the S matrix language.

For vectors, we demonstrate that describing the degrees of freedom across the wall in terms of 'wall polarisations' τ and λ is more convenient than using conventional transverse and longitudinal modes, as pointed out in [116]. The advantage of this approach is that $\tau_{1,2}$ and λ are not mixed with each other in the presence of the domain wall. These sets coincide only for zero transverse momentum $\boldsymbol{k}_\perp = 0$ (normal incidence on the wall), where rotations around the direction of propagation remain a symmetry.

In the case of gauge symmetry–breaking, λ smoothly interpolates between a Higgs degree of freedom on the symmetric side and a third massive vector degree of freedom on the broken side. We show how to perform calculations using this basis consistently, avoiding divergences that may appear in a naive analysis.

Although we explain how to (numerically) compute $\langle \Delta p \rangle$ for a general wall profile,

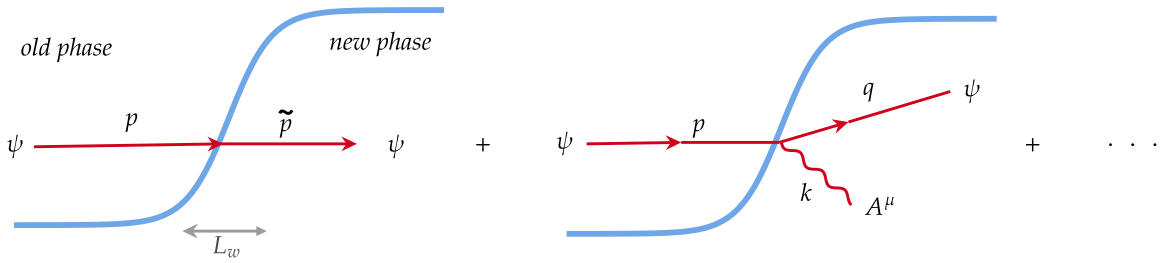

Figure 3.0.1: Diagrams corresponding to LO and NLO processes contributing to friction on a moving bubble wall. The emission of vectors with changing mass is generally the dominant $1 \to 2$ process for friction and the subject of this work. Tilde distinguishes objects in the new phase.

we dedicate most of the work to approximating it in a way that is independent of the particular shape, with the rough scale L_w playing the only role, while commenting on the sensitivity thereon. For the IR of the emitted spectrum $k^z \lesssim L_w^{-1}$ the wall appears effectively as a step function. This limit is particularly interesting theoretically (as well as phenomenologically important, as mentioned already) since everything can be computed analytically and relatively simply. For wavelengths shorter than the wall width $k^z > L_w^{-1}$, the WKB approximation becomes applicable. The integral over the phase space thus splits into two contributions and the averaged momentum exchange very schematically takes the form

$$\langle \Delta p \rangle \sim \int^{k^z < L_w^{-1}} d^3k \, \Delta p \, |\mathcal{M}^{\text{step}}|^2 \; + \; \int_{k^z > L_w^{-1}} d^3k \, \Delta p \, |\mathcal{M}^{\text{wkb}}|^2 \; . \tag{3.1}$$

where the $\mathcal{M}$ are matrix elements for emission calculated using the respective approximations. As the incoming flux scales like γ_w, we then have

$$\mathcal{P} \propto \gamma_w \langle \Delta p \rangle \; . \tag{3.2}$$

As a warm up, we study transition radiation in a theory with two scalars and observe some surprises. Though we find that the pressure from the emission of one scalar by the other always saturates at large velocities $\mathcal{P}^{\text{NLO,scalars}}_{\gamma_w \to \infty} \propto \gamma_w^0$, we find also that there can be an intermediate regime of linear growth $\mathcal{P}^{\text{NLO,scalars}}_{\text{intermediate}} \propto \gamma_w$. For scalars we find that the WKB contribution (second term in eq. (3.1)) dominates the momentum transfer in the asymptotic γ_w limit.

In the case of spontaneous breaking of gauge symmetry we find that the total friction from vector emissions scales as $\propto \gamma_w \log \frac{gT}{\tilde{v}}$ for $T/\tilde{v} \ll 1$, where $\tilde{v}$ is the Higgs' vev, in line with literature. We provide an updated fitted formula in eqs. (3.135) and (3.139). The logarithmic enhancement appears only for the τ polarisations, and is dominated by the step function contribution (the first term in the eq. (3.1)), however we also find that effects of the λ polarisations can lead to significant corrections for mild supercooling ($\frac{\tilde{v}}{T} \sim$ few). We compare the relative importance in fig. 3.0.2 (Left). The curves are only very weakly dependent on L_w. This and all of the rest of the figures in the chapter are in natural units with some arbitrary scale [arb.].

As a side application, we also compute the transition radiation when the bubble wall connects two vacua with broken gauge symmetry–but different vevs v and $\tilde{v}$. In this case, the contribution to friction from the longitudinal vector emission scales as

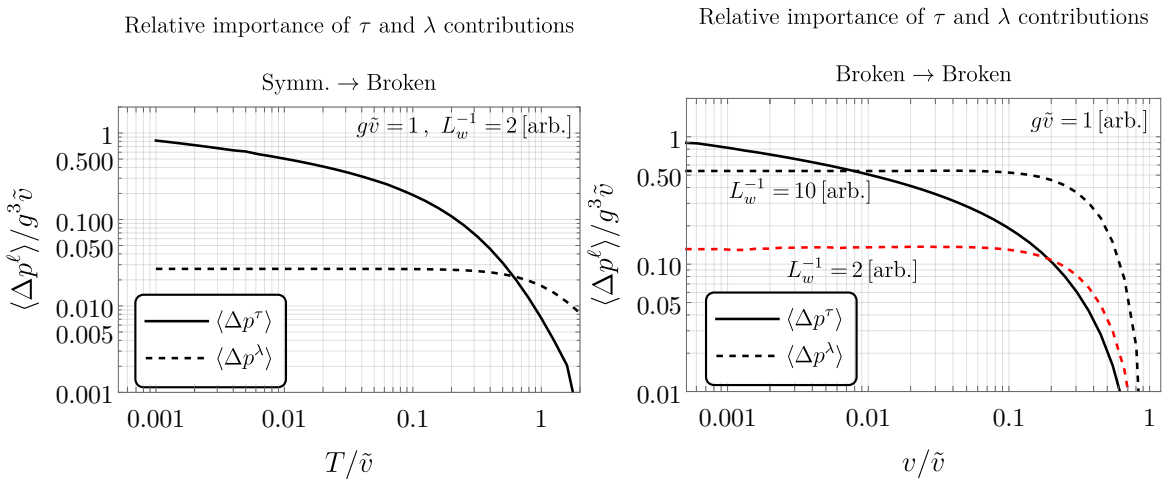

Figure 3.0.2: Comparison between the averaged exchanged momentum from transition radiation due to the emission of τ and λ vector polarisations, in the limit of large incoming particle energy $p_0 \to \infty$. **Left**: Symmetric → Broken transition at finite temperature T, shown as a function of temperature over Higgs vev $\tilde{v}$. T enters via thermal masses (for details see the discussion in section 3.3.2). Results do not change significantly in the limit $L_w \to 0$. **Right**: Broken → Broken transition. While the τ contribution does not change, λ emission can easily become dominant. We highlight the sensitivity on the wall thickness. [arb.] means arbitrary units.

$\mathcal{P}^{\text{NLO,vectors}}_{\gamma_w \to \infty} \propto \gamma_w L_w^{-1}$ (see fig. 3.0.2, Right) and can dominate over the transverse for thin wall.

Aside from the asymptotic $p^0 \to \infty$ limit, we are also able to explore regimes with intermediate – though large – γ_w. For symmetric → broken transition we find that the saturating value is reached at energies dependent on the mass of the emitter particle, as shown in fig. 3.0.3 (Left). In the case of the broken → broken transition we find that there is an intermediate regime where the pressure scales as $\mathcal{P}^{\text{NLO,vectors}}_{\text{intermediate}} \propto \gamma_w^2$ (right panel of fig. 3.0.3).

The chapter is organised as follows: in the section 3.1 we work through a toy model with only scalars, introducing various elements of the calculation. In section 3.2 we quantise an Abelian Higgs model in the presence of a symmetry–breaking domain wall and present the results for transition radiation of vectors in section 3.3. We summarise in section 3.4.

Summary of notation: In the rest of this chapter, we will adopt the following conventions:

1. We treat the bubble wall in the planar limit, where it is one dimensional and centred around $z = 0$.

2. We use a hybrid notation for four-vector Lorentz indices:
   $\mu = (n, z) \equiv (0, 1, 2, z)$. Coordinates are $x^\mu = (x^n, z) \equiv (t, \boldsymbol{x}_\perp, z)$.

3. Similarly for momenta $k^\mu = (k^n, k^z) \equiv (k_0, \boldsymbol{k}_\perp, k^z) \equiv (k_0, \boldsymbol{k})$.
   Also $E^2 = k^n k_n = k_0^2 - k_\perp^2$, where $k_\perp = |\boldsymbol{k}_\perp|$.

4. We define the change in mass across the wall $\Delta m \equiv \sqrt{\tilde{m}^2 - m^2}$.

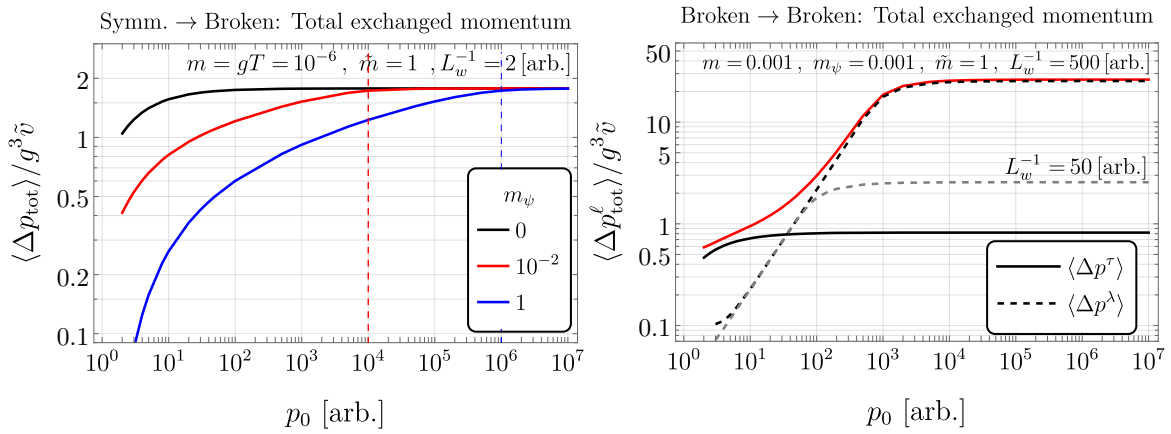

Figure 3.0.3: Total averaged momentum exchange as a function of incoming particle energy p^0. **Left**: Symmetric → Broken for different values of the mass of the *emitter* particle ψ. The asymptotic regime is reached around $p^0 \sim m_\psi \tilde{m}/m$ (dashed lines), with intermediate $\log(p^0/m_\psi)$ growth. **Right**: Broken → Broken with thin walls. Here the saturation value is reached around $p_0 \sim L_w^{-1}\text{Max}[1, m_\psi/m]$. Again we highlight the sensitivity to wall width. For small enough L_w we find an inter-relativistic regime with averaged exchange momentum growing linearly, which translates to pressure scaling like γ_w^2.

5. L_w is the thickness of the wall.

6. γ_w (v_w) is the boost factor (the velocity) of the wall.

7. The momenta p, q, k will always be used as in fig. 3.0.1 and we define:

$$\begin{aligned} \Delta p &\equiv p^z - q^z - k^z \ , \quad \Delta p_r \equiv p^z - q^z + k^z \ , \\ \Delta \tilde{p} &\equiv p^z - q^z - \tilde{k}^z \ , \quad \Delta \tilde{p}_r \equiv p^z - q^z + \tilde{k}^z \ . \end{aligned} \tag{3.3}$$

3.1 Simple example: scalars

In this section, as a warm up for the more complex case of gauge theories, we go through the quantisation of a scalar field theory in the presence of a domain wall and derive results for transition radiation for the case of one scalar emitting another. This toy example is sufficient to highlight many features of calculations in a spatially dependent background.

Consider two different scalar fields ϕ, ψ, the first of which feels the wall and has different mass depending on the phase, while the second for simplicity does not. The Lagrangian we consider is the following

$$\mathcal{L} = \frac{1}{2}(\partial\phi)^2 + \frac{1}{2}(\partial\psi)^2 - \frac{1}{2}m_\phi^2(z)\phi^2 - \frac{1}{2}m_\psi^2\psi^2 - y(z)\frac{1}{2}\psi^2\phi, \tag{3.4}$$

where $m(z)$ interpolates between $m^2(z)|_{z\to-\infty} = m^2 = const$ and $m^2(z)|_{z\to+\infty} = \tilde{m}^2 = const$. Similarly $y(z)$ goes from y to $\tilde{y}$. The profiles change on the scale of the wall width L_w around $z = 0$. The interactions in eq. (3.4) are not the most general, but are designed to mimic the vector case when $y = const$. The process that we will be studying is $\psi \to \psi\phi$, which would be forbidden by kinematics if it was not for the breaking of $z-$momentum.

Section summary: In section 3.1.1 and 3.1.2, we quantise the free theory, focusing on the ϕ field [1] , by defining a complete basis of solutions that solve its equations of motion. In section 3.1.3, we define a new basis that corresponds to *out-going* eigenstates of momentum. Later, in section 3.1.4, we calculate the amplitude for the $\psi \to \psi\phi$ transition in the step wall approximation, valid when $k^z L_w \lesssim 1$. In section 3.1.5, we present the proper domain for the phase space integration over the final state. In section 3.1.6, we complete the emission spectrum discussing the calculation of the amplitude in the (opposite) WKB regime $k^z L_w \gtrsim 1$. In section 3.1.7, we summarise and present master formulae for the calculation of the averaged momentum transfer $\langle \Delta p \rangle$. We conclude by discussing results for $\langle \Delta p \rangle$ and pressure $\mathcal{P}^{\rm NLO}$ in sections 3.1.8 and 3.1.9 respectively.

3.1.1 Complete basis

The quantisation of modes in the presence of a background profile arises in many corners of physics. A very similar task appears for example in the quantisation of field theory in black hole spacetimes. We found the treatment in [202] particularly useful. In the simple example of eq. (3.4) above, the discussion is relevant for ϕ, which satisfies

$$(\partial^2 + m_\phi^2(z))\phi = 0\,, \tag{3.5}$$

with a $z-$dependent mass term. To perform second quantisation we need to first find a convenient basis of solutions of this equation. Far away from the wall the solutions are plane waves. A convenient choice of complete orthonormal basis is given in terms of 'right' and 'left' moving solutions, which are defined by their boundary conditions as follows [2]

$$\phi_{R,k} = e^{-ik_n x^n}\chi_{R,k}(z) \equiv e^{-ik_n x^n}\begin{cases} e^{ik^z z} + r_{R,k}e^{-ik^z z}\,, & z \to -\infty \\ t_{R,k}e^{i\tilde{k}^z z}\,, & z \to +\infty \end{cases} \quad \text{(Right)} \tag{3.6}$$

with $k^0 > m$ and

$$\phi_{L,k} = e^{-ik_n x^n}\chi_{L,k}(z) \equiv e^{-ik_n x^n}\sqrt{\frac{k^z}{\tilde{k}^z}}\begin{cases} t_{L,k}e^{-ik^z z}\,, & z \to -\infty \\ r_{L,k}e^{i\tilde{k}^z z} + e^{-i\tilde{k}^z z}\,, & z \to +\infty \end{cases} \quad \text{(Left)} \tag{3.7}$$

with $k^0 > \tilde{m}$ and we take $k^z, \tilde{k}^z$ to be strictly positive [3]. The factor $\sqrt{k^z/\tilde{k}^z}$ is included in eq. (3.7) to ensure appropriate normalisation (see below, eq. (3.13)). In the limit of no domain wall the r_L, r_R (t_L, t_R) coefficients are zero (one) and ϕ_L, ϕ_R correspond simply to the plane waves with $\mp k^z$ momenta. The momentum along z is not conserved across the wall; however, asymptotically far it becomes constant and fixed by the relations

$$k^z \equiv \sqrt{k_0^2 - k_\perp^2 - m^2}, \quad \tilde{k}^z \equiv \sqrt{k_0^2 - k_\perp^2 - \tilde{m}^2}\,. \tag{3.8}$$

In general, we need to solve the equations of motion to find the expression of the coefficients $r_{L,R}, t_{L,R}$. Consequently, they will depend on the explicit form of the mass variation $m_\phi^2(z)$. However, here it will be sufficient to consider the *step wall* ansatz for the mass $m_\phi^2(z)$

$$m_\phi^2(z) = m^2 + \Delta m^2 \Theta(z)\,, \qquad \Delta m^2 \equiv \tilde{m}^2 - m^2\,. \tag{3.9}$$

[1] The quantisation of ψ, as it does not feel the wall, is instead completely standard.

[2] Recall that the index n designates $0, 1, 2$ and not the z direction.

[3] As is well known, the basis formed by just $\phi_{R,k}$ but allowing k^z to take both signs (and $\tilde{k}^z = \text{sign}(k)(\sqrt{k^2 - \Delta m^2})$ is also complete but not orthogonal and therefore less convenient. For example, the algebra of creation and annihilation operators would be more complicated.

using the Heaviside Theta function. The form of the coefficients for the scalar case under consideration can be obtained by matching ϕ and its first derivative at the origin $z = 0$, where the step wall lies. They take the form

$$r_{R,k} = \frac{k^z - \tilde{k}^z}{k^z + \tilde{k}^z} \ , \quad t_{R,k} = \frac{2k^z}{k^z + \tilde{k}^z} \ . \tag{3.10}$$

These expressions are specific to the step-wall assumption. However, the general treatment that we present here will hold for general r_k, t_k coefficients and could be easily adapted to a smooth wall case. Modes with $m < k_0 < \tilde{m}$ decay exponentially on the right of the wall and are automatically included as right-movers. For these, $\tilde{k}$ is purely imaginary with magnitude

$$|\tilde{k}^z|^2 = \Delta m^2 - k_z^2 \qquad \text{for} \qquad 0 < k^z < \Delta m \ . \tag{3.11}$$

In a similar fashion, for the left moving solution we find

$$r_{L,k} = -r_{R,k} = \frac{\tilde{k}^z - k^z}{k^z + \tilde{k}^z} \ , \quad t_{L,k} = \frac{\tilde{k}^z}{k^z} t_{R,k} = \frac{2\tilde{k}^z}{k^z + \tilde{k}^z} \ . \tag{3.12}$$

and we explicitly note the condition $k_0 > \tilde{m}$, to avoid the inclusion of solutions growing exponentially at infinity. The left and right moving modes are orthonormal in the sense that

$$\int_{-\infty}^{\infty} dz \ \chi_{I,k} \ \chi^*_{J,q} = 2\pi \delta_{IJ} \delta(k^z - q^z) \ , \qquad I, J \in \{R, L\} \ . \tag{3.13}$$

Computing integrals such as eq. (3.13) in the step function case requires the identity

$$\int_{-\infty}^{0} e^{i\beta z} dz = \text{PV}\left(\frac{1}{i\beta}\right) + \pi\delta(\beta) \ , \tag{3.14}$$

and its complex conjugate (which gives the integral from 0 to ∞). In eq. (3.13) the principle value (PV) pieces vanish as soon as we specify the relation between $\tilde{k}^z$ and k^z, i.e. $\tilde{k}_z^2 = k_z^2 + m^2 - \tilde{m}^2$. Notice we can discard terms proportional to $\delta(k^z + q^z)$ due to the strictly positive definition of k^z, q^z in our definition. If explicitly computing things like the Hamiltonian and operator algebra (see next subsection) it is also useful to know the other inner products:

$$\begin{aligned} \int_{-\infty}^{\infty} dz \ \chi_{R,k} \ \chi_{R,q} &= -\int_{-\infty}^{\infty} dz \ \chi_{L,k} \ \chi_{L,q} = 2\pi \frac{k^z - \tilde{k}^z}{k^z + \tilde{k}^z} \delta(k^z - q^z), \\ \int_{-\infty}^{\infty} dz \ \chi_{R,k} \ \chi_{L,q} &= 4\pi \frac{\sqrt{k^z \tilde{k}^z}}{k^z + \tilde{k}^z} \delta(k^z - q^z). \end{aligned} \tag{3.15}$$

Finally, we would like to comment that, in general, bound states may also appear in the spectrum, in addition to the scattering states studied above, if the function $m_\phi^2(z)$ is non-monotonic and has minima in the vicinity of the domain wall. These are of the form $\phi_{\text{b}} \propto e^{-ik^n x_n} \chi_{\text{b}}(z)$, with χ_{b} exponentially decaying for $|z| \to \infty$ and should be included in the upcoming expansion eq. (3.16). Further detail can be found in appendix 3.B.

3.1.2 Quantisation

Now that we have a complete orthonormal basis of eigenstates in the presence of the wall, we can proceed to quantise the theory. The field ϕ can be expanded in the form [4]

$$\phi(x,t) = \sum_{I=R,L} \int \frac{d^3k}{(2\pi)^3\sqrt{2k_0}} \left(a_{I,k}\phi_{I,k} + a^\dagger_{I,k}\phi^*_{I,k}\right) , \quad \text{where} \quad \phi_{L,k} \equiv 0 \quad \text{for} \quad E < \tilde{m} , \tag{3.16}$$

where $d^3k \equiv dk^z d^2k_\perp$, we recall $E \equiv \sqrt{k_0^2 - k_\perp^2}$ and k^z runs between $[0,\infty)$. We choose to label states by their quantum numbers outside the wall[5]. Note we have trivially extended the definition of the left moving modes to the region $E < \tilde{m}$ for convenience.

Using eqs. (3.13) and (3.15), one can show that

$$a_{I,p} = \int \frac{dz}{\sqrt{2p_0}} e^{ip_0 t} \chi^*_{I,p}(i\pi + p_0\phi) , \tag{3.17}$$

where $\pi \equiv \partial_t\phi$. Promoting Poisson brackets of ϕ and its conjugate momentum π to canonical commutation relations gives the familiar commutation algebra

$$\begin{aligned} [a_{I,k}, a^\dagger_{J,q}] &= (2\pi)^3\delta(\boldsymbol{k}-\boldsymbol{q})\delta_{IJ} , \\ [a_{I,k}, a_{J,q}] &= [a^\dagger_{I,k}, a^\dagger_{J,q}] = 0 , \qquad I,J \in \{R,L\} . \end{aligned} \tag{3.18}$$

We can define two types of states

$$|k_R\rangle \equiv \sqrt{2k_0}\, a^\dagger_{R,k}|0\rangle , \tag{3.19}$$

$$|k_L\rangle \equiv \sqrt{2k_0}\, a^\dagger_{L,k}|0\rangle , \tag{3.20}$$

which should be thought of as independent external states in any process. The space of physical states is thus the *Fock* space defined by arbitrary powers of $a^\dagger_{R,k}$ and $a^\dagger_{L,k}$ acting on the vacuum.

3.1.3 Out-going eigenstates of momenta

In the previous subsections we chose to quantise the orthonormal basis $\{\phi_{R,k}\,, \phi_{L,k}\}$ and defined associated one-particle states $|k_R\rangle$ and $|k_L\rangle$. As we explain in more detail in section 3.A by the use of wave-packets, these should be thought of as describing incoming particles with definite $z-$momenta k^z and $-\tilde{k}^z$ respectively at $t \to -\infty$, but at $t \to +\infty$ they correspond to a superposition between a transmitted and reflected particle. As a consequence, the functions $\phi_{R,L}$ are eigenstates of momenta only at $t \to -\infty$. They are well-suited for processes with asymptotic *in-state* ϕ particles.

On the other hand, in this work we will be interested in the momentum transfer to the wall, so it is more convenient to have a ϕ particle emitted as an asymptotic *out-state* with well-defined momentum at $t \to \infty$. A complete orthonormal basis of such late-time

[4] We use normalisation conventions in line with [203].

[5] This is more convenient than labeling with respect to $\tilde{k}^z$ since this becomes imaginary for the branch $0 < k^z < \Delta m$.

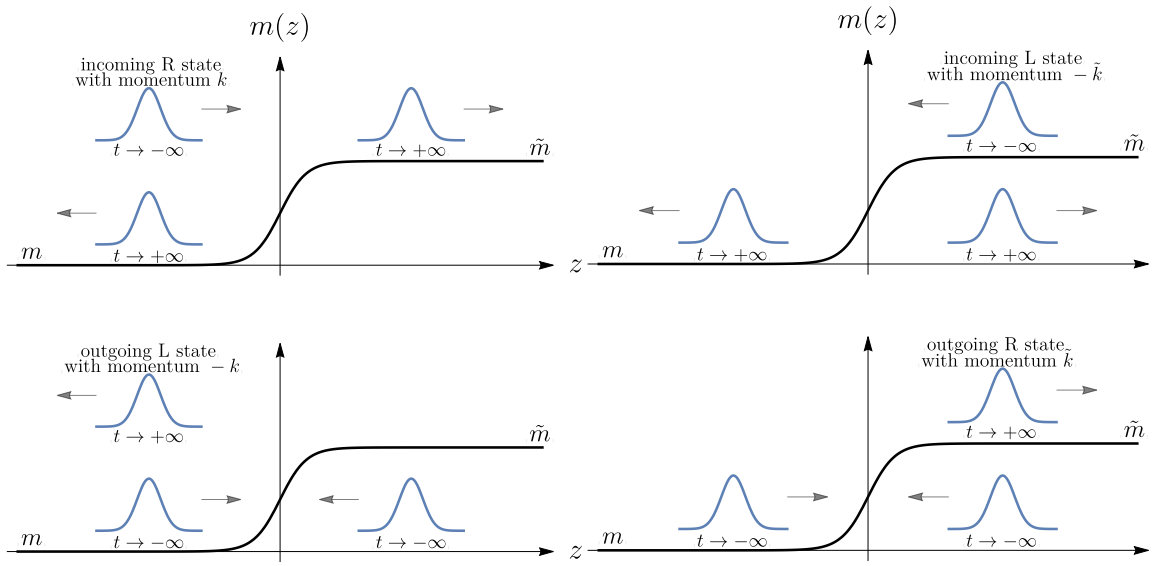

Figure 3.1.1: Summary of asymptotic external states with definite 4−momentum, to be used in calculating any process in the background of a domain wall (or any localised $z-$dependent potential). The upper panels represent in-state particles incoming from $z = -\infty$ and $z = \infty$. In the plane wave limit they correspond to states $|k_R\rangle$ and $|k_L\rangle$ with wavefunctions eqs. (3.6) and (3.7) respectively. The lower panels represent out-state particles travelling out towards $z = -\infty$ and $z = \infty$. They correspond to states eqs. (3.23) and (3.24) with wavefunctions eqs. (3.21) and (3.22) respectively.

eigenstates of momentum is given by

$$\phi^{\rm out}_{L,k} \equiv e^{-ik_n x^n}\zeta_{L,k}(z) = e^{-ik_n x^n}\chi^*_{R,k}(z) = e^{-ik_n x^n}\left(r^*_{R,k}\,\chi_{R,k} + t^*_{R,k}\sqrt{\frac{\tilde{k}^z}{k^z}}\,\chi_{L,k}\right) \ , \tag{3.21}$$

$$\phi^{\rm out}_{R,k} \equiv e^{-ik_n x^n}\zeta_{R,k}(z) = e^{-ik_n x^n}\chi^*_{L,k}(z) = e^{-ik_n x^n}\left(r^*_{L,k}\,\chi_{L,k} + t^*_{L,k}\sqrt{\frac{k^z}{\tilde{k}^z}}\,\chi_{R,k}\right) \ , \tag{3.22}$$

where in the last equalities we related them to the basis of section 3.1.1. We emphasise again that in our notation $k^z, \tilde{k}^z > 0$ always. $\phi^{\rm out}_{L,k}$ and $\phi^{\rm out}_{R,k}$ should be thought of as describing an outgoing final state particle with $-k^z$ and $+\tilde{k}^z$ momentum respectively. Recall that the function $\chi_{L,k}$ vanishes for $k^z < \Delta m$ and the corresponding Θ functions are implicit. At $t \to -\infty$ they are both superpositions of incoming particles from $z = \pm\infty$ and do not have well defined momentum. In practice we need to calculate the amplitudes with $\zeta_{L,R} = \chi^*_{R,L}$ wave functions. At the level of states, we have

$$|k^{\rm out}_L\rangle = r^*_{R,k}|k_R\rangle + t^*_{R,k}\sqrt{\tilde{k}^z/k^z}\ |k_L\rangle\ \Theta(k^z - \Delta m) \ , \tag{3.23}$$

$$|k^{\rm out}_R\rangle = t^*_{L,k}\sqrt{k^z/\tilde{k}^z}\ |k_R\rangle + r^*_{L,k}|k_L\rangle \ , \tag{3.24}$$

where we explicitly remind ourselves that when $0 < k^z < \Delta m$ the left mover state does not exist. The different asymptotic states are illustrated in the fig. 3.1.1.

We emphasise that both bases can be used to quantise the theory. In our present chapter however we will consider only outgoing ϕ particles so that the basis $\{\phi^{\rm out}_{R,k}, \phi^{\rm out}_{L,k}\}$ is actually more convenient. From now on we drop the label 'out' and we will refer to R (L) emission meaning using the mode functions $\{\zeta_R, \zeta_L\}$, if not stated otherwise.

3.1.4 Amplitudes

We now finally turn to compute the amplitude for the process $\psi \to \psi\phi$ in the background of a domain wall. We have not discussed the quantisation of ψ since it does not feel the wall directly and there are no complications with respect to the standard theory. In the previous sections we argued that there are two processes we have to consider separately: the emission of a left and right moving ϕ particle, with respective wavefunctions $\zeta_L(\zeta_R)$. Having quantised the free theory, the treatment of perturbative interactions proceeds as standard, by defining an S-matrix in terms of the interaction Hamiltonian $\mathcal{S} = \mathrm{T}\exp\left(-i\int d^4x\mathcal{H}_{\rm Int}\right)$ where T here denotes time ordering. We have the amplitudes of interest

$$\langle k_I^{\rm out}\ q|\ \mathcal{S}\ |p\rangle \equiv (2\pi)^3\delta^{(3)}(p^n - k^n - q^n)i\mathcal{M}_I \overset{\rm tree}{=} -i\int d^4x\langle k_I^{\rm out}\ q|\ \mathcal{H}_{\rm Int}\ |p\rangle \qquad (3.25)$$
$$\text{with} \quad I = L, R\ ,$$

where p and q stand for the initial and final one particle states for the ψ field and their respective 4−momenta, and the last equality is up to leading order in perturbation theory (tree level). Notice we have defined the matrix element $\mathcal{M}$ as closely as possible to standard theory. Of course, we cannot extract a z−momentum conserving delta function but rather $\mathcal{M}$ still contains the integral over z.

For the theory of scalars of eq. (3.4), we have $\mathcal{H}_{\rm Int} = -iy\psi^2(x)\phi(x)$ and we can now proceed to explicitly computing amplitudes. In the case of a ζ_L mode emission (where the emitted scalar has $-k^z$ momentum), the amplitude takes the form

$$\begin{aligned}\mathcal{M}_L &= \int_{-\infty}^{\infty} dz\ y(z)e^{i(p^z-q^z)z}\left[\zeta_{L,k} = \chi^*_{R,k}(z)\right]^* \\ &= \left[\frac{-iy}{p^z - q^z + k^z} + r_{R,k}\frac{-iy}{p^z - q^z - k^z} - t_{R,k}\frac{-i\tilde{y}}{p^z - q^z + \tilde{k}^z}\right]\ . \end{aligned} \qquad (3.26)$$

Instead, in the case of ζ_R mode emission (where the emitted scalar has $+\tilde{k}^z$ momentum):

$$\begin{aligned}\mathcal{M}_R &= \int_{-\infty}^{\infty} dz\ y(z)e^{i(p^z-q^z)z}\left[\zeta_{R,k} = \chi^*_{L,k}(z)\right]^* \\ &= \sqrt{\frac{k^z}{\tilde{k}^z}}\left[t_{L,k}\frac{-iy}{p^z - q^z - k^z} - \frac{-i\tilde{y}}{p^z - q^z - \tilde{k}^z} - r_{L,k}\frac{-i\tilde{y}}{p^z - q^z + \tilde{k}^z}\right]\ , \end{aligned} \qquad (3.27)$$

where the square root factor comes from the normalisation condition in eq. (3.7). To compute the total friction from $\psi \to \psi\phi$ we must sum the contributions from both processes. Then we can compute the amplitude squared for the emission of a right/left mover, under the assumption that $y = const.$, we obtain

$$|\mathcal{M}_R|^2 = y^2\frac{4k^z\tilde{k}^z(k^z - \tilde{k}^z)^2}{(\tilde{k}_z^2 - (p^z - q^z)^2)^2(k^z - p^z + q^z)^2}\ , \qquad (3.28)$$

$$|\mathcal{M}_L|^2 = y^2\frac{4k_z^2}{(k_z^2 - (p^z - q^z)^2)^2}\begin{cases}\frac{(k^z-\tilde{k}^z)^2}{(\tilde{k}^z+p^z-q^z)^2}\ , & k^z > \Delta m\ , \\ \frac{\Delta m^2}{\Delta m^2 - k_z^2 + (p^z-q^z)^2}\ , & k^z < \Delta m\ , \end{cases} \qquad (3.29)$$

where for L emission we distinguished between the two branches corresponding to $\tilde{k}^z$ purely real and imaginary, and used eq. (3.11) to simplify in the latter case.

3.1.5 Phase Space integration

We can now compute the average exchanged momentum due to transition radiation, $\langle \Delta p \rangle$ due to a single incoming particle. We integrate over the whole allowed phase space of the final two particles, weighting the amplitude squared for ψ to emit ϕ by the momentum lost. We add separately contributions from left and right movers with their respective slightly different phase space. $\langle \Delta p \rangle(p)$ is in general a function of the four-momentum p of the incoming ψ. From $\langle \Delta p \rangle$ we can compute the total friction pressure by integrating over the incoming flux.

For simplicity we take $\boldsymbol{p}_\perp = 0$ and parameterise the kinematics of the $1 \to 2$ process as follows

$$\begin{aligned} p^\mu &= (p_0, 0, 0, \sqrt{p_0^2 - m_\psi^2}), & q^\mu &= (q_0, -k_\perp, 0, q^z), \\ k^\mu &= (k_0, k_\perp, 0, k^z), & \tilde{k}^\mu &= (k_0, k_\perp, 0, \tilde{k}^z), \end{aligned} \tag{3.30}$$

where $\tilde{k}^z$ is defined in eq. (3.8) and $q^z = \sqrt{q_0^2 - k_\perp^2 - m_\psi^2}$, with $q_0 = p_0 - k_0$ from energy conservation. Note we have used the cylindrical symmetry of the set up to make the second spatial component of k^μ zero. $\langle \Delta p \rangle$ is given by the sum of left and right contributions

$$\begin{aligned} \langle \Delta p \rangle &= \langle \Delta p_R \rangle + \langle \Delta p_L \rangle \\ &\equiv \int d\mathbb{P}_{\psi \to \psi \phi_R} \underbrace{(p^z - q^z - \tilde{k}^z)}_{\Delta p_R^z} + \int d\mathbb{P}_{\psi \to \psi \phi_L} \underbrace{(p^z - q^z + k^z)}_{\Delta p_L^z} \, . \end{aligned} \tag{3.31}$$

where $d\mathbb{P}_{\psi \to \psi \phi_I}$ is the differential probability. The first and second terms on the RHS of eq. (3.31), will be different in their lower limits on the k^z integrals. The second term, left-mover emission, contains also the modes $k^0 < \tilde{m}$ which are exponentially decaying inside the wall. In section 3.A.2 we show that

$$\int d\mathbb{P}_{\psi \to \psi \phi_I} \Delta p_I^z = \int_{k_{\min}^{z,I}}^{k_{\max}^z} \frac{dk_z}{2\pi} \frac{1}{2k_0} \int_0^{k_{\perp,\max}^2} \frac{dk_\perp^2}{4\pi} \cdot \frac{1}{2p^z} \left[\frac{1}{2|q^z|} |\mathcal{M}_I|^2 \Delta p_I^z \right]_{q^z = \pm q_k^z} , \tag{3.32}$$

where $I = R, L$ and $[...]_{q^z = \pm q_k^z}$ is intended to be the sum over $q^z = \pm q_k^z$. The contribution with $q^z = -q_k^z$ corresponds to the reflection of the incoming particle ψ, a branch missing in the previous literature. Of course, in the ultra-relativistic regime, it is expected that this should be highly suppressed [6]. The limits of integration of eq. (3.32) are found demanding the reality of the q^z momentum, obtaining for the (R) modes

$$\begin{aligned} (\text{Right}): \; & k_{\min}^{z,R} \equiv \Delta m \le k^z \le k_{\max}^z \equiv \sqrt{(p_0 - m_\psi)^2 - m^2}, \\ & 0 \le k_\perp^2 \le k_{\perp,\max}^2 \equiv \frac{1}{4p_0^2}(p_0^2 + k_z^2 + m^2 - m_\psi^2)^2 - k_z^2 - m^2. \end{aligned} \tag{3.33}$$

For the (L) modes, the only difference is

$$(\text{Left}): \quad k_{\min}^{z,L} \equiv 0 \le k^z \le k_{\max}^z \, . \tag{3.34}$$

Following this discussion, in general, there will be four contributions:

$$\langle \Delta p_L^{q^z<0} \rangle, \langle \Delta p_L^{q^z>0} \rangle, \langle \Delta p_R^{q^z<0} \rangle, \langle \Delta p_R^{q^z>0} \rangle.$$

However, we explicitly checked that in all cases of interest, the contributions with $q^z < 0$ are largely subdominant and we will ignore them completely in the rest of this chapter.

[6] Notice that the sign change in Δp_R^z means that a process with $q^z < 0$ contributes more to momentum exchange, but it is the amplitude which is generally suppressed.

3.1.6 Emission in the WKB regime

So far we have been treating the bubble wall as a step function. This is a good approximation if the z momentum of the emitted particle is less than the inverse scale over which the background (in the case of eq. (3.4), the mass) changes significantly, i.e. $k^z \lesssim L_w^{-1}$. How can we proceed if the particles' momentum becomes comparable or larger than the width of the wall? First of all, if we know the shape of the potential exactly, we can solve for the left and right mover solutions as we did above for the step-wall, and proceed with these functions in precisely the same way as before. In principle, this can always be done numerically. However, we will argue that even in the case when we do not know the exact shape of the potential, we can still obtain reliable results.

Let us consider a particle hitting the wall with momentum $k^z \gg L_w^{-1}$. Reflection will be suppressed and the WKB approximation, which has been used extensively in the literature [95, 96, 107], becomes applicable. The approximate form of the z-dependent wavefunctions are now $\chi \approx \sqrt{k^z(z_0)/k^z(z)}e^{\pm i\int_{z_0}^{z} k^z(z')dz'}$, with z_0 some reference position. Having the approximate solutions to the $\chi_{R,L}(\zeta_{R,L})$ basis functions, we proceed in the same way as in section 3.1.4. Thus, in practice this means separating the phase space into two regions:

$$\begin{aligned} &\text{region (1)} \qquad k_\phi^z \ll L_w^{-1}, \quad \text{step wall,} \\ &\text{region (2)} \qquad k_\phi^z \gg L_w^{-1} \quad \text{WKB.} \end{aligned} \tag{3.35}$$

In the WKB regime the amplitude for a general $1 \to$ many right-movers[7] process, allowing for all masses to vary, can be schematically written as follows

$$\begin{aligned} \mathcal{M}_{\rm wkb} &= \int_{-\infty}^{+\infty} dz\, V(z) \exp\left[i\int_0^z \Delta p(z')dz'\right] \prod_i \sqrt{\frac{p_z^i(0)}{p_z^i(z)}}\,, \\ \Delta p(z') &\equiv p^z(z') - \sum_i p_i^z(z') = p^z(z') - \sum_i \sqrt{(p_0^i)^2 - (p_\perp^i)^2 - m_i^2(z')}\,, \end{aligned} \tag{3.36}$$

where i sums over final state particle momenta. Naively, computing this integral requires knowledge of the functions $m_i(z)$. However, these are changing only in the vicinity of the wall, while outside they quickly reach the asymptotic constant values. This means we can split the amplitude into two pieces

$$\begin{aligned} \mathcal{M}^{\rm wkb} = &\underbrace{\int_{-\infty}^{0} dz V(-\infty)e^{i\Delta p_z(-\infty)z} + e^{i\int_0^{L_w} dz'\Delta p(z')}\int_0^{\infty} dz V(+\infty)e^{i\Delta p_z(+\infty)z}}_{\mathcal{M}_{\rm outside}} \\ &+ \underbrace{\int_0^{L_w} dz V(z) e^{i\int_0^z dz'\Delta p(z')}}_{\mathcal{M}_{\rm inside}}\,, \end{aligned} \tag{3.37}$$

where the assumption is that things are varying only between $z \in [0, L_w]$. In the WKB regime, all the momenta of the particles are much larger than the inverse width of the wall $p^z L_w \gg 1$ so the overall modification of momenta $p(+\infty) - p(-\infty) \ll p(\infty)$ is much less than its absolute value (if the wall is not too thick $m(z)L \lesssim 1$), this is why we have approximated $\prod\sqrt{p/p(z)} \to 1$. Similarly $\Delta p(+\infty) - \Delta p(-\infty) \ll \Delta p(\infty)$, then from basic properties of Fourier transformations the amplitude

$$\mathcal{M} \to 0, \text{ if } \Delta p_z^{\rm max} L_w \gg 1\,, \tag{3.38}$$

[7] We will see later on how left mover emission is negligible for us in the WKB regime.

with $\Delta p_z^{\max} = \text{Max}[\Delta p_z(\pm\infty)]$. The physics behind this relation is very simple: the wall of the width L_w can lead to the momentum loss Δp_z at most L_w^{-1}. This is expected since the processes with $\Delta p_z \gg L_w^{-1}$ happen at distances $\sim \Delta p_z^{-1}$, much shorter than the typical wall width. However, at such small distances we recover translational symmetry along the z direction and transition radiation must be forbidden (we checked these statements for various wall ansatzes in appendix 3.J). From these arguments, we can see that independently of the wall ansatz the particle emission will be dominated by the region $\Delta p_z L_w \lesssim 1$. Then we can approximate the amplitude as follows

$$\begin{aligned}\mathcal{M}^{\text{wkb}} = &\int_{-\infty}^{0} dz V(-\infty) e^{i\Delta p_z(-\infty)z} + \int_{0}^{\infty} dz V(+\infty) e^{i\Delta p_z(+\infty)z} \\ &+ \int_{0}^{L_w} dz V(z) e^{i\int d\tilde{z}\Delta p(\tilde{z})} \ . \end{aligned} \tag{3.39}$$

Performing the z integrals for the first two terms is trivial and, using eq. (3.14), we get

$$\mathcal{M}^{\text{wkb}} \approx \frac{V(-\infty)}{i\Delta p_z(-\infty)} - \frac{V(+\infty)}{i\Delta p_z(+\infty)} + \int_{0}^{L_w} dz V(z) e^{i\int d\tilde{z}\Delta p(\tilde{z})} \tag{3.40}$$

The last term scales very roughly as $V(z \in [0, L_w])L_w$ then assuming $V(z \in [0, L_w]) \sim V(\infty) \sim V(-\infty)$ we can see it will be suppressed by the condition $\Delta p L_w \lesssim 1$. Thus we arrive at the Bodeker-Moore formula [95] for reduced matrix element

$$\mathcal{M}^{\text{wkb red.}} = \frac{V(-\infty)}{i\Delta p_z(-\infty)} - \frac{V(+\infty)}{i\Delta p_z(+\infty)} \ . \tag{3.41}$$

Now one can take this formula and perform the phase space integration. However, we would like to emphasise a simple but important point. Since we have ignored the contribution inside the wall, there is no guarantee that the matrix element will be suppressed in the region with $\Delta p_z L_w \gg 1$. In all of our calculations we always:

- impose $\Delta p_z L_w < 1$ – Fourier decomposition properties
- verify that $\mathcal{M}_{\text{inside}} \ll \mathcal{M}_{\text{outside}}$ – applicability of BM approximation (we will see that satisfying this inequality turns out to be non-trivial for longitudinal vector bosons).

Finally, from this discussion it is clear that we should not worry about left emission in the WKB regime since for left movers with $k^z > L_w^{-1}$ the total loss of momenta $\Delta p_z = p^z - q^z + k^z > L_w^{-1}$, meaning these processes must be strongly suppressed and we can safely ignore them.

Scalars example Let us apply this very generic discussion to the case of scalar radiation. Then the matrix element will be given by

$$\mathcal{M}^{\text{wkb red.}} = \frac{-iy}{p^z - q^z - k^z} - \frac{-iy}{p^z - q^z - \tilde{k}^z} \ , \tag{3.42}$$

for the contribution outside of the wall. The contribution inside the wall (which we ignore) scales roughly as

$$\frac{\mathcal{M}^{\text{inside}}_{\text{wkb}}}{\mathcal{M}^{\text{wkb red.}}} \sim \Delta p_z L_w \ , \tag{3.43}$$

which is always less than one. We conclude that the neglected corrections coming from inside of the wall contributions are indeed negligible for scalars.

3.1.7 Procedure for the momentum transfer calculation: summary

In this section we summarise the previous results and give a concise prescription for the momentum transfer calculation independent of the wall shape details. There are three contributions:

$$\langle \Delta p_L^{\text{step}} \rangle \ , \quad \langle \Delta p_R^{\text{step}} \rangle \ , \quad \langle \Delta p^{\text{wkb}} \rangle \ , \tag{3.44}$$

where the first two correspond to emission to the left and right in the step wall regime and the last one to the emission to the right in the WKB regime. These are given explicitly by the following phase space integrals:

$$\begin{aligned}
\langle \Delta p_L^{\text{step}} \rangle &= \int_0^{k_{\max}^z} \frac{dk_z}{2\pi} \frac{1}{2k_0} \int_0^{k_{\perp,\max}^2} \frac{dk_\perp^2}{4\pi} \cdot \frac{1}{2p^z} \left[\frac{1}{2|q^z|} |\mathcal{M}_L|^2 (p^z - q^z + k^z) \right] \Theta(L_w^{-1} - k^z) \ , \\
\langle \Delta p_R^{\text{step}} \rangle &= \int_{\Delta m}^{k_{\max}^z} \frac{dk_z}{2\pi} \frac{1}{2k_0} \int_0^{k_{\perp,\max}^2} \frac{dk_\perp^2}{4\pi} \cdot \frac{1}{2p^z} \left[\frac{1}{2|q^z|} |\mathcal{M}_R|^2 (p^z - q^z - \tilde{k}^z) \right] \Theta(L_w^{-1} - k^z) \ , \\
\langle \Delta p^{\text{wkb}} \rangle &= \int_{\Delta m}^{k_{\max}^z} \frac{dk_z}{2\pi} \frac{1}{2k_0} \int_0^{k_{\perp,\max}^2} \frac{dk_\perp^2}{4\pi} \cdot \frac{1}{2p^z} \left[\frac{1}{2|q^z|} |\mathcal{M}^{\text{wkb red.}}|^2 (p^z - q^z - \tilde{k}^z) \right] \\
&\quad \times \Theta\left(k^z - L_w^{-1}\right) \Theta\left(L_w^{-1} - (p^z - q^z - \tilde{k}^z)\right) \ ,
\end{aligned} \tag{3.45}$$

where the limits $k_{\max}^z, k_{\perp,\max}^2$ were defined in eq. (3.33) but we repeat them here for the reader's convenience,

$$\begin{aligned}
k_z^{\max} &\equiv \sqrt{(p_0 - m_\psi)^2 - m^2} \ , \\
k_{\perp,\max}^2 &\equiv \frac{1}{4p_0^2} (p_0^2 + k_z^2 + m^2 - m_\psi^2)^2 - k_z^2 - m^2 \ .
\end{aligned} \tag{3.46}$$

and also recall that $\Delta m^2 \equiv \tilde{m}^2 - m^2$. $\mathcal{M}_L, \mathcal{M}_R$ are the amplitudes for the process calculated using the step wall ansatz (see section 3.1.4) and $\mathcal{M}^{\text{wkb red.}}$ is the amplitude in the WKB approximation, without the contribution inside the wall, calculated following the discussion in section 3.1.6. Note the presence of various Theta functions imposing cuts on phase space. For the $\langle \Delta p_{L,R}^{\text{step}} \rangle$ cases, these ensure that $k^z < L_w^{-1}$, i.e. a step wall approximation is valid. Similarly $\Theta(k^z - L_w^{-1})$ for the WKB regime. For the latter, the second constraint $\Theta\left(L_w^{-1} - (p^z - q^z - \tilde{k}^z)\right)$ imposes that the momentum transfer not surpass the inverse wall width (see discussion near eq. (3.38)). In practice, all constraints can be implemented by cutting the integration limits, as is shown in Table 3.1.1. The $\Theta(\pm(L_w^{-1} - k^z))$ are easily implemented by cutting the k^z integration appropriately. For the WKB regime, the extra constraint $p^z - q^z - \tilde{k}^z < L_w^{-1}$ amounts to cutting also the $k_\perp^2$ integration as follows

$$k_\perp^2 \leq \begin{cases} k_{\perp,\text{wkb}}^2 \ , & k^z < k_*^z \\ k_{\perp,\max}^2 \ , & k^z > k_*^z \end{cases} \qquad \text{(WKB red.)} \tag{3.47}$$

where

$$k_{\perp,\text{wkb}}^2 \equiv \frac{1}{4p_0^2} \left(p_0^2 + k_z^2 + m^2 - m_\psi^2 - (p^z - \tilde{k}^z - L_w^{-1})^2\right)^2 - k_z^2 - m^2 \ , \tag{3.48}$$

$$k_*^z \equiv \sqrt{(p^z - L_w^{-1})^2 + \Delta m^2} \ . \tag{3.49}$$

To derive this, note that if $p^z - \tilde{k}^z - L_w^{-1} < 0$, the positivity of q^z means we are done with no extra condition. If instead $p^z - \tilde{k}^z - L_w^{-1} > 0$, squaring the constraint and solving for $k_\perp^2$ gives eq. (3.48).

Phase space integration limits				
	$L-$step	$R-$step	WKB red.	
k_z	$\left[0, \text{Min}[L_w^{-1}, k^z_{\text{max}}]\right]$	$\left[\Delta m, \text{Min}[L_w^{-1}, k^z_{\text{max}}]\right]$	$\left[L_w^{-1}, \text{Max}[L_w^{-1}, k^z_*]\right]$	$\left[\text{Max}[L_w^{-1}, k^z_*], k^z_{\text{max}}\right]$
$k_\perp^2$	$[0, k^2_{\perp,\text{max}}]$	$[0, k^2_{\perp,\text{max}}]$	$[0, k^2_{\perp,\text{wkb}}]$	$[0, k^2_{\perp,\text{max}}]$

Table 3.1.1: We report here all phase space integration limits for each emission contribution after explicitly taking into account constraints imposed by Theta functions in eq. (3.45). The WKB regime is divided into two regions having imposed the constraint $\Delta p_z L_w < 1$, as explained in section 3.1.7. All definitions Max & Min functions are included to also capture low p^0 or large L_w^{-1}.

3.1.8 Momentum transfer from scalar emission

Using the expressions summarised in section 3.1.7, we calculate the momentum transfer from scalar emission $\psi \to \psi\phi$ in our toy model eq. (3.4). As explained above, the total averaged momentum transfer is the sum of three separate contributions $\langle \Delta p^{\text{step}}_{L,R} \rangle$, $\langle \Delta p^{\text{wkb}}_R \rangle$. Numerical integration is relatively straightforward and representative results are shown in fig. 3.1.2. Analytical expressions can be derived, with some details given in section 3.G.1, and are presented when deemed useful. There are several parameters in the problem so which of the three contributions dominates is a function of different hierarchies. Generically we find that at large energies $p^0 \to \infty$ the WKB contribution always dominates and falls off as $1/p^0$. Computing the phase space integrals in this asymptotic limit, we obtain a very good approximation

$$\langle \Delta p^{\text{total}} \rangle \Big|_{p_0 \gg L_w^{-1}\text{Max}[1, m_\psi/m]} \approx \langle \Delta p^{\text{wkb}}_R \rangle \approx \frac{y^2 \tilde{m}}{32\pi^2 m_\psi^2} \times \tag{3.50}$$
$$\frac{p_0^{-1}}{2\tilde{m}} \left[2\tilde{m}^2 \ln\left(\frac{m}{\tilde{m}}\right) + \frac{2(m^2+\tilde{m}^2)m_\psi^2 - m^2\tilde{m}^2}{S(m)} \ln\left[D(m)\right] + S(\tilde{m}) \ln\left[D(\tilde{m})\right] \right] ,$$

where

$$D(m) \equiv \frac{m^2 - 2m_\psi^2 + S(m)}{2m_\psi^2} , \quad S(m) \equiv im\sqrt{4m_\psi^2 - m^2} .$$

On the other hand, at low and intermediate relativistic energies, the step function contributions typically dominate. This behaviour is amplified in two independent regimes. For very thin wall $L_w \to 0$ the WKB contribution naturally only turns on at higher energies $p_0 \gg L_w^{-1}$, with $\langle \Delta p^{\text{step}}_R \rangle$ temporarily dominating in its place (see bottom-right panel of fig. 3.1.2). Nonetheless, the trend is still reasonably approximated by interpolating backward the asymptotic result of eq. (3.50).

More interesting is the case when the initial mass of ϕ is very light $m \ll \tilde{m}, m_\psi$. Each contribution to momentum transfer becomes constant for an inter-relativistic plateau as can be observed in the leftmost panel of fig. 3.1.2. Moreover, it is actually $\langle \Delta p^{\text{step}}_L \rangle$ that dominates, with a value

$$\langle \Delta p^{\text{total}} \rangle \approx \langle \Delta p^{\text{step}}_L \rangle \approx \frac{y^2 \tilde{m}}{8\pi^2 m_\psi^2} \qquad \text{for} \quad p_0 \lesssim \tilde{m} m_\psi / m . \tag{3.51}$$

Further details can be found in section 3.G.1.

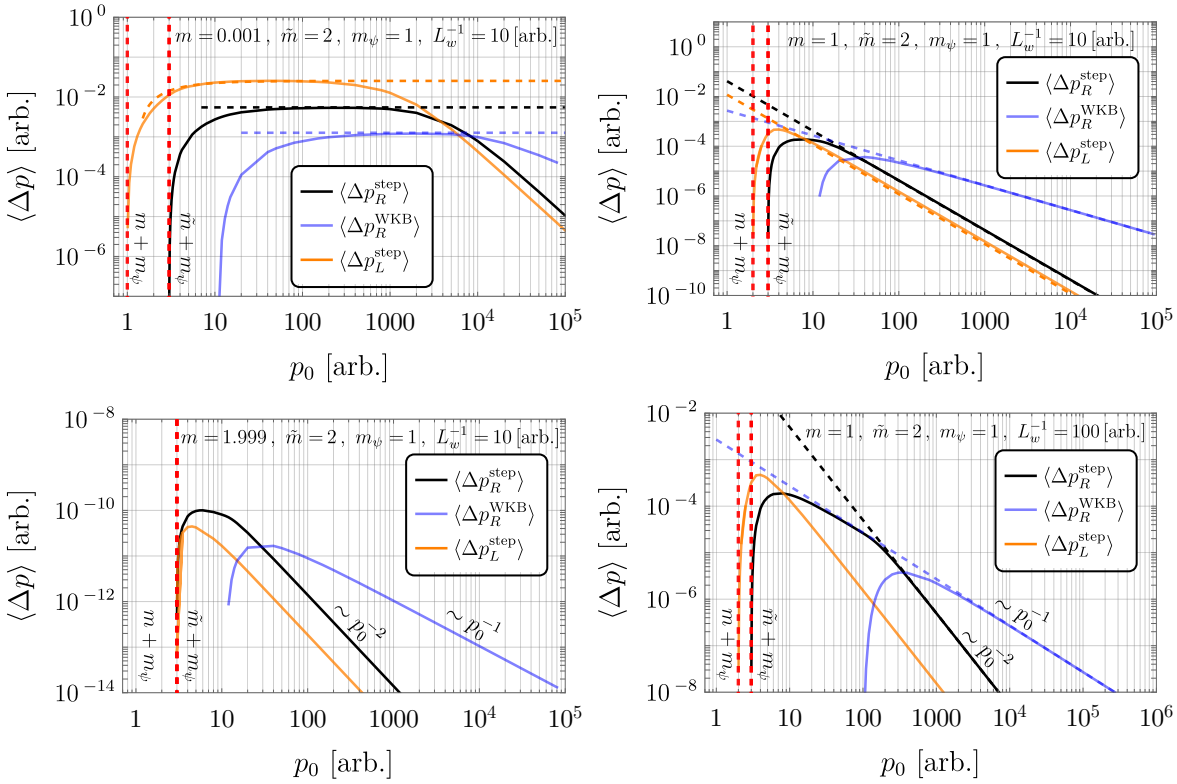

Figure 3.1.2: Numerical results for the averaged momentum transfer to the wall for each of the three contributions in eq. (3.45) as a function of incoming particle energy. Black and orange curves stand for right and left emission of soft quanta (using step wall), while blue is for the energetic quanta (using WKB). The vertical red dashed lines are the lower bounds on the minimal energy the incoming particle can have to emit right and left modes. We show four cases of interest, that respectively are: $\tilde{m} \gg m$, $\tilde{m} \sim O(1)m$, $\tilde{m} - m \ll 1$ and $L_w^{-1} \gg \tilde{m}$. The horizontal and oblique dashed lines are analytical estimates in eq. (3.50) ($\langle \Delta p_{\zeta_R}^{\rm wkb} \rangle$), in eq. (3.251) ($\langle \Delta p_{\zeta_L}^{\rm step} \rangle$) and in eq. (3.252) ($\langle \Delta p_{\zeta_R}^{\rm step} \rangle$). At the highest scales, the WKB contribution always dominates and falls as p_0^{-1} (while both step wall contributions fall as p_0^{-2}). In the limit $L_w \to 0$, R emission also falls off as p_0^{-1}. Most interestingly, for large hierarchy m_ψ/m, $\langle \Delta p \rangle$ is constant until $p_0 \lesssim \tilde{m} m_\psi / m$.

3.1.9 Pressure from scalar emission

The pressure induced on the bubble wall from scalar emission is finally obtained by integrating over the incoming flux

$$\mathcal{P} = \int \frac{d^3p}{(2\pi)^3} f_\psi(T, \gamma_w) \times \frac{p^z}{p_0} \langle \Delta p^{\text{total}} \rangle \ , \tag{3.52}$$

where f_ψ is the phase space distribution of incoming ψ particles in the frame of the wall. Let us first focus on the interesting regime when $m \ll m_\psi$, identified in eq. (3.51), where $\langle \Delta p \rangle^{\text{total}}$ is constant for a plateau lasting till $p_0 \lesssim \tilde{m} m_\psi / m$. In the ultra-relativistic limit $p^z/p_0 \to 1$, and the integration gives simply

$$\mathcal{P}^{\text{scalar}} = n_\psi(T, \gamma_w) \langle \Delta p^{\text{total}} \rangle = \gamma_w n_\psi(T) \langle \Delta p^{\text{total}} \rangle \ , \qquad p_0 \lesssim \frac{\tilde{m} m_\psi}{m} \ . \tag{3.53}$$

To go from the second equality to the third we used that the number density of ψ in the wall frame is boosted with respect to the FRW frame number density. Thus, even scalar emission can cause friction pressure that grows with γ_w. Combining the plateau and asymptotic contributions for scalar emission, we have approximately, for an incident thermal population,

$$\mathcal{P}^{\text{scalar}} \approx \begin{cases} \frac{T^3}{8\pi^4} \frac{y^2 \tilde{m}}{m_\psi^2} \times \gamma_w \ , & \gamma_w \lesssim \frac{\tilde{m} m_\psi}{mT} \\ \frac{T^2}{64\pi^3} \frac{y^2 \tilde{m}^2}{m_\psi m} \ , & \gamma_w \gtrsim \frac{\tilde{m} m_\psi}{mT} \end{cases} \ , \tag{3.54}$$

where the second expression was obtained by expanding eq. (3.50) for small m and simply multiplying by $n_\psi(T) \approx T^3/\pi^2$. The asymptotic constant pressure can be compared with the LO contribution from a thermal population of ϕ particles crossing the wall as per eq. (1.235), which gives $\sim T^2 \tilde{m}^2$. We observe that the NLO contribution is more important when $\frac{y^2}{64\pi m_\psi m} \gtrsim 1$.

We remind the reader that our results for scalar emission pressure were obtained for a particularly simple choice of interactions in the Lagrangian eq. (3.4) (with $y = \text{const}$) and we highlighted here a particular regime of parameters. Our main goal was to mimic as much as possible the vector radiation to be discussed in the next section. We will return to whether the pressure in eq. (3.54) can be phenomenologically relevant in future work.

3.2 Spontaneously broken gauge theories

We now proceed to the phase transitions related to the spontaneous breaking of gauge symmetry and the emission of vector bosons. The procedure will in essence be exactly the same as what we presented for the case of the scalar emission. We will quantise the theory of a gauge field in the background of a domain wall interpolating between a symmetric and broken phase. As should be expected, the extra difficulty will involve dealing with gauge-fixing, spin and the change of degrees of freedom due to the spatially-dependent rearrangement of the vacuum.

For simplicity, we will consider the Abelian Higgs model of a charged complex scalar H, whose potential $V(\sqrt{2}|H|)$ is responsible for the spontaneous breaking of the $U(1)$ gauge symmetry. A second scalar field ψ charged under the same $U(1)$ will play the role of matter; its potential is trivial. The Lagrangian is

$$\mathcal{L} = -\frac{1}{4} F_{\mu\nu} F^{\mu\nu} + |D_\mu H|^2 - V\left(\sqrt{2}|H|\right) + |D_\mu \psi|^2 - m_\psi^2 |\psi|^2, \tag{3.55}$$

where we are using the convention $D_\mu\psi = (\partial_\mu + igA_\mu)\psi$ and A_μ is the vector gauge field. We will in general not need to commit to a specific potential but will simply assume that it has two minima at $\sqrt{2}|H| = v, \tilde{v}$, where $v \to 0$ corresponds to the symmetric phase. We will quantise the theory in the background of a domain wall $\sqrt{2}\langle|H|\rangle = v(z)$. We will also be interested, both as a computational tool and as a phenomenological case in its own right, in imagining a distorted or more general class of potential with non-zero $v < \tilde{v}$. We will call this scenario a *broken to broken* phase transition, in opposition to the more familiar case of *symmetric to broken* phase transitions.

To work with the theory described by eq. (3.55), one has to make two independent choices: what field coordinates to use for H, such as Cartesian or polar, and what gauge to impose. The value of each choice is determined by the particular application. Much of the following pages will be dedicated to arguing for the most convenient choices for our application.

If we are interested in studying the geometry of the vacuum manifold, polar coordinates $H = \frac{1}{\sqrt{2}}(h+v)e^{i\theta}$ are most convenient. The potential depends only on the modulus. In the symmetric phase however, this coordinate choice is singular. On the other hand, Cartesian coordinates are well-defined everywhere

$$H = \frac{1}{\sqrt{2}}(h_1 + ih_2) \equiv \frac{1}{\sqrt{2}}\left(h + v(z) + ih_2\right) \ , \tag{3.56}$$

where we have expanded around the background solution $h_1 = v(z)$. The Lagrangian for the Higgs and gauge fields becomes

$$\begin{aligned}\mathcal{L}_{A,H} = &-\frac{1}{4}F_{\mu\nu}F^{\mu\nu} + \frac{1}{2}(\partial h)^2 + \frac{1}{2}(\partial h_2)^2 - gA^\mu\left[h_2\partial_\mu v(z) - v(z)\partial_\mu h_2\right] \\ &+ \frac{1}{2}g^2v^2(z)A^2 - \frac{1}{2}\partial_1^2V(v(z))h^2 - \frac{1}{2}\partial_2^2V(v(z))h_2^2 + \dots \ ,\end{aligned} \tag{3.57}$$

up to quadratic terms, where $\partial_i \equiv \partial/\partial h_i$, so that the last two terms are the z-dependent mass terms of h and h_2.

At a non-zero minimum of the potential, h_2 becomes massless and is the would-be Nambu-Goldstone boson (NGB). As always for gauge theories, when $v \neq 0$ a mixing term appears between this goldstone boson and the gauge boson. However, in the context of a varying background, there is also an extra mixing proportional to $\partial_z v$. When v is a constant, the mixing can be eliminated completely while also gauge fixing by adding the so called R_ξ gauge term

$$\delta\mathcal{L}_{g.f.} = -\frac{1}{2\xi}(\partial_\mu A^\mu - \xi g v h_2)^2 \ , \tag{3.58}$$

and integrating by parts. For $v = v(z)$, adding this same (now $z-$dependent) gauge-fixing term does not get rid of mixing entirely but localises it to the region of the wall

$$\begin{aligned}\mathcal{L}_{A,H} + \delta\mathcal{L}_{g.f.} = &-\frac{1}{4}F_{\mu\nu}F^{\mu\nu} - \frac{1}{2\xi}(\partial_\mu A^\mu)^2 + \frac{1}{2}(\partial h)^2 + \frac{1}{2}(\partial h_2)^2 \\ &- 2gh_2A^z\partial_z v(z) + \frac{1}{2}g^2v(z)^2A^2 - \frac{1}{2}\partial_1^2V(v(z))h^2 \\ &- \frac{1}{2}\left[\partial_2^2V(v(z)) + \xi g^2v^2(z)\right]h_2^2 + \dots \ .\end{aligned} \tag{3.59}$$

3.2.1 Particle content in the asymptotic regions

We briefly remind ourselves of the spectrum of the theory in the asymptotic regions $v = 0$ and $\tilde{v}$ at $z \to -\infty$ and $z \to \infty$ respectively, before discussing the full interpolating space.

Symmetric phase: The theory eq. (3.59) around the symmetric point minimum $v = 0$ describes two scalars $h_{1,2}$, with equal mass by symmetry

$$m_{h,s}^2 \equiv \partial_1^2 V(0) = \partial_2^2 V(0) \tag{3.60}$$

The gauge-fixing affects only the Maxwell equations of motion for the massless vector A^μ. Whatever the value of ξ, we can identify two physical transverse (in the sense that $A_\mu k^\mu$=0) degrees of freedom with polarisation vectors given by

$$\epsilon_{T_1}^\mu = (0,0,1,0) \ , \qquad \epsilon_{T_2}^\mu = \frac{1}{\sqrt{k_\perp^2 + k_z^2}}(0, k^z, 0, -k_\perp) \ , \tag{3.61}$$

for $k^\mu = (k_0, k_\perp, 0, k^z)$. The only (well-known) subtlety involves imposing on the Hilbert space a constraint to project out unphysical states, the so-called Gupta-Bleuler condition [204].

Broken phase(s): At a symmetry–breaking minimum $\partial_2^2 V(\tilde{v}) = 0$ and h_2 describes the would-be NGB. A particularly convenient choice is 'unitary gauge', corresponding to $\xi \to \infty$ in which the NGB decouples completely, making manifest the spectrum. We are left with a single massive scalar (the Higgs) h with mass squared equal to $\partial_1^2 V(\tilde{v})$ and a massive vector boson A_μ with mass

$$\tilde{m} \equiv g\tilde{v} \ , \tag{3.62}$$

and satisfying the Proca equation

$$\partial_\mu F^{\mu\nu} + \tilde{m}^2 A^\nu = 0 \ . \tag{3.63}$$

This reduces to a Klein-Gordon equation for each component of A^μ supplemented by the Lorenz condition:

$$\implies \partial^2 A^\mu + \tilde{m}^2 A^\mu = 0 \ , \qquad \partial_\mu A^\mu = 0 \ . \tag{3.64}$$

Solving this is straightforward and one adds to the transverse polarisations of eq. (3.61) a third longitudinal one parallel to 3−momentum

$$\epsilon_L^\mu = \left(\frac{k_0^2 - m^2}{k_0}, k_\perp, 0, k^z \right) \frac{k_0}{m\sqrt{k_0^2 - m^2}}. \tag{3.65}$$

3.2.2 Global degrees of freedom

Here will analyse the fields defined over the entire region and identify the appropriate global modes to quantise, where by global we simply mean they are good across the wall.

In principle, one could choose a convenient value of ξ in eq. (3.59) and push ahead with quantisation. However, we would have to deal with mixing when solving for the mode functions, as well as taking care to impose a non-trivial Gupta-Bleuler like condition on physical states. Luckily, we will argue that even when asymptotically approaching the symmetric point as $z \to -\infty$, it is possible to work with unitary gauge $\xi \to \infty$ with impunity. This approach was already made at the classical level in ref. [116], and we will re-derive and tweak some of their results using a slightly different language, before quantising.

In unitary gauge, the h_2 degree of freedom decouples and the theory becomes

$$\mathcal{L}^{U.G.}_{A,H} = -\frac{1}{4}F_{\mu\nu}F^{\mu\nu} + \frac{1}{2}g^2v^2(z)A^2 + \frac{1}{2}(\partial h)^2 - \frac{1}{2}\partial_1^2 V(v)h^2 + \dots \,, \tag{3.66}$$

and the equations of motion for eq. (3.57) reduce to just two uncoupled equations

$$\Box h = -V''(v)h \,, \tag{3.67}$$

$$\partial_\nu F^{\mu\nu} = g^2v^2(z)A^\mu \,. \tag{3.68}$$

The first one is the equation of motion for the physical Higgs boson h and we will not have any more to say about it here. The second will be the focus of our attention. While $v(z) > 0$, the theory is always in a broken phase and A^μ describes a massive vector. Unitary gauge is then manifestly a valid choice. Note that the usual transversality condition for massive vector bosons in this case becomes

$$\partial_\mu\partial_\nu F^{\mu\nu} = \partial_\mu(g^2v^2A^\mu) = 0 \,, \tag{3.69}$$

$$\implies \partial_n A^n + \partial_z A^z = -\frac{\partial_z v^2}{v^2}A^z \,, \tag{3.70}$$

which, in the presence of the domain wall, generalises the standard Lorenz condition for massive electrodynamics in eq. (3.64). The constraint above ensures this vector field has three polarisation degrees of freedom. Subbing this back into eq. (3.68) we get

$$\partial^2 A^\mu + \partial^\mu\left[\left(\frac{\partial_z v^2}{v^2}\right)A^z\right] + g^2v^2A^\mu = 0 \,. \tag{3.71}$$

The general Fourier mode can be written as

$$A^\mu_{k_0,k_\perp} = e^{-ik_nx^n}\sum_l a_l\,\chi^\mu_{l,k^n}(z) \,, \tag{3.72}$$

where l runs over three indices, a_l are some constant Fourier coefficients and the functions $\chi^\mu_{l,k_0,k_\perp}(z)$ have to be found by solving eq. (3.71). One might be tempted to define left and right moving χ^μ modes by fixing the incoming piece at infinity in terms of conventional transverse and longitudinal modes eqs. (3.61) and (3.65). However, under such a choice, transmitted and reflected pieces would contain also other polarisations. Fundamentally, this is because for non-zero $k_\perp$, rotations around $\boldsymbol{k}$ are not a symmetry and conventional spin is not conserved. We now construct more convenient 'wall polarisations', which instead do not mix.

τ polarisations: It is useful to define what we call $\tau-$polarisations by the condition $A^z = 0$, since for these we recover the Lorenz condition $\partial_\mu A^\mu = 0$, which in Fourier space reduces to

$$k_n\chi^n_\tau \equiv k_0\chi^0_\tau - k_\perp\chi^\perp_\tau = 0 \,, \tag{3.73}$$

and has solutions in terms of two *constant* vectors

$$\chi^\mu_\tau = \epsilon^\mu_{\tau_{1,2}}\,\chi_{\tau_{1,2}}(z) \,, \tag{3.74}$$

where

$$\epsilon^\mu_{\tau_1} = (0,0,1,0), \qquad \epsilon^\mu_{\tau_2} = (k_\perp,k_0,0,0)/\sqrt{k_0^2-k_\perp^2} \,, \tag{3.75}$$

and the equations of motion eq. (3.71) become the Klein-Gordon-like

$$\left[-E^2 - \partial_z^2 + g^2 v^2(z)\right] \chi_{\tau_{1,2}}(z) = 0 \ , \tag{3.76}$$

where we remind the reader of the definition $E = \sqrt{k_0^2 - k_\perp^2}$. Note that $\epsilon^\mu_{\tau_1}$ is one of the standard transverse polarisations, but ϵ_{τ_2} is not, since it has a non-zero time component, and is not orthogonal to three momentum. The wave equation to solve across the wall for τ d.o.f. is thus identical to the scalar case studied in section 3.1.

λ polarisation: It remains to solve for the remaining degree of freedom with $A^z \neq 0$. The wave equation to solve for is obtained by setting $\mu = z$ in eq. (3.71). We note already that it is significantly more complicated than what we found for τ. Whatever the solution for A^z, the other components of the vector are fixed. Requiring orthogonality with χ^μ_τ implies the form $\chi^\mu_\lambda(z) = (-ik^n\alpha(z), \chi^z_\lambda)$ where we recall $n = 0, \perp$. The generalised Lorenz condition in eq. (3.70) immediately leads to the relation

$$\alpha(z) = \frac{\partial_z \left(v^2 \chi^z_\lambda\right)}{E^2\, v^2} \ . \tag{3.77}$$

Plugging this back into the eq. (3.71), we obtain the equation in terms of the χ^z only

$$-E^2 \chi^z_\lambda - \partial_z \left(\frac{1}{v^2} \partial_z (v^2 \chi^z_\lambda)\right) + g^2 v^2(z) \chi^z_\lambda = 0 \ . \tag{3.78}$$

We can get rid of the linear in derivative term if we introduce a new function $\lambda(z)$

$$\chi^z_\lambda = \frac{E}{g v(z)} \lambda(z) \ , \tag{3.79}$$

and eq. (3.78) becomes Schrodinger-like

$$\left(-E^2 - \partial_z^2 + U_\lambda(z)\right) \lambda = 0 \ , \tag{3.80}$$

with effective potential

$$\begin{aligned} U_\lambda(z) &= g^2 v^2(z) - v\ \partial_z \left(\frac{\partial_z v}{v^2}\right) \\ &= g^2 v^2(z) + 2\left(\frac{\partial_z v}{v}\right)^2 - \frac{\partial_z^2 v}{v} \ . \end{aligned} \tag{3.81}$$

The solutions in terms of λ, unlike χ^z_λ, satisfy the usual orthogonality relations

$$\int dz \lambda_k(z) \lambda^*_q(z) = 2\pi \delta(k^z - q^z) \ . \tag{3.82}$$

It is easy to prove – and we do so explicitly in section 3.F – that for an interpolating solution $v(z)$ of a completely arbitrary Higgs potential V, we have $(v'/v)^2, v''/v \to m^2_{h,s}$ as $z \to -\infty$ so that $U_\lambda(z)$ is always finite even if $v = 0$. More precisely

$$\lim_{z\to-\infty} U_\lambda(z) = \begin{cases} g^2 v^2 \ , & v \neq 0 \\ m^2_{h,s} \ , & v = 0 \end{cases} \equiv m^2_\lambda \ . \tag{3.83}$$

We see that λ is the perfect cross-wall field. It interpolates between one of the massive (Higgs) degrees of freedom on the symmetric $v = 0$ side $z \to -\infty$ and a third component of the massive vector in the broken region $z \to \infty$. If instead $v \neq 0$, λ simply interpolates between the different mass vectors.

Let us look more closely at the A^μ vector formed by the λ field. Using the equations of motion forces the on-shell relation:

$$\begin{aligned}
\chi^z_\lambda &= \frac{E^2 \partial_z \alpha}{E^2 - g^2 v^2(z)} \Rightarrow \\
\chi^\mu_\lambda &= (-ik^n \alpha(z), \chi^z_\lambda) = (-ik^n, \partial^z)\ \alpha(z) + \frac{g^2 v^2(z)}{E^2} \chi^z_\lambda(0,0,0,1) \\
&= (-ik^n, \partial^z)\ \alpha(z) + \frac{gv(z)}{E} \lambda(z)(0,0,0,1)
\end{aligned} \tag{3.84}$$

So that the vector can be written as a total derivative plus a term sub-leading in energy. This form will turn out to be very useful in calculating the amplitudes for physical processes. Far from the wall, when $v \to const$, we can introduce the polarisation vector ϵ^μ_λ such that

$$\begin{aligned}
\chi^\mu_\lambda &\propto \epsilon^\mu_\lambda, \quad \epsilon^\lambda_\mu \epsilon^{\lambda\mu} = -1 \\
\epsilon^\mu_\lambda &= \left(k^n \frac{k^z}{E^2}\ , 1 \right) \times \frac{E}{gv} \\
&= \frac{k^z}{Egv}\ k^\mu + \frac{gv}{E}(0\ , 0\ , 0\ , 1)\ .
\end{aligned} \tag{3.85}$$

We emphasise again that these λ and τ differ from the conventional transverse and longitudinal polarisations. Far from the wall, all polarisations satisfy the same equation of motion and one can use any linear combination of either basis to decompose the vector field. We can relate the wall polarisations to the conventional longitudinal and transverse ones in eqs. (3.61) and (3.65) via the rotation matrix

$$\begin{pmatrix} \epsilon_{T_1} \\ \epsilon_{T_2} \\ \epsilon_L \end{pmatrix} = \begin{pmatrix} 1 & 0 & 0 \\ 0 & \frac{k_0 k^z}{E\sqrt{k_0^2 - m^2}} & -\frac{k_\perp m}{E\sqrt{k_0^2 - m^2}} \\ 0 & \frac{k_\perp m}{E\sqrt{k_0^2 - m^2}} & \frac{k_0 k^z}{E\sqrt{k_0^2 - m^2}} \end{pmatrix} \begin{pmatrix} \epsilon_{\tau_1} \\ \epsilon_{\tau_2} \\ \epsilon_\lambda \end{pmatrix}\ . \tag{3.86}$$

In the case of a very large $k^z, E \gg k_\perp, m$ the mixing angle between τ, λ transverse and longitudinal scales as m/E. We can see that the two bases of polarisations are exactly the same for the case $k_\perp = 0$. This is expected since for this configuration of momenta T_1, T_2 polarisations have zero components in the z direction. Using the unbroken part of the Lorentz symmetry (boosts in $x - y$ direction) we can obtain the polarisations for generic momenta, which indeed agrees with the τ, λ basis derived before. Our goal in this chapter is to calculate the total pressure acting on the domain wall and for this, we sum the contributions from all polarisations. We perform all of the calculations in the τ, λ basis, without even reporting the results for T, L polarisations.

$v \to 0$ limit

All of the previous discussion applied most manifestly for the case when the vev of the symmetry breaking field is $v \neq 0$. What happens in the case when the domain wall on one side approaches a vacuum where the gauge symmetry is unbroken? We saw in the

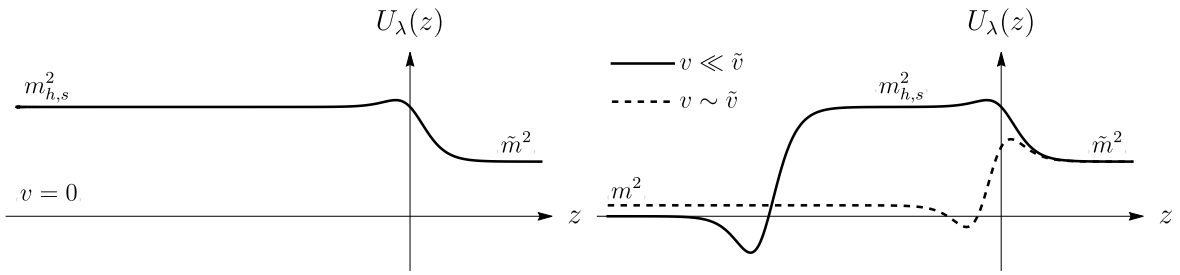

Figure 3.2.1: The potential for the λ degree of freedom, which is defined everywhere. Recall $m = gv$ and $\tilde{m} = g\tilde{v}$, plus thermal corrections. As $v \to 0$ a growing plateau develops ending at $z \sim m_{h,s}^{-1} \ln(v/\tilde{v})$ with value $m_{h,s}^2$ - the symmetric side mass of the Higgs in the case $v = 0$ exactly. These curves were drawn using the explicit profile eq. (3.92).

previous section that the potential of the λ mode has a property that as $v \to 0$ then $U_\lambda(z) \to m_{h,s}^2$, which together with our expectations from the Higgs phenomena hints that on the unbroken side λ should correspond to the would-be NGB

$$\lambda_{z\to-\infty} \to h_2\,. \tag{3.87}$$

To understand this matching better, let us look at the χ_λ^μ vector in the limit $v \to 0$

$$\begin{aligned}\chi_\lambda^\mu &= (-ik^n\alpha(z), \chi_\lambda^z) = \left(\frac{-ik^n\partial_z(v\lambda)}{gEv^2}, \frac{E}{gv}\lambda\right) \\ &= \frac{\lambda}{gv}\left(-\frac{ik^n}{E}\left[\frac{v'}{v}+\frac{\lambda'}{\lambda}\right], E\right)_{v\to0} = \frac{e^{-ikx}}{gv}\left(\frac{k^n}{E}\left[-im_{h,s}+k^z\right], E\right),\end{aligned} \tag{3.88}$$

where we have used that λ becomes a plane wave far from the wall and $v'/v \to m_{h,s}$. Note that the factor $(-im_{h,s}+k^z)/E$ is a pure phase if the λ dof is on shell. Let us see whether we can build exactly the same vector but from the field h_2. Indeed if we consider the vector

$$\partial^\mu\left(\frac{h_2}{gv}\right) = -\frac{e^{-ikx}}{gv}\left(k^n, k^z + i\frac{v'}{v}\right) = \frac{-iEe^{-ikx}}{gv(k^z - im_{h,s})}\left(\frac{k^n}{E}\left[-im_{h,s}+k^z\right], E\right). \tag{3.89}$$

So we can see, comparing with eq. (3.88), that the two vectors χ_λ^μ and $\partial_\mu(h_2/gv)$ are exactly the same apart from the constant phase factor, so indeed λ field in the $z \to -\infty$ limit corresponds to the Goldstone boson.

What about starting from a finite value and taking $v \to 0$? For concreteness let us consider the potential

$$V = \lambda_h(|h| - v)^2(|h| - \tilde{v})^2. \tag{3.90}$$

First of all the potential has a cusp at $|h| = 0$ so the limit $v \to 0$ becomes discontinuous. This can be seen also in the form of $U_\lambda(z)$. As v becomes smaller a longer finite plateau develops in the potential with value $\approx m_{h,s}^2$, as is shown in fig. 3.2.1. No matter how small v *eventually* the potential turns down and asymptotes to g^2v^2 as is to be expected. Thus for any finite though tiny v the asymptotic states at $z \to -\infty$ are those of a massive vector.

3.2.3 The step wall case

In order to proceed further we need to solve the equations of motion. In general, it is a complicated problem depending on the shape of the effective potential $V_{\text{eff}}(h)$ at the time of the phase transition. One needs to find the solitonic solution $v(z)$ connecting false and true vacuum and later the wavemodes describing perturbations of each field on this background. In the particular case of the domain wall

$$v(z) = \frac{1}{2}\tilde{v}\left(1 + \tanh\left(\frac{z}{L_w}\right)\right) \ , \tag{3.91}$$

solutions were found in [116] in terms of hypergeometric functions. In this chapter, we will consider an even simpler case, namely a step function ansatz for the wall. This approximation will of course be valid only if the momentum of the particle during the passage is (much) less than the inverse width of the wall $k, \tilde{k} \ll L_w^{-1}$. Typically, this width is controlled by the mass of the Higgs $L_w^{-1} \approx m_h$.

The solution of the equations of motion can be written down on each side immediately and the only challenge becomes deriving and implementing matching conditions. In this section, we report the matching conditions for τ and λ polarisations and write down the corresponding wave functions. We will do so first for the broken to broken case $v > 0$. As an explicit example, we can imagine distorting eq. (3.91) to

$$v(z) \to v + \frac{1}{2}(\tilde{v} - v)\left(1 + \tanh\left(\frac{z}{L_w}\right)\right) \ . \tag{3.92}$$

We then comment on the $v \to 0$ limit, which is straightforward for τ degrees of freedom but more delicate for λ.

(τ) polarisations

For the τ polarisations, we showed in section 3.2.2 that the equations of motion are exactly the same as for the scalar field ($\Box A^\mu_{(\tau)} = -g^2 v^2 A^\mu_{(\tau)}$) and so for the step wall the matching conditions become:

$$\chi_{\tau_i}|_{<0} \ = \chi_{\tau_i}|_{>0} \ , \tag{3.93}$$

$$\partial_z \chi_{\tau_i}|_{<0} = \partial_z \chi_{\tau_i}|_{>0} \ , \tag{3.94}$$

with $i = 1, 2$. The reflection and transmission coefficients are thus the same as for scalars and the wave functions become

$$\chi^\mu_{\tau_i,R,k}(z) = \epsilon^\mu_{\tau_i} \begin{cases} e^{ik^z z} + r^\tau_k e^{-ik^z z} \ , & z < 0 \\ t^\tau_k \ e^{i\tilde{k}^z z} \ , & z > 0 \end{cases} \ , \tag{3.95}$$

$$\chi^\mu_{\tau_i,L,k}(z) = \epsilon^\mu_{\tau_i} \sqrt{\frac{k^z}{\tilde{k}^z}} \begin{cases} \frac{\tilde{k}^z}{k^z} t^\tau_k \ e^{-ik^z z} \ , & z < 0 \\ e^{-i\tilde{k}^z z} - r^\tau_k e^{i\tilde{k}^z z} \ , & z > 0 \end{cases} \ , \tag{3.96}$$

where

$$r^\tau_k = \frac{k^z - \tilde{k}^z}{k^z + \tilde{k}^z} \ , \quad t^\tau_k = \frac{2k^z}{k^z + \tilde{k}^z} \ , \tag{3.97}$$

$$k_0 = \sqrt{k_z^2 + m_\tau^2 + k_\perp^2} \ , \quad \tilde{k}^z = \sqrt{k_0^2 - \tilde{m}_\tau^2 - k_\perp^2} \ , \quad m_\tau \equiv gv \ , \quad \tilde{m}_\tau \equiv g\tilde{v} \ .$$

Taking the $v \to 0$ limit for these degrees of freedom is simple and we approach the $v = 0$ case smoothly.

(λ) polarisation

The λ modes require more work. Again we first focus on the broken to broken case of $v > 0$. Matching conditions are easy to derive by integrating the wave equation for λ once and twice respectively (most easily done at the level of eq. (3.78)). These are

$$\left.\frac{\partial_z \lambda}{v(z)}\right|_{<0} = \left.\frac{\partial_z \lambda}{v(z)}\right|_{>0} ,$$
$$v(z)\lambda|_{<0} = v(z)\lambda|_{>0} , \tag{3.98}$$

which allows us to write down the expressions for (in-state) 'left' and 'right' movers:

$$\lambda_{R,k}(z) = \begin{cases} e^{ik^z z} + r_k^\lambda e^{-ik^z z} , & z < 0 \\ t_k^\lambda \, e^{i\tilde{k}^z z} , & z > 0 \end{cases} \tag{3.99}$$

$$\lambda_{L,k}(z) = \sqrt{\frac{k^z}{\tilde{k}^z}} \begin{cases} \frac{\tilde{k}^z}{k^z} t_k^\lambda e^{-ik^z z} , & z < 0 \\ e^{-i\tilde{k}^z z} - r_k^\lambda e^{i\tilde{k}^z z} , & z > 0 \end{cases} \tag{3.100}$$

where

$$r_k^\lambda = \frac{\tilde{v}^2 k^z - v^2 \tilde{k}^z}{\tilde{v}^2 k^z + v^2 \tilde{k}^z} , \quad t_k^\lambda = \frac{2 k^z v \tilde{v}}{\tilde{v}^2 k^z + v^2 \tilde{k}^z} , \tag{3.101}$$
$$k_0 = \sqrt{k_z^2 + m_\lambda^2 + k_\perp^2} , \quad \tilde{k}^z = \sqrt{k_0^2 - \tilde{m}_\lambda^2 - k_\perp^2} , \quad m_\lambda \equiv gv , \quad \tilde{m}_\lambda \equiv g\tilde{v} .$$

Notice that in the relativistic limit

$$r_k^\lambda \to \frac{\tilde{v}^2 - v^2}{\tilde{v}^2 + v^2} , \qquad \text{for} \quad k^z \gg m_\lambda, \tilde{m}_\lambda . \tag{3.102}$$

so that λ maintains a finite reflection probability as long as the step function is a valid approximation, as was pointed out in [79].

Interestingly we can see that $r_k^\lambda \to 1$ in the limit $v \to 0$, i.e. the wall becomes completely non-transparent for the λ polarisations in this limit. This in-penetrability of the wall deserves some discussion. Consider the explicit form of $U_\lambda(z)$ for the case of the *tanh* profile in eq. (3.92). As mentioned in section 3.2.2 and sketched in fig. 3.2.1, in the limit of $v \to 0$, $U_\lambda(z)$ develops a growing plateau with a height $\approx L_w^{-2} \sim m_{h,s}^2$ and width $L_{\text{plateau}} \sim L_w \log \tilde{v}/v$. In the step function approximation, the first scale is effectively treated as infinite. For $v = 0$ exactly, since $m_\lambda(-\infty) = m_{h,s}$, obviously there are no oscillating $\lambda_{R,k}$ modes at all in the step regime, while $\lambda_{L,k}$ are completely reflected. For v tiny but non-zero the potential *eventually* does instead relax to $m_\lambda^2 = g^2 v^2$ and both oscillating $\lambda_{L,R}$ solutions exist, though strongly constrained to live on opposite sides of the wall[8]: $|r_k| = 1 - \mathcal{O}(v^2/\tilde{v}^2)$. Back to the $v = 0$ exact case, one can also consider theories in which the two scales L_w and $m_{h,s}$ are decoupled (e.g. set $m_{h,s} = 0$ as an extreme case). Then again oscillating $\lambda_{L,R}$ modes will exist on both sides of the wall even as $L_w \to 0$. Still, by numerical inspection, we find total reflection ($|r_k| \to 1$) in the step wall limit, though we leave a proper proof to future work.

In conclusion, calculations in the step function regime for the symmetric to broken transition case ($v = 0$) can be computed starting from the $v \neq 0$ case, using wavemodes eqs. (3.99) and (3.100), and then finally setting $v \to 0$ in the amplitude at the end. Notice instead that the asymptotic masses in the phase space kinematics will need to be discontinuously changed from gv to $m_{h,s}$.

[8] One might question the validity of the step wall approximation for $k^z \gtrsim L_w^{-1}$ when the potential function $U_\lambda(z)$ has a very long plateau $v \ll \tilde{v}$. However, the solutions eqs. (3.99) and (3.100) capture exactly the qualitative behaviour described.

A comment on bound states: We have so far considered 'scattering state' solutions to the equations of motion, i.e. those which are plane waves far from the wall. What about bound states? In principle, such states are possible for λ polarisation. Ref [116] found the existence of one for the case $v = 0$ when the potential satisfies some specific constraints. The form of the potential for $v > 0$, for example, as sketched in fig. 3.2.1, suggests that a bound state might generically appear. The mass of these bound states is controlled by the scale L_w^{-1}, as is obvious by its absence in the step wall limit. One could in principle calculate in the WKB limit the amplitude for an incoming particle to excite this bound state. We leave this interesting exercise to future work.

3.2.4 Quantisation

Following on from the previous sections, we can expand the field into a complete basis of eigenmodes of the free theory in the background vev $v(z)$,

$$\begin{aligned} A^\mu &= \sum_{I,\ell} \int \frac{d^3k}{(2\pi)^3\sqrt{2k_0}} \left(a^{\text{in}}_{\ell,I,k}\, e^{-i(k_0 t - \boldsymbol{k}_\perp \boldsymbol{x})}\, \chi^\mu_{\ell,I,k}(z) + h.c. \right) \\ &= \sum_{I,\ell} \int \frac{d^3k}{(2\pi)^3\sqrt{2k_0}} \left(a^{\text{out}}_{\ell,I,k}\, e^{-i(k_0 t - \boldsymbol{k}_\perp \boldsymbol{x})}\, \zeta^\mu_{\ell,I,k}(z) + h.c. \right) \ , \end{aligned} \tag{3.103}$$

where $I = R, L$ denote right and left movers, $\ell = \tau_1, \tau_2, \lambda$ sums over different wall polarisations. The wave modes $\chi^\mu(z)$ are in general constructed via

$$\chi^\mu_{\tau_i,I,k} = \epsilon^\mu_{\tau_i}\, \chi_{\tau_i,I,k}(z) \ , \tag{3.104}$$

$$\chi^\mu_{\lambda,I,k} = \left(\frac{-ik^n \partial_z (v\lambda_{I,k})}{gEv^2}, \frac{E}{gv}\lambda_{I,k} \right) \overset{\text{on shell}}{=} \bar{\partial}^\mu \left(\frac{\partial_z \left(v\lambda^z_{I,k} \right)}{Eg\ v^2} \right) + \frac{gv(z)}{E}\lambda_{I,k}\, \delta^\mu_z \ , \tag{3.105}$$

where $\bar{\partial}^\mu \equiv (-ik^n, \partial^z)$, with the explicit form of scalar fields $\chi_{\tau_i,I,k}(z)$ and $\lambda_{I,k}(z)$ obtained by solving the respective Schrodinger-like wave eqs. (3.76) and (3.80) with appropriate R, L-mover boundary conditions. In the step wall approximation for the vev $v(z)$, these are given analytically in eqs. (3.95), (3.96), (3.99) and (3.100). In complete analogy to the case of fundamental scalars[9], the modes $\chi^\mu_{\ell,I,k}$ should be thought of as describing *incoming* (early time) eigenstates of momentum (particles) in the plane wave limit with physical $z-$momentum $k^z > 0$ and $-k^z$ for R and L respectively. Modes describing *outgoing* (late time) eigenstates of momenta $\zeta^\mu_{\ell,I,k}$ are instead obtained via

$$\zeta^\mu_{\tau_i,\{L,R\}} = \epsilon^\mu_{\tau_i}\, \chi^*_{\tau_i,\{R,L\}}(z), \tag{3.106}$$

$$\zeta^\mu_{\lambda,\{L,R\}} = \left(\frac{-ik^n \partial_z (v\lambda^*_{\{R,L\}})}{gEv^2}, \frac{E}{gv}\lambda^*_{\{R,L\}} \right) \overset{\text{on shell}}{=} \bar{\partial}^\mu \left(\frac{\partial_z (v\lambda^*_{\{R,L\}})}{Eg\ v^2} \right) + \frac{gv(z)}{E}\lambda^*_{\{R,L\}}\, \delta^\mu_z \ , \tag{3.107}$$

where we have dropped k labels to not clutter the notation. Notice the switch in L, R - labels. Both sets of eigenmodes form a complete orthonormal basis and can be used to expand the field operator in eq. (3.103). The associated Fourier operators carry in and out labels to emphasise that they create/annihilate in and out states in the $S-$matrix language

$$\left| k^{\text{in}}_{\ell,I} \right\rangle \equiv \sqrt{2k_0}\, (a^{\text{in}}_{\ell,I,k})^\dagger\, |0\rangle \ , \tag{3.108}$$

$$\left| k^{\text{out}}_{\ell,I} \right\rangle \equiv \sqrt{2k_0}\, (a^{\text{out}}_{\ell,I,k})^\dagger\, |0\rangle \ , \qquad I \in R, L \quad \& \quad \ell \in \tau_1, \tau_2, \lambda \ . \tag{3.109}$$

[9] See section 3.1.3 and section 3.A.

Both satisfy the usual algebra eq. (3.18) upon quantisation.

Ward identity and current conservation: We now comment on current conservation in the case of spontaneously broken Lorentz symmetry. If the gauge symmetry is preserved, vector bosons can couple only to conserved currents. This is not the case when it is spontaneously broken, but we may still choose to consider coupling to a conserved current [10]. In the Lorentz invariant theory, the statement of the current conservation can be expressed in terms of amplitudes. Given an arbitrary process with an external vector leg with momentum k^μ, we have the following identity

$$\mathcal{M}^{(4,J)} \equiv \epsilon_k^\mu \mathcal{M}_\mu^{(4,J)} = (\epsilon_k^\mu + k^\mu)\mathcal{M}_\mu^{(4,J)} \quad , \qquad \text{(no wall)}. \tag{3.110}$$

where the $(4, J)$ label indicates full 4-momentum conservation and the process is mediated by the conserved current J^μ, and ϵ_k^μ is the external particle's polarisation vector. This Ward identity implies that substituting the latter for the particle's momentum k^μ makes the amplitude vanish.

In the presence of a domain wall in the z direction, the generalised matrix element $\mathcal{M}^{(3)}$ as defined in eq. (3.25) includes an integral over z and the polarisation tensor is also a function thereof. The expression of conservation closest to eq. (3.110) is

$$\mathcal{M}^{(3,J)} \equiv \int dz\ \chi^\mu_{\ell,I,k}(z)\mathcal{M}_\mu^{(3,J)}(z) = \int dz\ \left(\chi^\mu_{\ell,I,k}(z) + \bar\partial^\mu f(z)\right)\mathcal{M}_\mu^{(3,J)}(z)\ , \tag{3.111}$$
$$\text{where} \quad \bar\partial^\mu \equiv (-ik^n, \partial^z)\ , \qquad\qquad \text{(with wall)}$$

and $f(z)$ is an arbitrary function.

To make this discussion more concrete we consider the coupling of the gauge field to the conserved current made out of ψ fields we introduced in eq. (3.55):

$$\mathcal{L} = igA_\mu J^\mu, \qquad J^\mu = i\left(\psi^\dagger\partial^\mu\psi - \psi\partial^\mu\psi^\dagger\right), \quad \partial^\mu J_\mu = 0\ . \tag{3.112}$$

Then the amplitude (defined in eq. (3.25)) corresponding to the emission of the (l, I) polarisation from the current will be equal to

$$\langle k_I^{\text{out}}\ q|\ \mathcal{S}\ |p\rangle \equiv (2\pi)^3\delta^{(3)}(p^n - k^n - q^n)\int dz\left(\zeta^\mu_{l,I,k}(z)\right)^*(p+q)_\mu e^{i(p^z-q^z)z}\ , \tag{3.113}$$

where as usual p, q are the initial and final momentum of the ψ particle. Note, modulo a numerical factor, the same expression will be valid for the emission of the vector boson from an arbitrary conserved current (not necessarily one made from scalars). The current conservation imposes that any interaction which can be written in the form

$$J^\mu\partial_\mu f \quad \Rightarrow \quad \langle final|\ \mathcal{S}_f\ |initial\rangle = \int d^4x\ \ \partial_\mu f(x)J^\mu(x) = 0\ , \tag{3.114}$$

has a vanishing matrix element. We see now the use of writing the polarisation vector for the λ d.o.f. as we did in eq. (3.107). The dangerous-looking first term is actually a total derivative and can be subtracted when computing amplitudes (see section 3.D). We comment further on this in the next section as well as discuss the case of non-conserved current in section 3.E.

[10] For example this is the case for the coupling of W boson to light quarks, in the high energy regime when the quark masses can be approximately neglected.

3.2.5 Subtleties with WKB regime

Before we start computing the amplitudes of interest, we highlight some important subtleties related to the calculation in the WKB regime. As we have discussed in section 3.1.6, our formulas are valid only if the contribution inside the wall can be ignored. Let us check whether this is a reasonable approximation for the vector emission. Consider the λ and τ cases separately:

- **τ polarisation**

  For the τ polarisations we can estimate the contribution to the amplitude inside and outside of the wall and we find:

  $$\frac{\mathcal{M}^{\tau}_{\text{inside}}}{\mathcal{M}^{\tau}_{\text{outside}}} \simeq \Delta p_z L_w \ . \tag{3.115}$$

  Similarly to the scalar case discussed in the section 3.1.6, the contribution inside the wall can be safely ignored.

- **λ polarisation**

  Now let us look at the λ polarisation, and the interactions between the current and λ field. Using the expansion for χ^{μ}_{λ} field (see for example eq. (3.88)) we get:

  $$\begin{aligned} g J^{\mu} A^{\mu(\lambda)} &= g(J_n \partial_n \alpha - J_z \chi^{\lambda}_z) \\ &= J_n \left[\frac{-ik_n}{E v(z)^2} \partial_z \left(v(z) \lambda(z) \right) \right] - J_z \frac{E}{v(z)} \lambda(z) \ , \end{aligned} \tag{3.116}$$

  outside of the wall, when $\lambda = e^{ikx}$ this becomes

  $$J_n \left[\frac{k_n k^z}{E v(z)} \right] - J_z \frac{E}{v(z)} \lambda = g J^{\mu} \cdot \epsilon^{(\lambda)}_{\mu} \ , \tag{3.117}$$

  see eq. (3.85). Let us consider the domain wall connecting the vacua with broken and restored gauge symmetry. In this case, the λ polarisation will interact with the ψ particle only on the broken side. Then the amplitude originating from the integration outside of the wall will be equal to

  $$\begin{aligned} &\mathcal{M}^{\text{wkb red.}}_{\lambda} \propto - \left(\frac{(p+q)^{\mu} \epsilon^{(\lambda)}_{\mu}(z \to -\infty)}{p^z - q^z - \tilde{k}^z} \right) \simeq - \left(\frac{\tilde{k}^z (p^z + q^z)}{\tilde{v} E} \right) , \\ &\tilde{v} \equiv v(z \to +\infty) \ , \end{aligned} \tag{3.118}$$

  where we have kept only the leading term in energy in the polarisation vector and simplified using the conservation of the current, $p^2 = q^2$. We can see that this matrix element is growing with energy and is singular in the limit $\tilde{v} \to 0$, which are very worrisome properties since the limit $\tilde{v} \to 0$ corresponds to the no domain wall and therefore no transition radiation, i.e. $\mathcal{M} \to 0$! Let us look now at the contribution coming from the integration inside the wall, using the interaction form of eq. (3.116)

  $$\begin{aligned} \mathcal{M}_{\text{inside}} \simeq &\int_0^{L_w} dz e^{-i(p-q)^z z} (p+q)_n \left[\frac{-ik_n}{E v(z)^2} \left(\partial_z v(z) + v(z) \partial_z \right) \right] e^{-i \int_0^z d\tilde{z} k^z(\tilde{z})} \\ &- \int_0^{L_w} dz e^{-i(p-q)^z z} (p+q)_z \frac{E}{v(z)} e^{-i \int_0^z d\tilde{z} k^z(\tilde{z})} \ . \end{aligned} \tag{3.119}$$

In the first integral there is a term $\propto \partial_z v(z)$, which upon integration will necessarily lead to

$$\mathcal{M}_{inside} \sim \frac{(p+q)_0}{E}\frac{1}{\tilde{v}} \ , \tag{3.120}$$

which is of the same size as the contribution outside of the wall. We see that the amplitude $\mathcal{M}_\lambda^{\text{wkb red.}}$ will definitely lead to incorrect results, so how can we proceed? One possibility would be to take some ansatz for the domain wall and then perform full WKB calculation keeping the terms inside the wall, which will lead to correct results without bad properties of eqs. (3.119)−(3.118). However, we can still make progress even without the knowledge of the shape of the wall using the following trick. By construction, we have been focusing on the case where the current built out of ψ fields is conserved

$$J_\mu = i(\psi^\dagger \partial_\mu \psi - \psi \partial_\mu \psi^\dagger) \ , \quad \partial_\mu J^\mu = 0 \ . \tag{3.121}$$

On the other hand, the λ mode can be written as a complete derivative plus a term subleading in energy (eq. (3.84))

$$A_\mu^{(\lambda)} = \partial_\mu \alpha + \frac{g v(z)}{E}\lambda(z)(0,0,0,1) \ . \tag{3.122}$$

The part $\partial_\mu \alpha$ does not couple to a conserved current, meaning that

$$g J^\mu A_\mu^{(\lambda)} \to -\frac{g^2 v(z)}{E} J_z \lambda \ . \tag{3.123}$$

With this simplification, we immediately see that all of the problems with λ polarisations are cured

$$\begin{aligned} &\mathcal{M}_{\text{outside}} \sim \frac{(p+q)^z g^2 \tilde{v}}{E \Delta p_z} \ , \quad \mathcal{M}_{\text{inside}} \sim L_w g^2 \tilde{v} \frac{(p+q)^z}{E} \ , \\ &\frac{\mathcal{M}_{\text{inside}}}{\mathcal{M}_{\text{outside}}} \sim L_w \Delta p_z \ . \end{aligned} \tag{3.124}$$

The contribution inside the wall is suppressed and the matrix element is not growing with energy but vanishes in the limit $\tilde{v} \to 0$.

So far we have been focusing only on the case when the current made out of ψ fields is conserved on both sides of the wall. This is not true generically, and in particular for SM fermions, where the Yukawa interactions will lead to current non-conservation. So how should one proceed in that case? As explained in more detail in section 3.E, it turns out that, with very minor modifications, a very similar trick can be used.

3.3 Transition radiation and pressure from vectors

We are now ready to calculate transition radiation and the resultant pressure from vector boson emission. We are working in the Abelian Higgs theory of eq. (3.55) and calculate the average momentum transfer during the radiation of a gauge boson from an incoming ψ particle of energy p^0. We evaluate the amplitudes of interest in the next section, comment on the final state phase space and masses employed in section 3.3.2, and finally present our results in section 3.3.3.

3.3.1 Amplitudes

All the relevant amplitudes for the particle process $\psi \to \psi A$ obtained from eq. (3.113) are reported here. These are τ and λ polarisation emission for left and right movers in the step wall and WKB regimes,

$$\mathcal{M}^{\text{step}}_{\tau,L} = -ig\epsilon^{\mu}_{\tau_2}(p+q)_\mu \left(\frac{1}{\Delta p_r} + \frac{r^\tau_k}{\Delta p} + \frac{t^\tau_k}{-\Delta \tilde{p}_r}\right) , \tag{3.125}$$

$$\mathcal{M}^{\text{step}}_{\tau,R} = -ig\epsilon^{\mu}_{\tau_2}(p+q)_\mu \sqrt{\frac{k^z}{\tilde{k}^z}} \left[\frac{\tilde{k}^z}{k^z}\frac{t^\tau_k}{\Delta p} - \frac{1}{\Delta \tilde{p}} + \frac{r^\tau_k}{\Delta \tilde{p}_r}\right] , \tag{3.126}$$

$$\mathcal{M}^{\text{wkb red.}}_{\tau} = -ig\epsilon^{\mu}_{\tau_2}(p+q)_\mu \left(\frac{1}{\Delta p} - \frac{1}{\Delta \tilde{p}}\right) , \tag{3.127}$$

$$\mathcal{M}^{\text{step}}_{\lambda,L} = -i\frac{g}{E}(p^z+q^z) \left[gv\left(\frac{1}{\Delta p_r} + \frac{r^\lambda_k}{\Delta p}\right) - g\tilde{v}\frac{t^\lambda_k}{\Delta \tilde{p}_r}\right] , \tag{3.128}$$

$$\mathcal{M}^{\text{step}}_{\lambda,R} = -i\frac{g}{E}(p^z+q^z) \sqrt{\frac{k^z}{\tilde{k}^z}} \left[gv\frac{\tilde{k}^z}{k^z}\frac{t^\lambda_k}{\Delta p} - g\tilde{v}\left(\frac{1}{\Delta \tilde{p}} - \frac{r^\lambda_k}{\Delta \tilde{p}_r}\right)\right] , \tag{3.129}$$

$$\mathcal{M}^{\text{wkb red.}}_{\lambda} = -i\frac{g}{E}(p^z+q^z) \left[\frac{gv}{\Delta p} - \frac{g\tilde{v}}{\Delta \tilde{p}}\right] , \tag{3.130}$$

where the scattering coefficients $r^{\tau,\lambda}_k, t^{\tau,\lambda}_k$ relevant for the amplitudes in the step wall regime are defined in section 3.2.3 and the Δp factors in denominator are defined in eq. (3.3). We presented amplitudes for $v \neq 0$. However, the symmetry-breaking transition case can be obtained smoothly at this level by sending $v \to 0$. Note that

$$\mathcal{M}^{\text{step}}_{\lambda,L} \to 0 \qquad \text{as} \quad v \to 0 , \tag{3.131}$$

in this limit. The discontinuity in asymptotic d.o.f. (and therefore masses) is hidden here inside the kinematic factors and are addressed in the following section.

For λ emission we used current conservation to simplify the computation of these amplitudes by subtracting the total derivative piece in the wavemode eq. (3.107), as explained in section 3.1.2. For $\mathcal{M}^{\text{step}}$ this simplification does not change the final expression since it is exact (in the limit of a step wall). However, we emphasise again that it does for $\mathcal{M}^{\text{wkb red.}}_{\lambda}$, which is an approximation as described in section 3.1.6, and the subtraction is *necessary* to be consistent with the approximations and avoid unphysical divergences, as explained in section 3.2.5.

3.3.2 Phase space integration for vector emission

In going from the amplitudes above to the averaged exchanged momentum $\langle \Delta p^\ell \rangle$, where $\ell = \tau, \lambda$, we integrate over final state phase space following the prescriptions and kinematics summarised in section 3.1.7, using $\mathcal{M}^{\text{step}}$ and $\mathcal{M}^{\text{wkb red.}}$ in their respective regimes of validity. However, there are some important subtleties to discuss compared to the simple theory of scalars of section 3.1, particularly for a symmetric to broken transition. In this case, the mass of the vector (and therefore τ d.o.f.) in the old phase ($z \to -\infty$) is zero by gauge invariance since $v = 0$. As shown explicitly in section 3.G.4, in principle we can get finite results working with $m = 0$ and integrating over the full phase space as long as the mass of the emitter is kept finite $m_\psi \neq 0$. However, thermal corrections ought to be important. We should expect our calculation to break down for momenta that are too soft (to be defined precisely), where thermal field theory becomes important.

To regularise the log divergence in transverse emission when m_ψ is set to zero, [96] cut the $k_\perp$ integration at the soft thermal scale $\sim gT$. This is roughly equivalent to using 'electric' thermal masses[11] in all asymptotic state kinematics

$$\begin{aligned}(\tau):&\begin{cases}\tilde{m}=m_\tau(z=+\infty)\approx g\sqrt{\tilde{v}^2+T^2}\ ,\\ m=m_\tau(z=-\infty)\approx gT\ ,\end{cases}\\ (\lambda):&\begin{cases}\tilde{m}=m_\lambda(z=+\infty)\approx g\sqrt{\tilde{v}^2+T^2}\ ,\\ m=m_\lambda(z=-\infty)=m_{h,s}(T)\ .\end{cases}\end{aligned}\qquad\text{(symmetric to broken)}\tag{3.132}$$

In this work we also impose the IR cut-off in this way, since our primary focus is the proper calculation of λ emission, which turns out to not need IR regulation. We note however that eq. (3.132) requires further scrutiny. As is well known, the self energy for $\boldsymbol{A}$ receives 'magnetic mass' thermal corrections only at two loops from charged matter, of parametric order $\sim g^2T$. Moreover, we are working in the frame of the wall, so the background plasma is boosted and standard results should be distorted. We leave the rigorous inclusion of finite temperature to a follow up study.

In eq. (3.132), $m_{h,s}$ is the mass of the Higgs d.o.f. in the symmetric phase (see eq. (3.83)) which will also be temperature dependent [12]. So now, for example, the integration limits for the k^z integral for $\langle\Delta p_R^{\lambda,\text{step}}\rangle$ in eq. (3.45) become explicitly $k^z\in\left[\sqrt{g^2\tilde{v}^2+g^2T^2-m_{h,s}^2(T)}\ ,\ k^z_{\text{max}}\right]$ [13].

It is worth stressing that for τ polarisation what appears in the amplitude and in the kinematics boundaries of the PS are always the masses m and $\tilde{m}$ as defined in eq. (3.132). However, for the λ polarisation the coupling appearing in the amplitude is really the bare $gv(\to 0)$ and does not receive thermal corrections, while in the kinematics and PS integration what appears is m and $\tilde{m}$ as defined as in eq. (3.132). So eq. (3.131) still holds even at finite T. For broken to broken transitions the vector masses are, for both λ and τ fields

$$m\approx g\sqrt{v^2+T^2}\ ,\quad \tilde{m}\approx g\sqrt{\tilde{v}^2+T^2}\ ,\qquad\text{(broken to broken)}\ .\tag{3.133}$$

In summary, $\langle\Delta p\rangle$ is computed as in section 3.1.7 with phase space integration limits in Table 3.1.1 and asymptotic masses defined here above. In general, there is a total of six contributions:

$$\begin{aligned}&\langle\Delta p_R^{\tau,\text{step}}\rangle\ ,\qquad\langle\Delta p_R^{\tau,\text{wkb}}\rangle\ ,\qquad\langle\Delta p_L^{\tau,\text{step}}\rangle\ ,\\ &\langle\Delta p_R^{\lambda,\text{step}}\rangle\ ,\qquad\langle\Delta p_R^{\lambda,\text{wkb}}\rangle\ ,\qquad\langle\Delta p_L^{\lambda,\text{step}}\rangle\ .\end{aligned}\tag{3.134}$$

3.3.3 Pressure on the bubble wall

We now report and comment on our results for the average NLO momentum transfer $\langle\Delta p\rangle$ due to transition radiation from a ψ particle travelling across the wall and thereby

[11] This is the thermal mass correction in the self-energy of A^0. It is the relevant scale for example in the Debye screening of the Coulomb field [11].

[12] We do not discuss the explicit form of it since our results are largely insensitive to it.

[13] When $m_{h,s}(T)<\tilde{m}(T)$ we are in line with our set up which assumed $m<\tilde{m}$, but if it is the other way around the lower limit of k^z becomes imaginary. This is signaling the fact that modes with $0<\tilde{k}<\sqrt{m^2-\tilde{m}^2}$ are now exponentially decaying in the old phase (right) side of the wall. Then it is more appropriate to define the step wall regime according to $k<\tilde{k}\lesssim L_w^{-1}$ and parameterise the PS integrals in terms of $(\tilde{k}^z,k_\perp^2)$. The integration limits for $\tilde{k}^z$ for $R-$mover emission would be $\tilde{k}^z\in[0,\tilde{k}^z_{\text{max}}]$, where $\tilde{k}^z_{\text{max}}=\sqrt{(p_0-m_\psi)^2-\tilde{m}^2}$.

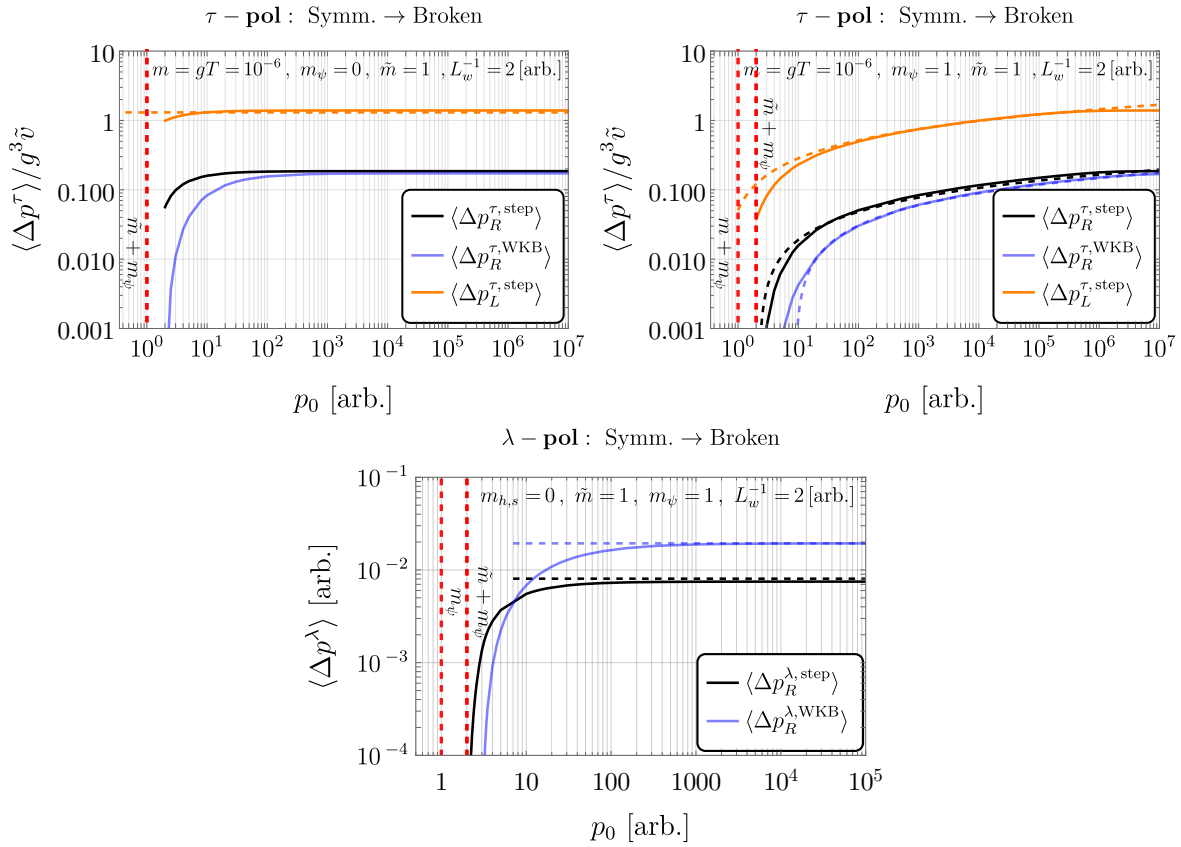

Figure 3.3.1: Symmetric $\to$ Broken. We present qualitatively the same plot as in fig. 3.0.3 (left panel), this time disentangling all the contributions, and highlighting the effect of a hierarchy $m \ll m_\psi$ for τ emission. **Top Left**: Averaged momentum exchange for τ polarisation contributions. The curves quickly saturate to their constant asymptotic values and the dominant contribution is $L-$mover emission in the step wall regime. Thick lines are numerics and the dashed line is the analytical expression in eq. (3.255). **Top Right**: Same as previous, but for $m/m_\psi \ll 1$. We see the transient inter-relativistic regime scaling as $\log(p_0)$, well described by the $m = 0$ analytical formulae (dashed lines) found in section 3.G.4. The regime ends around $p^0 \sim \tilde{m} m_\psi / m$. **Bottom**: λ polarisation contributions. The result is quite insensitive to the symmetric side λ mass $m_{h,s}(T)$ as long as it is $\lesssim \tilde{m}$. We plot for $m_\psi = 1$ [arb.], but varying it does not change much either; unlike for τ, there is no intermediate regime. Dashed lines are analytical formulae in eqs. (3.263) and (3.264).

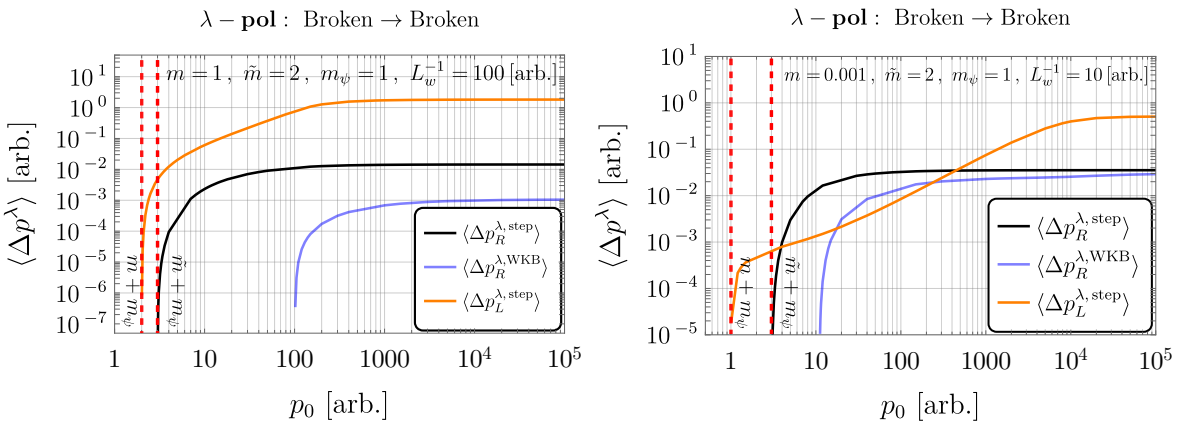

Figure 3.3.2: Broken $\to$ Broken. **Left**: Averaged momentum exchange for λ polarisation emission for relatively thin wall. The inter-relativistic regime of scaling with p^0 lasts till $p^0 \sim L_w^{-1}$. Taking $\Delta m \ll 1$ does not qualitatively change anything except for suppressing all values. Notice $m \lesssim \tilde{m}$. **Right**: Similar to previous, but in the case $m \ll \tilde{m}$. Here we see that the inter-relativistic regime is distorted at low p^0 and also extended up to $p_0 \sim L_w^{-1} m_\psi / m$.

compute the total pressure on the bubble wall. We show a break down of figs. 3.0.2 and 3.0.3 into all their contributions, as well as provide some analytical formulae. A comprehensive comparison (via numerical integration - see section 3.G for some analytical evaluation of phase space integrals) of all the different parts in eq. (3.134) is shown in figs. 3.3.1 and 3.3.2, as a function of the energy of the incoming emitter particle, ψ. In the asymptotic $p_0 \to \infty$ limit all contributions are constant. Their relative importance is displayed in fig. 3.3.3. We now discuss the two cases of interest $v = 0$ and $v \neq 0$ separately.

Symmetric to broken case ($v = 0$). We observe in fig. 3.3.1 that when the emitting particle is $m_\psi \lesssim m$ the contribution from τ saturates quickly to the constant $p_0 \to \infty$ value (top left in fig. 3.3.1), but if there is a hierarchy $m \ll m_\psi$, we observe an inter-relativistic regime of logarithmic dependence on p_0 up until $p_0 \sim \tilde{m} m_\psi / m$. This can be traced to a collinear log divergence of phase space integration in the limit $m = 0$ & $p_0 \to \infty$ as explained in section 3.G. This behaviour is not present in contributions from λ polarisation emission, which are insensitive to m_ψ for relativistic p^0, even when the symmetric side mass is set to zero $m_{h,s} = 0$.

In the asymptotic $p^0 \to \infty$ limit τ contributions depend significantly only on the ratio [14] $m/\tilde{m}$, which can be translated to $T/\tilde{v}$. While individual λ contributions depend also on L_w^{-1} their sum is constant. The total momentum transfer (summing over all contributions) can be fitted by the following expression

$$\lim_{p_0\to\infty}\langle\Delta p^{\text{total}}\rangle \simeq g^3\tilde{v}\left[0.135\log\left(\frac{\tilde{v}}{T}+2.26\right)-0.085-0.2\frac{\log\left(\frac{\tilde{v}}{T}+2.26\right)}{\tilde{v}/T}+\frac{0.19}{\tilde{v}/T}\right]. \tag{3.135}$$

We recall that to obtain this expression we cut the phase space integrals in the IR at energies $\sim gT$. The expression in eq. (3.135) becomes valid for the energies of initial particle $p_0 \gtrsim \frac{\tilde{v}}{T} \times m_\psi$, which in the case of massless emitter $m_\psi \to 0$ becomes $p_0 \gtrsim \tilde{v}$. At

[14] See for example the exact evaluation of the dominant contribution eq. (3.255).

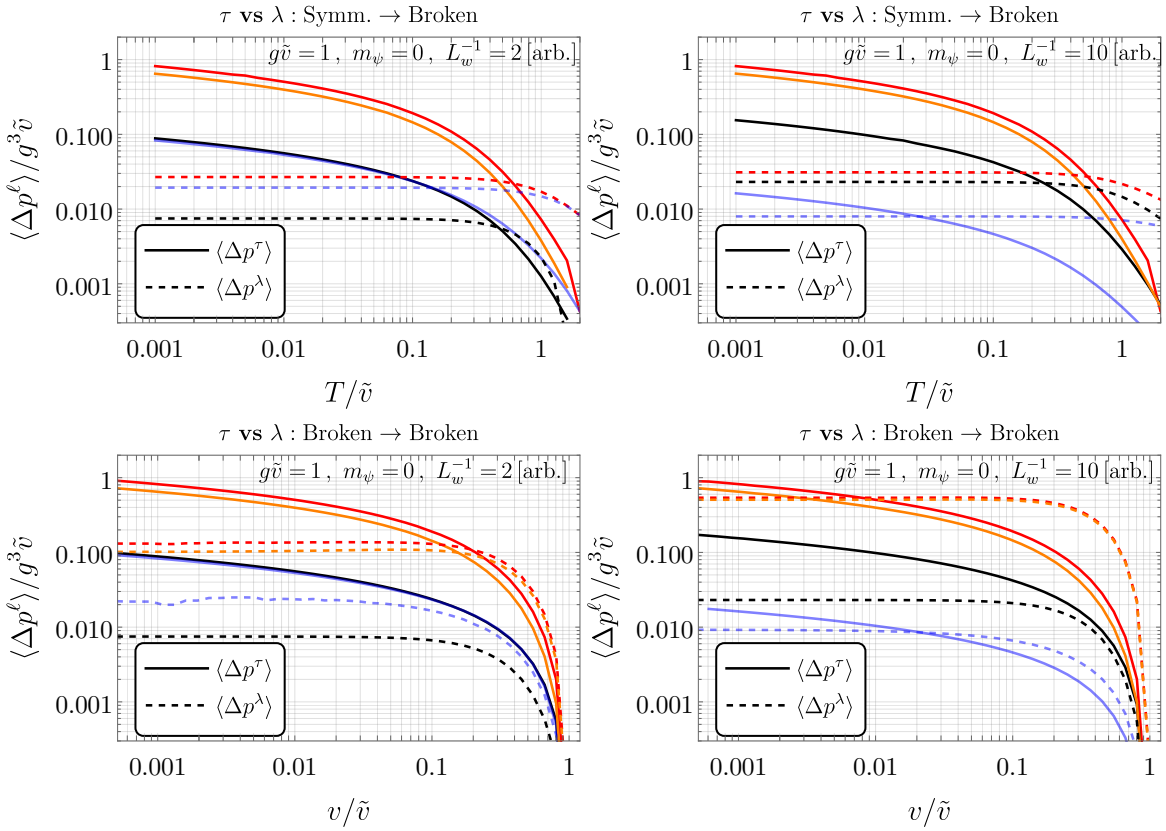

Figure 3.3.3: Here is presented the same plot as in fig. 3.0.2, but this time disentangling all the contributions. Solid lines refer to τ polarisation, while dashed to λ. The red lines are the total sum, for each polarisation. **Top**: Symmetric → Broken. It is shown two cases with different wall widths and it is worth noticing that while the total contribution for τ and λ does not change appreciably, the single contributions do, like R step wall versus WKB. **Bottom**: Broken → Broken. Here it happens the same as in the top panels, but, since in this case, L step contribution from λ polarisation has to be taken into account, we see that, depending on the value of L_w and the hierarchy between the different vevs, can be the most relevant contribution.

last we would like to remind the reader that the expression above was obtained just for the single vector emission, and one cannot trust it for very large values of log.

The contribution of the longitudinal modes is sub-leading except perhaps for mild super-cooling $\tilde{v}/T$ ∼few, and is equal approximately to

$$\lim_{p_0\to\infty}\langle\Delta p^{\lambda}\rangle \sim g^3\tilde{v}\times c_{\lambda}(L_w,T,\tilde{m},m_{\psi}),\quad c_{\lambda}\in[0.02,0.03]. \tag{3.136}$$

This result qualitatively agrees with the estimate in the Ref. [95]. An analytical form for the function c_λ is given in eq. (3.265).

So far we have been calculating the momentum transfer from individual collisions. In order to find the pressure acting on the bubble wall we need to perform the integration over the flux of incoming particles. This can be easily done in the thermal case since we know the distributions

$$\mathcal{P}=\int\frac{d^3p}{(2\pi)^3}f_{\psi}(T,\gamma_w)\times\frac{p^z}{p_0}\langle\Delta p\rangle. \tag{3.137}$$

If the average momentum transfer is a constant the integration is simple and we find, since in the ultra-relativistic case $p^z/p_0\to 1$,

$$\mathcal{P}=n_{\psi}(T,\gamma_w)\langle\Delta p\rangle=\gamma_w n_{\psi}(T)\langle\Delta p\rangle, \tag{3.138}$$

where n_ψ is the density of emitters ψ defined in the plasma frame. Then, for the symmetric to broken transition we obtain the following expression for the pressure:

$$\lim_{\gamma_w\to\infty}\mathcal{P}_{\text{th.}}\simeq\frac{\zeta(3)\gamma_w T^3}{\pi^2}\times \tag{3.139}$$
$$g^3\tilde{v}\left[0.135\log\left(\frac{\tilde{v}}{T}+2.26\right)-0.085-0.2\frac{\log\left(\frac{\tilde{v}}{T}+2.26\right)}{\tilde{v}/T}+\frac{0.19}{\tilde{v}/T}\right],$$

where th. stands for thermal.

Broken to broken case ($v\neq 0$). In fig. 3.3.2 we show the evolution of $\langle\Delta p\rangle(p_0)$ for a broken to broken transition. We focus only on λ contributions since the ones from τ are essentially the same as in fig. 3.3.1 with suitable re-interpretation of what $m,\tilde{m}$ mean (see section 3.3.2). Again the curves eventually saturate to a constant value but we highlight the strongly L_w-dependent novel contribution from $L-$mover emission, which easily comes to dominate in the thin wall regime. As in fig. 3.0.3, we highlight that in the left panel, we can clearly distinguish the inter-relativistic region where this last contribution develops a linear growth in p_0. In fig. 3.3.3 we see the dependence of the saturation value of the averaged exchanged momentum (in the limit $p_0\to\infty$) on the ratio between vevs (lower panels).

Broken to broken transitions were recently studied at leading order by [79] and it was found that reflection of the longitudinal vectors is efficient for the energies below L_w^{-1} (inverse width of the wall). This in its turn leads to the pressure scaling as γ_w^2, as long as $p_0<L_w^{-1}$. We find that a reminiscent effect happens at NLO level, the main difference is that the momentum of the vector is not fixed by the speed of the bubble expansion and is always integrated over all possible values. We find that the momentum transfer is dominated by left-mover modes and for the values of the energies of incoming particle $p_0<L_w^{-1}\text{Max}[1,m_\psi/m]$ it is proportional to $\propto p_0$

$$\lim_{p_0<L_w^{-1}\text{Max}[1,m_\psi/m]}\langle\Delta p_{v\neq 0}\rangle\sim 10^{-2}\times g^2\frac{(v^2-\tilde{v}^2)^2}{(v^2+\tilde{v}^2)^2}\times\frac{p_0}{\text{Max}[1,m_\psi/m]}\,. \tag{3.140}$$

In the case of large hierarchy $0 < m \ll m_\psi$, not only is the saturation point delayed, but a further slight distortion occurs at low p^0, as shown in fig. 3.3.2. Once the energy of the initial particle becomes larger than $\sim L_w^{-1}\text{Max}[1, m_\psi/m]$, we have

$$\lim_{p_0\to\infty, L_w\to 0}\langle \Delta p_{v\neq 0}\rangle \simeq 0.05 g^2 \frac{(v^2-\tilde{v}^2)^2}{(v^2+\tilde{v}^2)^2} L_w^{-1}. \tag{3.141}$$

Momentum transfer stops growing and reaches the saturation value. Note that the maximal value of this pressure is controlled by L_w^{-1} and not by the mass of the vector $g\tilde{v}$. This is related to the fact that at high energies Goldstone Boson equivalence theorem relates the longitudinal vectors to the Goldstone bosons, and the strength of their interaction with the bubble wall (Higgs field) is controlled by the mass of the Higgs (wall width). Consequently, in the case of broken to broken transition, there is an additional contribution to the pressure which scales as

$$\lim_{\gamma_w\to\infty} \mathcal{P}^\lambda_{v\neq 0} \sim 0.05 \frac{\zeta(3)\gamma_w T^3}{\pi^2} \times g^2 \frac{(v^2-\tilde{v}^2)^2}{(v^2+\tilde{v}^2)^2} \times L_w^{-1}. \tag{3.142}$$

with an intermediate regime scaling as $\mathcal{P}^\lambda \propto \gamma_w^2$ for the values of boost factor $\gamma_w < (L_w T)^{-1}$.

3.4 Summary

We conclude by summarising the main results of our work. We analysed in detail the phenomena of transition radiation in the presence of domain walls. We quantised from first principles scalar and vector theories on a translation-violating background and identified the correct asymptotic states. We split emission into soft and UV regimes and used a step wall and WKB approximation respectively to compute the desired matrix elements for transition radiation. Quantisation of vector field theories was naturally performed via the introduction of new degrees of freedom which do not coincide with the traditional transverse and longitudinal polarisation but are a convenient admixture. In this way, we have resolved some puzzles regarding the inclusion of longitudinal polarisations in the calculation of transition radiation.

We applied these results to calculate the pressure experienced by the bubble wall during the ultra-relativistic expansion. For the phase transitions with spontaneous breaking of the gauge symmetries in the regime of strong supercooling, we find the pressure which scales as

$$\mathcal{P} \propto \gamma_w g^3 \tilde{v} T^3 \log\frac{\tilde{v}}{T}, \quad \text{for} \quad \tilde{v}/T \gg 1, \tag{3.143}$$

and is dominated by the emission back out of the wall of transverse-like polarisations with momenta $k^z \in (0, \Delta m)$. This result qualitatively agrees with the previous literature on the subject. For moderate ratio $\tilde{v}/T \sim$ few we find that the contribution from the longitudinal-like polarisations can lead to significant corrections. We provide an updated fitted formula for the total pressure in eq. (3.139).

We also analysed the pressure in the case of transition between two vacua with broken gauge symmetry. Interestingly we find in this case the contribution from the longitudinal-like polarisation can easily become dominant for thin walls, with the asymptotic value controlled by the inverse wall width $\mathcal{P}^{\max} \propto \gamma_w g^2 T^3 L_w^{-1}$. Moreover, we find a transient intermediate regime of $\mathcal{P} \propto \gamma_w^2$ scaling for $p_0 \lesssim L_w^{-1}$.

Our results make an advance in understanding the balance between bubble acceleration and friction which plays a crucial role in determining most phenomenological consequences of FOPTs as well as their detection prospect at upcoming gravitational wave detectors.

Future outlook: The work can be improved and generalised in several ways. An important remaining question is the inclusion of finite temperature effects in a robust first principles fashion (see for example the discussion in section 3.3.2). It is relatively easy, though cumbersome, to allow also for the emitting particle to feel the wall $m_\psi \to m_\psi(z)$. Though in the $\gamma_w \to \infty$ limit, any dependence on $m_\psi(z)$ should drop out, we saw how m_ψ can distort the intermediate shape of $\mathcal{P}^{\rm NLO}(\gamma_w)$ and ultimately finding the equilibrium velocity v_w will require full knowledge of this curve. Similarly one could rigorously quantise fermionic fields that change mass across the wall.

A possibly important direction is the analysis of multiple vector emissions, particularly in regimes with large logs, possible IR enhancements, and back-reaction effects coming from the overdensity of soft vector bosons around the wall (see discussion in [96]). Furthermore, it would be interesting to compare our wall-shape-independent results with a full numerical calculation using a specific smooth wall ansatz (for example *tanh*). Finally, with some tweaks, our expressions can be used to analyse pressure in qualitatively different types of FOPTs, such as spontaneous breaking of *global* symmetries, or even symmetry *restoring* transitions. This latter case will be the subject of the next chapter.

While our interest here was in friction, we emphasise that our set up is useful for rigorously computing any process / Feynman diagram[15] in the presence of background walls which are not treated as a perturbation. Just as an example, one can easily re-purpose our expressions to compute the number of particles of a given species produced from collisions between an expanding bubble and surrounding particles [16]. The spontaneous breaking of Lorentz/translational symmetry in the early Universe results in a rich phenomenology that is only starting to be explored systematically.

[15] At tree or even loop level.

[16] These could be heavy, Dark matter candidates.

Appendix

3.A Wavepackets and asymptotic states

No wall: Let us recall a few things in the usual manifestly translation-invariant case (no wall background). For clarity, we will first focus on $1+1$ dimensions. For a scalar field theory, the field operator $\psi(t,z)$ is interpreted as creating a particle at position z at time $t=0$. The position space wavefunction of a state is thus given by its inner product with $\langle 0|\psi$. The wavefunction of a single particle eigenstate of momentum $|k\rangle = \sqrt{2k^0}a_k^\dagger|0\rangle$ is, as expected,

$$\langle 0|\psi(t,z)|k\rangle = e^{-ik_\mu x^\mu} \ . \tag{3.144}$$

To derive formulae for observables such as scattering cross sections or emission probabilities involving realistic particles we have to crucially go through appropriately defined wavepackets that describe those asymptotic states, taking a limit of sharp momentum only at the end. A wavepacket state describing a particle with momentum peaked around p and localised in space is given by

$$|\Psi_p\rangle \equiv \int_{-\infty}^{\infty} \frac{dk^z}{(2\pi)\sqrt{2k^0}} f_p(k^z)|k\rangle \ , \qquad \langle\Psi_p|\Psi_p\rangle = \int \frac{dk^z}{(2\pi)}|f_p(k^z)|^2 = 1 \ . \tag{3.145}$$

where $f_p(k^z)$ is like a sharp Gaussian in k^z peaked at p^z. Note there is no spacetime dependence in this expression (we are always in the Heisenberg picture). The limit to recover a momentum eigenmode is $f_p(k^z) \longrightarrow (2\pi)^3\sqrt{2k^0}\delta(p^z-k^z)$. However, the more appropriate limit used in the derivation of physical rates makes use of the normalisation condition above

$$|f_p(k^z)|^2 \longrightarrow (2\pi)\delta(p^z-k^z) \ , \quad \text{(peaked momentum limit)} \ . \tag{3.146}$$

To see the localisation we can look at the wavefunction of the wavepacket state:

$$\langle 0|\psi(t,z)|\Psi_p\rangle = \int_{-\infty}^{\infty} \frac{dk^z}{(2\pi)\sqrt{2k^0}} f_p(k^z) e^{-ik_\mu x^\mu} \ . \tag{3.147}$$

At $t=0$ this is an oscillating function of z (with wavelength controlled by p) with a Gaussian envelope so that it is indeed localised at $z=0$. As a function of time, the wavepacket moves in the direction of sign(p). Because each mode has a slightly different dispersion relation, the spatial width of the wavepacket tends to widen in time (dispersion) but this can be counteracted by making $f_p(k)$ a sharper Gaussian, taking an appropriate order of limits.

3.A.1 Asymptotic states in the wall background

In the presence of the wall we should still define asymptotic particle states as appropriate wavepackets to compute formulae for physical rates. A slight complication comes from the fact that the one particle states $|k_{L,R}\rangle$ we quantise are not eigenstates of momentum. Moreover, in general, the same state describes different types of particles in different regions of space[17]. Defining the asymptotic state carefully will get rid of any ambiguity.

We now consider an operator that feels the wall $\phi(t, \boldsymbol{x})$ expanded in left and right mover modes as in eq. (3.16). As before, the action of this on the vacuum should be thought of as creating a particle localised at $x^\mu = 0$. Contracting a state with $\langle 0|\phi$ still gives the wavefunction understood in the usual sense. In fact

$$\langle 0|\phi(t, \boldsymbol{x})|k_I\rangle = e^{-ik_n x^n}\chi_{I,k}(z) \ , \tag{3.148}$$

with $I = R, L$. To gain physical intuition of the one particle states $|k_I\rangle$, consider constructing wavepackets by superimposing exclusively right (left) movers:

$$|\Phi^{\rm in}_{I,p}\rangle \equiv \int_{0,\,\Delta m}^{\infty} \frac{dk^z}{(2\pi)\sqrt{2k^0}} f_p(k^z)|k_I\rangle \ , \tag{3.149}$$

where again we focus on $1+1$ dimensions and where the lower limit is 0 (Δm) for R (L) movers respectively. The 'in' labels will become clear shortly. Their wavefunctions are respectively

$$\langle 0|\phi(t, z)|\Phi^{\rm in}_{I,p}\rangle \equiv \int_{0,\,\Delta m}^{\infty} \frac{dk^z}{(2\pi)\sqrt{2k^0}} f_p(k^z)e^{-ik^0 t}\chi_{I,k}(z) \ . \tag{3.150}$$

Ignoring the slight dispersion mentioned at the end of the previous subsection, the time evolution of eq. (3.150) for $I = R(L)$ describes an isolated localised wavepacket travelling in towards the wall from $z < 0$ ($z > 0$) when $t < 0$. This wavemode scatters off the wall and for $t > 0$ splits into reflected and transmitted wavemodes travelling in opposite directions. Thus, $|\phi^{\rm in}_{R,p}\rangle$ ($|\phi^{\rm in}_{R,p}\rangle$) is a good asymptotic state for an *incoming* particle with positive (negative) $z-$momentum. It cannot however be used as an asymptotic state for any single *outgoing* asymptotic particle since at late times it describes a superposition.

So what about single localised *outgoing* particles? Clearly, when the wave equation is reduced to Schrodinger-like form with a real potential, these can be obtained by complex conjugation of the spacial part of the wavefunction. In other words we require states $|\Phi^{\rm out}_{I,p}\rangle$ such that

$$\begin{aligned} &\langle 0|\phi(t, z)|\Phi^{\rm out}_{I,p}\rangle \equiv \int_{\Delta m,\,0}^{\infty} \frac{dk^z}{(2\pi)\sqrt{2k^0}} f_p(k^z)e^{-ik^0 t}\zeta_{I,k}(z) \ , \\ &\text{with} \quad \zeta_{R,L}(z) = \chi^*_{L,R}(z) \ . \end{aligned} \tag{3.151}$$

In time, these correspond to two waves coming from opposite sides of the wall, hitting the wall around $t \approx 0$ and interfering in just the right way so that at late time there is only one wavemode travelling towards $z \to -\infty$ or $z \to \infty$ respectively. Notice the swap in labels. We adopt the convention that the right-mover R (left-mover L) label always denotes a particle of positive (negative) $z-$momentum. It is an easy exercise to write

[17] This can be simply because the mass changes or, as in the case of $\lambda(x)$ in a symmetric to broken transition, the field interpolates even between particles of different spin.

the $\zeta_{R,L}$ in terms of a linear composition of the complete basis $\chi_{R,L}$ as explicitly done in eqs. (3.21) and (3.22). The appropriate wavepacket for an outgoing state is thus

$$|\Phi^{\rm out}_{I,p}\rangle \equiv \int_{\Delta m,\,0}^{\infty} \frac{dk^z}{(2\pi)\sqrt{2k^0}} f_p(k^z)|k^{\rm out}_I\rangle \ , \tag{3.152}$$

where $|k^{\rm out}_I\rangle$ are the one-particle states with wavefunctions $\zeta_{I,k}(z)$ and are related to the $|k_I\rangle$ by

$$|k^{\rm out}_L\rangle = r^*_{R,k}|k_R\rangle + t^*_{R,k}\sqrt{\tilde{k}^z/k^z}\ |k_L\rangle\ \Theta(k^z-\Delta m) \ , \tag{3.153}$$

$$|k^{\rm out}_R\rangle = t^*_{L,k}\sqrt{k^z/\tilde{k}^z}\ |k_R\rangle + r^*_{L,k}|k_L\rangle \ , \tag{3.154}$$

where the reflection and transmission coefficients were defined in general for scalar d.o.f. in section 3.1.1, and given explicit form in the case of a step wall for fundamental scalars also in section 3.1.1 and for different vector polarisations in section 3.2.3.

Reflection and transmission probabilities: As a consistency check, we can compute reflection and transmission probabilities in this language. Focusing on the identity part of the S matrix $S = 1 + i\mathcal{T}$, the amplitude for a particle incoming from $z<0$ to reflect and transmit should be, respectively:

$$\langle\phi^{\rm out}_{L,p}|\phi^{\rm in}_{R,p}\rangle = \int_0^\infty \frac{dk}{2\pi}|f_p(k)|^2\ r_{R,k} \quad \to \quad r_{R,p} \ , \tag{3.155}$$

$$\langle\phi^{\rm out}_{R,p}|\phi^{\rm in}_{R,p}\rangle = \int_{\Delta m}^\infty \frac{dk}{2\pi}|f_p(k)|^2\ t_{L,k}\sqrt{\tilde{k}^z/k^z} \quad \to \begin{cases} t_{L,p}\sqrt{p/\tilde{p}}\ , & p>\Delta m \\ 0\ , & p<\Delta m \end{cases} \ , \tag{3.156}$$

where the arrow denotes taking the peaked momentum limit eq. (3.146) in the end. So the relative probability for a peaked-around-p incoming mode to reflect/transmit into a peaked-around-p outgoing mode is what one could have already guessed

$$\text{Reflection probability} = |\langle\phi^{\rm out}_{L,p}|\phi^{\rm in}_{R,p}\rangle|^2 \to |r_{R,p}|^2 \ , \tag{3.157}$$

$$\text{Transmission probability} = |\langle\phi^{\rm out}_{R,p}|\phi^{\rm in}_{R,p}\rangle|^2 \to \begin{cases} |t_{L,p}|^2 p/\tilde{p}\ , & p>\Delta m \\ 0\ , & p<\Delta m \end{cases} \ . \tag{3.158}$$

3.A.2 Phase space derivation from wavepackets

In this section we will obtain formulae for the averaged momentum exchanged by transition radiation processes in the background of the wall, deriving eq. (3.32) in the main text. Treating the incoming particle as a wavepacket as in eq. (3.145), we find the amplitude squared for splitting into ℓ particles, which may or may not feel the wall. These outgoing states are late-time eigenstates of momentum, obtained as limits of their own wave-packet forms. We have

$$\begin{aligned}
|\langle k^{\rm out}_1 \dots k^{\rm out}_\ell|\Phi_p\rangle|^2 &= \int \frac{d^3p_1 d^3p_2}{\sqrt{4p^0_1 p^0_2}} f_p(p_1) f^*_p(p_2)\delta^{(3)}\left(p_1 - \sum_{i=1}^{\ell} k_i\right)\delta^{(3)}\left(p_2 - \sum_{j=1}^{\ell} k_i\right)|\mathcal{M}^{(3)}_{1\to\ell}|^2 \\
&= \int \frac{d^3p_1 dp^z_2}{\sqrt{4p^0_1 p^0_2}} f_p(p_1) f^*_p(p_2)\delta^{(3)}\left(p_1 - \sum_{i=1}^{\ell} k_i\right)\frac{p^0_1}{|p^z_1|}\delta\left(p^z_1 - p^z_2\right)|\mathcal{M}^{(3)}_{1\to\ell}|^2 \\
&= \int \frac{d^3p_1}{2|p^z_1|}|f_p(p_1)|^2\delta^{(3)}\left(p_1 - \sum_{i=1}^{\ell} k_i\right)|\mathcal{M}^{(3)}_{1\to\ell}|^2 \\
&\longrightarrow \frac{(2\pi)^3}{2|p^z|}\delta^{(3)}\left(p - \sum_{i=1}^{\ell} k_i\right)|\mathcal{M}^{(3)}_{1\to\ell}|^2 \ ,
\end{aligned} \tag{3.159}$$

where the temporary label (3) on $\mathcal{M}$ emphasises only three of 4−momentum are conserved. In the last step, we take the peaked momentum limit of eq. (3.146). For the particular case of a $1 \to 2$ process as discussed in this work, we have

$$\begin{aligned}\langle \Delta p^z_{I=R,L} \rangle \equiv \int \mathcal{P}_{p\to q k_I^{\rm out}} \Delta p^z_I &= \int \frac{d^3k}{(2\pi)^3 2k^0} \int \frac{d^3q}{(2\pi)^3 2q^0} |\langle q\, k_I^{\rm out}|\Phi_p\rangle|^2 \Delta p^z_I \\ &= \int \frac{d^3k d^3q}{(2\pi)^3 8p^z k^0 q^0} \delta^{(3)}\left(p-k-q\right) |\mathcal{M}^{(3)}_I|^2 \Delta p^z_I \\ &= \int \frac{d^3k}{(2\pi)^3 8p^z k^0 |q^z_k|} \left[|\mathcal{M}^{(3)}_I|^2 \Delta p^z_I\right]_{q^z=\pm q^z_k} \end{aligned} \tag{3.160}$$

where in going to the last line we have used

$$\begin{aligned}\delta\left(p^0-k^0-q^0\right) &= \frac{q^0}{|q^z_k|}\left[\delta(q^z-q^z_k)+\delta(q^z+q^z_k)\right] \\ \text{with} \quad q^z_k &= \sqrt{(p^0-k^0)^2-k_\perp^2-m_q^2}\end{aligned} \tag{3.161}$$

Thus, in principle, one should sum contributions from both signs of q^z to obtain the full integrated rate. In practice, the $q^z < 0$ branch will be highly sub-leading at large energies.

Comparison with decay formula: One might wonder how to recover the familiar decay formula in the limit of no wall. The latter can be derived in terms of the full 4−momentum conserving matrix element $\mathcal{M}^{(4)}$ as

$$\begin{aligned}|\langle k_1 \dots k_\ell|p\rangle|^2 &= \int \frac{d^3p_1 d^3p_2 (2\pi)^2}{\sqrt{4p_1^0 p_2^0}} f_p(p_1) f_p^*(p_2) \delta^{(4)}\left(p_1 - \sum_{i=1}^{\ell} k_i\right) \delta^{(4)}\left(p_2-p_2\right) |\mathcal{M}^{(4)}_{1\to\ell}|^2 \\ &= \int \frac{d^3p_1 (2\pi)^2}{2p_1^0} |f_p(p_1)|^2 \delta^{(4)}\left(p_1 - \sum_{i=1}^{\ell} k_i\right) \underbrace{\delta\left(0\right)}_{T/2\pi} |\mathcal{M}^{(4)}_{1\to\ell}|^2 \\ &\longrightarrow \frac{(2\pi)^4}{2p_0} \mathbb{T}\, \delta^{(4)}\left(p - \sum_{i=1}^{\ell} k_i\right) |\mathcal{M}^{(4)}_{1\to\ell}|^2 \,, \end{aligned} \tag{3.162}$$

where $\mathbb{T}$ is total time (one can only define a decay probability per unit time). We can see how eq. (3.159) reduces to this result. In the absence of the wall, the matrix element gives

$$|\mathcal{M}^{(3)}_{1\to\ell}|^2 = 2\pi\, \mathbb{L}^z \delta\left(p^z - \sum_{i=1}^{\ell}\right) |\mathcal{M}^{(4)}_{1\to\ell}|^2 \tag{3.163}$$

where $\mathbb{L}^z$ is the distance traversed in the z direction. Finally, using that $\mathbb{L}^z = \mathbb{T}\, p^z/p^0$, eq. (3.159) reduces to eq. (3.162).

3.B Computations for scalar eigenmodes

In this appendix, we report, for completeness, the full computation of the orthogonality conditions for the eigenmodes computed in section 3.1.1. Starting from the KG equation for the ϕ field in presence of a z−dependent mass

$$(\Box + m^2(z))\phi = 0 \,, \quad \longrightarrow \quad \chi_k''(z) + m^2(z)\chi_k(z) = 0 \,, \tag{3.164}$$

where with k we refer to the momentum along the $z-$direction and $m^2(z) = m^2 + (\tilde{m}^2 - m^2)\theta(z)$. The general solution of this differential equation is of the form

$$\chi_k(z) \equiv \begin{cases} Ae^{ikz} + Be^{-ikz} \ , & z < 0 \\ Ce^{i\tilde{k}z} + De^{-i\tilde{k}z} \ , & z > 0 \end{cases} \tag{3.165}$$

where for this to be a solution we need to specify the relation $\tilde{k}^2 = k^2 + m^2 - \tilde{m}^2$. Integrating the KG equation around $\lim_{\epsilon\to 0}\int_{-\epsilon}^{+\epsilon} dz$ we find that the solution and its derivative should be continuous around $z = 0$, this lead to the following relations between the coefficients

$$\begin{cases} A + B = C + D \ , \\ k(A - B) = \tilde{k}(C - D) \ . \end{cases} \tag{3.166}$$

Since we have the freedom to set one of the four coefficients to zero, we can, without loss of generality, define two linearly independent solutions that describe right-movers and left-movers. The motivation for setting one of these coefficients to zero is to avoid describing a physical wave that comes from $z = \infty$ (for right-movers) or $z = -\infty$ (for left-movers). For the former, we set $D = 0$ and then

$$\chi_{R,k}(z) \equiv \begin{cases} A_R e^{ikz} + B_R e^{-ikz} \ , & z < 0 \\ C_R e^{i\tilde{k}z} \ , & z > 0 \end{cases} \tag{3.167}$$

where the coefficients are related by the conditions (3.166)

$$\begin{cases} A_R = \dfrac{k + \tilde{k}}{2k} C_R \ , \\ B_R = \dfrac{k - \tilde{k}}{2k} C_R \ . \end{cases} \tag{3.168}$$

Instead, for left-movers, we set $A = 0$, then

$$\chi_{L,k}(z) \equiv \begin{cases} B_L e^{-ikz} \ , & z < 0 \\ C_L e^{i\tilde{k}z} + D_L e^{-i\tilde{k}z} \ , & z > 0 \end{cases} \tag{3.169}$$

where the coefficients, from (3.166), are

$$\begin{cases} C_L = \dfrac{\tilde{k} - k}{2\tilde{k}} B_L \ , \\ D_L = \dfrac{\tilde{k} + k}{2\tilde{k}} B_L \ . \end{cases} \tag{3.170}$$

Without fixing any further relation among coefficients we already have constructed two linearly independent and orthogonal solution. Indeed

$$\int_{-\infty}^{+\infty} dz \ \chi_{L,k}\chi^*_{R,k'} = 0 \ . \tag{3.171}$$

In details

$$\begin{aligned} \int_{-\infty}^{+\infty} dz \ \chi_{L,k}\chi^*_{R,k'} &= \int_{-\infty}^{0} dz \left(B_L e^{-ikz}\right)\left(A'_R e^{-ik'z} + B'_R e^{+ik'z}\right) \\ &+ \int_{0}^{+\infty} dz \left(C_L e^{i\tilde{k}z} + D_L e^{-i\tilde{k}z}\right)\left(C'_R e^{-i\tilde{k}'z}\right) \\ &= A'_R B_L \int_{-\infty}^{0} dz \ e^{-i(k+k')z} + B'_R B_L \int_{-\infty}^{0} dz \ e^{i(k'-k)z} \\ &+ C'_R C_L \int_{0}^{+\infty} dz \ e^{i(\tilde{k}-\tilde{k}')z} + C'_R D_L \int_{0}^{+\infty} dz \ e^{-i(\tilde{k}'+\tilde{k})z}. \end{aligned}$$

Using the following relations

$$\int_0^{+\infty} dz\ e^{i\alpha z} = \pi\delta(\alpha) + \mathrm{PV}\left(-\frac{1}{i\alpha}\right), \quad \int_{-\infty}^{0} dz\ e^{i\alpha z} = \pi\delta(\alpha) + \mathrm{PV}\left(\frac{1}{i\alpha}\right) \ , \tag{3.172}$$

first we focus on the terms proportional to the deltas

$$\int_{-\infty}^{+\infty} dz\ \chi_{L,k}\chi^*_{R,k'} \supset A'_R B_L \pi\delta(k+k') + B'_R B_L \pi\delta(k-k') \tag{3.173}$$

$$+ C'_R C_L \pi\delta(\tilde{k}-\tilde{k}') + C'_R D_L \pi\delta(\tilde{k}+\tilde{k}') \ . \tag{3.174}$$

Expressing the deltas as function of the energy

$$\delta(k \pm k') = \left|\frac{dk}{dk_0}\right|^{-1} \delta(k_0 \pm k'_0) = \frac{k}{k_0}\delta(k_0 \pm k'_0),$$
$$\delta(\tilde{k} \pm \tilde{k}') = \frac{\tilde{k}}{k_0}\delta(k_0 \pm k'_0) \ ,$$

and enforcing the deltas we get

$$\int_{-\infty}^{+\infty} dz\ \chi_{L,k}\chi^*_{R,k'} \supset \frac{\pi}{k_0}\delta(k_0+k'_0)\left[kA_R B_L + \tilde{k} D_L C_R\right]$$
$$+ \frac{\pi}{k_0}\delta(k_0-k'_0)\left[kB_R B_L + \tilde{k} C_L C_R\right] = 0 \ , \tag{3.175}$$

where the first term is zero since $k_0+k'_0 > 0$, while the second is zero since the combination in the brackets vanishes as soon as we express the conditions in (3.168) and (3.170).
Now focusing on the PVs we get

$$\int_{-\infty}^{+\infty} dz\ \chi_{L,k}\chi^*_{R,k'} \supset A'_R B_L\ \mathrm{PV}\left[-\frac{1}{i(k+k')}\right] + B'_R B_L\ \mathrm{PV}\left[\frac{1}{i(k'-k)}\right]$$
$$+ C'_R C_L\ \mathrm{PV}\left[-\frac{1}{i(\tilde{k}-\tilde{k}')}\right] + C'_R D_L\ \mathrm{PV}\left[\frac{1}{i(\tilde{k}+\tilde{k}')}\right] \ .$$

Now dropping the PVs and using (3.168) and (3.170) we get

$$\ldots = \frac{iB_L C'_R (k-\tilde{k}')(k^2-k'^2-\tilde{k}^2+\tilde{k}'^2)}{(k-k')(k+k')(-\tilde{k}+\tilde{k}')(\tilde{k}+\tilde{k}')} = 0 \ ,$$

that vanishes as soon as we specify that $\tilde{k}^2 = k^2 + m^2 - \tilde{m}^2$.
The remaining two free parameter, C_R and B_L can be fixed with the normalisation conditions.

$$\int_{-\infty}^{+\infty} dz\ \chi_{L,k}\chi^*_{L,k'} = 2\pi\delta(k_0-k'_0) \ , \tag{3.176}$$

$$\int_{-\infty}^{+\infty} dz\ \chi_{R,k}\chi^*_{R,k'} = 2\pi\delta(k_0-k'_0) \ . \tag{3.177}$$

Then, we have

$$(LL) = \int_{-\infty}^{0} dz \left(B_L e^{-ikz}\right)\left(B'_L e^{ik'z}\right) \tag{3.178}$$

$$+ \int_0^{+\infty} dz \left(C_L e^{i\tilde{k}z} + D_L e^{-i\tilde{k}z}\right)\left(C'_L e^{-i\tilde{k}'z} + D'_L e^{i\tilde{k}'z}\right) \ . \tag{3.179}$$

The pieces proportional to the delta functions must give the normalisation condition among the coefficients while all the other pieces must vanish. Indeed, following the same tricks we have used for the orthogonality condition, we get

$$(LL) \supset \frac{\pi}{k_0}\left[kB_L^2+\tilde{k}(C_L^2+D_L^2)\right]\delta(k_0-k_0')+C_LD_L\frac{\pi\tilde{k}}{k_0}\delta(k_0+k_0')\ , \tag{3.180}$$

from which we read

$$kB_L^2+\tilde{k}(C_L^2+D_L^2)=2k_0 \quad \rightarrow \quad B_L=\pm\sqrt{2k_0}\frac{\sqrt{2\tilde{k}}}{k+\tilde{k}}. \tag{3.181}$$

It can be shown that all the other pieces, proportional to the PVs vanish, indeed

$$\begin{aligned}(LL) \supset\ & B_LB_L'\mathrm{PV}\left[\frac{1}{i(k'-k)}\right]+(C_LC_L'-D_LD_L')\mathrm{PV}\left[-\frac{1}{i(\tilde{k}-\tilde{k}')}\right]\\ &+(C_LD_L'-C_L'D_L)\mathrm{PV}\left[-\frac{1}{i(\tilde{k}+\tilde{k}')}\right]\\ &=\frac{-iB_LB_L'(k^2-k'^2-\tilde{k}^2+\tilde{k}'^2)}{(k-k')(\tilde{k}^2-\tilde{k}'^2)}=0\ .\end{aligned} \tag{3.182}$$

For the right-movers we have

$$(RR)=\int_{-\infty}^{0}dz\left(A_Re^{ikz}+B_Re^{-ikz}\right)\left(A_R'e^{-ik'z}+B_R'e^{ik'z}\right) \tag{3.183}$$

$$+\int_0^{\infty}dz\left(C_Re^{i\tilde{k}z}\right)\left(C_R'e^{-i\tilde{k}'z}\right)\ . \tag{3.184}$$

The pieces proportional to the delta functions must give the normalisation condition among the coefficient while all the other pieces must vanish. Indeed,

$$(RR) \supset \frac{\pi}{k_0}\left[k(A_R^2+B_R^2)+\tilde{k}C_R^2\right]\delta(k_0-k_0')+A_RB_R\frac{\pi k}{k_0}\delta(k_0+k_0')\ , \tag{3.185}$$

from which we read

$$k(A_R^2+B_R^2)+\tilde{k}C_R^2=2k_0 \quad \rightarrow \quad C_R=\pm\sqrt{2k_0}\frac{\sqrt{2k}}{k+\tilde{k}}\ . \tag{3.186}$$

It can be shown that all the other pieces, proportional to the PVs vanish, indeed

$$\begin{aligned}(RR) \supset\ & (A_RB_R'-A_R'B_R)\mathrm{PV}\left[\frac{1}{i(k+k')}\right]+(A_RA_R'-B_RB_R')\mathrm{PV}\left[\frac{1}{i(k-k')}\right]\\ &+C_RC_R'\mathrm{PV}\left[-\frac{1}{i(\tilde{k}-\tilde{k}')}\right]\\ &=\frac{iC_RC_R'(k^2-k'^2-\tilde{k}^2+\tilde{k}'^2)}{(k^2-k'^2)(\tilde{k}-\tilde{k}')}=0.\end{aligned} \tag{3.187}$$

In the end, we were able to fix all the coefficients and to construct a basis of eigenmodes suitable for second quantisation of the field ϕ, as in Eq. (3.16). In order to have the solution written as in Eq. (3.6) and (3.7) we need to divide the the eigenmodes by A_R and D_L, respectively, since

$$r_R=\frac{B_R}{A_R}\ ,\quad t_R=\frac{C_R}{A_R}\ ,\quad r_L=\frac{C_L}{D_L}\ ,\quad t_L=\frac{B_L}{D_L}\ . \tag{3.188}$$

3.C Diagonalisation of the Hamiltonian

In this appendix we investigate, for the case of longitudinal vector bosons, why the 'wall polarisation' λ is the most suitable dof for describing the change in dofs across the wall and what we really mean with orthogonality of the eigenmodes.

In unitary gauge, focusing only on the gauge sector, we get

$$\mathcal{L} = -\frac{1}{4}F_{\mu\nu}F^{\mu\nu} + \frac{m^2(z)}{2}A_\mu A^\mu \tag{3.189}$$

$$= \frac{1}{2}\left(\dot{A}^z + \partial_z A^0\right)^2 + \frac{1}{2}m^2(z)\left(A_0^2 - A_z^2\right) \ . \tag{3.190}$$

As is well known, this is a theory with a constraint, imposed by the Lagrange multiplier A^0. We can either work with the vector A_μ and get the Proca equation, or we can eliminate A^0 and get a wave equation with only the dynamical dof A^z. The equation of motion in each case is

$$\partial_\mu F^{\mu\nu} + m^2(z)A^\nu = 0 \ , \tag{3.191}$$

$$\ddot{A}^z - \partial_z\left(\frac{1}{m^2}\partial_z(m^2 A^z)\right) + m^2(z)A^z = 0 \ , \tag{3.192}$$

where we used the constrain $\partial_\mu(m^2 A^\mu) = 0$, which has been useful to rewrite as

$$A^0 = \frac{1}{m^2}\partial_z\left(\frac{m^2 A^z}{-\partial_t}\right) \ , \tag{3.193}$$

thus relating A^0 to A^z. The inverse derivative is to be understood in momentum space.

Solving à la Proca We found solutions to the equations of motion in vector form, which we call right-moving in analogy with the scalar case. These solutions are given by

$$A^\mu_{R,k}(t,z) = e^{-ik^0 t}\chi^\mu_{R,k}(z) \ , \tag{3.194}$$

where

$$\chi^\mu_{R,k}(z) = \begin{cases} \dfrac{1}{m}\begin{pmatrix} k \\ k^0 \end{pmatrix} e^{ikz} + \dfrac{r_k}{m}\begin{pmatrix} -k \\ k^0 \end{pmatrix} e^{-ikz}, & z < 0 \ , \\ \dfrac{1}{\tilde{m}}\begin{pmatrix} \tilde{k} \\ k^0 \end{pmatrix} t_k e^{i\tilde{k}z}, & z > 0 \ . \end{cases} \tag{3.195}$$

Here, $k^0 = \sqrt{k^2 + m^2}$, $k = \sqrt{k_0^2 - \tilde{m}^2}$, and the coefficients r_k and t_k are given by

$$r_k = \frac{\tilde{m}^2 k - m^2 k}{\tilde{m}^2 k + m^2 k}, \quad t_k = \frac{2km\tilde{m}}{\tilde{m}^2 k + m^2 k} \tag{3.196}$$

Similarly, we found the left-moving solutions

$$A^\mu_{L,k}(t,z) = e^{-ik^0 t}\chi^\mu_{L,k}(z) \ , \tag{3.197}$$

where

$$\chi^\mu_{L,k}(z) = \sqrt{\frac{k}{\tilde{k}}}\begin{cases} \dfrac{1}{m}\begin{pmatrix} -k \\ k^0 \end{pmatrix} \frac{\tilde{k}}{k} t_k e^{-ikz}, & z < 0 \ , \\ \dfrac{1}{\tilde{m}}\begin{pmatrix} -\tilde{k} \\ k^0 \end{pmatrix} e^{-i\tilde{k}z} - \dfrac{r_k}{\tilde{m}}\begin{pmatrix} \tilde{k} \\ k^0 \end{pmatrix} e^{i\tilde{k}z}, & z > 0 \ , \end{cases} \tag{3.198}$$

with the same coefficients r_k and t_k as for the right-movers.

However, we encountered a problem: the right-moving and left-moving solutions do not seem to be orthogonal in the naive way as expected, even for different momenta $p \neq q$

$$\int dz\, \chi^{\mu}_{R,p}(z)(\chi_{\mu,L,q}(z))^* \neq 0 \ . \tag{3.199}$$

This non-orthogonality issue needs further investigation.

Solving for A_z Consider solving for A_z from the start, setting $A_z = e^{-ik^0 t}\chi_{R,L,k}$ in (3.192). Upon integrating once and twice respectively, the matching conditions are

$$\partial_z(m^2(z)A_z) = \text{continuous at } z = 0 \ , \tag{3.200}$$
$$m^2(z)A_z = \text{continuous at } z = 0 \ . \tag{3.201}$$

The second condition implies that the first one can be simplified, yielding the matching conditions

$$\partial_z A_z = \text{continuous at } z = 0 \ , \tag{3.202}$$
$$m^2(z)A_z = \text{continuous at } z = 0 \ . \tag{3.203}$$

The right-moving wave modes are thus given by

$$A^z_{R,k} = e^{-ik^0 t}\chi_{R,k}(z) \equiv e^{-ik^0 t}\begin{cases} e^{ikz} + r_k e^{-ikz}, & z < 0 \\ t_k e^{i\tilde{k}z}, & z > 0 \end{cases} \tag{3.204}$$

with k, k^0, r_k, t_k defined above. Similarly, the left-moving wave modes are

$$A^z_{L,k} = e^{-ik^0 t}\chi_{L,k}(z) \equiv e^{-ik^0 t}\begin{cases} \frac{\tilde{k}\tilde{m}^2}{km^2} t_k e^{-ikz}, & z < 0 \\ e^{-i\tilde{k}z} - r_k e^{i\tilde{k}z}, & z > 0 \end{cases} \tag{3.205}$$

These are both exactly what one would expect by taking the $\mu = z$ component of the solutions to Proca's equations and then normalising by a constant.

Is it a general result that scattering states of wave equations with a term linear in derivative are not orthogonal in the naive sense? Instead, it seems that defining a new variable $\lambda = m(z)A^z/(-\partial_t)$ – which kill the linear in derivative term in the eom – its scattering states are naively orthogonal[18].

[18] In wave equations that include terms linear in the derivative, such as the Dirac equation or certain scalar field theories, the orthogonality of scattering states is generally not preserved in the naive sense. Unlike second-order wave equations like the Klein-Gordon equation, which have well-defined inner products ensuring orthogonality, these linear derivative terms introduce complexities that alter the standard inner product structure. Consequently, the naive inner product $\int \psi_1^* \psi_2 \, d^3x$ may not yield zero even for states that should be orthogonal. For example, in the Dirac equation, solutions are normalised using an inner product involving gamma matrices

$$\langle \psi_1 | \psi_2 \rangle = \int \psi_1^\dagger \gamma^0 \psi_2 \, d^3x \ . \tag{3.206}$$

This modified inner product ensures orthogonality but differs from the simple overlap integral used in second-order wave equations. Thus, for wave equations with linear derivative terms, it is essential to properly define an inner product that accurately reflect the orthogonality of the solutions.

But what do we mean by orthogonal? How do we know what the appropriate inner product on the space of solutions should be? The answer can be found by seeing if the modes diagonalise the Hamiltonian and read off from this what is the appropriate inner product. The Hamiltonian in the $1+1$ dimensional case, after some manipulation and eom use, is just

$$H = \int dx \frac{1}{2} \left((F^{0z})^2 + m^2 (A^z)^2 + m^2 (A^0)^2 \right) \ . \tag{3.207}$$

In order to evaluate the Hamiltonian most easily, we will further manipulate by using $F^{0z} = m^2 A^z / (-\partial_t)$ in the first term and using (3.193) in the last term

$$\begin{aligned} H &= \int dx \frac{1}{2} \left(m^4 \left(\frac{A^z}{-\partial_t} \right)^2 + m^2 (A^z)^2 + \frac{1}{m^2} \left(\partial_z \frac{m^2 A^z}{-\partial_t} \right)^2 \right) && (3.208) \\ &= \int dx \frac{1}{2} m^2 \left((A^z)^2 - \left(\frac{\ddot{A}^z}{-\partial_t} \right) \left(\frac{A^z}{-\partial_t} \right) \right) && (3.209) \\ &= \int dx \frac{1}{2} \left(\dot{\lambda}^2 - \ddot{\lambda} \lambda \right) \ . && (3.210) \end{aligned}$$

In going to the second line, we performed integration by parts on the last term and then applied the equation of motion for A^z given in (3.192). Our objective was to reformulate H to eliminate linear ∂_z terms, which are cumbersome to handle due to the difficulty of expressing $\partial_z \chi^z_{R,L,p}$ in terms of $\chi^z_{R,L,p}$, unlike $\partial_t \chi^z_{R,L,p} = -ip^0 \chi^z_{R,L,p}$. In the final line, it is noteworthy to observe how the Hamiltonian is expressed in terms of the λ field.

We can now expand A^z into the right and left movers above

$$A^z = \sum_I \int \frac{dp}{(2\pi)\sqrt{2p^0}} \left(c_{I,p} A^z_{I,p} + c.c. \right) \ , \tag{3.211}$$

where for the moment the Fourier coefficients are just functions of p and not operators. Therefore,

$$\begin{aligned} H = \sum_{I,J} \int \frac{dpdq}{(2\pi)^2 \sqrt{4p^0 q^0}} \int \frac{dz}{2} m^2(z) \Big[& c_{I,p} c_{J,q} \chi^z_{I,p} \chi^z_{J,q} e^{-i(p^0+q^0)t} \left(1 - p^0/q^0 \right) \\ & + c_{I,p} c^*_{J,q} \chi^z_{I,p} \chi^{z*}_{J,q} e^{-i(p^0-q^0)t} \left(1 + p^0/q^0 \right) \\ & + c^*_{I,p} c_{J,q} \chi^{z*}_{I,p} \chi^z_{J,q} e^{i(p^0-q^0)t} \left(1 + p^0/q^0 \right) \\ & + c^*_{I,p} c^*_{J,q} \chi^{z*}_{I,p} \chi^{z*}_{J,q} e^{i(p^0+q^0)t} \left(1 - p^0/q^0 \right) \Big] \ . \end{aligned} \tag{3.212}$$

So we can see that the appropriate inner product necessary so as to diagonalise the Hamiltonian is

$$\int dz \frac{m^2(z)}{p^0 q^0} \chi^z_{I,p} (\chi^{*,z}_{J,q}) = 2\pi \delta_{IJ} \delta(p-q) \ , \tag{3.213}$$

which we have checked that this is indeed satisfied by our modes defined above. Thus the Hamiltonian becomes diagonal

$$H = \sum_I \int \frac{dp}{2\pi} p^0 |c_{I,p}|^2 \ . \tag{3.214}$$

We also add the other 'inner products'

$$\int_{-\infty}^{\infty} dz \frac{m^2(z)}{p^0 q^0}\, \chi^z_{R,p}\, \chi^z_{R,q} = 2\pi\, r_p\, \delta(p-q)\ , \tag{3.215}$$

$$\int_{-\infty}^{\infty} dz \frac{m^2(z)}{p^0 q^0}\, \chi^z_{L,p}\, \chi^z_{L,q} = -2\pi\, r_p\, \delta(p-q)\ , \tag{3.216}$$

$$\int_{-\infty}^{\infty} dz \frac{m^2(z)}{p^0 q^0}\, \chi^z_{R,p}\, \chi^z_{L,q} = 2\pi \sqrt{\frac{\tilde{p}}{p}}\, t_p\, \delta(p-q)\ , \tag{3.217}$$

where r_p and t_p are given by eq. (3.196).

The conclusion is that the mode functions defined here do indeed diagonalize the Hamiltonian, however, it is crucial to select the appropriate inner product. For wave modes of A^z, the appropriate inner product is given in eq. (3.213). When working with A^μ instead, the inner product will take the form

$$\int dz\, \chi^\mu_{R,p} P_{\mu\nu} \chi^{*\nu}_{L,q} = 0\ , \tag{3.218}$$

where $P_{\mu\nu}$ is an appropriate projector. Although finding $P_{\mu\nu}$ should not be particularly difficult, it may turn out to be unnecessary.

3.D Current conservation in the presence of the wall

In the main text, we have discussed the modifications of the Ward identities in the presence of the wall and that in general the conserved current coupled to the total derivative must give zero matrix element,

$$J^\mu \partial_\mu f \quad \Rightarrow \langle final|\, \mathcal{S}_f\, |initial\rangle = 0\ . \tag{3.219}$$

Let us discuss the effects of various choices of the gauge transformation function f. For example let us consider $f = \chi^\tau_{1,2}(z)$, where $\chi^\tau_{1,2}$ are the wave functions for the τ polarisations (see section 3.2.2). Then the matrix element will be equal to

$$\begin{aligned} J^\mu \propto (p+q)^\mu \quad \Rightarrow \quad & \mathcal{M} = \frac{(p+q)_\mu k^\mu}{\Delta p} + r^\tau_k \frac{(p+q)_\mu k^\mu_r}{\Delta p_r} - t^\tau_k \frac{(p+q)_\mu \tilde{k}^\mu}{\Delta \tilde{p}}\ , \\ & k^\mu_r \equiv (k^m, -k^z), \quad \tilde{k}^\mu \equiv (k^m, \tilde{k}^z)\ . \end{aligned} \tag{3.220}$$

We can simplify the amplitude using the following identities:

$$\begin{aligned} (p+q)_\mu k^\mu &= (p+q)_m k^m - (p+q)_z k^z \\ &\overset{k_m=(p-q)_m}{=} (p+q)_m (p-k)^m - (p+q)_z k^z \\ &= p_z^2 + m_\psi^2 - q_z^2 - \tilde{m}_\psi^2 - (p+q)_z k^z \\ &\overset{m_\psi^2=\tilde{m}_\psi^2}{=} (p+q)_z (p-q-k)^z = (p+q)_z \Delta p\ . \end{aligned} \tag{3.221}$$

Performing similar manipulations for all of the terms we get:

$$\mathcal{M} = (p+q)_z (1 + r^\tau_k - t^\tau_k) = 0\ , \tag{3.222}$$

where we used the fact that $1 + r_k^\tau - t_k^\tau = 0$ for τ polarisations, as expected. Similarly we can choose $f = \alpha(z)$, of the λ. Then from the eq. (3.99) we can get

$$\begin{aligned}\alpha|_{z<0} &= \frac{ik^z}{gvE}\left(e^{ik^z z} - r_k^\lambda e^{-ik^z z}\right) \ , \\ \alpha|_{z>0} &= it_k^\lambda \times \frac{\tilde{k}^z}{gE\tilde{v}} e^{i\tilde{k}^z z} \ ,\end{aligned} \tag{3.223}$$

where we have used that $\alpha = \frac{1}{gv^2E}\partial_z(v\lambda) \to \frac{1}{gEv}\partial_z\lambda$ outside of the wall. Using the expression for reflection and transmission coefficients from eq. (3.101)

$$r_k^\lambda = \frac{\tilde{v}^2 k^z - v^2\tilde{k}^z}{\tilde{v}^2 k^z + v^2\tilde{k}^z} \ , \qquad t_k^\lambda = \frac{2k^z v\tilde{v}}{\tilde{v}^2 k^z + v^2\tilde{k}^z} \ , \tag{3.224}$$

we can compute the amplitude for the processes $J^\mu \to \chi_\lambda^\mu$ corresponding to the interaction $J_\mu \chi_\lambda^\mu$. The computation goes as follows

$$\begin{aligned}\mathcal{M} &= \frac{k^z}{gEv}\frac{(p+q)_\mu k^\mu}{\Delta p} - \frac{k^z}{Egv} r_k^\lambda \frac{(p+q)_\mu k_r^\mu}{\Delta p_r} - \frac{\tilde{k}^z}{gE\tilde{v}} t_k^\lambda \frac{(p+q)_\mu \tilde{k}^\mu}{\Delta\tilde{p}} \\ &= \frac{(p+q)_z}{E}\underbrace{\left(\frac{k^z}{gv} - \frac{k^z}{gv}r_k^\lambda - \frac{\tilde{k}^z}{g\tilde{v}}t_k^\lambda\right)}_{=0} = 0 \ ,\end{aligned} \tag{3.225}$$

the last expression in brackets is the matching condition for the λ field (eq. (3.98)) which must be satisfied. Note that terms cancelling each other in the brackets are growing in energy, which makes crucially important the calculation of exact values of reflection and transmission coefficients.

3.E WKB regime in the case of current non-conservation

In the main text we focus only on the transition radiation from the conserved current. How we can perform a similar calculation in the case when the current is not conserved? Let us consider the following example with scalar fields

$$\mathcal{L} = -\frac{1}{4}F_{\mu\nu}F^{\mu\nu} + |D_\mu H|^2 - V(|H|) + |D_\mu\phi|^2 - m_\psi^2|\phi|^2 + \left(\kappa\phi^2 H + h.c.\right) . \tag{3.226}$$

The charges under the gauged $U(1)$ symmetry are as follows: $Q_{U(1)}(H) = 1, Q_{U(1)}(\phi) = -1/2$. In the section 3.2.5, in order to perform the WKB calculation and get rid of interactions that can potentially lead to the divergences we have used the current conservation equations to modify the expression for the matrix elements. In the case of the system in eq. (3.226) the divergence of the current becomes equal to:

$$\partial_\mu J_\phi^\mu = \sqrt{2}v(z)\left(\kappa^*\phi^{*2} - \kappa\phi^2\right) \ , \quad J_\phi^\mu = i(\phi^*\partial^\mu\phi - \phi\partial^\mu\phi^*) \ . \tag{3.227}$$

The interaction between the λ polarisation and J_ϕ^μ and can be written as follows:

$$gQ_\phi J_\phi^\mu A_\mu^{(\lambda)} \to Q_\phi\left[-\sqrt{2}\left(\kappa^*\phi^{*2} - \kappa\phi^2\right)\frac{1}{Ev(z)}\partial_z\left(v(z)\lambda(z)\right) - \frac{g^2 v(z)}{E}\lambda(z)J_z\right] \ . \tag{3.228}$$

We can see that on top of the term λJ_z present in the conserved current case, there is an additional interaction. However, this interaction is not growing with energy, and in the limit $v(z) \to 0$, it is finite (see discussion in the appendix 3.F), thus the calculation of the vector emission becomes straightforward.

3.F Properties of the potential for λ field

In the main text we have shown that λ field satisfies the following equation of motion eq. (3.80)−(3.81)

$$\begin{aligned}\left(-E^2-\partial_z^2+U_\lambda(z)\right)\lambda=0\ ,\\ U_\lambda(z)=g^2v^2(z)+2\left(\frac{\partial_z v}{v}\right)^2-\frac{\partial_z^2 v}{v}\ .\end{aligned}\tag{3.229}$$

Let us investigate the properties of the function U_{λ_z}.

Broken→ Broken In this case

$$v_{z\to\pm\infty}\neq 0\ ,\tag{3.230}$$

and the potential has the limits :

$$U_\lambda(z)|_{z\to\pm\infty}=g^2v^2(z\to\pm\infty)\ ,\tag{3.231}$$

where we have used that $v', v''\to 0$ outside of the wall. Physics wise this result is expected since λ mode must have the mass of the vector gv outside of the wall.

Symmetric→Broken Here we will assume

$$v(z\to-\infty)=0\ ,\quad v(z\to\infty)=\tilde{v}\neq 0\ .\tag{3.232}$$

On the broken side as expected

$$U_\lambda(z\to\infty)=g^2v^2(z\to\infty)=g^2\tilde{v}^2\ ,\tag{3.233}$$

the potential becomes equal to the mass square of the vector boson. To find its limit on the symmetric side we need to look at the equation defining $v(z)$:

$$\partial_z^2 v(z)=V'(v(z))\ ,\tag{3.234}$$

where the prime stands for a derivative with respect to $v(z)$. Integrating this equation we get

$$\frac{1}{2}\left(\partial_z v(z)\right)^2=V(v(z))-C\ ,\tag{3.235}$$

where $C=-(\partial_z v(z_0))^2+V(v(z_0))$ is a 'constant of integration'. We can choose $z_0\to-\infty$, then using $v', v\to 0$ we get $C=V(v(-\infty))=V(0)$, which need not be zero. Now we look at the limits as $z\to-\infty$. At this point, using eqs. (3.234) and (3.235) we can write the various terms of the U_λ function in terms of the potential V and its derivatives V':

$$\begin{aligned}\frac{\partial_z^2 v(z)}{v(z)}=\frac{\partial_z^2 v}{v}=\frac{V'(v)}{v}\xrightarrow{v\to 0}V''(0)\ ,\\ \left(\frac{\partial_z v(z)}{v(z)}\right)^2=\left(\frac{\partial_z v}{v}\right)^2=2\frac{V(v)-V(0)}{v^2}\xrightarrow{v\to 0}V''(0)\ .\end{aligned}\tag{3.236}$$

However, in the limit $z \to -\infty, v \to 0$, we know that the first derivative of the potential V must be equal to zero at this point

$$\left.\frac{\partial V}{\partial v}\right|_{v\to 0} = 0 \ , \tag{3.237}$$

since there is a local minimum at $v = 0$. Thus in the region $v \to 0$ we can write down:

$$\begin{aligned} V(v)|_{v\to 0} &= \frac{V''(0)v^2}{2} + V(0) \Rightarrow \\ \left.\frac{V'(v))}{v}\right|_{v\to 0} &= V''(0) \ , \quad 2\frac{V(v) - V(0)}{v^2} = V''(0) \ . \end{aligned} \tag{3.238}$$

Combining these results we can see that

$$\lim_{z\to-\infty} U_\lambda(z) = V''(0) = m_{h,s}^2 \ , \tag{3.239}$$

where $m_{h,s}$ is the mass of the scalar on the symmetric side. We can see that as was discussed in the section 3.2.2 U_λ has the correct properties for a potential of a d.o.f interpolating between the scalar field and λ polarisation on different sides of the wall.

3.G Evaluation of phase space Integrals

In this appendix, we provide some details regarding the evaluation of the phase space integrals, and how to derive analytical expressions. We will always be interested in the limit of large incoming energy $p^0 \gg$ all masses. The types of integrals we deal with are all of the form

$$I(p^0) = \int_{\text{const}}^{l_1(p^0)} dk \int_{\text{const}'}^{l_2(p^0,k)} dk_\perp^2 \ \text{Int}(p^0, k, k_\perp^2) \ , \tag{3.240}$$

where the dependence on couplings and masses m_i is implicit. When $I(p^0)$ admits an expansion around infinity, this can be obtained in principle straightforwardly as

$$I(p^0) = I(1/x)|_{x\to 0} + \frac{d}{dx} I(1/x)\bigg|_{x\to 0} \frac{1}{p^0} + \ \ldots \tag{3.241}$$

and one can sometimes take this 'exact' approach. However, such an expansion does not always exist [19], or if it does, its coefficients might in practice be difficult to evaluate. Moreover, in the presence of large mass hierarchies, the regime where eq. (3.241) is actually a good approximation can begin at arbitrarily high energies [20]. One can often successfully use a different expansion instead, which we call 'collinear expansion', of $p^0, k^z \gg k_\perp, m_i$ where m_i stands for all masses. Keeping the leading term, reduces integrands to the form

$$\text{Int}(p^0, k, k_\perp^2) = \frac{N(k, k_\perp, m_i)}{\left[(k_{\perp,m}^{IR})^2 + k_\perp^2\right]^2} \qquad \text{for} \quad p^0, k^z \gg k_\perp, m_i, \tag{3.242}$$

[19] For example, in vector emission in symmetry–breaking transitions, for $m = 0$ we find logarithmic growth.

[20] We saw this for example when there are large scale other than p^0 such as $\tilde{m}m_\psi/m$ in plots in the main text figs. 3.0.3, 3.1.2, 3.3.1 and 3.3.2.

where

$$k_\perp^2 \lesssim (k_{\perp,m}^{IR})^2 \equiv \frac{k_z^2 m_\psi^2 - k^z m^2 p_0}{(p_0)^2} + m^2 > 0\,. \tag{3.243}$$

The function N depends on the contribution in question but we wish to highlight the factor in denominator. This form makes most manifest the properties of the phase space structure in particular for τ polarisation (and scalars), most importantly when m (and possibly m_ψ) is very small. For a given k^z, the integrand is peaked for $k_\perp^2 \lesssim (k_{\perp,m}^{IR})^2$. Notice the role of $k_{\perp,m}^{IR}$ - its presence regulates an otherwise logarithmically IR divergent integral. Indeed the momentum transfer diverges in the limit of $m, m_\psi \to 0$. It is easy to prove that $k_{\perp,m}^{IR} < k^z$ for small m, justifying the expansion. When m/m_ψ is very small, clearly there are two relativistic regimes, the first given by

$$p^0 \lesssim k^z m_\psi / m\,, \tag{3.244}$$

where k^z should be taken in the dominant region. Typically $k^z \sim \tilde{m}$ for step function contributions and $\sim L_w^{-1}$ for WKB. Above this scale instead one reaches the true asymptotic behaviour where eq. (3.241) is valid.

3.G.1 Scalars

Scalar R-mover emission (WKB) We begin with the most dominant contribution to scalar emission at the highest of energies $p^0 \to \infty$. The amplitude is the simplest that one can encounter,

$$\mathcal{M}_R^{\text{wkb}} = \left(\frac{y}{i\Delta p} + \frac{\tilde{y}}{-i\Delta\tilde{p}}\right)\,, \tag{3.245}$$

and

$$\langle \Delta p_R^{\text{wkb}} \rangle = \int_{L_w^{-1}}^{k^z_{\max}} dk^z \int_0^{k^2_{\perp,cut}} \frac{dk_\perp^2}{2} \frac{|\mathcal{M}_R^{\text{wkb}}|^2}{(2\pi)^2 8 p^z q^z k_0} \Delta p_R\,. \tag{3.246}$$

For $m \neq 0$, properly evaluating the expansion eq. (3.241) for this case is tricky [21]. However, the collinear expansion eq. (3.242) works extremely well, giving

$$\langle \Delta p_R^{\text{wkb}} \rangle \approx \frac{y^2 \Delta m^4}{32\pi^2} \int_{L_w^{-1}}^{k^z_{\max}} dk^z \int_0^{k^2_{\perp,cut}} dk_\perp^2 \frac{(k^z - p_0)^2/(p_0)^4}{\left[(k_{\perp,m}^{IR})^2 + k_\perp^2\right]^2 \left[(k_{\perp,\tilde{m}}^{IR})^2 + k_\perp^2\right]}\,, \tag{3.247}$$

where $k_\perp^{IR}$ is given by eq. (3.243). We see indeed that for large p^0 the integrand is relatively flat in k^z while $k_\perp$ is strongly IR dominated as anticipated in the preamble above, justifying the expansion. The integrals can now be computed exactly and we obtain eq. (3.50). We can see clearly however that there is also an intermediate regime for small m/m_ψ characterised by a plateau:

$$\langle \Delta p_R^{\text{wkb}} \rangle \approx \begin{cases} \frac{y^2 \tilde{m}^2 L_w}{32\pi^2 m_\psi^2}\,, & L_w^{-1} \ll p^0 \lesssim L_w^{-1} \frac{m_\psi}{m} \\ eq.\ (3.50)\,, & p^0 \gtrsim L_w^{-1} \frac{m_\psi}{m} \end{cases}\,, \tag{3.248}$$

[21] The coefficient of the $1/p^0$ term in eq. (3.241) is the first non-zero contribution as expected from fig. 3.1.2. Out of the three terms to evaluate only one is non-zero in the $x \to 0$ limit. Said limit cannot be taken before the integral is evaluated however and such a task proves unnecessarily difficult.

where we remind ourselves that there is no WKB contribution at all unless we can emit modes greater than the inverse wall length. The value of the plateau is easily obtained by setting $m = 0$ at the start and computing the leading order in eq. (3.241). However, in this regime, we find the step function contributions are more important and we move on there now.

Scalar R and L-mover emission (step wall) The step wall case is an interesting theory exercise in its own right, since everything can be done exactly. For scalars the contributions are

$$\langle \Delta p_R^{\rm step} \rangle = \int_{\Delta m}^{L_w^{-1}} dk^z \int_0^{k^2_{\perp,\rm max}} \frac{dk_\perp^2}{2} \frac{|\mathcal{M}_R^{\rm step}|^2}{(2\pi)^2 8 p^z q^z k_0} \Delta p_R \ . \tag{3.249}$$

$$\langle \Delta p_L^{\rm step} \rangle = \int_{0}^{L_w^{-1}} dk^z \int_0^{k^2_{\perp,\rm max}} \frac{dk_\perp^2}{2} \frac{|\mathcal{M}_L^{\rm step}|^2}{(2\pi)^2 8 p^z q^z k_0} \Delta p_L \ . \tag{3.250}$$

where the matrix elements are given by eqs. (3.28) and (3.29). Evaluating these in the asymptotic limit we obtain

$$\langle \Delta p_L^{\rm step} \rangle \approx \frac{y^2 \tilde{m}}{32\pi^2 m_\psi^2} \begin{cases} 4 \ , & p_0 \lesssim \tilde{m} m_\psi / m \\ \frac{4 m_\psi^2 \Delta m}{3 \tilde{m} m^2 p_0^2} \left[m^2 \left(\ln \frac{m^2}{\tilde{m}^2} - 1 \right) + \tilde{m}^2 \right] \ , & p_0 \gtrsim \tilde{m} m_\psi / m \end{cases} \tag{3.251}$$

$$\langle \Delta p_R^{\rm step} \rangle \approx \frac{y^2 \tilde{m}}{32\pi^2 m_\psi^2} \begin{cases} 1 - \tilde{m} L_w \ , & p_0 \lesssim 4\, \tilde{m} m_\psi / m \\ \frac{m_\psi^2 (L_w^{-1} - \Delta m)}{4 \tilde{m} m^2 p_0^2} \left[\Delta m^2 + 2 m^2 \ln \left(\frac{m}{\tilde{m}} \right) \right] \ , & p_0 \gtrsim L_w^{-1} m_\psi / m \end{cases} \tag{3.252}$$

For the $R-$contribution there is an intermediate regime well approximated by the WKB asymptotic formula in (3.50), as can be seen from fig. 3.1.2 (bottom right panel).

3.G.2 Vectors: τ emission

The three relevant amplitudes are repeated here again

$$\begin{aligned} \mathcal{M}_{\tau,L}^{\rm step} &= -ig \epsilon_{\tau_2}^\mu (p+q)_\mu \left(\frac{1}{\Delta p_r} + \frac{r_{\tau,k}}{\Delta p} + \frac{t_{\tau,k}}{-\Delta \tilde{p}_r} \right) \ , \\ \mathcal{M}_{\tau,R}^{\rm step} &= -ig \sqrt{\frac{k^z}{\tilde{k}^z}} \epsilon_{\tau_2}^\mu (p+q)_\mu \left[\frac{\tilde{k}^z}{k^z} \frac{t_k}{\Delta p} - \frac{1}{\Delta \tilde{p}} + \frac{r_k}{\Delta \tilde{p}_r} \right] \ , \\ \mathcal{M}_{\tau}^{\rm wkb} &= -ig \epsilon_{\tau_2}^\mu (p+q)_\mu \left(\frac{1}{\Delta p_r} + \frac{1}{-\Delta \tilde{p}} \right) \ . \end{aligned} \tag{3.253}$$

For τ polarisation we can treat both types of transitions of interest at the same time by interpreting the $m, \tilde{m}$ correctly.

3.G.3 $m \neq 0$ asymptotic p^0 regime

We present now the dominant contribution $\mathcal{M}_{\tau,L}^{\rm step}$ in detail [22]. The amplitude squared is

$$\left| \mathcal{M}_{\tau,L}^{\rm step} \right|^2 = \frac{16 g^2 k_z^2 k_\perp^2 p_0^2}{(k_z^2 + m^2)(k_z^2 - (p^z - q^z)^2)^2} \begin{cases} \frac{\Delta m^2}{\Delta m^2 - k_z^2 + (p^z - q^z)^2} \ , & k^z < \Delta m \\ \frac{(k^z - \tilde{k}^z)^2}{(\tilde{k}^z + p^z - q^z)^2} \ , & k^z > \Delta m \end{cases} \ , \tag{3.254}$$

[22] Similar asymptotic expressions can be derived for all contributions but we do not believe it useful to fill the chapter with multiple complicated formulae. We deem the total fitted formulae in the main text of more practical use given the overall uncertainties in the physics of FOPTs in the early Universe.

where, as usual, we make a distinction between two branches distinguished by $\tilde{k}$ being imaginary or real. We can explicitly evaluate the leading term in the large p^0 expansion eq. (3.241) for the total momentum exchanged. We report only the first, dominant, branch

$$\langle \Delta p_L^{\tau,\text{step}} \rangle \longrightarrow \frac{g^2 \tilde{m}}{8\pi^2} F_{\tau,L}^{\text{step}}(r \equiv \tilde{m}/m) \ , \qquad k^z < \Delta m \quad \text{branch} \ , \tag{3.255}$$

where the dimensionless function defined is

$$\begin{aligned} F_{\tau,L}^{\text{step}}(r) = \frac{1}{(r^2-1)} \Big\{ & 2\left(\pi(1+r)^2 - (1+r^2)\csc^{-1}[r]\right)\ln[r-\sqrt{r^2-1}] - 2\tan^{-1}[\sqrt{r^2-1}] \\ & - 4(1+r)^2\left(G - \Im \text{Li}_2\left[i(r+\sqrt{r^2-1})\right]\right) - 2(r^2-1)(r-1+\sqrt{r^2-1}) + 2\pi r \cosh^{-1}[r] \\ & - r^2\left(8\sqrt{r^2-1}\coth^{-1}\left[1-\frac{2r}{\sqrt{r^2-1}}\right] + \tan^{-1}[\sqrt{r^2-1}](4\sqrt{r^2-1}+4\log[r]-2)\right)\Big\} \ . \end{aligned}$$

$G \approx 0.916$ is Catalan's constant and $\Im$ stands for imaginary part. We caution the reader that, while the analytical evaluation of integrals is a fun endeavour, we believe that, at least at the present time, the numerical fits presented in the main text are more useful.

3.G.4 The $m \to 0$ regime

The inter-relativistic regime of growth $\propto \log(p_0)$ discussed in the main text when $m/m_\psi \ll 1$ can be found analytically by simply setting $m = 0$, keeping $m_\psi \neq 0$, and using the collinear expansion eq. (3.242) to evaluate the phase space integrals. We obtain

$$\langle \Delta p_L^{\tau,\text{step}} \rangle \simeq \frac{g^2\tilde{m}}{2\pi^2}\left(1 + 2\ln\left(\frac{p_0}{m_\psi}\right)\right), \tag{3.256}$$

$$\begin{aligned} \langle \Delta p_R^{\tau,\text{step}} \rangle \simeq & \frac{g^2\tilde{m}}{1800\pi^2}\left[526 - 900G - 195\pi + 480\ln\left(\frac{\sqrt{2}p_0}{m_\psi}\right)\right] \\ & + \frac{g^2\tilde{m}^2 L_w}{8\pi^2}\left[3 - 2\ln\left(\frac{\tilde{m}L_w p_0}{m_\psi}\right)\right] + \mathcal{O}\left((\tilde{m}L)^2\right), \end{aligned} \tag{3.257}$$

$$\langle \Delta p_R^{\tau,\text{wkb}} \rangle \simeq \frac{g^2\tilde{m}^2 L_w}{8\pi^2}\left[2\ln\left(\frac{\tilde{m}L_w p_0}{m_\psi}\right) - 3\right], \tag{3.258}$$

where $G \approx 0.916$ is Catalan's constant. The total contribution is dominated by L emission and then scales like

$$\langle \Delta p^{\tau,\,\text{tot}} \rangle \simeq \langle \Delta p_L^{\tau,\,\text{step}} \rangle \simeq \frac{g^2\tilde{m}}{2\pi^2}\left(1 + 2\ln\left(\frac{p_0}{m_\psi}\right)\right). \tag{3.259}$$

We remind the reader that these are the results for the single vector emission, to the expression above cannot be trusted for the large values of the log.

3.G.5 Vectors: λ emission

We report again the relevant amplitudes here with general $v \neq 0$:

$$\mathcal{M}_{\lambda,L}^{\text{step}} = -i\frac{g}{E}(p^z+q^z)\left[gv\left(\frac{1}{\Delta p_r} + \frac{r_k^\lambda}{\Delta p}\right) - g\tilde{v}\frac{t_k^\lambda}{\Delta\tilde{p}_r}\right] \ , \tag{3.260}$$

$$\mathcal{M}_{\lambda,R}^{\text{step}} = -i\frac{g}{E}(p^z+q^z)\sqrt{\frac{k^z}{\tilde{k}^z}}\left[gv\frac{\tilde{k}^z}{k^z}\frac{t_k^\lambda}{\Delta p} - g\tilde{v}\left(\frac{1}{\Delta\tilde{p}} - \frac{r_k^\lambda}{\Delta\tilde{p}_r}\right)\right] \ , \tag{3.261}$$

$$\mathcal{M}_{\lambda}^{\text{wkb red.}} = -i\frac{g}{E}(p^z+q^z)\left[\frac{gv}{\Delta p} - \frac{g\tilde{v}}{\Delta\tilde{p}}\right] \ . \tag{3.262}$$

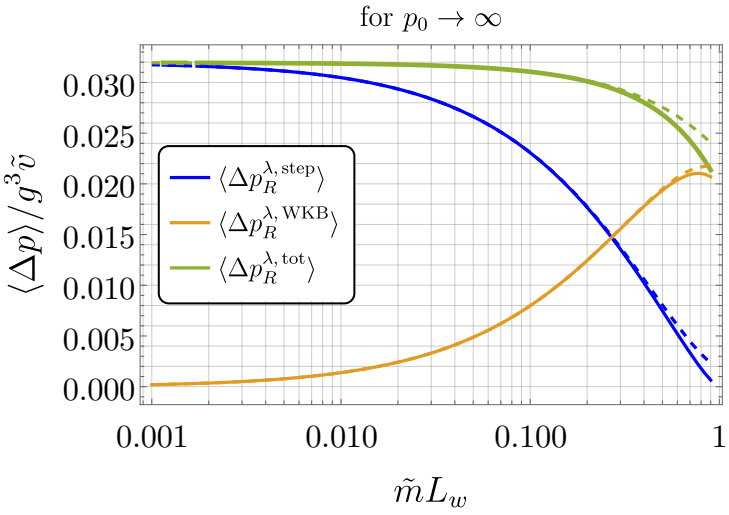

Figure 3.G.1: Analytically derived exact formulae for the exchanged momentum in the asymptotic limit $p^0 \to \infty$ from the emission of λ polarisations. Dashed lines correspond to the small $\tilde{m}L_w$ approximations reported in eq. (3.263). The sum of the two different contributions is roughly constant.

Unlike the case of τ we must consider the two transitions of interest separately.

Symmetric to Broken ($v = 0$): The symmetric side mass of the λ degree of freedom is $m_{h,s}$ – the mass of the Higgs in that phase. We find however that taking $m_{h,s} = 0$ incurs an error which is at most $\sim 10\%$ when $m_{h,s} \sim$ few $\times\, \tilde{m}$. One can rigorously prove that in the limit $p^0 \to \infty$ we have

$$\begin{aligned} \langle \Delta p_R^{\lambda,\mathrm{step}} \rangle \longrightarrow\ & \frac{g^4 \tilde{v}^2}{8\pi^2 \tilde{m}}\, F_{\lambda,R}^{\mathrm{step}}(\tilde{m}L_w) && (3.263) \\ =\ & \frac{g^4 \tilde{v}^2}{8\pi^2 \tilde{m}} \left[2 + 4G - \pi + \tilde{m}L_w \left(2\ln(\tilde{m}L_w) - 2\ln(2) - 1\right)\right] + \mathcal{O}\left((\tilde{m}L_w)^3\right)\ , \\ \langle \Delta p_R^{\lambda,\mathrm{wkb}} \rangle \longrightarrow\ & \frac{g^4 \tilde{v}^2}{8\pi^2 \tilde{m}} \left[\tan^{-1}\left(\frac{\tilde{m}L_w}{\sqrt{1 - \tilde{m}^2 L_w^2}}\right) - \tilde{m}L_w \ln\left(1 - \sqrt{1 - \tilde{m}^2 L_w^2}\right)\right]\ , && (3.264) \end{aligned}$$

where $G \approx 0.916$ is Catalan's constant. $F_{\lambda,R}^{\mathrm{step}}$ has a closed form in terms of (hyperbolic) trig functions and the dilogarithm, but we have deemed it more useful to explicitly report only its small $\tilde{m}L_w$ limit - an excellent approximation, as can be seen in fig. 3.G.1. There we also see that the sum of the two contributions is roughly constant, giving

$$\langle \Delta p^{\lambda,\mathrm{total}} \rangle \approx \langle \Delta p_R^{\lambda,\mathrm{step}} \rangle + \langle \Delta p_R^{\lambda,\mathrm{wkb}} \rangle \simeq \frac{g^4 v^2}{8\pi^2 \tilde{m}} \left[2 + 4G - \pi - \tilde{m}L_w \ln(2)\right]\ , \qquad (3.265)$$

to leading orders in $\tilde{m}L_w$. A more accurate expression when $\tilde{m}L_w \sim 1$ is eq. (3.264).

3.H Pressure in the EW phase transition

In this work, we computed the pressure in the context of an Abelian toy model, where the $U(1)$ gauge boson was emitted by a complex scalar. Emission from fermions will not significantly change our result per degree of freedom. Moreover, the emission can be straightforwardly expanded to the non-Abelian case.

For the SM case, the pressure at $1 \to 2$ level originates from the vertices inducing $\psi \to Z\psi$ (where the first particle in the final state is soft and ψ is some fermion of the SM), $\psi \to W^{\pm}\psi$ for the gauge bosons emitted from fermions $H \to W^{\pm}H$, $H \to ZH$ for the gauge bosons emitted from the Higgs and $A \to WW, W \to WA$, $Z \to WW, W \to WZ, W \to ZW$ for gauge bosons emitting gauge bosons. The careful counting of all the processes involved in the pressure was presented in Appendix C of [1]. This leads to a final pressure of the form

$$\begin{aligned}\mathcal{P}_{\mathrm{SM},1\to2} \approx & 157 \times \alpha_{\mathrm{em}} M_Z \frac{4\gamma_w \zeta(3) T^3}{\pi} \left[0.135 \log\left(\frac{\tilde{v}}{T} + 2.26\right) \right. \\ & \left. - 0.085 - 0.2 \frac{\log\left(\frac{\tilde{v}}{T} + 2.26\right)}{\tilde{v}/T} + \frac{0.19}{\tilde{v}/T} \right], \end{aligned} \tag{3.266}$$

where every contribution is normalised to the fine structure constant α_{em} and the Z boson mass M_Z in the broken phase. We caution the reader that this expression is still an estimate and may incur future revision, for example, from a better understanding of finite temperature corrections - see section 3.3.2.

3.I Sensitivity to wall width

In this work we separated the phase space of particles according to when the step wall and WKB approximations are justified

- $k^z < L_w^{-1}$, Step wall
- $k^z > L_w^{-1}$, WKB

where L_w is the width of the wall. However, this is a somewhat arbitrary quantity, significant up to some order 1 factor. Although we have discussed the sensitivity of our results to L_w in several places, we summarise it in this dedicated appendix.

We study numerically how pressure changes with wall width. For scalars, the dominant contribution comes from the WKB regime and dependence on L_w vanishes, as can be seen in explicitly by the analytical formulae eqs. (3.50) and (3.251). The results for vector emission are highlighted in fig. 3.I.1. The left and right columns show left and right mover emission respectively, while top and lower panels correspond to τ and λ polarisations. The first thing to notice is that $\langle \Delta p_L^{\tau,\,\mathrm{step}} \rangle$, which is the dominant contribution for super-cooled symmetric to broken transitions is largely insensitive to L_w. Secondly, $\langle \Delta p_R^{\lambda,\,\mathrm{step}} \rangle$ and $\langle \Delta p_R^{\lambda,\,\mathrm{wkb}} \rangle$ show almost linear dependence around $L_w \sim$ few $\tilde{m}$ but their *sum* is largely constant. This point was made also in fig. 3.G.1 using analytical asymptotic formulae. Instead, $\langle \Delta p_L^{\lambda,\,\mathrm{step}} \rangle$, which exists only in broken to broken transitions is linearly dependent on the cut-off (see eq. (3.141)).

3.J The suppressed region $\Delta p_z L_w \gg 1$: the Fourier constraint

In section 3.1.6 and afterward, we stated that in WKB approximation the region $\Delta p_z L_w \gg 1$ should have a very suppressed contribution to the pressure. In this appendix, we bring

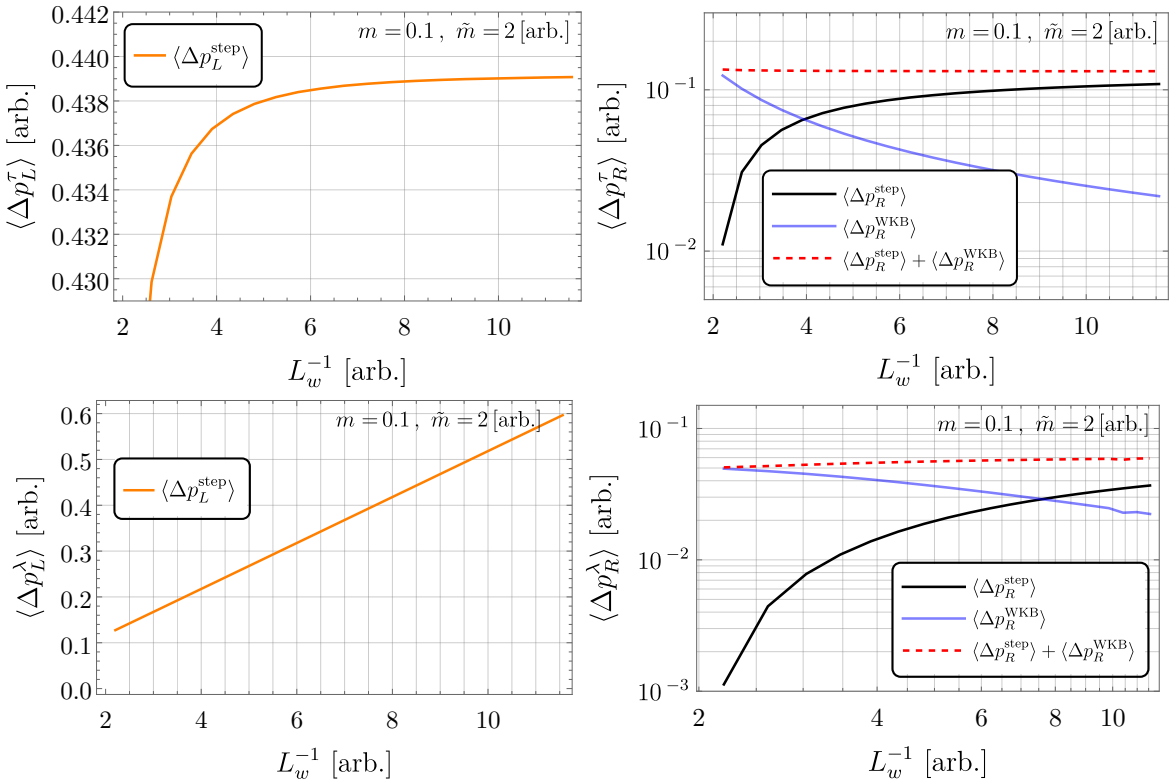

Figure 3.I.1: Dependence of various contributions to average momentum transfer, due to the emission of a vector boson, on the inverse wall width L_w^{-1} in the limit $p_0 \to \infty$. Top (Bottom) panels refer to τ (λ) emission, while left (right) column refers to L (R) emission. In this limit, any dependence on the mass of the emitter (m_ψ) vanishes.

some arguments to this claim (see also Appendix B.1 of [96] and Section V of [95] for previous discussion). The function that we have to study is typically the following integral

$$\mathcal{M} \approx \int_{-\infty}^{\infty} dz V(z) e^{i\int_{-\infty}^{z} \Delta p_z(z')dz'}\,, \tag{3.267}$$

where far from the wall both $\Delta p(z)$ and $V(z)$ are constant. In this case, we can always absorb $V(z) = V_0 \exp[\int_0^z (V'/V)dz]$ inside the exponent (redefining Δp) and thus we can focus only on the integrals where $V(z) = V_0$

$$\mathcal{M} \approx V_0 \int_{-\infty}^{\infty} dz e^{i\int_{0}^{z} \Delta p_z(z')dz'}\,. \tag{3.268}$$

In general, these integrals must be evaluated numerically for various wall shapes. However, for particular choices like

$$\Delta p_z(z) = \Delta p_z + \frac{\epsilon}{2}\tanh z/L_w, \tag{3.269}$$

we can evaluate the integrals analytically. In eq. (3.269), ϵ parameterises the change of the phase across the wall. This leads to

$$\mathcal{M} = V_0 \int_{-\infty}^{\infty} dz \exp\left[i\Delta p_z z + i\epsilon f(z)\right], \tag{3.270}$$

$$f(z) = \frac{L_w}{2}\log\cosh\frac{z}{L_w}\,, \tag{3.271}$$

and give finally

$$|\mathcal{M}|^2 = \frac{\pi\epsilon L_w |V_0|^2}{2\Delta p_z^2 - \epsilon^2/2} \times \frac{\sinh\left(\pi\epsilon L_w/2\right)}{\sinh\left(\pi(\Delta p_z - \epsilon/2)L_w/2\right)\sinh\left(\pi(\Delta p_z + \epsilon/2)L_w/2\right)} \tag{3.272}$$

$$\approx \frac{\pi\epsilon L_w |V_0|^2}{2\Delta p_z^2} \times \frac{\sinh\left(\pi\epsilon L_w/2\right)}{\sinh^2\left(\pi\Delta p_z L_w/2\right)}\,. \tag{3.273}$$

For $\epsilon L_w \lesssim 1, \Delta p_z L_w \gg 1$, we obtain

$$|\mathcal{M}|^2 \approx \frac{\pi\epsilon L_w |V_0|^2}{4\Delta p_z^2} \times \pi\epsilon L_w e^{-\pi\Delta p_z L_w} = \frac{(\pi\epsilon L_w)^2 |V_0|^2}{4\Delta p_z^2} \times e^{-\pi\Delta p_z L_w} \tag{3.274}$$

which shows that $|\mathcal{M}|^2 \propto e^{-\pi\Delta p_z L_w}$ and then decay exponentially with $\Delta p_z L_w \gg 1$. We have also checked numerically the behaviour of the amplitude for other wall shapes, with a similar behaviour (for example Erf function) and always find exponential suppression.

Chapter 4

NLO friction in symmetry–restoring phase transitions

After nucleation, bubbles expand at relativistic speeds if unimpeded, with their velocity determined by the balance between the energy density difference and the out-of-equilibrium pressure from surrounding matter. Bubbles can either reach an equilibrium velocity where energy is efficiently transferred to the medium or continue accelerating in a "runaway" scenario. The space of theories with this feature is a topic of recent and ongoing research, as sketched in fig. 4.0.1.

In this chapter, we take a step forward in charting this space by studying the particular case of phase transitions (PT) where gauge symmetry is restored. This goes in the opposite direction of most literature, which has focused rather on symmetry–breaking, for obvious reasons. In the SM, electroweak and chiral symmetry are spontaneously broken as the universe cools [1]. Nonetheless, it is still possible for the Universe to be stuck in a false vacuum of broken symmetry, as sketched in fig. 4.0.2, and transition to a deeper, symmetric one. We discuss this further and study a simple, concrete two-field model in section 4.D.

We start first by emphasising why the dynamics of such transitions are potentially interesting, or at least deserving of some consideration. We take symmetry–restoring PTs as the prime example of more general transitions where particles lose mass as they cross the bubble wall. This is true by definition for gauge bosons (and typically fermions in the theory as well). If the bubble expands into the broken phase at highly relativistic speeds, we can think of it interacting with individual particles. In the frame of the wall, those particles are highly boosted and by simple kinematics each degree of freedom (d.o.f.) i leads to a negative momentum transfer to the wall

$$\Delta p_i = p_i^z - \tilde{p}_i^z \approx -\frac{m_i^2}{2p_i^z} \,, \tag{4.1}$$

where p^μ, m_i are the incoming particle's 4−momentum and mass in the old (broken) phase, while a tilde will always denote a quantity in the new (symmetric) phase. We have in mind $m_i = gv$ or yv where v is the symmetry–breaking vev on the broken side, g is the gauge coupling and y is a Yukawa coupling. Multiplying by the incoming flux (assuming a thermal population at temperature T) gives the Bödeker-Moore result [94]

[1] To be precise, in the SM both transitions are smooth cross-overs, made first order only by the addition of BSM ingredients.

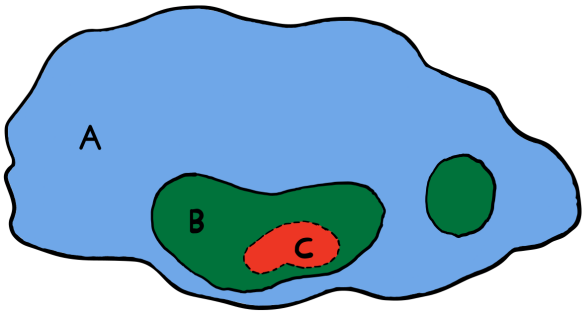

Figure 4.0.1: In the vast landscape of quantum field theories A, a subset B can undergo vacuum decay and first order phase transitions. Within B we can distinguish between phase transitions where nucleated bubbles can in principle accelerate forever, and that subset C where instead an equilibrium velocity always exists because friction from surrounding matter grows indefinitely with γ. The exact boundaries of C within B are a topic of ongoing research. The current work extends C to include gauge symmetry–restoring transitions with charged currents. Clearly, we have not attempted to draw the relative sizes of A, B and C to scale.

for relativistic pressure at leading order [2]

$$\mathcal{P}_{\rm LO} \sim -m_i^2 T^2 \ , \tag{4.2}$$

indicating a preference towards continued accelerated expansion of bubbles. This suggests that the phenomenology of these 'inverse' PTs can be quite different and the strength of signals potentially enhanced. It is thus necessary to examine whether there are other effects, in the relativistic regime, that counter (or reinforce) this dynamic.

In this chapter, we focus on friction pressure coming from the soft vector emission from a charged current, as it passes from a broken to a symmetric phase, as sketched later in fig. 4.0.3. It is 'NLO' in the sense that it is a $1 \to 2$ process involving an interaction vertex (proportional to the gauge coupling g). For the more commonly studied symmetry–breaking PTs, the analogous process (emission from a charged current going from symmetric to broken phase) leads to [2, 95, 96, 115]

$$\mathcal{P}_{NLO} \propto g^3 v \gamma_w T^3 \ . \qquad \text{(symmetric} \to \text{broken)} \tag{4.3}$$

The growth with γ_w means that in those PTs, this contribution eventually dominates over $1 \to 1$ processes in the highly relativistic limit. Clearly, it is, therefore, crucial to understand these effects also in the symmetry–restoring case.

For concreteness, we will be considering an Abelian Higgs model, with a complex scalar H charged under a gauged $U(1)$ that is restored in the true vacuum. The Lagrangian is

$$\mathcal{L} = -\frac{1}{4} F_{\mu\nu} F^{\mu\nu} + |D_\mu H|^2 - V\left(\sqrt{2}|H|\right) + g J^\mu(\psi) A_\mu + \dots \ , \tag{4.4}$$

where $\langle |H| \rangle = 0$ in the true vacuum and $\langle |H| \rangle \neq 0$ in the false vacuum, for some $T_{\rm nuc}$ and where $D_\mu \equiv (\partial_\mu + i g A_\mu)$, A^μ is the gauge field, V is a potential for H, and J^μ is a charged current made of fermionic or (complex) scalar matter ψ, minimally coupled [3].

[2] We are ignoring numerical coefficients in front, made precise by eq. (4.94).

[3] Finally, the dots in eq. (4.4) will be completely irrelevant for us, but are there to allow for possible other d.o.f.s contributing to the realisation of an effective (in general finite-T) potential drawn in fig. 4.0.2.

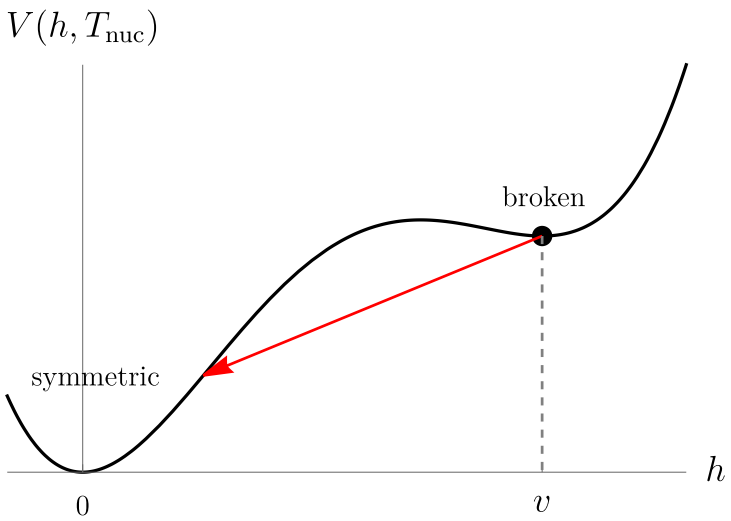

Figure 4.0.2: In this chapter we focus on friction effects on nucleated bubbles of restored gauge symmetry expanding into a surrounding false vacuum of broken symmetry. The effective potential for the order parameter h is thus of the form sketched, for some $T_{\rm nuc}$.

We will study friction effects involving all single quantum emissions resulting from the coupling $\propto J^\mu A_\mu$. In the main text, we will eventually take the mass of this charged d.o.f. to be constant $m_\psi(z) = m_\psi$, ignoring any (Yukawa-like) interaction it might have with the Higgs field, and moreover will set it to zero (a good approximation in the relativistic limit of interest). We comment on the absence of apparent soft divergences for this choice in section 4.A, which is in contrast to the symmetry–breaking case above. In section 4.B we argue that the effects of a spatially dependent $m_\psi(z)$ are subleading.

This chapter is organised as follows. In section 4.1 we present the setup of our calculation and review the canonical quantisation of the vector field in a background of broken translations [2], for a completely general wall profile. In section 4.2 we describe our strategy of using the step wall and WKB approximations in their respective, to some extent complementary, regimes of validity, without committing to a specific theory. The reader who is not interested in the many details of calculation can safely skip ahead to section 4.3, where we present our results, and more importantly to the final discussion in section 4.4. In section 4.C we discuss more generally about the possibility of negative friction.

4.1 Theoretical setup

We imagine that a bubble of true vacuum $\langle|H|\rangle = 0$ is nucleated and expands to a large (compared to its initial) radius. Since we will be interested in the local physics of medium particles interacting with the bubble wall, we will from now on consider the planar limit of a one dimensional domain wall $\langle|H|\rangle = v(z)/\sqrt{2}$ interpolating between the true vacuum at $z \to \infty$ and false vacuum $\langle|H|\rangle = v = \text{const}$ at $z \to -\infty$. Moreover, since we are taking $v(z)$ to be time-independent and using the Minkowski spacetime metric, we are therefore working in an assumed inertial rest frame of the wall. This will be self-consistent when the bubble reaches equilibrium and travels at constant speed [4]. The setup (as well as the

[4] More generally, it will be also if the timescale of the process on the wall we are interested in is short enough that an instantaneous rest frame can be assumed.

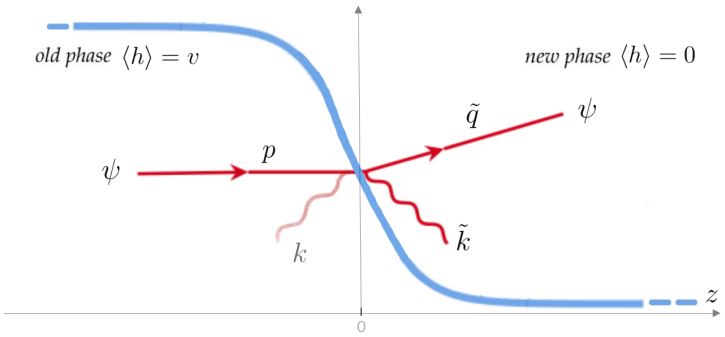

Figure 4.0.3: Our domain wall (in blue) describing the Higgs' vev $\langle h \rangle = v(z)$ is centred at $z = 0$ in its rest frame, interpolating between a false vacuum phase of broken gauge symmetry and a true vacuum phase of restored symmetry. Highly relativistic medium particles hit the wall from the left and can undergo many $z-$momentum violating processes. In this work, we focus on a charged current crossing the wall while emitting a single quantum through the minimal coupling interaction in eq. (4.4). Asymptotically, the emitted particle can be a transverse gauge boson or a Higgs/Goldstone degree of freedom if emitting to the right, or any of the three polarisations of the corresponding massive vector if emitting to the left. Globally, the emitted degrees of freedom are best described by so-called τ and λ polarisations, as presented in section 4.1.1. We use a tilde to denote quantities in the new phase.

process we wish to calculate) is summarised in fig. 4.0.3.

Expanding $H = (v(z) + h + i\,h_2)/\sqrt{2}$ in eq. (4.4) gives us a theory of perturbative quantum fields in the background of the domain wall. To calculate particle processes in this spatially dependent background, we start by properly defining and canonically quantising the free theory. We will now state and explain the key features, while for more details we refer the reader to [2]. The impatient or busy reader may skip directly to section 4.1.3 for a succinct summary.

4.1.1 Unitary gauge and 'wall' polarisations:

In this section, we aim to provide a concise summary of the construction of 'wall' polarisations, which was detailed in the previous chapter, and to introduce the differences with respect to the previous analysis. This summary is intended to remind the reader of the essential components needed for the computations presented in the following sections, but can be skipped by going directly to the end of section 4.1.3.

Despite the fact that the theory approaches the symmetric phase asymptotically on one side, we can make use of unitary gauge [2, 116]. The equations of motion (e.o.m.) of the quadratic action are then

$$\partial^2 h = -V''(v(z))\,h\ , \tag{4.5}$$

$$\partial_\nu F^{\mu\nu} = g^2 v^2(z) A^\mu\ , \quad \Longrightarrow\ \partial_\mu \left(v(z)^2 A^\mu\right) = 0\ . \tag{4.6}$$

The first will describe particle excitations of the Higgs h with mass $m_{h,s} \equiv V''(0)$ and $m_{h,b} \equiv V''(v)$ on the symmetric and broken sides respectively [5]. In this work we will only need to focus on the second - spatially dependent - Proca equation, which implies the

[5] As well as two discrete modes describing fluctuations in position and shape of the wall, see for example [205].

generalised Lorenz condition in eq. (4.6). The excitations of A^μ will describe three massive vector d.o.f.s deep in the broken phase, while only two (transverse) polarisations deep in the symmetric phase, *as well as the second Higgs d.o.f.* h_2. Since time and $\vec{x}_\perp = (x, y)$ translations remain symmetries of the theory, we can seek solutions to the quadratic e.o.m. that are eigenmodes of energy k^0 and transverse (w.r.t. the wall) momentum $\vec{k}_\perp$

$$A^\mu_k = e^{-i(k_0 t - \vec{k}_\perp \vec{x}_\perp)}\, \zeta^\mu_k(z) \ . \tag{4.7}$$

Using rotational symmetry around the $z-$axis we will always focus on

$$\vec{k}_\perp = (k_\perp,\ 0) \ , \quad \text{with } k_\perp > 0 \ , \tag{4.8}$$

unless otherwise stated. The $z-$dependence of the background leads to a non-trivial part of the mode functions $\zeta^\mu(z)$, which are *not* eigenmodes of $z-$momentum. Nonetheless one can choose boundary conditions such that $\zeta^\mu(z)$ describes the mode of choice asymptotically far away from the wall, with the full function everywhere else determined by solving the e.o.m..

A further complication in the presence of a spatially-dependent vector mass is that conventional transverse and longitudinal polarisations are in general not the best d.o.f.s to use. This is because the conventional spin angular momentum is associated with rotations around a particle's direction of propagation, for example, $\vec{k} = (\vec{k}_\perp, k^z)$ for a particle incoming from $z \to -\infty$. The presence of the domain wall background at $z = 0$ means that only rotations around the $z-$axis remain a symmetry, which implies that spin is not conserved unless the particle is exactly incident on the wall $\vec{k}_\perp = 0$. Physically this means, for example, that an incoming particle with conventional transverse polarisation has a finite amplitude to reflect a longitudinally polarised vector [6].

The appropriate, mutually orthogonal d.o.f.s in the presence of a wall were first pointed out in [116]. We call them τ (of which there are two) and λ 'wall' polarisations. The latter are easily obtained by setting $A^z_\tau = 0$, which leads to $\partial_\mu A^\mu_\tau = 0$ and $(\partial^2 + g^2 v(z)^2)\, A^\mu_\tau = 0$, while the former have the orthogonal form $A^\mu_\lambda = (\partial^n \alpha(z), A^z)$, with $n = t, x, y$, where $\alpha(x)$ is fixed in terms of A^z through the generalised Lorenz constraint in eq. (4.6). The $\zeta^\mu_{\ell=\tau_1,\tau_2,\lambda}(z)$ can be constructed from scalar functions $\tau_{i=1,2}(z)$ and $\lambda(z)$ as follows

$$\zeta^\mu_{\tau_i} = \epsilon^\mu_{\tau_i}\, \tau_i(z), \qquad \text{where} \quad \epsilon^\mu_{\tau_1} = (0,0,1,0) \ , \qquad \epsilon^\mu_{\tau_2} = (k_\perp, k_0, 0, 0)/\sqrt{k_0^2 - k_\perp^2} \ , \tag{4.9}$$

$$\zeta^\mu_\lambda = \left(\frac{-ik^n \partial_z(v(z)\lambda)}{gEv^2(z)}, \frac{E}{gv(z)}\lambda\right) \overset{\text{on shell}}{=} \bar{\partial}^\mu \left(\frac{\partial_z(v(z)\lambda)}{Eg\ v^2(z)}\right) + \frac{gv(z)}{E}\lambda\, \delta^\mu_z \ , \tag{4.10}$$

$$\text{with} \quad E^2 \equiv k_0^2 - k_\perp^2 \ , \equiv \quad \bar{\partial}^\mu \equiv (-ik^n, \partial^z) \ ,$$

where the scalars satisfy corresponding Schrodinger-like wave equations that can be derived from eq. (4.6):

$$\left(E^2 + \partial_z^2 - g^2 v^2(z)\right) \tau_{1,2} = 0 \ , \tag{4.11}$$

$$\left(E^2 + \partial_z^2 - U_\lambda(z)\right) \lambda = 0 \ . \tag{4.12}$$

The potential for τ modes is simply a changing vector mass. On the other hand, λ has a non-trivial effective potential

$$U_\lambda(z) = g^2 v^2(z) - v(z)\, \partial_z \left(\frac{\partial_z v(z)}{v^2(z)}\right) \to \begin{cases} g^2 v^2 \ , & \text{as } z \to -\infty \\ m^2_{h,s} \ , & \text{as } z \to +\infty \end{cases} \ , \tag{4.13}$$

[6] Since the full theory eq. (4.4) is invariant under the full Lorentz group, the angular momentum lost is in reality of course absorbed by the wall.

which exhibits the expected asymptotic behaviour describing a propagating vector in the broken phase and a Higgs particle in the symmetric phase. The limits in the last step are true for any interpolating solution $v(z)$ satisfying $\partial_z^2 v(z) = V'(v(z))$ for arbitrary potential with minima at v and 0 [2].

Orthonormal basis: Having identified the appropriate d.o.f.s and reduced the equations of motion to Schrodinger-like form, we must choose a convenient complete basis of solutions to expand in and eventually quantise. In this work, we will only be interested in processes with particles described by A^μ in the final state. We therefore choose boundary conditions corresponding to *outgoing* particles moving towards the right (R) and left (L) respectively

$$\phi^{\text{out}}_{\ell,R,k}(z) \longrightarrow \sqrt{\frac{k^z}{\tilde{k}^z}} \begin{cases} t^\lambda_{R,k} e^{-ik^z z} \ , & \text{as } z \to -\infty \\ e^{-i\tilde{k}^z z} + r^\lambda_{R,k} e^{i\tilde{k}^z z} \ , & \text{as } z \to +\infty \end{cases} \ , \qquad (\tilde{k}^z > 0) \tag{4.14}$$

$$\phi^{\text{out}}_{\ell,L,k}(z) \longrightarrow \begin{cases} e^{ik^z z} + r^\ell_{L,k} e^{-ik^z z} \ , & \text{as } z \to -\infty \\ t^\ell_{L,k}\ e^{i\tilde{k}^z z} \ , & \text{as } z \to +\infty \end{cases} \ , \qquad (k^z > 0) \tag{4.15}$$

$$\text{with} \quad k^0 = \sqrt{k_z^2 + k_\perp^2 + m_\ell^2} = \sqrt{\tilde{k}_z^2 + k_\perp^2 + \tilde{m}_\ell^2} \tag{4.16}$$

where $\phi_\ell \equiv (\tau_1(z), \tau_2(z), \lambda(z))$, the r_k, t_k coefficients are fixed by solving the equations of motion, and the factor in front of eq. (4.14) is for normalisation. The general orthonormality condition is

$$\int_{-\infty}^{\infty} dz\ \phi_{\ell,I,k}\ \phi^*_{\ell,J,q} = 2\pi\delta_{IJ}\delta(k^z - q^z) \ , \qquad I, J \in \{R, L\} \ . \tag{4.17}$$

While the solutions eqs. (4.14) and (4.15) are not eigenstates of $z-$momentum, wavepackets formed by the superposition of purely R or L movers do describe localised single wavemodes *at late time* with definite positive or negative central $z-$momentum respectively [7]. At finite z the behaviour of the solutions will of course depend on the details of the shape of $v(z)$. Before moving on we will consider the simple, exactly solvable case of a step function.

4.1.2 Step function

In this approximation we consider

$$v(z) = v\left[1 - \Theta(z)\right] \ , \tag{4.18}$$

where $\Theta(z)$ is the Heaviside theta function. The wavemodes are exactly solvable and determined by the appropriate matching conditions at $z = 0$. For the two τ polarisations, these are simply the continuity of the function and its first derivative, leading to

$$\left(\tau^{out}_{i,R,k}\right)^* = \sqrt{\frac{k^z}{\tilde{k}^z}} \begin{cases} \frac{\tilde{k}^z}{k^z} t^\tau_k\ e^{ik^z z} \ , & z < 0 \\ e^{i\tilde{k}^z z} - r^\tau_k e^{-i\tilde{k}^z z} \ , & z > 0 \end{cases} \ , \qquad (\tilde{k}^z > 0) \tag{4.19}$$

$$\left(\tau^{out}_{i,L,k}\right)^* = \begin{cases} e^{-ik^z z} + r^\tau_k e^{ik^z z} \ , & z < 0 \\ t^\tau_k\ e^{-i\tilde{k}^z z} \ , & z > 0 \end{cases} \ , \qquad (k^z > 0) \tag{4.20}$$

[7] At early times instead they describe *two* separate wavemodes incoming towards the wall which interfere in just the right way to describe a well–defined particle at late time.

where

$$r_k^\tau = \frac{k^z - \tilde{k}^z}{k^z + \tilde{k}^z} \ , \quad t_k^\tau = \frac{2k^z}{k^z + \tilde{k}^z} \ , \quad k_0 = \sqrt{k_z^2 + g^2 v^2 + k_\perp^2} = \sqrt{\tilde{k}_z^2 + k_\perp^2} \ .$$

The orthonormality condition eq. (4.17) can be checked exactly.

For λ, the step function limit is more tricky since on one side $\tilde{v} = v(z > 0) = 0$. However, we can obtain the right answer by starting from a broken to broken transition $\tilde{v} \neq 0$, as first studied in [79], and then sending $\tilde{v} \to 0$ subsequently. The matching conditions are continuity of $v(z)\lambda(z)$ and $\lambda'(z)/v(z)$ at $z = 0$, leading to

$$\left(\lambda^{\rm out}_{R,k}\right)^* = \sqrt{\frac{k^z}{\tilde{k}^z}} \begin{cases} \frac{\tilde{k}^z}{k^z} t_k^\lambda e^{-ik^z z} \ , & z < 0 \\ e^{-i\tilde{k}^z z} - r_k^\lambda e^{i\tilde{k}^z z} \ , & z > 0 \end{cases} \ , \qquad (\tilde{k}^z > 0) \tag{4.21}$$

$$\left(\lambda^{\rm out}_{L,k}\right)^* = \begin{cases} e^{ik^z z} + r_k^\lambda e^{-ik^z z} \ , & z < 0 \\ t_k^\lambda \ e^{i\tilde{k}^z z} \ , & z > 0 \end{cases} \ , \qquad (k^z > 0) \tag{4.22}$$

and

$$r_k^\lambda = \frac{\tilde{v}^2 k^z - v^2 \tilde{k}^z}{\tilde{v}^2 k^z + v^2 \tilde{k}^z} \ , \quad t_k^\lambda = \frac{2k^z v\tilde{v}}{\tilde{v}^2 k^z + v^2 \tilde{k}^z} \ , \quad k_0 = \sqrt{k_z^2 + m_\lambda^2 + k_\perp^2} = \sqrt{\tilde{k}_z^2 + \tilde{m}_\lambda^2 + k_\perp^2} \ ,$$

where $m_\lambda = gv$, and $\tilde{m}_\lambda = g\tilde{v}$ for $\tilde{v} \neq 0$ must be discontinuously changed to $\tilde{m}_\lambda = m_{h,s}$ in the case $\tilde{v} = 0$. Note

$$r_k^\lambda \to -1 \ , \qquad \text{for} \quad \tilde{v} \to 0 \ . \tag{4.23}$$

Thus, as long as the step wall is a good approximation, λ modes are totally reflected: R and L movers live completely on opposite sides of the symmetry–breaking wall. If we regularised eq. (4.18) with something like $v(z) = v\left(1 - \tanh(m_h z/2)\right)/2$, which comes from the standard double-well quartic potential $V(h) = \lambda_h h^2 (h - v)^2/4$ studied in [116], then the total reflection is trivial. The width of the wall is controlled by the mass of the Higgs $L_w \approx m_h^{-1}$ and particles with $k^z \lesssim L_w^{-1}$, for which the step function is a good approximation, do not have enough energy to make it to the other side. However, we stress that even for wall profiles with $m_h \to 0$ the reflective behaviour remains. A better interpretation of eq. (4.23) is that λ describes the would-be Nambu-Goldstone boson, that interacts derivatively with the background wall, as seen for example by the derivative terms in the potential $U_\lambda(z)$ in eq. (4.13).

4.1.3 Amplitudes and exchanged momentum

We choose to expand the field A^μ into a complete orthonormal basis of solutions to the quadratic equations of motion that are eigenmodes of energy k^0, transverse momentum $\vec{k}_\perp$ and describe outgoing particles of definite $z-$momentum,

$$\begin{aligned} A^\mu &= \sum_{I,\ell} \int \frac{d^3k}{(2\pi)^3 \sqrt{2k_0}} \left(a^{\rm out}_{\ell,I,k} \ A^\mu_{\ell,I,k} + h.c. \right) \ , \\ \text{with} \quad A^\mu_{\ell,I,k} &= e^{-i(k_0 t - \vec{k}_\perp \vec{x})} \ \zeta^\mu_{\ell,I,k}(z) \ , \end{aligned} \tag{4.24}$$

where $\ell = \tau_1, \tau_2, \lambda$ sums over the three different orthogonal 'wall' polarisations, and $I = R, L$ stand for right ($z \to +\infty$) and left ($z \to -\infty$) moving particles. In practice the $\zeta_{\ell,I,k}$ are constructed by solving the Shrödinger equations eqs. (4.11) and (4.12) with

boundary conditions of eqs. (4.14) and (4.15) (the latter defining the 'out' choice) and finally plugging the solutions into eqs. (4.9) and (4.10). Upon quantisation, the associated Fourier operators create out states

$$\left|k^{\rm out}_{\ell,I}\right\rangle \equiv \sqrt{2k_0}\,(a^{\rm out}_{\ell,I,k})^\dagger\,|0\rangle\ , \qquad I\in R,L \quad \& \quad \ell\in\tau_1,\tau_2,\lambda\ . \tag{4.25}$$

and satisfy the usual creation/annihilation operator algebra. Wick's theorem follows from this as usual and one may go ahead and compute amplitudes for arbitrary particle processes of interest in the background of the wall.

We will be focusing on the relatively simple single emission from the minimally coupled charged current J^μ in eq. (4.4). The tree level amplitude for this process is given by the following expression

$$\begin{aligned}
&\langle k^{\rm out}_{\ell,I}\ q|\ \mathcal{S}\ |p\rangle = (2\pi)^3\delta^{(3)}(p^n-k^n-q^n)i\mathcal{M}_{\ell,I}\ ,\\
&i\mathcal{M}_{\ell,I}\equiv\int dz\left(\zeta^\mu_{\ell,I,k}(z)\right)^*(p+q)_\mu e^{i(p^z-q^z)z}\ ,
\end{aligned} \tag{4.26}$$

where $S=\exp\left(i\int d^4x\ gA_\mu J^\mu\right)$ is the $S-$matrix and Right and Left mover emission are to be treated as separate processes. We emphasise that for a conserved current J^μ, which is the case we will focus on in this work, we can ignore the first term in eq. (4.10) since it is a total derivative. The total average momentum transfer is then given by summing over polarisations, as well as right and left contributions,

$$\langle\Delta p\rangle=\sum_{\ell,I}\langle\Delta p^\ell_I\rangle=\sum_\ell\ \langle\Delta p^\ell_R\rangle+\langle\Delta p^\ell_L\rangle\ , \tag{4.27}$$

and integrating appropriately over all final state phase space, giving the following master equations:

$$\langle\Delta p^\ell_L\rangle=\frac{1}{64\pi^2}\int_0^{k^z_{\rm max}}dk^z\int_0^{k^2_{\perp,\rm max}}\ dk^2_\perp\cdot\frac{|\mathcal{M}_{\ell,L}|^2}{k^0p^zq^z}\Delta p_L\ , \tag{4.28}$$

$$\langle\Delta p^\ell_R\rangle=\frac{1}{64\pi^2}\int_0^{\tilde{k}^z_{\rm max}}d\tilde{k}^z\int_0^{k^2_{\perp,\rm max}}\ dk^2_\perp\cdot\frac{|\tilde{\mathcal{M}}_{\ell,R}|^2}{k^0p^zq^z}\Delta p_R\ , \tag{4.29}$$

$$\text{and}\quad \Delta p_L=p^z-q^z+k^z\ ,\quad \Delta p_R=p^z-q^z-\tilde{k}^z\ ,$$

where $\tilde{k}^z_{\rm max}\,,k^2_{\perp,\rm max}$ are defined below, and we naturally choose to integrate in k^z for left emission and $\tilde{k}^z$ for right emission, since the lower kinematic limit is zero no matter the hierarchy between m_ℓ and $\tilde{m}_\ell$. The form of eq. (4.28) follows straightforwardly from our choice to second quantise and normalise modes of A^μ in the k^z variable (see eq. (4.17)). The reader can find an explicit derivation in terms of wave-packets in [2]. There, for the case of symmetry–breaking, all particles were gaining mass in the new phase and we also integrated eq. (4.29) in k^z, with a lower limit. On the other hand, for a symmetry–restoring transition, k^z takes on imaginary values for very soft τ emission to the right [8], so that $\tilde{k}^z$ is necessarily the better variable. Changing quantisation variable will only change the normalisation of the wavemodes, which translates into

$$\mathcal{M}\ \rightarrow\ \tilde{\mathcal{M}}\equiv\sqrt{\frac{\tilde{k}^z}{k^z}}\mathcal{M}\ , \tag{4.30}$$

[8] For λ emission, which of $k^z\ ,\tilde{k}^z$ have an imaginary branch depends on the relative sizes of $m_\lambda=gv$ and $\tilde{m}_\lambda=m_{h,s}$.

and thus in the final state phase space integration

$$dk^z|\mathcal{M}^2| \;\to\; d\tilde{k}^z|\tilde{\mathcal{M}}^2| \equiv d\tilde{k}^z \left|\frac{\tilde{k}_z}{k_z}\right| |\mathcal{M}^2| \;. \tag{4.31}$$

The upper limits of integration are in general given by

$$\begin{aligned} k^z_{\rm max} &= \sqrt{(p_0-\tilde{m}_\psi)^2 - m_\ell^2}\;, \quad \tilde{k}^z_{\rm max} = \sqrt{(k^z_{\rm max})^2 + m_\ell^2 - \tilde{m}_\ell^2}\;, \\ k^2_{\perp,{\rm max}} &= \frac{(p_0^2+E^2-\tilde{m}_\psi^2)^2}{4p_0^2} - E^2\;, \end{aligned} \tag{4.32}$$

where one chooses to write $E^2 \equiv k_0^2 - k_\perp^2$ in terms of $k_z^2 + m_\ell^2$ or $\tilde{k}_z^2 + \tilde{m}_\ell^2$ for left and right emission respectively. For gauge symmetry–restoration we have of course $\tilde{m}_\tau = 0$. In the main text we will also take the charged current to be massless $m_\psi = \tilde{m}_\psi = 0$ and comment on the insensitivity of our results thereon.

If one is powerful enough to compute the exact wavemodes for a given wall profile, the exact amplitude and average momentum transfer for transition radiation can be calculated using the expressions provided here. However, we will now explain our strategy to obtain approximate expressions, ignoring details of the wall shape.

4.2 Approximations in phase space

The main difficulty in calculating amplitudes and then ultimately $\langle\Delta p\rangle$ in the previous section is the computation of the $\zeta^\mu(z)$ wavemodes for a given wall profile $v(z)$. We could in principle simply try to use a step function. Not only is this a good theoretical exercise, but it is also a legitimate approximation for soft vectors. However, one should not overrely on it. Properties of the λ field, in particular, can be qualitatively quite different in the exact step function limit, such as the enhanced reflection, as studied already in [79] and then [2]. In practice we will then follow the procedure described in [2], where phase space was split into two regions: IR, where the step wall approximation is legitimately valid and UV, where instead the wave function of the vector bosons can be treated in a WKB approximation. Here, relative to the previous chapter, because of the symmetry–restoring pattern, we identify a more coherent approach to partitioning the phase space into its IR and ultraviolet UV components in order to capture the physics in both limits of thin and thick walls. Instead of using the cutoff $k^z \gtrless L_w^{-1}$, we will present this alternative method in the remainder of this section. We also verified that this more careful prescription does not change the result in the previous chapter.

4.2.1 Wavemodes

We now examine exactly when the step wall and WKB approximations are legitimate. The conditions will end up being slightly more refined than the simple cut used in [2]. We recall one more time the asymptotic masses for both τ, λ polarisations, defining $m \equiv gv$:

$$(\tau): \begin{cases} m_\tau(z=+\infty) = 0 \\ m_\tau(z=-\infty) = m \end{cases}, \qquad (\lambda): \begin{cases} m_\lambda(z=+\infty) = m_{h,s} \\ m_\lambda(z=-\infty) = m \end{cases}. \tag{4.33}$$

Step function limit (IR): The background wall can be well approximated by a step function for wavemodes which change on scales longer than those of the background. This should be expected for particles with momenta much less than the inverse width of the wall

$$\text{step}: \ \text{Max}\left[|k^z|\,, |\tilde{k}^z|\right] \ll L_w^{-1} \ . \tag{4.34}$$

The absolute value is necessary, since for example for τ polarisation there is a phase space region where

$$k_z^2 = E^2 - m^2 < 0 \ , \quad E^2 \equiv k_0^2 - k_\perp^2 = \tilde{k}_z^2 > 0 \ . \tag{4.35}$$

In other words, even if the mode is decaying for $z < 0$ as an $\exp(-|k_z z|)$, step wall approximation is valid only if $L_w^{-1} \ll |k_z|$. This constraint, when implemented in the integration limits, will in general cut both the extrema of integration.

WKB limit (UV): We now analyse the range of validity of the WKB approximation. In general, we are looking at the solutions of the Shrödinger-like equation:

$$\left(\partial_z^2 - V(z)\right)\psi = -E^2\psi, \quad \begin{cases} V(z) = g^2 v^2(z) & \text{for } \tau \text{ polarisations (see eq. (4.11))} \\ V(z) = U_\lambda(z) & \text{for } \lambda \text{ polarisations (see eq. (4.12))} \end{cases} . \tag{4.36}$$

We look for a solution of the form $\psi = e^{i\varphi(z)}$, which leads to

$$\left(i\varphi''(z) - \varphi'(z)^2 - V(z)\right) = -E^2 \ . \tag{4.37}$$

Then assuming $|\varphi''| \ll |\varphi'^2|, \ |E^2 - V(z)|$, we arrive at:

$$\varphi'^2 = E^2 - m^2(z) \equiv k_z^2(s) \implies \varphi(z) - \varphi(z_0) = \int_{z_0}^{z} ds \ k^z(s) \ . \tag{4.38}$$

The wave function solution becomes:

$$\psi = A \ e^{i\int_{z_0}^{z} ds \ k(s)} + \mathcal{O}\left(\frac{|\varphi''|}{|\varphi'^2|}\right) . \tag{4.39}$$

This approximation is valid if

$$|\varphi''| \ll |\varphi'^2| \implies |k_z'(z)| \ll |k_z^2(z)| \implies \frac{|\partial_z V(z)|}{2|k_z(z)|} \ll |k_z^2(z)| \ . \tag{4.40}$$

We approximate the derivative of the potential as $\partial_z V(z) \sim \Delta m^2 / L_w$, then we arrive at the following constraint:

$$\text{Min}\left[|k^z|\,, |\tilde{k}^z|\right] \gg \left(\frac{|\Delta m^2|}{2L_w}\right)^{1/3} . \tag{4.41}$$

4.2.2 Amplitudes

Having defined the two complementary approximations for the wavemodes $\zeta^\mu(z)$, one can attempt to evaluate the amplitudes eq. (4.26), which will then be valid in the corresponding regimes. This is completely straightforward for the case of the step function and exact expressions are presented below in eq. (4.44). For WKB, the matrix element for R emission is

$$\begin{aligned} &i\mathcal{M}_\ell^{\text{wkb}} = \int dz\, \mathcal{V}(z) e^{i\int_0^z ds\, \Delta p^z(s)} \ , \\ &\text{with} \quad \mathcal{V}(z) \equiv \epsilon^\mu_{\ell,k}(z)\, (p+q)_\mu \ , \quad \Delta p^z(s) \equiv (p^z - q^z - k^z(s)) \ , \end{aligned} \tag{4.42}$$

where the constant $\epsilon^\mu_{\tau_{1,2},k}$ were given in eq. (4.9), and we just take $\epsilon^\mu_{\lambda,k}(z) = \delta^\mu_z g v(z)/E$ using current conservation to ignore the total derivative in eq. (4.10). We can then reduce $\mathcal{M}_\ell^{\text{wkb}}$ to the form first explored by [95]

$$i\mathcal{M}_\ell^{\text{wkb red.}} \equiv \int_{-\infty}^0 dz\, \mathcal{V}(-\infty)\, e^{i(p^z - q^z - k^z)z} + \int_0^\infty dz\, \mathcal{V}(\infty)\, e^{i(p^z - q^z - \tilde{k}^z)z} \ , \tag{4.43}$$

plus contributions which are dependent on the specific shape of the wall. These additional contributions were shown to be important only if $\text{Min}_s\left[\Delta p^z(s)\right] L_w \gg 1$, as long as for λ emission we subtract the total derivative term in eq. (4.10) [9]. However, in this regime the full matrix element should vanish since we recover translation symmetry and the emission process is forbidden (see [2] for details). Ignoring the contribution inside the wall, it is not always guaranteed that this suppression is properly captured. Thus, in practice, we always complement eq. (4.43) by explicitly cutting out the region $\Delta p^z L_w \gg 1$ in the phase space integration. Finally, we do not consider left emission in the WKB approximation because there is no allowed phase space simultaneously satisfying all appropriate cuts.

For consistency of notations with [2] we report all amplitudes for the vector field quantised in terms of the k^z variable:

$$\begin{aligned} \mathcal{M}_{\tau,L}^{\text{step}} &= -ig\epsilon^\mu_{\tau_2}(p+q)_\mu \left(\frac{1}{\Delta p_r} + \frac{r_k^\tau}{\Delta p} - \frac{t_k^\tau}{\Delta \tilde{p}_r}\right) \ , \\ \mathcal{M}_{\tau,R}^{\text{step}} &= -ig\epsilon^\mu_{\tau_2}(p+q)_\mu \sqrt{\frac{k^z}{\tilde{k}^z}} \left[\frac{\tilde{k}^z}{k^z}\frac{t_k^\tau}{\Delta p} - \frac{1}{\Delta \tilde{p}} + \frac{r_k^\tau}{\Delta \tilde{p}_r}\right] \ , \\ \mathcal{M}_\tau^{\text{wkb red.}} &= -ig\epsilon^\mu_{\tau_2}(p+q)_\mu \left(\frac{1}{\Delta p} - \frac{1}{\Delta \tilde{p}}\right) \ , \\ \mathcal{M}_{\lambda,L}^{\text{step}} &= -i\frac{g^2 v}{E}(p^z + q^z)\left[\frac{1}{\Delta p_r} - \frac{1}{\Delta p}\right], \\ \mathcal{M}_{\lambda,R}^{\text{step}} &= 0 \ , \\ \mathcal{M}_\lambda^{\text{wkb red.}} &= -i\frac{g^2 v}{E}(p^z + q^z)\frac{1}{\Delta p} \ , \end{aligned} \tag{4.44}$$

where we have ignored terms proportional to delta functions since they ultimately don't contribute, and

$$\begin{aligned} &\Delta p \equiv p^z - q^z - k^z \ , && \Delta p_r \equiv \Delta p_L \equiv p^z - q^z + k^z \ , \\ &\Delta \tilde{p} \equiv \Delta p_R \equiv p^z - q^z - \tilde{k}^z \ , && \Delta \tilde{p}_r \equiv p^z - q^z + \tilde{k}^z \ . \end{aligned} \tag{4.45}$$

[9] If not, this piece will grow with energy and, ignoring the contribution inside the wall, one fails to see the cancellation that must necessarily occur. For more general processes, one should check case by case.

By τ here we mean τ_2. Amplitudes for the emission of τ_1 are zero. Because of rotational symmetry around the $z-$axis we can focus on the choice eq. (4.8), which manifestly leads to $\epsilon^{\mu}_{\tau_1}(p+q)_\mu = 0$.

4.2.3 Numerical procedure

Strictly speaking, the conditions eqs. (4.34) and (4.41) tell us that the respective approximations are valid only when the values of momenta are much less/greater than the corresponding thresholds. In practice in our calculation, we make the following approximation:

$$\text{step}: \ \text{Max}\left[|k^z|\,,|\tilde{k}^z|\right] < L_w^{-1}. \tag{4.46}$$

$$\text{WKB}: \left(\text{Min}\left[k^z,\tilde{k}^z\right] > \left(\frac{|\Delta m_\ell^2|}{2L_w}\right)^{1/3}\right) \cap \left(\text{Max}\left[|k^z|\,,|\tilde{k}^z|\right] > L_w^{-1}\right). \tag{4.47}$$

For the WKB approximation, we have added the second condition in order to avoid double counting, since for thin walls (e.g. $mL \ll 1$ for τ) there can be an overlap between the phase space regions defined by eqs. (4.34) and (4.41). Instead, for thick walls we comment that there can be a part of phase space not covered by our prescription, when

$$\left(\text{Min}\left[k^z,\tilde{k}^z\right] < \left(\frac{|\Delta m^2|}{2L_w}\right)^{1/3}\right) \cap \left(\text{Max}\left[k^z,\tilde{k}^z\right] > L_w^{-1}\ \right)\ . \tag{4.48}$$

However, this extra contribution will never significantly change our results.

We gather now for convenience all of the separate contributions to the momentum transfer in our calculation scheme:

$$\begin{aligned}
\langle\Delta p_L^{\text{step}}\rangle =& \frac{1}{64\pi^2}\int dk^z dk_\perp^2 \cdot \frac{|\mathcal{M}_L|^2}{p^z q^z k_0}\ (p^z - q^z + k^z)\ \Theta(\text{step})\ ,\\
\langle\Delta p_R^{\text{step}}\rangle =& \frac{1}{64\pi^2}\int d\tilde{k}^z dk_\perp^2 \cdot \left|\frac{\tilde{k}_z}{k_z}\right| \frac{|\mathcal{M}_R|^2}{p^z q^z k_0}\ (p^z - q^z - \tilde{k}^z)\ \Theta(\text{step})\ ,\\
\langle\Delta p^{\text{wkb}}\rangle =& \frac{1}{64\pi^2}\int d\tilde{k}^z dk_\perp^2 \cdot \left|\frac{\tilde{k}_z}{k_z}\right| \frac{|\mathcal{M}^{\text{wkb red.}}|^2}{p^z q^z k_0}\ (p^z - q^z - \tilde{k}^z)\\
&\times \Theta\left(\text{WKB}\right)\Theta\left(L_w^{-1} - (p^z - q^z - \tilde{k}^z)\right)\ ,
\end{aligned} \tag{4.49}$$

where the $\Theta(\text{WKB})$ and $\Theta(\text{step})$ are imposing the conditions in eqs. (4.46) and (4.47). In the WKB contribution an additional $\Theta\left(L_w^{-1} - (p^z - q^z - \tilde{k}^z)\right)$ is imposed to enforce that the momentum loss is always less than L_w^{-1}, as expected from Fourier transformation properties (see discussion below eq. (4.43), and [2] for more details). The integration ranges are given by

$$\begin{aligned}
&\tilde{k}^z \in [0\ , p_0 - m_\psi] \quad \& \quad k_\perp^2 \in \left[0\ , \frac{(p_0^2 + \tilde{k}_z^2 - m_\psi^2)^2}{4p_0^2} - \tilde{k}_z^2\right]\ ,\\
&k^z \in \left[0\ , \sqrt{(p_0 - m_\psi)^2 - m^2}\right] \quad \& \quad k_\perp^2 \in \left[0\ , \frac{(p_0^2 + k_z^2 + m^2 - m_\psi^2)^2}{4p_0^2} - k_z^2 - m^2\right]\ .
\end{aligned} \tag{4.50}$$

where, as mentioned before, we have taken $m_\psi = \tilde{m}_\psi$ to be constant, and moreover will set it to zero since it does not affect our results in the relativistic regime.

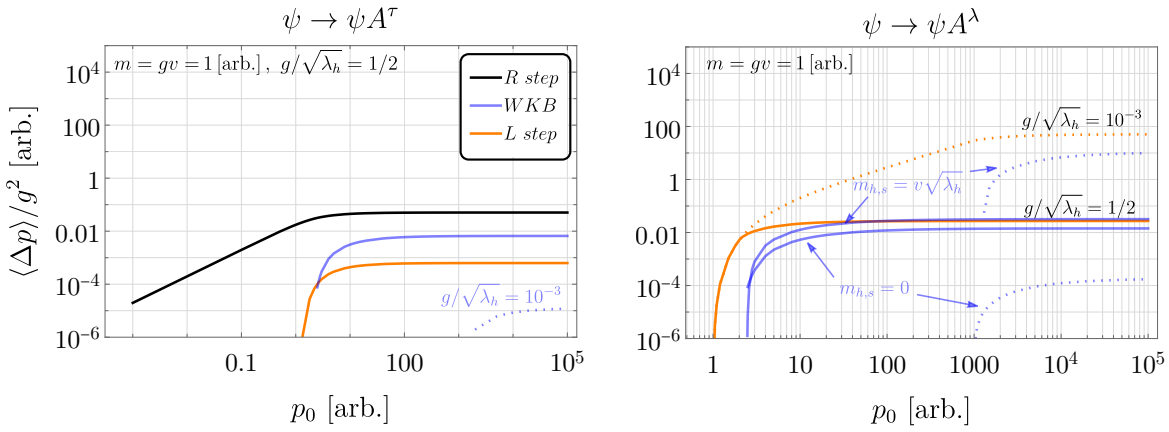

Figure 4.3.1: Average momentum transfer $\langle \Delta p \rangle$ from single emission by a charged particle with incoming energy $p_0 = p^z$, as it crosses the wall into the phase of restored gauge symmetry. We show the breakdown of all contributions in our calculation scheme (see section 4.2 for details): emission to the right (R) of low momentum modes (using the step function approximation), plus large momentum modes (using the WKB approximation), and emission to the left (L) of low momentum modes (step function). All are asymptotically constant, leading to friction on the wall that grows linearly with γ_w. We show results for two different values of wall length $mL_w = g/\sqrt{\lambda_h} = 1/2, 10^{-3}$, in units fixed by the broken phase gauge boson mass $m \equiv gv = 1$, described by solid and dotted lines respectively. **Left**: emission of $\tau-$polarisations. Only the WKB contribution changes appreciably in the thin wall limit, decaying as expected. **Right**: emission of λ polarisations. R emission in the step limit does not exist. L emission depends linearly on L_w^{-1}. We also highlight the dependence of the WKB contribution on the mass of the Higgs in the symmetric phase $m_{h,s}$, showing the natural identification $m_{h,s} = L_w^{-1} = v\sqrt{\lambda_h}$ (upper two blue curves) as well as $m_{h,s} = 0$ (lower two).

4.3 Results

In this section, we present our results for the average momentum transfer $\langle \Delta p \rangle$ from the NLO process of single emission of τ and λ polarisations from a charged particle in eq. (4.4) traversing the wall.

We break down all contributions as a function of incoming energy p_0 in fig. 4.3.1, where the main result is that $\langle \Delta p \rangle$ is constant and positive in the ultra-relativistic limit, and thus will lead to a pressure growing with γ_w when multiplied by the incoming flux. In fig. 4.3.2, we explore in more detail the dependence of the constant asymptotic values $\langle \Delta p \rangle_{p_0 \to \infty}$ on details of the theory. For τ emission the only scales in the problem (apart from p_0) are m and L_w. Thus, by dimensional analysis, we have $\langle \Delta p^\tau \rangle_{p_0 \to \infty} = g^3 v f_\tau(mL_w)$, for some function f_τ. We turn this into a dependence on couplings by defining $L_w^{-1} \equiv \sqrt{\lambda_h}\, v$, where λ_h will be a coupling related to the Higgs potential. On the other hand, for λ there is also a mass on the symmetric side $m_{h,s}$. In most models, it is natural to identify $m_{h,s} \approx L_w^{-1}$, which allows us to study λ emission also as a function of mL_w. We thus take as a primary benchmark

$$mL_w = \frac{g}{\sqrt{\lambda_h}} = \frac{m}{m_{h,s}} \,, \tag{4.51}$$

but we comment on disentangling L_w and $m_{h,s}$ when this make a significant difference. We also recall that we take the emitting charged particle to have constant mass $m_\psi(z) = m_\psi$

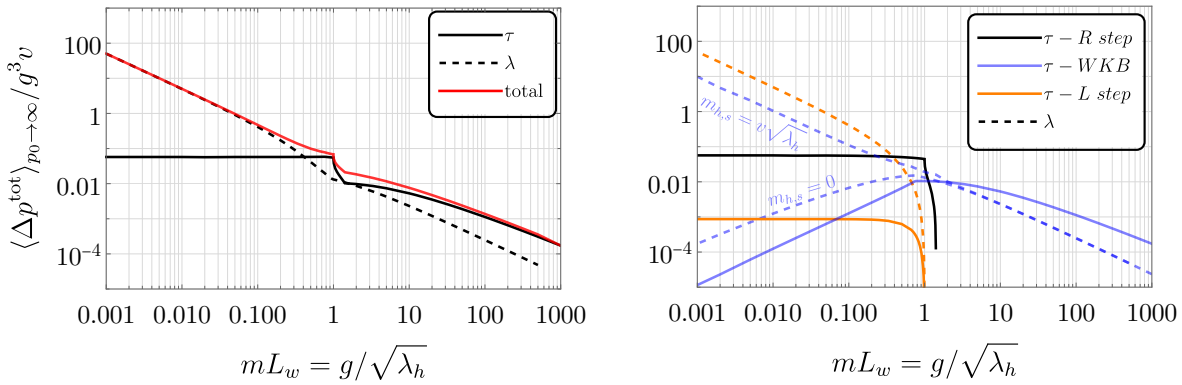

Figure 4.3.2: **Left**: Momentum transfer in the asymptotic limit, conveniently normalised, from τ and λ emission channels, and the total sum, as a function of the product mL_w, expressed in terms of couplings as $g/\sqrt{\lambda_h}$. In the region $g/\sqrt{\lambda_h} \ll 1$ (a 'thin wall' from the point of view of the τ field), λ is the dominant contribution. In the opposite ('thick wall') region we conservatively only keep WKB contributions. The jaggedness around $g/\sqrt{\lambda_h} \sim 1$ is purely a result of the brute cuts in phase space. **Right**: Breakdown of all contributions in our calculation scheme. Bold (dashed) lines refer to τ (λ) emission respectively. We show the λ WKB contribution for the most natural identification $m_{h,s} = L_w^{-1} = v\sqrt{\lambda_h}$, as well as $m_{h,s} = 0$.

and set it to zero. Turning on this mass distorts the curves at low energies but its effect is quickly lost for large p_0. In section 4.B we argue that our estimates for total $\langle \Delta p \rangle_{p_0 \to \infty}$ are also unaffected by allowing $m_\psi(z)$ to vary, although $\langle \Delta p \rangle$ can in general be even negative for low p_0.

We now provide some approximate formulae for all asymptotic contributions. Focusing first on τ emission, we obtain

$$\langle \Delta p_R^\tau \rangle_{p_0 \to \infty} \simeq \frac{g^3 v}{8\pi^2} \begin{cases} 4.4\ , & g/\sqrt{\lambda_h} \ll 1 \\ 0\ , & g/\sqrt{\lambda_h} \gg 1 \end{cases}\ , \tag{4.52}$$

$$\langle \Delta p_L^\tau \rangle_{p_0 \to \infty} \simeq \frac{g^3 v}{8\pi^2} \begin{cases} 0.07\ , & g/\sqrt{\lambda_h} \ll 1 \\ 0\ , & g/\sqrt{\lambda_h} \gg 1 \end{cases}\ , \tag{4.53}$$

$$\langle \Delta p_{wkb}^\tau \rangle_{p_0 \to \infty} \simeq \frac{g^3 v}{8\pi^2} \begin{cases} g/\sqrt{\lambda_h}\ , & g/\sqrt{\lambda_h} \ll 1 \\ 2\left(g/\sqrt{\lambda_h}\right)^{-1} \ln\left(g/\sqrt{\lambda_h}\right)\ , & g/\sqrt{\lambda_h} \gg 1 \end{cases}\ . \tag{4.54}$$

The first two contributions, coming from phase space where the step function is a good approximation, naturally dominate and remain constant in the thin wall limit $mL_w = g/\sqrt{\lambda_h} \ll 1$, while the contribution from the complimentary WKB regime vanishes. If instead one makes the wall look more and more broad $mL_w \gg 1$, in our scheme the WKB contribution dominates and is proportional to g^2/L_w, modulo an innocuous log. WKB domination follows from our cut in eq. (4.46); if we got rid of the absolute value, the R step contribution dominates over WKB. However, we would like to emphasise that in the limit $\lambda_h \to 0 \Rightarrow L_w \to \infty$ momentum transfer must vanish independently of prescription since the wall disappears, which is captured by the above equations. All contributions

manifestly vanish as g or $v \to 0$. For λ emission instead, we find

$$\langle \Delta p_L^\lambda \rangle_{p_0 \to \infty} \simeq \frac{g^3 v}{8\pi^2} \begin{cases} 4 \left(g/\sqrt{\lambda_h} \right)^{-1} , & g/\sqrt{\lambda_h} \ll 1 \\ 0 , & g/\sqrt{\lambda_h} \gg 1 \end{cases} , \tag{4.55}$$

$$\langle \Delta p_{wkb}^\lambda \rangle_{p_0 \to \infty} \simeq \frac{g^3 v}{8\pi^2} \begin{cases} 0.8 \left(g/\sqrt{\lambda_h} \right)^{-1} , & g/\sqrt{\lambda_h} \ll 1 \\ 1.6 \left(g/\sqrt{\lambda_h} \right)^{-1} , & g/\sqrt{\lambda_h} \gg 1 \end{cases} . \tag{4.56}$$

In the thin wall limit, the dominant contribution is from L movers, and it grows linearly with L_w^{-1}. This can be traced back to the total reflection of λ modes while the step function is a good approximation $k^z(z) \lesssim L_w^{-1}$, as discussed in section 4.1.2. For the natural identification $m_{h,s} \approx L_w^{-1}$, then $\langle \Delta p^\lambda \rangle$ can be interpreted as going like the mass gained $m_{h,s}$. However, we stress that even if we set $m_{h,s} = 0$, the behaviour remains. A better interpretation is again that λ describes the would-be Nambu-Goldstone boson, that interacts derivatively with the background wall. The WKB contribution appears to also increase in the thin wall limit, perhaps contrary to the reader's expectations. This is only because of the identification $m_{h,s} \approx L_w^{-1}$ in our benchmark choice. If we set $m_{h,s} = 0$, then we have instead

$$\langle \Delta p_{wkb}^\lambda \rangle_{p_0 \to \infty} \simeq \frac{g^3 v}{8\pi^2} 2.2 \left(g/\sqrt{\lambda_h} \right) \ln \left((g/\sqrt{\lambda_h})^{-1} \right) , \quad \text{for } m_{h,s} = 0 \quad \text{and} \quad g/\sqrt{\lambda_h} \ll 1 . \tag{4.57}$$

where again we have $L_w^{-1} = \sqrt{\lambda_h}\, v$, and it decays as expected as $\propto L_w^{-1}$. For the case $m_{h,s} \gg L_w^{-1}$ we found the WKB contribution to scale again like L_w^{-1}. This can be traced back to the fact that this limit is equivalent to the thick wall limit, happening for τ polarisation too. For the benchmark eq. (4.51), it is compensated by the mass gained $L_w^{-2} - m^2$, and increases linearly instead, as per eq. (4.56). The difference is highlighted in both figs. 4.3.1 and 4.3.2. Finally, we recall that we do not have a contribution from R emission in the step function limit since the amplitude is proportional to $g\tilde{v} \to 0$, as already stated section 4.2.2.

In fig. 4.3.2 the solid red line tracks the sum total of all contributions in our scheme, which we approximate by the following expression

$$\langle \Delta p \rangle_{p^z \to \infty} \simeq \frac{g^3 v}{8\pi^2} \begin{cases} 5 \left(g/\sqrt{\lambda_h} \right)^{-1} & g/\sqrt{\lambda_h} \ll 1 \\ 2 \left(g/\sqrt{\lambda_h} \right)^{-1} \left[1 + \ln \left(g/\sqrt{\lambda_h} \right) \right] & g/\sqrt{\lambda_h} \gg 1 \end{cases} , \tag{4.58}$$

where we have switched to $p^z \to \infty$ to be more accurate. To go to the friction pressure experienced by the wall expanding against a bath of particles charged under the restoring gauge symmetry, one should in principle integrate $\langle \Delta p \rangle$ against the distribution of incoming particles. Since this momentum transfer becomes constant for large p_0, to a very good approximation we can simply multiply eq. (4.59) by the incoming flux. Assuming a thermal distribution, this gives

$$\mathcal{P}_{\rm NLO} \simeq \frac{\zeta(3)}{\pi^2} \gamma_w T^3 \langle \Delta p \rangle_{p^z \to \infty} , \quad \text{for} \quad \gamma_w \gg 1 . \tag{4.59}$$

This expression of course should only be trusted when the bubble can be thought of as interacting with individual particles. A necessary condition is thus that the timescale of interactions between particles (in the plasma frame) $\Gamma_{\rm int.}^{-1}$ is longer than the wall cross time, i.e. $\gamma_w \gg L_w \Gamma_{\rm int.}$.

4.4 Summary and discussion

In this chapter, we studied the NLO friction in phase transitions of gauge symmetry–restoration, as a prime example of instances where particles may lose mass as they cross the phase boundary. To calculate, we reapplied the scheme developed in chapter 3 to study $1 \to 2$ processes in the translation-breaking background of a bubble/domain wall, in particular interpolating between different phases of a gauge theory. This amounts to a first principles quantisation of the gauge field using appropriate polarisations, and splitting final state phase space into regimes where the step function and WKB approximations are respectively valid.

The main result of this chapter is that the average momentum transfer due to a single emission from a particle charged under the gauge symmetry, as it passes from a broken to a restored phase, is positive, asymptotically constant, and roughly given by

$$\langle \Delta p \rangle_{p^z \to \infty} \sim \frac{g^2}{2\pi^2} L_w^{-1} \sim \frac{g^2}{2\pi^2} \sqrt{\lambda_h}\, v \ , \qquad \text{(symmetry–restoring)} \ , \tag{4.60}$$

where L_w is the width of the wall. We emphasise its typical relation to the Higgs vev (on the broken side) v and quartic coupling λ_h, to make manifest the physical vanishing limit $v \to 0$. This leads to a growing, positive, friction pressure eq. (4.59) for ultra-relativistic bubbles. Thus, we prove that symmetry–restoring phase transitions cannot have runaway behaviour $\gamma_w \to \infty$.

Comparison with gauge symmetry–breaking: We can compare eq. (4.60) to the far more studied case of symmetry–breaking transitions [2, 95, 96, 115], which is usually quoted as $\langle \Delta p \rangle \sim g^3 v / 2\pi^2$, ignoring a possible log term. A significant difference is present in the 'thin wall' limit $m L_w = g/\sqrt{\lambda_h} \ll 1$ due to the enhancement of λ ($\sim$ longitudinal) modes. The 'thick wall' limit $g/\sqrt{\lambda_h} \gg 1$ instead has not been explicitly quoted in the literature, but it will also go as eq. (4.60), since an extremely broad wall $L_w \to \infty$ is like having no wall at all so that the average momentum transfer in this limit vanishes also for symmetry–breaking transitions. Roughly speaking, one can imagine the black curve in the left panel of fig. 4.3.2 as describing the symmetry–breaking case. Another difference worth highlighting is the absence of naive soft divergences in any of the calculations in the main text. Unlike the symmetry–breaking case, nowhere did we have to resort to thermal masses to get a finite answer. We took a closer look at this in section 4.A. When testing the insensitivity of our results to turning on a change in current mass $m_\psi(z)$ in section 4.B, we did encounter a collinear log divergence, but this was always subleading with respect to the dominant contribution computed in the main text.

Anti-friction: Our motivation was guided partly by exploring the possibility of anti-friction, $\langle \Delta p \rangle < 0 \to \mathcal{P} < 0$, in instances when particles lose mass as they cross the wall. In symmetry–restoration, this is true at LO for τ ($\sim$ transverse) polarisations of the gauge field [10], and for any fermions with Yukawa couplings to the Higgs [11]. However, we found by direct computation that contributions to $\mathcal{P}$ from $1 \to 2$ NLO emission processes were positive and growing, and therefore always dominant for γ_w large enough. This positivity is almost trivial. The only thing that can possibly be negative in eqs. (4.28) and (4.29)

[10] We note that, on the other hand, it is not in general true for λ polarisations, whose mass changes from $m = gv$ to $m_{h,s}$.

[11] Interestingly, a toy model with symmetry–restoration discussed in section 4.D leads to a positive *total* $\mathcal{P}_{\rm LO}$. It is therefore not always straightforward to obtain $\mathcal{P}_{\rm LO} < 0$.

are $\Delta p_{L,R}$, and it is easy to prove that both are ≥ 0 for a constant charged particle mass $m_\psi = \tilde{m}_\psi$. Allowing ψ to lose mass in section 4.B lead to a negative contribution that was however subleading. This is no accident. As discussed in more detail in section 4.C, we argue that no particle physics process, with arbitrary number of incoming and outgoing states, can contribute an average momentum transfer more negative than $\langle \Delta p \rangle_{\min} = p^z - p_0$ per incoming d.o.f., in the limit $\gamma_w \to \infty$. The possibility of growing negative friction for low γ transient regimes has interesting, though model-dependent, phenomenological consequences, discussed briefly in section 4.C. We leave this exploration to future study.

Appendix

4.A Absence of soft divergences

In this section, we elucidate why the total momentum transfer to the bubble wall in the case of a symmetry–restoring phase transition calculated in the main text is IR finite. This result should be contrasted with the opposite case (when the true vacuum has a broken gauge symmetry) where an apparent logarithmic IR enhancement has been found [2, 96]. Let us look at the expressions for the matrix elements see eq. (4.44), the divergences in principle can appear when the momentum differences in the denominator are vanishing

$$\Delta\{p, p_r, \tilde{p}, \tilde{p}_r\} = 0 \ . \tag{4.61}$$

Let us consider for simplicity the case when the emitter particle has zero mass $m_\psi = 0$ both in the false and true vacuum. Then the energy conservation forces

$$\Delta p_r = p^z - q^z + k^z > p_0 - q_0 - k_0 = 0 \ , \tag{4.62}$$

$$\Delta \tilde{p}_r = p^z - q^z + \tilde{k}^z \geq p_0 - q_0 - k_0 = 0 \ , \tag{4.63}$$

where $k_z, \tilde{k}_z$ are positive by definition and in the last inequality $\Delta p_r = 0$ only for $k_0 = 0$.

$$\Delta p = p^z - q^z - k^z = p_0 - \sqrt{q_0^2 - k_\perp^2} - \sqrt{k_0^2 - k_\perp^2 - m^2} > 0 \ , \tag{4.64}$$

$$\Delta \tilde{p} = p^z - q^z - \tilde{k}^z = p_0 - \sqrt{q_0^2 - k_\perp^2} - \sqrt{k_0^2 - k_\perp^2} \geq 0 \ , \tag{4.65}$$

where in the last inequality $\Delta\tilde{p} = 0$ only for $k_\perp = 0$. So the divergences can appear only when $\Delta\tilde{p}$ and $\Delta\tilde{p}_r$ are equal to zero. Let us start by analysing the divergences appearing in the limit $\Delta\tilde{p} \to 0$: the relevant amplitudes are $\mathcal{M}^{\rm step}_{\tau,R}$ and $\mathcal{M}^{\rm wkb}_{\tau}$ and both of them diverge as $1/\Delta\tilde{p}$. For the scope of analysing the IR divergences we can safely focus only on the divergent pieces. Below we show the calculation for the 'step' contribution (WKB contribution differs just by some finite factor and proceeds in exactly the same way). The amplitude squared in the $\Delta\tilde{p} \to 0$ limit is

$$\lim_{\Delta\tilde{p}\to 0} |\mathcal{M}^{\rm step}_{\tau,R}|^2 = \frac{4k_\perp^2 p_0^2 |k_z|}{(\tilde{k}_z)^3} \times \frac{1}{(\Delta\tilde{p})^2} \ . \tag{4.66}$$

However, what is controlling the momentum transfer in the wall is the quantity

$$\langle \Delta p \rangle|_{IR} \propto \int_{k_\perp \to 0} \frac{d\tilde{k}_z}{2\pi} \frac{1}{2k_0} \frac{dk_\perp^2}{4\pi} \left|\frac{\tilde{k}_z}{k_z}\right| \cdot \frac{1}{2p^z} \left[\frac{1}{2|q^z|} |\mathcal{M}^{\rm step}_{\tau,R}|^2 (\Delta\tilde{p})\right] \ . \tag{4.67}$$

We change the integration variable using $\tilde{k}_z d\tilde{k}_z = k_0 dk_0$, and then focus only on the limit $k_\perp \to 0$, where potential IR divergences can in principle appear. Then we get

$$\langle \Delta p \rangle|_{IR} \propto \frac{1}{4\pi^2} \int \frac{dk_0}{k_0^2} k_\perp dk_\perp \ , \tag{4.68}$$

where the integral over $k_\perp$ is obviously finite. The integral over k_0 looks naively IR divergent, but remember that the upper bound of the $k_\perp$ integration is always below k_0, thus

$$\langle \Delta p \rangle|_{IR} \propto \frac{1}{4\pi^2} \int \frac{dk_0}{k_0^2} k_\perp dk_\perp < \frac{1}{8\pi^2} \int dk_0 = \quad \text{finite} \ . \tag{4.69}$$

Note that if we were calculating the probability of emitting the vector boson instead of the momentum transfer to the wall, we would have found a log divergence in $k_\perp$. Indeed,

$$\begin{aligned} \mathbb{P}_{1-\text{emission}} &\sim \int_{k_\perp \to 0} \frac{dk^z}{2\pi} \frac{1}{2k_0} \frac{dk_\perp^2}{4\pi} \cdot \frac{1}{2p^z} \left[\frac{1}{2|q^z|} |\mathcal{M}^{\text{step}}_{\tau,R}|^2 \right] \\ &\sim \frac{1}{4\pi^2} \int \frac{dk_0}{k_0^2} k_\perp dk_\perp \times \frac{2k_0 q_0}{p_0 k_\perp^2} = \quad \text{Log divergent} \ . \end{aligned} \tag{4.70}$$

What about $\Delta \tilde{p}_r = 0$? This term appears in $\mathcal{M}^{\text{step}}_{\tau,R}$ and in $\mathcal{M}^{\text{step}}_{\tau,L}$. However, the contribution of the left moving modes will be non-singular since $k_0 \geq m > 0$, and for the right moving modes we get

$$\lim_{k_0 \to 0} |\mathcal{M}^{\text{step}}_{\tau,R}|^2 \Delta \tilde{p} \propto \frac{m p_0^2}{k_0^2} \ . \tag{4.71}$$

Thus, we are back to the estimate

$$\langle \Delta p \rangle|_{IR} \propto \int \frac{dk_0}{k_0^2} k_\perp dk_\perp = \quad \text{finite} \ . \tag{4.72}$$

4.B Effects of a changing current mass

In the main text, we computed the average momentum transfer for a single emission from a charged current crossing into a gauge symmetry–restoring phase, assuming the charged matter did not change mass, i.e. $m_\psi(z) = m_\psi$. We then focused on $m_\psi = 0$, as our results did not depend on this parameter for large p_0 (large γ). These were positive and straightforwardly IR-finite. Of course, the more realistic case will have a varying mass, and our results are only phenomenologically useful if they are not appreciably affected by it. We will now argue that this is indeed the case.

If we suppose for concreteness that the charged current is a fermion, then the most natural way to gain mass is by the addition to the theory in eq. (4.4) of a Yukawa-like interaction

$$\delta \mathcal{L}_f = \bar{\psi} i \not{D} \psi - (y H \bar{\psi}_L \psi_R + h.c.) \ , \tag{4.73}$$

where gauge invariance forces ψ to be exactly massless on the symmetric side. If ψ were a complex scalar, we have more choice at the renormalisable level, such as

$$\delta \mathcal{L}_s = \frac{1}{2} |D_\mu \psi|^2 - \tilde{m}_\psi^2 |\psi|^2 \quad - (y \psi^2 H^2 + h.c.) \quad \text{or} \quad y |\psi|^2 |H|^2 \ . \tag{4.74}$$

The first interaction mimics the fermion case, with current non-conservation upon expanding around the vev. The second term shows that for a scalar one can also gain mass in a current preserving fashion. All these differences will not matter in what follows. For concreteness, we focus on the maximal change $\tilde{m}_\psi = 0$, in line with eq. (4.73).

A proper treatment would now require quantising also ψ modes into left and right movers, as we did for the vector in section 4.1. While this is certainly doable, it appears to us unnecessary, and we can argue qualitatively. On general grounds we expect the average momentum transfer to go as

$$\lim_{p_0\to\infty}\langle\Delta p\rangle \to vf\left(g,y,\sqrt{\lambda_h}\right)+\mathcal{O}\left(v^2/p^0\right)\ , \tag{4.75}$$

where f is some unknown function. In the main text, we computed the leading $\mathcal{O}\left(g^3\right)$ and $\mathcal{O}\left(g^2\sqrt{\lambda_h}\right)$ terms of f. This had dominant support from phase space where the vector was soft $k_0\sim gv$, or $\sim L_w^{-1}, m_{h,s}$ for λ, and the fermion hard $q_0\sim p_0$, consistent with our choice of ignoring the mass $m_\psi(z)\ll p_0$. Including $m_\psi(z)$, the greatest change will result in the part of phase space where the fermion is soft (and the vector hard).

Intuition for this possible contribution can be developed without much work by using the reduced WKB approximation for the matrix element, as per section 4.2.2. It was already pointed out in [95] that the amplitude for emission of a soft fermion is suppressed with respect to the emission of a soft vector [12]. We now go a bit further, estimating this WKB contribution, and show that indeed the contribution related to a change in ψ mass is suppressed for large incoming energies.

The matrix element for τ polarisation $\psi\to\psi A^\mu_\tau$ is

$$\mathcal{M}_\tau^{\text{wkb red.}}=-iy\epsilon^\mu_\tau\left(\frac{p^\mu+q^\mu}{p^z-q^z-k^z}-\frac{\tilde{p}^\mu+\tilde{q}^\mu}{\tilde{p}^z-\tilde{q}^z-\tilde{k}^z}\right)\ , \tag{4.76}$$

where, as in the main text, by τ we mean the non trivially zero τ_2. Defining $x=k^0/p^0$, the various four-momenta are explicitly

$$\begin{aligned}
&p^\mu=(p_0,0,0,\sqrt{p_0^2-m_\psi^2})\,,\quad \tilde{p}^\mu=(p_0,0,0,p_0)\,,\\
&q^\mu=(p_0(1-x),-k_\perp,0,\sqrt{p_0^2(1-x)^2-k_\perp^2-m_\psi^2})\ ,\quad \tilde{q}^\mu=(p_0(1-x),-k_\perp,0,\sqrt{p_0^2(1-x)^2-k_\perp^2})\ ,\\
&k^\mu=(p_0x,k_\perp,0,\sqrt{p_0^2x^2-k_\perp^2-m_A^2})\ ,\quad \tilde{k}^\mu=(p_0x,k_\perp,0,\sqrt{p_0^2x^2-k_\perp^2})\ .
\end{aligned} \tag{4.77}$$

The behaviour of eq. (4.76) is dictated by the collinear singularity of the second term for $k_\perp\to 0$, when

$$\mathcal{M}_\tau^{\text{wkb red.}}\to iy\frac{4p_0(1-x)}{k_\perp}\ . \tag{4.78}$$

We note that the momentum transfer in this region is actually negative

$$\Delta p_R=p^z-\tilde{q}^z-\tilde{k}^z\overset{k_\perp\to 0}{=}p^z-p_0+\frac{k_\perp^2}{2q^0k^0}+\dots\ . \tag{4.79}$$

We can estimate this 'negative' contribution from the loss in ψ mass in the large p_0 limit by

$$\langle\Delta p_R\rangle_\psi\propto\int\frac{dxdk_\perp k_\perp}{xp_0^2}\frac{x}{x(1-x)}\times\frac{16p_0^2(1-x)^2}{k_\perp^2}\times\frac{-m_\psi^2}{2p_0}\ . \tag{4.80}$$

We observe that this integral diverges logarithmically with respect to $k_\perp$, but not with respect to x, because the WKB contribution is only considered in the UV part of the

[12] See Table I in [95].

phase space, unlike the approach taken in Appendix 4.A, where we considered the step wall contribution. Nevertheless, the overall contribution must scale as

$$\langle \Delta p \rangle_{neg.} \propto -\frac{m_\psi^2}{p_0} \times \log(\text{divergence}) \ . \tag{4.81}$$

This divergence should be considered regulated by some mass scale. If we had allowed the mass of the emitter in the new phase to be non-zero, we would have found a dependence such as

$$\langle \Delta p \rangle_{neg.} \propto -\frac{m_\psi^2 - \tilde{m}_\psi^2}{p_0} \times \log\left(\frac{p_0}{\tilde{m}_\psi}\right) \ . \tag{4.82}$$

However, for large values of the initial momentum, this contribution will be highly subleading, regardless of the logarithmic divergence. Therefore, we can conclude that the contribution to the pressure we have identified is the only one that scales with the Lorentz boost factor. It is important to note that this divergence is related to the zero mass of the fermion on the symmetric side, and we expect it to be mitigated by interactions with the plasma.

We noticed that this negative contribution, coming from a particle losing mass across the wall, was subleading in $p_z \sim p_0$. This is true more generally as discussed in section 4.C, where we explore possible negative friction contributions in more general terms.

4.C Negative friction?

In this appendix, we attempt to examine more broadly the question of whether $1 \to 2$ processes, or indeed any multi-particle process in theories of broken translation, can source negative friction. We should emphasise that, in order to be phenomenologically interesting, a negative sign is not enough, but rather we would require $\langle \Delta p \rangle \sim (p^z)^n$ with $n > -1$. A contribution $n = -1$ is already obtained at LO when particles lose mass, while $n < -1$ would be inconsequential.

We start first with a generic $1 \to 2$ process, with incoming particle a and outgoing particles b and c and assign them 4−momenta p^μ, q^μ, k^μ respectively. There are four possible physical momentum transfers, corresponding to particles b, c being emitted to the right (R) or left (L) [13]. Defining $\Delta p_{I,J}$, with $I, J \in \{R, L\}$, as appropriate for the case b is $I-$emitted and c is $J-$emitted, these are

$$\begin{aligned}
\Delta p_{R,R} &\equiv p^z - \tilde{q}^z - \tilde{k}^z = \sqrt{p_0^2 - m_a^2} - \sqrt{(p_0 - k_0)^2 - k_\perp^2 - \tilde{m}_b^2} - \sqrt{k_0^2 - k_\perp^2 - \tilde{m}_c^2} \ , \\
\Delta p_{L,R} &\equiv p^z - \tilde{q}^z + k^z = \sqrt{p_0^2 - m_a^2} - \sqrt{(p_0 - k_0)^2 - k_\perp^2 - \tilde{m}_b^2} + \sqrt{k_0^2 - k_\perp^2 - m_c^2} \ , \\
\Delta p_{R,L} &\equiv p^z + q^z - \tilde{k}^z \ , \\
\Delta p_{L,L} &\equiv p^z + q^z + k^z \ ,
\end{aligned} \tag{4.83}$$

where, as always, we use a tilde to denote a quantity evaluated in the new phase when it changes across the wall, and $q^z, \tilde{q}^z, k^z, \tilde{k}^z \geq 0$. Further down, we study each contribution in more detail, in particular when it can be negative. However, it is easy to prove that,

[13] As explained in section 4.1, in theories of broken translations R and L emission are more properly considered on separate footing.

in any case, and over all phase space, the momentum transferred cannot be smaller than the absolute minimum

$$\Delta p \geq \Delta p_{\text{Min}} = p^z - q^0 - k^0 = p^z - p^0 = -\frac{m_a^2}{2p^z} + \mathcal{O}\left(\frac{1}{p_z^2}\right) , \tag{4.84}$$

the second equality by energy conservation. In the relativistic limit this is equal to the LO minimum eq. (4.1). We note that, although this *absolute minimum* is negative, it is going to zero in the asymptotic limit $p^z \to \infty$. It seems very difficult that the amplitude of the emission process might compensate for this. We can be more precise. A lower bound on the average momentum transfer is

$$\begin{aligned} \langle \Delta p_{I,J} \rangle &= \int d\Pi_{\text{BTPH}} \; |\mathcal{M}_{I,J}|^2 \; \Delta p_{I,J} \\ &\geq \Delta p_{\text{Min}} \int d\Pi_{\text{BTPH}} \; |\mathcal{M}_{I,J}|^2 \\ &= \Delta p_{\text{Min}} \; \mathbb{P}_{I,J} \; , \end{aligned} \tag{4.85}$$

where BTPH, which stands for broken translation phase space, is the positive-definite appropriate integration over final state momenta (such as in eqs. (4.28) and (4.29)), and $\mathcal{M}_{I,J}$ and $\mathbb{P}_{I,J}$ are the matrix element and *total integrated probability* for the corresponding process. Since $\mathbb{P}$ is an integrated probability for a physical process it cannot grow arbitrarily to infinity with incoming particle energy $p_0 \approx p^z$ (less it breaks unitarity), and we conclude that

$$\langle \Delta p \rangle > -\frac{m_a^2}{2p^z} , \qquad \text{for} \quad p^z \to \infty , \tag{4.86}$$

that is, asymptotic friction (obtained when multiplying by the flux $\propto \gamma_w \propto p_z$) will never dominate the LO contribution. We saw an explicit example of a negative contribution being subdominant in section 4.B.

The argument above can run again for an arbitrary $N_i \to N_f$ process. In this case, the absolute minimum momentum transfer is

$$\Delta p_{\text{Min}}^{N_i \to N_f} = p_1^z + \cdots + p_{N_i}^z - p_1^0 - \cdots - p_{N_i}^0 = -\sum_{j=1}^{N_i} \frac{m_{a,j}^2}{2p_j^z} + \mathcal{O}\left(\frac{1}{p_z^2}\right) , \tag{4.87}$$

which is independent of N_f. In the same way as eq. (4.85), we would conclude that the average momentum transfer, over all final phase space, cannot beat the leading order contribution of N_i particles simply crossing the wall, in the asymptotic limit.

We emphasise that our general argument applies only to the regime when individual particles can be thought of as interacting with the wall, usually the asymptotic $\gamma_w \to \infty$ regime, as opposed to a hydrodynamic regime when macroscopic fluid equations are more appropriate. We do not rule out negative friction for intermediate, possibly relativistic, bubble speeds, an exploration of which we leave to future work. We simply point out that potential intermediate regimes of negative pressure *growing* with v or γ could be phenomenologically quite interesting, as they could lead to instabilities. Fluctuations in the speed of expansion along the bubble's boundary can be expected, just as fluctuations in its position should be expected from finite temperature effects, collisions with the medium itself, or even quantum mechanically in the case of vacuum tunneling [206]. These fluctuations would grow in time and could lead to highly asymmetric bubbles at late time, which would greatly enhance the gravitational wave signal from single bubble expansion as well as collisions [14].

[14] Similar conclusions are emphasised in a recent work [207], although there the bubble of the new phase is already nucleated with significant asymmetry.

Further details of $1 \to 2$ processes. We examine a bit further the contributions in eq. (4.83). Clearly, $\Delta p_{L,L} > 0$ always. Furthermore, $\Delta p_{L,R}$ is clearly minimised when all of the kinetic energy available goes to b (i.e. $k^z = 0$)

$$\Delta p_{L,R} \geq p^z - q^z_{\max} = \sqrt{p_0^2 - m_a^2} - \sqrt{(p_0 - m_c)^2 - \tilde{m}_b^2} \tag{4.88}$$

$$\to m_c - \frac{m_a^2 - \tilde{m}_b^2}{2p_0} + \mathcal{O}\left(1/p_0^2\right) \ , \tag{4.89}$$

and similarly

$$\Delta p_{R,L} \geq p^z - k^z_{\max} = \sqrt{p_0^2 - m_a^2} - \sqrt{(p_0 - m_b)^2 - \tilde{m}_c^2} \tag{4.90}$$

$$\to m_b - \frac{m_a^2 - \tilde{m}_c^2}{2p_0} + \mathcal{O}\left(1/p_0^2\right) \ . \tag{4.91}$$

We see that the lower bounds eqs. (4.88) and (4.90) can be positive or negative, depending on the relative size of the three masses involved, but if p_0 is large enough, they can only be negative if $m_{c,b} = 0$ and $m_a > \tilde{m}_{b,c}$.

Finally, the most negative possible momentum transfer comes from

$$\Delta p_{R,R} \geq \Delta p_{R,R}\,|_{k_\perp = 0} = \sqrt{p_0^2 - m_a^2} - \sqrt{\left(p_0 - \sqrt{\tilde{k}_z^2 + \tilde{m}_c^2}\right)^2 - \tilde{m}_b^2} - \tilde{k}^z \ , \tag{4.92}$$

$$\geq \sqrt{p_0^2 - m_a^2} - \sqrt{p_0^2 - \tilde{m}_{b,c}^2} \ , \quad \text{if } \tilde{m}_{c,b} = 0 \ , \tag{4.93}$$

where we have highlighted the simple case of when either of the outgoing masses is zero. When both are non-zero, the precise location of the absolute minimum within the allowed range $\tilde{k}_z \in (0, \sqrt{(p_0 - \tilde{m}_b)^2 - \tilde{m}_c^2})$ is non-trivially located somewhere in between the extreme points, but it is always greater than $p^z - p^0$.

4.D Toy model with symmetry–restoring PT

In the main text, we computed friction without any discussion of specific models realising fig. 4.0.2. We now dedicate some space to this, mentioning some general possibilities, before studying a simple concrete model below.

In principle, for every symmetry–breaking FOPT that proceeds as the universe cools down, there is a potential symmetry–restoring FOPT that would follow if the universe were adiabatically heated up. This possibility was recently explored in [208], in the context of post-inflationary reheating. The picture in fig. 4.0.2 could also be true at zero temperature, for a non-renormalisable polynomial potential in (even powers of) the single field $|H|$ in eq. (4.4). Alternatively, by the addition of the right type of matter, one can arrange for radiative corrections to drive the effective quartic coupling of h to run slightly negative and then positive (as occurs in the Standard Model - see for example [209]). This leads to the existence of a second vacuum at very large field value, which can be tuned to have higher energy density. For a two field (or more) potential, fig. 4.0.2 can be obtained even at the renormalisable level. In all these 'cold' scenarios, one has to explain why the universe starts in the false vacuum, perhaps as a result of h random walking during inflation.

In the rest of this appendix, we explore a simple, though concrete, two field potential that can be considered as an existence proof for a first-order, symmetry–restoring phase

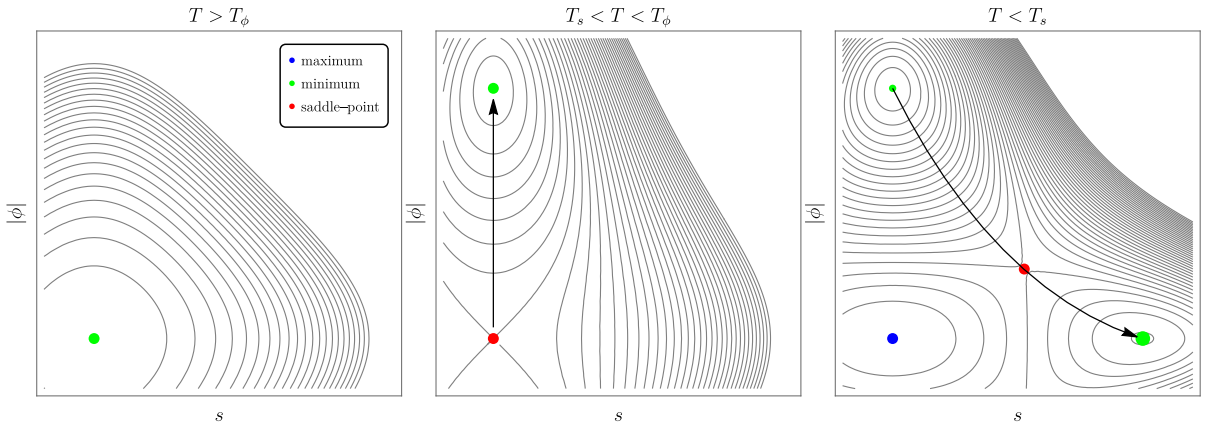

Figure 4.D.1: Sketch of the PT steps in the toy model described in section 4.D, where ϕ is charged and $s \to -s$ is a symmetry. At early times, for very high temperature, there is only one, symmetry preserving, vacuum at the origin. As the universe starts to cool down, the origin becomes unstable and a new minimum appears, spontaneously breaking gauge symmetry. As the universe cools down further, a pair of two $\mathbb{Z}_2$ symmetry–breaking minima appear (only one in the figure) and at some $T_{\rm nuc}$ the system will make the (1st order) transition to restore the gauge symmetry. The latter false and true vacua persist at zero temperature. Domain walls can in principle be avoided by introducing sufficient $\mathbb{Z}_2$ breaking. For the purposes of our work, we do not need to comment on this further.

transition that proceeds as the universe cools down, starting from a unique global minimum at high temperature. It does not therefore rely on inflation, or other initial condition selection mechanisms to start the universe in a false vacuum. For simplicity, we imagine the dynamics occurring in a hidden, thermal sector. For our purposes, we will not need to compute decay rates. We simply assume the transition will happen. We will however be interested in examining the leading order pressure mentioned around eq. (4.2). We remind the reader how the LO pressure, in the high temperature limit, is defined for a general particle content [94]

$$\mathcal{P}_{\rm LO} = \sum_i \frac{n_i c_i}{24} \left(m_i^2({\rm TV}) - m_i^2({\rm FV}) \right) T_{\rm nuc}^2 \ , \tag{4.94}$$

where i runs over all the particles present in the thermal plasma, n_i is the number of d.o.f.s of the particle i, $c_i = 1(1/2)$ for bosons(fermions) while $m_i^2({\rm TV}, {\rm FV})$ are the tree level field dependent masses computed at the true (false) vacuum. Interestingly, we will find it difficult for this particular scenario to lead to negative LO pressure.

Minimal concrete model: We examine a simple, renormalisable, toy model consisting of a complex field ϕ, charged under a gauged $U(1)$, and a real scalar s, endowed with a $\mathbb{Z}_2$ symmetry (a strong condition that we will later relax), with the following Lagrangian

$$\mathcal{L} = -\frac{1}{4} F_{\mu\nu} F^{\mu\nu} + |D_\mu \phi|^2 + \frac{(\partial_\mu s)^2}{2} + m_1^2 |\phi|^2 - \frac{\lambda_1 |\phi|^4}{4} + \frac{m_2^2 s^2}{2} - \frac{\lambda_2 s^4}{4} - \lambda_3 s^2 |\phi|^2 \ . \tag{4.95}$$

It is obvious from the form of eq. (4.95) that, at zero temperature and for λ_3 large enough, one has a spontaneously broken $U(1)$ local minumum and a spontaneously broken $\mathbb{Z}_2$ local minimum:

$$\langle |\phi| \rangle = \sqrt{2}\, m_1/\lambda_1 \ , \langle s \rangle = 0 \ , \qquad \langle |\phi| \rangle = 0 \ , \langle s \rangle = m_2/\sqrt{\lambda_2} \ . \tag{4.96}$$

We will argue that, for some particular choices of parameters, the cosmology will follow the steps sketched in fig. 4.D.1. Initially, at very high temperature, the (only) minimum of the system is at the origin of the potential, that is the symmetric configuration ($\langle|\phi|\rangle = 0, \langle s\rangle = 0$). Then, as the system cools down, $U(1)$ is spontaneously broken ($\langle|\phi|\rangle \neq 0, \langle s\rangle = 0$). At even lower temperatures, a new, deeper minimum appears, which breaks the $\mathbb{Z}_2$ but restores the gauge symmetry, giving the desired transition ($\langle\phi\rangle \neq 0, \langle s\rangle = 0) \to (\langle\phi\rangle = 0, \langle s\rangle \neq 0$).

For this to happen, we first need to explore the minima structure of the potential at low temperatures and require that the global minimum corresponds to ($\langle\phi\rangle = 0, \langle s\rangle \neq 0$). This leads to the condition

$$\frac{m_2^4}{4\lambda_2} > \frac{m_1^4}{\lambda_1} \ . \tag{4.97}$$

For our discussion, it is sufficient to use the tree level potential, and the leading terms in high temperature expansion, wherein appear the field dependent masses. They read

$$\begin{aligned} m_{\phi_1}^2 &= -m_1^2 + \frac{\lambda_1}{4}(3\phi_1^2 + \phi_2^2) + \lambda_3 s^2 \ , \\ m_{\phi_2}^2 &= -m_1^2 + \frac{\lambda_1}{4}(\phi_1^2 + 3\phi_2^2) + \lambda_3 s^2 \ , \\ m_s^2 &= -m_2^2 + 3\lambda_2 s^2 + 2\lambda_3|\phi|^2 \ , \\ m_A^2 &= 2g^2|\phi|^2 \ , \end{aligned} \tag{4.98}$$

where we separated two degrees of freedom of the complex scalar field $\phi = (\phi_1 + i\phi_2)/\sqrt{2}$. Then, the thermal corrections to the masses will be given by

$$\Pi_\phi = \left(\frac{g^2}{4} + \frac{\lambda_3 + \lambda_1}{12}\right) T^2 \ , \qquad \Pi_s = \left(\frac{\lambda_2}{4} + \frac{\lambda_3}{6}\right) T^2 \ . \tag{4.99}$$

Therefore, the requirement that $U(1)$ is broken before $\mathbb{Z}_2$ becomes

$$T_\phi^2 > T_s^2 \ , \tag{4.100}$$

where $T_{\phi,s}$ are the temperatures when the effective mass, $m_{s,\phi}^2 + \Pi_{s,\phi}$, vanishes and they are defined as

$$T_\phi^2 = \frac{12 m_1^2}{3g^2 + \lambda_1 + \lambda_3} \ , \qquad T_s^2 = \frac{12 m_2^2}{3\lambda_2 + 2\lambda_3} \ . \tag{4.101}$$

This requirement, written in terms of the couplings, reads

$$g^2 < -\frac{\lambda_3 + \lambda_1}{3} + \frac{m_1^2}{m_2^2}\left(\frac{2}{3}\lambda_3 + \lambda_2\right) \ . \tag{4.102}$$

The last condition will be that there is a barrier separating the two minima at ($\langle\phi\rangle \neq 0, \langle s\rangle = 0$) and ($\langle\phi\rangle = 0, \langle s\rangle \neq 0$), that is we need to require that they are local minima, then

$$\left.\frac{\partial^2 V_{\text{eff}}}{\partial s^2}\right|_{\langle\phi\rangle\neq 0, \langle s\rangle = 0} = -m_2^2 + \frac{4\lambda_3 m_1^2}{\lambda_1} + T^2\left[\frac{\lambda_2}{4} - \frac{\lambda_3(6g^2 + 2\lambda_3 + \lambda_1)}{6\lambda_1}\right] > 0 \ , \tag{4.103}$$

$$\left.\frac{\partial^2 V_{\text{eff}}}{\partial \phi_1^2}\right|_{\langle\phi\rangle = 0, \langle s\rangle\neq 0} = -m_1^2 + \frac{\lambda_3 m_2^2}{\lambda_2} + T^2\left[\frac{3g^2 - 2\lambda_3 + \lambda_1}{12} - \frac{\lambda_3^2}{6\lambda_2}\right] > 0 \ , \tag{4.104}$$

where $V_{\text{eff}} = V_{\text{tree}} + V_T$. These conditions turn out to be easy to satisfy.

Let us look at the LO pressure in this model, focusing on its sign. Since all the particles here are bosons, all we need to calculate is the sum of the mass squared, then we get

$$\sum m^2(\langle\phi\rangle \neq 0, \langle s\rangle = 0) = \frac{12m_1^2}{\lambda_1}g^2 + 2m_1^2 - m_2^2 + \frac{4\lambda_3 m_1^2}{\lambda_1} \ , \tag{4.105}$$

$$\sum m^2(\langle\phi\rangle = 0, \langle s\rangle \neq 0) = 2m_2^2 - 2m_1^2 + 2\lambda_3\frac{m_2^2}{\lambda_2} \ , \tag{4.106}$$

then the LO pressure will be negative if

$$\sum m^2(\langle\phi\rangle = 0, \langle s\rangle \neq 0) < \sum m^2(\langle\phi\rangle \neq 0, \langle s\rangle = 0) \ , \tag{4.107}$$

that translates into the condition

$$g^2 > -\frac{\lambda_3 + \lambda_1}{3} + \frac{\lambda_1 m_2^2}{4\lambda_2 m_1^2}\left(\lambda_2 + \frac{2}{3}\lambda_3\right) \ . \tag{4.108}$$

We can see that this is incompatible with the previous condition, in eq. (4.102), of the $U(1)$ breaking before $\mathbb{Z}_2$ and the requirement that in the true vacuum, the gauge symmetry is unbroken. So the total LO pressure is always positive in the concrete theory of section 4.D, despite the existence of a symmetry–restoring phase transition.

Including additional matter: One might think that, in order to change the above conclusion, we need only introduce additional matter fields to the theory, that lose mass during the final symmetry–restoring transition. Instead, we now show that, while maintaining our assumptions of renormalisability and $\mathbb{Z}_2$ symmetry, this is not so. We rewrite the theory in a slightly tidier fashion,

$$V = \lambda_f(f^2 - v_f^2)^2 + \lambda_t(t^2 - v_t^2)^2 + \lambda_{ft}f^2t^2 + \sum(\text{other fields not getting vev}) \ , \tag{4.109}$$

where f can be thought of as the radial mode of the charged field and t is the real scalar. The choice of labels reflects the fact that we will demand that, at $T = 0$, the true (degenerate) vacua are $\langle t\rangle = \pm v_t$, $\langle f\rangle = 0$, while the false vacuum is $\langle t\rangle = 0$, $\langle f\rangle = v_f$. Again, both can be (meta-)stable local minima for large enough λ_{ft}. The desired hierarchy translates to the requirement

$$\lambda_f v_f^4 < \lambda_t v_t^4 \ . \tag{4.110}$$

We take the additional sum in eq. (4.109) to be over an arbitrary number of extra fermions and scalars coupled at renormalisable level. For example, but not only, the Yukawa-like interactions in eqs. (4.73) and (4.74). Again, we also restrict the sum to respect the $\mathbb{Z}_2$ symmetry of t, and relax this assumption further below.

As before, at the highest of temperatures, the origin of field space will be the unique, symmetric vacuum. Next, we impose that the $U(1)$ breaking occurs first, to follow the steps of fig. 4.D.1. Thermal corrections to the potential, in the high temperature limit, are given by [6]

$$V_T(T) = T^2\sum_i \frac{n_i c_i}{24}m_i^2(f,t) + \dots \ , \tag{4.111}$$

where $m_i(f,t)$ are the field dependent tree level masses for every particle present in the thermal plasma, n_i is the number of the d.o.f.s of the particle i, while $c_i = 1(1/2)$ for bosons(fermions). Roughly speaking, the field f will develop a vev at the temperature T_f, defined as when its effective thermal mass at the origin vanishes

$$m_f^{\text{eff}}(f,t)^2\Big|_{f,t=0} = \frac{\partial^2}{\partial f^2}(V_{\text{tree}} + V_T(T_f))\Big|_{f,t=0} = 0 \ . \tag{4.112}$$

It is instructive to notice that the thermal correction to the mass can be rewritten in the following way

$$\frac{\partial^2 V_T}{\partial f^2}\Big|_{f,t=0} = \Pi_f(T_f) = T_f^2 \sum_i \frac{n_i c_i}{24} \frac{\partial^2 m_i^2(f,t)}{\partial f^2}\Big|_{f,t=0} \ . \tag{4.113}$$

Now, whichever is the form of $m_i^2(f,t)$ after the second derivative, computed at the origin, the only terms that will survive are the quadratic ones, then it is convenient to write the masses as

$$m_i^2(f,t) = m_i^2(0,0) + \frac{1}{2}\frac{\partial^2 m_i^2(f,t)}{\partial f^2}\Big|_{f,t=0} f^2 + \frac{1}{2}\frac{\partial^2 m_i^2(f,t)}{\partial t^2}\Big|_{f,t=0} t^2 + \dots \ , \tag{4.114}$$

where there is no linear term, or mixed second derivative, due to the $\mathbb{Z}_2$ symmetry. Restricting to renormalisable operators in eq. (4.109) means that there are no higher order terms and the series finishes here. We can then rewrite

$$\frac{\partial^2 m_i^2(f,t)}{\partial f^2}\Big|_{f,t=0} = 2 \cdot \frac{m_i^2(f,0) - m_i^2(0,0)}{f^2} \ . \tag{4.115}$$

Therefore a useful way to write the thermal correction is the following

$$\frac{\partial^2 V_T}{\partial f^2}\Big|_{f,t=0} = \Pi_f(T_f) = T_f^2 \sum_i \frac{n_i c_i}{12} \left(\frac{m_i^2(f,0) - m_i^2(0,0)}{f^2} \right) \ , \tag{4.116}$$

Since the RHS is actually independent of f, this allows us to evaluate it wherever we want, so even at $f = v_f$. An analogous expression follows for T_t evaluating at $t = \pm v_t$, and we can solve for both temperatures, finding

$$T_f^2 = \frac{-12 m_f^2(0,0) v_f^2}{\sum_i n_i c_i \left(m_i^2(v_f,0) - m_i^2(0,0)\right)} \ , \qquad T_t^2 = \frac{-12 m_t^2(0,0) v_t^2}{\sum_i n_i c_i \left(m_i^2(0,\pm v_t) - m_i^2(0,0)\right)} \ , \tag{4.117}$$

where we recall that $m_{f,t}^2(0,0) < 0$. Now the condition $T_f > T_t$, together with eq.(4.110), forces

$$\sum n_i c_i m_i^2(0,\pm v_t) - \sum n_i c_i m_i^2(v_f,0) > 0 \ , \tag{4.118}$$

but this is the condition of the LO pressure being positive.

Explicit $\mathbb{Z}_2$ breaking: Things become more complicated if we allow for explicit $\mathbb{Z}_2$ breaking terms in our theory. This could be simply done by including a cubic term in our tree level potential, or if one prefers to leave the cold potential unaltered, by adding to the sum of renormalisable operators in eq. (4.109), some $\mathbb{Z}_2$ breaking terms, such as a massive Dirac fermion with a Yukawa coupling to t

$$\mathcal{L} \supset \ \mu\, t^3 + (yt + m_\psi)\bar{\psi}\psi \ + \dots \tag{4.119}$$

We find that with these types of additions, it is naively possible to arrange for the cosmological history in fig. 4.D.1, with a negative LO pressure in the final symmetry–restoring FOPT. However, this is at the expense of significant tuning, which will be very sensitive to a more proper treatment of finite temperature corrections to the potential, and thus cannot be trusted.

Chapter 5

Hydrodynamics of inverse PTs

From a theoretical perspective, PTs between a local minimum and a deeper, local or global, minimum are commonplace in quantum field theory, where it is believed that the vacuum structure is a complicated manifold. A *direct* phase transition connects a local vacuum to a deeper vacuum of the zero–temperature potential, and the energy difference between the two minima manifests itself in the acceleration of the bubble wall. In this sense, the transition is triggered by the release of vacuum energy. On the other hand, an *inverse* phase transition connects a deeper minimum of the zero–temperature potential to a higher one, and the bubble actually expands against the vacuum energy. The transition is then triggered purely by thermal corrections. We study for the first time the hydrodynamics and the energy budget of inverse phase transitions. We find several modes of expansion for inverse bubbles, which are related to the known ones for direct transitions by a mirror symmetry. We finally investigate the friction exerted on the bubble wall and comment on the possibility of runaway walls in inverse phase transitions.

As already anticipated in the first chapter, we will try to characterise the bubble expansion modes during the PT in the limit in which the hydrodynamics description is a good approximation. We will review what has been done in the literature and extend it to what we called *inverse* PTs.

The hydrodynamics of cosmological PTs have been intensively studied in the past, alongside their hydrodynamical properties, their efficiency to turn vacuum energy into bulk motion, sound speed effects [73, 86, 210–215] and gravitational wave imprint [47, 48, 54] (see for example [216] for a review). A thorough classification of the different modes of expansion of bubbles wall has been presented [217–220]. Five consistent types of solutions survived the examination: weak and Chapman-Jouguet (CJ) deflagrations, weak and CJ detonations and hybrid solutions, which are supersonic deflagrations glued to rarefaction waves. The collapse of cosmological droplets, because of their possible impact on the production of GW [221] and PBH production [109], also received attention. In a direct phase transition, the vacuum undergoes a transition from a local higher minimum of the zero–temperature potential to a deeper minimum, as presented by the blue arrow (direct PT) in fig.5.0.1. The acceleration of the bubbles of the new phase is then triggered mostly by the vacuum energy release.

A much less studied situation is the expansion of bubbles of inverse phase transitions, where the transition is from a lower minimum (of the zero–temperature potential) to a higher one, as presented in solid darker red arrow (inverse PT) in fig.5.0.1. During inflation, we expect the true zero temperature vacuum to be populated and the symmetries to be broken by the vacuum expectation values of the scalar fields. The subsequent reheating will then increase the temperature of the bath and push the scalar fields to the

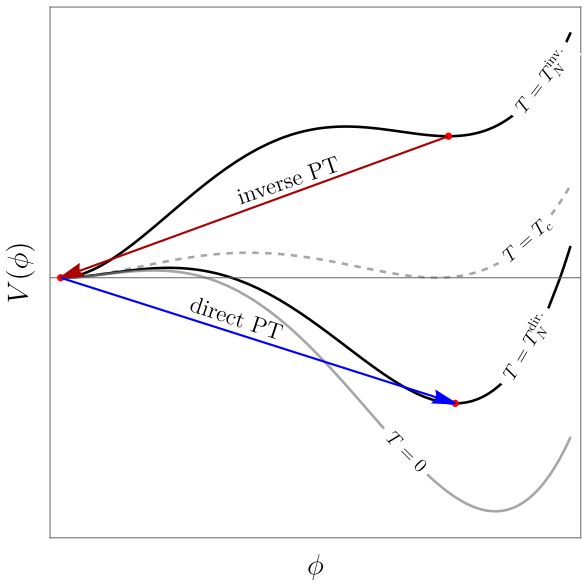

Figure 5.0.1: Schematic representation of the *thermally corrected* potential of a phase transition triggered by the vacuum energy, denoted as direct PT (blue arrow), and a phase transition against the vacuum energy, triggered by thermal corrections, referred to as inverse phase transition (darker red arrow).

origin, to the restoration of symmetries. The transition to the symmetric vacuum can then proceed via the nucleation of *inverse* bubbles expanding *against* the vacuum energy. Such a phenomenon has been studied in [208, 222] in the context of reheating after inflation, during the superheated deconfinement PTs of QCD that could occur during neutron stars mergers [223] and in some fast walls realisations of baryogenesis [224]. These "inverse" bubbles will however differ in many respects from the bubbles nucleated during direct PTs.

In this chapter, we present a thorough study of the modes of expansion of *inverse* phase transitions and discuss their energy budget. We also investigate the velocity of such bubbles. Here is a summary of the main results of our study:

- The main parameters controlling the expansion are the wall velocity ξ_w and the strength of the PT $-\alpha_N \equiv |\epsilon|/\rho_N$, where ϵ is the difference of vacuum energy, and ρ_N is the radiation energy density at the nucleation temperature T_N.

- We find five different types of consistent solutions: weak and Chapman-Jouguet (CJ) inverse deflagrations, weak and CJ inverse detonations, and inverse hybrid solutions. They however differ in several respects from their direct counterparts. In the plasma frame, the fluid velocities are typically negative (toward the inside of the bubble), meaning that the plasma is being sucked into the bubble.

- We calculate the efficiency of the energy transfer from the phase transition to the bulk flow motion, which acts as the source of gravitational waves.

- We also study the pressure exerted on inverse bubbles. We discover a hydrodynamic obstruction to the expansion of inverse phase transition, very similar to the obstruction to the expansion of direct ones. In the regime of fast bubbles, where the collisionless approach can be applied, we find a new Boltzmann suppression of the plasma pressure.

The remainder of this chapter is organised as follows: in Section 5.1 we present a review of known results of the hydrodynamics of the direct phase transitions, in Section 5.2, we present the study of the hydrodynamics of *inverse* phase transitions, in Section 5.3, we discuss the energy budget of the inverse phase transition as well as the efficiency factors. In Section 5.4, we discuss the friction effects on the bubble wall and in Section 5.4.2, the possibility of runaway solutions is discussed. Finally, we conclude in Section 5.5.

5.1 Direct phase transitions: a reminder

In this section, we review the expansion modes of a cosmological bubble that forms during a first-order PT within a primordial plasma background while the Universe cools down. This type of transition is the one considered in most cosmological applications, and it is characterised by a release of vacuum energy into the plasma. For this reason, we refer to it as *direct*. The case of *inverse* PTs against the vacuum energy will be the topic of Sec. 5.2.

5.1.1 Matching across discontinuities

The hydrodynamics of the coupled system, where a nucleated bubble expands within the primordial plasma, can be described by the conservation of the total energy-momentum tensor. The energy-momentum tensor contains two pieces: i) the scalar background, which generates the bubble wall profile that we denote ϕ, and ii) the plasma that we denote f and that we model as a perfect fluid. Those two contributions respectively read

$$T^{\mu\nu}_{\phi} = (\partial^{\mu}\phi)\partial^{\nu}\phi - g^{\mu\nu}\left[\frac{1}{2}(\partial\phi)^2 - V(\phi)\right] , \qquad \text{(scalar field component)} \tag{5.1a}$$

$$T^{\mu\nu}_{f} = (e_f + p_f)u^{\mu}u^{\nu} - g^{\mu\nu}p_f , \qquad \text{(plasma component)} \tag{5.1b}$$

where $u^{\mu} = \gamma(v)(1, \boldsymbol{v})$ is the fluid four-velocity in the plasma frame with the Lorentz boost factor $\gamma(v) = 1/\sqrt{1-v^2}$, e_f and p_f are the fluid energy density and pressure, that vanish at zero temperature. V is the effective (loop-resummed) scalar potential. However, one usually combines the fluid energy density and pressure with the effective scalar potential energy, $e = e_f + V(\phi)$, $p = p_f - V(\phi)$. The advantage of writing the energy-momentum tensors in terms of e and p is that the matching conditions for hydrodynamic quantities take the standard form that appears commonly in the literature. Note that the fluid *enthalpy* writes $w = e_f + p_f = e + p$. Therefore, in terms of e and p, the energy-momentum tensor for the fluid then takes the following form

$$T^{\mu\nu}_{f} = (e+p)u^{\mu}u^{\nu} - g^{\mu\nu}[p + V(\phi)] . \tag{5.2}$$

Then, the conservation of the energy-momentum tensor is given by

$$\nabla_{\mu}T^{\mu\nu} = \nabla_{\mu}\left(T^{\mu\nu}_{\phi} + T^{\mu\nu}_{f}\right) = 0 . \tag{5.3}$$

Hydrodynamical flows can develop discontinuities such as shock waves and reaction fronts, across which the bulk quantities undergo a jump, as pictorially presented in fig.5.1.1. The conservation equations in eq.(5.3) can then be used to derive junction conditions of these quantities. Those will serve as boundary conditions for the smooth

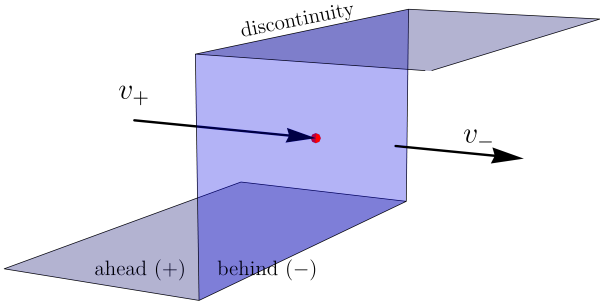

Figure 5.1.1: Pictorial representation of a discontinuity interface in the wall frame. The fluid ahead of the discontinuity, (+), is coming towards the wall in the region behind, (−). For direct PT (+) is (generically) the symmetric phase, while (−) is the broken one.

evolution of the fluid on both sides of the discontinuity. By integrating eq. (5.3) over a volume containing the interface and using Stokes' theorem, we arrive at the continuity equations governing the flow of energy-momentum

$$(T_+^{z\nu} - T_-^{z\nu})n_\nu = 0 \ , \qquad (T_+^{t\nu} - T_-^{t\nu})n_\nu = 0 \ , \tag{5.4}$$

where $n_\mu = (0,0,0,1)$ is the unit 4-vector perpendicular to the bubble interface. Under the assumption that the flux along the 3-direction is $u^\mu = \gamma(z)(1,0,0,-v(z))$, one can obtain the junction conditions

$$w_+\gamma_+^2 v_+ = w_-\gamma_-^2 v_- \ , \tag{5.5a}$$
$$w_+\gamma_+^2 v_+^2 + p_+ = w_-\gamma_-^2 v_-^2 + p_- \ , \tag{5.5b}$$

where $w \equiv e + p$ is the enthalpy and where the subscript "$\pm$" denotes quantities in front of/behind the bubble wall, so that $-$ always represents the interior of the bubble. To be explicit, $w_+ = w_s(T_+)$, $w_- = w_b(T_-)$ (and similarly for $p_\pm$), where the label "s/b" denotes the symmetric/broken phase, see fig. 5.1.1. Upon rearranging the junction conditions, we arrive at the familiar relations between the velocities, the energies and the pressures,

$$v_+ v_- = \frac{p_+ - p_-}{e_+ - e_-} \ , \qquad \frac{v_+}{v_-} = \frac{e_- + p_+}{e_+ + p_-} \ . \tag{5.6}$$

We remind that the velocities $v_\pm$ have to be understood in the *front frame* (the frame where the discontinuity is at rest). To advance and determine the solutions for the system of hydrodynamical equations, we must assume a specific equation of state (EoS) for the plasma. This EoS will represent a function that relates various thermodynamic quantities.

5.1.2 Introducing an Equation of State

To make further progress, we need to introduce an Equation of State (EoS), which for simplicity we take to be the bag EoS:

$$e_+(T) = a_+T^4 + \epsilon_+, \qquad p_+(T) = \frac{1}{3}a_+T^4 - \epsilon_+,$$
$$e_-(T) = a_-T^4 + \epsilon_-, \qquad p_-(T) = \frac{1}{3}a_-T^4 - \epsilon_-, \tag{5.7}$$

where $a_\pm$ and $\epsilon_\pm$ are constants and we used the convention $\epsilon_+ - \epsilon_- \equiv \Delta V$. Here, $a_\pm$ describes the different light degrees of freedom across the wall, and $T_\pm$ the different temperatures. One can explicitly compute the expression of the dof in the high–temperature limit, where they can be read from the thermal corrections to the effective potential:

$$a_\pm = \frac{\pi^2}{30} \sum_{i=\text{light dof}} \left[g_i^B + \frac{7}{8} g_i^F \right] , \tag{5.8}$$

where $B(F)$ stands for boson (fermion). From the EoS, it is easy to see that the relations in eq.(5.6) become

$$v_+ v_- = \frac{1-(1-3\alpha_+)r}{3-3(1+\alpha_+)r} , \qquad \frac{v_+}{v_-} = \frac{3+(1-3\alpha_+)r}{1+3(1+\alpha_+)r} , \tag{5.9}$$

where we have defined

$$\alpha_+ \equiv \frac{\epsilon_+ - \epsilon_-}{a_+ T_+^4} , \qquad r \equiv \frac{a_+ T_+^4}{a_- T_-^4} , \qquad \alpha_N \equiv \frac{\epsilon_+ - \epsilon_-}{a_+ T_N^4} , \tag{5.10}$$

with α_N characterizing the strength of the PT at the nucleation temperature T_N. It is then conventional to define the vacuum energy in the true minimum to be zero: $\epsilon_- = 0$ and $\epsilon_+ \equiv \epsilon$. Notice that by doing so we are specifying our transition to proceed from a phase with a higher vacuum energy to a phase with a lower one. This is the usual behaviour expected for a cooling phase transition, as it complies with the structure of the zero–temperature potential.

The parameter r can be eliminated from eq.(5.9) to write $v_+(v_-, \alpha_+)$,

$$v_+(v_-, \alpha_+) = \frac{1}{1+\alpha_+} \left[\left(\frac{v_-}{2} + \frac{1}{6v_-} \right) \pm \sqrt{ \left(\frac{v_-}{2} + \frac{1}{6v_-} \right)^2 + \alpha_+^2 + \frac{2}{3}\alpha_+ - \frac{1}{3} } \right] . \tag{5.11}$$

In fig. 5.1.2 are reported the two different branches $\pm$ for constant values of α_+. The left panel refers to direct PTs, with $\alpha_+ > 0$, while as we will discuss in Sec. 5.2 the right panel refers to inverse PTs, with $\alpha_+ < 0$.

Phase transitions and discontinuities are accompanied by an increase in the entropy of the plasma. We discuss the conservation of entropy current

$$\partial_\mu (s u^\mu) = 0, \qquad s \equiv \frac{w}{T} \qquad \text{(Entropy in continuous waves)} . \tag{5.12}$$

This is a reflection of the fact that the fluid in a continuous wave is in local thermal equilibrium. However, discontinuous boundaries are intrinsically dissipative and entropy will generically increase across them. Across a boundary, the following inequality has to be fulfilled:

$$s_+ \gamma_+ v_+ \leq s_- \gamma_- v_- \qquad \text{(Across discontinuities)} , \tag{5.13}$$

which imposes the increase of the entropy across the wall. Using the matching conditions in eq.(5.5), this relation can also be rephrased in the following way

$$\frac{\gamma_-}{\gamma_+} \leq \frac{T_+}{T_-} . \tag{5.14}$$

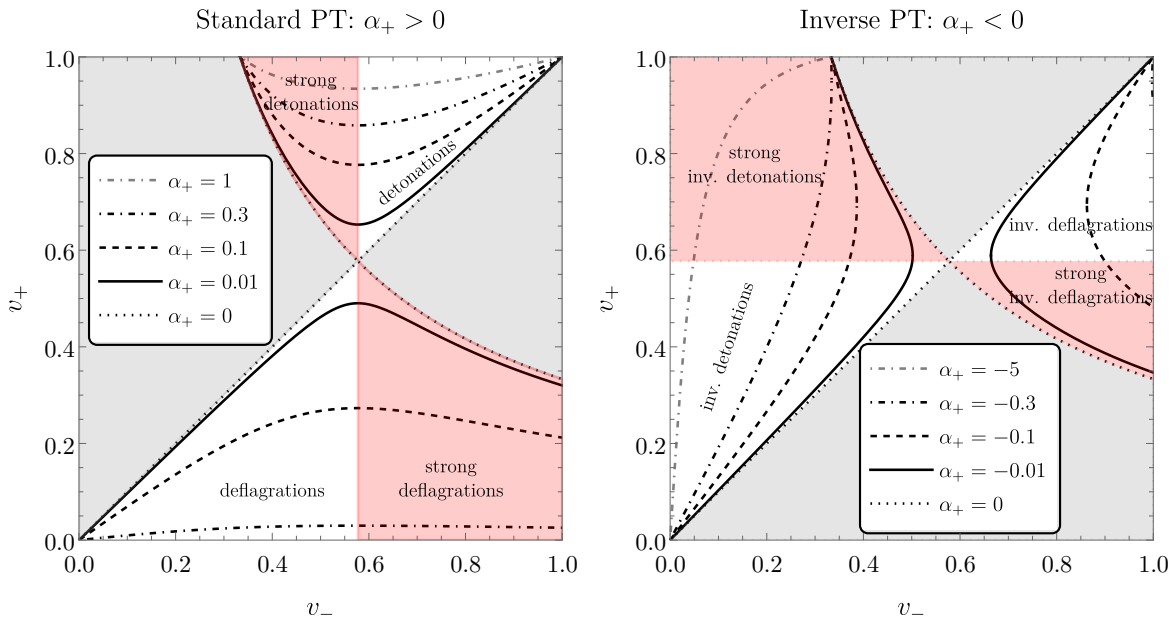

Figure 5.1.2: Left: In standard direct phase transitions with $\alpha_+ > 0$, we depict contours of constant α_+ in the allowed region in the plane (v_-, v_+), where $v_\pm$ are the fluid velocities in the wall frame. Shaded red regions indicate the presence of deflagrations and detonations, which are forbidden by hydrodynamical constraints, as we explain in the text. **Right**: Same as the left panel, but for the case of inverse phase transitions with $\alpha_+ < 0$. In the shaded red regions we similarly highlight the impossibility of strong inverse detonations ($v_+ \leq c_s$), while strong inverse deflagrations will decay to inverse hybrids.

5.1.3 The theory of discontinuities

So far we have addressed the hydrodynamic equations across discontinuities, focusing on matching conditions across the interfaces. The purpose here is to introduce the *Taub* and *reaction* adiabats that connect (and select) the physical fluid states across interfaces. In the study of phase transitions, two types of discontinuities will be relevant: i) the shock front and ii) the reaction front (or phase boundary). Additional details on the construction of the adiabats are provided in Appendix 5.C as well as in ref. [225].

Shock front The first type of discontinuity that can develop in a fluid is the shock front. It is characterised by an interface where there is no change in the chemical/physical composition of the fluid (vacuum), but there can be discontinuous jumps in the thermodynamic quantities.

The matching conditions across a discontinuity, using eq.(5.5a) and eq.(5.5b), can be expressed in the form

$$w_- x_- - w_+ x_+ = (p_- - p_+)(x_- + x_+) \ , \tag{5.15}$$

where we defined $x \equiv w/\rho^2$, being $\rho = nm$ the rest–mass density[1], which we find convenient[2] to represent in the plane (x, p). Now we need to express the $w_-(x_-, p_-)$ as a

[1]Here n is the number density and m the rest–mass of the system.

[2]In the case of nonrelativistic fluids, the shock adiabatic is typically plotted in the (V, p)-plane, with V representing the volume of the system. However, for the relativistic case, the natural variables for representing the relativistic shock adiabatic are $wV^2 = w/\rho^2$ and pc^2. Using these coordinates, the Taub adiabat offers a straightforward and graphical description of fluid properties across a shock. It can be visualised as the curve connecting the states ahead and behind a shock wave.

function of (x_-, p_-), where we consider x as the independent variable, and this can be done via the bag equation of state, describing a system for which there is no change in its microscopic nature across the interface, that is $\epsilon = 0$,

$$w_- = 4p_- \ , \qquad w_+ = 4p_+ \ . \tag{5.16}$$

Writing p_- in terms of the other quantities we obtain

$$p_- = \frac{3p_+x_+ - p_+x_-}{(3x_- - x_+)} \ . \qquad \text{(Taub adiabat)} \tag{5.17}$$

This is the *Taub* adiabat. Intuitively, the shock front can be understood as a discontinuity with vanishing latent heat $\alpha_+ \to 0$ ($\epsilon \to 0$), which implies, from eq.(5.9)

$$v_+v_- = \frac{1}{3} \ , \qquad \frac{v_+}{v_-} = \frac{3+\tilde{r}}{1+3\tilde{r}} \ , \qquad \tilde{r} \equiv \left(\frac{T_+}{T_-}\right)^4 \ , \tag{5.18}$$

since for a shock wave with no change of vev, the number of relativistic dof remains the same, i.e. $a_+ = a_-$. Finally, denoting the velocity of the shock wave $\xi_{\rm sh}$ and the velocity of the fluid after the shock wave $v_{\rm sh,-}$, we obtain the following matching conditions at the shock-wave front

$$\xi_{\rm sh} = c_s\sqrt{\frac{3+\tilde{r}}{1+3\tilde{r}}}, \qquad v_{\rm sh,-} = \frac{c_s^2}{\xi_{\rm sh}} \, . \tag{5.19}$$

The state of the plasma across a shock wave has always to lie on the same Taub adiabat. Moreover, as described in Appendix 5.C, entropy considerations require that the state of the plasma behind the shock lies on a point of the Taub adiabat with larger pressure

$$p_- > p_+ \qquad \text{(entropy increase for shocks)} \, , \tag{5.20}$$

or that the shock wave *goes up on the Taub adiabat*, as for example illustrated in fig.5.1.3 for the trajectory from the blue to the green dot.

Reaction front The second type of discontinuity is the reaction front, which is characterised by an interface where there is a change in the chemical/physical composition of the fluid. In other words, this requires a change in vacuum energy and in the equation of state, often manifested through a change in the number of relativistic degrees of freedom.

Now, using the matching conditions across a discontinuity, eq.(5.5a) and eq.(5.5b), and the bag equation of state, with $\epsilon \neq 0$, we get

$$p_- = \frac{(3p_+ + 4\epsilon)x_+ - p_+x_-}{(3x_- - x_+)} \ . \qquad \text{(reaction adiabat)} \tag{5.21}$$

This is the *reaction* adiabat. Let us notice that the reaction front clearly reduces to a shock wave in the limit $\epsilon \to 0$. Therefore, the reaction front connects states ahead of the interface, lying on the Taub adiabat, to states behind the interface, lying on the reaction adiabat.

In fig.5.1.3, we present the Taub and the reaction adiabat with the solid black and darker red line, respectively. Starting from a point (x_+, p_+) lying on the former adiabat, we can conclude that any other point on this adiabat can be reached upon crossing

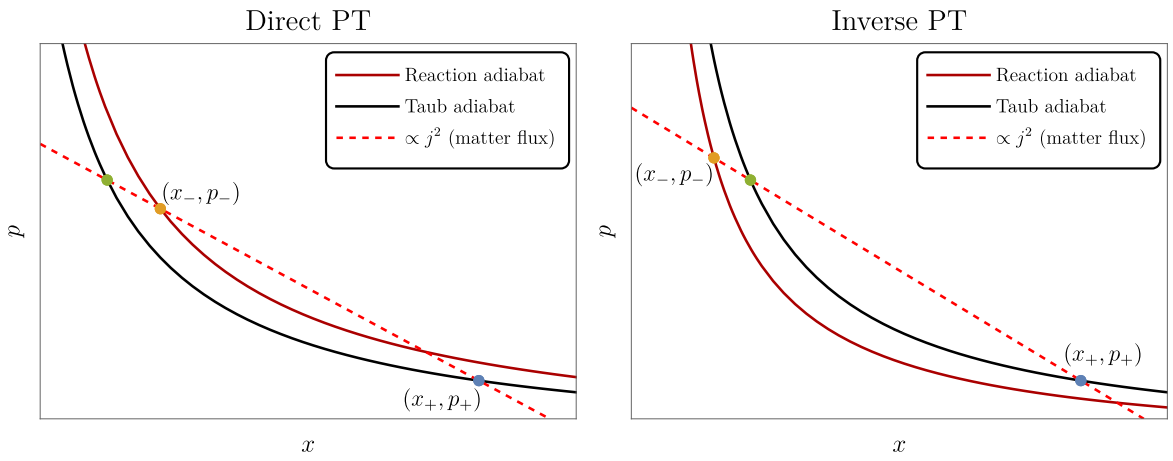

Figure 5.1.3: Left: Reaction and Taub adiabats for a direct PT. The trajectory connecting the blue dot with the green one is an example of a valid shock wave (connecting two points on the same Taub adiabat), while the trajectory connecting the blue dot to the orange one (from the Taub adiabat to the reaction one) is an example of valid reaction front with $\epsilon \neq 0$. Further details are presented in Appendix 5.C. **Right**: Same for the case of an inverse PT.

some shock wave. What selects the arrival point is the conserved flux going through the discontinuity. The matter flux j is defined by

$$\rho_+ \gamma_+ v_+ = \rho_- \gamma_- v_- \equiv j \ , \tag{5.22}$$

where, in these coordinates, it provides the slope of the chord from the initial point + on the adiabatic to any other point –, that is:

$$p_- = p_+ - j^2 (x_- - x_+) \ , \tag{5.23}$$

and it is shown with the dashed red line in fig.5.1.3. Given an initial point (x_+, p_+) (the blue dot lying on the Taub adiabat) and a straight line with the (conserved) matter flux as the slope (the dashed red line), we can obtain the state of the plasma behind the wall as the intersection between such line and the reaction adiabat (the orange dot). This shows the intuitive usefulness of such construction.

5.1.4 Hydrodynamical equations

Up to this point, we have discussed the relations between thermodynamic quantities across discontinuities. In this section, our focus shifts to examining the different types of solutions to the hydrodynamical equations and investigating their properties.

The relativistic hydrodynamics equations have been shown to allow for *self-similar* solutions. A hydrodynamic solution is said self-similar when it can be described by only two quantities with independent dimensions apart from space and time. In such cases, all relevant physical quantities can be expressed as functions of a similarity variable, typically a combination of spatial and temporal coordinates.

For large enough bubbles, when the solution reaches a terminal wall velocity, the fluid profile can be characterised by the *self-similar* variable $\xi \equiv r/t$ (for a comprehensive explanation, we refer to [225–227]). Notably, ξ possesses the dimension of a velocity but can be interpreted as a position as well. The velocity of the bubble wall, denoted as ξ_w, ranges between the centre of the bubble ($\xi \to 0$) and the lightcone ($\xi \to 1$).

Starting from the conservation of the energy-momentum tensor, projecting eq.(5.3) along and perpendicular to the flow, assuming spherical symmetry for the solutions and finally expressing the system of equations in terms of this self-similar variable, we obtain the following form

$$
\begin{aligned}
(\xi - v)\frac{\partial_\xi e}{w} &= 2\frac{v}{\xi} + [1 - \gamma^2 v(\xi - v)]\partial_\xi v \ , \qquad \text{(Euler eq.)} \\
(1 - v\xi)\frac{\partial_\xi p}{w} &= \gamma^2(\xi - v)\partial_\xi v \ . \qquad \text{(continuity eq.)}
\end{aligned} \tag{5.24}
$$

We emphasise that v denotes here the velocity of the fluid in the *plasma frame* (equivalently the centre of the bubble frame), as opposed to $v_\pm$ defined in the frame of the wall.

Combining those equations leads to the well–known equation for the fluid velocity:

$$
2\frac{v}{\xi} = \gamma^2(1 - v\xi)\left[\frac{\mu_{p\to w}^2}{c_s^2} - 1\right]\partial_\xi v, \qquad \mu_{p\to w}(\xi, v) = \frac{v - \xi}{1 - \xi v} \ , \tag{5.25}
$$

where $\mu_{p\to w}(\xi, v)$ is the Lorentz transformed fluid velocity, from the plasma to the wall frame. Two qualitatively different types of solutions emerge from the analysis of the equation eq.(5.25): i) the rarefaction wave and ii) the compression wave.

i) The rarefaction wave propagates from the head, moving at the largest velocity ξ_{head} to the tail, which moves at some smaller velocity $\xi_{\text{tail}} < \xi_{\text{head}}$. Consistency dictates that either $\xi_{\text{tail}} = c_s$ or $\xi_{\text{head}} = c_s$. While this is not true for generic flows, the symmetries of an expanding bubble dictate that the flow is at rest at the bubble centre and on the lightcone, meaning $v(\xi = 0) = v(\xi = 1) = 0$. By imposing these boundary conditions, we deduce from eq. (5.25) that for such solutions, $\partial_\xi v > 0$. Examining eq. (5.24) and focusing on the cases of interest for us, namely $\xi - v > 0$ and $\partial_\xi v > 0$, we conclude that the rarefaction waves are also decompression waves, since $\partial_\xi p > 0$, as we travel from $\xi = 1$ to $\xi = 0$, i.e. toward the centre of the bubble. Similar conclusions hold for the enthalpy w and the temperature T, which we will define, in terms of the wall velocity, at the end of this section.

ii) On the other hand, compression waves accelerate the motion of the plasma toward the centre of the bubble. The same reasoning as above indicates that the pressure, the temperature, and the enthalpy increase across the wave, as we travel toward the centre of the bubble, i.e. from $\xi = 1$ to $\xi = 0$.

Upon solving eq. (5.25) with the matching condition (5.5a), and obtaining the fluid velocity profile, we can subsequently compute the enthalpy profile

$$
w(\xi) = w(\xi_0)\ \exp\left[\int_{v(\xi_0)}^{v(\xi)} \left(\frac{1}{c_s^2} + 1\right)\gamma^2(v)\mu(\xi(v), v)\ dv\right] \ . \tag{5.26}
$$

From $\partial_\xi \ln T = \gamma^2(v)\mu(\xi, v)\partial_\xi v$, we can also obtain the temperature profile that reads

$$
T(\xi) = T(\xi_0)\ \exp\left[\int_{v(\xi_0)}^{v(\xi)} \gamma^2(v)\mu(\xi(v), v)\ dv\right] \ , \tag{5.27}
$$

where ξ_0 refers to the interface location, both for shock and reaction fronts. Properly computing the profile across the wall of the different thermodynamic quantities will be the subject of sec. 5.3.

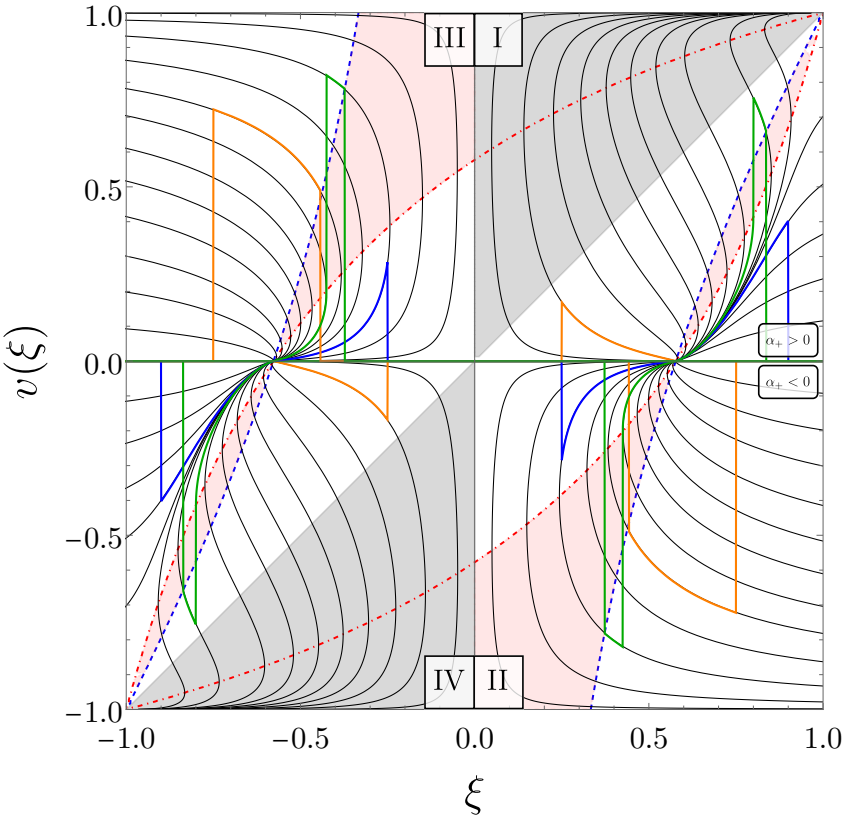

Figure 5.1.4: Profiles of the fluid velocity $v(\xi)$ in the plasma frame, both for the case of (standard) direct phase transitions ($\alpha_+ > 0$), and for inverse phase transitions ($\alpha_+ < 0$). The former case is described in the quadrant I and has $v(\xi) > 0$, while the latter is in the quadrant II with $v(\xi) < 0$. The grey shaded region is unphysical as it would imply that the fluid moves faster than the wall, $|v(\xi)| > |\xi|$. The red shaded region would similarly give unphysical velocity profiles as the dot–dashed red line indicates the maximum velocity that a detonation–type of solution can have, i.e. the sound speed in a frame moving at ξ, $v(\xi) = \mu(\xi, c_s)$. The dashed blue line shows the velocity of the shock front for deflagrations, that is $\mu(\xi_{sh}, v(\xi_{sh}))\xi_{sh} = c_s^2$. The different quadrants describe different physical systems: I) bubble and II) inverse bubble expansion as $\xi > 0$, III) droplet and IV) inverse droplet collapse with $\xi < 0$. The quadrants are related to each other by a mirror symmetry $v \to -v$ and $\xi \to -\xi$. The coloured profiles in orange, green and blue, in the I quadrant, describe a deflagration, a hybrid, and a detonation, respectively, and in the II quadrant an inverse deflagration, an inverse-hybrid, and an inverse detonation, respectively. The other profiles are obtained by symmetry (see also [225]).

Types of discontinuities for cosmological *direct* phase transitions		
	Detonations $p_+ < p_-, v_+ > v_-$	Deflagrations $p_+ > p_-, v_+ < v_-$
Weak	$v_+ > c_s, v_- > c_s$ Physical	$v_+ < c_s, v_- < c_s$ Physical
Chapman-Jouguet	$v_+ > c_s, v_- = c_s$ Physical	$v_+ < c_s, v_- = c_s$ Physical
Strong	$v_+ > c_s, v_- < c_s$ Forbidden	$v_+ < c_s, v_- > c_s$ Unstable

Table 5.1.1: Types of discontinuities for the direct phase transitions.

5.1.5 The types of solutions for direct PTs

In the previous sections, we have gathered the necessary tools to solve the thermodynamic profiles of bubbles. We now apply these tools to various modes of expansion of cosmological bubbles. As we shall see, constructing the velocity and temperature profiles of physical phase transitions requires glueing together discontinuous fronts and continuous waves.

In this section, we delineate the different types of solutions possible for direct cosmological phase transitions. In fig. 5.1.4 we present all the possible solutions of eq. (5.25). The four quadrants describe different physical situations: I) direct bubble expansion [218, 228, 229], II) inverse bubble expansion (this work), III) direct droplet collapse (see [230] for a recent study) and IV) inverse droplet collapse. In this section we will remind the solutions in quadrant I and study in depth the solutions of quadrant II in Sec. 5.2. Table 5.1.1 summarises the various flows that can exist across the discontinuity.

Direct phase transitions admit three bubble expansion modes: i) detonations ii) deflagrations and iii) hybrid solutions.

Detonations

In phase transitions proceeding as detonations, the wall moves colliding with the fluid at rest in front of it. In the wall frame, the fluid ahead of the wall moves at $v_+ = \xi_w$, and upon entering the new phase, it slows down to $v_- < v_+$. Detonations lie in in the upper half plane of the left panel of fig. 5.1.2.

To achieve a consistent solution, this setup needs a composition of a reaction front located at ξ_w, followed by a rarefaction wave. The fluid velocity right after the wall passage jumps to $v(\xi_w) = \mu(v_+, v_-)$ and then gradually slows down until it smoothly reaches zero at $\xi = c_s$. In this scenario, according to the junction conditions, we observe that $T_+ = T_N < T_-$ and $\alpha_+ = \alpha_N$. A family of solutions is parameterised by the parameter r, and we have indicated by T_N the nucleation temperature at which the bubbles nucleate.

In principle, three possible classes of detonations exist depending on v_-. *Weak* detonations exhibit $v_- > c_s$. In this case, the reaction front of the detonation is a *weak discontinuity* and its trajectory on the reaction adiabat is depicted in the left panel of fig.5.C.2. The *Chapman-Jouguet* (CJ) detonations have $v_- = c_s$. On the other hand, *strong* detonations have $v_- < c_s$, which display a strong discontinuity. The trajectory on the reaction adiabat of a strong discontinuity is presented in the left panel of fig. 5.C.3.

The velocity profile, in the plasma frame, for a weak detonation, is illustrated in the left panel of fig. 5.1.5.

Impossibility of strong detonations In this paragraph, we review why strong detonations are not feasible for cosmological phase transitions. This impossibility stems from the boundary conditions, which impose that the velocity asymptotically approaches

zero both far from the bubble and at its center [218]. This requirement translates to $v(\xi = 0) = v(\xi \to c_s) \to 0$ and $v(\xi = 1) = 0$. The resulting impossibility of strong detonation is readily apparent from eq. (5.25). Indeed, in the case of detonations, $v > 0$, and the decrease of velocity, $\partial_\xi v > 0$, from the position of the front $\xi > c_s$ to c_s is only possible if

$$\left[\frac{\mu_{p\to w}^2}{c_s^2} - 1\right] > 0\,, \tag{5.28}$$

which conversely requires that

$$|\mu_{p\to w}(\xi, v)| = \frac{\xi - v}{1 - \xi v} \equiv v_- > c_s\,. \tag{5.29}$$

From these considerations, we conclude that strong detonations with $v_- < c_s$ cannot satisfy the boundary conditions of a bubble with vanishing bulk velocity at the centre.

Deflagrations

For phase transitions described by deflagrations, the plasma is at rest immediately behind the wall, so the wall velocity is $\xi_w = v_-$. These solutions correspond to the lines in the lower half plane of the left panel in fig. 5.1.2, with the fluid velocity being higher behind the wall than in front, $v_- > v_+$. The fluid velocity in front of the wall jumps to $v(\xi_w) = \mu(v_-, v_+)$. Since $v_- > v_+$, we have $v(\xi_w) < \xi_w$, causing the deflagration solution profile to start below the line $v = \xi$, as shown in quadrant I of fig. 5.1.4.

These solutions are constructed from the combination of a shock wave, followed by a compression wave, and finally, the reaction front, as depicted on the right panel of fig. 5.1.5. Similarly to detonations, deflagrations can, in principle, be weak $v_- < c_s$ (see right panel of fig. 5.C.2 to see the trajectory on the reaction adiabats of the weak discontinuity), strong $v_- > c_s$ (right panel of fig. 5.C.3), or Chapman-Jouguet type $v_- = c_s$.

In the case of *subsonic* deflagrations, the wall velocity is $v_- = \xi_w < c_s$, leading to the conclusion that these deflagrations are weak. However, this is not the case if the deflagration is supersonic (yet slower than the Jouguet velocity) [219].

Impossibility of strong deflagrations It has been argued that strong (supersonic) deflagrations are forbidden [218, 219], primarily through two distinct arguments: stability and entropy law. The first argument, reviewed in Appendix 5.A, concludes that even if a supersonic deflagration can indeed be made to exist at some moment, it is inherently unstable with respect to perturbations. The second argument relies on the increase of entropy. In fig. 5.C.3, we show how a *strong* deflagration (left panel, blue to orange dot trajectory) can be seen as a shock (blue to green trajectory), followed by a *weak* detonation (green to orange trajectory). It is instructive to compare with the case of a strong detonation (right panel, blue to orange trajectory), which can be seen as a shock (blue to green trajectory) followed by a weak deflagration (green to orange trajectory).

But what is the nature of the shock wave in each case? For the strong detonation we observe that the shock (blue to green) goes up on the adiabat, constituting an *entropy-increasing* shock wave and satisfying the conditions in eq.(5.20). This makes the strong detonation seemingly viable[3]. However, in the case of deflagrations, where we have a

[3]As mentioned before, strong detonations are however not compatible with the boundary conditions of the nucleated bubble.

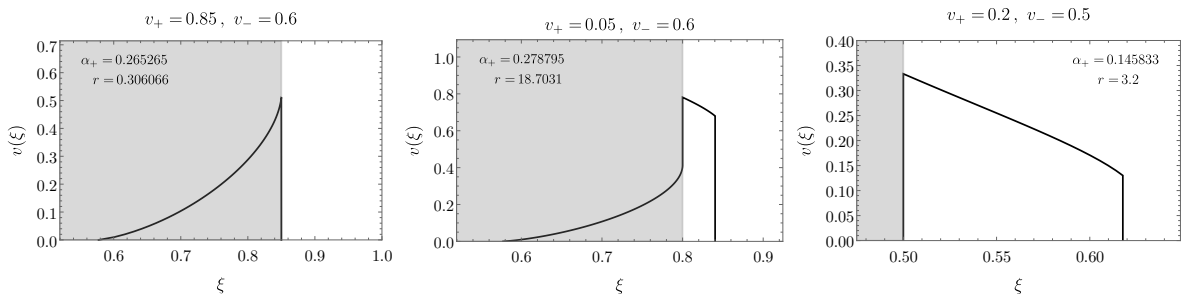

Figure 5.1.5: Velocity profiles for detonations (left), hybrids (middle) and deflagrations (right). The gray shaded region indicates the interior of the bubble.

shock from blue to green, going down on the adiabat, it consequently decreases entropy and violates the conditions in eq. (5.20). Due to these two reasons, we conclude that strong deflagrations are not viable modes of expansion of bubble walls. We however emphasise, as discussed in [219], that the nature of the cosmological phase transitions might allow for a direct jump between the blue and the orange point, making our argument inconclusive. In any case, we expect the stability argument to hold for cosmological phase transitions as well.

Hybrids

The previous reasoning by which strong deflagrations are forbidden does not necessarily mean that a supersonic deflagration–type of transition cannot exist. Although a solution with $v_- < c_s$ and $v_+ > c_s$ is unstable, the closest stable solution has $v_- = c_s$ and $v_+ > c_s$[4]. This type of solution can be achieved by combining a Chapman-Jouguet deflagration with a rarefaction wave behind the wall, ensuring the fulfilment of boundary conditions. This configuration is termed *hybrid solution* (or supersonic deflagration [219]), which become stable when $v_- = c_s$. In the middle panel of fig.5.1.5, we present an example of such a hybrid composition.

Evolving through the different profiles

When discussing the various modes of bubble expansion, it is more physical to fix the strength of the phase transition, α_N, and solve for all the other quantities in terms of it. Having fixed the strength there will be only one possible fluid profile for a given wall velocity. In fig. 5.1.6, we present the evolution of v_+ ans v_- as a function of ξ_w. Since α_N is not directly specified as an input parameter in the matching conditions, we conducted a scan over v_+ and v_- to determine which combination gives the appropriate α_N. Consequently, we also calculated α_+/α_N and the position of the shock wave, ξ_{sh}. The vertical grey lines indicate the speed of sound, c_s, and the Jouguet velocity, which represents the velocity distinguishing the fastest hybrid solution from the slowest detonation. We will properly define the Jouguet velocity in section 5.2.3. In the right panel, we illustrate the

[4]To be more precise, the condition $v_- = c_s$ is determined by the stability criteria for perturbations. As discussed in Appendix 5.A, linear perturbation analysis shows that for a deflagration front to be stable, we require $v_- \leq c_s$. Conversely, to ensure that the detonation solution is not double-valued, we need $v_- \geq c_s$. Therefore, to maintain a well-defined and stable front, it is necessary to have $v_- = c_s$. For a more rigorous treatment, one should also verify the stability of the deflagration front under *corrugation* (deformation or perturbation of the front, such as waves or ripples). This has been addressed (perturbatively) in [225], which demonstrates that the deflagration front remains stable if appropriate boundary conditions are specified for the velocity of the reaction front.

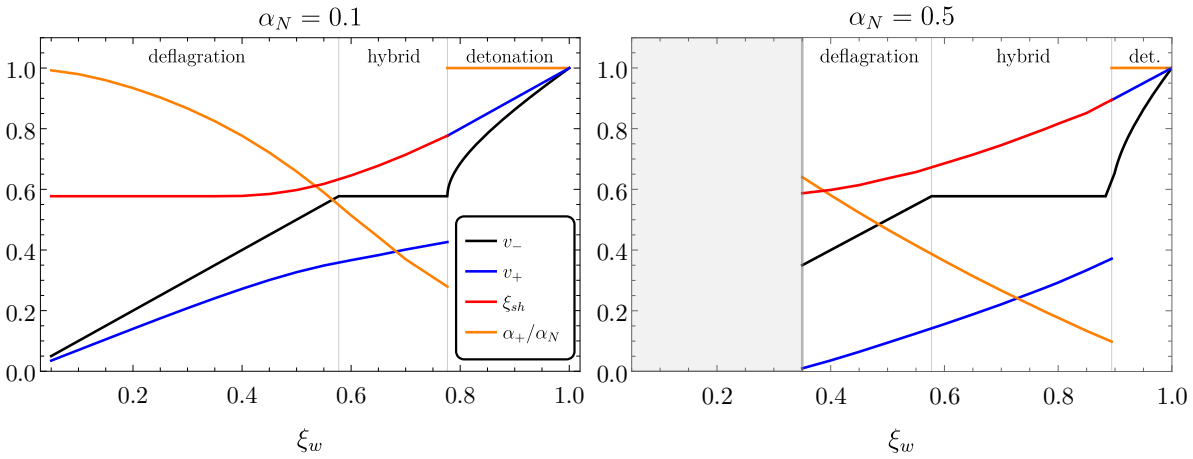

Figure 5.1.6: The quantities α_+/α_N, and v_+, v_-, ξ_{sh} as a function of ξ_w for fixed values of $\alpha_N = 0.1, 0.5$ varying the wall velocity. For deflagrations $\xi_w = v_-$, for hybrids neither v_+ nor v_- can be identified as the wall velocity, while for detonations $\xi_w = v_+$. The vertical lines represent the sound speed and the Jouguet velocity.

scenario where for sufficiently large values of α_N a solution with ξ_w within the grey band cannot be found. In other words, there cannot exist a (slow) deflagration compatible with such a (large) α_N.

Now that we have examined the relevant characteristics of the solutions for an expanding bubble during a direct phase transition and we have set all the necessary notation, we are ready, in the next section, to explore the second quadrant of fig. 5.1.4, which describes the case of bubble expansion during an inverse phase transition.

5.2 Inverse phase transitions

After reviewing the hydrodynamic solutions of direct PTs, we now turn to our main interest, namely the *inverse* PTs. These occur from a phase with vanishing vacuum energy to another phase with (positive) vacuum energy. We will follow the same presentation as before and identify all the expansion modes of inverse PTs.

5.2.1 Motivation and basics

When the system finds itself in a minimum with zero vacuum energy, typically located away from the origin of the potential, it may still be advantageous to transition to a state with non–zero vacuum energy, albeit with more relativistic (light) degrees of freedom.

How can this be realised? The simplest setup is the one where a direct transition proceeds in the opposite direction, namely if we simply heat up the zero–temperature phase as considered in ref. [208] in the context of reheating. If we stick to this picture, we do not need to go beyond the bag EoS. In fact, one can write the pressure in the broken and symmetric phases as in eq. (5.7) but inverting the roles of $\epsilon_\pm$, so that one can have a supercooled or superheated PT depending on which branch the system is coming from. Notice that if the two phases are well–defined in the temperature range relevant for a direct transition, they are typically well–defined for the inverse transition as well, as both transitions are supposed to take place around the same critical temperature. Therefore, if the direct PT is not extremely supercooled, also the inverse PT should be well established provided it is not extremely superheated.

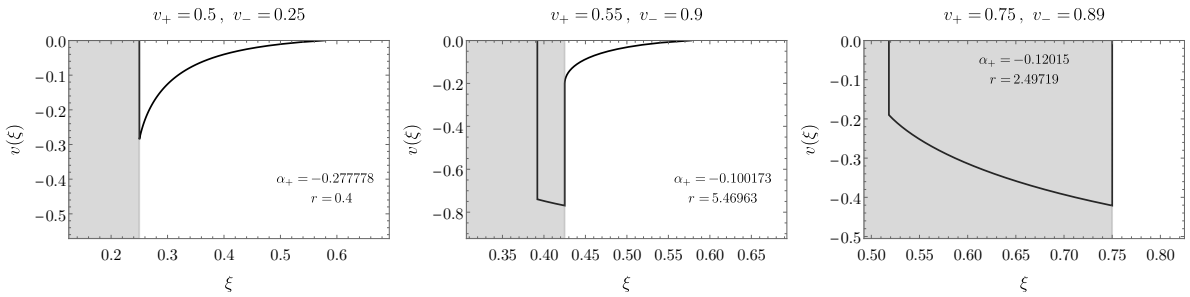

Figure 5.2.1: Velocity profiles for inverse detonations (left), inverse hybrids (middle) and inverse deflagrations (right).

Types of discontinuities for cosmological *inverse* phase transitions		
	Inverse Detonations $(p_+ < p_-, v_+ > v_-)$	Inverse Deflagrations $(p_+ > p_-, v_+ < v_-)$
Weak	$v_+ < c_s, v_- < c_s$	$v_+ > c_s, v_- > c_s$
Chapman-Jouguet	$v_+ = c_s, v_- < c_s$	$v_+ = c_s, v_- > c_s$
Strong	$v_+ > c_s, v_- < c_s$	$v_+ < c_s, v_- > c_s$

Table 5.2.1: Types of discontinuities for the inverse phase transitions.

The matching conditions of the inverse PT remain formally the same as in the direct case and we can refer to Sec. 5.1.1. As before, in order to complete the set of equations, we need to introduce an equation of state relating the various thermodynamic quantities. Keeping the same convention as in the previous section, for an inverse phase transition we require that the inside of the bubble $-$ expands into the outside of the bubble $+$, and the EoS takes the form in eq. (5.7). Since the matching conditions across the wall are formally unchanged once they are written in terms of the enthalpy and the velocities in the wall frame, the relations in eq. (5.9) still hold.

However, sticking to the definitions of eq. (5.10) for α_+ and r, one finds that inverse PTs display negative α_+:

$$\alpha_+ = \frac{\epsilon_+ - \epsilon_-}{a_+ T_+^4} = -\frac{\epsilon}{a_+ T_+^4} \ , \tag{5.30}$$

where here $\epsilon_+ = 0$ and $\epsilon_- \equiv \epsilon$. From now on, we will stick to the following characterisation: direct PTs have $\alpha_+ > 0$ while inverse PTs have $\alpha_+ < 0$.

Following the same steps as before and eliminating the pressures and the r parameter in favour of α_+ and v_-, we obtain the same relation between the velocities

$$v_+(v_-, \alpha_+) = \frac{1}{1 - |\alpha_+|}\left[\left(\frac{v_-}{2} + \frac{1}{6v_-}\right) \pm \sqrt{\left(\frac{v_-}{2} + \frac{1}{6v_-}\right)^2 + \alpha_+^2 - \frac{2}{3}|\alpha_+| - \frac{1}{3}}\right] , \tag{5.31}$$

with the only difference that α_+ is now negative. Notice that the limit $\alpha_+ \to -1$ is actually smooth. The isocontours with constant α_+ are reported in the right panel of fig. 5.1.2.

5.2.2 The types of solutions for inverse PTs

Similarly to the case of direct phase transitions, we expect that several types of fluid solutions can exist for inverse phase transitions. We found five different possible expansion

modes, analogously to the direct case, that we called: i) inverse detonations (weak and CJ), ii) inverse deflagrations (weak and CJ), and iii) inverse hybrids, displayed in the left, right, and middle panels, respectively, of fig. 5.2.1. Our naming of *inverse* detonations and deflagrations relies on the mirror symmetry that can be drawn from fig. 5.1.4 [5].

Inverse Detonations

The first possibility, in analogy with detonations, would be to build an *inverse detonation* by glueing a reaction front with $\xi_w = v_- < c_s$ and a rarefaction wave going from $v(\xi_w^+)$ to 0 at $\xi = c_s$. In the plasma frame, the velocity $v(\xi_w^+) = \mu(v_-, v_+)$ with $v_- < v_+$ is always negative. Notice however that since ξ is positive the bubble is actually expanding. As one can see from eq. (5.24), across the rarefaction wave, namely from $\xi = c_s$ to $\xi = \xi_w$, the pressure as well as the velocity decreases. Such solutions are displayed in the left panel of fig. 5.2.1.

For this type of wave with $v_- = \xi_w < c_s$, there are in principle three solutions for v_+, see the right panel of fig. 5.1.2: $v_+ < c_s$, which we call the *weak* inverse detonation, the CJ solution $v_+ = c_s$ and $v_+ > c_s$, which we call the *strong* inverse detonation. The corresponding trajectories in terms of reaction adiabats are shown in fig. 5.C.4 and fig.5.C.5.

Impossibility of strong inverse detonations Similarly to the case of direct strong detonations, one can show that inverse strong detonations are not compatible with the boundary conditions of the bubble. Taking into account that the fluid velocity is always negative, $v(\xi) \leq 0$, and requiring that $v(\xi \to c_s) \to 0$, one has $\partial_\xi v > 0$. From eq. (5.25) this implies that the velocity increases from the phase boundary to the outside of the bubble, so that $\left[\frac{\mu^2_{p\to w}}{c_s^2} - 1\right] < 0$ is required by the boundary conditions. This yields

$$|\mu_{p\to w}| = \frac{\xi - v}{1 - \xi v} \equiv v_+ < c_s \,, \tag{5.32}$$

where the subscript $p \to w$ means that we go from the plasma frame to the wall frame. We then conclude that strong inverse detonations are not compatible with our boundary conditions. This leaves the weak and CJ inverse detonations as the only physical solutions.

Inverse Deflagrations

A second type of solutions are *inverse deflagrations*, where we glue a reaction front with $v_+ = \xi_w$ and $v_- > c_s$ followed by a compression wave ending with a shock front. A typical fluid profile can be seen in the right panel of fig. 5.2.1. As we can see, these solutions are characterised by the fluid being sucked inside the bubble. This can be physically interpreted by noticing that, upon entering the bubble, particles losing their mass receive a kick toward the centre (as we shall see in Sec. 5.4), which then accelerates the fluid inward.

There are three possible solutions for inverse deflagrations depending on the value of v_+: $v_+ > c_s$ dubbed *weak* inverse deflagration, the CJ solution with $v_+ = c_s$, and the *strong* inverse deflagration with $v_+ < c_s$. The corresponding trajectories in terms of reaction adiabats can be found in fig. 5.C.4 and fig. 5.C.5.

[5] The distinguishing physical characteristic of detonations setting it apart from deflagrations, as stated in [231], is that the fluid just behind the reaction front is in motion rather than the propagation exceeding the speed of sound. The mirror symmetry flips this physical interpretation, as for instance for inverse detonations the fluid will be in motion ahead of the reaction front.

The impossibility of strong inverse deflagrations As for the case of direct PTs, strong inverse deflagrations can be argued to be forbidden by two arguments.

The first argument is about stability, and in Appendix 5.A we argue that strong inverse deflagrations cannot be stable by following the same reasoning as for direct PTs.

As a second argument, we can consider the behaviour of entropy across a strong inverse deflagration front. Referring to the right panel of fig. 5.C.5, we can interpret a strong inverse deflagration (blue to orange) as composed of a shock wave (blue to green) followed by a weak deflagration (green to orange). This is however forbidden, as the shock would imply negative entropy production (the pressure decreases across the shock)[6]. We again warn the reader that this second argument might not hold because of the nature of cosmological PTs.

Inverse Hybrids

The closer stable solution to a strong inverse deflagration is a CJ inverse deflagration with $v_+ = c_s$, which we dub *inverse hybrid*. Notice that here, contrarily to direct hybrids, it is the upstream velocity (v_+) that is fixed to the speed of sound. To build the velocity profile we glue a rarefaction wave to a detonation front, followed by a compression wave and finally a shock wave. This is shown in the middle panel of fig. 5.2.1. Moreover, the requirement that the shock wave is evolutionary (increases entropy) with $v_{-,sh} < c_s$ and $v_{+,sh} > c_s$, in the shock frame, imposes that $v_- > c_s$[7].

Fixing $v_+ = c_s$ actually sets an upper bound on $|\alpha_+|$. In particular, we find that for $|\alpha_+| \geq 2/\sqrt{3}-1 \sim 0.15$ inverse hybrids cannot be achieved. This is because these solutions are constrained to be in the region dubbed "strong inverse deflagration" in fig. 5.1.2, and by writing α_+ in terms of v_+ and v_-, we get from (5.11) that

$$\alpha_+(v_+, v_-) = \frac{(v_- - v_+)(1 - 3v_+v_-)}{3v_-(1 - v_+^2)} \ . \tag{5.33}$$

By setting $v_+ = c_s$, and the extremal value $v_- = 1$ in eq. (5.33), we obtain the largest possible $|\alpha_+|$ as $|\alpha_+^{\text{max, hybrid}}| = |\alpha_+(c_s, 1)|$.

We also find that the wall velocity of the inverse hybrid solution must satisfy

$$c_s^2 < \xi_w < c_s \ . \tag{5.34}$$

The lower bound comes from the fact that the slowest possible inverse hybrid is set by the slowest possible shock, that is the intersection of the blue dashed line with the horizontal axis $v(\xi) = -1$ in the quadrant II of fig. 5.1.4. This reads

$$\mu(\xi_w, v(\xi_w))\xi_w = c_s^2 \quad \overset{v=-1}{\longrightarrow} \quad \xi_w^{\text{min, hybrid}} = c_s^2 \ . \tag{5.35}$$

The upper bound comes from the fact that for $\xi_w > c_s$ there always exists an inverse deflagration which is stable.

[6] Similar considerations would show that strong inverse detonations are instead allowed in principle, even though incompatible with the required boundary conditions for the bubble as discussed above.

[7] Notice that in principle, another hybrid solution exists with $v_- < c_s$ and $v_+ = c_s$. However, this solution would require a shock wave behind the wall with $v_{sh,-} < c_s$ and $v_{sh,+} < c_s$, which is however forbidden by the thermodynamics of shocks.

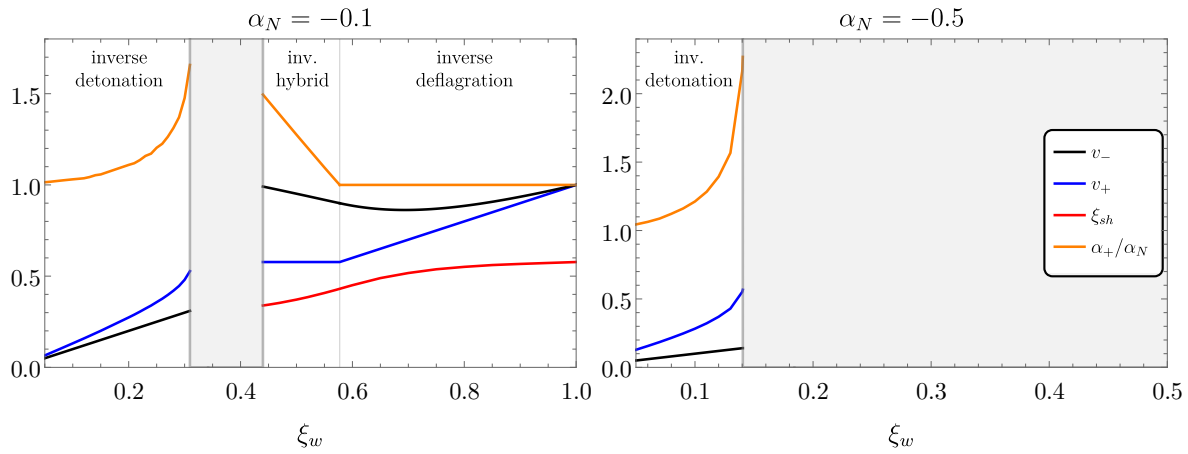

Figure 5.2.2: The quantities α_+/α_N, and v_+, v_-, ξ_{sh} for fixed $\alpha_N = -0.1, -0.5$ varying the wall velocity. The colour coding is the same as in fig. 5.1.6. For inverse detonations we can identify $\xi_w = v_-$, for inverse hybrids neither v_+ nor v_- can be identified with the wall speed, while for inverse deflagrations $\xi_w = v_+$. We can see that for large enough $|\alpha_N|$, a window opens up where no consistent solution can be found. For $\alpha_N < -1/3$, as in the right panel, only inverse detonations are allowed.

5.2.3 The Jouguet velocity for the transition between detonation and hybrid

In the context of direct phase transitions, the Jouguet velocity defines the wall velocity, $\xi_w = \xi_J^{\rm direct}$, for which the hybrid solution becomes a detonation, i.e. the velocity for which the bubble wall catches up with the shock wave. It reads

$$\xi_J^{\rm direct} = c_s \left(\frac{1 + \sqrt{3\alpha_N \left(1 - c_s^2 + 3c_s^2 \alpha_N\right)}}{1 + 3c_s^2 \alpha_N} \right), \tag{5.36}$$

which is obtained by substituting $v_- = c_s$ into eq.(5.11), and we have identified $\alpha_+ \equiv \alpha_N$ since the fluid to the right of the wall is at rest.

By a similar reasoning, in this section, we determine the inverse Jouguet velocity, $\xi_J^{\rm inv}$, which separates a pure inverse detonation from an inverse hybrid solution so that if $\xi_J^{\rm inv} < \xi_w < c_s$ the bubble grows as an inverse hybrid. To this end, we remind the reader that for an inverse detonation, one has

$$v_- = \xi_w < v_+ < c_s, \tag{5.37}$$

while the inverse hybrid solution implies

$$v_- > c_s \ , \qquad v_+ = c_s \ , \qquad c_s^2 < \xi_w < c_s \, . \tag{5.38}$$

We can now look for the wall velocity such that inverse detonations become impossible. Starting from $v_+ < c_s$ for a weak inverse detonation, the transition to a *forbidden* strong inverse detonation occurs when $v_+ > c_s$, so that the fastest allowed inverse detonation is given by the limit $v_+ \to c_s$. To find $\xi_J^{\rm inv}$ we can then set $v_- = \xi_J^{\rm inv}$ and $v_+ = c_s$ in eq. (5.11) to obtain

$$c_s = \frac{1}{1 - |\alpha_+|} \left[\left(\frac{\xi_J^{\rm inv}}{2} + \frac{1}{6\xi_J^{\rm inv}} \right) - \sqrt{\left(\frac{\xi_J^{\rm inv}}{2} + \frac{1}{6\xi_J^{\rm inv}} \right)^2 + \alpha_+^2 - \frac{2}{3}|\alpha_+| - \frac{1}{3}} \right], \tag{5.39}$$

which implicitly gives $\xi_J^{\rm inv}$ as a function of $|\alpha_+|$.

Notice that for an inverse hybrid solution, the region in front of the wall has a non–vanishing fluid velocity and one cannot identify α_+ with α_N. The latter needs to be solved for once we have fixed the strength of the PT. The value of $\xi_J^{\rm inv}$ as a function of the wall velocity resulting from this procedure is shown by the red dashed line in the right panel of fig. 5.3.2.

In fig. 5.2.2, we show the evolution of v_+, v_- (defined at the reaction front), the ratio α_+/α_N, and the position of the shock ξ_{sh}, as a function of the wall velocity ξ_w for the case of inverse phase transitions. Here we observe a gap of velocities between inverse detonations and inverse hybrids that cannot be realised for a given value of α_N. The gap widens as $|\alpha_N|$ increases, and for $\alpha_N < -1/3$ the forbidden region extends to all the inverse hybrids and inverse deflagrations, leaving the inverse detonations as the only possible solutions.

5.3 Energy budget of phase transitions

In this section, we examine the energy budget of inverse PTs. We begin by reviewing the direct PT case and calculating the enthalpy and other thermodynamic quantities for the various solutions. We then compute the efficiency factor, which quantifies how much of the available energy is converted into bulk fluid motion, thereby contributing to the production of GWs. Finally, we will present a similar analysis for inverse PTs and highlight the main differences.

5.3.1 Thermodynamic quantities for direct PTs

As discussed already in Sec. 5.1, once the fluid velocity profile is known it is possible to build the corresponding enthalpy and the temperature profiles. As these profiles are discontinuous at the wall and at the position of the shock, we need to use the junction condition in (5.5a) to provide a full characterisation. We consider the three types of solutions for the fluid and collect all the necessary results in Appendix 5.B. The resulting profiles are shown in the top row of fig. 5.3.1.

Efficiency factor The conservation of the energy–momentum tensor from eq. (5.3) tells us how much of the initial energy is converted into bulk fluid motion. We are interested in such a quantity because the kinetic energy density of the fluid, given by

$$\rho_{\rm kin} \propto v^2\gamma^2 w\,, \tag{5.40}$$

controls the amplitude of the GW signal from the PT. It is useful to split the conservation of energy in the following way:

$$\underbrace{\frac{\xi_w^3}{3}\epsilon}_{\text{vacuum energy}} + \underbrace{\frac{3}{4}\int w_N\xi^2 d\xi}_{\text{initial thermal energy}} = \underbrace{\int \gamma^2 v^2 w\xi^2 d\xi}_{\text{fluid motion}} + \underbrace{\frac{3}{4}\int w\xi^2 d\xi}_{\text{final thermal energy}}\,, \tag{5.41}$$

The integration range in eq. (5.41) needs to include all the regions of space where the fluid is perturbed ($v \neq 0$) for the conservation to hold. This is interpreted as the fact that the released vacuum energy and the initial thermal energy are converted into bulk fluid kinetic energy and thermal energy after nucleation. By defining

$$\rho_N \equiv \frac{3}{4}\int w_N\xi^2 d\xi\,, \qquad \rho_{\rm kin} = \int \gamma^2 v^2 w\xi^2 d\xi\,, \tag{5.42}$$

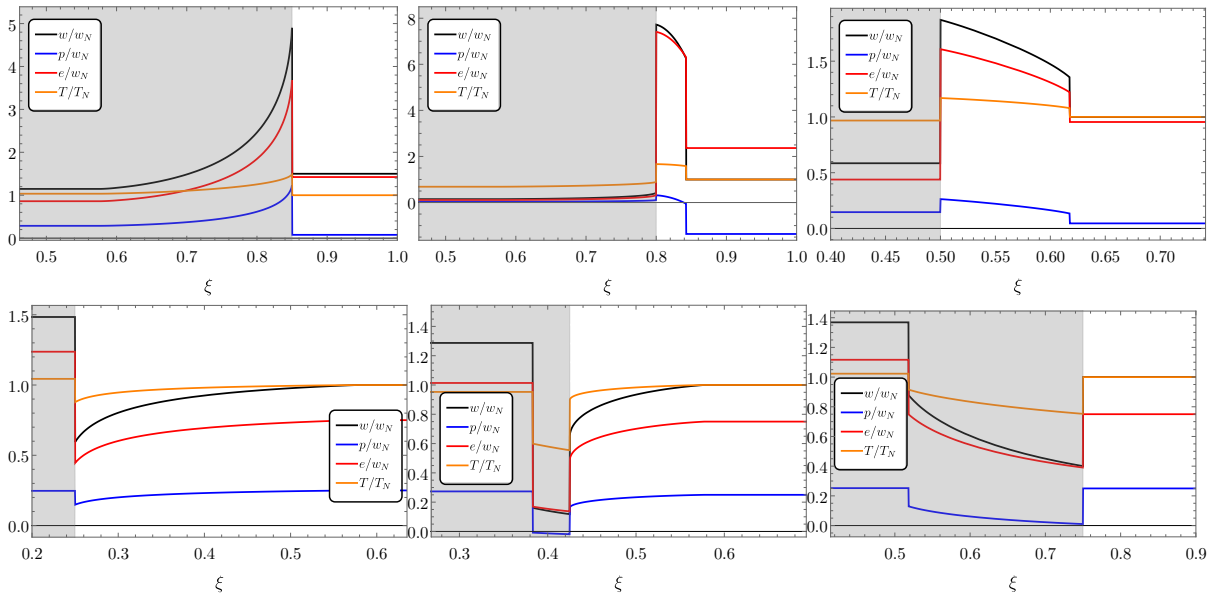

Figure 5.3.1: **Top**: Enthalpy, pressure, energy and temperature profiles across the bubble wall for detonations (left), hybrids (middle), and deflagrations (right). These correspond to the velocity profiles shown in fig. 5.1.5. The enthalpy and the temperature are normalised to w_N and T_N. For the temperature profiles, we have chosen $a_+/a_- = 1.5$. **Bottom**: Same as in the top row but for inverse PTs, for solutions corresponding to the profiles in fig. 5.2.1. For the temperature profiles, we have chosen $a_+/a_- = 0.8$.

one can introduce the *efficiency* parameter $\kappa_{\rm direct}$,

$$\frac{\rho_{\rm kin}}{\rho_{\rm tot}} \equiv \kappa_{\rm direct} \frac{\alpha_N}{1+\alpha_N} \ , \tag{5.43}$$

where $\rho_{\rm tot}$ is the total energy before nucleation, i.e. the LHS in eq. (5.41), and we have related the various quantities to α_N defined in eq. (5.10) via the bag EoS. The parameter $\kappa_{\rm direct}$ defined in this way is a measure of the efficiency for transferring the initial vacuum energy into bulk fluid motion and takes the form

$$\kappa_{\rm direct} = \frac{3}{\epsilon \xi_w^3} \int \gamma^2 v^2 w \xi^2 d\xi \ . \tag{5.44}$$

The fraction of the total energy going into thermal energy can then be directly estimated by $1 - \kappa_{\rm direct}$.

The numerical results for $\kappa_{\rm direct}$ are displayed in the left panel of fig. 5.3.2, where we actually plot the combination $\kappa_{\rm direct}\, \alpha_N/(1+\alpha_N)$ for a better comparison with the inverse case. The solid black lines are the isocontours with the same α_N, varying the wall velocity. We can note that the top right corner, where we have the fastest hybrid solutions, is the most efficient in converting the released vacuum energy into kinetic energy, saturating almost to 1 for $\alpha_N \gg 1$. The red dot-dashed line is the Jouguet velocity, defined in eq. (5.36), while the grey dashed line indicates the sound speed. It is worth noticing that not for every set of parameters a solution with a specific efficiency can be found. This is represented by the red shaded region, where no solution is available. This behaviour is similar to the right panel of fig. 5.1.6, where the grey shaded region was signalling that no solution could be found for a certain choice of α_N and ξ_w.

We also checked numerically energy conservation, eq. (5.41), which can be rewritten

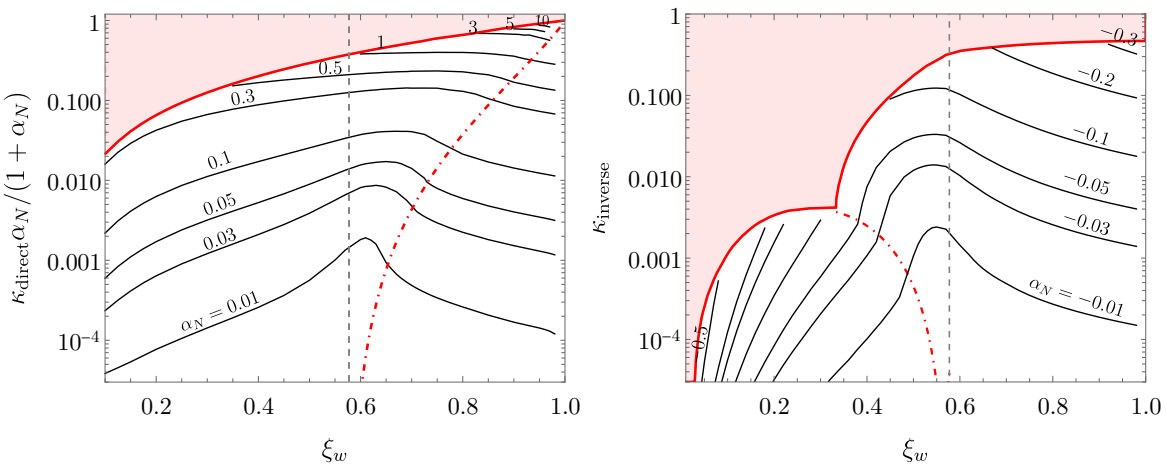

Figure 5.3.2: Efficiency factor for converting the energy budget into bulk fluid motion for direct PTs (left) and in the inverse case (right). The red dashed line is the Jouguet velocity. The red shaded region shows where no consistent solution with such a choice of wall velocity and efficiency can be found.

as

$$\int_0^1 \left[\left(\gamma^2 - \frac{1}{4}\right) w - \frac{3}{4} w_N\right] \xi^2 \, d\xi = \frac{\epsilon}{3} \xi_w^3 \, . \tag{5.45}$$

5.3.2 Thermodynamic quantities for inverse PTs

In this section, we aim to build the profiles for the thermodynamic quantities of interest for the inverse PTs. All the details are collected in Appendix 5.B and the profiles for the inverse transitions are presented in the bottom row of fig. 5.3.1.

Efficiency factor For the inverse PTs, we start by considering the energy density before the nucleation event to be the one of radiation,

$$\rho_{\rm tot} = e_R = \frac{3}{4} w_N \, , \tag{5.46}$$

where w_N is the enthalpy of the + phase at the nucleation temperature. On the other hand, the kinetic energy density of the fluid is given by

$$\rho_{\rm kin} \propto v^2 \gamma^2 w \, . \tag{5.47}$$

It is again instructive to split the conservation of energy. For the inverse PTs, we obtain

$$\underbrace{\frac{3}{4}\int w_N \xi^2 d\xi}_{\text{initial thermal energy}} = \underbrace{\frac{\xi_w^3}{3}\epsilon}_{\text{vacuum energy}} + \underbrace{\int \gamma^2 v^2 w \xi^2 d\xi}_{\text{fluid motion}} + \underbrace{\frac{3}{4}\int w \xi^2 d\xi}_{\text{final thermal energy}} \, , \tag{5.48}$$

where wrt to the standard case we see that the total amount of energy at our disposal is the initial thermal energy that will be converted not only into kinetic and final thermal energy, but also into vacuum energy. Indeed, it is apparent from eq. (5.48) that inverse phase transitions are happening “against the vacuum" and would not be possible at zero temperature.

In order to understand what are the appropriate boundaries of integration, we can consider the total enthalpy before nucleation inside a sphere that will contain all the space affected by the fluid perturbation after nucleation. This sphere has radius $\bar{v} = \mathrm{Max}(\xi_w, c_s)$, where for instance $\bar{v} = c_s$ for inverse detonations.

Then, it is possible to define the efficiency $\kappa_{\mathrm{inverse}}$ as the fraction of the critical energy inside this sphere that will go into bulk fluid motion:

$$\kappa_{\mathrm{inverse}} \equiv \frac{\rho_{\mathrm{kin}}}{\rho_{\mathrm{tot}}} = \frac{4\pi \int_0^{\bar{v}} \xi^2 d\xi \; v^2\gamma^2 w}{4\pi \int_0^{\bar{v}} \xi^2 d\xi \, \frac{3}{4} w_N} = \frac{4}{\bar{v}^3} \int \xi^2 d\xi \, v^2\gamma^2 \frac{w}{w_N} \; . \tag{5.49}$$

In the way it is defined the efficiency $\kappa_{\mathrm{inverse}}$ is the parameter directly entering the fits for the GW signal [8]. As before, we fix α_N and solve for all the other variables. Our numerical results for $\kappa_{\mathrm{inverse}}$ obtained in this way as a function of ξ_w and α_N are displayed in the right panel of fig. 5.3.2. The solid black lines are the isocontours with the same α_N, varying the wall velocity.

Similarly to the direct PT case, we note that the top right corner where we have the fastest inverse deflagrations is the most efficient in converting the initial energy into kinetic energy, saturating to $\kappa_{\mathrm{inverse}} \approx 0.5$ for $\alpha_N \gtrsim -1/3$. For more negative values of α_N, i.e. $\alpha_N \lesssim -1/3$, only inverse detonations are allowed and the efficiency drops. This effect may also be understood in terms of energy conservation, as for large and negative α_N a significant fraction of the energy budget is lost to the vacuum energy of the new phase and is not transferred into bulk kinetic energy of the fluid.

The red dot-dashed line is the Jouguet velocity, defined implicitly in eq. (5.39), while the grey dashed line indicates $\xi_w = c_s$. The limiting solid red curve separates physical solutions from forbidden ones, in shaded red. It is worth noticing that the region for which a consistent solution cannot be found is bigger than in the direct case. Indeed, increasing $|\alpha_N|$ beyond $|\alpha_N| \approx 0.07$, a window of forbidden solutions appears between the inverse detonation and inverse hybrid, as we can already observe in fig.5.2.2. This window induces the peculiar feature in the limiting red curve appearing at $|\alpha_N| \gtrsim 0.07$. At the dip, in $|\alpha_N| \gtrsim 0.07$ and $\xi_w = c_s^2$, it merges with the Jouguet velocity (dashed red line). This merging is due to the fact that the slowest possible velocity for a hybrid is $\xi_w = c_s^2$, as explained in section 5.2.2.

We have also checked numerically energy conservation from (5.48) for the inverse PT:

$$\int_0^1 \left[\left(\gamma^2 - \frac{1}{4} \right) w - \frac{3}{4} w_N \right] \xi^2 \; d\xi = -\frac{\epsilon}{3} \xi_w^3 \; . \tag{5.51}$$

5.3.3 The GW signal from sound waves

One of the main interesting features of cosmological phase transition is the copious gravitational wave signal induced [232–236]. For this reason, and in the context of several future GW experiments, it has become crucial to quantify the amplitude and the spectrum of GWs emitted during cosmological PTs. One of the strongest sources of GWs is the sound waves propagating in the plasma after the end of the transition [47, 48, 54], which are sourced by the kinetic energy deposited in the plasma.

[8] We could in principle also introduce another definition of the efficiency, $\tilde{\kappa}_{\mathrm{inverse}}$, which matches more closely the expression for the direct case:

$$\tilde{\kappa}_{\mathrm{inverse}} = \frac{3}{\epsilon \, \bar{v}^3} \int \xi^2 d\xi \, w \, v^2\gamma^2 \, , \quad \kappa_{\mathrm{inverse}} = |\alpha_N| \tilde{\kappa}_{\mathrm{inverse}}. \tag{5.50}$$

In the case of direct PTs, it has been showed that the amplitude of the signal from sound waves is controlled by [73]

$$\Omega_{\rm GW}^{\rm direct} \propto \left(\frac{\rho_{\rm kin}}{\rho_{\rm tot}}\right)^2 = \left(\frac{\kappa_{\rm direct}\alpha_N}{1+\alpha_N}\right)^2 , \tag{5.52}$$

where $\Omega_{\rm GW}$ is the fraction of energy in GW radiation today, where $\kappa_{\rm direct}\,\alpha_N/(1+\alpha_N)$ corresponds to the fraction of energy converted to bulk fluid motion.

In the context of inverse PTs, we expect the GW signal to analogously scale like

$$\Omega_{\rm GW}^{\rm inv} \propto \left(\frac{\rho_{\rm kin}}{\rho_{\rm tot}}\right)^2 = \kappa^2_{\rm inverse} \ . \tag{5.53}$$

We however emphasise that such claim should be confirmed by numerical simulations.

5.4 The pressure on the bubble wall

In this section we investigate the pressure and the driving force which acts on the bubble walls, first in the direct case and then in the inverse PT.

5.4.1 The driving force in the direct PT

Despite the difference in pressure, an important phase transition parameter which cannot in principle be fixed by hydrodynamics only, is the velocity of the bubble wall expansion, ξ_w. To investigate it we need to rely on a microphysics analysis. The EoM of the scalar field is given by [100, 101]

$$\Box\phi + \frac{dV(\phi)}{d\phi} + \sum_i \frac{dm_i^2(\phi)}{d\phi}\int \frac{d^3\boldsymbol{p}}{(2\pi)^3 2E_i} f_i(p,x) = 0 \ , \tag{5.54}$$

where f_i are the distribution functions of the different particles coupling to the wall. The distribution functions are unknown and need to be solved via Boltzmann equations. Following the lines of [73], we can integrate the EoM in eq.(5.54) $\int dz\partial_z\phi$. Upon this operation, we obtain the driving force for the expansion of the bubble[9]

$$F_{\rm vacuum} \equiv \int_{\rm inside}^{\rm outside} dz\partial_z\phi\frac{dV(\phi)}{d\phi} = \epsilon_+ - \epsilon_- \ , \tag{5.55}$$

which is positive for a direct phase transition and negative for an inverse phase transition, and the resisting friction originating from the plasma

$$\mathcal{P}_{\rm plasma} \equiv -\int dz\partial_z\phi\sum_i \frac{dm_i^2(\phi)}{d\phi}\int \frac{d^3\boldsymbol{p}}{(2\pi)^3 2E_i} f_i(p,z,T) = \mathcal{P}_{\rm LTE} + \mathcal{P}_{\rm dissipative} \, . \tag{5.56}$$

Using a separation of the form $f_i(p,T,z) = f^{\rm eq}(p,T,z) + \delta f_i(p,T,z)$, the friction has been conventionally split into a LTE (local thermal equilibrium) contribution and dissipative contribution. From now on, we will follow the following convention: positive pressure will contribute to the acceleration of the bubble wall while negative pressure will resist it.

[9] Notice that there is an intrinsic freedom in determining what is called the *driving force* and what is called the *friction force*. Here we follow the split explained in [237], and used typically in particle physics computation of the pressure [94] as opposed to [73].

The dissipative force originates from departure from equilibrium piece $\delta f_i(p,T,z)$, while the LTE originates from heating effects and the $f^{\rm eq}(p,T,z)$ piece. The LTE contribution can be further separated in

$$\mathcal{P}_{\rm LTE} = -\int_{\rm inside}^{\rm outside} dz \partial_z \phi \frac{dV_T(\phi,T)}{d\phi} = -\Delta V_T + \int_{\rm inside}^{\rm outside} dz \frac{\partial V_T}{\partial T}\frac{\partial T}{\partial z} \,. \tag{5.57}$$

Finally, the pressure budget on the wall is given by

$$F_{\rm vacuum} - \mathcal{P}_{\rm plasma} = \epsilon_+ - \epsilon_- + \Delta V_T - \int_{\rm inside}^{\rm outside} dz \frac{\partial V_T}{\partial T}\frac{\partial T}{\partial z} - \mathcal{P}_{\rm dissipative} \,. \tag{5.58}$$

Let us first neglect the contribution of the dissipative forces. In the context of the direct phase transition $\epsilon_- = 0$ and we define $\epsilon_+ \equiv \epsilon$, so that eq.(5.58) becomes

$$F_{\rm vacuum} - \mathcal{P}_{\rm plasma} = \epsilon + \Delta V_T - \int_{-\infty}^{\infty} dz \frac{\partial V_T}{\partial T}\frac{\partial T}{\partial z} \,, \tag{5.59}$$

where the integral is to be performed from the *inside* of the bubble to the *outside* of it. We cannot solve exactly the integral without a microscopic description of the phase transition and the change of d.o.f. As a first approximation, we can assume that the phase transition is weak enough so that $T_+ \approx T_-$[10] obtaining

$$F_{\rm vacuum} - \mathcal{P}_{\rm plasma} \approx \epsilon - \frac{1}{3}\Delta a T_+^4 \,, \tag{5.60}$$

which we can express in the equivalent form

$$F_{\rm vacuum} - \mathcal{P}_{\rm plasma} \approx \frac{3w_+}{4}\left(\alpha_+ - \frac{1}{4}(1-b)\right) \,, \qquad b \equiv a_-/a_+ \,. \tag{5.61}$$

with $b \leq 1$ being the ratio of the number of relativistic d.o.f inside and outside the bubble. The driving force is maximised when $b = 1$ (this remains true even if there is a large heating in front of the wall and $T_+ \gg T_N$). A more precise expression can be obtained within the purely local thermal equilibrium approximation by imposing the conservation of entropy across the reaction front, as was followed in [104, 105, 237]. Our simplified picture in (5.61) captures nevertheless the physics we are interested in.

We observe that in the instance of $\epsilon \to \frac{1}{3}\Delta a T_+^4$, the driving force vanishes. This is an example of the *hydrodynamic obstruction* discussed for in details in [103–105, 237–240]. Intuitively, from a purely hydrodynamic point of view, this can be understood from the presence of a shock wave in front of the wall, which heats up the plasma. It has been showed that this hydrodynamic obstruction is maximal at the Jouguet velocity, which is the crossing between the hybrid and the detonation regime. From fig. 5.2.2 we observe that α_+ has a minimum at the Jouguet velocity, which turns into a weaker driving force in eq. (5.61).

The dissipative force $\mathcal{P}_{\rm dissipative}$ can be estimated within a particle physics model. It originates from

$$\mathcal{P}_{\rm dissipative} = \int dz \partial_z \phi \sum_i \frac{dm_i^2(\phi)}{d\phi} \int \frac{d^3\boldsymbol{p}}{(2\pi)^3 2E_i} \left(f_i(p,z,T) - f_i^{\rm eq}(p,z,T)\right) \,. \tag{5.62}$$

It however requires a careful solving of the Boltzmann equations to be accounted for [74–78, 100, 101].

[10] Notice that the strict equality $T_+ = T_-$ is technically not consistent with the LTE assumption, which imposes the conservation of entropy current and thus the saturation of eq. (5.13).

The runaway solution for direct PTs

In the regime of fast bubbles, the wall can reach a terminal velocity, described by a boosted detonation, or keep accelerating until the collision. We call the latter, a runaway wall. This type of runaway wall can be studied neglecting the collisions among particles in the wall [2, 94–96, 102, 106, 115, 241], where it is assumed that the distribution is fixed all along the wall by the incoming flux: $f_i(p,T) = f_{\rm outside}(p,T_N)$. This avoids the usual split into an equilibrium and an out-of-equilibrium piece, as performed in the previous subsection. This is approximately verified when particles entering do not scatter inside the wall. In the regime of fast bubbles, $\gamma_w \gg 1$, where we defined $\gamma_w \equiv 1/\sqrt{1-\xi_w^2}$ the boost factor of the wall to the plasma, it is known that while the contribution from LTE decreases, the most important contribution originates from the particles coupling to the scalar field and thus gaining a mass [94]. In the case of the fast walls, it has been obtained

$$\mathcal{P}_{\rm plasma}^{\rm LO,\gamma_w\to\infty} \approx \sum_i c_i g_i \frac{\Delta m_i^2 T^2}{24} \,, \tag{5.63}$$

where $\Delta m^2 \equiv m_b^2 - m_s^2 > 0$ and where $c_i = 1(1/2)$ for bosons (fermions), and g_i is the number of d.of of each particle. On top of those contributions, pressure from particle splittings studied in [2, 95, 96, 115] has been also shown to be able to stop the acceleration of the bubble wall. Notice that such contributions are by definition *not* accounted in eq. (5.54). This is an open question of how to express particle splittings in the framework of eq. (5.54).

In a given model the condition for runaway behaviour is usually formulated as

$$|\mathcal{P}_{\rm plasma}^{\rm max}(T_{\rm nuc})| < \epsilon \,, \tag{5.64}$$

where $\mathcal{P}_{\rm plasma}^{\rm max}(T_{\rm nuc})$ contains several pieces: the LO plasma pressure dominated by the expression in eq.(5.63), possibly pressure from mixing particles [107] and pressure from emission of soft gauge bosons, scaling like the wall boost factor γ_w.

5.4.2 The driving force in the inverse PT

In the case of an inverse phase transition, the difference of vacuum energy becomes a resisting pressure and the driving force originates from the plasma effects. We reinterpret the various contributions in the following way: the resisting force is given by

$$F_{\rm vacuum} \equiv \int dz \partial_z \phi \frac{dV(\phi)}{d\phi} = \epsilon_+ - \epsilon_- \,, \tag{5.65}$$

and the pushing plasma effect is given by

$$\mathcal{P}_{\rm plasma} \equiv -\int dz \partial_z \phi \sum_i \frac{dm_i^2(\phi)}{d\phi} \int \frac{d^3\boldsymbol{p}}{(2\pi)^3 2E_i} f_i(p,z,T) = \mathcal{P}_{\rm LTE} + \mathcal{P}_{\rm dissipative} \,. \tag{5.66}$$

As before, we first ignore the dissipative contributions. In the inverse PT case $\epsilon_+ = 0$, and we define $\epsilon_- \equiv \epsilon$. The approximate LTE expression becomes (when we can approximate $T_+ \approx T_-$):

$$F_{\rm vacuum} - \mathcal{P}_{\rm plasma} \approx \frac{3w_+}{4}\left(\frac{1}{4}(b-1) - |\alpha_+|\right) \,, \quad b \equiv a_-/a_+ \,, \tag{5.67}$$

where now $b > 1$. We observe that the driving force fuelling the expansion now originates from the change of d.o.f. and has to overcome the resisting force from the vacuum. This requires $b > 1 + 4|\alpha_+|$. This approach misses potentially important physical effects, as already stated in the previous section, as for example effects coming from the change of temperature across the wall. We leave this for further studies.

Looking back at fig. 5.2.2, we observe that even at constant α_N, α_+ is a function of the wall velocity ξ_w and presents a peak at the crossing between the inverse detonation and the inverse hybrid profile. Notice that, since in the case of inverse transitions the pressure associated with $|\alpha_+|$, as observed in the RHS of eq. (5.67), is resisting the expansion, this behaviour implies a hydrodynamical obstruction very similar to the one that has been largely studied in direct phase transitions [104, 237, 238] and recalled in the subsection above. Like in the direct case, the obstruction shows a peak at the (inverse) Jouguet velocity. This trend would deserve more investigation, we however leave the study of the subtleties of such effects to future studies.

The runaway solution for inverse PTs

So far, we have studied the steady states of the expansion modes. A steady state is reached when the vacuum force is balanced by the plasma pressure. It remains the possibility that a steady state is not reached at all and the bubble keeps accelerating until the collision.

What about the possibility of the runaway solution for the inverse PT? In principle, this can be studied in the collisionless limit, since we consider $\gamma_w \gg 1$: the pressure from the exchange of momentum originates from some particles losing their mass and inducing a kick on the wall. Let us sketch the analysis in the collisionless regime. Since the particles lose their mass when entering the wall, we expect the reflection from outside to be negligible. Let us then as a first approximation only consider the entering species: in the wall frame, we can apply the conservation of energy along the particle trajectory,

$$E = \sqrt{m^2 + p_z^2 + p_\perp^2}\,, \qquad \frac{dE}{dz} = \left(\frac{dm^2}{dz} + \frac{dp_z^2}{dz}\right)\frac{1}{2E} = 0\,, \qquad \Rightarrow \Delta p_z^{\rm part} \approx -\frac{|\Delta m^2|}{2p_z} \tag{5.68}$$

From eq.(5.68), we see that particles entering the wall and losing their mass are accelerated *inward* by a negative Δp_z. By conservation of momentum, the wall receives an equal and opposite kick, $\Delta p_z^{\rm part} = -\Delta p_z^{\rm wall} > 0$, which accelerates it forward. This leads us to conclude that the wall is *aspired* as the particles lose their mass. This behaviour was dubbed *anti friction* in the analysis of ref. [208].

We need however to convolute with the incoming flux to have a pressure

$$\begin{aligned}\mathcal{P}_{\rm plasma} &= -\int dz \partial_z\phi \sum_i g_i \frac{dm_i^2(\phi)}{d\phi} \int \frac{d^3\boldsymbol{p}}{(2\pi)^3 2E_i} f_i(p,z,T) \\ &\approx -\sum_i g_i \int \frac{d^3p}{(2\pi)^3} \frac{|\Delta m_i^2|}{2E_i} f^{\rm eq}_{\rm outside}(p,T)\end{aligned} \tag{5.69}$$

where the sum is performed over particles losing their mass and g_i is the number of d.o.f of each particle. The integral over the phase space is frame-independent and we compute it in the plasma frame. We obtain the final expression

$$\mathcal{P}_{\rm plasma}^{\gamma_w\to\infty} \approx -\sum_i C_{\rm eff,i}(m^i_{\rm out}/T) c_i g_i \frac{|\Delta m_i^2| T^2}{24}\,, \tag{5.70}$$

where again $c_i = 1(1/2)$ for bosons (fermions). We also defined $C_{\rm eff} \leq 1$ to take into account the Boltzmann suppression of the particles outside the bubble. It has an analytical expression in two limits

$$C_{\rm eff}(m^i_{\rm out}/T)\frac{T^2}{24} \equiv \int \frac{d^3p}{(2\pi)^3 2E_i} f_i(p,T) \approx \begin{cases} \dfrac{T^2}{24} & \text{if} \quad m_i^{\rm out} \ll T\,, \\ \dfrac{1}{2m_i^{\rm out}}\left(\dfrac{m_i^{\rm out}T_{\rm nuc}}{2\pi}\right)^{3/2} e^{-m_i^{\rm out}/T} & \text{if} \quad m_i^{\rm out} \gg T\,, \end{cases} \tag{5.71}$$

and we emphasise that the particles with large masses outside of the bubble become Boltzmann suppressed. Therefore, if the following inequality is satisfied,

$$\epsilon < \left| \sum_i C_{\rm eff,i}(m^i_{\rm out}/T) c_i g_i \frac{|\Delta m_i^2|T^2}{24} \right|, \tag{5.72}$$

then the wall can in principle runaway. However, we will expect, in the same case as in the direct phase transition [2], that there might be other sources of pressure from the splitting of particles passing through the wall [3].

Notice that the presence of the Boltzmann suppression factor in (5.72) implies that the BM pressure for inverse and direct transitions can actually be different (in absolute value) for the cooling and the heating phase transition happening in the very same particle physics model. This could change the conclusion in ref. [208] that runaway for the direct PT would imply non–runaway for the inverse PT, and viceversa.

Let us however notice that from the point of view of hydrodynamics, the situation for inverse phase transitions appears different than in the case of direct phase transitions. In the case of direct phase transitions the hydrodynamical solutions with $\xi_w \sim 1$ corresponding to ultra–relativistic detonations are in principle possible for any value of $\alpha_+ = \alpha_N$. In an inverse phase transition steady–wall solutions with $\xi_w \sim 1$ correspond to inverse deflagrations. These solutions exist only for $-1/3 < \alpha_+ < 0$. It is then conceivable that when α_+ becomes too negative the runaway behaviour is prevented. This reflects the fact that the vacuum energy is now opposed to the bubble expansion rather than fueling it. On the other hand, runaway walls are not steady-state solutions, so this reasoning cannot firmly invalidate runaway for $\alpha_+ < -1/3$.

5.5 Summary

The reheating of the Universe, for example at the end of cosmic inflation [208], or after a period of matter domination, might lead to inverse phase transitions against the vacuum energy of the zero–temperature potential. Formally, we find that these transitions can be studied by taking $\alpha_N \to -\alpha_N$ in the expression for the fluid velocity as computed from the matching conditions in the case of direct phase transitions.

In this chapter, we have focused on the hydrodynamics of inverse transitions, and we have identified five different modes of bubble expansion: weak and CJ inverse detonations, weak and CJ inverse deflagrations and finally inverse hybrids. We have excluded strong inverse detonations as they are inconsistent with the boundary conditions of the bubble, as well as strong inverse deflagrations because they are unstable and likely excluded by entropy considerations. We show schematically a summary of the possible fluid velocity profiles for inverse PTs in fig. 5.5.1, alongside the direct PT profiles for comparison.

We have provided the velocity, enthalpy, and temperature profiles for each of these solutions and examined the efficiency for transferring energy into bulk fluid motion after

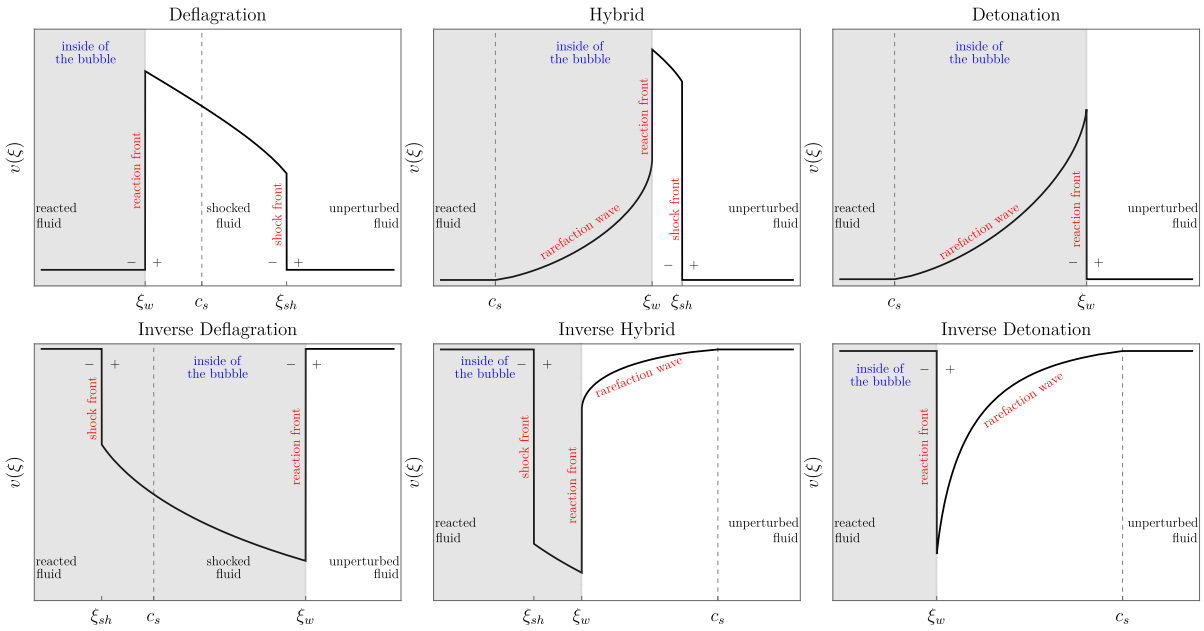

Figure 5.5.1: Cartoon illustrating the various fluid solutions, and the corresponding discontinuities and interfaces for direct PTs (top) and inverse PTs (bottom).

nucleation. This can be used to assess the amplitude of the gravitational waves produced during such a transition.

Finally, we have studied the pressure exerted on the bubble wall of the inverse phase transition. As opposed to the direct case, the driving force originates from the plasma rather than from the vacuum energy. We also find an analogous hydrodynamic obstruction, where the resistance to the expansion is maximal at the crossing of the inverse Jouguet velocity.

While our study clearly has applications in the case of heating phase transitions, we leave the exploration of particle physics models that could lead to the realisation of such inverse phase transitions for future studies.

Appendix

5.A Stability of the hydrodynamical solutions

The stability of the direct phase transitions has been thoroughly studied in previous works [227] and [225] (sections 4.8 and 5.5) and more specifically in [242, 243]. In this context, the stability of discontinuities has been related to the concept of *evolutionarity* of the front. A front is said to be evolutionary if any type of infinitesimal perturbations acting on it remains infinitesimal.

To determine if a front is *evolutionary*, it is sufficient to compute its degree of underdeterminacy D_U [225, 227], which is defined as the difference between the unknown parameters associated with the front and the number of boundary conditions applied on the front.

The boundary conditions applied on the wall are the three conservation equations, the conservation of mass, momentum, and energy across the front and possibly a fourth condition imposing the front velocity ξ. On the other hand, the number of unknown parameters is given by i) the number of acoustic $\lambda^{\pm}_{1,2}$ and 2) the entropy perturbations $\lambda^{\pm}_0$ *that can be transmitted* from the front [227]. We call those perturbations *propagating*. We can obtain that

- The perturbations $\lambda^{\pm}_{1,2}$ in the front frame have the form

$$\text{Ahead}: \qquad \lambda^{+}_1 = \frac{v_+ + c_s}{1 + v_+ c_s} \propto v_+ + c_s \qquad \lambda^{+}_2 = \frac{v_+ - c_s}{1 - v_+ c_s} \propto v_+ - c_s\,, \tag{5.73}$$

$$\text{Behind}: \qquad \lambda^{-}_1 = \frac{v_- + c_s}{1 + v_- c_s} \propto v_- + c_s \qquad \lambda^{-}_2 = \frac{v_- - c_s}{1 - v_- c_s} \propto v_- - c_s\,, \tag{5.74}$$

  where the proportionality is valid in the Newtonian limit and is simply the composition between an acoustic perturbation propagating with a velocity $\pm c_s$ in a fluid with bulk velocity v_- downstream or v_+ upstream. A propagating perturbation (for a *left* propagating front) ahead of the wall needs to have $\lambda^+ < 0$ while a propagating perturbation behind the wall will have $\lambda^- > 0$. Those are the conditions for the perturbations to be propagated away from the front. Perturbations violating those conditions remain stuck on the front and do not propagate.

- $\lambda^{\pm}_0$: On the other hand, the entropy perturbations $\lambda^{\pm}_0$ are always transmitted [225, 227]. The count is thus always two from the entropy perturbations.

Let us illustrate the computation with the case of $v_+ > c_s, v_- < c_s$, we have

$$\lambda^{+}_1 > 0 \qquad \lambda^{+}_2 > 0 \qquad \lambda^{-}_1 > 0 \qquad \lambda^{-}_2 < 0\,, \tag{5.75}$$

where we can conclude that only λ^-_1 is propagating. Put in a more intuitive way, in the region where the flow is upstream (toward) the front, $v_+ > c_s$, and so the two acoustic

perturbations which propagate with velocity c_s cannot propagate away from the front, since $v_+ > c_s$. On the other hand, downstream, the flow goes out from the wall with velocity $v_- < c_s$ and so, while the perturbation propagating toward the front cannot escape from it, the perturbation propagating away from the front can escape it because $v_- < c_s$. This leads us to the conclusion that for $v_+ > c_s, v_- < c_s$, there are three propagating disturbances, two entropy and one acoustic. If the velocity of the shock is not imposed, the degree of under-determinacy is finally $D_U^{v_+>c_s,v_-<c_s} = 3-3 = 0$, and the front is *evolutionary*. Following a very similar computation,

$$D_U^{v_+>c_s,v_-<c_s} = 3-3 = 0, \quad D_U^{v_+>c_s,v_->c_s} = 1, \quad D_U^{v_+<c_s,v_-<c_s} = 1, \quad D_U^{v_+<c_s,v_->c_s} = 2, \tag{5.176}$$

assuming that the velocity of the front is not imposed. This implies that only a shock wave with $v_+ > c_s, v_- < c_s$ is evolutionary.

5.A.1 Application to direct PTs

The same analysis can be followed to study the *reaction fronts* like detonations and deflagrations. There is however one important physical difference: while the shock wave velocity cannot be fixed as a boundary condition, the velocity of a phase transition boundary is controlled by hydrodynamics and particle physics. This consists of one more boundary condition. The very same analysis leads to

$$D_U^{v_+>c_s,v_-<c_s} = 3-4 = -1, \quad D_U^{v_+>c_s,v_->c_s} = 0, \quad D_U^{v_+<c_s,v_-<c_s} = 0, \quad D_U^{v_+<c_s,v_->c_s} = 1 \tag{5.177}$$

The case $v_+ > c_s, v_- < c_s$ corresponds to strong detonations that are not realised in a cosmological phase transition, $v_+ > c_s, v_- > c_s$ and $v_+ < c_s, v_- < c_s$ correspond respectively to weak detonations and weak deflagrations and are evolutionary. Finally, $v_+ < c_s, v_- > c_s$ corresponds to the strong deflagrations and are *not* evolutionary, because even fixing the velocity of the wall does not set the degree of under-determinacy to zero. This analysis has been confirmed by numerical simulations [217].

5.A.2 Application to inverse PTs

We now turn to the stability of the solutions for inverse phase transitions that we discussed in the main text. The results in eq.(5.77) remain valid, as they apply directly to the phase boundary, which have the same structure for the direct and the inverse transitions.

We can thus conclude in exactly the same way: the case $v_+ > c_s, v_- < c_s$ corresponds to the inverse strong detonations, $v_+ < c_s, v_- < c_s$ and $v_+ > c_s, v_- > c_s$ correspond respectively to weak inverse detonations and weak inverse deflagrations and are evolutionary, and finally $v_+ < c_s, v_- > c_s$ corresponds to strong inverse deflagrations and are *not* evolutionary.

We conclude that direct and inverse strong deflagrations are not evolutionary and then very likely unstable. If they can be made to exist initially, they will split into the hybrid solutions identified in the main text.

5.B Profiles of the thermodynamic quantities across the waves

In this appendix, we collect all the necessary results to compute the plots of fig.5.3.1 and the profiles of temperature and enthalpy.

5.B.1 Direct PTs

We begin by studying the direct phase transitions, with deflagrations, hybrids and detonations:

Deflagrations Here there are two discontinuities, at the shock and at the wall position, as we can see in fig. 5.5.1. The matching conditions at the shock position are again

$$\text{(matching at the shock)} \qquad w_+^{sh} v_+^{sh} \gamma_+^2 = w_-^{sh} v_-^{sh} \gamma_-^2 \ , \tag{5.78}$$

where + refers to the right region wrt the shock, i.e. the unperturbed fluid, and – refers to the left region wrt the shock, the perturbed region. Then we can identify

$$w_+^{sh} = w_N \ , \quad v_+^{sh} = \xi_{sh} \ , \quad v_-^{sh} = \mu(\xi_{sh}, v(\xi_{sh}^-)) \, . \tag{5.79}$$

To obtain the enthalpy after the shock, w_-^{sh}, we can plug eq.(5.79) into eq.(5.78) to obtain

$$w_-^{sh} \equiv w(\xi_{sh}^-) = w_N \cdot \frac{\xi_{sh}}{1-\xi_{sh}^2} \cdot \frac{1-\mu(\xi_{sh}, v(\xi_{sh}^-))^2}{\mu(\xi_{sh}, v(\xi_{sh}^-))} \ . \tag{5.80}$$

Now, evolving the solution back to the wall position we have that

$$w(\xi_w^+) = w(\xi_{sh}^-) \cdot \exp\left[\int_{v(\xi_{sh}^-)}^{v(\xi_w^+)} \left(1 + \frac{1}{c_s^2}\right) \gamma(v)^2 \mu(\xi(v), v) \, dv \right] \ . \tag{5.81}$$

Proceeding in a similar way as above, the matching conditions at the wall position imply

$$w_- \equiv w(\xi_w^-) = w(\xi_w^+) \cdot \frac{\mu(\xi_w, v(\xi_w^+))}{1-\mu(\xi_w, v(\xi_w^+))^2} \cdot \frac{1-\xi_w^2}{\xi_w} \ . \tag{5.82}$$

Summarizing the total profile is

$$w(\xi) = \begin{cases} w_N & \xi \geq \xi_{sh}^+ \\ w(\xi_{sh}^-) \cdot \exp\left[\int_{v(\xi_{sh}^-)}^{v(\xi)} \left(1 + \frac{1}{c_s^2}\right) \gamma(v)^2 \mu(\xi(v), v) \, dv \right] & \xi_w^+ \leq \xi \leq \xi_{sh}^- \\ w(\xi_w^-) & \xi \leq \xi_w^- \end{cases} \tag{5.83}$$

The same can be applied to the temperature profile which is

$$T(\xi) = \begin{cases} T_N & \xi \geq \xi_{sh}^+ \\ T(\xi_{sh}^-) \cdot \exp\left[\int_{v(\xi_{sh}^-)}^{v(\xi)} \gamma(v)^2 \mu(\xi(v), v) \, dv \right] & \xi_w^+ \leq \xi \leq \xi_{sh}^- \\ T(\xi_w^-) & \xi \leq \xi_w^- \end{cases} \tag{5.84}$$

where

$$T(\xi_{sh}^-) = T_N \left(\frac{w(\xi_{sh}^-)}{w_N} \right)^{1/4} \ , \tag{5.85}$$

$$T(\xi_w^+) = T(\xi_{sh}^-) \ \exp\left[\int_{v(\xi_{sh}^-)}^{v(\xi_w^+)} \gamma(v)^2 \mu(\xi(v), v) \, dv \right] \ , \tag{5.86}$$

$$T(\xi_w^-) = T(\xi_w^+) \left(\frac{w(\xi_w^-)}{w(\xi_w^+)} \cdot \frac{a_+}{a_-} \right)^{1/4} \ . \tag{5.87}$$

The resulting profiles are shown in the right panel (first row) of fig. 5.3.1.

Detonations For the detonations, we only have the discontinuity at the wall position. We skip the detailed derivation and give the resulting profile, that for the enthalpy is

$$w(\xi) = \begin{cases} w_N & \xi \geq \xi_w^+ \\ w(\xi_w^-) \cdot \exp\left[\int_{v(\xi_w^-)}^{v(\xi)} \left(1 + \frac{1}{c_s^2}\right) \gamma(v)^2 \mu(\xi(v), v)\, dv\right] & c_s \leq \xi \leq \xi_w^- \\ w(c_s) & \xi \leq c_s \end{cases} \tag{5.88}$$

while the temperature is

$$T(\xi) = \begin{cases} T_N & \xi \geq \xi_w^+ \\ T(\xi_w^-) \cdot \exp\left[\int_{v(\xi_w^-)}^{v(\xi)} \gamma(v)^2 \mu(\xi(v), v)\, dv\right] & c_s \leq \xi \leq \xi_w^- \\ T(c_s) & \xi \leq c_s \end{cases} \tag{5.89}$$

where

$$w(\xi_w^-) = w_N \cdot \frac{1 - \xi_w^2}{\xi_w} \cdot \frac{\mu(\xi_w, v(\xi_w^-))}{1 - \mu(\xi_w, v(\xi_w^-))^2}\ , \tag{5.90}$$

$$w(c_s) = w(\xi_w^-)\ \exp\left[\int_{v(\xi_w^-)}^{v(c_s)} \left(1 + \frac{1}{c_s^2}\right) \gamma(v)^2 \mu(\xi(v), v)\, dv\right]\ , \tag{5.91}$$

$$T(\xi_w^-) = T_N \left(\frac{w(\xi_w^-)}{w_N} \cdot \frac{a_+}{a_-}\right)^{1/4}\ , \tag{5.92}$$

$$T(c_s) = T(\xi_w^-)\ \exp\left[\int_{v(\xi_w^-)}^{v(c_s)} \gamma(v)^2 \mu(\xi(v), v)\, dv\right]\ . \tag{5.93}$$

The profiles are shown in the left panel (first row) in fig. 5.3.1.

Hybrids Here we have two discontinuities and we have to glue the two previous solutions in order to have a consistent one. Skipping the details the resulting enthalpy profile is

$$w(\xi) = \begin{cases} w_N & \xi \geq \xi_{sh}^+ \\ w(\xi_{sh}^-) \cdot \exp\left[\int_{v(\xi_{sh}^-)}^{v(\xi)} \left(1 + \frac{1}{c_s^2}\right) \gamma(v)^2 \mu(\xi(v), v)\, dv\right] & \xi_w^+ \leq \xi \leq \xi_{sh}^- \\ w(\xi_w^-) \cdot \exp\left[\int_{v(\xi_w^-)}^{v(\xi)} \left(1 + \frac{1}{c_s^2}\right) \gamma(v)^2 \mu(\xi(v), v)\, dv\right] & c_s \leq \xi \leq \xi_w^- \\ w(c_s) & \xi \leq c_s \end{cases} \tag{5.94}$$

and analogously for the temperature profile. What is worth noticing is that here, in order to build a consistent solution we glued a CJ deflagration with a rarefaction wave, this means that the velocity of the fluid behind the wall, in the wall frame, has to be $v_- = c_s$, and the matching condition reads

$$w(\xi_w^-) = w(\xi_w^+) \cdot \frac{\mu(\xi_w, v(\xi_w^+))}{1 - \mu(\xi_w, v(\xi_w^+))^2} \cdot \frac{1 - c_s^2}{c_s}\ . \tag{5.95}$$

5.B.2 Inverse PTs

We now turn to inverse phase transitions.

Inverse Deflagrations Here, as in the standard case, we have two discontinuities, but now the phases + and − are inverted. We remind the reader that even in this case we keep the identification + to be the region to the right of the discontinuity, while − to be the region to the left. Therefore, using the matching condition, at the wall position we have to impose that

$$w(\xi_w^-) = w_N \cdot \frac{1-\mu(\xi_w, v(\xi_w^-))^2}{\mu(\xi_w, v(\xi_w^-))} \cdot \frac{\xi_w}{1-\xi_w^2} \ , \tag{5.96}$$

and evolving backwards to the shock position we get

$$w(\xi_{sh}^+) = w(\xi_w^-) \ \exp\left[\int_{v(\xi_w^-)}^{v(\xi_{sh}^+)} \left(1+\frac{1}{c_s^2}\right)\gamma(v)^2\mu(\xi(v),v)\ dv\right] \ . \tag{5.97}$$

Now, at the shock position, we get that

$$w(\xi_{sh}^-) = w(\xi_{sh}^+) \cdot \frac{1-\xi_{sh}^2}{\xi_{sh}} \cdot \frac{\mu(\xi_{sh}, v(\xi_{sh}^+))}{1-\mu(\xi_{sh}, v(\xi_{sh}^+))^2} \ . \tag{5.98}$$

Summarizing, the enthalpy profile is described by

$$w(\xi) = \begin{cases} w_N & \xi \geq \xi_w^+ \\ w(\xi_w^-) \cdot \exp\left[\int_{v(\xi_w^-)}^{v(\xi)} \left(1+\frac{1}{c_s^2}\right)\gamma(v)^2\mu(\xi(v),v)\ dv\right] & \xi_{sh}^+ \leq \xi \leq \xi_w^- \\ w(\xi_{sh}^-) & \xi \leq \xi_{sh}^- \end{cases} \tag{5.99}$$

The same can be applied to the temperature profile which is

$$T(\xi) = \begin{cases} T_N & \xi \geq \xi_w^+ \\ T(\xi_w^-) \cdot \exp\left[\int_{v(\xi_w^-)}^{v(\xi)} \gamma(v)^2\mu(\xi(v),v)\ dv\right] & \xi_{sh}^+ \leq \xi \leq \xi_w^- \\ T(\xi_{sh}^-) & \xi \leq \xi_{sh}^- \end{cases} \tag{5.100}$$

where

$$T(\xi_w^-) = T_N \left(\frac{w(\xi_w^-)}{w_N} \cdot \frac{a_+}{a_-}\right)^{1/4} \ , \tag{5.101}$$

$$T(\xi_{sh}^+) = T(\xi_w^-) \ \exp\left[\int_{v(\xi_w^-)}^{v(\xi_{sh}^+)} \gamma(v)^2\mu(\xi(v),v)\ dv\right] \ , \tag{5.102}$$

$$T(\xi_{sh}^-) = T(\xi_{sh}^+) \left(\frac{w(\xi_{sh}^-)}{w(\xi_{sh}^+)}\right)^{1/4} \ . \tag{5.103}$$

The resulting profiles are shown in the right panel (second row) of fig. 5.3.1.

Inverse Detonations Here we only have the discontinuity at the wall position. As before, we skip the detailed derivation and give the resulting profile, that the enthalpy is

$$w(\xi) = \begin{cases} w_N & \xi \geq c_s \\ w_N \cdot \exp\left[\int_{v(c_s)}^{v(\xi)} \left(1+\frac{1}{c_s^2}\right)\gamma(v)^2\mu(\xi(v),v)\ dv\right] & \xi_w^+ \leq \xi \leq c_s \\ w(\xi_w^-) & \xi \leq \xi_w^- \end{cases} \tag{5.104}$$

while the temperature is

$$T(\xi) = \begin{cases} T_N & \xi \geq c_s \\ T_N \cdot \exp\left[\int_{v(c_s)}^{v(\xi)} \gamma(v)^2 \mu(\xi(v), v)\, dv\right] & \xi_w^+ \leq \xi \leq c_s \\ T(\xi_w^-) & \xi \leq \xi_w^- \end{cases} \tag{5.105}$$

where

$$w(\xi_w^-) = w(\xi_w^+) \cdot \frac{1-\xi_w^2}{\xi_w} \cdot \frac{\mu(\xi_w, v(\xi_w^+))}{1-\mu(\xi_w, v(\xi_w^+))^2}\ , \tag{5.106}$$

$$w(\xi_w^+) = w_N\ \exp\left[\int_{v(c_s)}^{v(\xi_w^+)} \left(1+\frac{1}{c_s^2}\right) \gamma(v)^2 \mu(\xi(v), v)\, dv\right]\ , \tag{5.107}$$

$$T(\xi_w^-) = T(\xi_w^+) \left(\frac{w(\xi_w^-)}{w(\xi_w^+)} \cdot \frac{a_+}{a_-}\right)^{1/4}\ , \tag{5.108}$$

$$T(\xi_w^+) = T_N\ \exp\left[\int_{v(c_s)}^{v(\xi_w^+)} \gamma(v)^2 \mu(\xi(v), v)\, dv\right]\ . \tag{5.109}$$

The profiles are shown in the left panel (second row) in fig. 5.3.1.

Inverse Hybrids Here we have two discontinuities and we have to glue the two previous solutions in order to have a consistent one. Skipping the details the resulting enthalpy profile is

$$w(\xi) = \begin{cases} w_N & \xi \geq c_s \\ w_N \cdot \exp\left[\int_{v(c_s)}^{v(\xi)} \left(1+\frac{1}{c_s^2}\right) \gamma(v)^2 \mu(\xi(v), v)\, dv\right] & \xi_w^+ \leq \xi \leq c_s \\ w(\xi_w^-) \cdot \exp\left[\int_{v(\xi_w^-)}^{v(\xi)} \left(1+\frac{1}{c_s^2}\right) \gamma(v)^2 \mu(\xi(v), v)\, dv\right] & \xi_{sh}^- \leq \xi \leq \xi_w^- \\ w(\xi_{sh}^-) & \xi \leq \xi_{sh}^- \end{cases} \tag{5.110}$$

and analogously for the temperature profile. What is worth noticing, even in the inverse case, is that, in order to build a consistent solution we glued a CJ inverse deflagration with an inverse rarefaction wave, this means that the velocity of the fluid in front of the wall, in the wall frame, has to be $v_+ = c_s$, and the matching condition reads

$$w(\xi_w^-) = w(\xi_w^+) \cdot \frac{1-\mu(\xi_w, v(\xi_w^-))^2}{\mu(\xi_w, v(\xi_w^-))} \cdot \frac{c_s}{1-c_s^2}\ . \tag{5.111}$$

The resulting profiles are shown in the middle panel (second row) of fig.5.3.1.

5.C Taub and Poisson's adiabats

In this section, we introduce how discontinuities are treated within hydrodynamics and how to connect states across such interfaces. We will introduce the Taub adiabat and summarise the main features. First seminal works, to name a few, were done by [244, 245], but we will follow the more modern approach presented in [225, 227].

In the presence of discontinuity waves, like shock and reaction fronts, the profile can be mathematically described by a discontinuity surface with a region ahead of the shock

(upstream) and one behind it (downstream). The discontinuity prevents to use of the relativistic hydrodynamic equation across the discontinuity, which can be replaced by the relativistic version of the Rankine-Hugoniot junction conditions. We can recast the hydrodynamic equations

$$\nabla_\mu(\rho u^\mu) = 0 \ , \qquad \nabla_\mu T^{\mu\nu} = 0 \ , \tag{5.112}$$

in global equation in the sense that they are not anymore only locally defined. To do so we choose an arbitrary function f and a 4−vector λ_ν and, using the previous expression, we can write

$$\nabla_\mu(\rho u^\mu f) = \rho u^\mu \nabla_\mu f \ , \qquad \nabla_\mu(T^{\mu\nu}\lambda_\nu) = T^{\mu\nu}\nabla_\mu\lambda_\nu \ . \tag{5.113}$$

We then integrate both sides over an arbitrary region $\mathcal{V}$ containing the shock surface and all his history, Σ, and then apply Stoke's theorem on the LHS, obtaining

$$\int_{\mathcal{S}} \rho u^\mu f n_\mu \ dV \ = \int_{\mathcal{V}} \rho u^\mu \nabla_\mu f \ d^4x \ , \tag{5.114}$$

$$\int_{\mathcal{S}} T^{\mu\nu}\lambda_\nu n_\mu \ dV = \int_{\mathcal{V}} T^{\mu\nu}\nabla_\mu\lambda_\nu \ d^4x \ , \tag{5.115}$$

where n_μ is the 4−vector perpendicular to $\mathcal{S}$. We can now shrink $\mathcal{V}$ to zero while comprising a portion Σ' of the 3D worldline relative to the shock front. In this limit, LHS$\to 0$ while the RHS is the quantity computed at each side of the shock, then

$$\int_{\Sigma'} \ f[\![\rho u^\mu]\!] n_\mu \ dV = 0 \ , \qquad \int_{\Sigma'} \ \lambda_\mu [\![T^{\mu\nu}]\!] n_\mu \ dV = 0 \ , \tag{5.116}$$

where we introduced the double bracket notation $[\![A]\!] = A_+ - A_-$. Then the conditions

$$[\![\rho u^\mu]\!] n_\mu = 0 \ , \qquad [\![T^{\mu\nu}]\!] n_\mu = 0 \ , \tag{5.117}$$

are exactly the junction conditions written in the main text, in eqs. (5.5a) and (5.5b). Now, defining the mass flux as $J = \rho\gamma v = const.$, and taking $u^\mu = (0, 0, 0, 1)$, we can recast the first the conditions $\rho u^z = const.$ and $T^{zz} = const.$ in the following expressions

$$[\![J^2]\!] = 0 \ , \qquad J^2 = -\frac{[\![p]\!]}{[\![w/\rho^2]\!]}. \tag{5.118}$$

Now, from $T^{tz} = const.$ we get

$$w\gamma^2 v = const. \quad \to \quad [\![\gamma w/\rho]\!] = 0 \ . \tag{5.119}$$

Taking the right expression in eq. (5.118) multiply it by $\frac{w_+}{\rho_+^2} + \frac{w_-}{\rho_-^2}$, and subtracting from it the square of the previous expression we end up in

$$\left[\!\!\left[\frac{w^2}{\rho^2}\right]\!\!\right] = \left(\frac{w_+}{\rho_+^2} + \frac{w_-}{\rho_-^2}\right) [\![p]\!] \ . \tag{5.120}$$

This expression is the relativistic generalisation of the classical Hugoniot adiabat for Newtonian shock fronts. Equations (5.118) and (5.120) are known as Taub's junction conditions for shock waves, serving as the relativistic counterparts to the Rankine–Hugoniot junction conditions for Newtonian shocks.

When examining the $(p, w/\rho^2)$ plane, the Taub adiabat offers a straightforward and visual representation of fluid properties across a shock. We plotted the shock adiabatic

in this plane since the natural variables for representing the relativistic shock adiabatic are $w/\rho^2 = wV^2$ and pc^2; in these coordinates, J^2 gives the slope of the chord from the initial point 1 on the adiabatic to any other point 2. Here, the Taub adiabat appears as the curve connecting the states before and after a shock wave, as illustrated in fig. 5.C.1. Upon defining the state "+" of the fluid ahead of the front in terms of pressure p_+ and the ratio w_+/ρ_+^2, condition (5.120) constrains the possible states of the fluid in the shocked region "−" to lie on the adiabat. Similar to the Newtonian result, the chord connecting the two states is proportionate to the square of the mass flux, J^2, implying that for the same initial state "+", a new state "−" with higher pressure will also entail a greater mass flux across the shock.

From the definition of the sound speed

$$c_s^2 = \left(\frac{dp}{de}\right)_s \ , \tag{5.121}$$

and using that for the isoentropic transformation we have that $de = hd\rho$ we can see that

$$c_s^2 = \left(\frac{dp}{de}\right)_s = \left(\frac{dp}{d(h/\rho)}\right)_s \left(\frac{d(h/\rho)}{de}\right)_s = \left(\frac{dp}{d(h/\rho)}\right)_s \frac{c_s^2 - 1}{\rho^2} \ , \tag{5.122}$$

that translate in

$$\left(\frac{dp}{d(h/\rho)}\right)_s = -\frac{\rho^2 c_s^2}{1 - c_s^2} = -\rho^2 \gamma_s^2 c_s^2 < 0 \ , \tag{5.123}$$

meaning that the slope at any point along the Taub adiabat is inherently negative and directly proportional to the local sound speed. Consequently, shocked states with higher pressures and densities will exhibit larger sound speeds.

For weak discontinuities[11] the jumps in the specific entropy and in the pressure scale, according to [245], as

$$[\![s]\!] = \left[\frac{1}{12hT}\left(\frac{d(h/\rho)}{dp}\right)_s\right][\![p]\!]^3 + O([\![p]\!]^4) \ . \tag{5.124}$$

The meaning of the previous equation lies in the necessity for a change in entropy across a shock, albeit only slightly. Because of the second law of thermodynamics, this change must manifest as an increase. Hence,

$$s_- > s_+ \ . \tag{5.125}$$

This inequality mirrors the intricate irreversible processes occurring within the narrow region of the shock front. It enables the exclusion of unphysical shocks that fail to induce an increase in entropy.

Let's visualise the situation described: consider the point (p_+, x_+) where $x = h/\rho = w/\rho^2$ in the $p-x$ plane. We draw two curves through this point: the shock Taub adiabatic and the Poisson adiabatic. The equation of the Poisson adiabatic, being an isoentropic transformation, is given by $s_+ - s_- = 0$. One can demonstrate that the Poisson and Taub adiabats passing through a given state share identical first and second derivatives at that particular state. Moreover, excluding non-convex equations of state, it can be proven that the second derivative of the Taub adiabat is always positive. To determine

[11] Discontinuity for which every quantity is small, i.e. the states ahead and behind the shock are not very different.

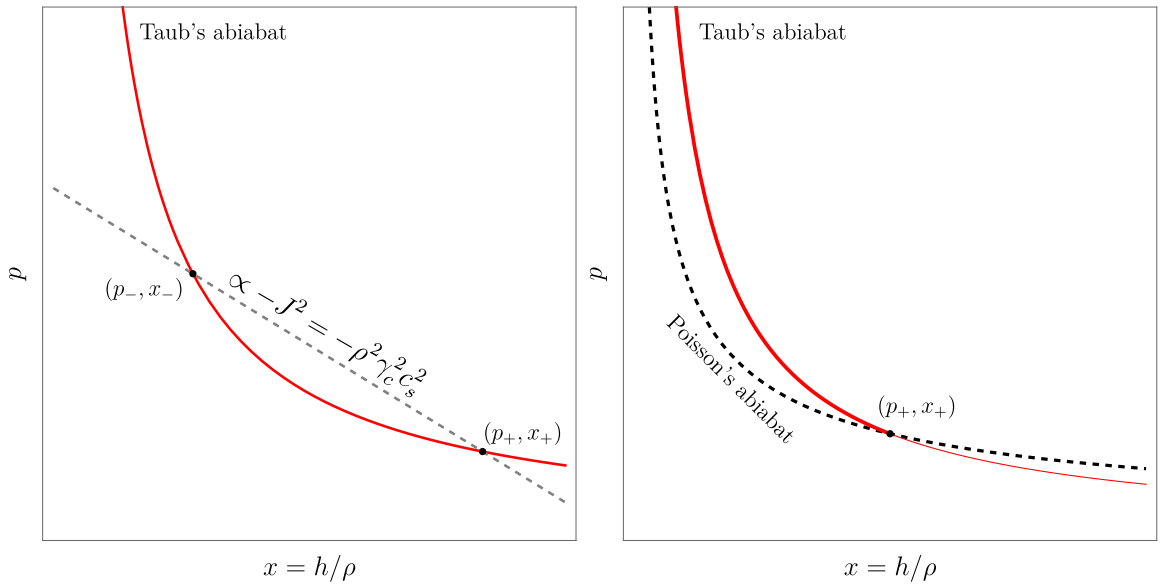

Figure 5.C.1: Taub and Poisson's adiabats. In the left panel, it is presented the Taub adiabat connecting two different states, $(x_\pm, p_\pm)$, across a shock, whose chord connecting them is proportional to the (conserved) matter flux J^2. In the right panel, the Poisson adiabad is compared to the Taub one. Since this latter is an isoentropic adiabat, i.e. connect states with the same entropy, it selects the physical branch of the Taub adiabat, for which the final state, across the shock, has increased its entropy.

the relative position of the two curves near point 1, we consider the fact that we must have $s_- > s_+$ on the shock adiabatic for $p_- > p_+$, while on the Poisson adiabatic $s_- = s_+$. Consequently, the abscissa of a point on the shock adiabatic must exceed that of a point on the Poisson adiabatic with the same ordinate p_-. When combined, $s_- > s_+$ and $p_- > p_+$, they establish that the Poisson adiabat selects the "physical" branch of the Taub adiabat, ensuring it always lies above the constant-entropy curve.

Under the assumption that the concavity of the Taub adiabat is always positive, combined with the increase in pressure across the discontinuity and eq. (5.120), we also conclude that $\rho_- w_- > \rho_+ w_+$. Furthermore, since $w_- > w_+$, we deduce $\rho_- > \rho_+$.

These inequalities provide crucial insights into the flow velocities on either side of the shock and how they compare with the local sound speed. By using eq. (5.5b) and the aforementioned inequalities, we arrive at the conclusion that the velocity must decrease in magnitude across the shock.

$$|v_-| < |v_+| \ . \tag{5.126}$$

Furthermore, from eq. (5.123), along with the previous expression, we can demonstrate that the flow entering a shock front is always supersonic, while the flow exiting it is necessarily subsonic

$$J^2 > -\left(\frac{\partial p}{\partial x}\right)_+ \quad \rightarrow \quad v_+ > c_{s,+} = c_s \ , \tag{5.127}$$

$$J^2 < -\left(\frac{\partial p}{\partial x}\right)_- \quad \rightarrow \quad v_- < c_{s,-} = c_s \ . \tag{5.128}$$

It's important to emphasise that the previous inequalities hold true for relativistic (as well as non-relativistic) shock waves, irrespective of the thermodynamic conditions. This is due to the necessity for the shock to be evolutionary, i.e., stable under small perturbations.

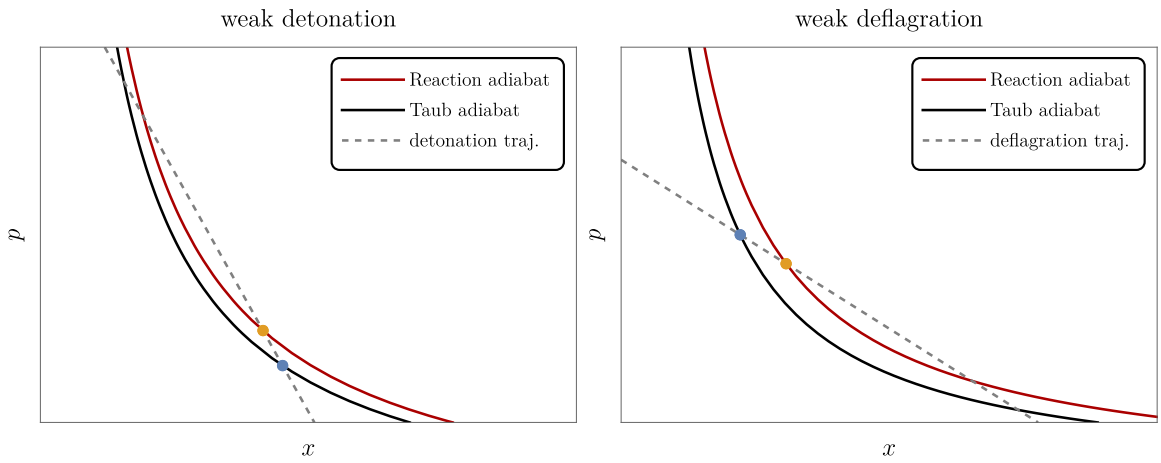

Figure 5.C.2: Representation of a weak detonation (left) and a weak deflagration (right). The state of the plasma *ahead* of the wall is represented by the blue dot and lies on the *Taub* adiabat, while the state of the plasma *behind* the discontinuity is represented by the orange dot and lies on the reaction adiabat.

In summary, across a shock, several changes occur: entropy, enthalpy, pressure, and rest-mass density increase, while the velocity relative to the shock decreases. Additionally, the flow is supersonic ahead of the shock and subsonic behind it. Moreover, both the mass flux and the entropy jump increase for states further along the physical branch of the Taub adiabat. These findings hold even for strong shocks, where the jumps in states ahead and behind the shock can be arbitrarily large. Finally, we here collect all the representations of the Taub and reaction adiabats for the strong and weak, direct and inverse deflagration and detonation in fig.5.C.2, 5.C.3, 5.C.5 and 5.C.4.

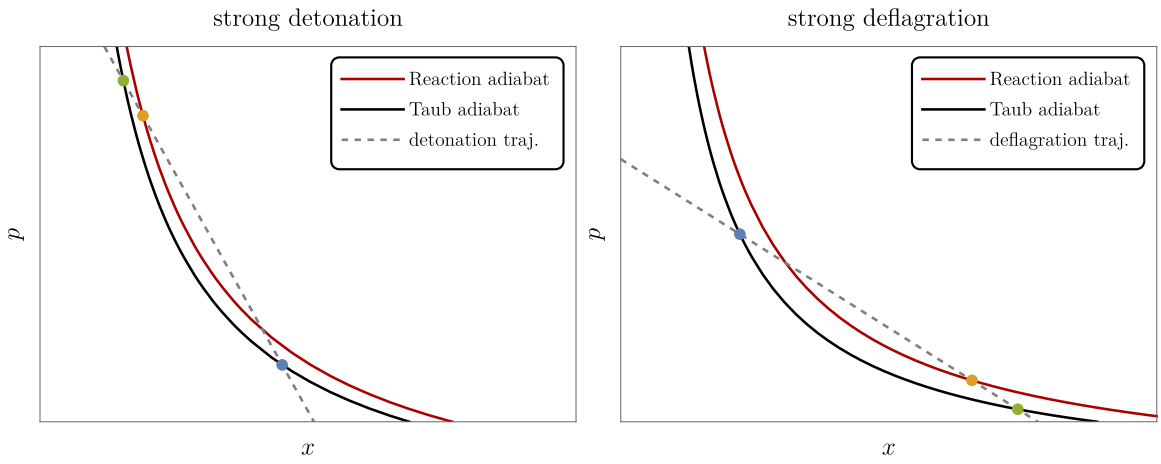

Figure 5.C.3: Left: Strong detonation: the physical detonation is the trajectory between the blue point and the orange one (from Taub to the reaction adiabat). However, we can virtually see it as the trajectory from the blue dot to the green one (from Taub to Taub, so a shock wave) and then back to orange (from Taub to the reaction adiabat). **Right**: Strong deflagration: the physical deflagration is the trajectory from the blue dot to the orange one, but, here too, we can see it as the trajectory from the blue to the green and then back to orange.

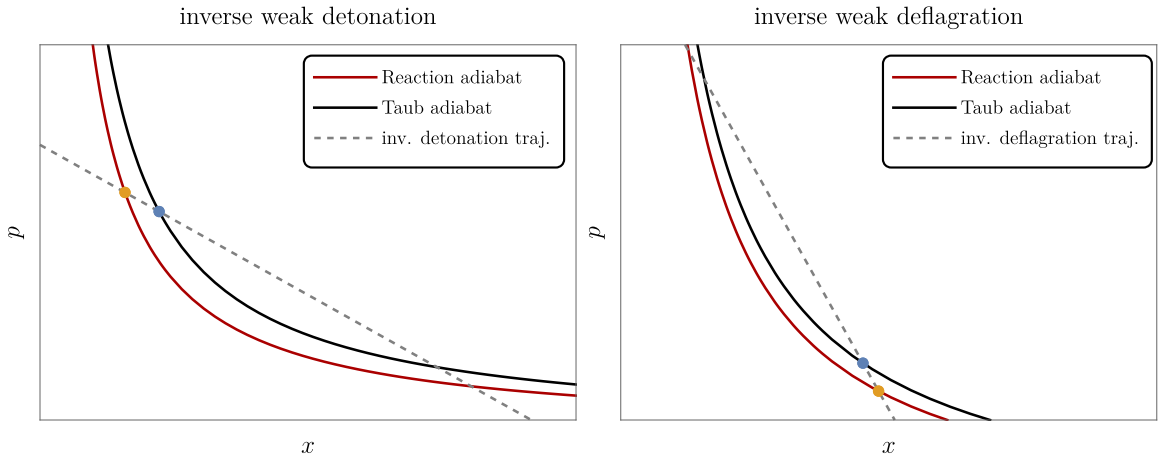

Figure 5.C.4: Same as in fig. 5.C.2 for inverse PT.

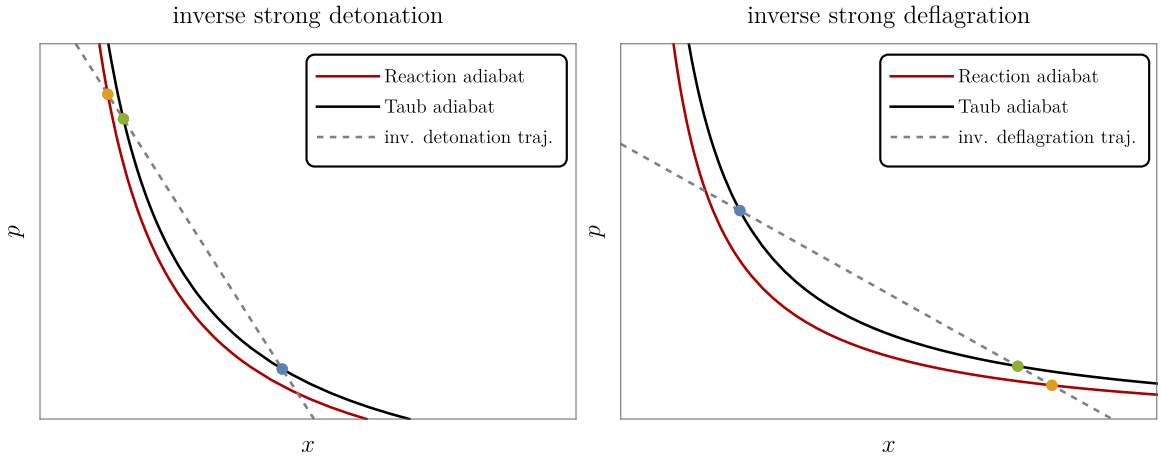

Figure 5.C.5: Same as in fig. 5.C.3 for inverse PT.

Chapter 6

Conclusion

In this thesis, we focused on the impact of cosmological first-order phase transitions, particularly highlighting the non-trivial dynamics they induce during the early stages of the evolution of the Universe. We tried to present one of the open problems in this research field, which is a reliable computation of the bubble wall velocity during the expansion. Although this question remains unresolved for a general theory with no approximations on the velocity range, we hope the reader has gained some intuition about the challenges involved and what can be done to improve the methods we presented.

In more detail, in chapter 1, we provided the foundational framework needed for this work. We began with a discussion of the standard Hot Big Bang theory, detailing the thermal history of the Universe and its expansion. We then covered the basics of QFT at finite temperature, which is crucial for computing the effective potential of a given theory. This is essential for understanding the dynamics of phase transitions. We examined different types of phase transitions and the role of symmetries, focusing on first-order phase transitions. The chapter concluded with an analysis of the challenging task of computing the velocity of bubble expansion during a FOPT, reviewing existing literature, and identifying weaknesses.

In chapter 2, we examined a specific example of a FOPT within the SM augmented by a real scalar singlet. The novel aspect of our study was the detailed analysis of the parameter space where first-order phase transitions could occur, particularly where bubbles of true vacuum could achieve relativistic velocities. This area is significant because it can lead to new mechanisms for baryogenesis and Dark Matter production. We thoroughly analysed various models for Dark Matter production and baryogenesis and explored the potential for discoveries in current and future experiments.

In chapter 3, we quantised field theories on the background of a bubble wall in the planar limit, with a focus on spontaneous gauge symmetry breaking. Using these tools, we calculated the average momentum transfer from transition radiation, focusing on the longitudinal polarisation of vectors. We found that longitudinal polarisations were comparable to transverse polarisations in symmetry-breaking transitions with mild super-cooling and dominant in broken-to-broken transitions with thin walls. Our results have practical implications for bubble expansion during first-order phase transitions. Our framework allows for robust calculations of particle processes in such translation-breaking backgrounds.

In chapter 4, we analysed the friction pressure on relativistic walls in phase transitions where gauge symmetry is restored. This analysis was motivated by the observation that this pressure could be negative at leading order since some particles lose mass as they cross into the new phase. However, we found that at next-to-leading order (NLO), the

soft emission of vectors from a charged current leads to positive pressure scaling with the wall's Lorentz boost factor γ_w, similar to gauge symmetry breaking. Unlike the latter case, the dominant contribution in single emission is free from infrared divergences and shows a strong dependence on the wall shape. Finally, we argued that in any phase transition, no multi-particle process on the wall can impart negative pressure greater than the leading-order result in the asymptotic limit of large velocity.

In the final chapter 5, we explored the hydrodynamic approach to bubble expansion to characterise all expansion modes. We reviewed the literature on direct PT and extended the study to inverse PTs. In a direct PT, a local vacuum transitions to a deeper vacuum of the zero-temperature potential, with the energy difference manifesting as bubble wall acceleration, driven by vacuum energy release. In an inverse PT, a deeper minimum transitions to a higher one, with bubbles expanding against vacuum energy, driven purely by thermal corrections. We conducted the first study on the hydrodynamics and energy budget of inverse PTs. We discovered several expansion modes for inverse bubbles, related to known modes for direct transitions by mirror symmetry. We also investigated the friction on the bubble wall and discussed the possibility of runaway walls in inverse PTs.

In conclusion, this thesis has explored the dynamics of FOPTs in the early Universe, focusing on the intricate computation of friction exerted on the bubble wall. By integrating various approaches, we have developed a cohesive framework to predict and compute such a contribution, in a general theory, in the ultrarelativistic limit. Our findings offer valuable insights into these fundamental processes that could have governed the early Universe, contributing to the broader field of cosmology and particle physics. This work lays the groundwork for future research, providing a deeper understanding of the mechanisms driving cosmological phase transitions.

Bibliography

[1] A. Azatov, G. Barni, S. Chakraborty, M. Vanvlasselaer, and W. Yin, *Ultra-relativistic bubbles from the simplest Higgs portal and their cosmological consequences*, *JHEP* **10** (2022) 017, [2207.02230].

[2] A. Azatov, G. Barni, R. Petrossian-Byrne, and M. Vanvlasselaer, *Quantisation across bubble walls and friction*, *JHEP* **05** (2024) 294, [2310.06972].

[3] A. Azatov, G. Barni, and R. Petrossian-Byrne, *NLO friction in symmetry restoring phase transitions*, 2405.19447.

[4] G. Barni, S. Blasi, and M. Vanvlasselaer, *The hydrodynamics of inverse phase transitions*, 2406.01596.

[5] E. W. Kolb and S. M. Turner, *The Early Universe*, vol. 69. Taylor and Francis, 5, 2019.

[6] M. Quiros, *Finite temperature field theory and phase transitions*, in *ICTP Summer School in High-Energy Physics and Cosmology*, pp. 187–259, 1, 1999. hep-ph/9901312.

[7] M. D. Schwartz, *Quantum Field Theory and the Standard Model*. Cambridge University Press, 3, 2014.

[8] S. Coleman and E. Weinberg, *Radiative corrections as the origin of spontaneous symmetry breaking*, *Phys. Rev. D* **7** (Mar, 1973) 1888–1910.

[9] E. J. Weinberg, *Radiative corrections as the origin of spontaneous symmetry breaking*. PhD thesis, Harvard U., 1973. hep-th/0507214.

[10] J. I. Kapusta and C. Gale, *Finite-Temperature Field Theory: Principles and Applications*. Cambridge Monographs on Mathematical Physics. Cambridge University Press, 2 ed., 2006.

[11] M. L. Bellac, *Thermal Field Theory*. Cambridge Monographs on Mathematical Physics. Cambridge University Press, 3, 2011.

[12] M. Laine and A. Vuorinen, *Basics of Thermal Field Theory*, vol. 925. Springer, 2016.

[13] D. Goodstein, *States of Matter*. Dover Books on Physics. Dover Publications, 1985.

[14] D. Curtin, P. Meade, and H. Ramani, *Thermal Resummation and Phase Transitions*, *Eur. Phys. J.* **C78** (2018), no. 9 787, [1612.00466].

[15] A. D. Linde, *Fate of the False Vacuum at Finite Temperature: Theory and Applications*, *Phys. Lett.* **100B** (1981) 37–40.

[16] D. Croon, O. Gould, P. Schicho, T. V. I. Tenkanen, and G. White, *Theoretical uncertainties for cosmological first-order phase transitions*, *JHEP* **04** (2021) 055, [2009.10080].

[17] O. Gould, S. Güyer, and K. Rummukainen, *First-order electroweak phase transitions: A nonperturbative update*, *Phys. Rev. D* **106** (2022), no. 11 114507, [2205.07238].

[18] A. Ekstedt, O. Gould, and J. Löfgren, *Radiative first-order phase transitions to next-to-next-to-leading order*, *Phys. Rev. D* **106** (2022), no. 3 036012, [2205.07241].

[19] A. Ekstedt, *Two-loop hard thermal loops for vector bosons in general models*, *JHEP* **06** (2023) 135, [2302.04894].

[20] A. Ekstedt, *Propagation of gauge fields in hot and dense plasmas at higher orders*, 2304.09255.

[21] C. Delaunay, C. Grojean, and J. D. Wells, *Dynamics of Non-renormalizable Electroweak Symmetry Breaking*, *JHEP* **04** (2008) 029, [0711.2511].

[22] E. J. Weinberg and A. Wu, *Understanding complex perturbative effective potentials*, *Phys. Rev. D* **36** (Oct, 1987) 2474–2480.

[23] T. W. B. Kibble, *Topology of Cosmic Domains and Strings*, *J. Phys. A* **9** (1976) 1387–1398.

[24] P. Auclair *et al.*, *Probing the gravitational wave background from cosmic strings with LISA*, *JCAP* **04** (2020) 034, [1909.00819].

[25] Y. Cui, M. Lewicki, D. E. Morrissey, and J. D. Wells, *Cosmic Archaeology with Gravitational Waves from Cosmic Strings*, *Phys. Rev. D* **97** (2018), no. 12 123505, [1711.03104].

[26] S. Blasi, R. Jinno, T. Konstandin, H. Rubira, and I. Stomberg, *Gravitational waves from defect-driven phase transitions: domain walls*, *JCAP* **10** (2023) 051, [2302.06952].

[27] S. Blasi and A. Mariotti, *QCD Axion Strings or Seeds?*, 2405.08060.

[28] S. R. Coleman, *The Fate of the False Vacuum. 1. Semiclassical Theory*, *Phys. Rev.* **D15** (1977) 2929–2936. [Erratum: Phys. Rev.D16,1248(1977)].

[29] C. G. Callan and S. Coleman, *Fate of the false vacuum. ii. first quantum corrections*, *Phys. Rev. D* **16** (Sep, 1977) 1762–1768.

[30] A. Linde, *Fate of the false vacuum at finite temperature: Theory and applications*, *Physics Letters B* **100** (1981), no. 1 37–40.

[31] *Decay of the false vacuum at finite temperature: A. linde, nucl. phys. b216 (1983) 421*, *Nuclear Physics B* **223** (1983), no. 2 544.

[32] U. Sarid, *Tools for tunneling*, *Phys. Rev. D* **58** (1998) 085017, [hep-ph/9804308].

[33] J. Ellis, M. Lewicki, J. M. No, and V. Vaskonen, *Gravitational wave energy budget in strongly supercooled phase transitions*, *JCAP* **1906** (2019), no. 06 024, [1903.09642].

[34] A. H. Guth and S. H. H. Tye, *Phase Transitions and Magnetic Monopole Production in the Very Early Universe*, *Phys. Rev. Lett.* **44** (1980) 631. [Erratum: Phys. Rev. Lett.44,963(1980)].

[35] A. H. Guth and E. J. Weinberg, *Cosmological consequences of a first-order phase transition in the* su_5 *grand unified model*, *Phys. Rev. D* **23** (Feb, 1981) 876–885.

[36] J. Ellis, M. Lewicki, and J. M. No, *On the Maximal Strength of a First-Order Electroweak Phase Transition and its Gravitational Wave Signal*, 1809.08242. [JCAP1904,003(2019)].

[37] M. Gleiser, E. W. Kolb, and R. Watkins, *Phase transitions with sub-critical bubbles*, *Nuclear Physics B* **364** (1991), no. 2 411–450.

[38] L. Darmé, J. Jaeckel, and M. Lewicki, *Towards the fate of the oscillating false vacuum*, *Phys. Rev. D* **96** (2017), no. 5 056001, [1704.06445].

[39] R.-G. Cai and S.-J. Wang, *Effective picture of bubble expansion*, 2011.11451.

[40] J. Ellis, M. Lewicki, and J. M. No, *Gravitational waves from first-order cosmological phase transitions: lifetime of the sound wave source*, *JCAP* **07** (2020) 050, [2003.07360].

[41] A. Azatov, D. Barducci, and F. Sgarlata, *Gravitational traces of broken gauge symmetries*, *JCAP* **07** (2020) 027, [1910.01124].

[42] R. Jinno, T. Konstandin, and M. Takimoto, *Relativistic bubble collisions-a closer look*, *JCAP* **09** (2019) 035, [1906.02588].

[43] A. Mégevand and F. A. Membiela, *Thin and thick bubble walls. Part I. Vacuum phase transitions*, *JCAP* **06** (2023) 007, [2302.13349].

[44] S. Weinberg, *Gravitation and Cosmology: Principles and Applications of the General Theory of Relativity*. John Wiley and Sons, New York, 1972.

[45] B. F. Schutz, *A FIRST COURSE IN GENERAL RELATIVITY*. Cambridge Univ. Pr., Cambridge, UK, 1985.

[46] M. Hindmarsh, S. J. Huber, K. Rummukainen, and D. J. Weir, *Gravitational waves from the sound of a first order phase transition*, *Phys. Rev. Lett.* **112** (2014) 041301, [1304.2433].

[47] M. Hindmarsh, S. J. Huber, K. Rummukainen, and D. J. Weir, *Numerical simulations of acoustically generated gravitational waves at a first order phase transition*, *Phys. Rev. D* **92** (2015), no. 12 123009, [1504.03291].

[48] M. Hindmarsh, S. J. Huber, K. Rummukainen, and D. J. Weir, *Shape of the acoustic gravitational wave power spectrum from a first order phase transition*, *Phys. Rev.* **D96** (2017), no. 10 103520, [1704.05871].

[49] D. Cutting, M. Hindmarsh, and D. J. Weir, *Gravitational waves from vacuum first-order phase transitions: from the envelope to the lattice*, *Phys. Rev.* **D97** (2018), no. 12 123513, [1802.05712].

[50] D. Cutting, M. Hindmarsh, and D. J. Weir, *Vorticity, kinetic energy, and suppressed gravitational wave production in strong first order phase transitions*, *Phys. Rev. Lett.* **125** (2020), no. 2 021302, [1906.00480].

[51] O. Gould, S. Sukuvaara, and D. Weir, *Vacuum bubble collisions: From microphysics to gravitational waves*, *Phys. Rev. D* **104** (2021), no. 7 075039, [2107.05657].

[52] D. J. Weir, *Gravitational waves from a first order electroweak phase transition: a brief review*, *Phil. Trans. Roy. Soc. Lond. A* **376** (2018), no. 2114 20170126, [1705.01783].

[53] M. B. Hindmarsh, M. Lüben, J. Lumma, and M. Pauly, *Phase transitions in the early universe*, *SciPost Phys. Lect. Notes* **24** (2021) 1, [2008.09136].

[54] C. Caprini *et al.*, *Detecting gravitational waves from cosmological phase transitions with LISA: an update*, 1910.13125.

[55] C. Badger *et al.*, *Probing early Universe supercooled phase transitions with gravitational wave data*, *Phys. Rev. D* **107** (2023), no. 2 023511, [2209.14707].

[56] R. Caldwell *et al.*, *Detection of early-universe gravitational-wave signatures and fundamental physics*, *Gen. Rel. Grav.* **54** (2022), no. 12 156, [2203.07972].

[57] C. Caprini, R. Durrer, and G. Servant, *Gravitational wave generation from bubble collisions in first-order phase transitions: An analytic approach*, *Phys. Rev.* **D77** (2008) 124015, [0711.2593].

[58] L. Kisslinger and T. Kahniashvili, *Polarized Gravitational Waves from Cosmological Phase Transitions*, *Phys. Rev. D* **92** (2015), no. 4 043006, [1505.03680].

[59] R. Jinno and M. Takimoto, *Gravitational waves from bubble dynamics: Beyond the Envelope*, *JCAP* **1901** (2019) 060, [1707.03111].

[60] T. Konstandin, *Gravitational radiation from a bulk flow model*, *JCAP* **1803** (2018), no. 03 047, [1712.06869].

[61] R. Jinno and M. Takimoto, *Gravitational waves from bubble collisions: An analytic derivation*, *Phys. Rev. D* **95** (2017), no. 2 024009, [1605.01403].

[62] L. Delle Rose, G. Panico, M. Redi, and A. Tesi, *Gravitational Waves from Supercool Axions*, *JHEP* **04** (2020) 025, [1912.06139].

[63] B. Sathyaprakash *et al.*, *Scientific Objectives of Einstein Telescope*, *Class. Quant. Grav.* **29** (2012) 124013, [1206.0331]. [Erratum: Class. Quant. Grav.30,079501(2013)].

[64] **KAGRA, LIGO Scientific, VIRGO** Collaboration, B. P. Abbott *et al.*, *Prospects for Observing and Localizing Gravitational-Wave Transients with Advanced LIGO, Advanced Virgo and KAGRA*, *Living Rev. Rel.* **21** (2018), no. 1 3, [1304.0670].

[65] **LIGO Scientific** Collaboration, J. Aasi *et al.*, *Advanced LIGO*, *Class. Quant. Grav.* **32** (2015) 074001, [1411.4547].

[66] T. Robson, N. J. Cornish, and C. Liug, *The construction and use of LISA sensitivity curves*, *Class. Quant. Grav.* **36** (2019), no. 10 105011, [1803.01944].

[67] K. Schmitz, *New Sensitivity Curves for Gravitational-Wave Signals from Cosmological Phase Transitions*, *JHEP* **01** (2021) 097, [2002.04615].

[68] K. Yagi, N. Tanahashi, and T. Tanaka, *Probing the size of extra dimension with gravitational wave astronomy*, *Phys. Rev.* **D83** (2011) 084036, [1101.4997].

[69] K. Yagi, *Scientific Potential of DECIGO Pathfinder and Testing GR with Space-Borne Gravitational Wave Interferometers*, *Int. J. Mod. Phys.* **D22** (2013) 1341013, [1302.2388].

[70] H. Kurki-Suonio and M. Laine, *Bubble growth and droplet decay in cosmological phase transitions*, *Phys. Rev. D* **54** (Dec, 1996) 7163–7171.

[71] P. J. Steinhardt, *Relativistic detonation waves and bubble growth in false vacuum decay*, *Phys.*

Rev. D **25** (Apr, 1982) 2074–2085.

[72] M. Kamionkowski, A. Kosowsky, and M. S. Turner, *Gravitational radiation from first-order phase transitions*, *Phys. Rev. D* **49** (Mar, 1994) 2837–2851.

[73] J. R. Espinosa, T. Konstandin, J. M. No, and G. Servant, *Energy Budget of Cosmological First-order Phase Transitions*, *JCAP* **1006** (2010) 028, [1004.4187].

[74] S. De Curtis, L. D. Rose, A. Guiggiani, A. G. Muyor, and G. Panico, *Bubble wall dynamics at the electroweak phase transition*, 2201.08220.

[75] S. De Curtis, L. Delle Rose, A. Guiggiani, A. Gil Muyor, and G. Panico, *Collision integrals for cosmological phase transitions*, *JHEP* **05** (2023) 194, [2303.05846].

[76] S. De Curtis, L. Delle Rose, A. Guiggiani, A. Gil Muyor, and G. Panico, *Non-linearities in cosmological bubble wall dynamics*, *JHEP* **05** (2024) 009, [2401.13522].

[77] B. Laurent and J. M. Cline, *Fluid equations for fast-moving electroweak bubble walls*, *Phys. Rev. D* **102** (2020), no. 6 063516, [2007.10935].

[78] B. Laurent and J. M. Cline, *First principles determination of bubble wall velocity*, *Phys. Rev. D* **106** (2022), no. 2 023501, [2204.13120].

[79] I. Garcia Garcia, G. Koszegi, and R. Petrossian-Byrne, *Reflections on Bubble Walls*, 2212.10572.

[80] D. G. Figueroa, A. Florio, F. Torrenti, and W. Valkenburg, *The art of simulating the early universe. part i. integration techniques and canonical cases*, *Journal of Cosmology and Astroparticle Physics* **2021** (apr, 2021) 035.

[81] D. G. Figueroa, A. Florio, F. Torrenti, and W. Valkenburg, *Cosmolattice: A modern code for lattice simulations of scalar and gauge field dynamics in an expanding universe*, *Computer Physics Communications* **283** (2023) 108586.

[82] J. Braden, J. R. Bond, and L. Mersini-Houghton, *Cosmic bubble and domain wall instabilities i: parametric amplification of linear fluctuations*, *Journal of Cosmology and Astroparticle Physics* **2015** (mar, 2015) 007.

[83] J. Braden, J. R. Bond, and L. Mersini-Houghton, *Cosmic bubble and domain wall instabilities ii: fracturing of colliding walls*, *Journal of Cosmology and Astroparticle Physics* **2015** (aug, 2015) 048.

[84] J. R. Bond, J. Braden, and L. Mersini-Houghton, *Cosmic bubble and domain wall instabilities iii: the role of oscillons in three-dimensional bubble collisions*, *Journal of Cosmology and Astroparticle Physics* **2015** (sep, 2015) 004.

[85] G. C. Dorsch, S. J. Huber, and T. Konstandin, *A sonic boom in bubble wall friction*, 2112.12548.

[86] F. Giese, T. Konstandin, K. Schmitz, and J. van de Vis, *Model-independent energy budget for LISA*, *JCAP* **01** (2021) 072, [2010.09744].

[87] R. Jinno, T. Konstandin, and H. Rubira, *A hybrid simulation of gravitational wave production in first-order phase transitions*, *JCAP* **04** (2021) 014, [2010.00971].

[88] R. Jinno, T. Konstandin, H. Rubira, and I. Stomberg, *Higgsless simulations of cosmological phase transitions and gravitational waves*, *JCAP* **02** (2023) 011, [2209.04369].

[89] M. Lewicki, V. Vaskonen, and H. Veermäe, *Bubble dynamics in fluids with N-body simulations*, *Phys. Rev. D* **106** (2022), no. 10 103501, [2205.05667].

[90] T. Krajewski, M. Lewicki, and M. Zych, *Hydrodynamical constraints on the bubble wall velocity*, *Phys. Rev. D* **108** (2023), no. 10 103523, [2303.18216].

[91] G. D. Moore and T. Prokopec, *How fast can the wall move? a study of the electroweak phase transition dynamics*, *Phys. Rev. D* **52** (Dec, 1995) 7182–7204.

[92] B. H. Liu, L. McLerran, and N. Turok, *Bubble nucleation and growth at a baryon-number-producing electroweak phase transition*, *Phys. Rev. D* **46** (Sep, 1992) 2668–2688.

[93] A. Azatov and M. Vanvlasselaer, *Bubble wall velocity: heavy physics effects*, *JCAP* **01** (2021) 058, [2010.02590].

[94] D. Bodeker and G. D. Moore, *Can electroweak bubble walls run away?*, *JCAP* **0905** (2009) 009, [0903.4099].

[95] D. Bodeker and G. D. Moore, *Electroweak Bubble Wall Speed Limit*, *JCAP* **1705** (2017), no. 05 025, [1703.08215].

[96] Y. Gouttenoire, R. Jinno, and F. Sala, *Friction pressure on relativistic bubble walls*, *JHEP* **05** (2022) 004, [2112.07686].

[97] A. Azatov, M. Vanvlasselaer, and W. Yin, *Dark Matter production from relativistic bubble walls*, *JHEP* **03** (2021) 288, [2101.05721].

[98] A. Azatov, M. Vanvlasselaer, and W. Yin, *Baryogenesis via relativistic bubble walls*, *JHEP* **10** (2021) 043, [2106.14913].

[99] S. Höche, J. Kozaczuk, A. J. Long, J. Turner, and Y. Wang, *Towards an all-orders calculation of the electroweak bubble wall velocity*, *JCAP* **03** (2021) 009, [2007.10343].

[100] G. D. Moore and T. Prokopec, *Bubble wall velocity in a first order electroweak phase transition*, *Phys. Rev. Lett.* **75** (1995) 777–780, [hep-ph/9503296].

[101] G. D. Moore and T. Prokopec, *How fast can the wall move? A Study of the electroweak phase transition dynamics*, *Phys. Rev.* **D52** (1995) 7182–7204, [hep-ph/9506475].

[102] M. Barroso Mancha, T. Prokopec, and B. Swiezewska, *Field theoretic derivation of bubble wall force*, 2005.10875.

[103] S. Balaji, M. Spannowsky, and C. Tamarit, *Cosmological bubble friction in local equilibrium*, *JCAP* **03** (2021) 051, [2010.08013].

[104] W.-Y. Ai, B. Garbrecht, and C. Tamarit, *Bubble wall velocities in local equilibrium*, *JCAP* **03** (2022), no. 03 015, [2109.13710].

[105] W.-Y. Ai, B. Laurent, and J. van de Vis, *Model-independent bubble wall velocities in local thermal equilibrium*, *JCAP* **07** (2023) 002, [2303.10171].

[106] M. Dine, R. G. Leigh, P. Y. Huet, A. D. Linde, and D. A. Linde, *Towards the theory of the electroweak phase transition*, *Phys. Rev.* **D46** (1992) 550–571, [hep-ph/9203203].

[107] A. Azatov and M. Vanvlasselaer, *Phase transitions in perturbative walking dynamics*, *JHEP* **09** (2020) 085, [2003.10265].

[108] M. Lewicki and V. Vaskonen, *Gravitational waves from bubble collisions and fluid motion in strongly supercooled phase transitions*, *Eur. Phys. J. C* **83** (2023), no. 2 109, [2208.11697].

[109] M. Lewicki, K. Müürsepp, J. Pata, M. Vasar, V. Vaskonen, and H. Veermäe, *Dynamics of false vacuum bubbles with trapped particles*, *Phys. Rev. D* **108** (2023), no. 3 036023, [2305.07702].

[110] I. Baldes, M. Dichtl, Y. Gouttenoire, and F. Sala, *Bubbletrons*, 2306.15555.

[111] I. Baldes, M. Dichtl, Y. Gouttenoire, and F. Sala, *Particle shells from relativistic bubble walls*, 2403.05615.

[112] S. Blasi, A. Mariotti, A. Rase, A. Sevrin, and K. Turbang, *Friction on ALP domain walls and gravitational waves*, *JCAP* **04** (2023) 008, [2210.14246].

[113] S. Blasi, A. Mariotti, A. Rase, and A. Sevrin, *Axionic domain walls at Pulsar Timing Arrays: QCD bias and particle friction*, *JHEP* **11** (2023) 169, [2306.17830].

[114] M. Barroso Mancha, T. Prokopec, and B. Swiezewska, *Field-theoretic derivation of bubble-wall force*, *JHEP* **01** (2021) 070, [2005.10875].

[115] A. Azatov and M. Vanvlasselaer, *Bubble wall velocity: heavy physics effects*, *JCAP* **01** (2021) 058, [2010.02590].

[116] G. R. Farrar and J. W. McIntosh, Jr., *Scattering from a domain wall in a spontaneously broken gauge theory*, *Phys. Rev. D* **51** (1995) 5889–5904, [hep-ph/9412270].

[117] I. Baldes, S. Blasi, A. Mariotti, A. Sevrin, and K. Turbang, *Baryogenesis via relativistic bubble expansion*, *Phys. Rev. D* **104** (2021), no. 11 115029, [2106.15602].

[118] A. D. Sakharov, *Violation of CP Invariance, C asymmetry, and baryon asymmetry of the universe*, *Pisma Zh. Eksp. Teor. Fiz.* **5** (1967) 32–35. [Usp. Fiz. Nauk161,no.5,61(1991)].

[119] V. A. Kuzmin, V. A. Rubakov, and M. E. Shaposhnikov, *On the Anomalous Electroweak Baryon Number Nonconservation in the Early Universe*, *Phys. Lett. B* **155** (1985) 36.

[120] M. Shaposhnikov, *Possible Appearance of the Baryon Asymmetry of the Universe in an Electroweak Theory*, *JETP Lett.* **44** (1986) 465–468.

[121] K. Kajantie, M. Laine, K. Rummukainen, and M. E. Shaposhnikov, *A Nonperturbative analysis of the finite T phase transition in SU(2) x U(1) electroweak theory*, *Nucl. Phys. B* **493** (1997) 413–438, [hep-lat/9612006].

[122] M. D'Onofrio and K. Rummukainen, *Standard model cross-over on the lattice*, *Phys. Rev. D* **93** (2016), no. 2 025003, [1508.07161].

[123] D. E. Morrissey and M. J. Ramsey-Musolf, *Electroweak baryogenesis*, *New J. Phys.* **14** (2012) 125003, [1206.2942].

[124] D. N. Schramm, *Phase Transitions and Dark Matter Problems*, *Nucl. Phys. B* **252** (1985) 53–71.

[125] M. J. Baker and J. Kopp, *Dark Matter Decay between Phase Transitions at the Weak Scale*, *Phys. Rev. Lett.* **119** (2017), no. 6 061801, [1608.07578].

[126] M. J. Baker and L. Mittnacht, *Variations on the Vev Flip-Flop: Instantaneous Freeze-out and Decaying Dark Matter*, *JHEP* **05** (2019) 070, [1811.03101].

[127] L. Heurtier and H. Partouche, *Spontaneous Freeze Out of Dark Matter From an Early Thermal Phase Transition*, *Phys. Rev. D* **101** (2020), no. 4 043527, [1912.02828].

[128] T. Cohen, D. E. Morrissey, and A. Pierce, *Changes in Dark Matter Properties After Freeze-Out*, *Phys. Rev. D* **78** (2008) 111701, [0808.3994].

[129] L. Bian and Y.-L. Tang, *Thermally modified sterile neutrino portal dark matter and gravitational waves from phase transition: The Freeze-in case*, *JHEP* **12** (2018) 006, [1810.03172].

[130] L. Hui and E. D. Stewart, *Superheavy dark matter from thermal inflation*, *Phys. Rev. D* **60** (1999) 023518, [hep-ph/9812345].

[131] D. Chung, A. Long, and L.-T. Wang, *Probing the Cosmological Constant and Phase Transitions with Dark Matter*, *Phys. Rev. D* **84** (2011) 043523, [1104.5034].

[132] D. J. H. Chung and A. J. Long, *Cosmological Constant, Dark Matter, and Electroweak Phase Transition*, *Phys. Rev. D* **84** (2011) 103513, [1108.5193].

[133] T. Hambye, A. Strumia, and D. Teresi, *Super-cool Dark Matter*, *JHEP* **08** (2018) 188, [1805.01473].

[134] I. Baldes, Y. Gouttenoire, and F. Sala, *String Fragmentation in Supercooled Confinement and Implications for Dark Matter*, *JHEP* **04** (2021) 278, [2007.08440].

[135] J. Shelton and K. M. Zurek, *Darkogenesis: A baryon asymmetry from the dark matter sector*, *Phys. Rev. D* **82** (2010) 123512, [1008.1997].

[136] K. Petraki, M. Trodden, and R. R. Volkas, *Visible and dark matter from a first-order phase transition in a baryon-symmetric universe*, *JCAP* **02** (2012) 044, [1111.4786].

[137] I. Baldes, *Gravitational waves from the asymmetric-dark-matter generating phase transition*, *JCAP* **05** (2017) 028, [1702.02117].

[138] E. Hall, T. Konstandin, R. McGehee, and H. Murayama, *Asymmetric Matters from a Dark First-Order Phase Transition*, 1911.12342.

[139] A. Falkowski and J. M. No, *Non-thermal Dark Matter Production from the Electroweak Phase Transition: Multi-TeV WIMPs and 'Baby-Zillas'*, *JHEP* **02** (2013) 034, [1211.5615].

[140] M. J. Baker, J. Kopp, and A. J. Long, *Filtered dark matter at a first order phase transition*, *Phys. Rev. Lett.* **125** (Oct, 2020) 151102.

[141] D. Chway, T. H. Jung, and C. S. Shin, *Dark matter filtering-out effect during a first-order phase transition*, *Phys. Rev. D* **101** (2020), no. 9 095019, [1912.04238].

[142] D. Marfatia and P.-Y. Tseng, *Gravitational wave signals of dark matter freeze-out*, 2006.07313.

[143] S. Ramazanov, E. Babichev, D. Gorbunov, and A. Vikman, *Beyond freeze-in: Dark matter via inverse phase transition and gravitational wave signal*, *Phys. Rev. D* **105** (2022), no. 6 063530, [2104.13722].

[144] E. Babichev, D. Gorbunov, S. Ramazanov, and A. Vikman, *Gravitational shine of dark domain*

walls, *JCAP* **04** (2022), no. 04 028, [2112.12608].

[145] I. Baldes, Y. Gouttenoire, and F. Sala, *Hot and heavy dark matter from a weak scale phase transition*, *SciPost Phys.* **14** (2023) 033, [2207.05096].

[146] A. Katz and A. Riotto, *Baryogenesis and Gravitational Waves from Runaway Bubble Collisions*, *JCAP* **11** (2016) 011, [1608.00583].

[147] P. Baratella, A. Pomarol, and F. Rompineve, *The Supercooled Universe*, *JHEP* **03** (2019) 100, [1812.06996].

[148] N. Craig, N. Levi, A. Mariotti, and D. Redigolo, *Ripples in Spacetime from Broken Supersymmetry*, *JHEP* **21** (2020) 184, [2011.13949].

[149] J. R. Espinosa and M. Quiros, *Novel Effects in Electroweak Breaking from a Hidden Sector*, *Phys. Rev. D* **76** (2007) 076004, [hep-ph/0701145].

[150] A. Noble and M. Perelstein, *Higgs self-coupling as a probe of electroweak phase transition*, *Phys. Rev. D* **78** (2008) 063518, [0711.3018].

[151] A. Ashoorioon and T. Konstandin, *Strong electroweak phase transitions without collider traces*, *JHEP* **07** (2009) 086, [0904.0353].

[152] P. H. Damgaard, D. O'Connell, T. C. Petersen, and A. Tranberg, *Constraints on New Physics from Baryogenesis and Large Hadron Collider Data*, *Phys. Rev. Lett.* **111** (2013), no. 22 221804, [1305.4362].

[153] T. Alanne, K. Tuominen, and V. Vaskonen, *Strong phase transition, dark matter and vacuum stability from simple hidden sectors*, *Nucl. Phys. B* **889** (2014) 692–711, [1407.0688].

[154] P. Huang, A. J. Long, and L.-T. Wang, *Probing the Electroweak Phase Transition with Higgs Factories and Gravitational Waves*, *Phys. Rev. D* **94** (2016), no. 7 075008, [1608.06619].

[155] A. Beniwal, M. Lewicki, J. D. Wells, M. White, and A. G. Williams, *Gravitational wave, collider and dark matter signals from a scalar singlet electroweak baryogenesis*, *JHEP* **08** (2017) 108, [1702.06124].

[156] V. Barger, P. Langacker, M. McCaskey, M. J. Ramsey-Musolf, and G. Shaughnessy, *LHC Phenomenology of an Extended Standard Model with a Real Scalar Singlet*, *Phys. Rev. D* **77** (2008) 035005, [0706.4311].

[157] J. R. Espinosa, T. Konstandin, and F. Riva, *Strong Electroweak Phase Transitions in the Standard Model with a Singlet*, *Nucl. Phys. B* **854** (2012) 592–630, [1107.5441].

[158] J. Kozaczuk, M. J. Ramsey-Musolf, and J. Shelton, *Exotic Higgs boson decays and the electroweak phase transition*, *Phys. Rev. D* **101** (2020), no. 11 115035, [1911.10210].

[159] Z. Wang, X. Zhu, E. E. Khoda, S.-C. Hsu, N. Konstantinidis, K. Li, S. Li, M. J. Ramsey-Musolf, Y. Wu, and Y. E. Zhang, *Study of Electroweak Phase Transition in Exotic Higgs Decays at the CEPC*, 3, 2022. 2203.10184.

[160] J. Ellis, M. Lewicki, M. Merchand, J. M. No, and M. Zych, *The scalar singlet extension of the Standard Model: gravitational waves versus baryogenesis*, *JHEP* **01** (2023) 093, [2210.16305].

[161] P. Agrawal, S. Blasi, A. Mariotti, and M. Nee, *Electroweak phase transition with a double well done doubly well*, *JHEP* **06** (2024) 089, [2312.06749].

[162] G. Kurup and M. Perelstein, *Dynamics of Electroweak Phase Transition In Singlet-Scalar Extension of the Standard Model*, *Phys. Rev. D* **96** (2017), no. 1 015036, [1704.03381].

[163] Z. Kang, P. Ko, and T. Matsui, *Strong first order EWPT & strong gravitational waves in Z_3-symmetric singlet scalar extension*, *JHEP* **02** (2018) 115, [1706.09721].

[164] L. Niemi, P. Schicho, and T. V. I. Tenkanen, *Singlet-assisted electroweak phase transition at two loops*, *Phys. Rev. D* **103** (2021), no. 11 115035, [2103.07467].

[165] B. Gripaios, A. Pomarol, F. Riva, and J. Serra, *Beyond the Minimal Composite Higgs Model*, *JHEP* **04** (2009) 070, [0902.1483].

[166] J. R. Espinosa, B. Gripaios, T. Konstandin, and F. Riva, *Electroweak Baryogenesis in Non-minimal Composite Higgs Models*, *JCAP* **01** (2012) 012, [1110.2876].

[167] L. Bian, Y. Wu, and K.-P. Xie, *Electroweak phase transition with composite Higgs models:*

calculability, gravitational waves and collider searches, *JHEP* **12** (2019) 028, [1909.02014].

[168] S. De Curtis, L. Delle Rose, and G. Panico, *Composite Dynamics in the Early Universe*, *JHEP* **12** (2019) 149, [1909.07894].

[169] **CMS** Collaboration, A. M. Sirunyan *et al.*, *A measurement of the Higgs boson mass in the diphoton decay channel*, *Phys. Lett. B* **805** (2020) 135425, [2002.06398].

[170] M. B. Einhorn and D. R. T. Jones, *A NEW RENORMALIZATION GROUP APPROACH TO MULTISCALE PROBLEMS*, *Nucl. Phys. B* **230** (1984) 261–272.

[171] P. Schicho, T. V. I. Tenkanen, and G. White, *Combining thermal resummation and gauge invariance for electroweak phase transition*, 2203.04284.

[172] P. M. Schicho, T. V. I. Tenkanen, and J. Österman, *Robust approach to thermal resummation: Standard Model meets a singlet*, *JHEP* **06** (2021) 130, [2102.11145].

[173] J. M. Cline and K. Kainulainen, *Electroweak baryogenesis and dark matter from a singlet Higgs*, *JCAP* **01** (2013) 012, [1210.4196].

[174] D. Curtin, P. Meade, and C.-T. Yu, *Testing Electroweak Baryogenesis with Future Colliders*, *JHEP* **11** (2014) 127, [1409.0005].

[175] V. Vaskonen, *Electroweak baryogenesis and gravitational waves from a real scalar singlet*, *Phys. Rev. D* **95** (2017), no. 12 123515, [1611.02073].

[176] D. Buttazzo, F. Sala, and A. Tesi, *Singlet-like Higgs bosons at present and future colliders*, *JHEP* **11** (2015) 158, [1505.05488].

[177] S. Profumo, M. J. Ramsey-Musolf, and G. Shaughnessy, *Singlet Higgs phenomenology and the electroweak phase transition*, *JHEP* **08** (2007) 010, [0705.2425].

[178] H. H. Patel and M. J. Ramsey-Musolf, *Stepping Into Electroweak Symmetry Breaking: Phase Transitions and Higgs Phenomenology*, *Phys. Rev. D* **88** (2013) 035013, [1212.5652].

[179] W. Huang, Z. Kang, J. Shu, P. Wu, and J. M. Yang, *New insights in the electroweak phase transition in the NMSSM*, *Phys. Rev. D* **91** (2015), no. 2 025006, [1405.1152].

[180] M. Jiang, L. Bian, W. Huang, and J. Shu, *Impact of a complex singlet: Electroweak baryogenesis and dark matter*, *Phys. Rev. D* **93** (2016), no. 6 065032, [1502.07574].

[181] C.-W. Chiang, M. J. Ramsey-Musolf, and E. Senaha, *Standard Model with a Complex Scalar Singlet: Cosmological Implications and Theoretical Considerations*, *Phys. Rev. D* **97** (2018), no. 1 015005, [1707.09960].

[182] V. Guada, M. Nemevšek, and M. Pintar, *FindBounce: Package for multi-field bounce actions*, *Comput. Phys. Commun.* **256** (2020) 107480, [2002.00881].

[183] R. Barbieri and G. F. Giudice, *Upper Bounds on Supersymmetric Particle Masses*, *Nucl. Phys. B* **306** (1988) 63–76.

[184] K. Enqvist, J. Ignatius, K. Kajantie, and K. Rummukainen, *Nucleation and bubble growth in a first order cosmological electroweak phase transition*, *Phys. Rev.* **D45** (1992) 3415–3428.

[185] I. Baldes, Y. Gouttenoire, F. Sala, and G. Servant, *Supercool composite Dark Matter beyond 100 TeV*, *JHEP* **07** (2022) 084, [2110.13926].

[186] P. Amaro-Seoane, H. Audley, S. Babak, J. Baker, E. Barausse, P. Bender, E. Berti, P. Binetruy, M. Born, D. Bortoluzzi, J. Camp, C. Caprini, V. Cardoso, M. Colpi, J. Conklin, N. Cornish, C. Cutler, K. Danzmann, R. Dolesi, L. Ferraioli, V. Ferroni, E. Fitzsimons, J. Gair, L. G. Bote, D. Giardini, F. Gibert, C. Grimani, H. Halloin, G. Heinzel, T. Hertog, M. Hewitson, K. Holley-Bockelmann, D. Hollington, M. Hueller, H. Inchauspe, P. Jetzer, N. Karnesis, C. Killow, A. Klein, B. Klipstein, N. Korsakova, S. L. Larson, J. Livas, I. Lloro, N. Man, D. Mance, J. Martino, I. Mateos, K. McKenzie, S. T. McWilliams, C. Miller, G. Mueller, G. Nardini, G. Nelemans, M. Nofrarias, A. Petiteau, P. Pivato, E. Plagnol, E. Porter, J. Reiche, D. Robertson, N. Robertson, E. Rossi, G. Russano, B. Schutz, A. Sesana, D. Shoemaker, J. Slutsky, C. F. Sopuerta, T. Sumner, N. Tamanini, I. Thorpe, M. Troebs, M. Vallisneri, A. Vecchio, D. Vetrugno, S. Vitale, M. Volonteri, G. Wanner, H. Ward, P. Wass, W. Weber, J. Ziemer, and P. Zweifel, *Laser interferometer space antenna*, 2017.

[187] B. Von Harling, A. Pomarol, O. Pujolàs, and F. Rompineve, *Peccei-Quinn Phase Transition at*

LIGO, *JHEP* **04** (2020) 195, [1912.07587].

[188] V. Brdar, A. J. Helmboldt, and J. Kubo, *Gravitational Waves from First-Order Phase Transitions: LIGO as a Window to Unexplored Seesaw Scales*, *JCAP* **02** (2019) 021, [1810.12306].

[189] V. Corbin and N. J. Cornish, *Detecting the cosmic gravitational wave background with the big bang observer*, *Class. Quant. Grav.* **23** (2006) 2435–2446, [gr-qc/0512039].

[190] J. Crowder and N. J. Cornish, *Beyond LISA: Exploring future gravitational wave missions*, *Phys. Rev. D* **72** (2005) 083005, [gr-qc/0506015].

[191] N. Seto, S. Kawamura, and T. Nakamura, *Possibility of direct measurement of the acceleration of the universe using 0.1-Hz band laser interferometer gravitational wave antenna in space*, *Phys. Rev. Lett.* **87** (2001) 221103, [astro-ph/0108011].

[192] K. Yagi and N. Seto, *Detector configuration of DECIGO/BBO and identification of cosmological neutron-star binaries*, *Phys. Rev. D* **83** (2011) 044011, [1101.3940]. [Erratum: Phys.Rev.D 95, 109901 (2017)].

[193] S. Isoyama, H. Nakano, and T. Nakamura, *Multiband Gravitational-Wave Astronomy: Observing binary inspirals with a decihertz detector, B-DECIGO*, *PTEP* **2018** (2018), no. 7 073E01, [1802.06977].

[194] S. Hild *et al.*, *Sensitivity Studies for Third-Generation Gravitational Wave Observatories*, *Class. Quant. Grav.* **28** (2011) 094013, [1012.0908].

[195] M. Maggiore *et al.*, *Science Case for the Einstein Telescope*, *JCAP* **03** (2020) 050, [1912.02622].

[196] L. Badurina *et al.*, *AION: An Atom Interferometer Observatory and Network*, *JCAP* **05** (2020) 011, [1911.11755].

[197] **AEDGE** Collaboration, Y. A. El-Neaj *et al.*, *AEDGE: Atomic Experiment for Dark Matter and Gravity Exploration in Space*, *EPJ Quant. Technol.* **7** (2020) 6, [1908.00802].

[198] C. Caprini *et al.*, *Science with the space-based interferometer eLISA. II: Gravitational waves from cosmological phase transitions*, *JCAP* **1604** (2016), no. 04 001, [1512.06239].

[199] S. Argyropoulos, O. Brandt, and U. Haisch, *Collider Searches for Dark Matter through the Higgs Lens*, *Symmetry* **2021** (9, 2021) 13, [2109.13597].

[200] S. Bruggisser, B. Von Harling, O. Matsedonskyi, and G. Servant, *Electroweak Phase Transition and Baryogenesis in Composite Higgs Models*, *JHEP* **12** (2018) 099, [1804.07314].

[201] S. Blasi and A. Mariotti, *Domain Walls Seeding the Electroweak Phase Transition*, *Phys. Rev. Lett.* **129** (2022), no. 26 261303, [2203.16450].

[202] A. Shkerin and S. Sibiryakov, *Black hole induced false vacuum decay from first principles*, *JHEP* **11** (2021) 197, [2105.09331].

[203] M. E. Peskin and D. V. Schroeder, *An Introduction to quantum field theory*. Addison-Wesley, Reading, USA, 1995.

[204] D. Tong, *Lectures on quantum field theory*, *Part III Cambridge University Mathematics Tripos, Michaelmas* (2006).

[205] J. J. Blanco-Pillado, D. Jiménez-Aguilar, and J. Urrestilla, *Exciting the domain wall soliton*, *JCAP* **01** (2021) 027, [2006.13255].

[206] K. Blum and M. Mirbabayi, *A single-bubble source for gravitational waves in a cosmological phase transition*, 2403.20164.

[207] S. Hassan, J. March-Russell, and G. Obied, *Chern-Simons bubbles: Lopsided false vacuum decay in axion electrodynamics*, 2402.00119.

[208] M. A. Buen-Abad, J. H. Chang, and A. Hook, *Gravitational wave signatures from reheating*, *Phys. Rev. D* **108** (2023), no. 3 036006, [2305.09712].

[209] G. Degrassi, S. Di Vita, J. Elias-Miro, J. R. Espinosa, G. F. Giudice, G. Isidori, and A. Strumia, *Higgs mass and vacuum stability in the Standard Model at NNLO*, *JHEP* **08** (2012) 098, [1205.6497].

[210] F. Giese, T. Konstandin, and J. van de Vis, *Model-independent energy budget of cosmological*

first-order phase transitions—A sound argument to go beyond the bag model, *JCAP* **07** (2020), no. 07 057, [2004.06995].

[211] X. Wang, F. P. Huang, and Y. Li, *Sound velocity effects on the phase transition gravitational wave spectrum in the sound shell model*, *Phys. Rev. D* **105** (2022), no. 10 103513, [2112.14650].

[212] M. A. Ajmi and M. Hindmarsh, *Thermal suppression of bubble nucleation at first-order phase transitions in the early Universe*, *Phys. Rev. D* **106** (2022), no. 2 023505, [2205.04097].

[213] T. V. I. Tenkanen and J. van de Vis, *Speed of sound in cosmological phase transitions and effect on gravitational waves*, *JHEP* **08** (2022) 302, [2206.01130].

[214] S.-J. Wang and Z.-Y. Yuwen, *The energy budget of cosmological first-order phase transitions beyond the bag equation of state*, *JCAP* **10** (2022) 047, [2206.01148].

[215] X. Wang, C. Tian, and F. P. Huang, *Model-dependent analysis method for energy budget of the cosmological first-order phase transition*, *JCAP* **07** (2023) 006, [2301.12328].

[216] P. Athron, C. Balázs, A. Fowlie, L. Morris, and L. Wu, *Cosmological phase transitions: From perturbative particle physics to gravitational waves*, *Prog. Part. Nucl. Phys.* **135** (2024) 104094, [2305.02357].

[217] J. Ignatius, K. Kajantie, H. Kurki-Suonio, and M. Laine, *The growth of bubbles in cosmological phase transitions*, *Phys. Rev. D* **49** (1994) 3854–3868, [astro-ph/9309059].

[218] M. Laine, *Bubble growth as a detonation*, *Phys. Rev. D* **49** (1994) 3847–3853, [hep-ph/9309242].

[219] H. Kurki-Suonio and M. Laine, *Supersonic deflagrations in cosmological phase transitions*, *Phys. Rev. D* **51** (1995) 5431–5437, [hep-ph/9501216].

[220] L. Giombi and M. Hindmarsh, *General relativistic bubble growth in cosmological phase transitions*, *JCAP* **03** (2024) 059, [2307.12080].

[221] D. Cutting, E. Vilhonen, and D. J. Weir, *Droplet collapse during strongly supercooled transitions*, *Phys. Rev. D* **106** (Nov, 2022) 103524.

[222] H. Kolesova and M. Laine, *Update on gravitational wave signals from post-inflationary phase transitions*, *Phys. Lett. B* **851** (2024) 138553, [2311.03718].

[223] J. Casalderrey-Solana, D. Mateos, and M. Sanchez-Garitaonandia, *Mega-Hertz Gravitational Waves from Neutron Star Mergers*, 2210.03171.

[224] C. Caprini and J. M. No, *Supersonic Electroweak Baryogenesis: Achieving Baryogenesis for Fast Bubble Walls*, *JCAP* **01** (2012) 031, [1111.1726].

[225] L. Rezzolla and O. Zanotti, *Relativistic Hydrodynamics*. Oxford University Press, 09, 2013.

[226] D. Giulini, *Luciano rezzolla and olindo zanotti: Relativistic hydrodynamics*, *General Relativity and Gravitation* **47** (2015) 1–2.

[227] L. Landau and E. Lifshitz, *Fluid Mechanics: Landau and Lifshitz: Course of Theoretical Physics*. 09, 2013.

[228] M. Laine, *The Two loop effective potential of the 3-d SU(2) Higgs model in a general covariant gauge*, *Phys. Lett. B* **335** (1994) 173–178, [hep-ph/9406268].

[229] M. Laine and K. Rummukainen, *What's new with the electroweak phase transition?*, *Nucl. Phys. B Proc. Suppl.* **73** (1999) 180–185, [hep-lat/9809045].

[230] D. Cutting, E. Vilhonen, and D. J. Weir, *Droplet collapse during strongly supercooled transitions*, *Phys. Rev. D* **106** (2022), no. 10 103524, [2204.03396].

[231] L. Heinz, *The hydrodynamic theory of detonation*, *NTRS - NASA Technical Reports Server* **19930094517** (Jun, 1939).

[232] E. Witten, *Cosmic Separation of Phases*, *Phys. Rev.* **D30** (1984) 272–285.

[233] C. J. Hogan, *Gravitational radiation from cosmological phase transitions*, *Mon. Not. Roy. Astron. Soc.* **218** (1986) 629–636.

[234] A. Kosowsky and M. S. Turner, *Gravitational radiation from colliding vacuum bubbles: envelope approximation to many bubble collisions*, *Phys. Rev.* **D47** (1993) 4372–4391, [astro-ph/9211004].

[235] A. Kosowsky, M. S. Turner, and R. Watkins, *Gravitational waves from first order cosmological*

phase transitions, *Phys. Rev. Lett.* **69** (1992) 2026–2029.

[236] M. Kamionkowski, A. Kosowsky, and M. S. Turner, *Gravitational radiation from first order phase transitions*, *Phys. Rev.* **D49** (1994) 2837–2851, [astro-ph/9310044].

[237] W.-Y. Ai, X. Nagels, and M. Vanvlasselaer, *Criterion for ultra-fast bubble walls: the impact of hydrodynamic obstruction*, *JCAP* **03** (2024) 037, [2401.05911].

[238] T. Konstandin and J. M. No, *Hydrodynamic obstruction to bubble expansion*, *JCAP* **02** (2011) 008, [1011.3735].

[239] M. Sanchez-Garitaonandia and J. van de Vis, *Prediction of the bubble wall velocity for a large jump in degrees of freedom*, 2312.09964.

[240] T. Krajewski, M. Lewicki, and M. Zych, *Bubble-wall velocity in local thermal equilibrium: hydrodynamical simulations vs analytical treatment*, *JHEP* **05** (2024) 011, [2402.15408].

[241] W.-Y. Ai, *Logarithmically divergent friction on ultrarelativistic bubble walls*, *JCAP* **10** (2023) 052, [2308.10679].

[242] A. Megevand and F. A. Membiela, *Stability of cosmological detonation fronts*, *Phys. Rev. D* **89** (2014), no. 10 103503, [1402.5791].

[243] A. Megevand and F. A. Membiela, *Stability of cosmological deflagration fronts*, *Phys. Rev. D* **89** (2014), no. 10 103507, [1311.2453].

[244] A. H. Taub, *General relativistic variational principle for perfect fluids*, *Phys. Rev.* **94** (Jun, 1954) 1468–1470.

[245] K. S. Thorne, *Relativistic Shocks: the Taub Adiabat*, *Astrophysical Journal* **179** (Feb., 1973) 897–908.